Tool wear and tool protection in metal cutting

in-process interaction between workpiece, tool, and environment

Bjerke, Axel

2025

Citation for published version (APA):
Bjerke, A. (2025). *Tool wear and tool protection in metal cutting: in-process interaction between workpiece, tool, and environment*. [Doctoral Thesis (compilation), Department of Industrial and Mechanical Sciences]. Lund University.

Total number of authors:
1

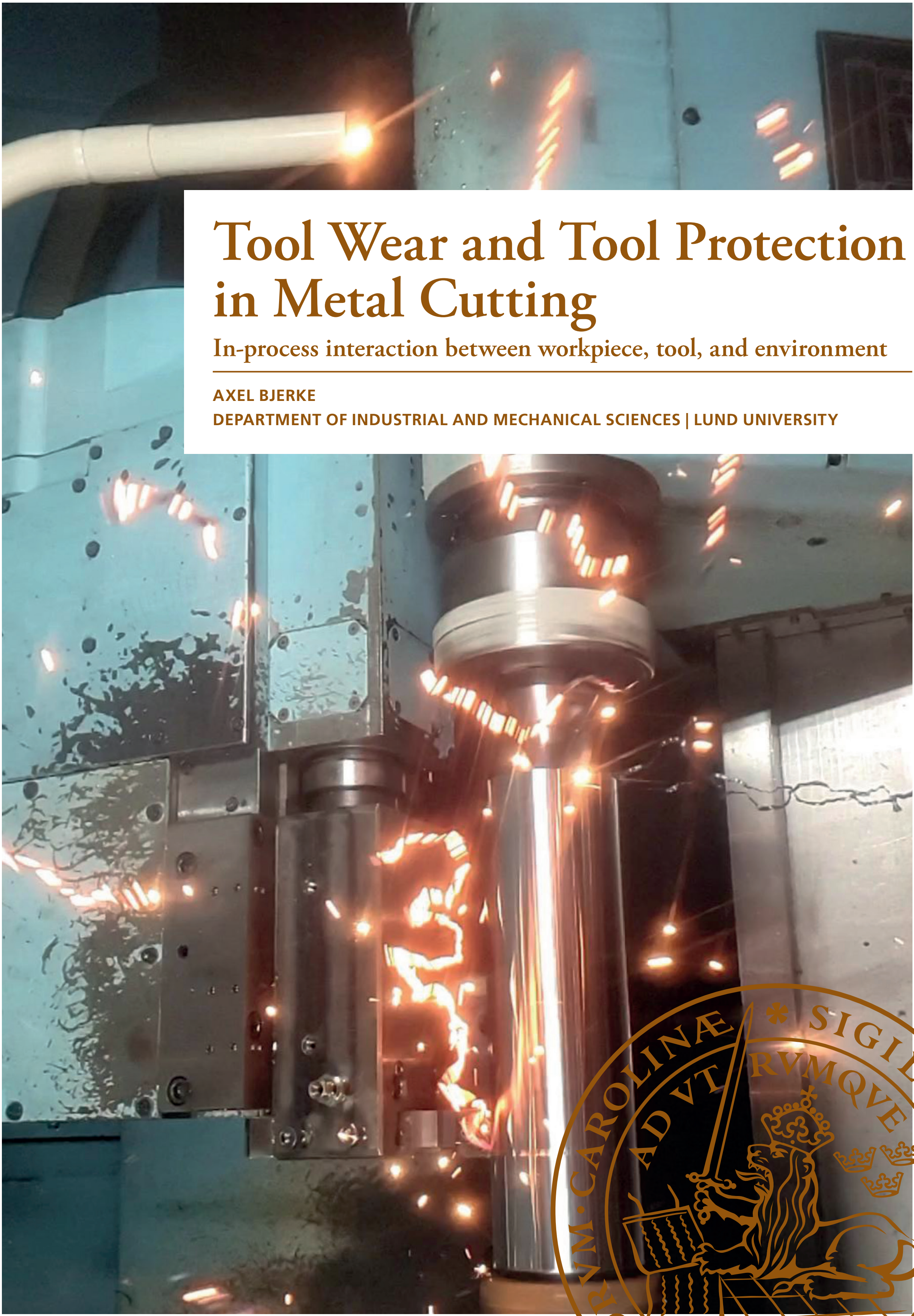

Tool Wear and Tool Protection in Metal Cutting

In-process interaction between workpiece, tool, and environment

AXEL BJERKE
DEPARTMENT OF INDUSTRIAL AND MECHANICAL SCIENCES | LUND UNIVERSITY

There is always more room for cutting edge science,
from the continuum to k-space, and even on the back of this book.

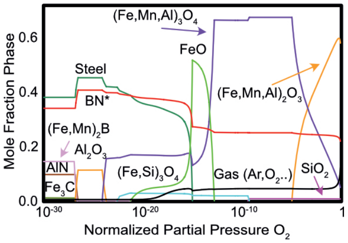

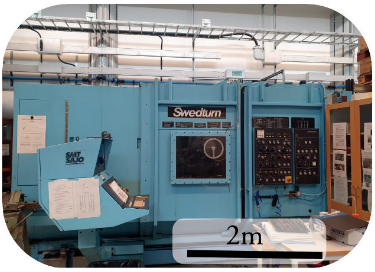

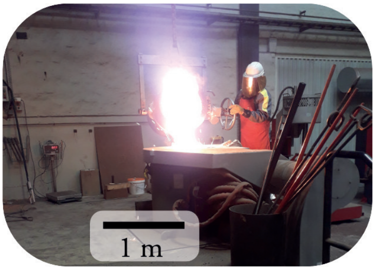

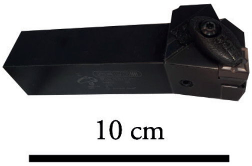

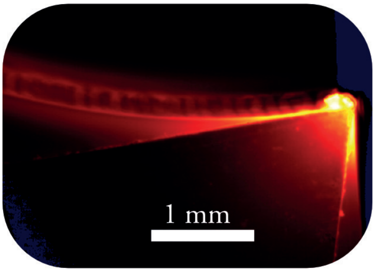

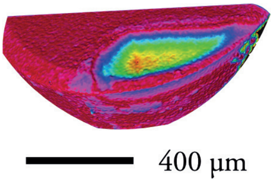

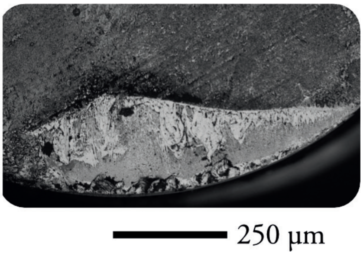

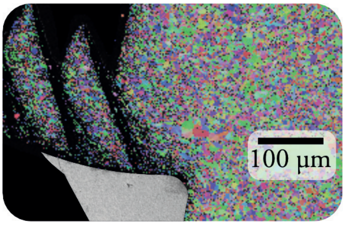

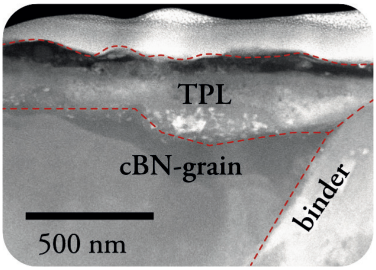

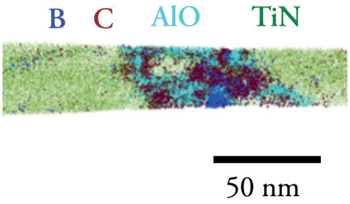

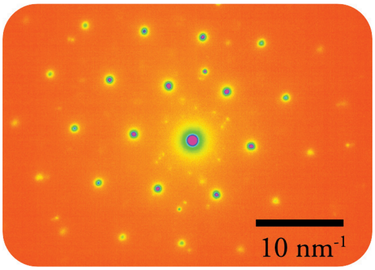

Lund University

Faculty of Engineering
Department of Industrial and Mechanical Sciences
Division of Production and Materials Engineering

ISBN 978-91-8104-491-1

Printed by Media-Tryck, Lund 2025 NORDIC SWAN ECOLABEL 3041 0903

Tool Wear and Tool Protection in Metal Cutting

In-process interaction between workpiece, tool, and environment

Axel Bjerke

LUND UNIVERSITY

DOCTORAL DISSERTATION

Doctoral dissertation for the degree of Doctor of Philosophy (PhD) at the Faculty of Engineering at Lund University to be publicly defended on 28th of May at 09.00 in lecture hall M:B, Department of Industrial and Mechanical Sciences, Ole Römers väg 1, Lund

Faculty opponent

Associate Professor Raquel de Oro Calderon, Technischen Universität Wien, Austria

Organization: LUND UNIVERSITY

Document name: DOCTORAL DISSERTATION **Date of issue:** 2025-05-28

Author(s): Axel Bjerke

Title and subtitle: Tool Wear and Tool Protection in Metal Cutting - In-process interaction between workpiece, tool, and environment

Abstract:

In an era where 3D printing and AI are at the forefront, turning, milling, and metal cutting might seem like niche research topics from the past. But metal cutting is all around you. If what you have lying on your desk was not machined, then the tools used to create it certainly were. Even 3D-printed or additively manufactured parts must be machined if a good surface quality is needed for an industrial application or to look shiny and nice.

Being bad at machining is very expensive—not only wasting the limited resources available to us on this planet but also most likely putting you out of business. A tool used in an industrial setting to machine metal costs at least 10 euros but can exceed 100 euros. A tool lasts about 15 minutes and can be used one to four times. The tool is not even the most expensive part of the process, as the cost of the operator, machine, workpiece material, and workshop are also a big part of the cost. A tool breakage during machining is even more expensive, as it might require reworking or scrapping a part worth tens of thousands of euros.

One may think that tools are worn only through mechanical wear, but these tools are extremely hard; for example, diamond is the hardest known material. This resistance to mechanical wear makes chemical degradation play an important role. Modeling this chemical wear can save industry resources and reduce lead times in research projects. It is also a scientifically interesting topic, as chemical degradation at high temperatures and high material flow rates is a complex process that appears in many other research fields.

This thesis combines experiments, advanced microscopy, and chemical simulations to study how and why tools wear and how we can limit it. This allows us to combine the right tool material, workpiece, and process to limit tool wear. It also enables us to optimize the machining process so that a protective layer forms on the tool, further limiting wear. This discovery adds a new dimension to a research field that has been studied for over a century within a manufacturing practice spanning thousands of years.

Keywords: machinability, thermodynamic modeling of tool wear, electron microscopy of cutting tools, tool protection layers (TPL)

Language: **English** **Number of pages**: 100

ISBN: 978-91-8104-491-1 (printed), ISBN 978-91-8104-492-8 (digital)

Signature Date 2025-04-08

Tool Wear and Tool Protection in Metal Cutting

In-process interaction between workpiece, tool, and environment

Axel Bjerke

LUND
UNIVERSITY

Cover by Axel Bjerke

Faculty of Engineering
Department of Industrial and Mechanical Sciences
Division of Production and Materials Engineering

ISBN 978-91-8104-491-1 (printed)
ISBN 978-91-8104-492-8 (digital)

Printed in Sweden by Media-Tryck, Lund University
Lund 2025

Printed matter
3041 0903

Media-Tryck is a Nordic Swan Ecolabel
certified provider of printed material.
Read more about our environmental
work at www.mediatryck.lu.se

MADE IN SWEDEN

To anyone trying to study
machining using microscopy and
thermodynamic modeling,
I hope you find this helpful!

Table of Contents

Acknowledgments

My PhD studies have been far from a one-man show. Five to nine people have co-authored each article, and I have authored the articles with 23 different people. This does not even include the countless hours of help I have gotten from research engineers, technicians, administrators, colleagues, friends, family, companies, organizations, and relentless reviewers! These years have been great! I will keep this acknowledgment to one page, even though it could be a book!

First, I would like to thank my advisors, Volodymyr Bushlya, Filip Lenrick, Rachid M'Saoubi, Andrii Hrechuk, and Jan-Eric Ståhl. I have learned so much from you, thank you for a fantastic journey! I would also like to thank our research engineers, technicians, and administrators because they have helped me realize all the experiments and helped me through the jungle of administration. Thank you Mikael Hörndahl, Ryszard Wierzbicki, Klas Holger Jönsson, Svante Bouvin, and Rose-Marie Hermansson! There are also several corridors in Lund, especially the Department of Industrial and Mechanical Sciences that are full of friendly, amazing, and helpful people!

Henrik Larsson, Andreas Markström, and Susanne Norgren, you provided me with valuable guidance on modeling and simulating metal cutting, although you were not my official supervisors. I would also like to thank Rebecka Lindvall, Armin Salmasi, and Felix Ekholm, for some great discussions about metal cutting, thermodynamics, and kinetics.

This thesis was also made possible by several funding agencies, governments, and companies, as mentioned in the individual papers. But I would like to thank them not just for the funding but for their willingness to share knowledge with me; thank you, Seco Tools, Thermo-Calc, Sandvik Coromant, Sandvik SRP, Outokumpu, OVAKO, National Action for Metallic Materials organized by Vinnova and Jernkontoret, V. Bakul Institute for Superhard Materials of the National Academy of Sciences of Ukraine.

I would also like to thank my extended family and friends for their help and support, both big and small! Lastly, I would like to acknowledge the support I have received from the most important people in my life: my wife, Lizette, and my children, Eli and Kai!

Popular science summary

In an era where 3D printing and AI are at the forefront, turning, milling, and metal cutting might seem like niche research topics from the past. But metal cutting is all around you. If what you have lying on your desk was not machined, then the tools used to create it certainly were. Even 3D-printed or additively manufactured parts must be machined if a good surface quality is needed for an industrial application or to look shiny and nice.

Being bad at machining is very expensive—not only wasting the limited resources available to us on this planet but also most likely putting you out of business. A tool used in an industrial setting to machine metal costs at least 10 euros but can exceed 100 euros. A tool lasts about 15 minutes and can be used one to four times. The tool is not even the most expensive part of the process, as the cost of the operator, machine, workpiece material, and workshop are also a big part of the cost. A tool breakage during machining is even more expensive, as it might require reworking or scrapping a part worth tens of thousands of euros.

One may think that tools are worn only through mechanical wear, but these tools are extremely hard; for example, diamond is the hardest known material. This resistance to mechanical wear makes chemical degradation play an important role. Modeling this chemical wear can save industry resources and reduce lead times in research projects. It is also a scientifically interesting topic, as chemical degradation at high temperatures and high material flow rates is a complex process that appears in many other research fields.

This thesis combines experiments, advanced microscopy, and chemical simulations to study how and why tools wear and how we can limit it. This allows us to combine the right tool material, workpiece, and process to limit tool wear. It also enables us to optimize the machining process so that a protective layer forms on the tool, further limiting wear. This discovery adds a new dimension to a research field that has been studied for over a century within a manufacturing practice spanning thousands of years.

Populärvetenskaplig sammanfattning

Om sakerna på ditt skrivbord inte har tillverkats genom skärande bearbetning, så har definitivt verktyget som användes för att tillverka dem gjort det. Skärande bearbetning har en stor men ganska dold inverkan på ditt liv. Då den enda skärande bearbetning du kanske har upplevt är att göra en ljusstake i träslöjden i grundskolan. Svarvningen och fräsningen i denna avhandling rör ej ljusstakar i trä, utan i stället svarvning av betydligt starkare legeringar av järn, nickel och titan. Verktygen i denna avhandling är inte häller av legerat stål, utan av extremt slitstarka och hårda keramiska material.

Ett verktyg i industrin håller cirka en kvart, och kan användas en till fyra gånger och kostar från 100 kr till flera tusen kr, och då ska man ha i åtanke att oftast är det inte verktyget som är det dyra, utan även maskinen, materialet man bearbetar, operatören och lokalen är en stor del av kostanden. Att behöva kassera eller ombearbeta om en nästan färdig produkt på grund av ett verktyg som har fallerat kan bli en ännu större kostnad speciellt vid tillverkning av turbindelar i legeringar av nickel och titan (hundratusentals kronor).

Man kan tro att verktygsmaterialen slits enbart mekaniskt, men så är inte fallet, verktygsmaterialen är mycket resistenta mot denna typ av förslitning. Diamant är till exempel det hårdaste materialet människan känner till. Förslitning på grund av kemisk nedbrytning spelar därför en betydande roll. Att välja rätt material är då extremt viktigt, diamant slits till exempel ner efter ett par sekunder om man svarvar rostfritt stål. Att kunna modellera spar både dyra resurser ute in industrin och spar ledtid vid utveckling av nya verktygsmaterial. Det är också vetenskapligt intressant att studera diffusion, kemisk nedbrytning och oxidation vid höga temperaturer och vid höga materialflöden eftersom det är en komplex process som även dyker upp i andra forskningsområden.

Denna avhandling kombinerar experiment, avancerad mikroskopi och kemiska simuleringar av svarvning för att förstå hur och varför skärverktyg slits, och hur vi kan få dem att slitas mindre. Forskningsresultaten hjälper oss att kombinera rätt verktygsmaterial med rätt arbetsmaterial mer effektivt. Vi kan vidare använda dessa simuleringar för att kombinera material och process så att skyddsskikt bildas på verktyget under svarvningen. Att kunna göra detta är en ny upptäckt, i detta hundraåriga forskningsfält av en tusenårig tillverkningsmetod!

Appended publications and author's contribution

This dissertation is based on the research presented in the following publications. In the text, these publications are referred to using Roman numerals I-X.

I **On the wear mechanisms of uncoated and coated pcBN tools during turning of 17–4 PH martensitic stainless steel**
A. Bjerke, J. Casas, F. Lenrick, J.M. Andersson, R. M'Saoubi, V. Bushlya. Int. J. Refract. Met. Hard Mat. 127, February 2025, 106984
https://doi.org/10.1016/j.ijrmhm.2024.106984
- Bjerke was the main author and performed the majority of the work and data analysis and presented the paper at the 12th International Conference on the Science of Hard Materials in March 2024.

II **On chemical interactions between an inclusion engineered stainless steel (316L) and (Ti,Al)N coated tools during turning**
A. Bjerke, F. Lenrick, A. Hrechuk, K. Slipchenko, R. M'Saoubi, J.M. Andersson, V. Bushlya. Wear. 532–533 (2023) 205093
https://doi.org/10.1016/j.wear.2023.205093
- Bjerke was the main author and performed the majority of the work and data analysis.

III **Onset of the degradation of CVD α-Al_2O_3 coating during turning of Ca-treated steels**
A. Bjerke, A. Hrechuk, F. Lenrick, R. M'Saoubi, H. Larsson, A. Markström, T. Björk, S. Norgren, J.-E. Ståhl, V. Bushlya. Wear. (2021) 203785
https://doi.org/10.1016/j.wear.2021.203785
- Bjerke was the main author and performed the majority of the work and data analysis.

IV **Understanding wear and interaction between CVD α-Al_2O_3 coated tools, steel, and non-metallic inclusions in machining**
A. Bjerke, F. Lenrick, S. Norgren, H. Larsson, A. Markström, R. M'Saoubi, I. Petrusha, V. Bushlya. Surf. Coatings Technol. 450 (2022) 128997
https://doi.org/10.1016/j.surfcoat.2022.128997
- Bjerke was the main author and performed the majority of the work and data analysis.

V **On the wear mechanisms of uncoated and coated carbide tools in milling titanium alloys**
R. Lindvall, J.M. Bello Bermejo, A. Bjerke, J.M. Andersson, E. Vikenadler, R. M'Saoubi, V. Bushlya. Int. J. Refract. Met. Hard Mater. 124 (2024) 106806.
https://doi.org/10.1016/j.ijrmhm.2024.106806
- Bjerke performed the thermodynamic calculations, aided in the data analysis, and wrote parts of the paper. Lindvall was the main author and presented the paper at the 12th International Conference on the Science of Hard Materials in March 2024.

VI **Predicting wear mechanisms of ultra-hard tooling in machining Ti6Al4V by diffusion couples and simulation**
R. Lindvall, A. Bjerke, A. Salmasi, F. Lenrick, R. M'Saoubi, J.-E.E. Ståhl, V. Bushlya, R. M'Saoubi, J.-E.E. Ståhl, V. Bushlya J. Eur. Ceram. Soc. 43 (2023) 291–303. https://doi.org/10.1016/j.jeurceramsoc.2022.10.005
- Bjerke performed the thermodynamic calculations and wrote part of the paper jointly with Salmasi. Lindvall was the main author.

VII **On chemical and diffusional interactions between PCBN and superalloy Inconel 718: Imitational experiments**
V. Bushlya, A. Bjerke, V.Z.Z. Turkevich, F. Lenrick, I.A.A. Petrusha, K.A.A. Cherednichenko, J.-E. Ståhl. J. Eur. Ceram. Soc. 39 (2019) 2658–2665.
https://doi.org/10.1016/j.jeurceramsoc.2019.03.002
- Bjerke performed the thermodynamic calculations jointly with Turkevich and aided in the data analysis and wrote parts of the paper. Bushlya was the main author.

VIII **Tool wear mechanisms of PcBN in machining Inconel 718: Analysis across multiple length scale**

V. Bushlya, F. Lenrick, A. Bjerke, H. Aboulfadl, M. Thuvander, J.-E. Ståhl, R. M'Saoubi. CIRP Ann. 70 (2021) 73–78. https://doi.org/10.1016/j.cirp.2021.04.008
- Bjerke performed the thermodynamic calculations and aided in the data analysis and wrote parts of the paper. Bushlya was the main author.

IX **Thermodynamic modeling framework for prediction of tool wear and tool protection phenomena in machining**
A. Bjerke, A. Hrechuk, F. Lenrick, A. Markström, H. Larsson, S. Norgren, R. M'Saoubi, T. Björk, V. Bushlya. Wear. 484–485 (2021) 203991
https://doi.org/10.1016/j.wear.2021.203991
- Bjerke was the main author and performed the majority of the work and data analysis.

X **Machinability improvement by in-operando Tool Protection Layers through designed steel alloying: The case of manganese steel**
A. Bjerke, S. Norgren, H. Larsson, A. Markström, F. Lenrick, R. M'Saoubi, J. Petersson, L. Melk, V. Bushlya. J. Mater. Process. Technol. 330 (2024) 118496.
https://doi.org/10.1016/j.jmatprotec.2024.118496
- Bjerke was the main author and performed the majority of the work and data analysis.

Selected abbreviations and symbols

Cutting parameters and phenomena

a_p – cutting depth/depth of cut [mm]
f – feed [mm/rev]
v_c – cutting speed [m/min]
VB – width of the flank wear land
KT – depth of the crater wear
NMI – non-metallic inclusion
TPL – tool protection layer

Thermodynamics and materials

bcc – body-centered cubic
pcBN – polycrystalline cubic boron nitride
PCD – polycrystalline diamond
fcc – face-centered cubic
hcp – hexagonal close-packed
PP_x – normalized or effective partial pressure of species x [unitless]

Microscopy and spectroscopy

EBSD – electron backscatter diffraction
FIB – focused ion beam
HAADF – high-angle annular dark field
LAADF – low-angle annular dark field
SEM – scanning electron microscopy
TEM – transmission electron microscopy
SAED – selected area electron diffraction
STEM – scanning transmission electron microscopy
XEDS – X-ray energy dispersive spectroscopy
XRD – X-ray diffraction

Introduction

Vad fan får jag för pengarna?

—Leif Östling [1]

Interdisciplinary research can be complex and create some dilemmas, but it is the most rewarding. For example, should the introduction be about tool wear and metal cutting or the economic impact and history of machining [2–6], to motivate the money spent on this research? Should it be about thermodynamics, kinetics, and CALPHAD [7], and how metal cutting is a fascinating case of diffusion and reactions in a moving frame of reference? Maybe about microscopy [8–10], and how to study multi-element and multi-phase materials that have interacted? Or the geopolitical and environmental aspects of critical raw materials and efficient use of scarce resources [11]? Metal cutting has a profound impact on your life and is a fascinating topic, regardless of your interests or background.

Background and objective

There are numerous alloys, and new alloys are constantly entering the market. We need some way to machine them if a good surface quality and tolerances are required for an industrial application, whether the part is additively manufactured, cast, wrought, forged, or pressed.

Coatings, tool materials, cutting parameters, and workpieces can be combined in an infinite number of ways. Determining how to machine a material typically follows the process–structure–property–performance (PSPP) relationship. We can experimentally test or model the effect that new processes for making tools and alloys have on performance by studying the relationship in steps: process → structure → property → performance [12]. If we know what performance we need, then we can design the process required to make that tool or alloy: performance → property → structure → process. This can be done both experimentally or using the Integrated Computational Materials Engineering (ICME) approach [13].

Linking process and performance has been done informally since the discovery of metal cutting during the bronze age (circa 3000 BC) [14], and there has been a lot of success in linking processing to the performance of both tools [15] and workpieces [16] since the innovation of cemented carbides (hardmetal) over a hundred years ago [4]. Metal cutting is challenging because studying the PSPP relationship between the tool and workpiece separately is insufficient.

For example, cutting steel requires a material with high hardness. Diamond is the hardest known material, but cutting stainless steel at reasonable speeds with diamond tools results in catastrophic tool failure within seconds [17–19]. The diamond tool transforms into graphite and carbon dioxide or monoxide, while the steel and chip acquire a slightly higher carbon content due to the carbon diffusion from the tool.

Alumina ceramic tools would then be a good choice according to the PSPP roadmap for the tool, as they are generally chemically inert. Further adding Ca-inclusions to the steel would protect the tool from chemical wear and improve machinability, according to the PSPP roadmap for the steel. But this is a very poor combination, as shown in a series of papers on the anomalous wear of ceramic tools and coatings when machining Ca- and Si-deoxidized steels [20–23]. We must therefore combine the PSPP roadmap of both the tool and the workpiece!

Machining alloys at high metal removal rates with hard tool materials such as cemented carbide, ceramics, diamond, and cubic boron nitride leads to high temperatures and to tool wear through a combination of diffusion, oxidation, chemical degradation, and thermomechanical mechanisms [2–6]. We need to study and model what is happening to the tool-workpiece combination in-operando, rather than just studying the tool post-mortem, to be able to combine the PSPP roadmap of the tool with that of the workpiece.

Studying metal cutting in-operando [24] and modeling [25] the cutting process is difficult, and studies focus mainly on the effect of stress and strain rather than chemical interactions [2,5,6]. Combining post-mortem analysis of worn tools using advanced microscopy and thermodynamic modeling has significantly contributed to the pursuit of linking processing to performance with regard to diffusion, oxidation, and chemical degradation [26–31].

These methods have been used since the 1970s, and a lot has happened in the last 25 years due to the improvement and increased availability of computational thermodynamics [26–31] and transmission electron microscopes [32–35]. The studies of chemical, diffusion, and oxidation wear continued through the 80s [36] and 90s [37,38]. This topic has also been covered in many recent theses [39–42], books [2,3,5,6], and countless articles. There is still much to learn about metal cutting, particularly concerning tool wear and protection related to chemical interactions, diffusion, and oxidation.

The *first objective* of this thesis is to add to the body of knowledge by combining experimental studies (in-operando and in-situ), microscopy, and spectroscopy (in-situ and post-mortem) with thermodynamic modeling and kinetic simulations. By combining these methods, we can understand not only the types of wear that have occurred on the tool during metal cutting, such as flank wear, crater wear, or loss of carbon, but also the underlying in-process cause of this wear related to chemical degradation, diffusion, and oxidation.

The *second objective* is to better predict how to pair the tool and the workpiece to improve performance of the machining process. For example, the first objective is to better understand why there is anomalous wear of ceramic tools and coatings when machining Ca- and Si-deoxidized steel [20–23]. The second objective is then to better predict whether a selected tool and Ca-treated steel combination will perform better, given our understanding of the wear process. This need for prediction and pairing is not limited to inclusion engineering. It is also key when limiting wear through oxidation, diffusion, and chemical degradation of clean alloys. For example, Co may not readily diffuse into Fe alloys during metal cutting. But that is not the property of the Co binder, since it can diffuse into Ti alloys. It is the property of the Co and Fe-alloy pair during machining.

The *third objective* is to utilize the understanding and predictive power to develop requirements and specifications for the materials, and to a limited extent in this thesis, the cutting parameters, shifting from a discovery mindset to a design mindset. For example, the first objective is to understand why and how a tool is worn by diffusion. The second objective would then be to predict whether a specific tool-workpiece pair will experience less wear due to diffusion and, consequently, perform better. This third objective is to model, simulate, predict, and set requirements for a more optimal tool-workpiece pair, or design a new material altogether, that experiences less wear due to diffusion. The objective is to move beyond simply discovering that a non-metallic inclusion improves machinability or that a new binder, coating, or ceramic performs better. Instead, try to increase performance by setting requirements on the properties of the tool-workpiece combination. The objective is to design alloys and tools that lead to improved machinability and to combine the PSPP roadmap [12] for both the tool and the workpiece.

The *fourth objective* is related to tool protection layers (TPL) [43], which are in-process chemical interactions that lead to the formation of refractory phases, providing tool protection and enhancing tool performance. Interactions between the tool, workpiece, and environment can either lead to aggressive wear or, if controlled correctly, provide tool protection and improve tool performance. Consequently, the fourth objective is to leverage our knowledge, predictive power, and ability to select or design tool-workpiece pairs that result in these protective layers.

The overall aim is to expand our understanding of wear-related in-process interactions, enabling increased tool life and performance in machining processes. Achieving this aim shortens the research and development cycle of new tool materials and alloys, saving time, money, and resources. It will also save time, money, and resources in the factories due to improved machining performance. A shorter development cycle is also necessary to rapidly adapt our use of critical raw materials used in the tool and alloy industry when needed [11].

Hypothesis and research questions

The hypothesis is that the in-process interaction determines wear in machining through diffusion, oxidation, and chemical mechanisms, alongside the conventional thermomechanical wear phenomena, and that we can purposefully combine process parameters, tool material, workpiece material, and the environment to control such in-process interaction, using knowledge gained from experiments, thermodynamics, and advanced microscopy.

The following research questions are formulated and addressed to achieve the aim and objectives, as well as to test the hypothesis:

RQ1. How can our understanding of in-process interaction leading to tool wear in machining be improved through a combination of focused experiments, microscopy, and thermodynamics?

RQ2. Can tool wear and protection mechanisms related to chemical, diffusional, and oxidation phenomena be described and predicted based on thermodynamic modeling and kinetic simulation?

RQ3. Can thermodynamics, experiments, and microscopy be utilized to more efficiently design, combine, and select workpiece materials, tool materials, and cutting parameters to achieve increased tool performance?

RQ4. How can in-process chemical interactions leading to the formation of refractory phases be leveraged for tool protection and improved tool performance?

Methodology, scope, and limitations

This research employs inductive methods (searching for patterns in observations) to draw conclusions and deductive reasoning (collecting data to test a rejectable hypothesis) to test ideas.

The scope of this thesis is to limit wear by diffusion, oxidation, and chemical degradation in metal cutting by combining experiments, thermodynamic and kinetic modeling, microscopy, and spectroscopy.

Some limitations are needed because this can be done in a myriad of ways. This thesis focuses on continuous and stable longitudinal turning using single-point tools in a laboratory environment. One article concerned external circular down milling with a single tooth; however, the author's contribution was focused on modeling the oxidation of the tool. The tools, tooling systems, and cutting data are based on the recommendations of the tool and workpiece manufacturers, with some exploration of cutting speeds. The study is limited to commercial or near-commercially available tools and coatings. The workpieces are all commercial alloys except the developed Hadfield steel.

There are various other interesting factors to study when machining, and these have been observed and noted to some extent but not researched—for example, tool geometries, vibrations, coating delamination and other mechanical failure modes, and much more. The tool life was measured to test the hypothesis; but there is no explicit tool life modeling. There are also some inherent limitations related to time, cost, availability, and the basic principles of the techniques, which are further discussed in separate chapters.

Turning and Metal Cutting

> *-I can't find any literature on what we discussed; did you say there was any?*
> *-Don't worry; there is plenty, and I'll show you!*
> *[Comes back the next day with a pile of books and unpublished internal reports in Cyrillic, German, and Japanese]*
>
> —A conversation between Volodymyr Bushlya and me.

There is a wealth of accumulated knowledge and experience concerning machining, some of which is available online and some in archives; but this cannot even be compared to the amount of knowledge accumulated by researchers and operators around the globe. This thesis focuses on continuous and stable longitudinal turning using single-point tools, a subsection of machining or metal cutting. This chapter provides an overview the turning processes, the cutting parameters, and their effect on physical quantities. It aims to help the reader understand the impact of cutting parameters on chemical, thermodynamic, and kinetic phenomena in metal cutting under the influence of such physical quantities. This section is designed to keep an interest of the metal cutting expert, who is knowledgeable about cutting parameters and geometries, but perhaps less so about chemical activity. Additionally, it will hopefully appeal to materials scientists or microscopists who are less familiar with metal cutting but more knowledgeable about thermodynamics and oxidation, as well as serving as a review for those already researching this interdisciplinary topic.

Cutting parameters

Continuous longitudinal turning is the main operation performed in the appended papers. It is one of the most stable and controllable machining operations, making it suitable for research purposes. The workpiece rotates while the tool moves longitudinally across it, resulting in a helical trajectory of the insert across the surface (Figure 1).

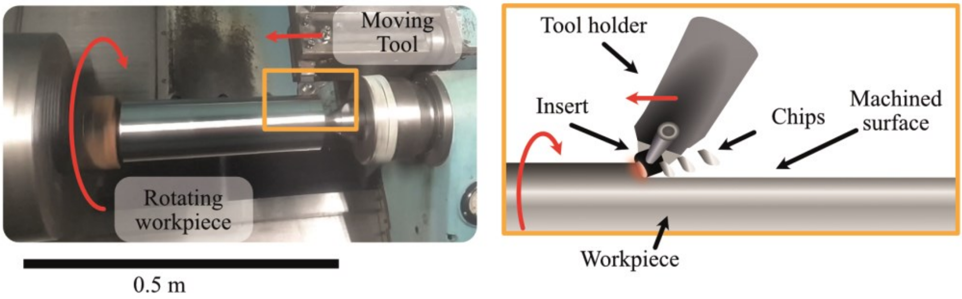

Figure 1. Image of longitudinal turning. The bar rotates and the tool holder with the clamped insert moves along the length of the bar, creating a bar with a smaller and desired diameter.

The cutting parameters can be translated from longitudinal turning to other machining operations, such as orthogonal turning, milling, and drilling, with due care. Milling can, for example, be seen as intermittent cutting from the reference frame of the insert. This will lead to the addition of other cutting parameters, changes in the forces acting on the tool, and further modifications [2,3,5,6]. However, the physics and chemistry of tool wear are somewhat transferable.

The main cutting parameters are cutting speed (v_c) defined in m/min; this is the relative velocity between the cutting tool and the workpiece. The feed rate (f) defined in mm/rev is the rate at which the tool moves in the axial distance per revolution. The depth of cut (a_p) is how much of the bar's radius is reduced per revolution, measured in mm. The product of these three parameters is termed as the material removal rate MRR (cm^3/min). These, along with the other essential cutting parameters and forces, are shown in Figure 2 [2,3,5,6].

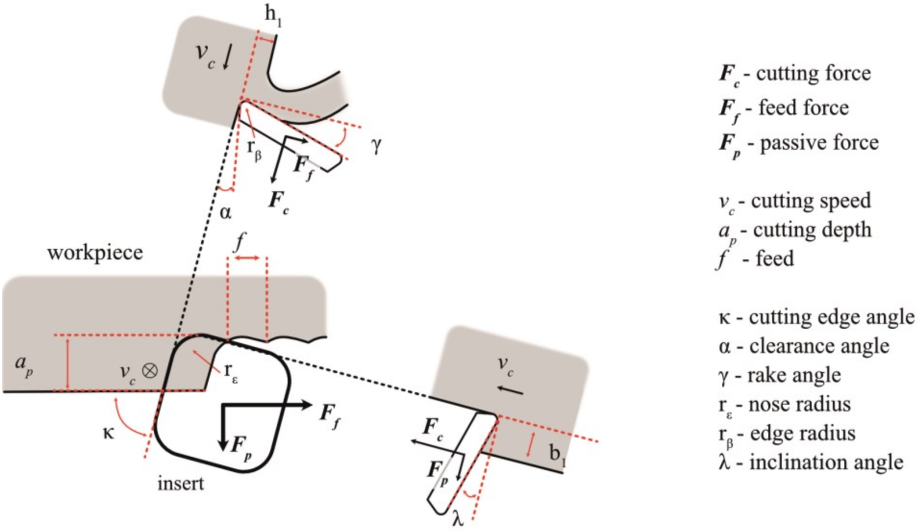

Figure 2. The main cutting parameters and forces, based on [2,5,6].

The forces commonly measured using a dynamometer are the cutting force ($\boldsymbol{F_c}$), the feed force ($\boldsymbol{F_f}$), and the passive force ($\boldsymbol{F_p}$) shown in Figure 2. $\boldsymbol{F_c}$ is usually the largest in longitudinal turning, and $\boldsymbol{F_p}$ is generally the smallest of the three [2]. The magnitude of the resulting vector is the total force (F_t) on the insert (Eq.1). However, these forces are neither constant over time nor evenly distributed over the insert [2,3].

$$F_t = \sqrt{|\boldsymbol{F_c}|^2 + |\boldsymbol{F_f}|^2 + |\boldsymbol{F_p}|^2} \qquad (1)$$

The rate of insert wear, the forces acting on the tool, and the heat generated are also dependent on the geometry of the insert and the angles at which it cuts the workpiece [2,3,5,6,44]. The optimization of the tool holder, insert, and chip-breaker size and shape are not addressed in this thesis, but they are nonetheless very important [2,3,5,6,44]. These angles are also not always explicitly stated in the appended papers, as they can be inferred from the ISO 25.100 designation of the insert and tool holder combination, as well as the shape and size of the chip breaker.

Coolants are also used for various purposes and can affect the cutting process in different ways depending on the type, machining process, composition, pressure, and flow rate during machining [5,45–47]. The coolant in this thesis is supplied either as flood coolant or directed jets (Figure 11b). The coolant supplied is typically measured by the pump's pressure, ranging from a couple of bars to nearly 100 bars. This might sound like a misleading parameter that would tell us very little about the amount of coolant supplied. Since the pressure of the coolant leaving the nozzle is nearly 1 atm. The convention in the field is to do so because the same result is achieved on different machines when using the same coolant nozzles. The pressure and nozzle size can also easily be used to estimate the flow rate. Coolants are generally avoided unless necessary since they have a cost associated with them, are not ideal for the working environment [2,5,6]. Compressed air can be an alternative in some cases, but it has its own drawbacks [2,5,6].

The effect of the cutting parameters on physical quantities

The above cutting parameters are very convenient in machining, as we can set the feed, speed, and cutting depth on any modern computer numerically controlled (CNC) lathe. We can also set the desired cutting angles by selecting the appropriate tool holder and insert. We can also readily measure the forces acting on the tool using a dynamometer.

The effect of the cutting parameters in Figure 2 and their influence on the parameters used in thermodynamic models, such as thermodynamic pressure, temperature, and chemical composition, is not always intuitive. We need a general understanding of the effect of cutting parameters on physical quantities to comprehend metal cutting and compare results across experiments and with previous literature.

For example, can we compare the different tool materials in Paper IX? The v_c, f, and a_p are fixed in Paper IX, and the inserts all have the same general geometry (CNMG120408) and can be mounted in the same tool holder (PCLNL2525M12). But the cemented carbide tool has a chip breaker, and the different ceramics have different cutting edge conditions (Table 2, Paper IX). Are the results then comparable, even with different r_β and γ? To understand this, we need to comprehend the impact of cutting parameters on the cutting process and, to some extent, translate these parameters into physical quantities.

Forces, contact pressure, and stress

The forces acting on the tool, the generated contact pressures on the tool surface, and the stress experienced by the tool material are major research areas due to their importance in the design of machine elements, tools, and the performance of the operation [2,3,5,6]. We can readily measure the forces acting on the tool using a dynamometer [2,3]. It is also possible but challenging to measure the contact pressure using, for example, a split-tool dynamometer arrangement [3,6]. Measuring the stress experienced by the tool material is also challenging but possible using photoelastic-sensitive tools [2,3,6]. Modeling the forces, pressures, and stresses in metal cutting is another significant area of research [25].

There is considerable knowledge about the general effect of changing the cutting parameters on the forces acting on the tool. Changing f and a_p (Figure 2) has the most direct and strongest influence on the cutting forces, as it changes the contact area. A larger contact area generally leads to an increase in cutting forces, provided that cutting speed and material properties remain constant. There is almost a linear relationship between the contact area and F_c, F_f, and F_p [2,5].

The effect of changing other cutting parameters is not as clear and significant. An increase in the rake angle (γ) generally decreases F_c, F_f, and F_p because the tool appears sharper [2]. A negative rake angle (γ), generally increases F_c, F_f, and F_p [2] while providing more strength to the cutting edge. Similarly, a smaller edge radius r_β makes the tool appear sharper, decreasing F_c, F_f, and F_p [2]. Having a clearance angle (α) of zero or negative leads to rubbing against the workpiece and higher forces. A more negative inclination angle (λ) mainly affects the strength of the edge during intermittent cutting, but it also increases the passive force [2]. Increasing the cutting edge angle (κ) increases F_f and F_p [2].

It is more difficult to draw conclusions about the effect of changing v_c on the forces [2,3,5,6]. It is very common that the forces decrease in certain speed ranges when the cutting speed increases, which is due to the thermal softening of the material cut, changes in the contact area, and chip flow [2,6]. The effect of cutting speed on cutting forces can only then be understood in relation to the material being cut and the material flow.

The stress experienced by the insert material due to the forces per unit area acting on the insert can result in crack formation, chipping, flaking, deformation, and, ultimately, tool breakage. Studying this is essential for understanding whether the tool will deform or fracture [2,3,5,6]. High forces can still lead to low stresses, for example, by having a negative λ, γ, or a chamfer [2,5,6]. The normal stress experienced by the tool is due to a force acting perpendicular (or normal) to the rake. The maximum global principal (normal) stress occurs on the rake side; this is where the tool edge is likely to break off. The maximum global effective stress is on the flank side; this is where the tool is likely to deform. The relationship between forces and stresses also depends on material properties and temperature.

Is the comparison between the tools in Paper IX then valid? The contact area is almost identical, the tools are the same size and shape, and f, a_p, κ, and r_ε are the same. The (Ti,Al)N-coated cemented carbide tool has a chip breaker, and the ceramic tools have slightly different edge preparation and chamfers. The main cutting forces remain largely unchanged, but the stress experienced by the insert material differs. The edge micro-geometry and chip breakers are optimized for the tool material and intended operation. Hence, the comparison between the tools would not be fair if one wanted to study the tool materials' resistance to chipping, cracking, or deformation. However, their resistance to chemical wear, oxidation, and diffusion can still be compared to some extent. Using commercially available and optimized geometries did not significantly impede this specific study. Instead, it made the research more industrially relevant and helped prevent premature tool cracking.

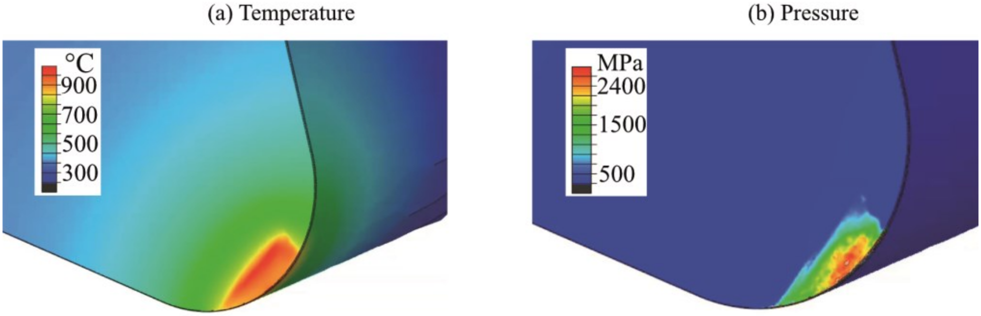

Figure 3. Results from finite element method simulations in Paper VIII when machining A718 at $v_c = 250$ m/min, $f = 0.15$ mm/rev, and $a_p = 0.25$ mm, (a) temperature and (b) contact pressure within the tool chip interface.

The contact pressure on the tool surface (sometimes called contact stress) can be measured using the split-tool dynamometer arrangement [3,6] or estimated using finite element method simulations [25], as shown in Paper VIII and in Figure 3. But how do we translate this to thermodynamic pressure? This can be quite confusing and is seldom discussed in machining literature.

Firstly, why is it important? Inserts and coatings often contain C (tungsten carbide, diamond, and TiC), B (cubic boron nitride), O (SiAlON and Al_2O_3) and N (TiN and (Ti,Al)N). Understanding whether the tool or coating will become a liquid (B_2O_3), a gas (N_2), or undergo a phase change or decomposition is essential. These transformations depend on both pressure and temperature [48], and one does not want the tool to become a liquid, gas, or graphite.

Secondly, why is it confusing? Pressure in thermodynamics is a scalar quantity, and it is always positive, has no direction, and only a magnitude. It is defined as the negative change in internal energy (U) with respect to a change in volume (V), when the entropy (S) and number of particles (N_i) are fixed (Eq. 2).

Machining studies mainly focus on modeling stresses, contact pressures, and measuring forces because these determine whether the tool will fracture or deform, how much the energy the process will consume, what the contact conditions are, and how well the tool performs [2,3,5,6]. One can either model the stresses to find the hydrostatic stress, calculated as the absolute value of the average of the trace of the stress tensor, or the normal stress if the stress is isotropic (Eq.3) [49,50]. Alternatively, one can measure the forces and estimate the contact pressure [2,3,5,6].

One can assume that if the insert is rigid (at least locally), then the normal pressure or contact pressure applied at a point on the insert would result in isotropic stress of equal magnitude, assuming strain and thermal pressure are negligible. We can then approximate thermodynamic pressure as being equal in magnitude to the contact pressure or normal stress (Eq. 4) [49,50]. So, we can disregard the fact that the measured contact pressure or calculated normal stress is not the same as the thermodynamic pressure because they are equal in magnitude [49]. Measuring and estimating contact pressure, or modeling the normal stress experienced by the tool, provides a very good approximation of thermodynamic pressure used in thermodynamic modeling of metal cutting. This allows us to assess whether a nitride or nitrogen gas will form on the tool surface, as shown in Papers VII and VIII.

$$P_{thermodynamics} \equiv -\left(\frac{\partial U}{\partial V}\right)_{S,N_i} \tag{2}$$

$$P_{contact} \sim \left|\frac{1}{3}tr(\boldsymbol{\sigma})\right| \sim |\sigma_N| \tag{3}$$

$$P_{thermodynamics} \sim P_{contact} \sim |\sigma_N| \tag{4}$$

We can then discuss the range of thermodynamic pressures involved in metal cutting. Thermodynamic pressure is generally never below 1 atm (≈ 10^5 Pa), which corresponds to a non-machining state where the insert and workpiece are just on the floor or table. The highest pressure occurs at the cutting edge (maximum global principal stress and maximum contact pressure) and ranges from hundreds of MPa to several GPa, as seen in Figure 3 in Paper VIII and in [2,5,6]. The exact value at a specific point requires modeling and measurement. Still, the approximate thermodynamic pressure and boundary values can be estimated from literature and experiments, depending on the cutting parameters and material. The effect can be studied to understand if the insert material is likely to perform well or become a liquid, gas, decompose, or experience reverse phase transformation (graphitization).

Temperature

We need an understanding of the energy and power involved in metal cutting to discuss the temperature distribution in the tool. Most of the mechanical energy is converted into thermal energy during metal cutting [2,5,6]. The power generated can be easily estimated as force times velocity; the approximate power is the product of v_c and F_c. Higher cutting speeds and forces result in more energy per unit of time. But how does this relate to the tool's temperature?

Temperature both influences and is influenced by the cutting process as well as the properties of the workpiece and insert. It can be rather challenging to predict the temperature in the cutting zone before doing any cutting experiment [2,3,5,6]. For example, the temperature in the cutting zone becomes hotter if the heat conductivity of the tool is lower since less heat is transported away from the cutting zone. But thermal conductivity decreases with temperature for many cutting tool materials, further reducing heat dissipation and leading to even higher temperatures [2]. Predicting the heat flux into and away from the insert is an open area of research, explored using both experimental and modeling techniques [51–53]. Papers III and IX include temperature measurements, while Paper VIII includes temperature modeling primarily to estimate parameters for the thermodynamic calculations.

Temperature distribution is also an essential factor. The maximum temperature does not occur at the edge of the cutting tool but at some distance away (Figure 3) [52,54]. The maximum temperature in the cutting zone can range from 200°C when machining leaded brass [55] to more than 1000°C when machining nickel-based superalloys [52,54], as shown in Paper VIII.

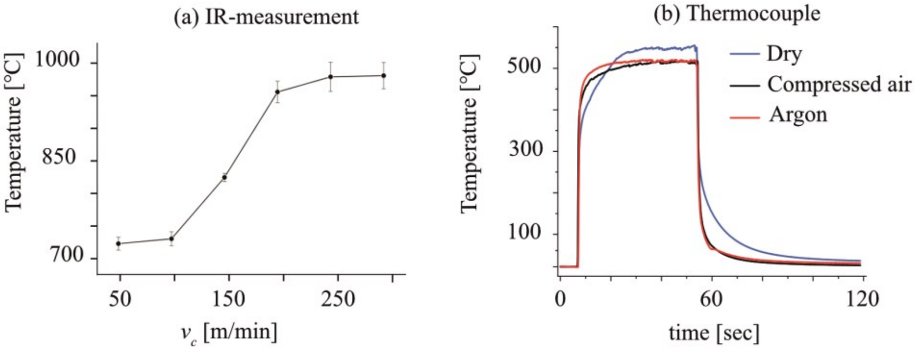

Figure 4. a) Influence of cutting speed on maximum tool temperature (Paper IX), b) effect of using compressed air and coolant on the temperature 500 µm from the tool tip (Paper III).

But we can still generalize some basic principles. Higher cutting speeds result in a hotter contact area within the speed ranges in the appended papers [2,3,5,6], as shown in Paper IX and Figure 4. Increasing the feed also leads to both higher temperatures and higher forces, while increasing the depth of cut has the least effect on temperature but a large effect on forces. Increasing a_p and decreasing f at a constant cutting speed can lower temperatures while still maintaining the metal removal rate, though this increases the force acting on the tool [56,57].

Effective concentration and partial pressure

Determining the activity (effective concentration) of species (atoms, ions, and molecules) in metal cutting is not a trivial task. This may seem strange, given that the chemical and phase compositions of the tool and workpiece materials are thoroughly studied and well understood. The workpiece material that comes into contact with the insert is freshly cut but undergoes severe stress, strain, heating, oxidation, diffusion, and reactions. While the tool material is experiencing stress, strain, heating, oxidation, diffusion, and reactions and is being continuously worn. Modeling the interaction between the insert material and workpiece materials is not as simple as modeling a perfect mixture of half insert material and half workpiece material or a static diffusion couple [29,58].

Two extreme examples help illustrate this complexity, and the truth lie somewhere in between depending on the cutting process. At one extreme, there is a constant supply of fresh workpiece material passing over the tool surface if the cutting speed (v_c) is high and there is no adhesion. There is almost then a limitless supply of fresh workpiece material (hence a fixed activity of the workpiece elements) while the amount of tool material remains fixed or decreases as the tool is worn. For example, an infinite amount of Ni from the workpiece material could diffuse into or react with the binder of the tool, and this process would never stop. Similarly, N from a cBN insert could continuously diffuse into the alloy [35,59] as the insert encounters new material. The other extreme case is a and complete and very thick adhesion layer [60–62]. If there is never any material flow across the insert surface due to a build-up edge and the thickness of this edge is large, then there is limited supply of fresh workpiece material. The true way of modeling the interaction between the workpiece, chip, environment, and insert lies somewhere between these two extremes. The importance of this distinction will be demonstrated later in the modeling section and is highlighted in Paper VI and other studies [29,58]. The appropriate method for modeling tool-workpiece-environment interactions then depends on the cutting speed and the flow of the workpiece material across the tool surface. The material flow is typically higher on the flank than on the rake, and a near-stagnation point may exist even without workpiece adhesion [2,3,5,6,44].

Partial pressure is another important concept when studying insert or coating oxidation [30,31,63,64]. It represents the availability of one or a mixture of gas species and is analogous to thermodynamic activity, but for gas species. The cutting zone is more exposed to air during milling (Paper V), but air also affects the tool during turning [65,66].

One way to quantify this is by using the effective (or normalized) partial pressure of O_2 (PP_{O_2}) [31]. It does not exceed 0.21 under ambient conditions, as air contains 21% O_2. This number is independent of the contact pressure since it is normalized. PP_{O_2} will decrease if, for example, oxygen is consumed, cannot reach the contact zone, or if the oxygen concentration is artificially lowered by introducing Ar (Papers III and IX) or other gases [67–69].

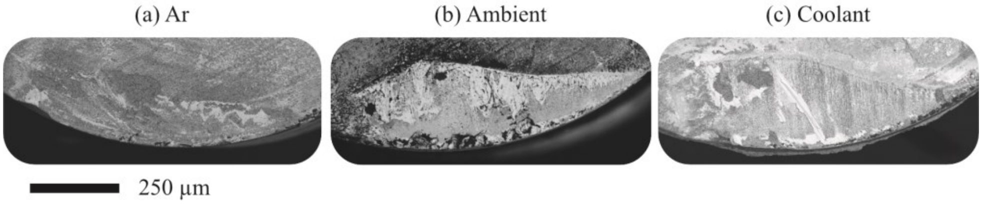

Figure 5. Tool rake of tools machined in a) an Ar atmosphere, b) in ambient air (dry), and c) using coolant. The lighter contrast areas in b) and c) are due to the formation of metal oxides in the contact zone of the rake, adapted from Paper IX.

Materials

> *What is this material!?*
>
> —My colleagues [70]

The appended papers investigate a wide range of coatings, tool materials, and alloys. These range from machinability-improved general structural steels (19MnVS6) to difficult-to-cut Ti-alloys (Ti-5553), and from uncoated cemented carbides to polycrystalline diamond (PCD) tools. This diverse selection of materials enables the study of various tools, environments, and workpiece interactions. This chapter summarizes the tool, coating, and workpiece combinations investigated in the appended papers, highlighting the differences and similarities between these materials. Table 1 provides an overview of the materials studied.

Table 1. Overview of workpiece and tool materials. A "+" indicates the presence of a coating material, "-" the binder, and "$_w$" whisker reinforcement. Consequently, (Ti,Al)N+cBN-TiC is a (Ti,Al)N-coated pcBN tool with a TiC binder.

Workpiece material	**Machined with tool material**	**Paper**
17-4PH	(Ti,Al)N+cBN-TiC, cBN-TiC	I
316L	(Ti,Al)N+WC-Co	II
19MnVS6	Al_2O_3+WC-Co	III, IV
Ti-6242	(Ti,Al)N/NbN+WC-Co, WC-Co	V
Ti-6246	(Ti,Al)N/NbN + WC-Co, WC-Co	V
Ti-5553	(Ti,Al)N/NbN + WC-Co, WC-Co	V
Ti-64	WC-Co, PCD-Co, cBN-(Co,Mo,Ni,W,Cr,Ti,Al)	VI
Inconel 718	cBN-Ti(C,N)	VII, VIII
Hybrid steel 55	cBN-TiC, (Ti,Al)+WC-Co, Si_3N_4, Al_2O_3-SiC_w, SiAlON, Al_2O_3-TiC	IX
Hadfield Steels	cBN-AlN/AlB_x	X

Tool materials and coatings

The nomenclature used for cutting tool materials can be confusing at first. This is because the terms ceramic, cemented carbide, cermet, and hardmetal are defined differently by various authors, organizations, and over time as new materials are invented [4]. This thesis will explicitly state the phases present in the tool material when relevant. For example, cBN-TiC refers to polycrystalline cubic boron nitride (pcBN) with a TiC binder when the distinction from other pcBN grades are important.

The material types present in the tools in this thesis can be divided into four groups based on their hard phase: cemented carbide tools, which are based on tungsten carbide (WC) and Co, pcBN tools, PCD tools, and ceramic tools, which have no cobalt binder or WC hard phase, such as silicon aluminum oxynitride (SiAlON). Two other important material groups in the metal cutting industry are high-speed steels and cermets, but they are not covered in this thesis. Cermets (**cer**amic **met**al**s**) are comparable to WC-Co cemented carbides but have a different primary hard phase, typically titanium carbide or nitride (TiC/TiN), with a binder that containing both Ni and Co. High-speed steels are a group of alloyed and heat-treated steels which have a martensitic matrix containing carbide precipitates.

The tools can also be coated to further enhance their performance. The coatings studied in this thesis are oxide and nitride coatings. These are mainly applied to cemented carbide tools (Papers II-V and IX), but also to pcBN tools in Paper I.

Cemented carbides and coatings

Cemented carbide consists of WC grains in a Co binder matrix. WC-Co has been around for nearly a century and remains the backbone of the metal cutting industry as the most widely used cutting tool material [15]. This is due to its combination of hardness (500–3000 HV), fracture toughness (K_{IC} = 4–28 MPa·m$^{1/2}$), and the ability to modify these properties [71]. Metal cutting tools are not limited to but usually have a hardness between 1000 and 2000 HV and a K_{IC} between 5 and 20 MPa·m$^{1/2}$. Finer WC grains result in a harder material while more binder results in a tougher material [71]. WC grains have a hexagonal close-packed (hcp) structure, while Co has a metastable face-centered cubic (fcc) structure retained after sintering. Although the thermodynamic equilibrium phase of Co at room temperature is hcp, but this is more brittle and generally not preferred in cutting tools [2–6]. The WC grain size in metal cutting tools in the appended papers is in the range of 0.4 to 2 μm, with a Co content between 5 and 15 wt.%.

Coatings are mainly used on cemented carbide tools to combine their toughness with the enhanced properties of solid carbides, nitrides, or oxides [72]. The coatings in the appended papers were produced using cathodic arc evaporation, a physical vapor deposition (PVD) technique, and thermally activated chemical vapor deposition (CVD). PVD coatings provide greater flexibility in composition and layering but are limited to a thickness of around 5 µm [2,3,5,6]. CVD coatings are usually limited to TiN, Ti(C,N), and Al_2O_3, but can be as thick as 20 µm and with a controlled crystal structure and orientation [2–6], such as the (001)-textured α-Al_2O_3 coating in Papers II and III. In general, CVD coatings are preferred when high abrasion resistance is needed, due to their greater thickness. PVD coatings are used when sharp tool geometry and toughness are important, since the coatings are thinner and allow for multilayers that prevent crack propagation [2–6].

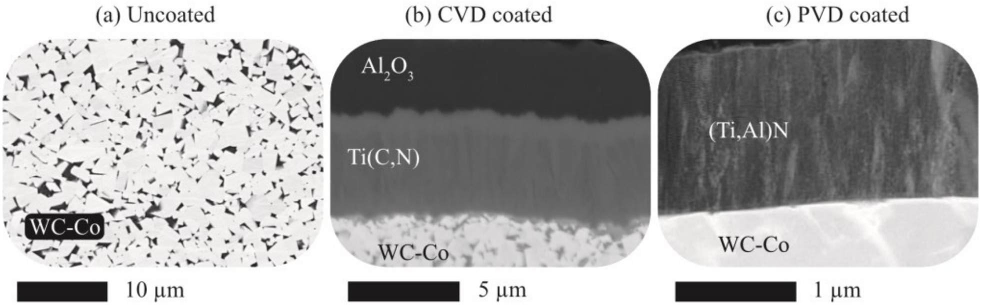

Figure 6. a) WC-Co, b) CVD Al_2O_3 coated WC-Co with Ti(C,N) bonding layer, c) PVD (Ti,Al)N coated WC-Co, adapted from Papers II and III.

Diamond, cubic boron nitride, and mixed ceramics

Diamond is the hardest material known, but it is very brittle. Diamond-based cutting tools are most commonly polycrystalline, consisting of diamond grains bonded together with a binder. Diamond is also metastable at room temperature since graphite is the stable form, but the rate of transformation is neglectable. The binder material in Paper VI is cobalt, as in cemented carbide. Diamond tools are mainly used for non-ferrous alloys [2–6].

Cubic boron nitride (cBN) is the second hardest material known. It does not exist naturally and is also metastable. It is made by high-temperature and high-pressure sintering [2–6]. The stable form of BN is hexagonal graphite-like (hBN), but it can also exist as a hexagonal wurtzite form (wBN). The rate of transformation to hBN at room temperature is negligible, much like the transformation of diamond to graphite [2–6]. All cBN inserts in the appended papers are polycrystalline, consisting of hard cBN particles and a binder or sintering agent. The properties of cBN-based tool material can be tuned by changing the grain size, binder content, and binder type [2–6]. The cBN grades in the appended papers have a cBN content ranging from 45% to 95% by volume. A “binderless” grade is used for the experimental studies in Paper VIII. PcBN-based tools are primarily used for harder workpiece materials (greater than 45 HRC) and at higher cutting speeds [2–6]. For example, the selected cutting speed would be below 100 m/min in Paper I if cemented carbides were used [73], whereas cBN tools can be used at cutting speeds ranging from 200 to 600 m/min [74].

There is a significant difference between optimizing the properties of pcBN tools and cemented carbides [2–6]. The binder phase in pcBN tools is often comparable to the hardness of the WC phase in cemented carbides. PcBN grades consisting of 45-65% cBN by volume have ceramic binders such as TiC (Papers I and IX) or a mixture of Ti(C,N) with smaller fractions of Al_2O_3 and SiC whiskers (Papers VII and VIII). This is mainly to reduce chemical wear, rather than to increase toughness as in the case of increasing the Co content in cemented carbide. PcBN grades with >70% cBN by volume can either have a metallic binder such as Co (Paper VI) [75] or an Al sintering agent resulting in a binder phase of AlN, AlB_x, and Al_2O_3 (Paper X) [76]. This leads to higher fracture toughness for heavy or interrupted machining.

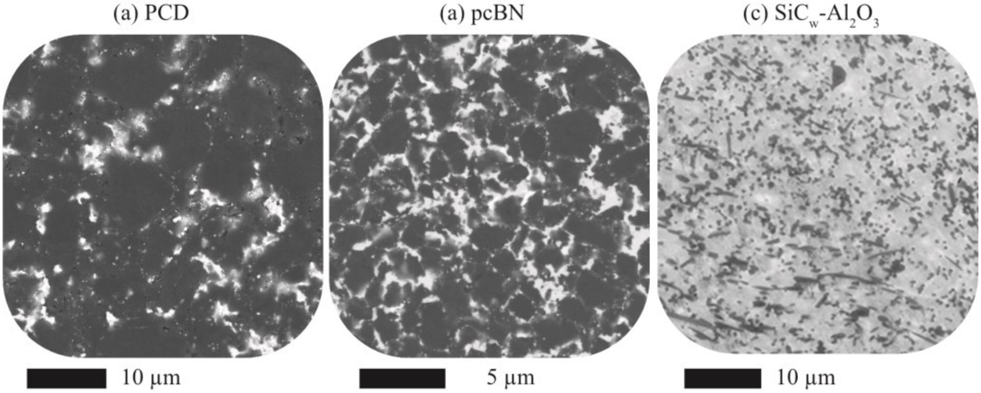

Figure 7. a) PCD grade with a 12% Co, b) pcBN grade with a high cBN content and 15% metallic binder, c) SiC whisker reinforced Al_2O_3, adapted from Papers V and IX.

All the above tools could be classified as ceramic tools since diamond, WC, and cBN are considered ceramics depending on how you define the term. Most people in the metal cutting field do not consider WC-Co, pcBN, and PCD as ceramic tool materials [4]. The term ceramic or mixed ceramic refers to tool materials containing only ceramics phases. Examples of such tools include aluminum oxide mixed with titanium carbide (Al_2O_3-TiC), silicon carbide whisker-reinforced alumina (Al_2O3-SiC_w), silicon aluminum oxynitride (SiAlON), and silicon nitride (Si_3N_4), all used in Paper IX.

Aluminum oxide (Al_2O_3) tools, sometimes referred to as alumina, are more wear resistant and chemically resistant to ferrous alloys compared to WC-Co tools but are much more brittle. This allows for stable machining at very high cutting speeds (above 600 m/min) in some cast irons [2–6]. The addition of TiC or SiC_w (silicon carbide whiskers) makes the tools tougher and more resistant to thermal shock. SiAlON is similar to Si_3N_4 with some Si-N bonds being replaced by Al-N and Al-O bonds. Si_3N_4 is tougher but less hard than alumina, while SiAlON is harder than Si_3N_4 but not as tough [2–6].

Workpiece materials

Steels

Steels are iron-based alloys with a low percentage of carbon, usually combined with other elements such as Mn, Si, Cr, V, Ti, and Ni. The carbon content in the steels included in this thesis ranges from 1.4 wt.% for Hadfield steel down to 0.02 wt.% for 316L.

Steel is an interesting engineering alloy because its chemical composition, heat treatment, and workability allow for great variability in material properties. This is primarily due to the numerous allotropes of iron, as well as the ability to form additional phases and modify their properties by adding alloying elements. The steel alloys in this thesis will, therefore, be grouped by their phase composition.

The two most important allotropes of iron are ferrite (α-iron), which has a body-centered cubic (bcc) structure, and austenite (γ-iron), which has a face-centered cubic (fcc) structure. Austenite is stable at higher temperatures than ferrite, but it can be retained at room temperature by having a low carbon content, by alloying, and by rapid cooling.

This is the case of the austenitic stainless steel 316L in Paper II, which also contains small amounts (<<1% wt.) of non-metallic inclusions (NMIs), namely MnS and several complex oxides $(Ca, Si, Al, Mg)_xO_y$. These NMIs are added to ease chip formation and create protective deposits on the tool during cutting. This is one of the most common stainless steels, with a hardness of around 150–200 HV depending on heat treatment.

A combination of ferrite and cementite (Fe_3C/Orthorhombic) can then be formed during cooling or heat treatment. The structure of 19MnVS6 in Papers III and IV is a mix of ferrite and a lamellar structure of ferrite and cementite called pearlite.

19MnVS6 contains small amounts (<<1% wt.) of the non-metallic inclusions (Mn,Ca)S and $(Mg,Ca,Al)_xO_y$, for the same reason as 316L. 19MnVS6 is a general structural steel with a hardness of about 200–400 HV depending on heat treatment.

17-4 PH in Paper I is a martensitic stainless steel with a hardness ranging from 250 HV to 460 HV. Hybrid Steel 55® (or X20NiCrAlMoV6-5-2-1) in Paper IX is a medium alloy, low-carbon steel with a hardness ranging from 300 HV to 600 HV. The maximum aged hardness is much higher than that of 316L and 19MnVS6. This is in large part due to the α'-martensite phase, which has a body-centered tetragonal (bct) or highly strained bcc structure. Hybrid Steel 55 differs from 17-4 PH in that it has Ni_3Al precipitates, while 17-4 PH contains mainly NbN, as well as CrN, Cu-rich, and Mn, Ni, Si-rich precipitates, along with some Al and Ca oxides.

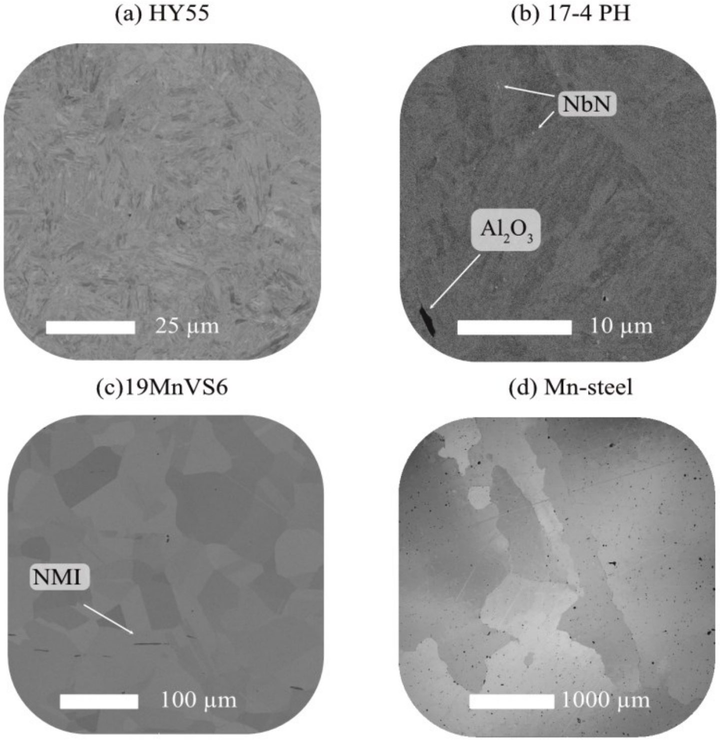

Figure 8. a) Medium alloyed low-carbon steel, b) martensitic stainless steel, c) machinability improved soft Ca-treated steel, d) Hadfield or Mn-steel austenitic steel, adapted from Papers I, IV, IX, and X.

Hadfield steels, or manganese steels, contain 12–15 wt.% manganese. These are initially austenitic steels when heat treated but transform into ε-martensite, a hexagonal close-packed (hcp) structure, through mechanical work. This is called transformation-induced plasticity (TRIP), which can also lead to α’-martensite. It is called twinning induced plasticity (TWIP) if the mechanical work leads to twinning. The formation of mainly ε-martensite, but also α’-martensite and twinning, results in a change in hardness from around 200 HV to 400-500 HV during use.

Nickel-based superalloys and Ti-alloys

Nickel-based alloys, also known as nickel superalloys, are highly alloyed materials used in environments ranging from cryogenic (-250°C) to high temperatures (700°C and above), where high strength, resistance to thermal fatigue, and exceptional corrosion and oxidation resistance are required. The Ni-superalloy investigated in this thesis is Inconel 718® (sometimes called Alloy 718 or A718). Titanium alloys also retain their high strength, resistance to thermal fatigue, and high corrosion and oxidation resistance at high temperatures.

The main difference between Ti-alloys and Ni-superalloys is that Ti-alloys have a better strength-to-weight ratio, while Ni-superalloys can operate at higher temperatures. This is why Ti-alloys are used in the jet engines compression section while Ni-superalloys are used in the engines’ combustion section [77,78]. Ti-alloys are also biocompatible and used in orthopedic implants and surgical instruments, whereas developing a nickel contact allergy is not uncommon.

The matrix phase in nickel alloys is always a nickel-rich fcc phase called nickel-γ (or austenite). This austenite phase is analogous to the austenite phase in steels. There is usually a higher percentage of other elements in solid solution, than in steels. The strengthening of these alloys is mainly due to precipitates. The most important precipitates are the intermetallic phases $Ni_3(Al,Ti)$ called γ' (also an fcc phase) and the Ni_3Nb called γ'' (a body-centered tetragonal (bct) phase). The delta phase δ, an orthorhombic Ni_3Nb, and carbides such as NbC and TiC (fcc) are also common [77] (Figure 9).

The combination of precipitates as well as their size and distribution is what primarily determines the material properties of Ni-superalloys. The exact ratios of γ, γ', γ'', δ, and carbides depend on the heat treatment of the material. Therefore, all A718 alloys do not have the same ratio of precipitates. But A718 generally has a high volume fraction of γ'' (Ni_3Nb) and some γ', δ, and carbides. Aged A718 has a hardness of around 400–500 HV, which is similar to aged 17-4 PH and Hybrid 55, but A718 retains its toughness, hardness, and fatigue resistance at much higher temperatures than these steels, which makes Ni-superalloys unique.

(a) A718 (b) Ti-6242

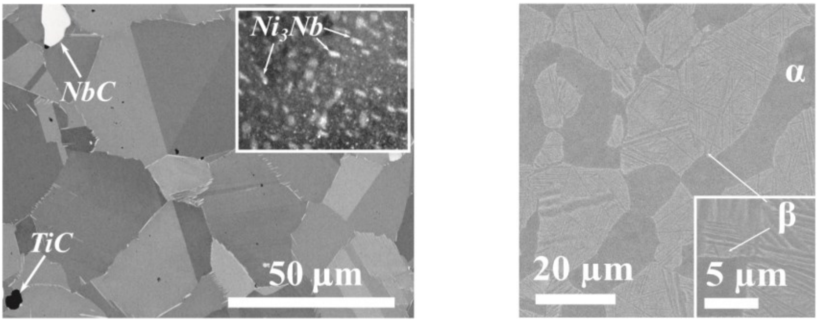

(c) Ti-64 (d) Ti-6246 (e) Ti-5553

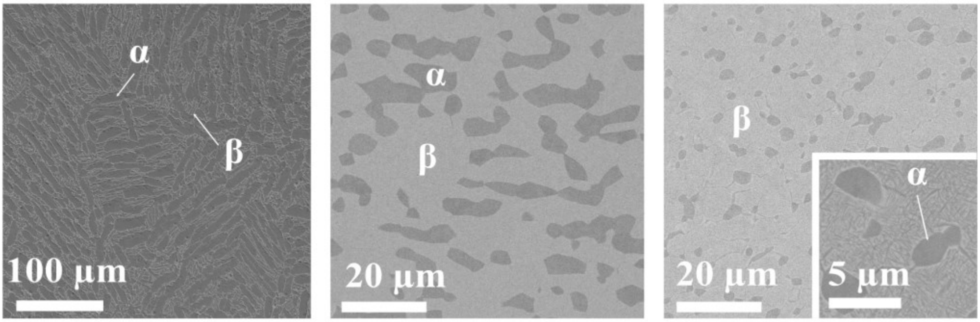

Figure 9. a) The nickel alloy Inconel 718 or Alloy 718, b) near α Ti-6242, c) α+β Ti-64, d) α+β Ti-6246 e) near-β Ti-5553, adapted from Papers V, VI, and VIII.

Ti is either in a hexagonal close-packed (hcp) phase called α-phase stable up to 882°C, at which it is transformed into a bcc phase called β-phase, which is stable up to the melting point of 1668°C. The Ti-alloys are categorized by the amount of α and β phases, and the alloying elements are classified depending on which phase they stabilize. Common α-stabilizing elements are Al, O, N, and C, while Mo, V, Nb, Ta, and W are β-stabilizing, Sn and Zn can be regarded as neutral but can lead to grain refinement [79]. This effect can be seen in the four titanium alloys studied (Figure 9), which are: near α Ti-6Al-2Sn-4Zr-2Mo (Ti-6242), α+β Ti-6Al-4V (Ti-64), α+β Ti-6Al-2Sn-4Zr-6Mo (Ti-6246), and near-β alloy Ti-5Al-5V-5Mo-3Cr (Ti-5553). More β-phase leads to a stronger material, while alloys with more α-phase make for a lighter, more corrosion-resistant, and ductile material.

Experimental Methods

> *... For your specific parameters ($v_c = 600$ m/min, $a_p = 1.5$ mm, $f = 0.2$ mm/rev, no coolant), the tool life for the PCD tool when machining 316L stainless steel will likely be in the range of 20 to 50 min.*
>
> —ChatGPT, 2025-02-26

> *...the approximate tool life would be around 16 minutes.*
>
> —Copilot, 2025-02-26

We should probably use artificial intelligence and large language models for their intended purpose, although they are useful in many applications. The ultimate performance test will always be to put theory into practice by actually machining the material. Measuring the temperature using thermal cameras and thermocouples, or machining in argon, can further evaluate whether it is possible to activate or deactivate wear mechanisms, such as oxidation. Diffusion couples and the ability to cast new alloys can deepen our understanding of the effects of different elements and tool-workpiece interactions. The importance and difficulty of measuring contact pressure and forces were discussed in earlier sections, but how is this actually done? This chapter provides a brief description of the methods used.

Metal cutting

Turning tests were performed using continuous longitudinal turning on computer numerically controlled (CNC) lathes with single-point inserts at constant or pre-set cutting data v_c, f, and a_p. Only Paper V studies milling, which was also performed on a CNC machine using external circular down milling with a single tooth, at constant cutting parameters. The experiments were conducted in a laboratory environment using industrial equipment.

The tests were conducted in intervals based on a fixed cutting distance (or its engagement time equivalent). After each interval, the insert was removed, and wear was measured using visible light microscopy (VB, KT, KF, etc.). The test continued until either a predetermined distance was reached or tool life criterion reached. Cutting parameters were selected based on pre-tests to identify a suitable process window based on previous literature, manufacturer recommendations, calculations, and experience. The final experiments were conducted within a stable and repeatable process window, limiting the time, cost, and result variability. Additionally, tools were saved at selected intervals for later investigations.

Force measurements in the papers were conducted using a piezoelectric multicomponent dynamometer, measuring the three orthogonal force components $F_{c,}$ F_f, and F_p acting on the tool. This was used in most cutting tests even if the results were not published, as cutting forces increase with tool wear. Thus, force data revealed insights into both the cutting process and tool condition.

Thermal measurements were performed via thermography using a high-speed infrared (IR) camera in Papers III and IX as well as embedded thermocouples in Paper III to get an estimate of process temperature and its distribution (Figure 10). The thermography setup for side-view measurements was limited to orthogonal cutting. While speed and feed could be almost directly translated between orthogonal and longitudinal cutting, the cutting depth a_p was instead translated into cutting width. The benefit of IR thermography is the comparable ease of use and relative accuracy. The downside is the difficulty of calibration and knowing the emissivity of the insert, coating, and workpiece material over a wide temperature range, creating uncertainty in absolute temperature.

Embedded thermocouples have an accuracy better than 1°C, and provide a point measure several hundred µm away from the contact zone. These can be used for any cutting operation, but the tools need to be prepared, including inserting and securing thermocouple wires with thermal paste. Combining thermography and thermocouples and with heat flux models had shown to be promising [51].

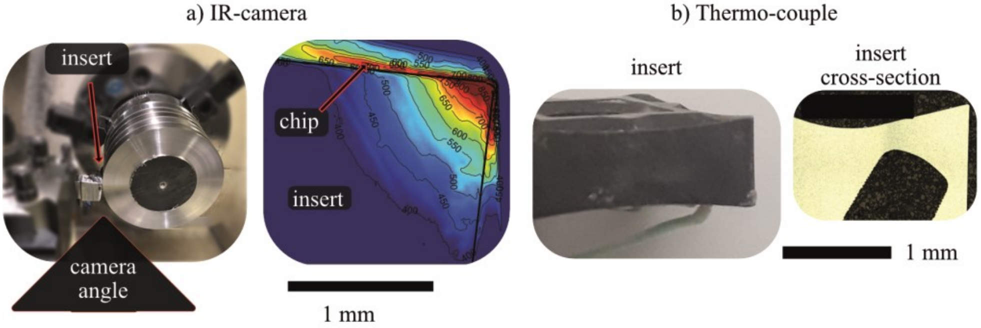

Figure 10. a) Setup and image of IR measurement, b) insert with thermocouple wire and corresponding cross-section, adapted from Paper III.

Controlling the atmosphere is seldom done in industrial settings. But displacing oxygen with inert gas can reveal how O_2 in the air affects the tool wear process by promoting oxidational wear and tool material loss or the formation of protective oxides [65]. To investigate this, a special chamber was built around the tool holder. In Paper IX, the cutting zone was flooded with 400 l/min of Ar through nozzles in this chamber and through the tool holder's coolant channels. But the chamber caused problems with chips getting stuck during longer cutting distances in Paper III. A different setup was therefore used in that paper, where Ar was supplied through both the jet and flood coolant nozzles in the tool holder instead of using a chamber. This achieved the same result but without the need for a chamber (Figure 11). These controlled atmosphere experiments provided insight into both degradation and protection mechanisms.

The cutting zone was also flooded with compressed air at the same pressure and flow rate as the Ar setup in Paper III, To study the effects of oxidation while maintaining the same temperatures, Which ensured that any observed differences were due to oxidation rather than cooling effects (Figure 4 and Paper III).

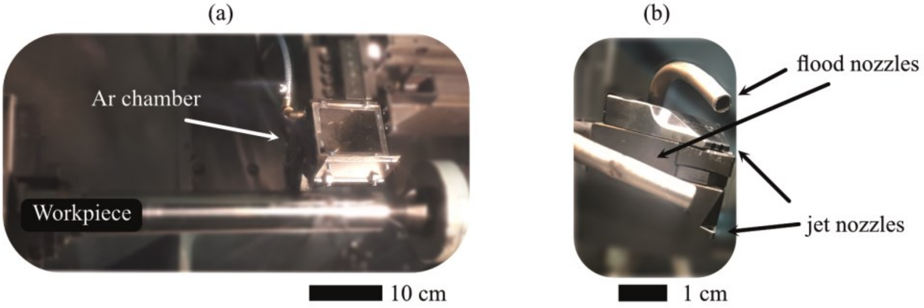

Figure 11. a) Ar chamber covering part of the tool shank and the insert, b) flood coolant and jet coolant nozzle connected to compressed Ar supply, adapted from Paper III.

Casting

The Mn-steel in Paper X is the only alloy not industrially cast but still heat-treated at a commercial facility. All other alloys were both commercially produced and heat-treated. Mn-steel bars for turning (500 mm long, 150 mm in diameter) were cast at a "pilot foundry" using an open oxide-lined induction furnace and poured into molds. The melt was protected from oxygen by the slag. This enabled different alloys to be cast from the same batch through successive alloying, measurement, and pouring. Mn-steel bars for diffusion couples (100 mm long, 20 mm in diameter) were cast in a resistance tube furnace, pumped down to vacuum (10^6 mbar) and then flooded with Ar to avoid oxidation and loss of elements with lower boiling points. Heat treatments were done by reheating and oil quenching.

Diffusion couples

The reactions between the insert, workpiece, and air are difficult to study after turning. TPLs are on the order of 100 nm or sometimes less. Some reactions lead to tool and coating degradation, resulting in poor properties that are immediately abraded away, making them difficult to analyze. Studying diffusion into the chip is also challenging because the elements diffusing away from the tool will be spread over several kilometers of chips. The reaction products will not be abraded away in a diffusion couple, resulting in reaction layers on the order of microns.

The diffusion couple method serves as a bridge between modeling and machining. Diffusion couples are static, whereas machining is dynamic; new workpiece material flows past the tool surface, resulting in a constant influx of new material and fixed workpiece element activities. A diffusion couple is thus closer to resembling a stagnant and thick adhesion layer or build-up edge. It then underestimates the supply (activity) of workpiece elements, a factor that must be considered. Nonetheless, properly accounted for, this method provides valuable insights and allows for hypothesis testing.

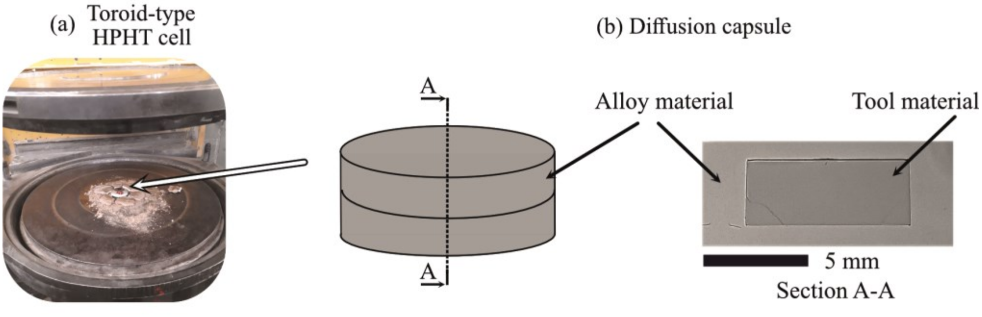

Figure 12. a) The opened toroid type HPHT cell after the experiment with the diffusion capsule highlighted, b) the diffusion capsule and cross-sectioned sample showing how the tool material is inside a workpiece material capsule.

The main diffusion couple method used in the appended papers is a high-pressure (2.5-3 GPa) and high-temperature (900–1300°C) (HPHT) process. This involves encapsulating the tool material in a capsule made of the workpiece material, then heating the puck in a toroid-type HPHT cell for 10 minutes, followed by rapid quenching (<1 minute). The high pressure is used to capture the formation of nitrides, borides, oxides, and other products that are not captured in low-pressure diffusion couples. The differences between high pressure and low pressure are investigated in Paper VII. The addition of powders and the entrapment of air in the corners enable the investigation of the effects of oxygen and NMI on tool degradation (Paper IV).

Thermodynamics and Kinetics of Metal Cutting

> *Perhaps it will be wise to approach the subject cautiously.*
>
> —David L. Goodstein [80]

One could argue that thermodynamic equilibrium is not reached during a metal cutting process or that it is not even in a steady state. You might even have noticed that most of the tool and workpiece phases are metastable at room temperature and under cutting conditions, such as diamond, cBN, (Ti,Al)N, austenite, and fcc Co. Cementite (Fe_3C) should not even present in the equilibrium Fe-C phase diagrams. But the postulate of local thermodynamic equilibrium holds for a broad range of systems and conditions [81,82], and evidence suggests that the surface of the cutting tool during metal cutting behaves as such a system. Some understanding of thermodynamics, kinetics, and CALPHAD is necessary to assess which assumptions, simplifications, and shortcuts are acceptable and which might mislead us.

CALPHAD

Thermo-Calc and DICTRA [7] are the CALPHAD-based software that are used for the thermodynamic simulations and kinetic modeling in the appended papers. The benefit of CALPHAD-based software is its ability to reliably extrapolate and predict thermodynamic, kinetic, and other properties of multicomponent material systems based on experimental data from unary, binary, and ternary systems [7,83].

CALPHAD is a phenomenological method based on fitting model parameters to describe the Gibbs energy of phases. How the model data is created and collected using ab-initio calculations and experiments, as well as the assessment, optimization, and creation of databases using the PARROT model [7], are outside the scope of this thesis. Still, understanding the possibilities and limitations of this approach remains important for evaluating the validity of modeling efforts.

The Gibbs energy (*G*) of each phase (*α,β,..*) is described using the compound energy formalism as a function of temperature (*T*), pressure (*P*), and composition (X_i). The structure of every phase is then represented by a sublattice model $(A,B)_k(D,E,F..)_l(..)_{..}$, where *A* and *B* is the mix in the first sublattice etc. and k and l is the stoichiometric coefficients [84]. For example, a M_7C_3 carbide containing Cr, Fe, C could be written as $(Cr,Fe)_7(C)_3$. The Gibbs energy of the whole system is the sum of the Gibbs energy of the individual phases and the amount of each phase (*N)*, as shown in Eq. 5 [83]. Equilibrium is reached when the Gibbs energy of the entire system is minimized in an isothermal isobaric system.

$$G(P,T,N,X_i \dots) = G^{\alpha}(P,T,N^{\alpha},x_i^{\alpha} \dots) + G^{\beta}(P,T,N^{\beta}x_i^{\beta} \dots) \qquad (5)$$

The accuracy of the model is then dependent on how well the Gibbs energy of the individual phases is described [7,83]. The CALPHAD-based expression for the molar Gibbs energy of a phase is typically given as Eq. 6 [83].

$$G_m = {}^{\circ}G_m - TS_m^{cnf} + G_m^{magn} + {}^{E}G_m \qquad (6)$$

The first term ${}^{\circ}G_{\mathrm{m}}$ represents the surface of reference and is a weighted average of all the end members in the phase. The second term is ideal entropy of mixing, where the $\mathrm{S}_{\mathrm{m}}^{\mathrm{cnf}}$ is the configurational entropy per mol and T is the temperature in K. The third term G_m^{magn} is the magnetic contribution. The fourth term ${}^{E}G_m$ is the excess Gibbs energy representing the deviation from an ideal mixture not captured by the first three terms.

There is also, in general, no temperature and pressure dependence on the molar volume. But still, a dependence of molar volume on the Gibbs energy, making calculations accurate up to a 1-10 GPa, dependent on the difference in bulk modulus and thermal expansion between phases [85]. This might lead to underestimations of the stability of gases and liquids, as they are more compressible than solids. Consequently, melting and boiling points may appear artificially high at elevated pressures [85]. But this can be accounted for by the manual addition of parameters, which was done to some extent in Paper VII.

A much more common and significant source of error when modeling a cutting process is misinterpretation. Interpreting and translating the metal cutting into thermodynamics, setting up correct calculations, and interpreting the results are the key challenges addressed in the appended papers.

Kinetics and DICTRA

Diffusion simulations can further aid in understanding these interactions. This was attempted in Paper VI to understand and predict the interactions between PCD, pcBN, or WC-Co with Ti-64. DICTRA is based on solving Onsager's extension of Fick's law, where diffusion is driven by differences in chemical activities calculated using Thermo-Calc [7,86,87]. It can simulate diffusion through a multiphase mixture using homogenization models. The chemical and phase composition can differ along only one axis, but the geometry can be planar, spherical, or cylindrical; it is thus a 1D model at its core [86,87].

The multiphase diffusion problem in 1D is solved by turning it into an equilibrium single-phase problem using a homogenization (or simply averaging) method. This is done by calculating the flux (J) of each chemical component (often element) (k) in each phase according to Eq. 7, where $\mathrm{M}_{\mathrm{k}}^{\alpha}$ is the mobility, $\mathrm{c}_{\mathrm{k}}^{\alpha}$ the concentration, $\mu_{\mathrm{k}}^{\alpha}$ the chemical potential of component k in phase α, and z the position [86,87].

$$J_k^{\alpha} = -M_k^{\alpha} c_k^{\alpha} \frac{\partial \mu_k^{\alpha}}{\partial z} \tag{7}$$

The product of $\mathrm{M}_{\mathrm{k}}^{\alpha}\mathrm{c}_{\mathrm{k}}^{\alpha}$ is the permeability ($\Gamma_{\mathrm{k}}^{\alpha}$) of component (k) in phase (α) [86,87]. This product was used in both Paper VI and X as a simple and effective way to estimate how fast and to what extent a component moves in each phase without having to run full diffusion simulations. A homogenization function is then needed to calculate the locally averaged flux (Γ_{k}^{*}) of each component k through the multiphase mixture (*). The simplest approach is the rule of mixtures, also known as the upper Wiener bound (Eq. 8) [86,87], which was used in Paper VI. Here, f^{ϕ} is the local volume fraction of each phase.

$$\Gamma_k^{*} = \sum_{\phi} f^{\phi} \Gamma_k^{\phi} \tag{8}$$

The flux of a component in the multiphase region is then given by Eq. 5, where V_{s} is the molar volume of all substitutional elements, assuming that interstitial components do not contribute to volume. The "l.eq." indicates the assumption of local equilibrium.

$$J_k = \frac{-1}{V_S} - \Gamma_k^{*} \frac{\partial \mu_k^{l.eq}}{\partial z} \tag{9}$$

There are many other homogenization functions, and much more detailed descriptions of diffusion modeling are available in the references [7,86,87].

Applying models

Minimizing Gibbs energy can be done analytically with pen and paper for simple systems. Phase diagrams and Ellingham diagrams might already be available in such cases. Diffusion calculations, such as carburization of a single phase, can also be solved by hand. However, calculating the interactions between the workpiece, air, tool, and coating can result in a system containing about fourteen elements and nine phases, many of which are metastable. These multielement and multiphase systems, with numerous metastable phases, require computational power, which is precisely what we will utilize!

The temperature, pressure, and effective concentration (activity) changes across the tool chip interface and over time. There is no global equilibrium state for the entire tool, but every point on the tool surface is in (a possibly constrained) local equilibrium [81,82,88]. Furthermore, thermodynamics can also be useful even if equilibrium is never reached, as it can tell us what can and cannot happen. Diffusion, oxidation, and chemical degradation cannot occur without a driving force, and they are more likely to occur when the temperature and driving forces are high.

Putting everything into one big equation and modeling everything simultaneously would be overwhelming. A comprehensive model of workpiece oxidation would likely result in a PhD thesis on high-temperature oxidation rather than metal cutting. Knowing what to exclude from the model is then as important as knowing what to include in the model.

Figure 13 from Paper IX attempts to break down the key aspects of metal cutting models. There are: i) oxidation of the workpiece material, ii) oxidation of the tool materials, iii) interaction between the tool and workpiece, and iv) combined interactions, such as those between the tool and workpiece oxides. The specific cutting parameters and materials will determine the modeling efforts that should be undertaken.

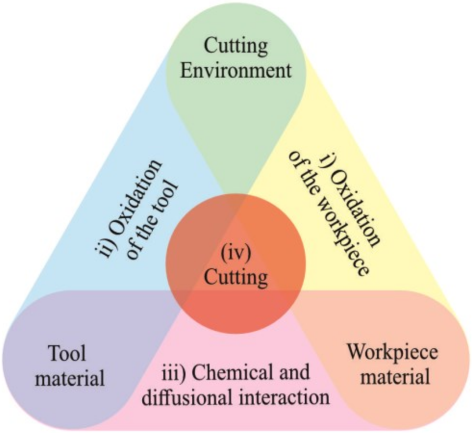

Figure 13. The different interactions modeled, i) the oxidation of the workpiece material, ii) the oxidation of the tool materials, iii) the interaction between the tool and workpiece, and iv) a combination of them, such as the interaction between the tool and workpiece oxides.

Modeling the oxidation of i) the workpiece and ii) the tool involves investigating which oxides are in equilibrium and which have a high driving force to form depending on the temperature, pressure, and oxygen availability. This approach can help determine how tool oxidation progresses (Paper V), whether a passivation film might form (Paper IX), or at what temperature and pressure cBN oxidizes to from B_2O_3 and when this oxide melts (Paper X) [77,89]. Extensive literature is available on the oxidation of alloys and tool materials, including which oxides are stable or porous [66,89]. Plotting the effective partial pressure of O_2 against equilibrium mole fractions and normalized driving forces can be used to evaluate which oxides might or might not form [31]. These results can then be compared to literature data or further modeled. This can be done separately for the alloy (Figure 14a), the tool (Figure 14b), or a combination (Figure 14c). For example, in Paper IX, the oxidation of cBN-TiC does not change significantly in the presence of Hybrid 55, whereas interactions between the alloy, air and silicon-based tool materials result in the formation of Al_2SiO_5 and Fe_2SiO_4.

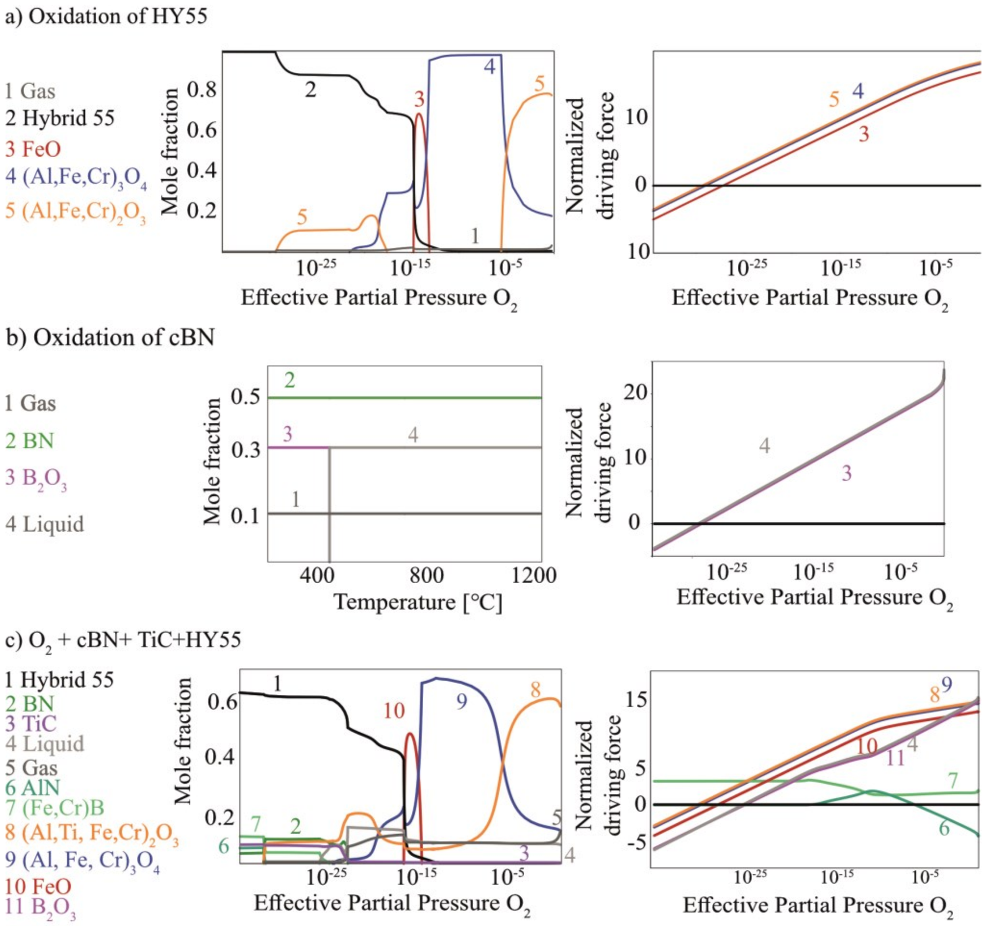
a) Oxidation of HY55

b) Oxidation of cBN

c) O_2 + cBN+ TiC+HY55

Figure 14. Adapted from Paper IX, a) possible oxidation of the workpiece at equilibrium and the driving force for the formation of different oxides, b) possible cBN oxidation at different temperatures and the driving for the formation of B_2O_3 solid and liquid, c) possible interactions between tool, workpiece, and oxygen.

Modeling iii) the interaction between the workpiece and tool can focus on different interactions, such as the chemical interactions between the coating material and NMIs, as in Papers II, III, and IV (Figure 15a), or the solubility, mobility, and permeability of tool elements in the alloy, as in Paper XI (Figure 15b). The tool-alloy interactions can also be studied at different temperatures and pressures (Papers XII and XIII, Figure 15c), or a combination, as in Papers X and IX.

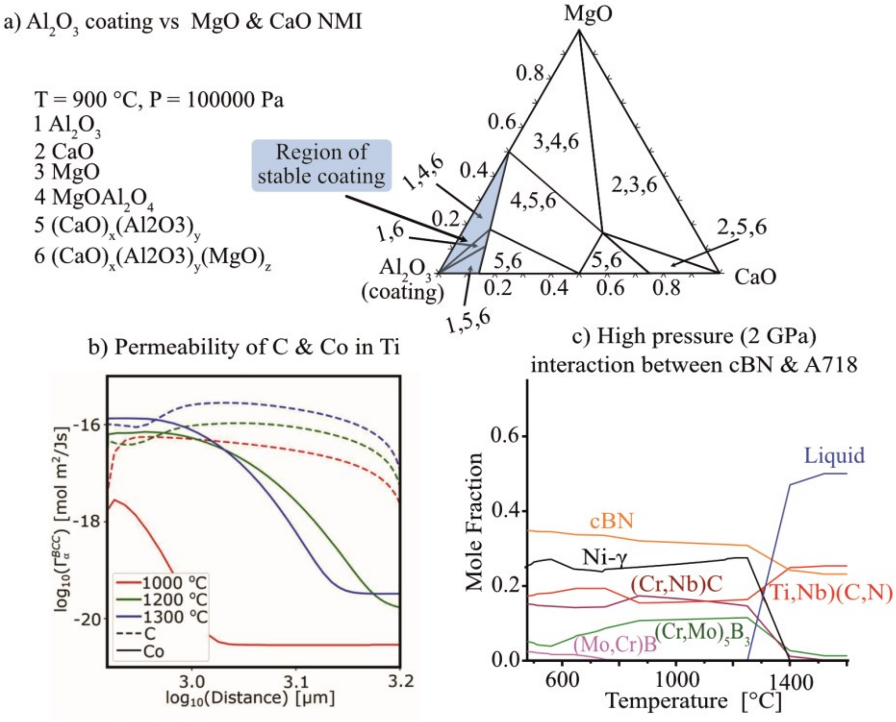

Figure 15. a) A ternary phase diagram between the coating Al_2O_3 and some common steel oxides (Paper III), b) the permeability of tool elements in Ti-64 at different temperatures and distances (concentrations) (Paper VI), c) the equilibrium phase composition at 2 GPa and different temperatures when cBN-TiC and A718 interact (Paper VII).

The benefit of these calculations is that they provide a quick way to explore potential outcomes, such as oxidation, diffusion, or reactions. They also help predict how the tool will degrade as it wears and when it will no longer interact with the workpiece and environment.

These are all equilibrium calculations. For example, in thermodynamic calculations, diamond tools are always considered to transform into graphite at cutting temperatures. But it is well known that diamonds are very stable in vacuum up to about 1000°C and in oxygen up to about 900°C [90]. Thermodynamics alone cannot account for this; researchers must rely on literature and experience to recognize such discrepancies. Hence, there could be “false degradation”, but not false stability.

There are ways to work around this. In well-understood systems, some phases can be explicitly suppressed, such as graphite when modeling PCD and hBN when modeling cBN. Ranking can also be done by comparing their driving forces (Figure 14). The rate of solid state reactions is often limited by diffusion [88] and hence the permeability [87] can be used to rank and estimate how elements diffuse through different phases (Figure 15b). These combinations of estimates make it possible to predict and rank tool materials both with respect to limiting degradation and TPL formation (Paper II-IX), as well as predicting and ranking successful alloying for TPL formation (Paper X).

Diffusion simulations are, of course, more precise than permeability estimates only, and are a useful tool when the permeabilities of different elements are similar (Paper VI). However, it is more complicated and not as fast for large-scale screening. Setting up the diffusion calculation is not trivial and depends on the cutting process [29,58]. A diffusion couple or diffusion simulation is more similar to the interaction between the tool and completely adhered workpiece material. But chip flow can be modeled by fixing the activity of the workpiece elements at the boundary, which might be a better way to model the constant flow of the chip or workpiece sliding across the tool’s flank and rake [58], because there is a constant influx of new workpiece material. Diffusion simulations must then be carefully interpreted to investigate and predict the correct formation sequence under well-defined boundary conditions.

Characterization

> *Oh, I love dirty dark field!*
>
> —Filip Lenrick

VLM

Visible light microscopy (VLM), sometimes referred to as light optical microscopy (LOM), is probably the microscope most people are familiar with (the normal tabletop microscope). I will use the term VLM, because a synchrotron using X-rays could also be considered a LOM since it involves light, optics, and microscopy.

A visible light microscope uses visible light to illuminate a sample, with the image then received by your eye or a detector. The benefit of VLM is its relative affordability and ease of use. Several VLMs were used to measure and inspect flank wear, notching, cracks, etc. Sample preparation is also optional and easy when using VLM.

VLM has a limited resolution and limited depth of focus, due to the limitations of lenses and the wavelength of visible light. Image stitching of multiple images is necessary to capture tool wear, as the entire tool cannot be in focus.

This limited depth of focus can be an advantage when measuring crater wear or surface roughness. By combining focus variation with a stepping motor, the relative height difference between two regions that are not in focus simultaneously can be determined. This is the basic principle behind the optical profilometers used for measuring crater wear and making 3D maps of worn tools (Figure 19).

Limited chemical information can be gained from VLM when it comes to metals, as most are grey and shiny. However, the use of etchants, polarizers, and recognizing the distinct colors of different carbides, oxides, nitrides, and ceramics can reveal chemical information. A polarizer was, for example, used in Paper III to estimate when the different layers of the Ti(C,N)-Al_2O_3 coating were worn through.

SEM and FIB

Scanning electron microscopy (SEM) and focused ion beam scanning electron microscopy (FIB-SEM) are inherently different from VLM. SEM uses electrons while FIB-SEM uses ions, which are scanned across the sample [91]. Different detectors can be used to detect electrons, ions, or photons. This method of scanning electrons across the sample makes the resolution of SEM much higher and the depth of focus much greater than VLM.

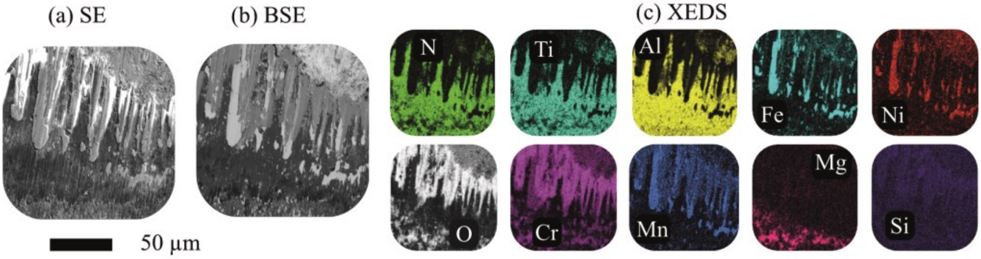

Figure 16. a) Topography contrast SE image of the periphery of the contact zone, b) Z-contrast BSE image, c) elemental XEDS-maps, adapted from Paper II.

The secondary electron (SE) detector collects low-energy electrons that have inelastically scattered off the surface of the sample. This makes the SE image topography sensitive [91]. The backscatter electron (BSE) detector collects higher-energy electrons that have elastically scattered from the sample. Since heavier atoms scatter more, BSE images are Z-contrast sensitive, heavy elements will appear light, and light elements will appear dark [91], as seen in Figure 16. The X-ray energy dispersive spectrometer (XEDS), sometimes called EDS, EDX, EDXS, EDAX, or EDXMA, should not be confused with the slower but more precise wavelength-dispersive X-ray spectrometer (WDS or WDXS) [91]. These instruments measure characteristic X-rays emitted from the sample. The X-ray is generated when an outer shell electron loses energy to be able to fill a hole left by an inner shell electron that was knocked out. The problem with this technique is that H and He do not have any characteristic X-rays, and measuring atoms below Na ($Z < 11$) is only semi-quantitative. Additionally, multiple scattering events can occur, resulting from a signal outside the incident beam path.

Electron backscatter diffraction (EBSD) and transmission Kikuchi diffraction (TKD/t-EBSD) use the same detector and are essentially the same technique.

However, EBSD measures electrons scattered off the surface while TKD/t-EBSD measures electrons scattered through the sample. Electron backscatter diffraction patterns, sometimes called Kikuchi patterns, are analyzed using these techniques. The incident beam is first scattered both elastically and inelastically. These initially scattered electrons then diffract, resulting in many diffraction spots that form Kikuchi lines and ultimately Kikuchi patterns [91], (Figure 18c). These can give information about the crystal orientation, structure, deformation, and more (Figure 17 b, c, and d).

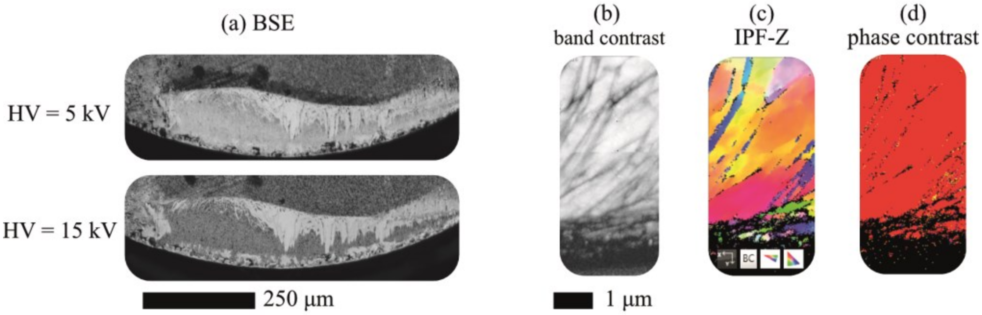

Figure 17. a) SEM of tool rake at different HV, HV = 5 kV results in a smaller excitation volume revealing the presence of a thin surface film, adapted from Paper IX, b) band contrast EBSD map of the highly deformed austenite grains after abrasion test, c) IPF-Z EBSD-map, d) phase contrast EBSD map, adapted from Paper X.

The SEM/FIB requires a vacuum to image, but sample preparation is optional if the sample is conductive and basic imaging is needed. But more rigorous sample preparation can and should be done depending on the investigation’s goal, especially for high-quality EBSD mapping.

Creating a spot size of sub 4 nm can routinely be done in an SEM, which makes for high-resolution SE images, as this signal originates only from the surface. But the excitation volume is much larger. Because X-rays and backscattered electrons can originate from 50 to 100 nm into the sample at an acceleration voltage or high tension (HV) of 5 kV (in Fe), the spatial resolution of the BSE image or XEDS maps is much lower than the initial 4 nm beam size [91]. The excitation volume gets even larger at higher HV, which is needed to reliability measure the characteristic X-rays of many elements, resulting in an excitation volume of 300 to 800 nm (for HV = 30 kV in Fe). The characteristic X-rays measured by the XEDS detector might also have originated from multiple scattering events, causing the

XEDS signals to come from outside the original beam path [91]. This can sometimes create confusion since one might be looking at the coating of the tool or a thin film formed on the tool using the SE detector (Figure 17 a), but the BSE image shows the bulk, and the XEDS signal might mainly detect the bulk material as well. Similarly but opposite, the SE image might only show dirt on the surface of a worn tool that was poorly cleaned, while the BSE and XEDS is good.

TEM

Transmission electron microscopy (TEM) is a good complement to SEM. It also uses a beam of electrons, which can be parallel (in standard TEM mode) or focused into a scanning beam (much like SEM). This is called scanning transmission electron microscopy (STEM). There are a myriad of different STEM and TEM modes and different contrast mechanisms [9]. The sample must be transparent to electrons and typically range in thickness from 50 to 200 nm. Hence a large excitation volume is not a problem, and STEM-XEDS can be used, but multiple scattering events still cause XEDS signals to originate from outside the original beam path [9].

Sample preparation is needed for samples thicker than this, which is the case in metal cutting. All TEM samples in this study were prepared using the FIB lift-out technique [10]. Most images in the appended papers are STEM images, as they are the most intuitive for the reader, though a lot of the investigation was done in TEM mode. Bright-field TEM (BF-TEM) uses the objective aperture to select the unscattered electron beam [9]. Anything scattering the beam will appear darker, such as crystalline areas, high mass areas, or defects, while the vacuum appears bright [9]. One can also look at the back focal plane to see the diffraction pattern of the sample. A selected-area aperture can be used to select an area of interest, a technique called selected area electron diffraction (SAED) [9]. This provides information about the crystal structure of the selected area.

Dark-field TEM (DF-TEM) is the opposite of BF-TEM; the center of the beam is excluded, and only a selection of scattered electrons are observed. In this mode, the vacuum therefore appears dark, while crystalline areas, high-mass areas, or defects appear bright [9]. Areas with coinciding diffraction spots, meaning they have similar crystal orientation and structure, can be located by tilting a particular diffraction spot into the center of the aperture or just selecting it using displaced-aperture dark field (DADF) [9]. This technique, also known as “dirty dark field”, is demonstrated in a false color DADF-TEM image in Paper VII to locate precipitates.

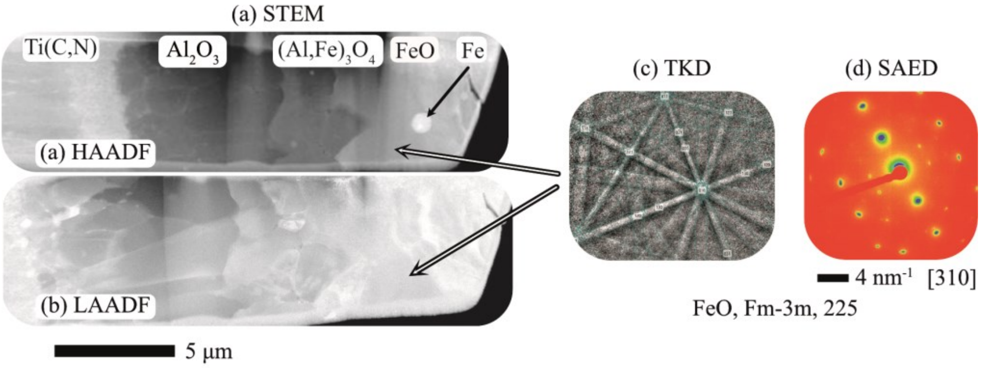

Figure 18. a) Z-contrast HAADF image, b) diffraction contrast LAADF image, c) TKD pattern with indexed Kikuchi lines, d) SAED image of the same region. Adapted from Paper IV.

BF-STEM and annular dark filed (ADF-STEM) are analogous to BF-TEM and DF-TEM, but use a scanning beam. There is also low-angle annual dark field (LAADF-STEM), which shows diffraction contrast or differences in specimen thickness, and high-angle annual dark field (HAADF-STEM), where the higher the angle the higher the Z-contrast [9]. Hence a HAADF-STEM image is analogous to a BSE-SEM image but offers a much higher resolution and more capabilities [9].

XEDS-STEM is therefore analogous to very high-resolution XEDS-SEM, since the beam is smaller and the sample thinner. However, multiple scattering still pose a problem, when measuring elements with $Z < 11$. For example, when using a copper TEM grid, a Cu signal will be present in all TEM-XEDS spectra. Electron energy loss spectroscopy (EELS) can accurately measure B, C, N, and O and does not suffer from false detection due to multiple scattering events, which makes it a good complement to XEDS and WDS. However, quantification is more difficult [9].

XEDS-TEM or XEDS-SAED works but provides the composition of everything that is illuminated, not only the area selected by the image plane or diffraction plane apertures. Hence, you cannot collect the XEDS signal only from the area visible in the diffraction pattern, selected using the objective aperture. You would instead need to make the beam smaller by using the condenser lenses and apertures. The nuances and possibilities when operating a TEM create many more possibilities but put higher demands on the operator [9].

Synchrotron, XRD, OES and other techniques

The main spectroscopy and microscopy techniques used in the appended papers are VLM, SEM, and TEM because they are readily available and give spatially resolved information about physical structure and chemical composition. But other instruments were used too.

A spark optical emission spectrometer (OES) was used to measure the composition of the different manganese steels in Paper X. The instrument works by vaporizing a small portion of the sample and then measuring the emission lines of the elements. The benefit of this method is that it quickly and accurately measures alloy compositions, including light elements such as carbon.

Atom probe tomography (APT) was used in Paper VIII. The sample is smaller than a TEM sample, but the sample preparation is similar. APT is based on field evaporation of ions and detection, allowing for nm to atomic resolution of a 3D sample, with the added benefit of being able to detect light elements as effectively as heavy elements.

X-ray diffraction (XRD) was also used in almost all papers to measure the phase composition of the received tools and workpieces, with XRD spectra shown in Papers VII, VIII, and IX. The XRD and SAED are related, but XRD uses X-rays while SAED uses electrons. The basic principle is constructive and destructive interference of scattered X-rays or electrons, which depends on the crystal lattice spacing. This gives information about the crystal structure, but offers no direct chemical information or spatial resolution. For example, all the Mn-steels in Paper IX have identical XRD patterns.

Energy dispersive X-ray diffraction (EDXRD) is a more advanced XRD technique. The benefits of a synchrotron are many and depend on the synchrotron and end station. The benefit of the ERL PSICHÉ beamline at SOLEIL is that EDXRD can be done in-situ. The X-ray diffraction pattern can be measured under high pressure and during sample heating and quenching, which would otherwise be impossible. Hence, we could study phase formation and dissolution during heating and cooling at high pressures.

Classifying Tool Wear and Protection

Good luck, have fun!

—Rebecka Lindvall

This thesis distinguishes between wear mechanisms and wear types. The wear mechanism explains why the insert wears, for example through abrasion, chemical degradation, or a combination. The wear type describes how we identify this wear, such as flank or rake wear.

Wear types

Different tool materials are prone to different wear types and mechanisms [2,3,5,6]. The two main types studied in the appended papers are the flank wear and crater wear, respectively quantified by the average width of the flank wear land (VB_B) and crater wear (KT) parameters, as shown in Figure 19. Flank wear is the most desirable type of wear, if tool wear can ever be desirable. This is because it is predictable and progressive [2,3,5,6]. The tool can be used until it does not generate the desired quality of the surface, which is dependent on the flank wear [2,3,5,6]. The tool wear can be easily monitored and accurately predicted, making the machining process very efficient.

The rate of crater wear can progress predictably to a certain point. But an increase in crater size leads to a weakening of the cutting edge and may result in failure of the cutting edge. The difference between a well-performing tool and catastrophic failure can be a matter of seconds. For example, no significant wear occurred on the rake or flank of the (Ti,Al)N-coated cemented carbide tool in Paper IX until 180 seconds of machining, when a crater formed after the coating was worn away. The growth of the crater then led to the complete collapse of the cutting tool after 210 seconds. Hence, the tool went from almost no VB during 180 sec of machining to 250 µm of VB in the next 30 seconds. Having these unpredictable tool failures forces you to stop earlier than necessary to avoid a collapsed edge destroying the surface of the workpiece.

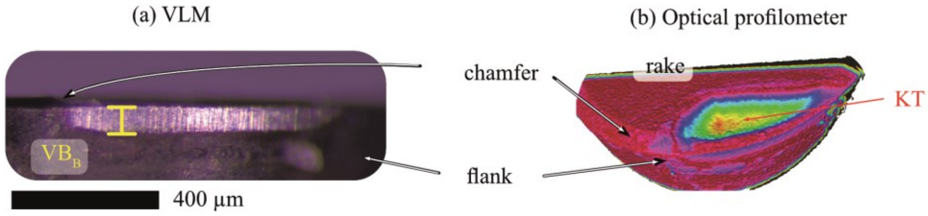

Figure 19. a) VLM image of the average width of the flank wear land (VB$_B$), b) optical profilometer measurement of the depth of the crater wear (KT).

Another wear type present in the appended papers is coating delamination, which is when the coating detaches from the insert, leaving the substrate exposed. Notch wear is a type of localized flank wear occurring at the edge of the contact zone on the major or minor cutting edge. Cracks can also form in the coating or substrate. Other types of wear include plastic deformation, comb cracks, flaking, and more [2,3,5,6].

Wear mechanisms

Diffusion, oxidation, and chemical degradation are the main focus of this thesis, rather than thermomechanical wear mechanisms, such as abrasion, adhesion and attrition. These are often related and occur simultaneously, but a distinction should be made between them.

Chemical degradation is when the tool and the workpiece react, such as the Al_2O_3 coating in Papers III and IV reacting with Ca, Mg, and O as well as other NMI, leading to its degradation into calcium aluminates (Figure 20a). Oxidation degradation is when oxygen from the air reacts with the tool materials, such as the formation of Co-W-O shown in Paper V (Figure 20b). Diffusion wear is when an element leaves or enters the tool. For example, in Paper VIII, both B and N from the cBN grains diffused into the alloy leading to B and N precipitates in the adhered workpiece material (Figure 20c).

A combination of these three is also common. For example, Fe does not react with Al_2O_3, but oxidized iron can react with Al_2O_3 to form the $FeAl_2O_4$ spinel, as seen in Papers III and IV. Chemical reactions in metal cutting are often diffusion controlled, resulting in diffusion occurring first followed by a reaction.

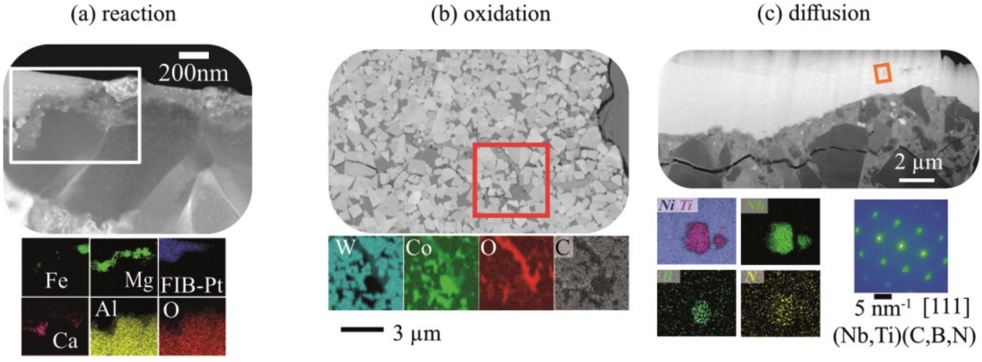

Figure 20. a) STEM and XEDS images showing chemical degradation of Al_2O_3 in Paper IV, b) SEM and XEDS images showing oxidation of the binder in Paper V, c) STEM, XEDS, and SAED of diffusion of B and N followed by re-precipitation in the adhered workpiece material in Paper VIII.

Abrasive wear in the appended papers is due to hard particles like inclusions (Al_2O_3) and precipitates (TiC, NbC) sliding across the tool surface, abrading or almost polishing and grinding away mostly the softer binder phase. The matrix phase in the steels (austenite, ferrite, and martensite), Ni-superalloy (nickel-γ), and Ti-alloys (α- and β-titanium) are not hard enough to significantly abrade the hard phases, such as WC, cBN, and diamond, hence their impact on abrasive wear is minimal.

Abrasion can also occur after a softening of the tool material or coating. The Al_2O_3 coating in Papers III and IV is very resistant to abrasion, but it transformed into a soft calcium aluminate that is more easily abraded.

There is also abrasion due to the dislodging of tool material grains (WC, cBN, and diamond), which then slide across the tool surface, resulting in self-abrasion. But the underlying wear mechanism is not abrasion itself but the loss of binder that allows hard grains to be removed and subsequently contribute to tool wear [2,3,5,6].

Abrasive wear can exist on both the flank and the rake, but it is most prominent on the flank of the tool, where the relative speed of the workpiece material across the tool surface is the highest.

Adhesive wear occurs when the material being cut adheres to the tool material or coating. This is most common when the relative speed of the workpiece across the tool surface is lower, such as at low cutting speeds or near the cutting edge. This effect is seen in Paper I when machining 17-4 PH at $v_c = 200$ m/min, where the material adheres to the cutting edge followed by a peel-off, which does not happen at higher cutting speeds $v_c = 300 – 600$ m/min. It is also seen on the edge line of a (Ti,Al)N-coated tool when machining 316L in Paper II. Adhesive wear can also occur due to chemical bonding between the tool material and workpiece, driven by diffusion, chemical reactions, or both.

In operando tool protection

The use of non-metallic inclusions (NMIs) has long been the norm for improving the machinability of steels. Adding sulfur leads to the formation of sulfides such as (Ca, Mn)S while calcium treatments lead to the formation of calcium oxides, or combinations of Si, Al, and Ca oxides such as $Al_2Ca_2SiO_7$ in the steel [92]. These additions of Ca, S, and other non-metals also lead to the dissolution and embedment of hard oxides in soft non-metallic inclusions. This decreases the abrasiveness of the metal, improves chip formation, and hence improves machinability. But it also forms a protective deposit, sometimes called tribofilm, build-up layer, belag, or transfer layer on the tool surface, limiting tool wear as seen in Paper II. This protective effect of NMIs is well known [92–94].

There are, however, limitations. The addition of NMIs cannot be done for all materials since it decreases corrosion resistance, weldability, impact toughness, and fatigue strength [95]. These NMIs do not protect the cutting edge of the tool when the contact pressure is high, or at the periphery of the contact zone where the coating oxidation takes place (Paper II). NMIs also have to be optimized for specific tool materials and coatings, since CaO can react with oxide ceramics and coatings [23], as seen in Papers III and IV.

A more recent discovery is that of in-operando tool protection layers (TPLs) [43,62,65,96–101]. These TPLs are different from deposited inclusions or workpiece material. They consist of phases that form between the environment and tool and the workpiece, or chip materials during cutting. Examples include Al_2O_3 in Paper X, $Al_2(Fe,Cr)O_4$ in Paper IX, (Ti,Nb,Cr)N and Al-oxides in Paper XII and XIII, and (Ti,V)C, $(Ti,V)B_2$ in diffusion couples in Paper VI and during machining [98]. The W layer in Paper VI may be considered a TPL, but it is rather a layer formed due to an absence of a reaction with W after Co and C have diffused out of the tool (Paper VI and [98]).

TPLs form during machining due to interactions between the workpiece material, tool, and air. These work as barriers against chemical degradation, oxidation, and diffusion.

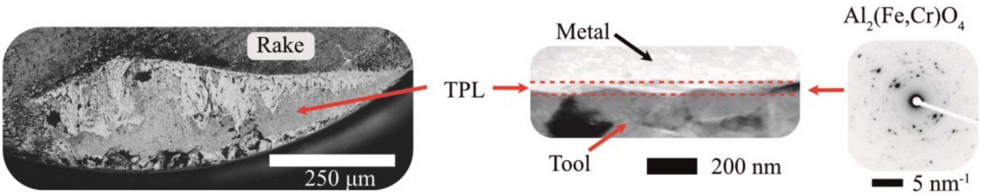

Figure 21. BSE-SEM image at low HV, HAADF-STEM, and SAED view of aluminum-rich oxide TPL forming on top of the pcBN tool in Paper IX.

TPLs, however, do not ease chip formation or decrease abrasiveness, and their thickness is usually measured in hundreds of nanometers rather than micrometers (Figure 21). But alloying or selecting tool materials and cutting parameters that lead to TPL formation does not have detrimental effects on the alloy's corrosion resistance, weldability, impact toughness, or fatigue strength. Furthermore, abrasive wear is often initiated and accelerated by diffusion, oxidation, and chemical degradation, as seen by the degradation of alumina coating in Papers III and IV. Hence, limiting these wear mechanisms can have larger effects than one might initially expect, as seen when removing oxygen [65] and consequently, TPL formation seen in Paper IX or the additions of Al in Paper X.

The difficulty with TPLs is that the tool, workpiece, and cutting parameters must be paired for TPL formation, while NMI inclusions have broader applicability. Hence TPLs are a new way to improve machinability when the use of NMIs is not appropriate.

Striking the right balance for TPL formation is crucial. A TPL will not form if the reactions are too slow, and the tool will wear fast if the reactions are too aggressive. The interaction between the tool, workpiece, air, or coolant must be properly balanced.

Tool Degradation and Protection

If you thought that science was certain – well, that is just an error on your part.

—Richard P. Feynman [102]

This section combines the previously explained methods and concepts to understand and limit tool wear as well as promote tool protection.

Diffusion, oxidation, and chemical degradation

Paper I examines how tool wear by adhesion, diffusion, oxidation, and chemical degradation changes with increasing cutting speed when machining 17-4 PH with coated and uncoated pcBN tools. The pcBN tool with a TiC binder experiences both flank and crater wear, with notch wear also detected but not limiting tool life. There is adhesion at low speeds (v_c = 200 m/min), and the crater wear becomes more aggressive as the speed and process temperature increase (v_c > 400 m/min, Figure 22b). A $(Ti_{0.45}Al_{0.55})N$ coating is applied to the PcBN tool, but it does not survive on the tool flank or rake, though it does protect the chamfer.

There are definite signs of oxidation as the tool becomes covered by a mixed layer of metal and workpiece oxides (Figure 22a), which thickens as the speed increases. This limits the adhesion seen at v_c = 200 m/min. TiO_2 or B_2O_3 would be the expected oxidation products when there is tool oxidation, but neither is identified on the tool surface. This is most likely because they are abraded away by the moving chip, though it is possible that they never form.

The cBN grains show preferential wear over the TiC binder (Figure 22a). The boron and nitrogen from cBN grains can diffuse and dissolve into the chip and potentially react with the workpiece to form borides and nitrides, in addition to oxidation. No nitrides or borides are identified. This could be because these never form due to the high solubility and mobility and hence high permeability of B, N, and C in stainless steel, or they may not be detected because they are abraded away.

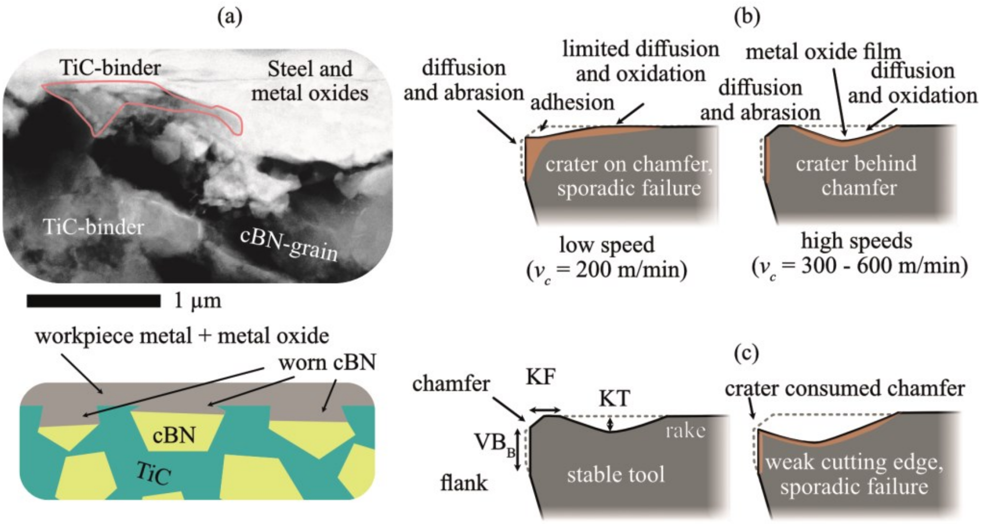

Figure 22. a) HAADF-STEM image of worn cBN-TiC tool with a schematic image showing preferential wear of cBN and oxidation, b) schematic image showing how the speed shifts the crater wear, c) schematic image showing how the growing crater weakens the cutting edge

Diffusion, oxidation, and chemical degradation is also present when machining with Si based tool materials in Paper IX. The thermodynamic modeling in Paper IX predicts that silicon-containing ceramic tools Si_3N_4, Al_2O_3-SiC_w, and SiAlON should fail due to oxidation and chemical degradation as well as diffusional loss when machining Hybrid Steel 55 (Figure 23a). C, Si, and N also have a positive driving force and high solubility in the steel. There is also a positive driving force for SiO_2 formation, and a positive driving force for the formation of softer mixed oxides with workpiece oxides such as Fe_2SiO_4 and Al_2SiO_5.

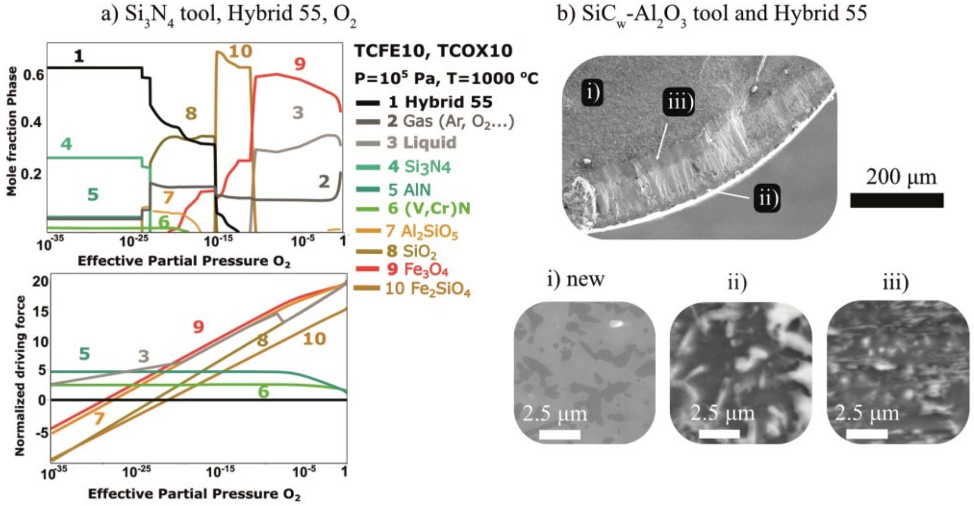

Figure 23. a) thermodynamic calculation showing potential degradation of Si-based tool materials, b) the corresponding chemical, oxidation, and diffusion wear of a Si-based tool material, adapted from Paper IX.

An example of this can be seen on the surface of the Al_2O_3-SiC_w, tool, where the whiskers are depleted from Si. Note the contrast change of the whiskers from i) to ii) and iii) in Figure 23b, and the formation of a glassy oxide layer Figure 23b iii). The silicon-containing ceramic tools then fail due to crater formation after very short engagement times.

Discussion and conclusion

The shift from adhesion to diffusion, oxidation, and chemical degradation is the expected shift in wear mechanisms with increasing speed [2,5,6]. But it is very difficult to determine the exact cutting parameters at which this shift occurs. Previous research on turning 17-4 PH and other martensitic stainless steels has mainly focused on the wear mechanisms of coated and uncoated cemented carbides. The recommended speed for turning 17-4 PH with cemented carbide is below v_c = 100 m/min [73]. Few comparable studies on turning exist [74], but one showed that machining at high speeds (v_c = 300–600 m/min) with pcBN can achieve a good surface finish. Hence, there was a knowledge gap in how to select and develop tool materials for the machining of this material at speeds above 100 m/min, and how coatings could be used.

The study on machining 17-4PH with pcBN in Paper I shows that the tool and coating combination performs well. The coating used decreases the adhesion at low speeds and protects the chamfer at all speeds, potentially leading to less sporadic failure, since the tool edge will collapse without a chamfer. This collapse also happens if a tool without a chamfer is selected or if the chamfer is consumed by the crater (Figure 21b). It also shows that the tool material has the required fracture toughness and abrasion resistance. But future work could focus on increasing fracture toughness, possibly through whisker reinforcement, which might make it possible to machine even with a larger crater, limiting the sporadic edge failure. New materials have to resist oxidation, diffusion, and chemical degradation, making Al-based binders promising. Investigating cutting conditions and tool materials that can form Cr, Nb, and Ta TPLs is another possible research direction.

The Hybrid Steel 55 in Paper IX is a recently developed alloy with unknown machinability, and a method to select the appropriate tool material is needed. Selecting tool material based on previous experience with similar materials might lead to suboptimal performance. This study demonstrates that the combination of modeling the oxidation of both the tool and workpiece, and their interactions in both unoxidized and oxidized steel, shows how one can understand and predict which tools are likely to perform well. Si-based tools should not be used for machining HY55 at speeds where the cutting conditions are such that diffusion, oxidation, and chemical degradation can occur at a high rate. Other tool materials such as cBN-TiC and Al_2O_3-TiC should be used instead, as shown in Paper IX and in the next sections.

Transfer layers

Papers II, III and IV investigated the interaction between non-metallic inclusions and coatings. The steel in Paper II is a 316L, an austenitic stainless steel which also contains MnS and various complex oxides $(Ca, Si, Al, Mg)_xO_y$ as engineered NMIs. The steel in Papers III and IV is 19MnVS6, a general structural steel containing various sulfides (Mn,Ca)S and oxides $(Ca, Si, Al, Mg)_xO_y$. The differences between the machining experiments were the workpiece material, the coating, and the use of coolant. Since both materials were machined under similar conditions (a_p = 1.5mm, f = 0.2 mm), the tool geometries and tool substrates were the same and tool holders provided the same cutting angles. 316L was machined only at v_c =185 m/min using coolant, and 19MnVS6 was machined at different speeds between v_c =100 to 600 m/min and dry. The cutting of these materials is at least somewhat comparable, but the interaction between the workpiece coating is the complete opposite.

Figure 24 illustrates how the NMIs protect the (Ti,Al)N coating in Paper II, while the NMIs consume the Al_2O_3 coating in Paper III. Papers II, III, and IV model these interactions to suggest how to better pair NMIs, workpiece material, cutting conditions, and coatings.

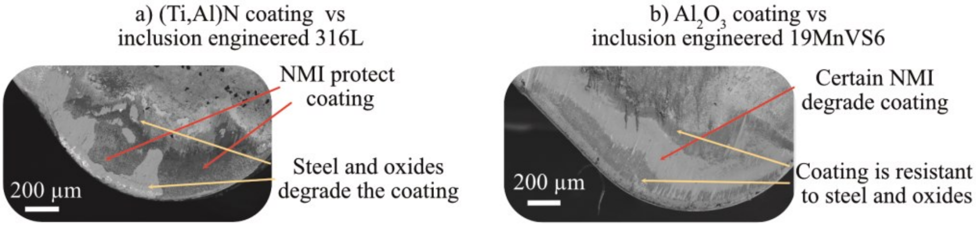

a) (Ti,Al)N coating vs inclusion engineered 316L

b) Al_2O_3 coating vs inclusion engineered 19MnVS6

Figure 24. a) The (Ti,Al)N is protected from oxidation and chemical degradation by workpiece oxides as well as diffusion by protective NMI, b) Al_2O_3 is resistant to oxidation, diffusion, and chemical degradation by steel, while reactions between the Al_2O_3 coating an NMI and oxidized steel result in a degradation of the Al_2O_3 into softer aluminates. Images adapted from Papers II and III.

Paper II shows how (Ti,Al)N coatings can suffer from oxidation, diffusion, and chemical degradation when machining steels. The deposition of NMIs on the rake during machining hinders these degradation routes, in addition to providing other machining benefits.

The Al_2O_3 in Paper III and IV is on the other hand a very stable phase. It does not measurably react with the steel after 10 minutes in a diffusion couple even at 1300°C and 2.5 GPa. It is not thermodynamically impossible for a reaction to occur depending on the workpiece alloying, especially in machining where there is a constant supply of material, but the solubility of workpiece elements in Al_2O_3 is not comparable to what happens when iron oxides or Ca and Mg oxides are present. Oxides and sulfides of Ca, Mg, Si, and Fe can all react with and degrade the Al_2O_3 coating. This degradation is strongly driven by thermodynamics, as verified using SEM and TEM in both in diffusion couples and machining experiments in Papers III and IV. The worn rake of the Al_2O_3-coated tool (Figure 24b) appears as an inverse image of the worn rake of (Ti,Al)N (Figure 24a). The Al_2O_3 coating remains almost intact at the edge line and the periphery of the contact zone, while NMIs attack the Al_2O_3 coating in the middle of the contact zone.

Discussion and conclusion

Both alloys are very machinable with both coatings. There are, however, both limitations and possible improvements when pairing coatings with inclusion-engineered steels using thermodynamic modeling.

Thermodynamic models of (Ti,Al)N coatings are not straightforward since (Ti,Al)N has a metastable fcc structure, while TiN is fcc and AlN is hcp at equilibrium. The hcp phase needs to be suppressed in the calculation to force (Ti,Al)N to appear as an equilibrium phase in the calculations. Alternatively, the coating can be modeled as AlN (hcp) and TiN (fcc), though this overestimates the stability of the coating. Hence, if TiN and AlN are not stable, then (Ti,Al)N is definitely not stable, and this approach was used in Paper II.

a) (Ti,Al)N, 316L and O_2 - Calculation

	O_2	316L	NMI : $Mg_1Al_2O_4$ / $Al_2Ca_2Si_1O_7$
TiN	Ti_xO_y	Cr react with coating Ti, N diffuse into steel	Stable coating
AlN	Al_2O_3	Al, N diffuse into steel	Stable coating

b) (Ti,Al)N, 316L and O_2 - TEM

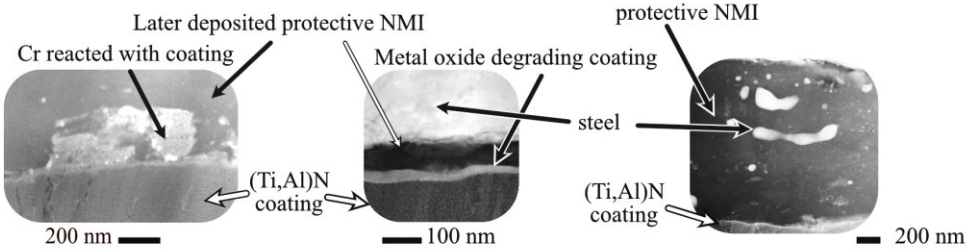

Figure 25. a) Results from thermodynamic calculation of the interaction between the (Ti,Al)N coating, 316L, oxygen, and NMI. b) HAADF-STEM images of the same interactions on the rake of the tool after machining. Adapted from Paper II.

The thermodynamic equilibrium calculations and TEM analysis show that the coating does not react with NMIs such as $Mg_1Al_2O_4$ and $Al_2Ca_2SiO_7$, which were present in the rake (Figure 25). Both the thermodynamic calculations and TEM results show that the elements in the steel can react and chemically degrade the coating and coating elements can diffuse into the workpiece chip (Figure 25). The coating can oxidize according to calculations (Figure 25 and Paper II). The (Ti,Al)N experiences mechanical adhesion, delamination, chemical degradation, and diffusion at the edge line, as well as chemical degradation and oxidation in the periphery of the contact zone (Figure 24a and Paper II). But it is protected from oxidation, diffusion, chemical and mechanical wear in the rake by the NMIs. Creating more favorable conditions for the tool edge and periphery of the contact zone is therefore important to avoid delamination and coating oxidation because the middle of the contact zone, which is usually prone to crater wear, is protected by the NMIs (Figure 24a and Figure 25).

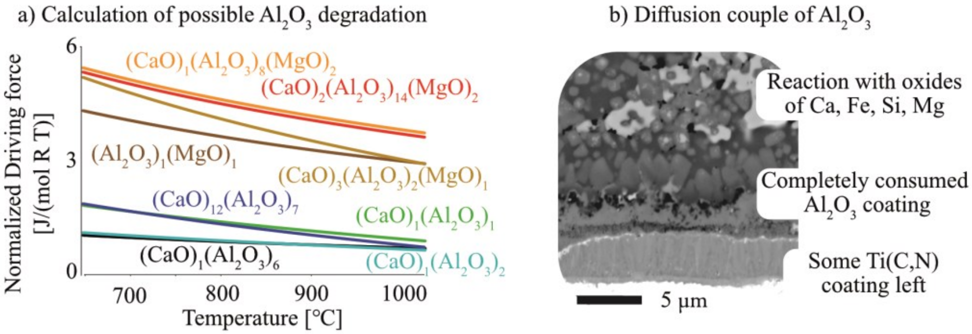
a) Calculation of possible Al_2O_3 degradation

b) Diffusion couple of Al_2O_3

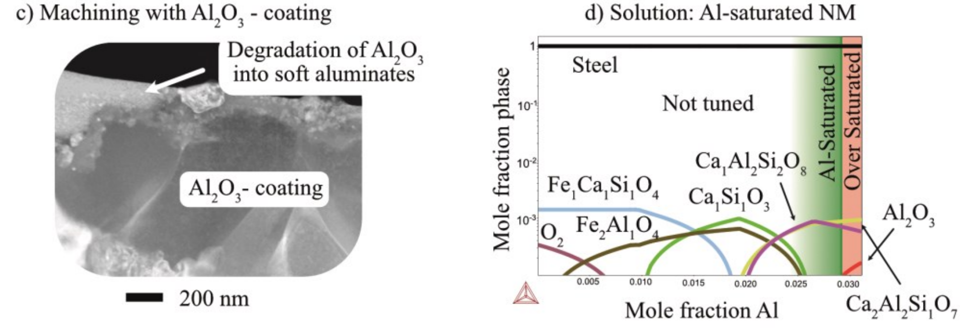
c) Machining with Al_2O_3 - coating

d) Solution: Al-saturated NM

Figure 26. a) Thermodynamic calculations show that there is a positive driving force for the degradation of the Al_2O_3 coating by reactions with NMI such as Ca and Mg oxides, b) diffusion couple BSE-SEM image of the complete degradation of Al_2O_3 due to reactions with Ca, Fe, Si, and Mg oxides, c) TEM image of Al_2O_3 coating degradation due to reactions with NMI during turning, d) thermodynamic calculations show that Al-saturating of the NMI is possible in this steel, which will limit the coating degradation. Adapted from Paper III and IV.

The case is the opposite for the Al_2O_3 coating. It is a stable equilibrium phase under these conditions and it does not react measurably with the alloy compared to (Ti,Al)N. NMIs, however, thermodynamic calculations, diffusion couple experiments, and TEM images of used tools show that NMI react with the coating and degrade it into soft mixed oxides (Figure 26a-c). Hence, Al_2O_3 should be used when machining clean steels, or the NMI inclusions can be Al-saturated, such as $Ca_1Al_{12}O_{19}$, $Ca_1Al_2Si_1O_7$, and $Ca_1Al_2Si_2O_8$ (Figure 26d and Paper IV). Aluminum saturation of NMIs is possible for this steel (Figure 26d), this would hinder the NMI from reacting with the coating, and this is also possible without the formation of Al_2O_3 in the steel, which would otherwise be very abrasive. The Al-saturated $Ca_1Al_{12}O_{19}$ inclusion is also the high melting point NMI that are preferred at high cutting speeds [103].

Cobalt diffusion and W protection

It is well known that Ti-alloys have high strength and toughness. They are also adhesive during machining and have low thermal conductivity. Ti-alloys also readily react with many elements, and many elements can diffuse and dissolve into Ti-alloys at high rates. This combination of properties and conditions results in high temperatures, high pressures, and high chemical loads on the tools when machining Ti-alloys [79]. There are no abrasive particles or inclusions in the T-alloys studied in Papers V and VI. The wear mechanisms during turning are mainly diffusion and chemical degradation, combined with tough mechanical loads that lead to tool failure. The tool is also intermittently exposed to coolant and oxygen during milling in Paper V, shifting the wear balance more towards oxidation and cracking due to thermal cycling and cyclic mechanical loading.

Combining the results from thermodynamic calculations, diffusion simulations, diffusion couples, turning, and milling experiments of Ti-alloys with cemented carbide provides a detailed insight into the wear mechanisms. The diffusion couples, thermodynamic calculations, and diffusion simulations show how both C and Co diffuse into the Ti-alloy (Paper V and VI and Figure 27 and 28). What is interesting is that the permeability for C (an interstitial element) is not always more than Co (a substitutional element). This is because the solubility of Co in the β-phase of Ti is high compared to C, and their mobilities are comparable (Figure 27b). C can diffuse both through the Co binder and from the WC grains into the Ti-alloy. This diffusional loss of Co and C can continue indefinitely if there is fresh workpiece material passing over the tool surface. However, adhesion and the formation of a diffusion barrier can slow this down.

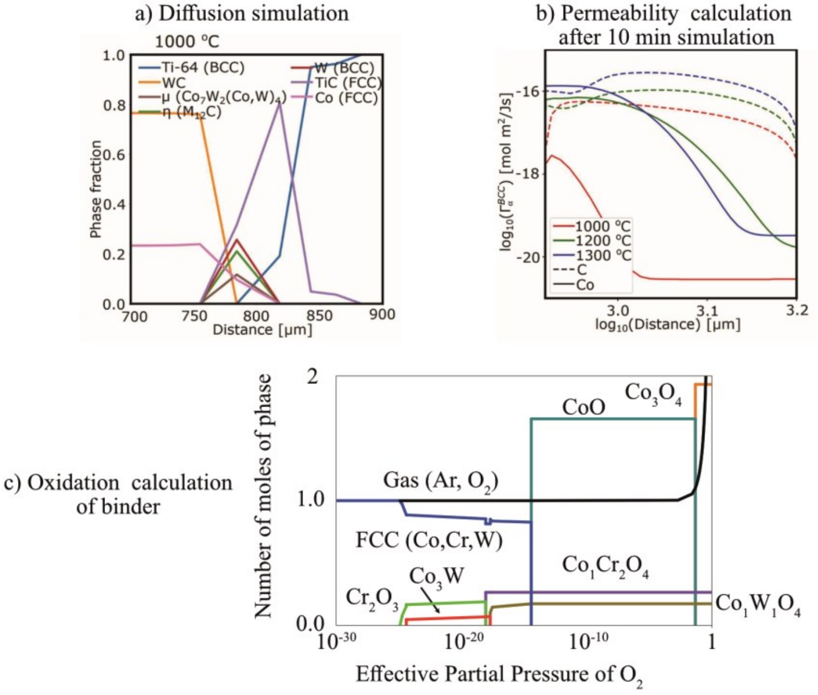

Figure 27. a) Modeling diffusion of WC-Co in Ti-64, b) calculating the permeability of C and Co in Ti dependent on distance (concentration) and temperature, c) modeling the different possible tool oxides during milling of Ti-alloys, adapted from Papers V and VI.

A TiC and (Ti,V)C barrier can form in diffusion couple experiments (Figure 28a), but the protective mechanism of these carbides is not as prominent when investigating worn tools in these papers and other machining studies [104,105]. This can be because the solubility limit of C in the Ti-alloy is not reached during machining or because TiC is removed away by the chip flow, if not attached strongly to the tool. The reason for more TiC formation in diffusion couples than during turning and milling is that there is a constant influx of new material when machining, while the diffusion couple is static. This is also discussed in Paper V concerning Ti-5553 and WC-Co, as well as for other tool materials. In consequence TiC can form in the presence of adhered workpiece materials, but it is less likely to form if the adhesion layer is not stable.

The C and Co loss results in excess W (Figure 27a, Figure 28a, and Paper VI). This can result in metallic W forming, intermetallic Co-W phases, or η-phase carbides (M_6C and $M_{12}C$) (Figure 28a and Paper VI), which form first and which remains stable depends on the temperature and nucleation rates of the phases and the permeabilities of Co and C at the specific temperatures and cutting conditions. The metallic W can function as a diffusion barrier limiting Co and C loss. The intermetallic Co-W phases or η-phase carbides form mainly on the grain boundaries of the WC grains and are probably very brittle, not providing stable protection

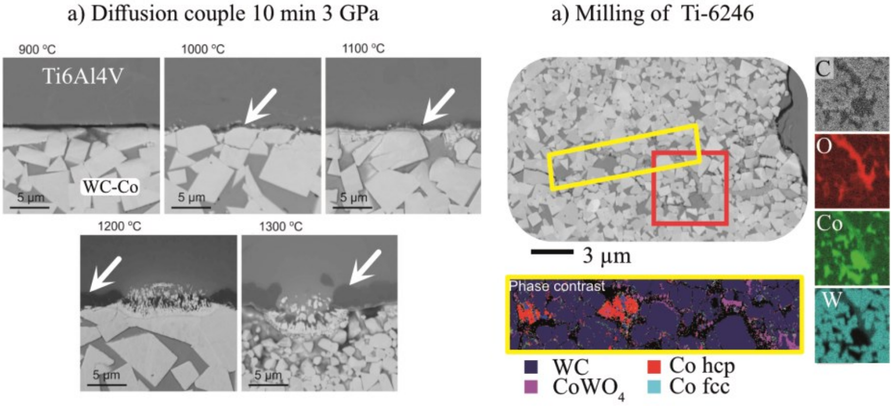

Figure 28. a) BSE-SEM images of diffusion couples between WC-Co and Ti6Al4V at different temperatures, resulting in the formation of TiC, Co (hcp),W, Co_3W_3C, and Co_6W_6C, b) BSE-SEM, XEDS, and EBSD images of the oxidation of WC-Co during milling of Ti-624, which resulted in the formation $CoWO_4$. Adapted from Paper V and VI.

The cyclic loading of the tool and the thermal cycling during milling, together with tool oxidation, diffusion, and chemical degradation, lead to large cracks (Figure 28b). The formation of $CoWO_4$, detected in the cracks, results from oxidation of the Co binder with dissolved W (Figure 27c and Figure 28b). The formation of this phase leads to a volume increase, aiding crack propagation. The WC grains also become rounded due to C diffusion, while Co is transformed into more brittle hcp. Furthermore, the loss of Co, either by diffusion or embrittlement, leads to voids between the WC grains, resulting in grain pullout by adhesion.

Discussion and conclusion

It is important to limit Co and C diffusion, as well as oxidation, during both turning and milling of different Ti-alloys, as shown in Papers V and VI. The metallic W can function as a diffusion barrier to some extent. But we need to understand the difference between the α-phase and β-phase of Ti and the relation between the permeability of Co and C in order to understand how to limit diffusion and oxidation.

The β-phase presents several challenges from a machining perspective. More β-phase leads to a more ductile and adhesive material with higher tensile strength, resulting in harsher cutting conditions. Additionally, the mobility of the tool elements Co and C in the β-phase is also higher than in the α-phase, leading to more diffusional wear. The physical and chemical properties of the β-phase mean that the cutting speed and machining performance had to be lowered during milling for the near-β alloy Ti-5553 compared to the α + β alloy Ti-6246, which was also more difficult to machine than near-α alloy Ti-6242, when doing the milling experiments in Paper V.

Oxidation was most prominent during milling of the α + β alloy Ti-6246. Milling Ti-5553 at a lower speed and milling the more machinable α alloy Ti-6242 likely resulted in lower process temperatures and less oxidation. The limited ingress of oxygen into the contact zone during turning of α + β Ti-64 limited the oxidation. Oxidation seems to be mainly a problem when milling under aggressive conditions, leading to high temperatures.

The only oxide detected using SEM, XEDS, and EBSD was $CoWO_4$. This phase remains stable everywhere except in the W-rich corner of the W-Co-O ternary phase diagram at 900°C (Figure 27c). Although this phase has neither the highest driving force nor is the first phase that forms at the lowest oxygen partial pressure. Other oxides may have formed but were either abraded away or remain undetected. All oxide formation leads to volume expansion, which aids crack propagation. Avoiding this oxidation would require either machining below the temperature at which oxidation is rapid or developing more oxidation-resistant binder systems.

Limiting diffusion would either require developing binders with less solubility and mobility in Ti-alloys or promoting the W layer or carbide TPLs. Saturating the Co binder with W and C to form more W layers and TiC is difficult while still being able to sinter the tools without graphite or η-phase formation. Alternatively, switching the hard phase from WC to diamond could increase the chances of carbide TPLs, as shown in the next section.

Tool protection layers

Carbide and boride TPL

Using cemented carbide while milling different Ti-alloys in Paper V and turning in Paper VI showed how the tools suffered from loss of C and Co due to diffusion and oxidation. The excess W created a slight diffusion barrier. The formation of TiC in diffusion couples showed promise as a diffusion barrier, but its formation was marginal in the actual cutting experiments [104,105]. Using diamond as a hard phase instead of WC significantly increases C activity. This results in more

TiC formation in both diffusion couples and simulations. The higher carbon activity in polycrystalline diamond (PCD) compared to cemented carbide should make the formation of TiC tool protection layers (TPL) more likely during machining. Paper VI includes diffusion couple, microscopy, thermodynamic and kinetics modeling, and machining tests comparing cemented carbide and PCD. These results show how Ti-rich carbides can act as TPLs when machining with PCD. In-depth microscopy of the TiC and (Ti,V)C layers during turning with a similar PCD grade can also be found in a different study [98].

Understanding how diffusion and reactions change between diffusion couples, turning, and milling, along with the effect of adhesion and chip flow, make it possible to translate diffusion couples and simulations into machining applications. Conclusions can therefore be drawn about the effect of changing the hard phase, binder, or machining alloys with different α + β ratios, or changing cutting conditions from thermodynamic calculations of chemical activities, solubilities, mobilities, and permeabilities, as well as diffusion simulations.

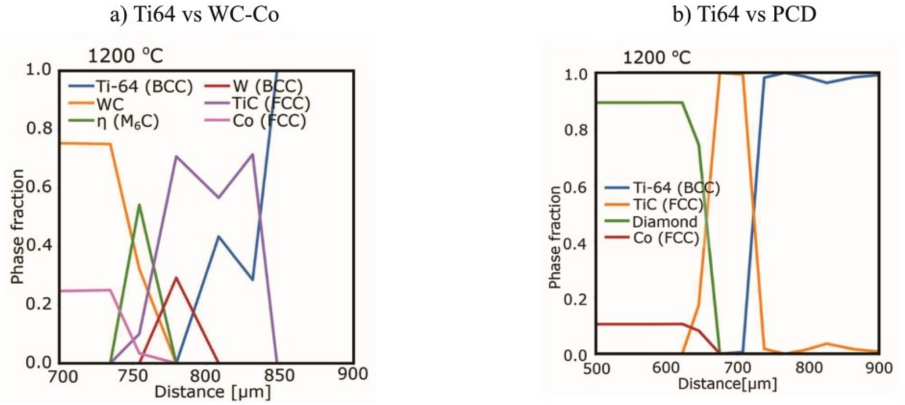

Figure 29. Ti-64 diffusion simulation at 1200 °C after 10 min for a) WC-Co and b) PCD, showing how there is a much stronger tendency to form TiC with PCD, which is in agreement with both the diffusion couples and machining experiments Paper VI and [98].

It is well known that machining any nickel- or iron-based alloys with diamond is usually catastrophic, with some exceptions. But could it be possible to form a carbide TPL in Ni- or Fe-alloys and machine with PCD or at least carbide TPL when machining with cemented carbide? It might be possible if the alloys were carbon saturated or have low carbon mobility, such as ferrous alloys with high amounts of cementite or graphite. But none of these were studied in this work. Instead, nitride, boride, and oxide TPLs are explored as possible solutions when machining Ti-alloys, Ni-alloys, and Fe-alloys in the appended papers.

Boride, nitride, and oxide-based TPL

Studying the interaction between Ti-alloys and pcBN is a bit different than WC-Co and PCD. Boron, much like C in WC-Co and PCD, has a low solubility in the β-phase. But both B and N in pcBN have higher permeability in the β-phase than Co. B has higher mobility in the β-phase than N, while N has a higher solubility. Therefore, the permeability of B versus N depends on the alloy's saturation and temperature, as shown in Paper V. These variations in solubility, diffusivity, and consequently permeability make for some interesting results when comparing diffusion couples and machining. Nitrides form in diffusion couples, but they might not form during machining without major adhesion since the solubility limit is high. In contrast, borides form both in the diffusion couple and during machining since the solubility is low and mobility is high. This is verified by diffusion couples, simulations in Paper VI. Further in-depth microscopy of the Ti-rich borides during machining with a similar pcBN grade can be found in a different study [98].

Turning Hybrid Steel 55 with Si-based tool materials at certain cutting conditions results in temperatures that allow for oxidation, diffusion, and chemical interactions, leading to rapid tool degradation. (Ti,Al)N-coated cemented carbide, Al_2O_3-TiC ceramics, and pcBN with TiC binders perform rather well.

TiC, BN and (Ti,Al)N, and WC-Co can all suffer from oxidation, diffusion, and chemical degradation at high temperatures. But the oxides that have the highest driving force to form are not glassy Si-based oxides, such as Fe_2SiO_4 and Al_2SiO_5, but refractory Al-based oxides, such as $(Fe,Al,Ti)_2O_3$ and $(Fe,Al,Ti)_3O_4$. Machining with the (Ti,Al)N-coated cemented carbide tool leads to almost no crater wear initially, as chemical and diffusional mechanisms are suppressed or slowed down by the TPLs. But pits formed on the rake and the tool edge as a result of coating loss due to adhesion wear, which lead to a tool failure as these pits grow, coalesce, and rapidly developed into crater wear (Figure 30).

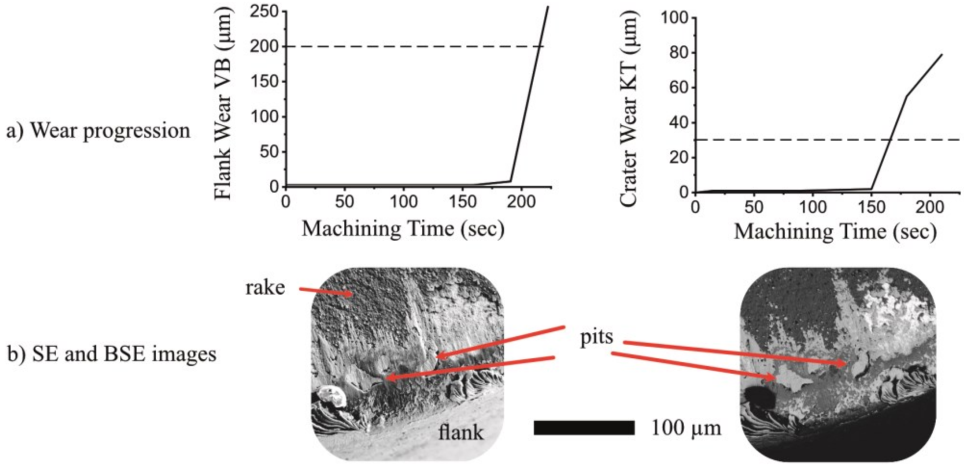

Figure 30. The wear of (Ti,Al)N when machining Hybrid 55 is very limited until the pits coalesce leading to rapid failure.

Machining with cBN-TiC performs the best, and Al_2O_3-TiC performs well (Paper IX). There should be a speed (temperature) and oxygen effect (Figure 31a) on the TPL formation as predicted from calculations (Paper IX). This is confirmed by temperature measurements and machining at different speeds and by machining in a chamber with Ar flow to suppress oxygen (Figure 31 b and c). No TPL forms at low speeds (v_c = 50 m/min), due to the low temperatures. Lowering the oxygen availability also prevents TPL formation, which leads to adhesion and tool fracture. This is also shown in the performance tests (Figure 31d)

a) Thermodynamic calculation of interaction and TPL formation between PcBN, HY55, and O_2

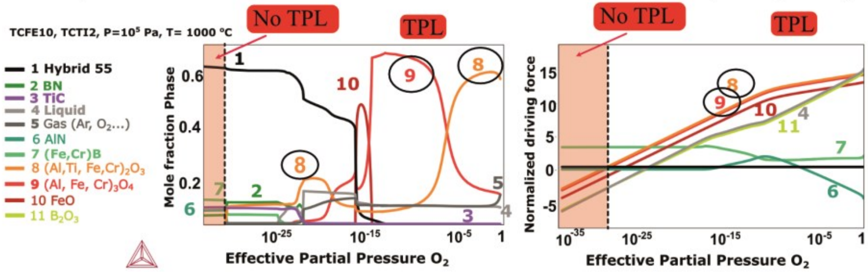

b) Speed (temperature) effect on TPL

c) Effect of O_2 on TPL

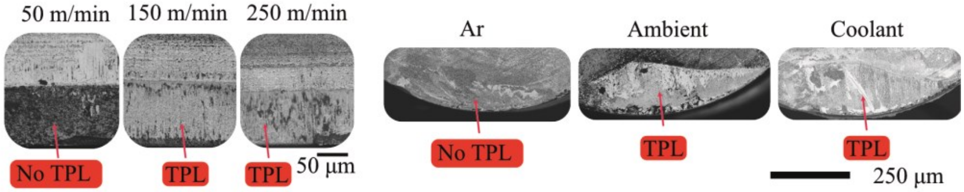

d) Machining result (v_c = 300 m/min, f = 0.1 mm/rev, a_p = 0.3 mm)

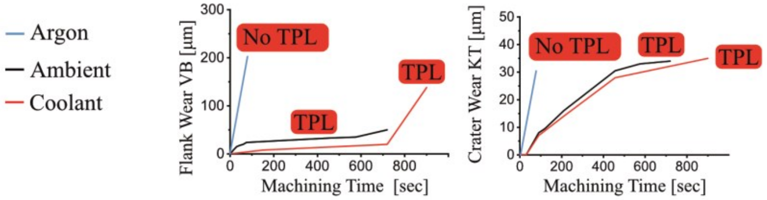

Figure 31. There is a minimum process temperature (cutting speed) required and there is a minimum oxygen activity needed for the formation of a TPL. Shown by a) thermodynamic calculations, and confirmed by b) cutting at different speeds, c) machining in different environments and d) performance tests, adapted from Paper IX.

Alloy 718 (Inconel 718), contains many elements that can form borides, nitrides, and oxides, such as Cr, Mo, Nb, Ti, and Al. A718 then has the potential to form oxide, nitride, and boride TPLs with pcBN tools. The positive effect of oxygen when machining A718 with pcBN has been shown previously [65]. The solubility of B and N is low in A718, but the mobility of B is slightly higher than N. Boron reacts with oxygen to form B_2O_3, which melts around 450°C, BN is stochiometric, thus N forms N_2 gas. These reactions occur at rather slow rates below 800°C [89], but constant abrasion can destroy the passivation B_2O_3 film seen in oxidation experiments [89]. However, the pressure in the cutting zone can reach several GPa, which would stabilize cBN, borides, and nitrides. This is seen in Paper VII, where we compared vacuum annealing (10^{-1} Pa) of powders with high pressure annealing ($2.5{\cdot}10^{9}$ Pa) using in-situ EDXRD, high-pressure diffusion couples ($2.5{\cdot}10^{9}$ Pa), and thermodynamic calculations. The diffusion and interaction experiments in Paper VII show how cBN grains can diffuse into the Ni-alloy at a higher rate than the TiC binder, similar to the machining experiments of 17-4PH in Paper I. But nitrides of Ti and Nb and borides of Cr, Mo, and Nb as well as Al_2O_3 form during these experiments. The turning experiments in Paper VIII with a similar tool material show that the Al_2O_3 and $(Al,Cr,Ti)_3O_4$ spinel, as well as (Ti,Nb,Cr)N, are the main contributors to the formation of TPL (Figure 32). Limited borides form because the mobility of B is high and because there is high chip flow and not as much adhesion as when machining Ti-alloys.

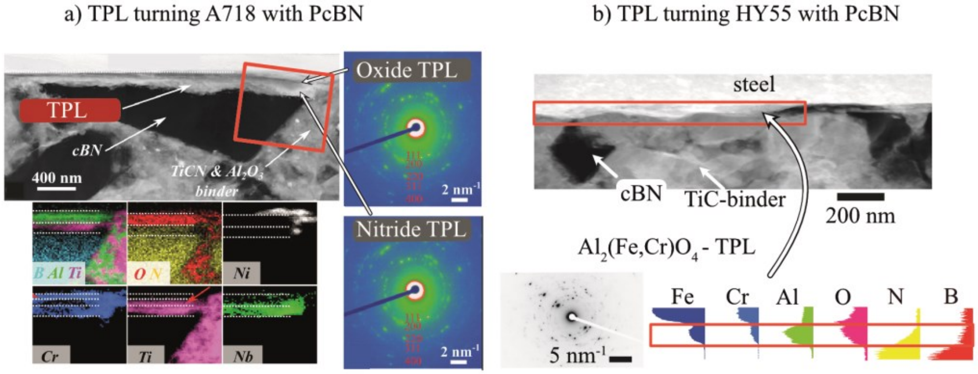
a) TPL turning A718 with PcBN

b) TPL turning HY55 with PcBN

Figure 32. HAADF-TEM, SAED, TEM-XEDS of TPLs, a) sandwich TPL of nitrides (Ti,Nb,Cr)N and oxides γ-Al_2O_3 / $(Al,Cr,Ti)_3O_4$, on pcBN tools during machining of Alloy 718, b) an oxide $Al_2(Fe,Cr)O_4$ TPL on top of pcBN tool during machining of Hybrid 55

Discussion and conclusion

The solubility and mobility of tool elements such as C, B and N in the alloys must be low for a TPL to form, or there must be a lot of workpiece adhesion, so the solubility limit is reached. Oxide TPLs are preferable if they form due to workpiece oxidation rather than tool oxidation, as tool oxidation leads to wear. High melting point oxides are favored over soft glassy phases. Thermodynamic equilibrium calculations and calculating the normalized driving force has proven to be a good approximation for what will form in the cutting zone. The addition of pressure to modeling is important when assessing if an element will form a liquid or gas, as well as when comparing different phases with different molar volumes and compressibility.

Turning and milling are complicated processes, and we cannot model and measure the exact temperature, pressure, workpiece material flow, and wear rate. We can, nonetheless, optimize the tool binder, hard phase, and cutting conditions to promote TPL formation based on thermodynamic and kinetic modeling. We can also use electron microscopy and thermodynamics to translate results from diffusion couple studies to machining. Machining tests are needed, but the number of tests needed for finding optimal tool, workpiece, and cutting data combinations can be greatly reduced through the use of modeling.

Machining Ti-alloys with PCD-Co instead of WC-Co leads to more TiC, which acts as a TPL due to increased carbon activity. Using Si-based ceramics to machine Hybrid 55 leads to glassy silica-alumina oxides and aggressive crater wear, while machining with (Ti,Al)N, Al_2O_3-TiC, and cBN-TiC produces Al_2O_3 and Al_2FeO_4 TPLs. Si-containing tools should thus only be used to machine Hybrid 55 at low speeds, that do not lead to oxidation and diffusion, while (Ti,Al)N coated can only be used at high speeds as long as the coating is intact. In contrast, pcBN and Al_2O_3-TiC perform well under cutting conditions where oxidation, diffusion, and chemical degradation are active, both with and without coolant. A718 has the alloying to potentially form borides, nitrides, and oxides, but boride TPLs do not form due to the high chip flow and high mobility of B. The formation of nitrides is dependent on the high contact pressures, since N_2 is more stable at low pressures.

Both understanding and predicting the effects of changing the workpiece composition, tool material, and cutting conditions allows for much more extensive and faster screening of new workpiece-tool combinations and their optimal cutting conditions.

Machinability improvement by TPL alloying

Some research is available on the machining of high manganese austenitic steels, commonly called Hadfield steels [106], but very little has been done on machining using pcBN [107]. Machining with pcBN is common in industry to reach high material removal rates. The initial alloy contains Fe, Mn, C, Si, and Cr as well as some trace elements. It has very poor machinability and is used in safes and locks as an anti-saw and anti-drill material, but its main use is in heavy industrial applications and the rail industry. This is because it work hardens under impact, resulting in an increase in hardness from around 200 HV to around 450 HV, due to the transformation from austenite (fcc) to mainly ε-martensite (hcp) and some α'-martensite (bcc).

The tool material in the study is a high-cBN (90%) pcBN grade with an Al-based binder. The tool experiences a combination of crater and flank wear. The crater wear weakens the cutting edge, which accelerates flank wear and occasionally leads to catastrophic tool failure where the whole cutting edge collapses.

The aim of Paper X is to alloy the original manganese steel material so that a TPL can form to protect the tool from oxidation, diffusion, and chemical degradation. Alloying the original material with Al, Ti, V, Zr, Mo, Nb, and Ta, which are the eight most promising nitride, boride, and oxide-forming alloying elements, in steps of 0.1 at % from 0 to 3%, results in around $8.5\cdot10^{11}$ combinations. Being efficient and only testing with a fixed amount for every element would result in 255 semi-random combinations. This is still a very large number of alloys to cast and do machining tests with. Many of these 255 alloys would be unoptimized and of limited value. Previous literature can help, but a lot of testing would still be needed.

Computational power is then needed, but $8.5\cdot10^{11}$ is almost a tera-number of combinations, so brute force is possible but not wise. This is just for modeling the tool material against the alloy at one machining process condition. As a top up, changes in temperature, pressure, and oxygen availability will further need to be accounted for to evaluate the onset of diffusion, oxidation, chemical degradation, and TPL formation.

We know that the Hadfield steel must be fully austenitic after quenching, containing a limited number of carbides, and should work harden during its use. Alloying cannot compromise the abrasive wear resistance and should not lead to excessive carbide formation. The alloying should also lead to a decrease in the permeability of B, N, and Al as well as to the formation of nitrides, borides, and oxides that are stable at cutting temperatures, pressures, and in a normal atmosphere.

The first step was to determine the maximum amount of alloying that does not lead to carbide formation at the quenching temperature, which means calculating the maximum solubility of different alloy elements in the steel. This brings the number of combinations down from $8.5\cdot10^{11}$ to 184 million. The second step is to see what carbide-free combinations do not significantly change the work hardenability of the material, modeled by a change in stacking fault energy. This brings the number of combinations down from 184 million to 13 million.

a) Diffusion couple of reference material

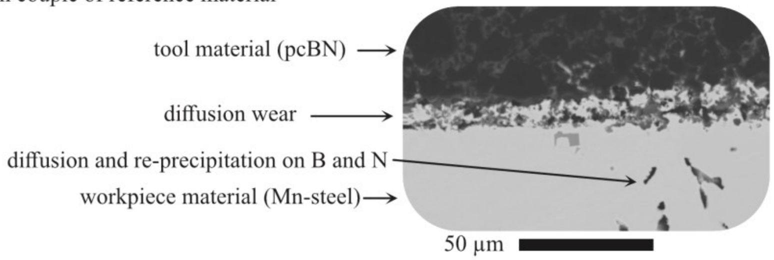

b) Diffusion couple of Al-alloyed reference material

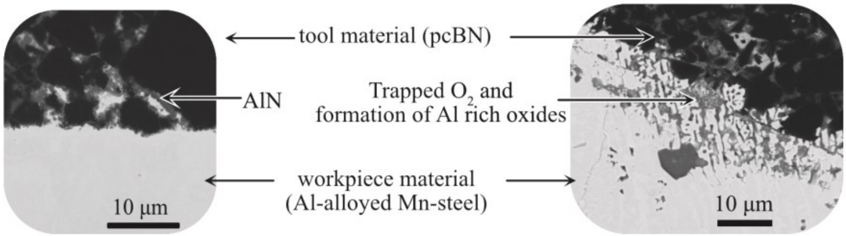

Figure 33. Diffusion couple between a) reference alloy and cBN-Al_2O_3 tool, resulting in major diffusional loss of cBN and even reprecipitation of BN more than 50 µm into the steel, while b) Al-alloying leads to AlN and alumina oxide formation and limited diffusional loss of cBN.

Modeling only the 255 maximum alloyed versions of these 13 million acceptable combinations against the tool material shows that only alloying with Al is very promising, as it lowers the solubility of all tool elements and forms oxides, borides, and nitrides. But it also shows that alloying with combinations of Al, Ti, Nb, and V shows some promise, while Zr, W, and Ta are too strong carbide formers and Mo forms a non-promising $(Fe,Mo)_2B$. The maximum single-element alloys were also verified by diffusion couples (Figure 33).

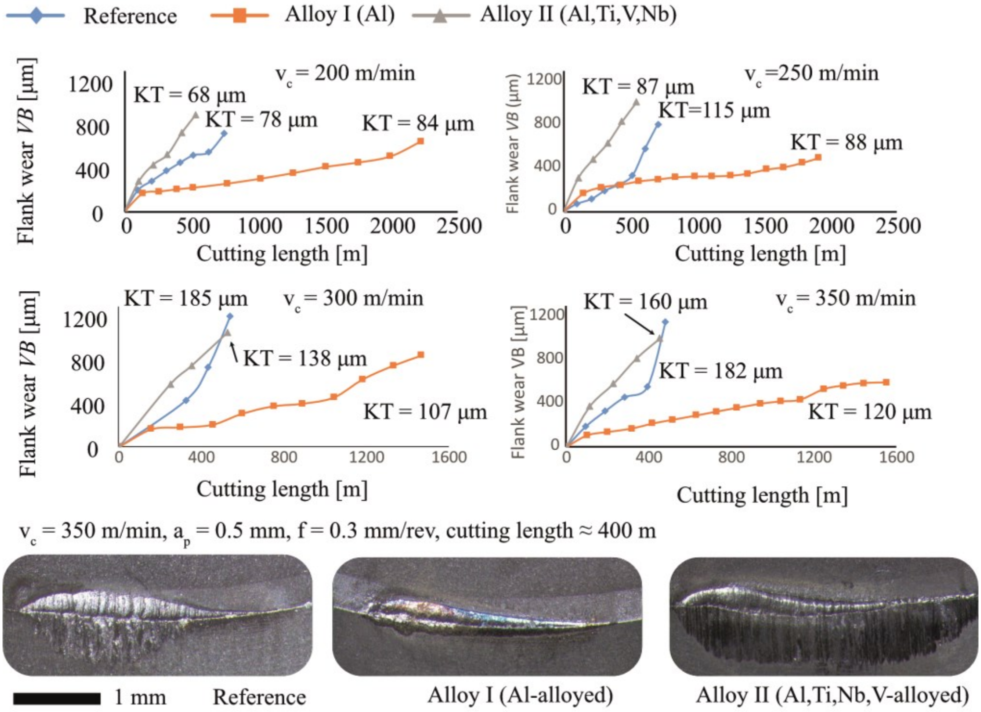

Figure 34. The Al alloyed Alloy I results in the same mechanical properties and abrasion resistance as the reference but leads to a TPL formation and less tool wear, the carbide formation in Alloy II leads more flank wear at low speeds, but less crater wear at all speeds.

This brings the total down from 13 million to 840 very promising combinations. The calculations verified by diffusion couples have narrowed the interesting alloying elements from eight to one very promising element (Al) and an additional three reasonably promising elements (Ti, Nb, V). A lot of casting and machining tests would still be needed if we want to evaluate all options in increments of 0.1 at %, but this level of precision is not necessary given the insights gained from the calculations. The calculations showed the maximum amount of alloying that can be quenched, is abrasion-resistant, and is likely to form TPLs. The maximum amounts are extremes, as they require perfect quenching, may still lead to some carbide formation, and push the limits of how much one should change the stacking fault energy.

We therefore decided to cast a reference, a moderately Al-alloyed (0.30 at. %) version and an Al, Ti, Nb, and V alloyed from the same melt, by consecutive alloying. This modeled set of 840 interesting combinations could be compared to $8.5 \cdot 10^{11}$ possible combinations at the start, and the set of two tested combinations could be compared to the 255 combinations "maximum alloy" combinations.

The change in hardness, structure, and abrasion resistance was not significant between the reference and Al alloyed versions. An increase in Si was detected in the Al, Ti, Nb, and V alloyed material due to the slight collapse of the lining during casting. This led to the formation of abrasive carbide particles in the Al, Ti, Nb, and V alloyed material (Alloy II). This resulted in similar or slightly increased flank wear, but the crater wear decreased, and the wear was more predictable and stable, for this over alloyed case (Figure 34).

However, both the reference and the Al-alloyed (Alloy I) was casted successfully. The tool life more than tripled between the reference and the Al-alloyed (Alloy I) version (Figure 34), due to the formation of alumina TPL during cutting (Figure 35) as predicted in Paper X, also in agreement with the diffusion couples (Figure 33).

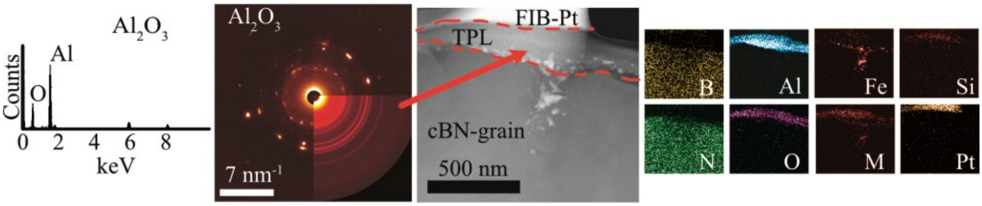

Figure 35. STEM-XEDS point measure, TEM-SAED, HAADF-STEM, and STEM-XEDS maps of alumina TPL formed on the tool during machining of Alloy I (Al-alloyed Mn-steel), due to alloying according to Paper X, resulting in improved machinability (Figure 34). Figure adapted from Paper X.

Discussion and conclusion

Paper X shows that it is not only possible to understand and predict wear mechanisms during cutting using thermodynamics, but also to predict which alloying, tool material, and pressure and temperature ranges will support the formation of a TPL. This allows for very efficient screening and a new method for improving machinability.

This approach could potentially be used for pairing other alloys and tool materials. By understanding the limitations on how much an alloy and tool can be changed without degrading other properties such as hardness, corrosion resistance, or fracture toughness. The accuracy of this modeling will continue to improve when combined with other modeling methods and as measurement accuracy and our understanding of tool wear increases.

Conclusions

> *Yesterday is history, Tomorrow is a mystery, but Today is a gift. That is why it's called the Present.*
>
> —Grand Master Oogway [108]

Combining in-operando machining measurements (Papers III and IX) with in-situ imitational studies (Papers VII), post-mortem microscopy (Papers I-X), and thermodynamics (Papers II-X) allows for a deeper understanding of in-process interaction and tool wear occurring in machining. Thermodynamic modeling and kinetic simulations are crucial in steering the experiments and microscopy that should be performed. They can also serve as tools to explain observed experimental results and microscopy findings.

The in-situ experiments in Paper VII, as well as the high-pressure and high-temperature diffusion couple experiments in Papers IV, VI, VII, and X, would have been much easier to perform at ambient pressure. Ambient pressure does not result in, for example, the formation of nitrides, as nitrogen tends to form N_2 gas at low pressure. High-pressure experiment must then be conducted to imitate the in-process interaction during metal cutting which indeed has the contact pressure present for nitride formation Paper VIII. Measuring the in-operando temperature in Papers III and IX or machining in Ar in Papers III and IX is not a trivial task, but calculations show that temperature and oxygen availability are key to the onset of both wear and protection phenomena.

Furthermore, combining advanced microscopy, experiments, and modeling provides new insights into in-process interactions. Because how can we determine what happened when the material we want to study has abraded away or diffused into the chip? SEM, TEM, and APT can show us the results from interactions at a nanoscale or even with atomic resolution but not in-process events. But combining these techniques with thermodynamics can fill in the gaps. The opposite is also true, we cannot possibly model everything, so we need to know what to focus our modeling efforts on, based on experiments and microscopy. For example, oxidation is important in milling Ti in Paper V, while the differences in permeability between Co and C are significant in turning Ti in Paper VI.

The *second research question* focuses on prediction using the understanding gained from the *first research question*. Again, we cannot model the cutting process without understanding it. There is no point in modeling oxidation if the tool lacks the necessary hardness and toughness to cut the workpiece. But the mechanical properties can locally degrade due to oxidation, diffusion, and chemical degradation. Predicting if the tool will suffer from oxidation is possible, as shown in Papers II-V and VIII-X. We can also predict which tool material is chemically more resistant to a particular workpiece material or NMI, and which element is likely to diffuse into a specific phase at a certain rate (Papers II-IV and VI-X). We can even predict what tool protective layers will likely form at what temperatures (Papers VI-X). These predictive thermodynamic models and kinetic simulations are not an exact science, but require knowing what to model based on experiments, microscopy, previous knowledge, or other types of modeling. Nonetheless, we can still use them to rank and to save time, money, and resources by testing only tool and workpiece combinations that are promising based on thermodynamics and kinetics.

The first research question concerns incremental progress in the study of metal cutting. The second research question concerns the application of this knowledge to predict future outcomes. The *third research question* is really about moving from discovery to design using not only the PSPP relationships [12] and the ICME approach [13], but by combining the PSPP roadmap of the tool, workpiece, environment, and cutting parameters. Papers III and IV demonstrate how NMIs interact with the Al_2O_3 coating, which is generally considered inert, resulting in degradation into soft aluminates. This does not have to be the case if the non-metallic inclusions are Al-saturated, which is possible in this steel, as shown in Papers III and IV. Paper IX develops a method and demonstrates how to select tool materials to ensure the formation of a tool protection layer, which can only be done by understanding the tool-workpiece-environment interaction. Paper X further shows how to select a tool material and how to alloy a steel to form a TPL that triples the tool life without degrading the functional properties of the steel. Designing based on thermodynamics and verified by microscopy and experiment, rather than a conventional trial-and-error discovery, resulted in having to cast and machine two alloys to find a promising alloy, rather than testing 255 alloys and maybe finding a promising alloy.

Improving machinability by forming tool protective layers is a relatively recent discovery [43,62,65,96–101]. While these TPLs were not coincidental by any means, they were not actively designed by setting boundary conditions for the requirements of the tool-workpiece-environment-cutting parameter combination. The answer to the *fourth research question* is connected to the three previous ones. Because we need to understand, predict, and/or design the right combination of tool-workpiece-environment-cutting parameters to achieve the desired in-process chemical interactions. Which lead to the formation of refractory phases and TPLs, thereby improving tool performance. This can, of course, be achieved without combining thermodynamics, focused experiments, and microscopy; however, it will more often result in adhesion at low speeds and aggressive crater wear at high speeds rather than TPL formation, as observed in Paper I. In contrast, TPL formation was successfully used to improve performance in Papers VIII, IX, and X, and the work in Papers VI and VII explained the formation of TPL in [98] and Paper VIII respectively.

Future work

This thesis was an exploratory study that combined machining experiments, microscopy, and thermodynamic modeling. The aim was to understand, predict, and design combinations of tools, workpieces, environments, and, to some extent, cutting parameters that reduce wear caused by diffusion, chemical reactions, and oxidation. This was achieved either by limiting wear, promoting the formation of transfer layers of NMI, or creating TPLs, while exploring the possibilities of the techniques currently available to us.

This work is a small but fascinating contribution to the field of metal cutting. Using the developed framework for more materials and studying its possibilities and limitations is of interest. The machining processes in the appended papers are primarily continuous and stable longitudinal turning with single-point tools in a laboratory environment. This is good for research, but exploring other materials, cutting conditions, and operations would be very interesting. Tool geometries were not fully explored, and the focus on cutting parameters was limited. There is considerable potential for adjusting other parameters beyond adjusting the cutting speed and toggling the coolant supply on and off. We can also further develop and use more advanced modeling techniques and microscopy, for example, accounting for grain boundary diffusion and using EELS to better measure light elements.

But we can now, to some extent, already approximate and predict the requirements on tool, coating, and alloy combinations. An interesting next step would be to integrate these findings with other models of sintering, coating, casting, and machining which would provide deeper insights into how to develop tools and alloys that meet these combined requirements. Such as other thermodynamic models, finite element modeling, molecular dynamics, density functional theory, and more experiments to study the workpiece, tool, environment, and cutting conditions together and not separately.

References

[1] Leif Östling, chairman of the Confederation of Swedish Enterprise, Uppdrag, SVT, Gransking, (2017).

[2] J.-E. Ståhl, Seco Tools AB, Metal Cutting: Theories and Models, Seco Tools AB, 2012.

[3] T. Childs, Metal Machining, Elsevier, 2000. https://doi.org/10.1016/C2009-0-23990-0.

[4] H.M. Ortner, P. Ettmayer, H. Kolaska, The history of the technological progress of hardmetals, Int. J. Refract. Met. Hard Mater. 44 (2014) 148–159. https://doi.org/10.1016/j.ijrmhm.2013.07.014.

[5] M.C. Shaw, J.O. Cookson, Metal Cutting Principles (Vol. 2), 2005.

[6] E.M. Trent, P.K. Wright, Metal Cutting Fourth Edition, 2000.

[7] J.-O. Andersson, T. Helander, L. Höglund, P. Shi, B. Sundman, Thermo-Calc & DICTRA, computational tools for materials science, Calphad. 26 (2002) 273–312. https://doi.org/10.1016/S0364-5916(02)00037-8.

[8] P.W. Hawkes, J.C.H. Spence, Science of Microscopy, Springer New York, New York, NY, 2007. https://doi.org/10.1007/978-0-387-49762-4.

[9] C.B. Carter, D.B. Williams, eds., Transmission Electron Microscopy, 1st ed. 20, Springer International Publishing, Cham, 2016. https://doi.org/10.1007/978-3-319-26651-0.

[10] L.A. Giannuzzi, F.A. Stevie, eds., Introduction to Focused Ion Beams, Springer US, Boston, MA, 2005. https://doi.org/10.1007/b101190.

[11] E.C.J.R. Center, E. Garbarino, F. Ardente, D. Blagoeva, F. Bouraoui, G. Blengini, C. Pavel, C. Torres De Matos, F. Mathieux, T. Hámor, S. Solar, P. Nuss, D. Wittmer, E. Tzimas, B. Gawlik, P. Alves Dias, G. Orveillon, H. Saveyn, D. Huygens, S. Bobba, Critical raw materials and the circular economy – Background report, Publications Office, 2017. https://doi.org/doi/10.2760/378123.

[12] G.B. Olson, Computational Design of Hierarchically Structured Materials, Science 277 (1997) 1237–1242. https://doi.org/10.1126/science.277.5330.1237.

[13] The Minerals Metals & Materials Society (TMS), Modeling Across Scales: A Roadmapping Study for Connecting Materials Models and Simulations Across Length and Time Scales, TMS, Warrendale, PA, 2015. https://doi.org/10.7449/multiscale_1.

[14] The Editors of Encyclopaedia Britannica, Bronze Age, Encyclopedia Britannica, (2025). https://www.britannica.com/event/Bronze-Age.

[15] J. García, V. Collado Ciprés, A. Blomqvist, B. Kaplan, Cemented carbide microstructures: a review, Int. J. Refract. Met. Hard Mater. 80 (2019) 40–68. https://doi.org/10.1016/j.ijrmhm.2018.12.004.

[16] H. Liu, X. Xu, J. Zhang, Z. Liu, Y. He, W. Zhao, Z. Liu, The state of the art for numerical simulations of the effect of the microstructure and its evolution in the metal-cutting processes, Int. J. Mach. Tools Manuf. 177 (2022) 103890. https://doi.org/10.1016/j.ijmachtools.2022.103890.

[17] A.G. Thornton, J. Wilks, Tool wear and solid state reactions during machining, Wear. 53 (1979) 165–187. https://doi.org/10.1016/0043-1648(79)90226-6.

[18] C. Evans, J.B. Bryan, Cryogenic Diamond Turning of Stainless Steel, CIRP Ann. 40 (1991) 571–575. https://doi.org/10.1016/S0007-8506(07)62056-3.

[19] E. Paul, C.J. Evans, A. Mangamelli, M.L. McGlauflin, R.S. Polvani, Chemical aspects of tool wear in single point diamond turning, Precis. Eng. 18 (1996) 4–19. https://doi.org/10.1016/0141-6359(95)00019-4.

[20] N. Narutaki, A. Murakoshi, Effect of Small Quantity Inclusions in Steels on the Wear of Ceramic Tools, J. Japan Soc. Precis. Eng. 42 (1976) 221–226. https://doi.org/10.2493/jjspe1933.42.221.

[21] A. Nordgren, A. Melander, Tool wear and inclusion behaviour during turning of a calcium-treated quenched and tempered steel using coated cemented carbide tools, Wear. 139 (1990) 209–223. https://doi.org/10.1016/0043-1648(90)90046-D.

[22] J. Barry, G. Byrne, Cutting tool wear in the machining of hardened steels, Wear. 247 (2001) 139–151. https://doi.org/10.1016/S0043-1648(00)00531-7.

[23] Y. Yamane, H. Usuki, B. Yan, N. Narutaki, The formation of a protective oxide layer in machining resulphurized free-cutting steels and cast irons, Wear. 139 (1990) 195–208. https://doi.org/10.1016/0043-1648(90)90045-C.

[24] M. Moreno, J.M. Andersson, J. Eriksson, P. Alm, K. Hedström, R. M'Saoubi, I.C. Schramm, N. Schell, M.P. Johansson-Jöesaar, M. Odén, L. Rogström, Strain and phase evolution in TiAlN coatings during high-speed

metal cutting: An in operando high-energy x-ray diffraction study, Acta Mater. 263 (2024) 119538. https://doi.org/10.1016/j.actamat.2023.119538.

[25] M. Agmell, Applied FEM of metal removal and forming : a practical course in Abaqus modeling., First edit, Studentlitteratur, 2018.

[26] A. Malakizadi, B. Shi, P. Hoier, H. Attia, P. Krajnik, Physics-based approach for predicting dissolution–diffusion tool wear in machining, CIRP Ann. 69 (2020) 81–84. https://doi.org/10.1016/j.cirp.2020.04.040.

[27] S. Giménez, O. Van der Biest, J. Vleugels, The role of chemical wear in machining iron based materials by PCD and PCBN super-hard tool materials, Diam. Relat. Mater. 16 (2007) 435–445. https://doi.org/10.1016/j.diamond.2006.08.017.

[28] S. Odelros, B. Kaplan, M. Kritikos, M. Johansson, S. Norgren, Experimental and theoretical study of the microscopic crater wear mechanism in titanium machining, Wear. 376–377 (2017) 115–124. https://doi.org/10.1016/j.wear.2017.01.104.

[29] A. Graves, R. Lindvall, A. Salmasi, W. Wan, C. Xiao, H. Larsson, V. Bushlya, M. Jackson, S. Norgren, A Combined Experimental and Modelling Approach to Understand Chemical Wear in Titanium Turning, 15th World Conf. Titan. Proc. (2024).

[30] J. Vleugels, L. Vandeperre, O. Van Der Biest, Influence of alloying elements on the chemical reactivity between Si–Al–O–N ceramics and iron-based alloys, J. Mater. Res. 11 (1996) 1265–1276. https://doi.org/10.1557/JMR.1996.0161.

[31] E. Epifano, D. Monceau, Ellingham diagram: A new look at an old tool, Corros. Sci. 217 (2023) 111113. https://doi.org/10.1016/j.corsci.2023.111113.

[32] S. Shoja, O. Bäcke, A. Fazi, S. Norgren, H.-O. Andrén, M. Halvarsson, Enhanced steel machining performance using texture-controlled CVD alpha-alumina coatings: Fundamental degradation mechanisms, Int. J. Mach. Tools Manuf. 197 (2024) 104137. https://doi.org/10.1016/j.ijmachtools.2024.104137.

[33] K. Sobiyi, I. Sigalas, Chip Formation Characterisation and Tem Investigation of Worn PcBN Tool during Hard Turning, Mach. Sci. Technol. 19 (2015) 479–498. https://doi.org/10.1080/10910344.2015.1051542.

[34] R. Bejjani, M. Collin, T. Thersleff, S. Odelros, Multi-scale study of initial tool wear on textured alumina coating, and the effect of inclusions in low-alloyed steel, Tribol. Int. 100 (2016) 204–212.

https://doi.org/10.1016/j.triboint.2016.01.021.

[35] J. Angseryd, H.-O. Andrén, An in-depth investigation of the cutting speed impact on the degraded microstructure of worn PCBN cutting tools, Wear. 271 (2011) 2610–2618. https://doi.org/10.1016/j.wear.2010.11.059.

[36] J. Kannatey-Asibu E., A Transport-Diffusion Equation in Metal Cutting and its Application to Analysis of the Rate of Flank Wear, J. Eng. Ind. 107 (1985) 81–89. https://doi.org/10.1115/1.3185971.

[37] J.A. Yeomans, T.F. Page, Studies of ceramic-liquid metal reaction interfaces, J. Mater. Sci. 25 (1990) 2312–2320. https://doi.org/10.1007/BF00638021.

[38] J. Vleugels, O. Van Der Biest, Chemical wear mechanisms of innovative ceramic cutting tools in the machining of steel, Wear. 225–229 (1999) 285–294. https://doi.org/10.1016/S0043-1648(98)00362-7.

[39] A. Salmasi, ICME guided study of mass transport in production and application of cemented carbides, [Doctoral Thesis], Materials Science and Engineering, KTH Royal Institute of Technology, 2022.

[40] R. Lindvall, Wear Mechanisms in Cutting Tools for Machining Applications: Interfacial Phenomena, Characterization, and Relation to Performance, [Doctoral Thesis], Production and Materials Engineering, Department of Mechanical Engineering and Sciences, Faculty of Engineering LTH, Lund University, 2024.

[41] A. Graves, Towards an understanding of high strength metastable β titanium alloy machinability, [Doctoral Thesis], Department of Materials Science and Engineering, The University of Sheffield, 2021.

[42] S. Shoja, Microstructure and Wear Mechanisms of Textured CVD Alumina and Titanium Carbonitride Coatings, [Doctoral Thesis], Department of Physics, Chalmers University of Technology, 2022. https://research.chalmers.se/publication/530092/file/530092_Fulltext.pdf.

[43] J.-E. Ståhl, Requirements and potential for high performance cutting tools based on superhard phases in new applications, in: De Beers Diamond Conference hosted by Warwick University, UK, 2016. https://portal.research.lu.se/en/publications/requirements-and-potential-for-high-performance-cutting-tools-bas.

[44] G. Schneider, Cutting Tool Applications, George Schneider, Jr., 2002.

[45] E.O. Ezugwu, J. Bonney, Effect of high-pressure coolant supply when machining nickel-base, Inconel 718, alloy with coated carbide tools, J. Mater. Process. Technol. 153–154 (2004) 1045–1050. https://doi.org/10.1016/j.jmatprotec.2004.04.329.

[46] Y. Kamata, T. Obikawa, High speed MQL finish-turning of Inconel 718 with different coated tools, J. Mater. Process. Technol. 192–193 (2007) 281–286. https://doi.org/10.1016/j.jmatprotec.2007.04.052.

[47] P. Sivaiah, D. Chakradhar, Effect of cryogenic coolant on turning performance characteristics during machining of 17-4 PH stainless steel: A comparison with MQL, wet, dry machining, CIRP J. Manuf. Sci. Technol. 21 (2018) 86–96. https://doi.org/10.1016/j.cirpj.2018.02.004.

[48] N. Norrby, M.P. Johansson, R. M'Saoubi, M. Odén, Pressure and temperature effects on the decomposition of arc evaporated Ti0.6Al0.4N coatings in continuous turning, Surf. Coatings Technol. 209 (2012) 203–207. https://doi.org/10.1016/j.surfcoat.2012.08.068.

[49] T.H.K. Barron, R.W. Munn, Thermodynamics of solids under stress, Pure Appl. Chem. 22 (1970) 527–534. https://doi.org/10.1351/pac197022030527.

[50] B.E. Hobbs, A. Ord, Does non-hydrostatic stress influence the equilibrium of metamorphic reactions?, Earth-Science Rev. 163 (2016) 190–233. https://doi.org/10.1016/j.earscirev.2016.08.013.

[51] V. Kryzhanivskyy, V. Bushlya, O. Gutnichenko, R. M'Saoubi, J.-E. Ståhl, Heat flux in metal cutting: Experiment, model, and comparative analysis, Int. J. Mach. Tools Manuf. 134 (2018) 81–97. https://doi.org/10.1016/j.ijmachtools.2018.07.002.

[52] B.M. Pereira Guimarães, C.M. da Silva Fernandes, D. Amaral de Figueiredo, F.S. Correia Pereira da Silva, M.G. Macedo Miranda, Cutting temperature measurement and prediction in machining processes: comprehensive review and future perspectives, Int. J. Adv. Manuf. Technol. 120 (2022) 2849–2878. https://doi.org/10.1007/s00170-022-08957-z.

[53] M. Bacci da Silva, J. Wallbank, Cutting temperature: prediction and measurement methods—a review, J. Mater. Process. Technol. 88 (1999) 195–202. https://doi.org/10.1016/S0924-0136(98)00395-1.

[54] N.A. Abukhshim, P.T. Mativenga, M.A. Sheikh, Heat generation and temperature prediction in metal cutting: A review and implications for high speed machining, Int. J. Mach. Tools Manuf. 46 (2006) 782–800. https://doi.org/10.1016/j.ijmachtools.2005.07.024.

[55] J. Johansson, P. Alm, R. M'Saoubi, P. Malmberg, J.-E. Ståhl, V. Bushlya, On the function of lead (Pb) in machining brass alloys, Int. J. Adv. Manuf. Technol. 120 (2022) 7263–7275. https://doi.org/10.1007/s00170-022-09205-0.

[56] V.F. Bobrov, The Basics of Metal Cutting Theory, Mashinostroene, Moscow, 1975.

[57] K. M., F. E., Y. P., Cutting Therory, 2nd ed., Minsk: Novoe znanie, 2006.

[58] A. Graves, A. Salmasi, S.J. Graham, W. Wan, C. Xiao, M. Jackson, H. Larsson, S. Norgren, An experimental and theoretical investigation on Ti-5553/WC–Co(6%) chemical interactions during machining and in diffusion couples, Wear. 516–517 (2023) 204604. https://doi.org/10.1016/j.wear.2022.204604.

[59] B.M. Kramer, B.F. von Turkovich, A Comprehensive Tool Wear Model, CIRP Ann. 35 (1986) 67–70. https://doi.org/10.1016/S0007-8506(07)61840-X.

[60] R. M'Saoubi, H. Chandrasekaran, Innovative Methods for the Investigation of Tool-Chip Adhesion and Layer Formation during Machining, CIRP Ann. 54 (2005) 59–62. https://doi.org/10.1016/S0007-8506(07)60049-3.

[61] J. Gerth, F. Gustavsson, M. Collin, G. Andersson, L.-G. Nordh, J. Heinrichs, U. Wiklund, Adhesion phenomena in the secondary shear zone in turning of austenitic stainless steel and carbon steel, J. Mater. Process. Technol. 214 (2014) 1467–1481. https://doi.org/10.1016/j.jmatprotec.2014.01.017.

[62] M. Olsson, F. Lenrick, R. M'Saoubi, H. Larsson, A. Markström, I. Petrusha, J.-E. Ståhl, V. Bushlya, Study of wear mechanisms of cemented carbide tools during machining of single-phase niobium, Wear. 450–451 (2020) 203244. https://doi.org/10.1016/j.wear.2020.203244.

[63] E.D. Doyle, J.G. Horne, D. Tabor, Frictional interactions between chip and rake face in continuous chip formation, Proc. R. Soc. London. A. Math. Phys. Sci. 366 (1979) 173–183. https://doi.org/10.1098/rspa.1979.0046.

[64] L. Zou, J. Yin, Y. Huang, M. Zhou, Essential causes for tool wear of single crystal diamond in ultra-precision cutting of ferrous metals, Diam. Relat. Mater. 86 (2018) 29–40. https://doi.org/10.1016/j.diamond.2018.04.012.

[65] V. Bushlya, F. Lenrick, J.-E. Ståhl, R. M'Saoubi, Influence of oxygen on the tool wear in machining, CIRP Ann. 67 (2018) 79–82. https://doi.org/10.1016/j.cirp.2018.03.011.

[66] G.J. Tennenhouse, F.D. Runkle, The effects of oxygen on the wear of Si3N4 against cast iron and steel, Wear. 110 (1986) 75–81. https://doi.org/10.1016/0043-1648(86)90153-5.

[67] C. Bagnall, J. Capo, W.J. Moorhead, Oxidation Behavior of Tungsten Carbide-6% Cobalt Cemented Carbide, Metallogr. Microstruct. Anal. 7 (2018) 661–679. https://doi.org/10.1007/s13632-018-0493-7.

[68] S.N. Basu, V.K. Sarin, Oxidation behavior of WC-Co, Mater. Sci. Eng. A. 209 (1996) 206–212. https://doi.org/10.1016/0921-5093(95)10145-4.

[69] G.J. Tennenhouse, F.D. Runkle, The effects of oxygen on the wear of tungsten-carbide-based materials, Wear. 118 (1987) 365–375. https://doi.org/10.1016/0043-1648(87)90078-0.

[70] We completely failed to use cut-off wheels and milling small test samples of alloyed Mn-steel. Because I had failed to quench them properly, the material both worked hardened and contained W, Zr, and other carbides., (2022).

[71] A. Chychko, J. García, V. Collado Ciprés, E. Holmström, A. Blomqvist, HV-KIC property charts of cemented carbides: A comprehensive data collection, Int. J. Refract. Met. Hard Mater. 103 (2022) 105763. https://doi.org/10.1016/j.ijrmhm.2021.105763.

[72] K.-D.D. Bouzakis, N. Michailidis, G. Skordaris, E. Bouzakis, D. Biermann, R. M'Saoubi, Cutting with coated tools: Coating technologies, characterization methods and performance optimization, CIRP Ann. - Manuf. Technol. 61 (2012) 703–723. https://doi.org/10.1016/j.cirp.2012.05.006.

[73] W.-T. Chien, C.-S. Tsai, The investigation on the prediction of tool wear and the determination of optimum cutting conditions in machining 17-4PH stainless steel, J. Mater. Process. Technol. 140 (2003) 340–345. https://doi.org/10.1016/S0924-0136(03)00753-2.

[74] K. Sobiyi, I. Sigalas, High-speed machining of martensitic stainless steel using PcBN, J. Superhard Mater. 38 (2016) 34–39. https://doi.org/10.3103/S1063457616010056.

[75] Y. Huang, Y.K. Chou, S.Y. Liang, CBN tool wear in hard turning: a survey on research progresses, Int. J. Adv. Manuf. Technol. 35 (2007) 443–453. https://doi.org/10.1007/s00170-006-0737-6.

[76] A. McKie, J. Winzer, I. Sigalas, M. Herrmann, L. Weiler, J. Rödel, N. Can, Mechanical properties of cBN–Al composite materials, Ceram. Int. 37 (2011) 1–8. https://doi.org/10.1016/j.ceramint.2010.07.034.

[77] R.C. Reed, The Superalloys: Fundamentals and Applications, Cambridge University Press, Cambridge, 2006. https://doi.org/DOI: 10.1017/CBO9780511541285.

[78] R. M'Saoubi, D. Axinte, S.L. Soo, C. Nobel, H. Attia, G. Kappmeyer, S. Engin, W.-M. Sim, High performance cutting of advanced aerospace alloys and composite materials, CIRP Ann. 64 (2015) 557–580. https://doi.org/10.1016/j.cirp.2015.05.002.

[79] E.O. Ezugwu, Z.M. Wang, Titanium alloys and their machinability—a review, J. Mater. Process. Technol. 68 (1997) 262–274. https://doi.org/10.1016/S0924-0136(96)00030-1.

[80] D.L. Goodstein, States of Matter, Dover Publications, 1985.

[81] E.B. Tadmor, R.E. Miller, R.S. Elliott, Continuum Mechanics and Thermodynamics: From Fundamental Concepts to Governing Equations, Cambridge University Press, Cambridge, 2011. https://doi.org/DOI: 10.1017/CBO9781139017657.

[82] E.B. Tadmor, R.E. Miller, Modeling Materials, Cambridge University Press, Cambridge, 2011. https://doi.org/10.1017/CBO9781139003582.

[83] M. Hillert, M. Selleby, Thermodynamics for Materials Scientists and Engineers, Stockholm, 2018.

[84] M. Hillert, The compound energy formalism, J. Alloys Compd. 320 (2001) 161–176. https://doi.org/10.1016/S0925-8388(00)01481-X.

[85] X.-G. Lu, M. Selleby, B. Sundman, Implementation of a new model for pressure dependence of condensed phases in Thermo-Calc, Calphad. 29 (2005) 49–55. https://doi.org/10.1016/j.calphad.2005.04.001.

[86] H. Larsson, L. Höglund, Multiphase diffusion simulations in 1D using the DICTRA homogenization model, Calphad. 33 (2009) 495–501. https://doi.org/10.1016/j.calphad.2009.06.004.

[87] H. Larsson, A model for 1D multiphase moving phase boundary simulations under local equilibrium conditions, Calphad. 47 (2014) 1–8. https://doi.org/10.1016/j.calphad.2014.06.001.

[88] J.-C. Zhao, Methods for Phase Diagram Determination, Elsevier, Oxford, 2007. https://doi.org/10.1016/B978-0-08-044629-5.X5000-9.

[89] İ. Özkan, E. Dokumacı, A.B. Önay, Cyclic Oxidation Behavior of c-BN and h-BN at Elevated Temperatures, Acta Phys. Pol. A. 134 (2018) 61–63. https://doi.org/10.12693/APhysPolA.134.61.

[90] G.E. Spriggs, 13.5 Properties of diamond and cubic boron nitride, in: P. Beiss, R. Ruthardt, H. Warlimont (Eds.), Powder Metall. Data. Refract. Hard Intermet. Mater., Springer-Verlag, Berlin/Heidelberg, n.d.: pp. 118–139. https://doi.org/10.1007/10858641_7.

[91] P.W. Hawkes, J.C.H. Spence, eds., Science of Microscopy, Springer New York, New York, NY, 2007. https://doi.org/10.1007/978-0-387-49762-4.

[92] N. Ånmark, A. Karasev, P. Jönsson, The Effect of Different Non-Metallic Inclusions on the Machinability of Steels, Materials (Basel). 8 (2015) 751–783. https://doi.org/10.3390/ma8020751.

[93] W. König, Einfluss nichtmetallischer Einschlüsse auf die Zerspanbarkeit von Kohlenstoffstählenitle, Maschinenmarkt. 87 (1965).

[94] K. Watari, J. Fujiwara, T. Nishi, M. Egashira, Micro Structure of Belag and Oxide Inclusions in Ca-deoxidized Steels, J. Japan Soc. Precis. Eng. 78 (2012) 787–791. https://doi.org/10.2493/jjspe.78.787.

[95] N. Ånmark, Steel characteristics and their link to chip breaking and tool wear in metal cutting, [Doctoral Thesis], Materials Science and Engineering, KTH Royal Institute of Technology, 2016.

[96] V. Bushlya, F. Lenrick, O. Gutnichenko, I. Petrusha, O. Osipov, S. Kristiansson, J.-E. Stahl, Performance and wear mechanisms of novel superhard diamond and boron nitride based tools in machining Al-SiCp metal matrix composite, Wear. 376–377 (2017) 152–164. https://doi.org/10.1016/j.wear.2017.01.036.

[97] V. Bushlya, D. Johansson, F. Lenrick, J.-E. Ståhl, F. Schultheiss, Wear mechanisms of uncoated and coated cemented carbide tools in machining lead-free silicon brass, Wear. 376–377 (2017) 143–151. https://doi.org/10.1016/j.wear.2017.01.039.

[98] R. Lindvall, F. Lenrick, H. Persson, R. M'Saoubi, J.-E. Ståhl, V. Bushlya, Performance and wear mechanisms of PCD and pcBN cutting tools during machining titanium alloy Ti6Al4V, Wear. 454–455 (2020) 203329. https://doi.org/10.1016/j.wear.2020.203329.

[99] H. Persson, V. Bushlya, L. Franca, J. Zhou, J.-E. Ståhl, F. Lenrick, Performance and wear mechanisms of different PcBN tools when machining superalloy AD730, Ceram. Int. 48 (2022) 22733–22742. https://doi.org/10.1016/j.ceramint.2022.04.042.

[100] T. Aiso, T. Matsumura, Effect of Si and Al Additions to Steel on Machinability in Gear Cutting, ISIJ Int. 62 (2022) 1957–1966. https://doi.org/10.2355/isijinternational.ISIJINT-2022-145.

[101] T. Aiso, U. Wiklund, M. Kubota, S. Jacobson, Effect of Si and Al additions to carbon steel on material transfer and coating damage mechanism in turning with CVD coated tools, Wear. 368–369 (2016) 379–389. https://doi.org/10.1016/j.wear.2016.10.011.

[102] R.P. Feynman, The Quotable Feynman, Princeton University press, 2015.

[103] A. Larsson, S. Ruppi, Structure and composition of built-up layers on coated tools during turning of Ca-treated steel, Mater. Sci. Eng. A. 313 (2001) 160–169. https://doi.org/10.1016/S0921-5093(01)00964-9.

[104] B. Kaplan, S. Odelros, M. Kritikos, R. Bejjani, S. Norgren, Study of tool wear and chemical interaction during machining of Ti6Al4V, Int. J.

Refract. Met. Hard Mater. 72 (2018) 253–256. https://doi.org/10.1016/j.ijrmhm.2017.12.012.

[105] R. Lindvall, F. Lenrick, J.M. Andersson, R. M'Saoubi, V. Bushlya, On wear of TiAlN coated tools with and without NbN overlayer in machining titanium alloys, Int. J. Mach. Tools Manuf. 198 (2024) 104148. https://doi.org/10.1016/j.ijmachtools.2024.104148.

[106] D. Handayani, V.F. Okhuysen, N. Wagner, Machinability of High Mn Steel Using Tool Life Criteria, Int. J. Met. 18 (2024) 600–607. https://doi.org/10.1007/s40962-023-01044-3.

[107] J. Kopac, Hardening phenomena of Mn-austenite steels in the cutting process, J. Mater. Process. Technol. 109 (2001) 96–104. https://doi.org/10.1016/S0924-0136(00)00781-0.

[108] Kung Fu Panda, (2008).

Paper I

International Journal of Refractory Metals and Hard Materials 127 (2025) 106984

Contents lists available at ScienceDirect

International Journal of Refractory Metals and Hard Materials

journal homepage: www.elsevier.com/locate/IJRMHM

On the wear mechanisms of uncoated and coated pcBN tools during turning of 17–4 PH martensitic stainless steel

A. Bjerke [a,*], J. Casas [a], F. Lenrick [a], J.M. Andersson [b], R. M'Saoubi [a,b], V. Bushlya [a]

[a] *Division of Production and Materials Engineering, Lund University, Box 118, 22100 Lund, Sweden*
[b] *R&D Materials and Technology Development, Seco Tools AB, 737 82 Fagersta, Sweden*

ARTICLE INFO

Keywords
PcBN tool wear during turning of 17–4 PH
(Ti,Al)N coating wear turning 17–4 PH
High speed machining of 17–4 PH SAE 630
UNS S17400
TEM investigation of worn PcBN tools

ABSTRACT

Polycrystalline cubic boron nitride (pcBN) is a very promising tool material for turning martensitic stainless steels at high cutting speeds ($v_c > 200$ m/min). The competitive advantage of pcBN over cemented carbide increases as the cutting speed is increased. Changing the speed might lead to a shift in the wear balance and hence the knowledge about tool wear below $v_c = 200$ m/min might not be applicable at $v_c = 600$ m/min. The coatings designed for the lower speed range might also not be performing in the same way at higher speeds. This paper investigates the wear mechanism of uncoated and (Ti,Al)N coated pcBN tools when turning 17–4 PH in a hardened condition at speeds $v_c = 200$–600 m/min. Both scanning and transmission electron microscopy are used to study the worn tools. The in-depth analysis reveals that adhesive wear is only active at low speeds. Increasing the speed does however lead to more wear by diffusion and oxidation. The cBN is preferentially worn out, leaving the TiC binder at the tool-chip interface. Oxidation results in the accelerated wear of the pcBN but also in the formation of metal oxides within the adhered build up layer. The (Ti,Al)N coating does not significantly extend the tool life within this speed range, but it suppresses the adhesive wear mechanism preventing premature tool failure.

1. Introduction

17–4 PH (SAE 630 / UNS S17400) is a martensitic stainless steel with good corrosion resistance and high hardness. It is mainly used in processing industries, marine environments, and in engine or turbine components. Machining 17–4 PH in a hardened condition can be done using uncoated cemented carbide tools. But the optimal cutting speed for such process is below $v_c = 100$ m/min [1], and the wear mechanisms are mainly mechanical (abrasion, adhesion, and fracture) [1–3]. There are limited studies of machining 17–4 PH in any condition with pcBN. The authors found one study using pcBN [4] which showed that it is possible to achieve a high surface finish at speed $v_c = 150$–500 m/min during machining of hardened 17–4 PH, which avoids the need for grinding. The focus was on the surface quality and not the machining performance or wear mechanisms. There are a limited number of high-resolution microscopy studies, such as transmission electron microscopy (TEM), of worn pcBN tools used in machining any hardened martensitic stainless steels [5], and no studies of pcBN tools used at cutting speeds above $v_c = 200$ m/min. It is not obvious that the wear mechanism are the same when cutting other materials with similar hardness but with different chemical compositions [6], similar composition but different hardness [7], or similar material but at a lower speed [5]. Not knowing the dominant wear mechanism and not understanding the wear progression makes it difficult to select the correct cutting conditions, tool material, tool geometry, and tool coating. Hence this investigation aims at providing an in-depth study of the wear mechanisms when turning the hardened martensitic stainless steel (17–4 PH) at high speeds using coated and uncoated pcBN tools.

2. Experimental details

Machining tests of longitudinal turning were performed on a DMG MORI NLX 2500 CNC machine. The same workpiece is used for all tests, it is a martensitic stainless steels 17–4 PH (SAE 630 / UNS S17400). The composition of the workpiece is shown in Table 1 and unetched microstructure in Fig. 1b. It was machined in a precipitation hardened condition, with a measured hardness of HRC 46. It contains mainly Nb nitrides but also Cr nitrides, there are also Cu rich and Mn, Ni, Si rich precipitates as well as of Al and Ca oxides (Fig. 1b).

Machining was performed with pcBN tools which consist of 50 %

---

* Corresponding author.
E-mail address: axel.bjerke@iprod.lth.se (A. Bjerke).

https://doi.org/10.1016/j.ijrmhm.2024.106984
Received 21 August 2024; Received in revised form 26 November 2024; Accepted 26 November 2024

cBN with an average grain size of 2 μm, and a ceramic binder whose main component is TiC. Lesser amounts of W and Al_2O_3 are present (Fig. 1a). The tools were used both uncoated and coated with a commercially available physical vapor deposited (PVD) $(Ti_{0.45}Al_{0.55})N$ coating. This coating is commonly used when machining similar stainless steels due to its hot hardness and oxidation resistance [8].

The inserts used have the CNGA120408S-01020-L1-B ISO geometry with two brazed pcBN tips to a carbide carrier. With a chamfer width and angle of 0.1 mm and 20° respectively. The toolholder with designation DCLNL2525X12-JETI was used in all tests. The toolholder has internal coolant channels allowing for the coolant to be supplied to the rake through two nozzles in a 3D-printed insert clamp and one nozzle directed at a flank below the insert. The coolant used is a 6 % oil-water emulsion (CIMSTAR 501FF) supplied only through the specified tool holder at 80 bars pressure. All tests are performed as longitudinal turning at a constant feed $f = 0.1$ mm/rev and depth of cut $a_p = 0.3$ mm. Cutting speed between $v_c = 200$ to 600 m/min were evaluated. This represents industrially relevant finishing conditions for this type of tool and workpiece material.

Three series of machining tests, further denoted as Test 1 to 3, are performed in this study at different cutting speeds to understand the effect of changing the cutting speed and the addition of a coating on tool wear mechanisms. Test 1 studies how the wear of pcBN tools changes with cutting speed for uncoated tools. This is done by studying the tool wear after a fixed cutting distance at different speeds, $v_c = 200$, 300, 400, 500, and 600 m/min. A distance of 2400 m is selected to be able to compare all speeds, as this is the maximum distance cut at $v_c = 600$ m/min. Test 2 investigates the evolution of the tool wear over time and quantifies the tool life at different cutting speeds for uncoated tools. The speeds investigated are $v_c = 200$, 400, and 600 m/min. The tool life criterion is here defined as a flank wear width $VB_B = 200$ μm, a crater wear depth KT = 90 μm. A larger flank wear (VB_B) results in poor surface quality, and hence was avoided because one of the potential benefits of using pcBN is to avoid final grinding [4]. Larger crater wear (KT) as discovered experimentally in this study, results in an unpredictable catastrophic tool failure. These criteria are in accordance with ISO 3685 - Tool life testing with single-point turning tool. Test 3 analyzes the effect of the addition of a $(Ti_{0.45}Al_{0.55})N$ coating on the wear mechanisms and machining performance of coated pcBN tools, using the same test strategic as in Test 1 and 2.

VB_B is measured using an Olympus SZX7 stereo visible light microscope (VLM). Crater wear (KT) is measured using focus-variation measurements with an Alicona Infinite Focus 3D VLM which enables topographically sensitive measurements. VB_B and KT are measured at the end of Test 1 and 3, but for Test 2 these wear criteria are measured continuously after every 600 m of cutting.

Further in depth analysis of selected tools is conducted on a scanning electron microscope (SEM) TESCAN Mira3. The SEM is equipped with a topography sensitive secondary electron (SE) detector, composition sensitive backscatter electron (BSE) detector, and X-ray energy dispersive spectrometer (XEDS) for measuring local chemical composition. This enables a spatially resolved study of the tool surfaces with respect to chemical composition and topography.

Lamellae for transmission electron microscopy (TEM) investigation is prepared by a lift-out procedure using a SEM equipped with a focused ion beam (FIB-SEM) FEI Nova NanoLab 600. TEM work is conducted on a JEOL 3000F. The TEM images presented in the paper are mainly STEM-HAADF images which are z-contrast sensitive. A XEDS detector in the STEM mode is used for measuring chemical composition. This enables a highly spatially resolved investigations of the tool cross-sections with respect to structure and chemical composition.

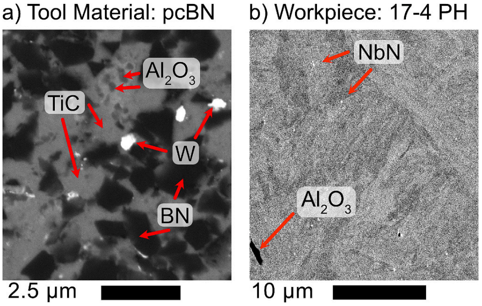

Fig. 1. SEM-BSE image of a) tool material and b) workpiece material. The main constituents in the pcBN are cBN and TiC, with lesser amounts of Al_2O_3 and W. The workpiece contains some NbN and Al_2O_3 as well as intermetallic precipitates and calcium oxides.

3. Results

3.1. Results Test 1, different speeds same distance

Test 1 is aimed at investigating how the tool wear of uncoated tools changes with speed after machining a constant length or spiral distance. The speeds investigated are $v_c = 200$, 300, 400, 500, and 600 m/min. The tool used at 600 m/min reached its tool life criteria after 2400 m in cut, this fixed distance is therefore used for comparison between all tools.

The main wear morphologies observed after the machining tests are flank wear (VB_B) and crater wear (KT) (Fig. 2). The behavior of the crater on the rake is strongly dependent on the speed. At the lowest cutting speed of $v_c = 200$ m/min, the crater is covering the entire tool-chip contact zone, including the chamfer. At the same time the width of the crater is the smallest. Furthermore, the crater width increases with speed seen in the 3D scans in Fig. 2. The crater is constrained to the tool-chip contact region outside the chamfer, and the chamfer remains intact, at higher cutting speeds, up to $v_c = 500$ m/min. However, the chamfer is also worn out at $v_c = 600$ m/min, as seen in both the VLM image (left) of the flank and the 3D scan (right) in Fig. 2. The crater depth KT and flank wear VB_B do not significantly vary between speeds 200–400 m/min, which is more surprising. There is even a slight decrease in the KT and VB_B at a cutting speed of $v_c = 300$ m/min, as compared to 200 m/min. This suggests a shift in the dominating wear mechanism, since higher speeds generally results in more wear keeping other things fixed.

The cutting edge of the uncoated pcBN tool used at $v_c = 200$ m/min is unevenly worn suggesting some form of adhesion wear, as compared to the tools used at 300–600 m/min, all resulting in an evenly worn cutting edge. The flank wear VB_B increases almost linearly with speed within the range of 300–600 m/min. While the crater wear KT accelerates at $v_c = 500$ m/min and rapidly increases at $v_c = 600$ m/min, leading to the crater consuming the chamfer and reaching the flank, see Fig. 2.

3.2. Results Test 2, tool life at different speeds

Test 2 is subsequently aimed at investigating the evolution of tool

Table 1
Composition of 17–4 PH. All numbers in wt%.

Fe	C	Mn	P	S	Si	Cr	Ni	Cu	Nb, Ta
bal.	<0.07	<1.0	<0.04	<0.03	<1.0	15.0–17.5	3.0–5.0	3.0–5.0	0.15–0.45

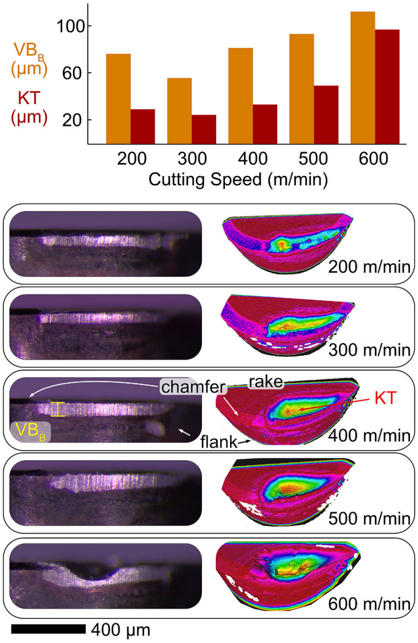

Fig. 2. Tool wear after 2400 m at different speeds. The left column is VLM images of the flank, used to measure VB_B. The right column is the corresponding 3D scan used to measure KT; the color scale is normalized for every image. The crater width increases with speed, but not necessarily flank width and crater depth.

wear during the tool engagement time and exploring the tool life at different cutting speeds and if there is a shift in the dominant wear mechanism with changing the speed. Flank and crater wear is still the dominating wear mechanism. But in some cases, an insignificant notching on the major cutting edge could be observed – i.e. at the depth of cut line. Edge chipping was also observed in cases of excessive cratering. Occasionally, catastrophic edge failure occurred if the machining was continued after the edge chipping was detected.

The tool life at $v_c = 600$ m/min was already reached in Test 1. Because the uncoated pcBN tool suffered from aggressive crater wear. The crater consumed the chamfer and had reached the flank wear land. Turning at $v_c = 400$ m/min resulted in progressive flank wear and was stopped after 8.5 km of machining due to the flank wear reaching the wear criterion of $VB_B = 200$ μm. Crater wear at the end of tool life was KT = 76 μm, see Fig. 3. Machining at the lowest speed, 200 m/min, resulted in a severe edge chipping between 8.5 and 9 km of machining (Fig. 4). The size of the resulting chipping led to a VB_{Bmax} of 480 μm, while in the VB_B was 138 μm in the regions of a uniform wear and KT = 53 μm. The cutting edge line of the pcBN tool used at 200 m/min is jagged and unevenly worn indicating adhesion and pluck out of the tool material during turning. Hence, understanding the wear mechanism behind the flank wear and crater wear are both of interest.

3.3. *In-depth analysis of wear mechanisms for Test 1 and Test 2*

The flank wear is significant on all tools at all speeds, but the mechanism is not necessarily only an abrasive wear mechanism. A limited number of distinct scratches are detectable on the flanks of the tools, the flanks appear to have smooth groves instead of distinct scratches (Fig. 5). The microstructure of the 17–4 PH workpiece material (Fig. 1b) contain only a limited number of hard particles such as NbN and Al_2O_3 which has a hardness comparable to the phases in the tool material (Fig. 1a). Therefore, the flank wear most likely originates due to a combination of several mechanisms. The smooth grooved appearance is most likely due to abrasion and diffusion wear by the martensitic matrix [9], or can be associated with preferential diffusional wear around cutting edge defects [10]. The few scratches can be due to the harder NbN and Al_2O_3 inclusions [9] as well self-abrasion by loose cBN particles which plough the flank resulting in some scratches [11].

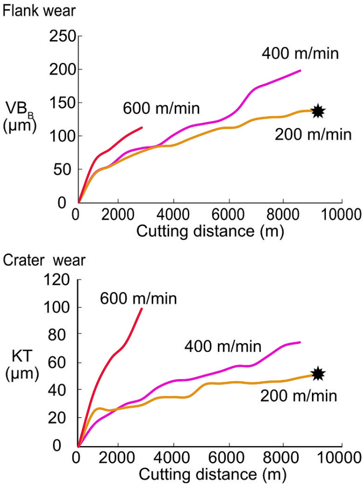

Fig. 3. Tool life at different speeds. Turning at 600 m/min resulted in aggressive cratering. 200 m/min and 400 m/min resulted in progressive flank and crater wear. There was a sudden edge failure between 8.5 and 9 km during machining at 200 m/min indicated by a star.

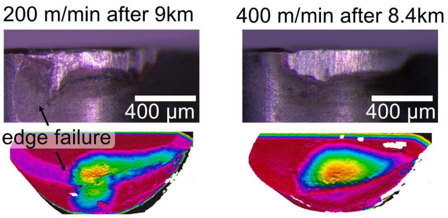

Fig. 4. Comparison between 200 and 400 m/min. Top images are VLM for the two speeds, bottom image is the corresponding 3D scan; the color scale is normalized for each image. The tool used at 400 m/min experience progressive flank wear and a growing crater. The tool used at 200 m/min was less worn at equal distance, but the cutting edge was unevenly worn, and the edge failed at a lower KT and VB_B than the tools at other speeds. 600 m/min is shown in Fig. 2.

Generally speaking, the gradual increase in wear between $v_c = 300$ and 600 m/min can be explained by more aggressive conditions leading to higher process temperature and to more wear, both crater and flank [12,13]. But further in-depth microscopic analysis of the worn tools is needed to understand why the speed $v_c = 200$ m/min resulted in the

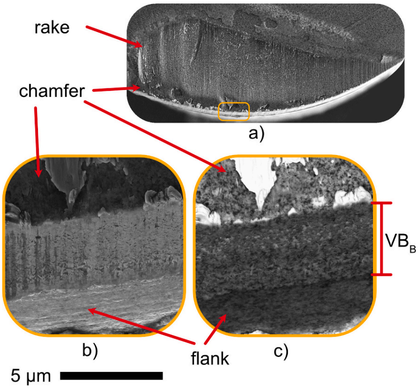

Fig. 5. SEM images of the worn edge of a tool machined at 400 m/min after 1800 m. a) Overview of the rake, b) topography sensitive SEM-SE image of the chamfer and flank, and c) z-contrast sensitive SEM-BSE image of the same area. The flank at other speeds has a similar appearance.

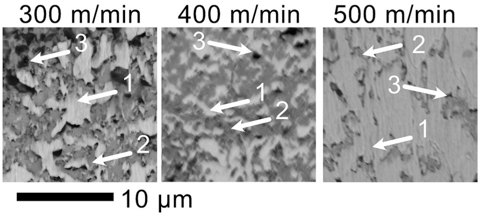

Fig. 7. BSE-SEM of the rake at different speeds. The features are identified using XEDS. Which are (1) steel with oxygen the bright areas, (2) binder the grey areas, and (3) cBN the black areas.

unexpected edge failure at a much lower VB$_B$ and KT and why there is a slight decrease in the wear when the speed is increased from speed 200 m/min to 300 min/m.

The crater wear on all tools has indications of wear by diffusion, oxidation or chemical reactions leading to the degradation of the tool material. SEM revealed that there is a significant difference in the wear pattern between the tool used at 200 m/min and the tools used at speeds above 300 m/min. There is substantial adhesion and pluck out of pcBN at v_c = 200 m/min, especially in the region where the cutting edge chipped and failed (red region Fig. 6). The rake, and also the chamfer has areas of adhered metal and areas where the tool material has been plucked out both microscopically and similarly to flaking. There is also a region in the crater where there are limited signs of adhesion, but rather a mix of oxides which did not suffer from cratering to the same extent as the rest of the contact zone (yellow region Fig. 6). This adhesion and pcBN pluck out explain the uneven appearance of the cutting edge in Fig. 4.

The tools used to machine at speeds v_c = 300–600 m/min have no signs of similar adhesion leading to severe cratering and pcBN pluck out, as in the red region Fig. 6 for v_c = 200 m/min. Three distinct features are visible using SEM which are the same in the whole contact zone of the rake on the tools used at speeds 300–600 m/min. The cBN grains and TiC binder is visible in the rake wear scar, but there is also a thin build up layer or tribo film of the workpiece material with a significant oxygen content (Fig. 7). This is similar to the yellow region at 200 min/min seen in Fig. 6. The main difference between the wear scars for the different speeds is the extend and appearance of the adhered build up layer (BUL) and amount of oxidized wear features and the degree of their oxidation (Fig. 7). Additionally, it is seen that the cBN phase is less visible than the binder, this difference is most pronounced for the higher cutting speeds.

Fig. 8 shows an overview of the rake at 400 m/min after 1800 m, it is representative of the rake of the tools at the other speeds and cutting distances. The change in acceleration voltage (HV) from 30 kV to 8 kV shows how the build-up layer or the film of adhered material is thinnest close to the cutting edge, in particular on the chamfer (Fig. 8). Two TEM lamellas are extracted from a tool to further study of the wear scar

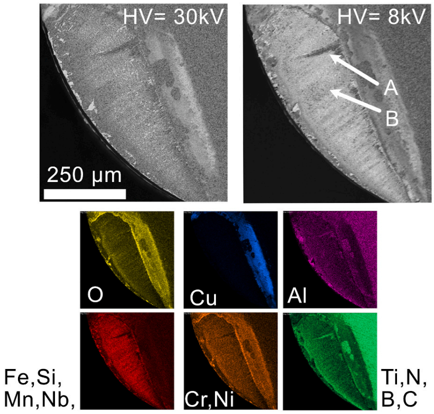

Fig. 8. BSE-SEM at 30 and 8 kV and XEDS maps of a tool machined at 400 m/min after 1800 m. The tool is covered with a thin layer of oxygen and steel, which is different from tools machined at 200 m/min, but similar to tools machined at 300–600 m/min. A and B indicate the location of the extracted TEM lamellae.

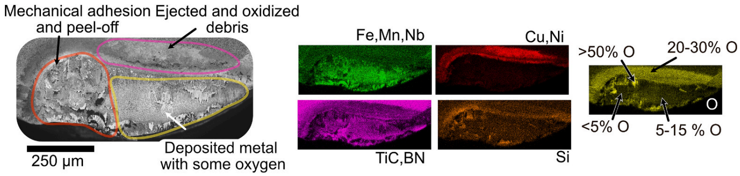

Fig. 6. Rake after 9 km of cutting at 200 m/min. SEM-BSE image with corresponding XEDS maps and point measurements of O in at. %. There is one area in the contact zone with lots of adhesion and peel-off with limited O signal, marked in orange, this is where the tool edge failed. The other area marked in yellow in the contact zone is covered with metal and some oxygen. (For interpretation of the references to color in this figure legend, the reader is referred to the web version of this article.)

features. The regions are from an area with a thick build up layer, the exact location is indicated in Fig. 8.

Fig. 9 shows that the bright features in Fig. 7 and 8 are not monolithic oxide products of the steel but rather a mechanical mixture of original 17–4 PH steel with an Fe, Cr, and Mn rich oxide O. The oxides are thin, less than 10 nm thick in Fig. 9 making them hard to identify by diffraction, but STEM-XEDS suggest that the oxide is the spinel phase $(Fe,Cr,Mn)_3O_4$. The difference in the microscopy z-contrast in the top part of the adhered layer is not a difference in thickness, but rather a difference in composition where brighter-contrast areas are steel, and the darker areas are oxides.

Fig. 10 give evidence to explain why there is much less cBN visible in the SEM images compared to binder (see Fig. 7), whereas the pcBN microstructure consists of an equal volumetric mixture of binder and cBN grains (see Fig. 1). It seems that the TiC and Al_2O_3 binder phases are more resistant to oxidation, diffusion, and chemical degradation while the cBN phase is preferentially removed and replaced by the steel at the tool-workpiece interface surface. Such preferential removal of cBN phase has been earlier reported in machining austenitic [7] and martensitic [14] workpiece materials where the diffusion dissolution rate of cBN exceeds the dissolution of the binder phases, hence resulting in the preferential wear. There is also CaO which might act as a diffusion barrier for a further attack on the cBN grains [7], but the amount of such phase in 17–4 PH is very limited compared to usual inclusion engineered steels. Consequently, CaO has only a sparse presence on the tool-workpiece interface (Fig. 10).

Fig. 11 confirms the formation of a metal oxide, most likely $(Cr,Mn,Fe)_3O_4$ spinel, as a result of the oxidation of the 17–4 PH steel. The spinel is richer in Cr and Mn compared to Fig. 9. It also further confirms the preferential attack on cBN over TiC and Al_2O_3. These features suggest that wear by oxidation and diffusion is acting simultaneously. However, no oxides of the tool material phases or oxidation products (i.e. B_2O_3 or TiO_2) are identified, most likely because B_2O_3 and TiO_2 are immediately abraded away due to their very low strength and hardness [14], but the presence of metal oxide spinel confirms the oxidation taking place in the cutting zone [6,15]. No reaction products such as nitride, borides, carbides are identified while preferential wear of cBN is clear, hence diffusion wear is dominant over chemical degradation and formation of reaction products [16].

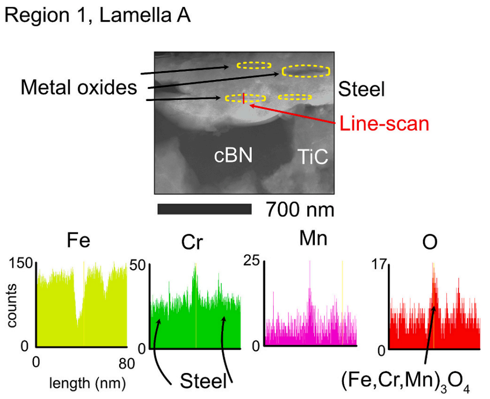

Fig. 9. STEM-HAADF image and STEM-XEDS line scan of region in lamella A from Fig. 8. The adhered material is not one layer but a mixture of steel and metal oxides.

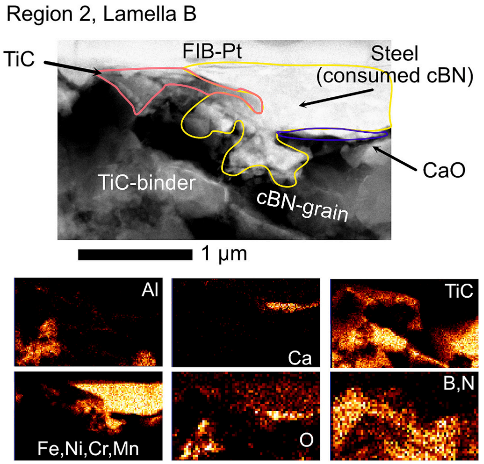

Fig. 10. STEM-HAADF image and STEM-XEDS maps of a region in lamella B from Fig. 8. The cBN is replaced by the steel/oxide due to diffusion and oxidation. The TIC binder is more resistant to this type of wear.

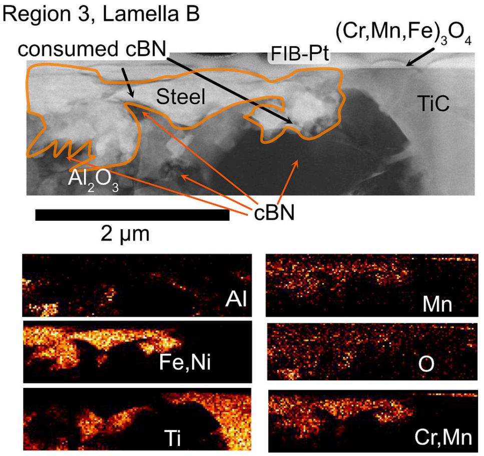

Fig. 11. STEM-HAADF image and STEM-XEDS maps of a region in lamella B from Fig. 8. Both TIC and Al_2O_3 from the binder is more resistant to wear in the crater than the cBN grains.

3.4. Test 3 addition of coatings

The addition of a $(Ti_{45}Al_{55})N$ coating to the pcBN insert leads to improvement in the tool performance at the tested speeds after 2400 m (Fig. 12). The flank wear VB_B is less at $v_c = 200$ m/min than 300 m/min, which was not the case for the uncoated tools, see dashed lined bars graphs in Fig. 12 or Fig. 3. This suggests that the coating protects the tool from the adhesive wear seen on the uncoated tool at $v_c = 200$ m/min.

This effect is of course only while the coating is intact. The coating is rapidly consumed in the crater and hence there is modest improvement in KT. However, the coating survives on the part of the chamfer not

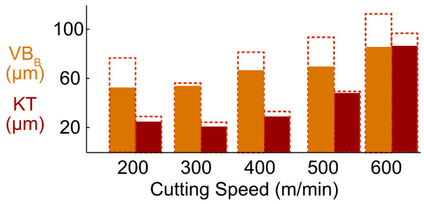

Fig. 12. Tool wear after 2400 m at different speeds of coated tools. Solid bars are coated tools, and dashed bars are for uncoated tools for comparison, also in Fig. 3.

consumed by the crater, and this is true at all cutting speeds. Fig. 13 shows the intact coating on the chamfer at $v_c = 400$ m/min compared to the uncoated tool. The chamfer region seems to coincide with the sticking zone where the tangential stress has a plateau as a result of an intense adhesion between the tool and workpiece material and internal material flow [12,13]. However, the adhesive wear mechanism registered for the uncoated pcBN tool at speed of $v_c = 200$ m/min (Fig. 6) is not detectable on the coated tool at any speed. Consequently, there is less edge chipping detected on $(Ti_{45},Al_{55})N$ coated pcBN tool at the speed $v_c = 200$ m/min.

But there is not a significant improvement in performance of the tool life (Fig. 14), since the coating only survives on the chamfer. The chamfer will also eventually be consumed when the crater wear expands towards the edge line and wears out the remnants of the chamfer as seen in one location in Fig. 13. This is the reason for the edge fracture observed for the $(Ti_{45},Al_{55})N$ coated pcBN tool at $v_c = 400$ m/min (Fig. 13 and 14). Removal of the chamfer and the presence of the crater right at the cutting edge creates a positive rake angle as opposed to the $\gamma = -26°$ for the new tool. Consequently, the created positive rake angle produces a weaker tool geometry which fails under the mechanical load. But the exact time of the edge failure was not predictable. This applies to both coated and uncoated tools. But this is different from the adhesion seen when machining an uncoated tool at $v_c = 200$ m/min which resulted in a failed edge (Fig. 6), comparing with Fig. 13 at $v_c = 400$ m/min which has a failed edge but show no signs of adhesion.

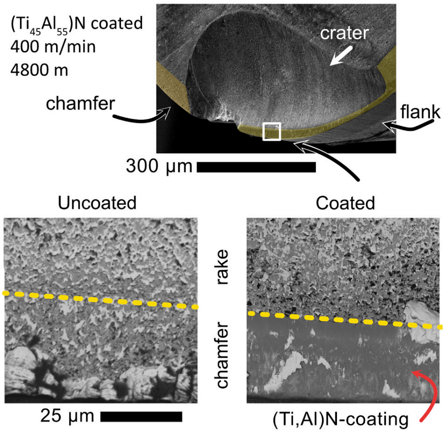

Fig. 13. BSE-SEM images of a coated and an uncoated tool at cutting speed 400 m/min. The coating on the chamfer is intact, until the crater consumes the chamfer.

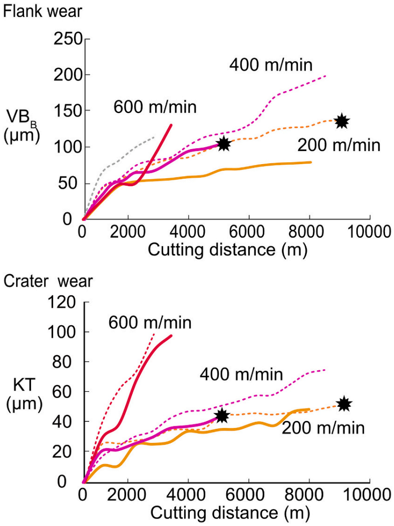

Fig. 14. Tool life at different speeds of coated tools. Solid lines represent coated tools, the same-colored dashed line represent the same speed but uncoated tool (from Fig. 3). The star represents a broken edge.

4. Discussion

Flank wear is present at all speeds and appears as polished grooves (Fig. 2, 4, and 5). Abrasion alone does not contribute to the development of flank wear VB_B (Fig. 2,3, 4, 12, and 14). The hardness of the 17–4 PH after the heat treatment is rather modest (HRC 46) compared to cBN, TiC and Al_2O_3 (Fig. 1). However, the NbN and Al_2O_3 in the steel (Fig. 1b) have high enough hardness to possibly abrade the pcBN, or at least the binder phases of TiC and Al_2O_3. The worn insert flanks in this study are more similar in appearance to martensitic steels containing no precipitates then martensitic steels containing a high concentration of hard precipitates, a comparison is shown in [9]. Hence the flank wear is due to a combination of abrasion, adhesion, and diffusion wear by the martensitic matrix [9], diffusional wear around cutting edge defects [10], abrasion by hard precipitates [9], and self-abrasion by loose cBN particles [11].

There are definite signs of oxidation wear mechanisms on the rake confirmed by the formation of oxidation reaction products of the workpiece material adhered to the tool surfaces [4,6] (Fig. 9–11), which are not present in the original steel (Fig. 1b). B_2O_3 and TiO_2 which are potential oxidation products of the pcBN phases may have formed, but cannot be conclusively detected with the advanced microscopy as they are of very low hardness and will be instantly abraded away [14,16].

There is also evidence of a diffusional attack on cBN (Fig. 9–11). Chemical degradation of the tool may potentially be present due to reactions between the tool and steel such as the formation of metal borides and nitrides which are not as wear resistant as the original tool material [6], however none of such products have been found on the tools surface and the tool-chip interface. This suggests that the diffusional rate is high, and such products never form as the concentration of nitrogen or boron is insufficient, or that these phases form but are instantly abraded away [14–16].

The cBN is preferentially worn over the TiC binder (Fig. 9–11) which explains why more TiC is visible on the surface than what could be expected (Fig. 7). This is not unexpected [6], but the extent and absence of any formation of reaction between tool and steel would be hard to predict without experimental investigation and thermodynamic calculations [16]. Fig. 15 shows a simple schematic of the wear mechanism on the rake, summarizing the conclusions drawn from SEM images in Fig. 5 and 7 as well as TEM images in Fig. 9–11.

Adhesion and tool material pluck out is only observed on uncoated tools at speed 200 m/min (Fig. 6). There is a shift of the wear balance when the speed increases (Fig. 2). The shift in wear is from the adhesive wear mechanism to more wear by diffusion and oxidation. These observations follow the conventional relationship [12,13] between the wear mechanisms and the cutting speed and process temperature. The onset of the intensive oxidation seems to create two effects, the build-up layer with mixed in oxides (Fig. 8–11) softened due to the temperature and is weakened by the extensive amount of spinel oxides. All such effects contributing to lowering the pcBN pluck out, but it also leads to more cratering due to rapid oxidation of the cBN and binder phases and their removal alongside with the diffusional dissolution [7]. The extreme cases being 600 m/min (Fig. 2). This shift away from adhesion at increasing speeds is well known [17], but the results of the current study reveal the exact range for the given tool-workpiece pair. Fig. 16 shows how the crater is located on the chamfer at low speeds creating a weaker cutting edge compared to higher speeds, shown in in detail in Fig. 2, 4–8.

The flank wear VB_B and crater depth KT wear criteria do not fully enable an accurate prediction of the tool life due to edge fracture. VB_B is a good indicator of the quality of the machined surface, the KT has been instrumental in assessing weakening of the edge geometry. However, the cutting edge did fail twice (out of 12 tests) before either of the wear criteria was met. This is because the growth of the crater and flank wear leads to the removal of the chamfer. The crater is then at the cutting edge which creates a positive rake angle producing a weaker tool geometry, which sporadically fails under the mechanical load. Tools without a chamfer were also assessed in a pre-study but failed rapidly, due to the weaker tool geometry even without significant crater wear.

Hence an additional wear criterion might be appropriate to avoid sporadic edge failure, such as crater front distance (KF) [7,18]. This is true particularly for the cases where the edge failures occurred due to the crater consuming the chamfer as seen in (Fig. 4 and 13). The importance of the intact chamfer can be expected from similar machining experiments [7], but it is difficult to predict the extent of this. Fig. 17 schematically shows how the crater consuming the chamfer led to a positive rake angle and weaker tool geometry also seen detail in Fig. 2, 4, 6, 13 and 14.

The (Ti,Al)N coating survived on the chamfer (Fig. 13 and 18). This changes the wear pattern especially at speed 200 m/min. But the coating did not survive on either the tool flank or in the crater and if the chamfer is consumed (Fig. 17). A larger test matrix is needed to investigate this resistance to adhesion and if this protection of the chamfer leads to significantly less sporadic edge failures. The results also suggest that the coating might affect the performance at more moderate speeds.

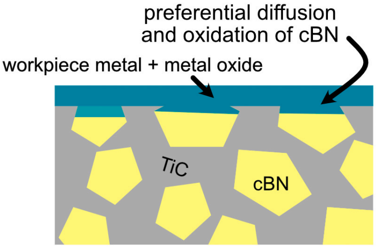

Fig. 15. Wear mechanism. A film consisting of a mixture of metal and metal oxide is formed on the tool, increasing in thickness with speed. There is also preferential attack on cBN grains over the TiC binder.

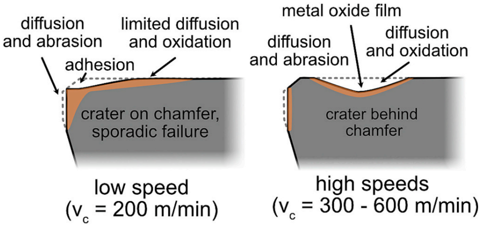

Fig. 16. Wear at different speeds. The crater is located on the chamfer at low speeds, leading to sporadic failure, it also suffers from more adhesive wear. The crater is located behind the chamfer at higher speed, and the tool suffer from more wear by diffusion and oxidation.

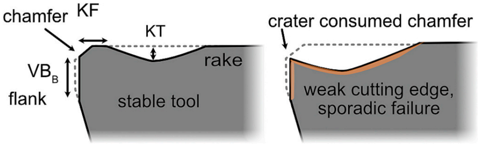

Fig. 17. The change in rake angle due to crater wear. Severe crater wear leads to the chamfer being consumed. Creating a positive and weak rake angle. Leading to sporadic failure. KF should be monitored in addition to VB_B and KT.

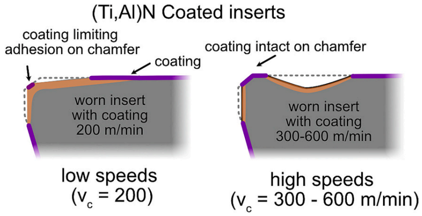

Fig. 18. The effect of the addition of a coating. The coating does not survive on the flank or in the crater but protects the chamfer.

5. Conclusion

Turning 17–4 PH in a precipitation hardened condition (HRC 46) within a high-speed machining regime of $v_c = 200$–600 m/min can be done successfully with pcBN tooling for a machining distance of 2.5 to 10 km with less than 200 μm of flank wear (Fig. 2 and 3). This allows for faster cycle time and longer tool life compared to cemented carbide, with the possibility to avoid heat treatment post-machining and final grinding.

The wear mechanisms are not the same across the speed range. Flank wear is present at all speeds, but the nature of the smooth grooved appearance with a limited number of scratches is not only abrasive. It is most likely due to a combination of abrasion, adhesion, and diffusion. The few scratches can be due to the harder NbN and Al_2O_3 inclusions, as well self-abrasion by loose cBN particles which plough the flank resulting in scratches.

The tool material loss by adhesive wear and edge failure was observed only on the uncoated tool at the speed of $v_c = 200$ m/min (Fig. 6 and 16). The cBN grains are worn faster than the TiC binder

(Fig. 9–11 and 15), due to a higher rate of oxidation and diffusion. These mechanisms contribute to the accelerated wear with the increase of the cutting speed which eventually results in the severe cratering at 600 m/min within 4 min of machining (Fig. 2 and 3). The oxidation process primarily affects the adhered build up layer at speeds of $v_c = 300$–500 m/min the, resulting in formation of metal oxides, such as $(Cr,Mn,Fe)_3O_4$ spinel (Fig. 7–11).

The intactness of the chamfer is of importance, because the removal of the chamfer by adhesion at low speeds ($v_c = 200$) or a growing crater at higher speeds ($v_c = 300$–600 m/min), leads to a positive and weak rake angle leading to sporadic edge failure. In this way the chamfer and crater front distance KF should be measured and monitored alongside the VB_B and KT (Fig. 17). The tool should be exchanged when the crater and flank wear consume the chamfer monitored by KF, to prevent a spontaneous edge failure.

The (Ti,Al)N coating plays a role in suppressing the adhesive wear mechanism at $v_c = 200$ m/min but it also remains intact on a part of the chamfer not consumed by the crater or flank wear at all speeds (Fig. 13 and 18).

CRediT authorship contribution statement

A. Bjerke: Writing – review & editing, Writing – original draft, Visualization, Validation, Methodology, Investigation, Formal analysis, Data curation, Conceptualization. **J. Casas:** Writing – review & editing, Methodology, Investigation, Formal analysis, Data curation, Conceptualization. **F. Lenrick:** Writing – review & editing, Visualization, Supervision, Investigation, Formal analysis. **J.M. Andersson:** Writing – review & editing, Validation, Supervision, Resources, Methodology, Formal analysis, Conceptualization. **R. M'Saoubi:** Writing – review & editing, Supervision, Resources, Project administration, Methodology, Investigation, Funding acquisition, Formal analysis, Conceptualization. **V. Bushlya:** Writing – review & editing, Visualization, Validation, Supervision, Resources, Project administration, Methodology, Investigation, Funding acquisition, Formal analysis, Conceptualization.

Declaration of competing interest

The authors declare that they have no known competing conflict of interest that could have appeared to influence the work reported in this paper.

Acknowledgement

This research was partly funded by the Global Training Programme by the Basque Government and Mondragon University and partly by the Vinnova project DETECT (grant 2023-03561). The authors would like to express gratitude to Seco Tools AB for their support with the custom tooling and coating solutions.

Data availability

Data will be made available on request.

References

[1] W.-T. Chien, C.-S. Tsai, The investigation on the prediction of tool wear and the determination of optimum cutting conditions in machining 17-4PH stainless steel, J. Mater. Process. Technol. 140 (2003) 340–345, https://doi.org/10.1016/S0924-0136(03)00753-2.

[2] P. Sivaiah, D. Chakradhar, Effect of cryogenic coolant on turning performance characteristics during machining of 17-4 PH stainless steel: A comparison with MQL, wet, dry machining, CIRP J. Manuf. Sci. Technol. 21 (2018) 86–96, https://doi.org/10.1016/j.cirpj.2018.02.004.

[3] F. Clavier, F. Valiorgue, C. Courbon, M. Dumas, J. Rech, A. Van Robaeys, F. Lefebvre, A. Brosse, H. Karaouni, Impact of cutting tool wear on residual stresses induced during turning of a 15-5 PH stainless steel, Procedia CIRP 87 (2020) 107–112, https://doi.org/10.1016/j.procir.2020.02.074.

[4] K. Sobiyi, I. Sigalas, High-speed machining of martensitic stainless steel using PcBN, J. Superhard Mater. 38 (2016) 34–39, https://doi.org/10.3103/S1063457616010056.

[5] K. Sobiyi, I. Sigalas, Chip formation characterisation and TEM investigation of worn PcBN tool during hard turning, Mach. Sci. Technol. 19 (2015) 479–498, https://doi.org/10.1080/10910344.2015.1051542.

[6] J. Angseryd, H.-O. Andrén, An in-depth investigation of the cutting speed impact on the degraded microstructure of worn PCBN cutting tools, Wear 271 (2011) 2610–2618, https://doi.org/10.1016/j.wear.2010.11.059.

[7] H. Persson, F. Lenrick, L. Franca, J.-E. Ståhl, V. Bushlya, Wear mechanisms of PcBN tools when machining AISI 316L, Ceram. Int. (2021), https://doi.org/10.1016/j.ceramint.2021.08.075.

[8] S. PalDey, S. Deevi, Single layer and multilayer wear resistant coatings of (Ti,Al)N: a review, Mater. Sci. Eng. A. 342 (2003) 58–79, https://doi.org/10.1016/S0921-5093(02)00259-9.

[9] G. Poulachon, B. Bandyopadhyay, I. Jawahir, S. Pheulpin, E. Seguin, Wear behavior of CBN tools while turning various hardened steels, Wear 256 (2004) 302–310, https://doi.org/10.1016/S0043-1648(03)00414-9.

[10] V. Bushlya, J. Zhou, P. Avdovic, J.-E. Ståhl, Performance and wear mechanisms of whisker-reinforced alumina, coated and uncoated PCBN tools when high-speed turning aged Inconel 718, Int. J. Adv. Manuf. Technol. 66 (2013) 2013–2021, https://doi.org/10.1007/s00170-012-4477-5.

[11] V. Bushlya, R. Lindvall, F. Lenrick, L. Magnusson Åberg, R. M'Saoubi, J.-E. Ståhl, Effect of ageing on machining performance of grey cast iron and its compensation by cutting speed management, CIRP Ann. 73 (2024) 45–48, https://doi.org/10.1016/j.cirp.2024.04.061.

[12] E.M. Trent, P.K. Wright, Metal Cutting, Fourth Edition, 2000.

[13] J.-E. Ståhl, Seco Tools AB, Metal Cutting: Theories and Models, Seco Tools AB, 2012.

[14] V. Bushlya, F. Lenrick, J.-E. Ståhl, R. M'Saoubi, Influence of oxygen on the tool wear in machining, CIRP Ann. 67 (2018) 79–82, https://doi.org/10.1016/j.cirp.2018.03.011.

[15] A. Bjerke, S. Norgren, H. Larsson, A. Markström, F. Lenrick, R. M'Saoubi, J. Petersson, L. Melk, V. Bushlya, Machinability improvement by in-operando Tool Protection Layers through designed steel alloying: The case of manganese steel, J. Mater. Process. Technol. 330 (2024) 118496, https://doi.org/10.1016/j.jmatprotec.2024.118496.

[16] A. Bjerke, A. Hrechuk, F. Lenrick, A. Markström, H. Larsson, S. Norgren, R. M'Saoubi, T. Björk, V. Bushlya, Thermodynamic modeling framework for prediction of tool wear and tool protection phenomena in machining, Wear 484–485 (2021) 203991, https://doi.org/10.1016/j.wear.2021.203991.

[17] K. Sobiyi, I. Sigalas, G. Akdogan, Y. Turan, Performance of mixed ceramics and CBN tools during hard turning of martensitic stainless steel, Int. J. Adv. Manuf. Technol. 77 (2015) 861–871, https://doi.org/10.1007/s00170-014-6506-z.

[18] ISO, Tool-Life Testing with Single-Point Turning Tools (ISO 3685), 1993.

Paper II

Wear 532-533 (2023) 205093

Contents lists available at ScienceDirect

Wear

journal homepage: www.elsevier.com/locate/wear

On chemical interactions between an inclusion engineered stainless steel (316L) and (Ti,Al)N coated tools during turning

Axel Bjerke [a,*], Filip Lenrick [a], Andrii Hrechuk [a], Kateryna Slipchenko [a], Rachid M'Saoubi [a,b], Jon M. Andersson [b], Volodymyr Bushlya [a]

[a] *Division of Production and Materials Engineering, Lund University, Ole Römers väg 1, Lund, Sweden*
[b] *R&D Materials and Technology Development, Seco Tools AB, 737 82, Fagersta, Sweden*

ABSTRACT

Non-metallic inclusions offer one of the most effective routes for improving the machinability of steels. However, the wear-reducing mechanisms activated by such inclusions are not fully understood. The interactions are notoriously difficult to predict due to the wide variety of steel grades, cutting conditions, and tool materials employed in industry. The interaction between PVD (Ti,Al)N coated cemented carbide tools, non-metallic inclusions, atmospheric oxygen, and the stainless steel 316L in a turning operation is therefore investigated here as a case study. The study includes turning experiments, nanometer resolution microscopy, and thermodynamic calculations. The paper explains how not only too high a contact pressures hinder the formation of protective deposits at the tool edge, but also how too low a contact pressure leads to excessive wear. A range of conditions specified in this paper must therefore be met for the two observed protective non-metallic inclusions $Mg_1Al_2O_4$ and $Al_2Ca_2Si_1O_7$ to be preferentially deposited on a tool. Hence the coating wear is experimentally investigated, explained, and a thermodynamic calculation method for predicting the protective or degenerative potential of a deposit on the coating is presented.

1. Introduction

(Ti,Al)N coated carbide tools are often used in the metal cutting industry when turning stainless steels [1,2]. Physical vapor deposited (PVD) (Ti,Al)N coatings are known to have superior hot hardness and improved oxidation resistance to other common Ti-based coatings, such as TiN, TiC, and Ti(C,N) [3,4].

Non-metallic inclusions (NMI) are an inherent part of the steel-making process. Controlling their distribution, composition and morphology is a common method for improving machinability and castability. However, the inclusions often have a negative impact on the corrosion and mechanical properties of the material [5]. Inclusion engineering can improve machinability by decreasing abrasive tool wear, easing chip formation, improving the tribological contact, and forming chemically protective deposits on the tool [6–8]. Inclusion engineering for improved machinability was initially developed for uncoated cemented carbide and high-speed steel tools [9–11].

Inclusion engineering has also been used to improve machinability when turning with coated tools. Nordgen and Melander [12] studied multilayered TiC-Al_2O_3-TiN coated tools during turning of Ca-treated quenched and tempered steel. They concluded that MnS inclusions contribute to machinability at low cutting speeds, and calcium sulfides and calcium aluminates at higher speeds. Ruppi et al. [13] compared chemical vapor deposition (CVD) coatings of TiC, Ti(C,N), TiN, and Al_2O_3 types when turning Ca-treated quenched and tempered Al-killed steels. They noted that the protective and degenerative action of the deposits depends on the hardness and chemical composition of the NMI in relation to the hardness and chemical stability of the coating. Larsson and Ruppi [14] also used transmission electron microscopy (TEM) to investigate the relationship between steel inclusions and deposits on tools. They observed that cubic (Ca,Mn)S and hexagonal $Ca_1Al_{12}O_{19}$ were the most significant inclusions contributing to the adhered layer at higher speeds. The distribution and thickness of adhered materials on Ti(C,N)-Al_2O_3-TiN coated tools when machining Ca-treated 316L has also been studied using laser ablation time-of-flight mass spectrometry (LA-TOMS) [15,16]. These studies showed that the inclusions were thickest where the temperature was around 800 °C in the second half of the tool–chip contact area, and not at the maximum temperature in the first half of the chip contact area. The combined results from these studies show that inclusion deposits can function both as mechanical and diffusion protection layers when machining inclusion engineered steels using Al- and Ti-based nitride coatings [13,14,17–20]. However, the distribution, type, and thickness of the layers depend on the tool, steel, and cutting conditions [15,16].

Certain tool and coating materials are not compatible with certain types of inclusions. Studies by Narutaki and Murakoshi [21] and Brandt

---

* Corresponding author.
E-mail address: axel.bjerke@iprod.lth.se (A. Bjerke).

https://doi.org/10.1016/j.wear.2023.205093
Received 19 April 2023; Received in revised form 14 July 2023; Accepted 12 August 2023

and Mikus [22] compared cemented carbide and Al_2O_3 ceramic tools with an addition of TiC when turning steels with and without inclusion engineering. The results highlighted the importance of pairing the correct tool material with the correct inclusion type. Silicon- and calcium oxide inclusions increase the degradation of the aluminum oxide tool material [21,22]. This was also observed on the rake of the tool in recent studies when machining inclusion engineered steels with alumina coated tools [23,24]. The CVD Al_2O_3 coating reacted with the steel, air, and inclusions during turning, and formed a less wear resistant aggregate of complex oxides, leading to rapid tool wear [23]. The explanation offered and shown by experiments and calculation [25] was that there is a positive thermodynamic driving force for the CVD Al_2O_3 coating to react with the steel, air and inclusions. This reaction degrades the Al_2O_3 coating into softer mixed oxides. One type of deposit can act as a diffusion barrier for one tool material while degrading another tool material, because the elements in one coatings might be able to diffuse well in the deposit, while the elements in another coating might not be able to diffuse in that deposit at all (differences in mobilities) and some coatings cannot react with the deposits while other coatings readily react (differences in reactivity) [25–28]. However, this has not been thoroughly investigated for the industrially common (Ti,Al)N coated tools, using the combination of thermodynamics and experiments.

The effectiveness and performance of a specific inclusion type will thus change from case to case, depending on the interplay between the cutting conditions, tool material, and workpiece material. For example, a Ca-treatment can improve the machinability of a stainless steel using a TiN coated tool [13], but can lead to increased rake wear of alumina coated tools during machining of a low alloy steel [24].

High resolution microscopy studies of turning steels with (Ti,Al)N based coatings have observed adhered steel and inclusions on top of the coating [19,29–31]. These studies have mostly focused on the performance of the coating, and not on the interplay between the deposits and adhered material with the coating. Thus while inclusions and steel have been shown adhered to (Ti,Al)N based coatings, how the (Ti,Al)N coating interacts with inclusions and steel deposits has not been sufficiently investigated. Without this knowledge it is difficult to model and predict the mechanism of tool wear in order to properly pair the correct inclusion engineering steels with (Ti,Al)N tools. An incorrect choice risks the inclusion consuming the coating, rather than protecting it. The difficulty increases further when dealing with doped, multilayered, and nanolayered (Ti,Al)N coatings.

Therefore this work specifically studies how the coating interacts with adhered steel and inclusions for a (Ti,Al)N coated tool. The study investigates differences across the tool rake face and how they change as the wear progresses. The investigation will include why and how certain materials adhere to the rake and degrade or protect the coating. This is achieved by employing scanning electron microscopy (SEM) and transmission electron microscopy (TEM) combined with thermodynamic calculations. This combination of electron microscopy and thermodynamics show how the interaction between the coating and the adhered material can be predicted.

2. Methods

Prodec® 316L, an austenitic machinability-improved stainless steel with controlled distribution and morphology of NMIs, was used for the machining tests. The chemical composition of the 316L steel is provided in Table 1. The NMIs in this steel are MnS and various complex oxides of (Ca, Si, Al, Mg)$_x$O$_y$. This enables the study of how a variety of inclusions interact with the coating during turning.

Table 1
Chemical composition of 316L, wt. %.

C	Cr	Ni	Mo	Fe
0.02	17	10	2	Balance

A cemented carbide tool with a PVD cathodic arc ($Ti_{45}Al_{55}$)N coating deposited by the method outlined in Ref. [30] was used. The tool has the ISO CNMG120408-MF1 geometry, and was used with the tool holder PCLNL2525M12. Longitudinal turning was done on a CNC lathe SMT 500 (70 kW) with flood coolant consisting of a 6% oil-water emulsion supplied at 8 bars pressure. Cutting conditions were selected to provide sufficient tool life to investigate the onset of wear, medium coating degradation, and severe coating degradation and to reflect actual production usage. This was done using iterative testing initially based on tool and steel manufacturers recommendations. Thus, a feed of $f = 0.2$ mm/rev, a depth of cut $a_p = 1.5$ mm, and a cutting speed of $vc = 185$ m/min were selected, which provides a coating life of at least 15 min. The tool life is longer, meaning that the tool can be used further after the coating is worn through, but this is not the focus of this study. Three separate machining tests with engagement times of T = 2, 6.3, and 15 min were performed to represent different states of coating wear. A new tool was used each time.

The coating wear was examined using a SEM (TESCAN Mira3) equipped with secondary electron (SE), backscatter electron (BSE) and X-ray energy dispersive spectroscopy (XEDS) detectors. SEM images are acquired using 10 keV and 30 keV is used to make more quantitative XEDS measurements. Lamellas for TEM investigation were prepared by a lift-out procedure using a focused ion beam (FIB, FEI Nova NanoLab 600). A TEM (JEOL 3000F) equipped with XEDS was used to investigate the lift-out lamellas. Scanning transmission electron microscopy (STEM) micrographs were obtained using both low-angle (LAADF) and high-angle annular dark field detectors (HAADF). Selected area electron diffraction (SAED) was also undertaken to achieve high resolution and in-depth understanding of the tool and deposit interaction.

The thermodynamic calculations were performed using the CALPHAD method, which enables the calculation of phase equilibria of multicomponent systems. Thermo-Calc® was used for these calculations [32] using the TCFE12 and TCOX11 databases. This enabled the study of the chemical stability and the driving force for degradation of the coating in contact with the steel, inclusions, and oxygen.

3. Results

Flank wear remained marginal compared to rake wear throughout the turning test, and the main coating damage was sustained on the tool rake surface. The edge region of the tool rake suffers from mechanical failure, leading to partial delamination of the coating. The cemented carbide substrate on the edge is exposed, and then covered by inclusions and adhered steel. The initial adhesion and delamination is likely due to the edge experiencing the highest normal stress and hence contact pressure [33,34]. This leads to mechanical spalling of the coating and adhesion to the substrate [35]. This edge delamination is similar to the results of Wiklund et al. when turning 316L using TiN tools [35]. They showed that adhered Fe acts as preferential sites for more adhesion, which leads to more coating delamination. The edge of the tool with exposed cemented carbide substrate becomes covered with adhered metal. The edge of the tool then acts like an uncoated tool, as has been studied elsewhere [7,26,36].

The analysis of the progression of coating wear in this study is therefore mainly focused on three areas on the rake. The wear progression is the same within each area, but differs between the areas. Hence studying each area separately and investigating it progressively, makes the analysis more coherent. The areas are: ***P*** – the periphery of the contact area, ***Max*** – the area of maximum chip thickness, and ***Min*** – the area of minimum chip thickness. These are shown in Fig. 1. Separating the tool into the.

The thermodynamic calculations are focused on how the chemical, oxidation, and diffusion wear differ and progress in these areas. The highlights from the analysis of the progression of wear are described in sections 3.1 Onset of coating wear, 3.2 Medium coating degradation and 3.3 Severe coating degradation. For additional data, refer to the

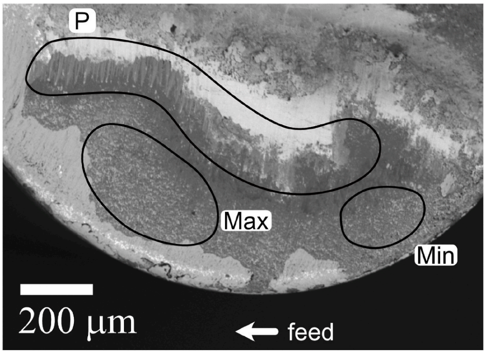

Fig. 1. Overview of rake of the tool showing the three areas selected for investigating the progression of wear. **P** – the periphery of the contact area, **Max** – the area of maximum chip thickness, **Min** – the area of minimum chip thickness,.

supplementary material.

3.1. Onset of coating wear

Fig. 2a shows a composition-sensitive backscatter electron (BSE) image of the rake after the onset of wear, which occurs after 2 min in cut. BSE relies on Z-contrast and thus illustrates compositional variations.

The adhered material in the periphery (***P***) of the contact area (Fig. 2b and Fig. 3) exhibits varying composition and thickness, as shown by the brightness difference in the BSE image (Fig. 2b). Grooves in the adhered material and large tooth-like deposits are clearly seen in the topography-sensitive secondary electron (SE) image in Fig. 3. The (Ti,Al)N coating is intact in this area, as shown by the strong XEDS signal from Ti, Al, and N (the lower part of Fig. 3). The (Ti,Al)N coating is not detectable through the large tooth-like deposits of Cr, Mn and O in the upper part of Fig. 3. This deposit located on the periphery of the tool–chip contact experiences the lowest contact pressure and high oxygen availability [33]. These thick deposits are comparable to the deposited and oxidized workpiece material seen both in turning [37,38] and in pin-on-disk tests [39]. There is preferential oxidation of Cr and Mn over Fe and Ni in the tooth-like deposits. Formation of $MnCr_2O_4$ spinel in a similar region of the tool–chip contact was reported when machining 316L with PcBN tools [40]. The ratio of Cr and Mn to O in the tooth-like deposits measured using XEDS agrees with such a Cr oxide spinel. The inclusions in the steel do not contain Cr and Mn is only present in the inclusions, hence the deposit must form as a result of workpiece and inclusion deposition, oxidation, and build-up.

The coating has also been severely worn in the region left of the teeth (Fig. 3a), as shown by the W-signal (substrate) in Fig. 3f and the low signal from Ti, Al, and N (coating) (Fig. 3b–**d**). The EDX maps can be misleading since they show concentration differences. However, point analysis shows that the substrate is detectable (W-signal), but not exposed enough to get a strong Co signal. It is also covered with a Cr and Fe oxide. Point analysis of the periphery of the cutting zone outside the tooth-like area shows that the deposits consist of a mixed oxide rich in Fe, Cr, and Mn that is thinner than the tooth-like deposits. Ca and S were not present in significant amounts.

The second area (***Max)*** with maximum chip thickness (Fig. 2a, Fig. 2c and Fig. 4) has closely spaced streaks in the chip flow direction that have an appearance typical of abrasive wear marks. However, these abrasion marks are in the deposits located atop the original coating, not in the coating itself. Two types of deposits are present in this region. The central region has higher concentrations of Fe, Ni, Cr, Mn, Mg, and O, while the region closer to the periphery has higher concentrations of Ca, Mg, Cr, and O. The brightness difference in the Ti-, Al-, and N-signals is due to the thickness of the adhered material rather than the coating thickness. Adhered steel is seen in the bottom left of Fig. 4a, which shows the edge of the larger area of exposed cemented carbide covered with adhered steel in Fig. 2. Sulfide deposits are not significant in this region.

The cutting temperature and shear stress are highest in this region of maximum chip thickness [33,34], which is often the location of the highest rake wear when machining non-machinability-improved 316L with (Ti,Al)N coated tools in similar conditions [20,30]. However, in our case, this is the area of thickest deposits and least rake wear.

Fig. 5a shows a SEM SE image of the third area (***Min***) with the minimum chip thickness (Fig. 2d). It is similar to region ***Max***, however it is located on the opposite side of the rake face, where the contact pressure and temperature are lower. There are deposits of high Fe, Ni,

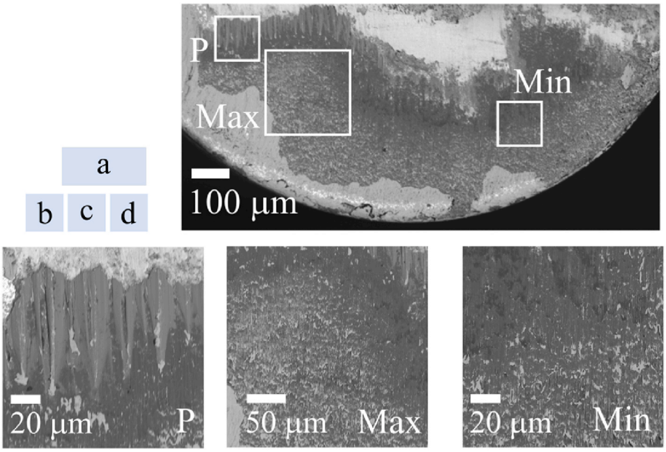

Fig. 2. (a) SEM BSE overview of rake face of the tool after 2 min in cut; (b–d) additional larger magnification images of the three areas selected for further analysis.

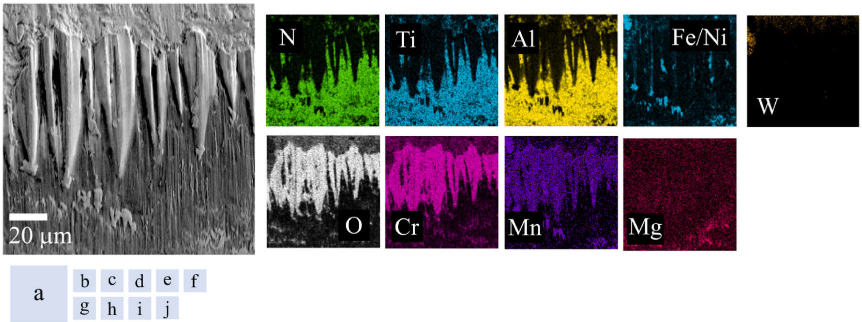

Fig. 3. (a) SEM SE and (b–j) XEDS analysis of the tooth-like deposits in the periphery, region **P** in Fig. 3, after 2 min of machining, displaying deposits of metal oxides on top of the coating at the end of the contact zone.

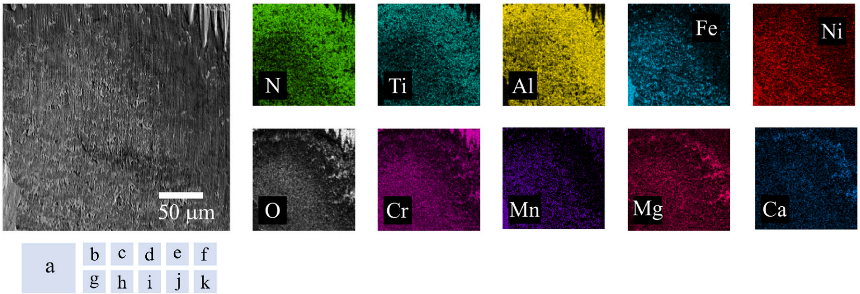

Fig. 4. (a) SEM SE and (b–k) XEDS analysis of deposit in area ***Max*** from Fig. 2 after 2 min of machining. This shows an area of Fe, Cr, Mn, Mg, Ni, and O rich deposit in the center and a Ca, Mg, Cr, and O rich deposit outside the center region.

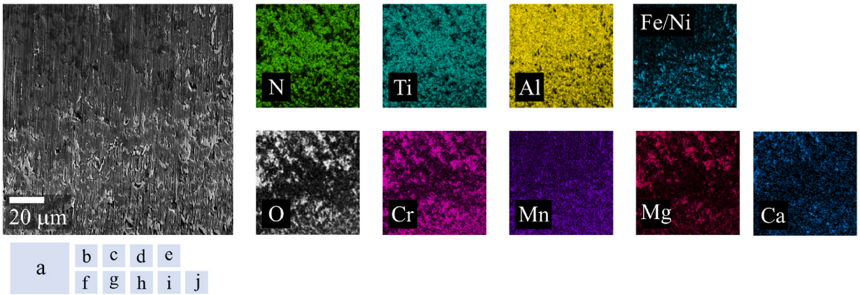

Fig. 5. (a) SEM SE and (b-k) XEDS images of deposits in area ***Min*** from Fig. 2 after 2 min of machining. Areas of Fe, Cr, Mn, Mg, and O rich deposits and streaks of Ca, Mg, Al, Cr, and O rich deposits are present.

Cr, Mn, Mg, and O concentration (the central region of Fig. 5) and areas of high Ca, Mg, Cr, and O concentration (upper region of Fig. 5a).

It should also be noted that there are dark spots in the XEDS maps from the coating elements Ti and N (Fig. 5b and **c**). There was, however, signal from the coating element Al (Fig. 5d) where there is a lack of Ti and N, indicating that the Al-signal originated both from the coating and from the workpiece. Therefore, the upper region of area ***Min*** most likely contained Ca, Mg, Cr, O and Al. Streaks and deposits in the chip flow direction in the deposits were also visible in this area (Fig. 5a). Sulfide deposits are not significant in this region.

3.2. *Medium coating degradation*

Fig. 6 is an overview SEM BSE image of the tool after 6.3 min machining, which leads to medium coating degradation. SEM BSE images of the regions ***P***, ***Max***, and ***Min*** are shown in Fig. 6b–d. The selected

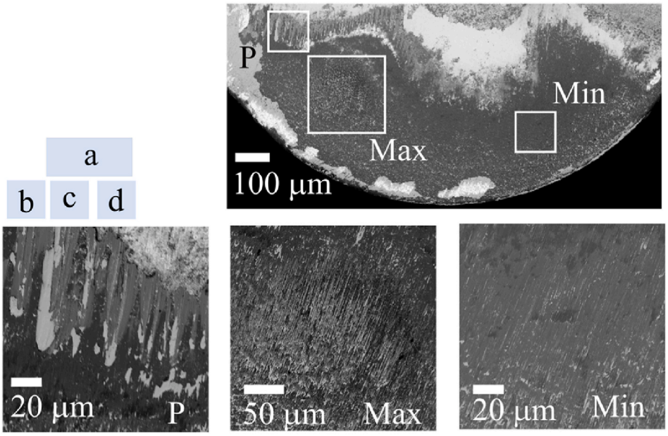

Fig. 6. (a) SEM BSE overview of the rake after 6.3 min in cut; (b–d) zoomed-in images of the areas selected for further analysis. The locations ***P*** (Fig. 6b), ***Max*** (Fig. 6c), ***Min*** (Fig. 6d) after 6.3 min are the same as the locations investigated after 2 min machining.

areas ***P***, ***Max***, and ***Min*** correspond to similar locations to those investigated for the tool studied at the onset of coating wear after 2 min (Fig. 2).

The tooth-like deposits on the periphery of the contact zone ***P*** (Fig. 6b and Fig. 7) contain Al and Si oxides, in addition to the Cr and Mn oxides seen after 2 min. The bright area of the tooth-like deposits in Fig. 6b is adhered steel with the same composition as the original material, hence Fe, Ni, Cr, and Mo (Mo not shown in the map). Significant amounts of Mg oxides are found in the lower part of this region as seen in Fig. 7j, which was also the case after 2 min. More substantial deposits of oxides are observed at the periphery of the contact area than after 2 min. A very weak signal from W (not shown in the map) was detected. The Ti, Al, and N signals were weaker, indicating a thinner (Ti,Al)N coating.

Sulfur is not significant in region ***P***. The deposits in this area have higher Cr content than the adhered material in the center of the rake. The build-up of oxidized material in this region is compositionally more similar to the adhered and oxidized material seen during high temperature tribology tests of (Ti,Al)N and 316L [39] than the inclusions present in the steel.

The deposits in the ***Max*** region (Fig. 6c) are similar but much thicker, and the abrasion tracks in the deposited layer are more pronounced than for a tool after 2 min in cut (Fig. 4a). Sulfide deposits are not significant in this region. In region ***Min*** (Fig. 6d), as in region ***Max***, the deposit after 6.3 min is thicker compared to the case after 2 min of machining (Fig. 5a). Abrasion tracks in the adhered layer are also clearer. Three types of deposits are identified: adhered workpiece material, MnS deposit, and Mg, Cr, Si, Ca, and O deposits. Additional BSE, SE and XEDS SEM images can be found in the supplementary material**.**

3.3. *Severe coating degradation s*

Fig. 8 is an overview SEM SE and BSE image of the tool after severe coating degradation that occurred after 15 min machining. A cross-section was made to investigate the periphery region (***P)***. TEM lamellas were extracted to investigate the ***Max*** and ***Min*** regions. These areas correspond to the regions ***P, Max,*** and ***Min*** of Fig. 2 (2 min) and Fig. 6 (6.3 min). The coating is severely worn, and the delaminated region has grown from the edge along the rake in two directions. The WC-Co substrate of the tool is exposed in these locations (the brightest areas in BSE) and is covered by adhered material (gray in BSE) seen in Fig. 8b. Pits have formed in the periphery of the contact zone (***P***) and are filled with adhered steel, (indicated in Fig. 8b). The coating is intact in the regions of maximum (***Max***) and minimum (***Min***) chip thickness***,*** and is still covered by deposits. The two TEM lamellas were extracted using a

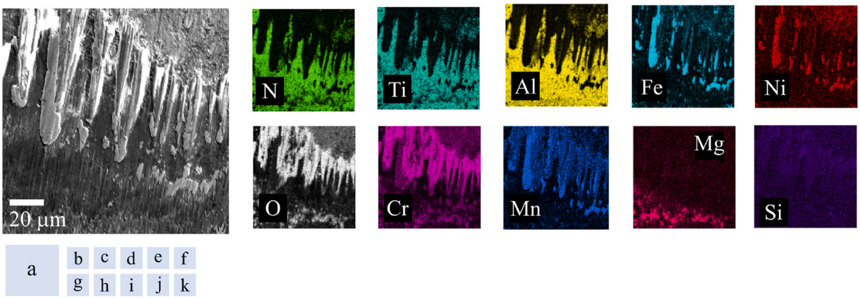

Fig. 7. (a) SEM SE and (b–k) XEDS analysis of deposit in the ***Max*** area from Fig. 6 after 6.3 min of machining. This displays deposits of metal and oxides on top of the coating. The weak W and Mo signals are not included.

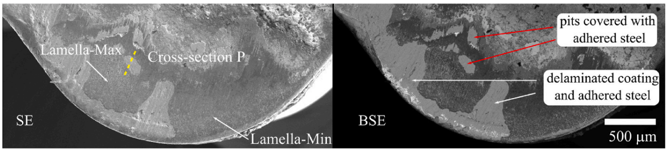

Fig. 8. A topography-sensitive SEM SE and a composition-sensitive BSE image of the severely worn coating after 15 min of machining.

FIB lift-out technique from the marked areas. Lamella ***Max*** corresponds to region ***Max*** and lamella ***Min*** to region ***Min*** investigated at initial and medium tool wear. The flank wear is still limited.

The coating is perforated in region ***P***. At the initial (2 min) and medium (6.3 min) tool wear stages, this region was covered by adhered steel and Mn and Cr oxide with tooth-like morphology (Fig. 3 and Fig. 7). The cross-section (Fig. 9h) shows how the adhered oxides and coating becomes thinner and thinner, ending with a pit where there is no coating. The pit is filled with adhered steel.

The deposit is thick in lamella **Max**, where the contact pressure and temperature are high [33]. There is steel adhered on top of the deposit. The two regions marked in Fig. 10 were investigated further.

Fig. 11a shows a composition-sensitive high-angle annular dark field (HAADF-STEM) image of Region 1 of lamella **Max**. The lamella is uniform in thickness, and the contrast in HAADF is therefore directly correlated to a variation in local average atomic mass. Fig. 11b is a crystal structure sensitive low-angle annular dark field (STEM-LAADF) image. SEM images of this region at shorter machining durations (Fig. 4 and Fig. 6c) showed that it contained a deposit containing Al, Fe, Cr, Mg, Si, Ca, Mn, S, and O. The STEM images (Fig. 11) show that this is not a homogeneous layer containing one oxide, but a distributed multilayer arrangement of different oxides and steel. The STEM-LAADF image shows the presence of a band structure consisting of coarse and fine grains. The borders between bands are marked by the yellow lines in Fig. 11b. The STEM-HAADF and accompanying XEDS maps show that three types of deposits are present in this region: i) A metal-rich deposit of similar composition to the workpiece material, seen as bright spots in Fig. 11a ii) An oxide phase that has a fine-grained structure with a composition approximately corresponding to $(Mg,Fe,Mn)_1Al_2O_4$. The highest content is Mg followed by Fe and Mn. iii) A coarse-grained oxide phase corresponded approximately to $Al_2Ca_2Si_1O_7$.

Formation of both Al-rich oxide deposits was likely the reason for an increased XEDS Al-signal in the same areas where the other coating elements (Ti and N) were absent in the SEM-XEDS maps. The smallest light gray spots in the HAADF image were identified as MnS, which can also be distinguished in region **Max** at medium coating degradation.

Fig. 12a shows the selected area electron diffraction (SAED) pattern from the fine-grain area. The XEDS measured composition and the diffraction pattern are in reasonable agreement with the spinel phase $(Mg,Fe,Mn)_1Al_2O_4$. Fig. 12b displays the diffraction pattern from the coarse-grain area, and is in reasonable agreement with $Al_2Ca_2Si_1O_7$ gehlenite. A diffraction pattern was also taken from the adhered metal (Fig. 12c) and from the (Ti,Al)N coating (Fig. 12d), both in good agreement with metallic austenite phase and the cubic (Ti,Al)N coating, respectively.

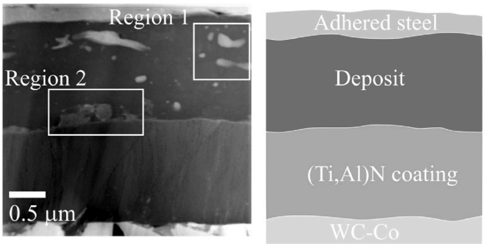

Fig. 10. STEM-HAADF image (left) and schematic illustration (right) of lamella **Max**. The lamella was extracted from region **Max** on the rake after 15 min of machining, as shown in Fig. 8. Regions 1 and 2 are investigated further.

Fig. 13 show a STEM-HAADF image and XEDS maps of Region 2 of lamella **Max** (Fig. 10), which was located closer to the coating. The phases identified as $(Mg,Fe,Mn)_1Al_2O_4$ and $Al_2Ca_2Si_1O_7$ layers are present across the entire lamella and hence are also observed in this region. Limited amounts of Fe and S could also be seen in this region. However, (Ti,Cr)N has formed directly on the coating–oxide interface, which is indicative of a reaction between the coating and the deposit or the steel. The formation of (Ti,Cr)(C,N) from Ti(C,N) has been shown in wetting experiments with steel on TiC-WC-Co tools [41]. The new product (Ti, Cr)N likely originates due to a reaction with Cr from the steel and the coating.

The location of lamella **Min** is shown in Fig. 8. This lamella, made after 15 min of machining, corresponds to region **Min** for the tools used for 2 min (Fig. 4) and 6.3 min (Fig. 6d) of machining.

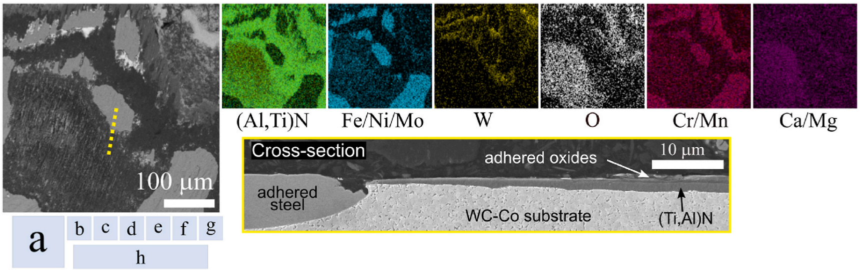

Fig. 9. (a) SEM BSE of the periphery (***P***) after 15 min of machining, (b–g) XEDS analysis, (h) cross-section of the region from the location marked by the dashed yellow line. (For interpretation of the references to colour in this figure legend, the reader is referred to the Web version of this article.)

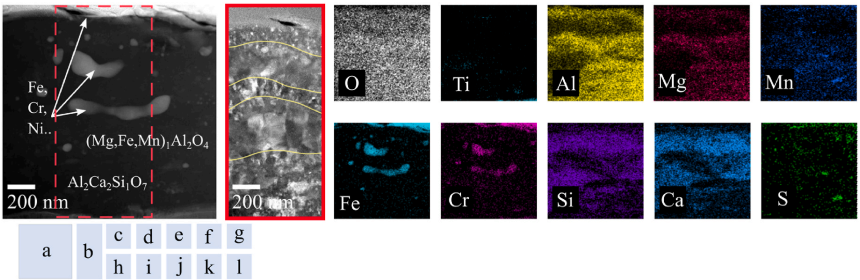

Fig. 11. (a) STEM-HAADF and (b) STEM-LAADF images of Region 1 of lamella **Max** of the tool used for 15 min with (c–l) the corresponding XEDS maps.

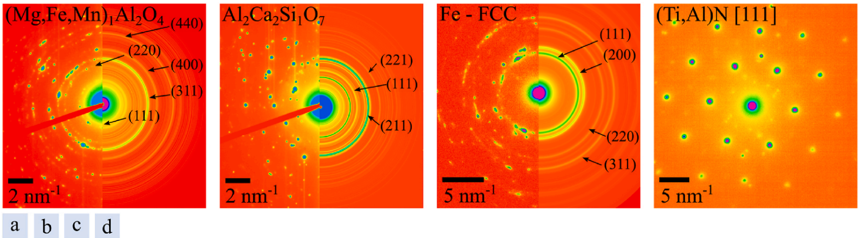

Fig. 12. SAED patterns from Region 1 of lamella **Max** (Fig. 8 and Fig. 9). The combination of STEM-XEDS and diffraction indicates that (a) the Al, Mg, Fe, Mn, and O phase was a $(Mg,Fe,Mn)_1Al_2O_4$ spinel phase, (b) the Al, Ca, Si, and O phase was $Al_2Ca_2Si_1O_7$ gehlenite, (c) the metal deposit (Fe,Ni,Cr, and Mo) was austenite, and (d) the (Ti,Al)N coating is cubic.

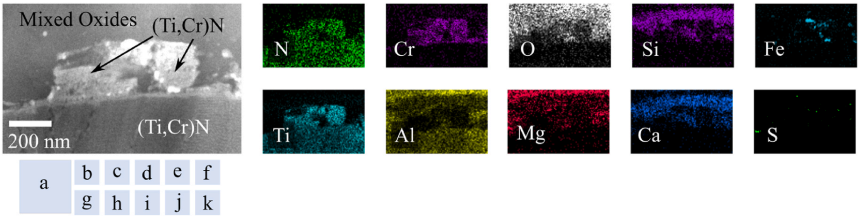

Fig. 13. (a) STEM-HAADF image and (b–k) XEDS maps of Region 2 of lamella **Max**. Similar mixed oxides are present in Region 2 as in the Region 1 (Fig. 11). However, (Ti,Cr)N has formed on the interface between the coating (Ti,Al)N and the deposit.

Fig. 15 shows a STEM-LAADF and XEDS of Region 3 in lamella **Min**. The coating and deposit was much thinner in this region. A multilayered oxide deposit structure was observed. The top layer is the adhered workpiece material (Fe, Cr, Ni, Mo), the second layer is the previously identified oxides, and the third layer is a workpiece metal oxide (Fe, Cr, Ni, and O) on the coating–deposit interface. Region 3 lamella **Min** is thus similar to lamella **Max**, but with a metal oxide layer separating the inclusion-based oxides from the coating. The Ti and N have diffused or reacted with the adhered material, since there are no detectable amounts of Ti or N in the steel, but there are Ti and N signals originating from the adhered material. Al is not as clear since the NMI contain Al.

The STEM-LAADF and XEDS images in Fig. 16 are from Region 4 of lamella **Min** (Fig. 14). There was no Fe, Cr, and Ni in direct contact with the coating as in Region 3, or metal globules as in Region 1, but two similar oxides one containing Al, Mg, Fe, and Mn and one containing Al, Ca and Si.

3.4. *Thermodynamics of steel–coating interactions*

The microscopy data of **Section 3.3** identified two oxides $(Mg,Fe,Mn)_1Al_2O_4$ and $Al_2Ca_2Si_1O_7$ on the surface where the coating remained intact during the cutting tests (Region ***Min*** and ***Max*** in Fig. 1). Data from region ***Max*** (Fig. 13) indicate that chromium from the steel can react with the coating to form (Ti,Cr)N. Data from the periphery (Region ***P*** in Fig. 1) indicate a correlation between a reaction of oxygen and Fe, Cr, and Ni oxides with the coating and the complete degradation of the coating and formation of pits (Fig. 9). Thermodynamic modeling is therefore focused on the possibility of calculating and potentially predicting what adhered material lead to either degradation or protection of the coating.

Table 2 shows what is thermodynamically favorable when the coating encounters adhered workpiece material, NMIs, or oxygen. The results are from equilibrium calculations between 1 mol of coating elements and 1 mol of the deposit, steel, or oxygen. One mole of Ar was

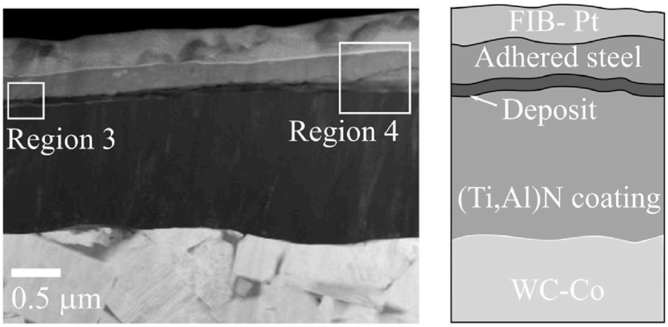

Fig. 14. STEM-HAADF image (left) and schematic illustration (right) of lamella **Min** located on the rake after 15 min of machining (Fig. 8). Region 3 and 4 are investigated further.

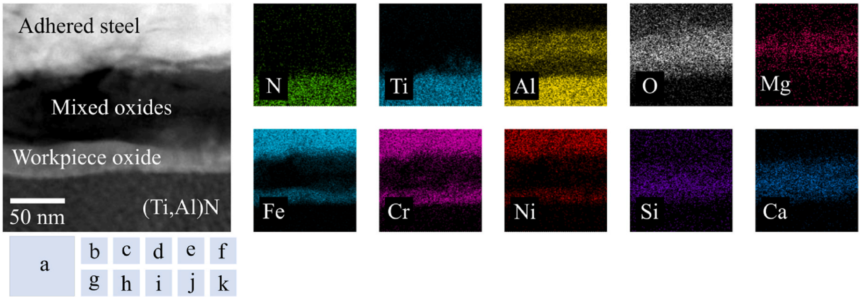

Fig. 15. a) STEM-HAADF image and accompanying (b–k) XEDS maps of Region 3 of lamella **Min**. The adhered layer was thinner and there was a metal oxide layer between the coating and the inclusion oxide layer, which is different compared to lamella **Max**.

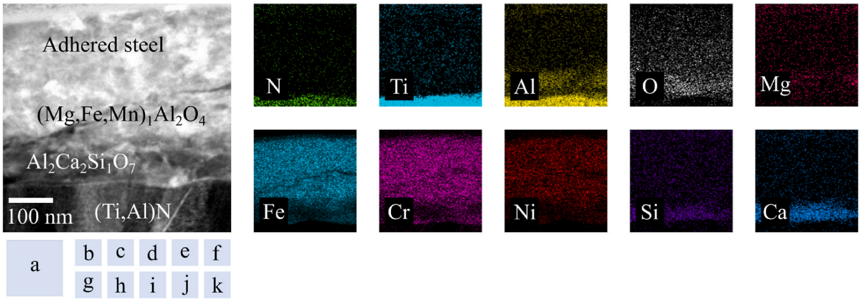

Fig. 16. (a) STEM-LAADF image and (b–k) XEDS maps of Region 4 lamella **Min**.

added to apply pressure. The calculation is performed by minimizing the Gibbs free energy of a system using Thermo-Calc software and the TCOX11 and TCFE12 databases [32]. Built correctly, this can be an efficient method to investigate whether the (Ti,Al)N coating is resistant to chemical, oxidation, or diffusion wear by a specific material. This method also calculates which phases the coating is likely to degrade into if it is not stable. In-depth explanations of this method can be found elsewhere [23,25,27,42–45].

Typical temperatures in the cutting zone for this type of machining operation range from 700 °C to 1100 °C [16,46] and contact pressures from 10^5 Pa to 10^9 Pa [34]. While the calculations were performed within the range of these parameters, only selected results for 800 °C at 10^5 Pa are shown for comparison, but the trend remains stable across pressures and temperatures. (Ti,Al)N is a metastable coating, hence the coating will be modeled by its equilibrium phases of hexagonal AlN and cubic TiN, which are thermodynamically more stable. The (Mg,Fe,

Table 2
Calculations of the stability of the coating and showing what phase may form when the (Ti,Al)N coating encounters the steel, oxygen, or an NMI at 800 °C and 10^5 Pa.

	O_2	*316L*	*316L + O_2*	*Spinel: $Mg_1Al_2O_4$*	*Gehlenite: $Al_2Ca_2Si_1O_7$*
TiN	Ti_xO_y	$(Ti_x,Cr_{1-x})N$ + Ti, N diffuse into steel	$(Ti_xCr_{1-x})N$ $+Ti_xO_{2y}$ + Ti, N diffuse into steel	Stable coating	Stable coating
AlN	Al_2O_3	Al, N diffuse into steel	Al_2O_3 + Al, N diffuse into steel	Stable coating	Stable coating

$Mn)_1Al_2O_4$ spinel contains much more Mg than Fe and Mn, and for simplicity it was modeled as $Mg_1Al_2O_4$. The stainless steel was modeled by its major elements ($Fe_{0.73}Cr_{0.18}Ni_{0.10}$). All phases available in the database are included. TCFE12 was used for metals and nitrides, and TCOX11 for oxides.

The results in Table 2 show that there is a positive thermodynamic driving force for the (Ti,Al)N coating to degrade when it comes into contact with air, steel, or oxidized steel deposits. The coating is, however, protected from diffusion, chemical, and oxidational attack when the mixed oxides adhere to the coating.

Fig. 17a is a plot of the equilibrium phase composition at 900 °C and 10^5 Pa, as the ratio of Cr_2O_3 to (Ti,Al)N increases. This is a simplified model of what happens to the (Ti,Al)N when more and more oxidized chromium is deposited on the coating, similar to what is seen in the cutting experiment in the periphery of the contact zone (***P***). The interaction of oxidized Cr from the steel with the (Ti,Al)N coating leads to the degradation of the coating into $(Ti_xCr_{1-x})N$ and $(Cr, Al)_2O_3$. These products are not necessarily epitaxial, may not adhere to the coating, and are hence much less resistant to abrasion. This eventually leads to mechanical removal of the reaction products and thus exposure of the substrate (Fig. 9).

Fig. 17b is a plot of the normalized driving force for new phases to form when 1 mol of (Ti,Al)N and 1 mol of 316L ($Fe_{0.73}Cr_{0.18}Ni_{0.09}$) are exposed to an increasing amount of O_2, expressed as the effective partial pressure of O_2. This ratio 1 mol–1 mol is a simplified model of what happens to the coating when the steel is adhered and oxygen is available. The ratio of steel, inclusions, and the coating (or more precisely the activity of the elements in the steel, inclusions, and the coating elements) depend on various factors. These include how the material adheres, the chip flow, and how the elements diffuse, dissolve, and react with the coating, inclusions, steel, and oxygen. Changing the activity of the individual elements was performed within this investigation; however, this simplified 1 to 1 mol ratio captures the main degradation mechanism. A low effective partial pressure of O_2 represents the case of limited oxygen, such as in the middle of the contact zone (e.g., regions **Max** and **Min**). A high effective partial pressure of O_2 represents the case when there is more ambient oxygen, such as at the periphery (**P**) of the contact zone. There is no driving force for the formation of new phases when the coating meets the steel, where there is limited oxygen. However outward diffusion of Ti, Al, and N is probable, and Cr can be dissolved in the (Ti,Al)N phase (Table 2). Furthermore, the driving force for the degradation of the coating into $(Cr,Al)_2O_3$, $(Fe,Ni,Cr,Al)_3O_4$ and TiO_2 is large and increases further when the availability of oxygen increases (Fig. 17b).

4. Discussion

The reason for the order in which the coating fails, as shown in Fig. 18, is not intuitively obvious. The edge line region fails first (white arrows), then the pits of the periphery (orange area), and lastly the center of the rake (red area).

The coating delaminated around the tool edge after less than 2 min of machining, as indicated by the white arrows in Fig. 18a. This area then grew into two large pits after 15 min (Fig. 18c). The initiation of the coating delamination is most likely due to adhesion. Abrasive wear of the intact coating was not seen as a major factor in this test since almost no flank wear was present, and flank wear is a good indicator of wear driven by abrasion [34,47,48]. The initial adhesion and delamination is likely due to the edge experiencing the highest normal stress and hence contact pressure [33,34]. This leads to mechanical adhesion [35], as well as possible diffusion welding, as shown in Table 2, since Al, Ti, and N are able to diffuse into the steel, and Cr from the steel can diffuse into the coating. This edge delamination is similar to the results by Wiklund et al. when turning 316L using TiN tools [35]. They showed that adhered Fe acts as a preferential site for more adhesion, which leads to more coating delamination.

The temperature and shear stress are highest [33,34] in the center (red area in Fig. 18) [33,34]. This is often the location of the highest rake wear when machining 316L with (Ti,Al)N coated tools in similar conditions [20,30]. However, in our case, the center (red area) is the region of least crater wear and has the thickest deposits (Fig. 10 and Fig. 14), except for the two growing areas of delamination, driven by the initial edge delamination. The periphery of the contact area (orange region in Fig. 18) experiences the lowest temperature and the least normal and tangential stress [33,34], but has the most access to oxygen. The center is expected to wear faster than the periphery if there are no protective inclusions [20,30]. But the periphery (orange area) experiences more coating degradation and the formation of large pits and exposed cemented carbide (Fig. 9), compared to the center (red area). However, the coating failure at the periphery is not driven by mechanical wear mechanisms but by oxidation and reactions with the adhered and

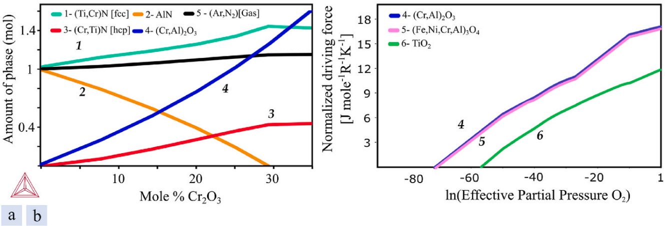

Fig. 17. (a) Modeling of the equilibrium phase composition of the interaction between (Ti, Al)N and Cr_2O_3 shows how the coating degrades as more Cr oxide is deposited, as seen in region **P.** (b) The normalized driving force for new phases to form between 1 mol of steel and 1 mol of coating depends on the availability of oxygen. The modeling shows how the combination of steel and oxygen drives the degradation of the coating seen in region **P**.

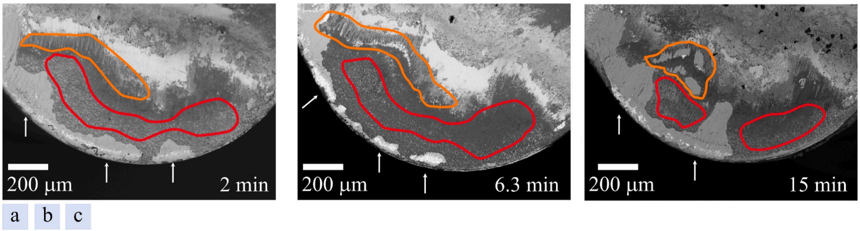

Fig. 18. SEM image showing the wear process: (a) onset of coating wear, (b) medium coating degradation, and (c) severe coating degradation. White arrows indicate delaminated coating, red areas indicate protective deposits and orange areas indicate non-protective deposits leading to pits of exposed cemented carbide. (For interpretation of the references to colour in this figure legend, the reader is referred to the Web version of this article.)

oxidized steel (Fig. 3, Fig. 7, and Fig. 9). The chemically degraded coating is then mechanically worn away. These types of oxide deposits are similar to those seen in tribology tests [39] and are also seen in Refs. [30,49]. The types of deposits in this area are not protecting the coating but degrading it. The availability of oxygen and the adhered and oxidized Fe, Mn, Ni, and Cr drives the coating degradation. It is seen by the formation of large pits in region **P** in Fig. 3, Fig. 7, and Fig. 9, and is explained by the positive thermodynamic driving force for coating degradation by oxygen, steel, and oxidized steel (Table 2 and Fig. 17).

This is the opposite of the deposits of the mixed oxide inclusions found in the center (regions **Min** and **Max** in Fig. 10–Fig. 16). The coating is the least worn in areas where (Mg,Fe,Mn)$_1$Al$_2$O$_4$ and Al$_2$Ca$_2$Si$_1$O$_7$ adhered to the coating. The coating was slightly thinner in regions where workpiece oxides adhered between the coating and inclusion oxides.

The reason for this is that certain oxides (two identified as (Mg,Fe, Mn)$_1$Al$_2$O$_4$ and Al$_2$Ca$_2$Si$_1$O$_7$) do not interact with the coating. Hence there is limited thermodynamic driving force for Ti, Al, or N to react or diffuse into these mixed oxides (Table 2). Hence, inclusions that do not interact with the coating act as protective deposits not only against mechanical wear but also against chemical, diffusion, and oxidation wear [5,23,25]. The abrasive tracks seen in the center are the tracks in the adhered layer, not in the coating seen in the TEM images.

The tool rake surface can thus be divided into three regions: the "edge" region that is similar to machining a inclusion free steel since no NMI adhered, the "center" region with limited wear due to protective NMI action, and the "periphery" region with formation of pits due to oxidation, diffusion, and reactions with the adhered steel (Fig. 19).

The success of the pairing of the coating and inclusion engineering thus depends on a few factors. The chip flow has to be high so that the NMI encounter the tool, and the NMI have to survive to be able to adhere [14]. A very limited number of MnS inclusions survive in this study, this is due to the aggressive cutting condition, because of the lower melting point and lower hardness MnS at these cutting temperatures [50]. Which NMI will adhere and whether the steel will adhere likely depend on their high temperature softening [14]. Hence, if steel adheres first, then the NMIs cannot protect the coating from degradation (Table 2 and Fig. 13) and the situation becomes similar to the case of machining inclusion free steels [2,5]. Limited chip flow and too high a pressure also lead to limited NMI being deposited, which is the case at the edge of the tool [14,35] which becomes a "no NMI deposit" region.

The most overlooked factor that this paper focuses on is the importance of pairing the tool material and the NMI. The reverse process can occur when the coating is thermodynamically stable with respect to the steel but not stable with respect to the type of NMI inclusion adhered [23,25]. Such cases lead to the inclusions consuming the coating. Matching NMI and coatings can be predicted and estimated by thermodynamic modeling (Table 2 and Fig. 17).

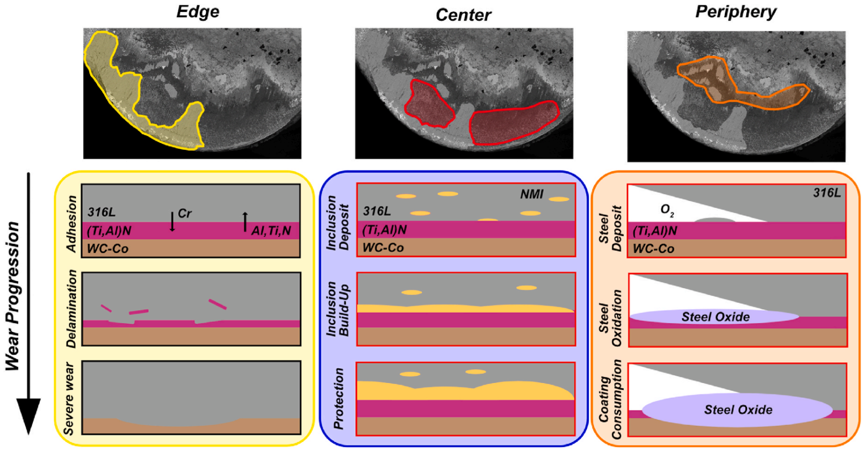

Fig. 19. Simplified schematic of how the regions differ. The edge region suffers from mechanical adhesion, delamination, and diffusion, resulting in coating delamination. The center region is chemically and mechanically protected from wear. The periphery region suffers from diffusion, oxidation, and chemical wear.

5. Conclusion

This study has undertaken an in-depth investigation of the interaction between the (Ti,Al)N coating and NMI in the machinability-improved stainless steel 316L (Prodec®) during longitudinal turning. Deposits were identified using SEM, TEM, and XEDS analysis of bulk samples, TEM lamellas, and cross-sectioned tools. The phenomena identified by microscopy of worn tools were also modeled with thermodynamics. This analysis aims to understand what drives the protection and degradation of the coating.

It was found that deposition and adhesion during turning of $(Mg,Fe,Mn)_1Al_2O_4$ (spinel) and $Al_2Ca_2Si_1O_7$ (gehlenite) introduces a positive protective action in limiting tool wear by retarding the oxidation and chemical wear of the (Ti,Al)N coating, in addition to providing protection against abrasive wear. These protective deposits are preferentially formed in the middle of the tool–chip contact zone. Oxides of the steel itself form at the periphery of the contact zone, due to the absence of NMI protective oxides. The interaction of the (Ti,Al)N coating with these metal oxides and atmospheric oxygen in these locations results in accelerated wear and coating perforation. At the tool edge, the pressure is too high and chip flow too low, leading to adhesion of steel and coating delamination.

- Too high a contact pressure and too low a chip flow lead to adhesion of steel and coating delamination. This occurred at the edge where there are no NMI deposits (Fig. 19).
- Lower normal stresses, high chip flow, and limited oxygen are optimal conditions for stable adhesion and deposition of protective NMI. These occurred in the center region of the contact (Fig. 19). A prerequisite is that the NMI survive these conditions. The NMI should also not thermodynamically interact with the coating, which can be predicted by thermodynamics.
- When the availability of oxygen is high, the temperature is high enough for oxidation, and the conditions are such that steel adhere (Fig. 19). This leads to oxidation, diffusion, and reactions degrading the (Ti,Al)N coating. This is seen in the periphery regions at the end of the chip–tool contact.

Knowledge of the cutting conditions and the use of thermodynamics can be used to both explain and predict both intuitive and non-intuitive wear and protection mechanisms. Such as edge delamination of the coating or why the coating is being worn more rapidly in the periphery of the contact zone than the center when it is normally the opposite since the center is the location of crater wear.

Author statement

Axel Bjerke: Conceptualization, Methodology, Software, Validation, Formal analysis, Investigation, Data Curation, Writing - Original Draft, Visualization, Project administration.

Filip Lenrick: Conceptualization, Methodology, Validation, Formal analysis, Investigation, Writing - Review & Editing, Visualization, Supervision, Funding acquisition.

Andrii Hrechuk: Conceptualization, Methodology, Validation, Formal analysis, Investigation, Data Curation, Writing - Review & Editing, Visualization.

Kateryna Slipchenko: Conceptualization, Methodology, Validation, Formal analysis, Data Curation, Writing - Review & Editing, Visualization.

Rachid M`Saoubi: Conceptualization, Methodology, Validation, Writing - Review & Editing, Supervision, Funding acquisition.

Jon M. Andersson: Conceptualization, Methodology, Validation, Writing - Review & Editing, Supervision.

Volodymyr Bushlya: Conceptualization, Methodology, Validation, Formal analysis, Investigation, Writing - Review & Editing, Visualization, Supervision, Project administration, Funding acquisition.

Declaration of competing interest

The authors declare that they have no known competing financial interests or personal relationships that could have appeared to influence the work reported in this paper.

Data availability

Data will be made available on request.

Acknowledgments

This work was funded by the national strategic innovation program National Action for Metallic Materials, organized by Vinnova and Jernkontoret (Sweden) under DEMO project (ID 2017–02915). The authors would also like to acknowledge the Sustainable Production Initiative (SPI), a cooperation between Lund University and Chalmers University of Technology.

Appendix A. Supplementary data

Supplementary data to this article can be found online at https://doi.org/10.1016/j.wear.2023.205093.

References

[1] K.-D.D. Bouzakis, N. Michailidis, G. Skordaris, E. Bouzakis, D. Biermann, R. M`Saoubi, Cutting with coated tools: coating technologies, characterization methods and performance optimization, CIRP Ann. - Manuf. Technol. 61 (2012) 703–723, https://doi.org/10.1016/j.cirp.2012.05.006.

[2] V.F.C. Sousa, F.J.G. Da Silva, G.F. Pinto, A. Baptista, R. Alexandre, Characteristics and wear mechanisms of TiAlN-based coatings for machining applications: a comprehensive Review, Metals 11 (2021) 260, https://doi.org/10.3390/met11020260.

[3] K. Bobzin, High-performance coatings for cutting tools, CIRP J. Manuf. Sci. Technol. 18 (2017) 1–9, https://doi.org/10.1016/j.cirpj.2016.11.004.

[4] A. Hörling, L. Hultman, M. Odén, J. Sjölén, L. Karlsson, Mechanical properties and machining performance of Ti1−xAlxN-coated cutting tools, Surf. Coating. Technol. 191 (2005) 384–392, https://doi.org/10.1016/j.surfcoat.2004.04.056.

[5] N. Ånmark, A. Karasev, P. Jönsson, The effect of different non-metallic inclusions on the machinability of steels, Materials 8 (2015) 751–783, https://doi.org/10.3390/ma8020751.

[6] L.E.K. Holappa, A.S. Helle, Inclusion control in high-performance steels, J. Mater. Process. Technol. 53 (1995) 177–186, https://doi.org/10.1016/0924-0136(95)01974-J.

[7] N. Matsui, K. Watari, Wear reduction of carbide tools observed in cutting Ca-added steels for machine structural use, ISIJ Int. 46 (2006) 1720–1727, https://doi.org/10.2355/isijinternational.46.1720.

[8] N. Ånmark, T. Björk, Effects of the composition of Ca-rich inclusions on tool wear mechanisms during the hard-turning of steels for transmission components, Wear 368–369 (2016) 173–182, https://doi.org/10.1016/j.wear.2016.09.016.

[9] H. Yamada, S. Yoshida, A. Kimura, K. Kato, T. Ito, On the relationship between machinability and inclusion morphology of Ca bearing free machining steels, Tetsu-To-Hagane 57 (1971) 2111–2127, https://doi.org/10.2355/tetsutohagane1955.57.13_2111.

[10] W. König, Einfluss nichtmetallischer Einschlüsse auf die Zerspanbarkeit von Kohlenstoffstählenitle, Maschinenmarkt 87 (1965).

[11] W. König, Der Einfluss nichtmetallischer Einschlüsse auf die Zerspanbarkeit von unlegierten Baustählen, Ind. Anzeiger 87 (1965).

[12] A. Nordgren, A. Melander, Tool wear and inclusion behaviour during turning of a calcium-treated quenched and tempered steel using coated cemented carbide tools, Wear 139 (1990) 209–223, https://doi.org/10.1016/0043-1648(90)90046-D.

[13] S. Ruppi, B. Högrelius, M. Huhtiranta, Wear characteristics of TiC, Ti(C,N), TiN and Al2O3 coatings in the turning of conventional and Ca-treated steels, Int. J. Refract. Met. Hard Mater. 16 (1998) 353–368, https://doi.org/10.1016/S0263-4368(98)00039-0.

[14] A. Larsson, S. Ruppi, Structure and composition of built-up layers on coated tools during turning of Ca-treated steel, Mater. Sci. Eng. A. 313 (2001) 160–169, https://doi.org/10.1016/S0921-5093(01)00964-9.

[15] H. Chandrasekaran, M. Granfors, R. M`Saoubi, Tribological aspects of tool–chip and tool–work contact in machining and the application of laser spectrometry, Wear 260 (2006) 319–325, https://doi.org/10.1016/j.wear.2005.04.023.

[16] R. M`Saoubi, H. Chandrasekaran, Innovative methods for the investigation of tool-chip adhesion and layer formation during machining, CIRP Ann 54 (2005) 59–62, https://doi.org/10.1016/S0007-8506(07)60049-3.

[17] J.-E. Desaigues, C. Lescalier, A. Bomont-Arzur, D. Dudzinski, O. Bomont, Experimental study of Built-Up Layer formation during machining of high strength

free-cutting steel, J. Mater. Process. Technol. 236 (2016) 204–215, https://doi.org/10.1016/j.jmatprotec.2016.05.016.

[18] A. Flink, R. M'Saoubi, F. Giuliani, J. Sjölén, T. Larsson, P.O. Persson, M. P. Johansson, L. Hultman, Microstructural characterization of the tool-chip interface enabled by focused ion beam and analytical electron microscopy, Wear 266 (2009) 1237–1240, https://doi.org/10.1016/j.wear.2009.03.001.

[19] A. Vereschaka, V. Tabakov, S. Grigoriev, N. Sitnikov, F. Milovich, N. Andreev, J. Bublikov, Investigation of wear mechanisms for the rake face of a cutting tool with a multilayer composite nanostructured Cr–CrN-(Ti,Cr,Al,Si)N coating in high-speed steel turning, Wear 438–439 (2019), 203069, https://doi.org/10.1016/j.wear.2019.203069.

[20] A. Knutsson, M.P. Johansson, L. Karlsson, M. Odén, Machining performance and decomposition of TiAlN/TiN multilayer coated metal cutting inserts, Surf. Coating. Technol. 205 (2011) 4005–4010, https://doi.org/10.1016/j.surfcoat.2011.02.031.

[21] N. Narutaki, A. Murakoshi, Effect of small quantity inclusions in steels on the wear of ceramic tools, J. Jpn. Soc. Precis. Eng. 42 (1976) 221–226, https://doi.org/10.2493/jjspe1933.42.221.

[22] G. Brandt, M. Mikus, The formation of protective layers when machining steel with ceramic cutting tools, Wear 118 (1987) 99–112, https://doi.org/10.1016/0043-1648(87)90007-X.

[23] A. Bjerke, A. Hrechuk, F. Lenrick, R. M'Saoubi, H. Larsson, A. Markström, T. Björk, S. Norgren, J.-E. Ståhl, V. Bushlya, Onset of the degradation of CVD α-Al2O3 coating during turning of Ca-treated steels, Wear (2021), 203785, https://doi.org/10.1016/j.wear.2021.203785.

[24] R. Bejjani, S. Odelros, S. Öhman, M. Collin, Shift of wear balance acting on CVD textured coatings and relation to workpiece materials, Proc. Inst. Mech. Eng. Part J J. Eng. Tribol. 235 (2021) 114–128, https://doi.org/10.1177/1350650120926781.

[25] A. Bjerke, F. Lenrick, S. Norgren, H. Larsson, A. Markström, R. M'Saoubi, I. Petrusha, V. Bushlya, Understanding wear and interaction between CVD α-Al2O3 coated tools, steel, and non-metallic inclusions in machining, Surf. Coating. Technol. 450 (2022), 128997, https://doi.org/10.1016/j.surfcoat.2022.128997.

[26] P. Hoier, A. Malakizadi, U. Klement, P. Krajnik, Characterization of abrasion- and dissolution-induced tool wear in machining, Wear 426–427 (2019) 1548–1562, https://doi.org/10.1016/j.wear.2018.12.015.

[27] A. Malakizadi, B. Shi, P. Hoier, H. Attia, P. Krajnik, Physics-based approach for predicting dissolution−diffusion tool wear in machining, CIRP Ann 69 (2020) 81–84, https://doi.org/10.1016/j.cirp.2020.04.040.

[28] A. Bjerke, A. Hrechuk, F. Lenrick, A. Markström, H. Larsson, S. Norgren, R. M'Saoubi, T. Björk, V. Bushlya, Thermodynamic modeling framework for prediction of tool wear and tool protection phenomena in machining, Wear 484–485 (2021), 203991, https://doi.org/10.1016/j.wear.2021.203991.

[29] M. Moreno, J.M. Andersson, M.P. Johansson-Jöesaar, B.E. Friedrich, R. Boyd, I. C. Schramm, L.J.S. Johnson, M. Odén, L. Rogström, Wear of Mo- and W-alloyed TiAlN coatings during high-speed turning of stainless steel, Surf. Coating. Technol. 446 (2022), 128786, https://doi.org/10.1016/j.surfcoat.2022.128786.

[30] M. Moreno, J.M. Andersson, R. Boyd, M.P. Johansson-Jöesaar, L.J.S. Johnson, M. Odén, L. Rogström, Crater wear mechanism of TiAlN coatings during high-speed metal turning, Wear (2021) 484–485, https://doi.org/10.1016/j.wear.2021.204016.

[31] K.M. Calamba, M.P. Johansson Jöesaar, S. Bruyère, J.F. Pierson, R. Boyd, J. M. Andersson, M. Odén, The effect of nitrogen vacancies on initial wear in arc deposited (Ti0.52,Al0.48)Ny, (y < 1) coatings during machining, Surf. Coating. Technol. 358 (2019) 452–460, https://doi.org/10.1016/j.surfcoat.2018.11.062.

[32] J.-O. Andersson, T. Helander, L. Höglund, P. Shi, B. Sundman, Thermo-Calc & DICTRA, computational tools for materials science, Calphad 26 (2002) 273–312, https://doi.org/10.1016/S0364-5916(02)00037-8.

[33] N. Norrby, M.P.P. Johansson, R. M'Saoubi, M. Odén, Pressure and temperature effects on the decomposition of arc evaporated Ti0.6Al0.4N coatings in continuous turning, Surf. Coating. Technol. 209 (2012) 203–207, https://doi.org/10.1016/j.surfcoat.2012.08.068.

[34] J.-E. Ståhl, Seco Tools AB, Metal Cutting: Theories and Models, Seco Tools AB, 2012.

[35] U. Wiklund, S. Rubino, K. Kádas, N.V. Skorodumova, O. Eriksson, S. Hedberg, M. Collin, A. Olsson, K. Leifer, Experimental and theoretical studies on stainless steel transfer onto a TiN-coated cutting tool, Acta Mater. 59 (2011) 68–74, https://doi.org/10.1016/j.actamat.2010.09.005.

[36] S. Saketi, U. Bexell, J. Östby, M. Olsson, On the diffusion wear of cemented carbides in the turning of AISI 316L stainless steel, Wear 430–431 (2019) 202–213, https://doi.org/10.1016/j.wear.2019.05.010.

[37] R. Bejjani, M. Collin, T. Thersleff, S. Odelros, Multi-scale study of initial tool wear on textured alumina coating, and the effect of inclusions in low-alloyed steel, Tribol. Int. 100 (2016) 204–212, https://doi.org/10.1016/j.triboint.2016.01.021.

[38] J. Gerth, F. Gustavsson, M. Collin, G. Andersson, L.-G. Nordh, J. Heinrichs, U. Wiklund, Adhesion phenomena in the secondary shear zone in turning of austenitic stainless steel and carbon steel, J. Mater. Process. Technol. 214 (2014) 1467–1481, https://doi.org/10.1016/j.jmatprotec.2014.01.017.

[39] P.V. Moghaddam, B. Prakash, E. Vuorinen, M. Fallqvist, J.M. Andersson, J. Hardell, High temperature tribology of TiAlN PVD coating sliding against 316L stainless steel and carbide-free bainitic steel, Tribol. Int. 159 (2021), 106847, https://doi.org/10.1016/j.triboint.2020.106847.

[40] H. Persson, F. Lenrick, L. Franca, J.-E. Ståhl, V. Bushlya, Wear mechanisms of PcBN tools when machining AISI 316L, Ceram. Int. (2021), https://doi.org/10.1016/j.ceramint.2021.08.075.

[41] P. Helistö, A.S. Helle, J. Pietikäinen, Interface phenomena between oxide layers and cemented carbide tools, Wear 139 (1990) 225–234, https://doi.org/10.1016/0043-1648(90)90047-E.

[42] V. Bushlya, A. Bjerke, V.Z.Z. Turkevich, F. Lenrick, I.A.A. Petrusha, K.A. A. Cherednichenko, J.-E.E. Ståhl, On chemical and diffusional interactions between PCBN and superalloy Inconel 718: imitational experiments, J. Eur. Ceram. Soc. 39 (2019) 2658–2665, https://doi.org/10.1016/j.jeurceramsoc.2019.03.002.

[43] J. Angseryd, H.-O. Andrén, An in-depth investigation of the cutting speed impact on the degraded microstructure of worn PCBN cutting tools, Wear 271 (2011) 2610–2618, https://doi.org/10.1016/j.wear.2010.11.059.

[44] J. Vleugels, O. Van Der Biest, Chemical wear mechanisms of innovative ceramic cutting tools in the machining of steel, Wear 225–229 (1999) 285–294, https://doi.org/10.1016/S0043-1648(98)00362-7.

[45] R. Lindvall, A. Bjerke, A. Salmasi, F. Lenrick, R. M'Saoubi, J.-E.E. Ståhl, V. Bushlya, R. M'Saoubi, J.-E.E. Ståhl, V. Bushlya, Predicting wear mechanisms of ultra-hard tooling in machining Ti6Al4V by diffusion couples and simulation, J. Eur. Ceram. Soc. 43 (2023) 291–303, https://doi.org/10.1016/j.jeurceramsoc.2022.10.005.

[46] R. M'Saoubi, H. Chandrasekaran, Experimental tool temperature distributions in oblique and orthogonal cutting using chip breaker geometry inserts, J. Manuf. Sci. Eng. 128 (2005) 606–610, https://doi.org/10.1115/1.2162904.

[47] M.C. Shaw, J.O. Cookson, Metal Cutting Principles, vol. 2, 2005.

[48] E.M. Trent, P.K. Wright, Metal Cutting, fourth ed., 2000.

[49] L. Rogström, M. Moreno, J.M. Andersson, M.P. Johansson-Jöesaar, M. Odén, K. Klementiev, L.-Å. Näslund, M. Magnuson, Structural changes in Ti1-xAlxN coatings during turning: a XANES and EXAFS study of worn tools, Appl. Surf. Sci. 612 (2023), 155907, https://doi.org/10.1016/j.apsusc.2022.155907.

[50] C.-H. Leung, L.H. Vlack, Solution and precipitation hardening in (Ca, Mn) sulfides and selenides, Metall. Trans. A. 12 (1981) 987–991, https://doi.org/10.1007/BF02643479.

Paper III

Wear 477 (2021) 203785

Contents lists available at ScienceDirect

Wear

journal homepage: http://www.elsevier.com/locate/wear

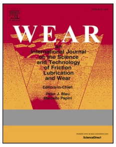

Onset of the degradation of CVD α-Al2O3 coating during turning of Ca-treated steels

Axel Bjerke [a,*], Andrii Hrechuk [a], Filip Lenrick [a], Rachid M'Saoubi [b], Henrik Larsson [c], Andreas Markström [d], Thomas Björk [e], Susanne Norgren [f], Jan-Eric Ståhl [a], Volodymyr Bushlya [a]

[a] *Division of Production and Materials Engineering, Lund University, Ole Römers väg 1, Lund, Sweden*
[b] *R&D Materials and Technology Development, Seco Tools AB, 737 82 Fagersta, Sweden*
[c] *Unit of Structures, Dept Materials Science and Engineering, KTH, SE-10044, Stockholm, Sweden*
[d] *Thermo-Calc Software AB, Råsundavägen 18, SE-169 67, Solna, Sweden*
[e] *Ovako Group, Olof Hjorts väg 2, 813 35 Hofors, Sweden*
[f] *Sandvik Coromant R&D, Lerkrogsv. 13, 126 80 Stockholm, Sweden*

ARTICLE INFO

Keywords:
Steel
CVD coatings
Cutting tools
Optical microscopy
Electron microscopy
Wear modelling

ABSTRACT

The ability to control the shape, distribution and composition of non-metallic inclusions has had an important impact on many aspects of steel making. One such impact is on the machinability. Ca-treatments have shown to be able to reduce the abrasiveness of oxide inclusions, improve chip-breaking and lead to formation of deposits that reduce tool wear. However, machining Ca-treated steels with Al_2O_3 coated cemented carbide tools has not been as advantageous as expected. This study investigates the mechanisms behind the anomalous wear of Al_2O_3 coatings when turning soft Ca-treated steels.

Longitudinal turning tests at a range of speeds ($v_c = 100$–600 m/min) show rapid localized degradation of the Al_2O_3 coating limited to the sliding zone. Detailed analysis of the degradation mechanisms was performed using scanning and transmission electron microscopy. The results demonstrate a presence of chemical interactions between the alumina coating and non-metallic inclusions. The interaction resulted in the formation of mainly calcium aluminates and partly alumina-magnesia spinel. *In-operando* infrared thermography measurements indicate cutting temperatures of 850–1000 °C. Thermodynamic calculations give that CaO and MgO readily reacts with Al_2O_3, while the reaction with CaS requires presence of additional oxygen at these cutting conditions. Additional turning experiments investigate the influence of oxygen by controlling the cutting environment by adding oxygen (compressed air) or removing oxygen (supply argon). These additional tests show that the presence of additional oxygen has a limited impact on the possible Ca–Al_2O_3 interaction. This demonstrat a potential for further machinability improvements by controlling the chemical interaction between Ca and Mg based non-metallic inclusions and alumina coatings.

1. Introduction

Calcium treatments and non-metallic inclusion (NMI) was not originally intended as a means of improving the machinability of steel. However, the use of Ca, S, Si and Al NMIs to improve machinability has been researched and used industrially since the 1960's [1,2]. It is still in use and researched as one effective way to enhance the machinability of steels [3]. On the cutting tool side, the development of texture-controlled α-Al_2O_3–Ti(C,N) multilayered coatings have led to increased performance. Especially the development of the (001) textured α-Al_2O_3 that is suggested to be more resistant to plastic deformation and shear stress at elevated temperatures [4].

Previous research on wear of alumina coated cemented carbide tools and Ca-treated steels claim that abrasive wear and plastic deformation of the coating are the most common wear types [4–12]. It is also reported that machinability improvement by Ca-treatment of steels results in the dissolution and embedment of hard oxides. This decreases the abrasiveness, improves chip formation and forms protective deposits [13–15]. Hence, Ca-treatments lead to an increase in the tool life [3, 13–16]. However, it can lead to an increase in rake wear compared to non Ca-treated steel [17], and the positive effects of NMIs are not always as prominent when machining with alumina coated tools [18]. An

---

* Corresponding author.
E-mail address: axel.bjerke@iprod.lth.se (A. Bjerke).

https://doi.org/10.1016/j.wear.2021.203785
Received 8 September 2020; Received in revised form 31 January 2021; Accepted 2 February 2021

extreme example of alumina degradation by Ca-inclusions is seen when not only the coating but the whole tool is alumina based, such as alumina ceramic tools [19,20].

Flank wear is typically a sign of predominant abrasive wear, whereas rake wear is a sign of predominant chemical, diffusional or oxidational wear [21,22]. Wear models based on deformation, dislocations and abrasion of the coating can therefore only explain part of the increased rake wear, when there is a decrease in flank wear. Earlier research suggests dissolution or a chemical reaction leading to coating degradation [23,24], similar to the effect seen when using alumina ceramic tools [19,20]. However, such suggestions have not found support due to the commonly assumed chemical inertness of alumina [5,7,10,17]. Hence, the anomalous wear of alumina coatings when machining calcium treated steels is therefore further investigated, especially with regards to the claimed inertness of alumina coatings.

2. Methods

An appropriate steel has to be selected to study the onset of the wear of alumina coated tools when turning machinability improved soft Ca-treated steels. A calcium treated 19MnVS6 E470 steel was used as workpiece material. This grade is a characteristic Ca machinability improved general structural steel with non-metallic inclusions. The typical NMIs for this grade are different variations of sulfides and oxi-sulfides commonly (Mn,Ca)S and $(Mg,Ca,Al)_xO_y$, shown in Fig. 1. No pure oxides were found in the steel. The chemical composition of the steel is shown in Table 1. A Ca content of about 53 ppm and O content of about 11 ppm is reported. This combination makes the 19MnVS6 workpiece material a good choice for the study. Only the outermost 15 mm of the bar is used for the machining tests, in order to limit the effect of an uneven solidification and related distribution of NMI.

All cutting tools in this study consist of a bi-layered CVD coating with an inner Ti(C,N) layer followed by outermost layer of (001) textured α-Al2O3 deposited on a cemented carbide substrate, shown in Fig. 2.

2.1. Onset of the coating wear

The first machining test was performed to investigate the onset of the tool wear, which was performed by continuous turning in an SMT Sajo 500 Swedturn CNC-lathe. The onset of the wear of the coating was examined by carrying out a set of turning experiments in intervals of 100 m/min for cutting speeds between v_c = 100–600 m/min. While having the other cutting parameters fixed: cutting length $l = 130$ m, depth of cut $a_p = 1.5$ mm and feed rate $f = 0.2$ mm/rev. The insert geometry was CNMG120408-MF1 that provide a nose radius of 0.8 mm and an edge radius of 25 μm, and was combined with PCLNL3225P12JETL tool holder.

Table 1
Elemental composition of 19MnVS6 E470 workpiece material in wt.%.

	C	Si	Mn	P	S	Cr	V	Fe
Min.	0.16	0.25	1.30	–	0.015	–	0.07	Balance
Max.	0.22	0.50	1.55	0.025	0.035	0.50	0.11	

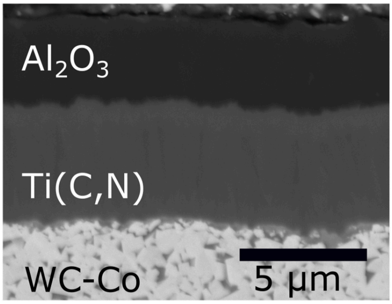

Fig. 2. BSE-SEM image of the tool and the coating.

The tool wear characteristics were investigated using an Olympus SZX7 stereo visible light microscope (VLM), an Alicona Infinite Focus 3D VLM microscope equipped with a polarizer. A Tescan Mira3 scanning electron microscope (SEM), equipped with secondary electron (SE), backscatter electron (BSE) and an X-ray energy-dispersive spectroscopy (XEDS) detectors. This enabled the comparison of the onset of the degradation process of the alumina coating at different cutting speeds.

2.2. Wear mechanism of coating

The next test was aimed toward investigating the progressive wear of the coating by use of the previous cutting conditions but only at cutting speed vc = 300 m/min. The wear evolution of the coating was measured using the 3D VLM. The use of the polarizer and the creation of 3D images

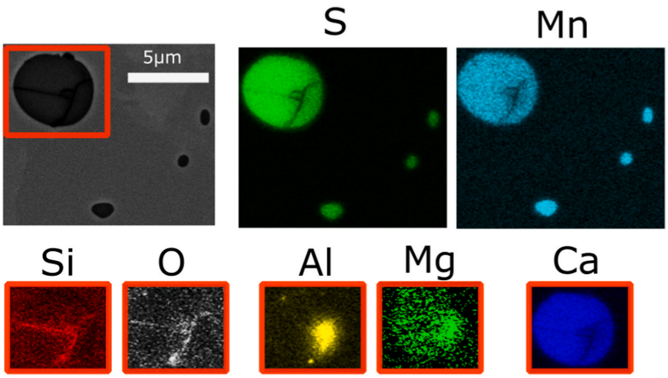

Fig. 1. A combination of SEM and XEDS maps showing an example of the NMI inclusions. The inclusion are a mixture of oxides and sulfides of (Mn,Ca)S and $(Mg,Ca,Al)_xO_y$, the SiO_2 is remnants from the polishing media.

enabled the measurement of the progression of coating removal, and the method was verified by SEM-XEDS measurements. Analysis of wear mechanism were conducted with SEM using SE, BSE, and XEDS detectors. Specific areas of interest were studied on lamellas extracted vertically from the worn tool rake. These lamellas were extracted using FEI Nova NanoLab 600 focused ion beam (FIB) SEM and were examined using transmission electron microscope (TEM) JEOL 3000F additionally equipped with a XEDS detector.

2.3. *Temperature measurements*

The following test was carried out to determine the temperature in the cutting zone. Orthogonal turning was performed on BOEHRINGER VDF DUS560 TI CNC-lathe with a high-speed Flir x6580sc IR-Camera fitted for measurement of tool temperature distribution. The thermal camera had a temperature discretization range of 300–1130 °C (Fig. 3a) and attained images with a frequency of 350 FPS (Hz). The same coated cemented carbide tool material was used but in TNMA160408 geometry allowing for orthogonal cutting. The test was conducted at speed $v_c =$ 200 and 300 m/min, feed $f = 0.2$ mm/min and cutting depth $a_p = 1.5$ mm. This gave an estimation of the temperature reached in the cutting zone and in the chips.

2.4. *Thermodynamic calculations*

The results from temperature measurement were used for thermodynamic equilibrium calculations. The calculations were done to give an understanding of the effect of NMI on the thermodynamic stability of the alumina-coating and the driving force for its degradation. These calculations were carried out using Thermo-Calc [25] and the TCFE10 steels/Fe-Alloys and TCOX10 metal oxide solutions database. It is a CALPHAD based software which models each phase by a Gibbs energy function. The calculation of the interaction between the tool, NMI and environment is dependent on determining the thermodynamic boundary conditions of pressure *(P)*, temperature *(T)* and elemental composition (X_i) in the cutting zone. The temperature boundary conditions (T) is determined by the experimental result from the thermal camera measurement. The pressure in the cutting zone can reach 1 GPa [21] and the local elemental (X_i) and phase composition used in the modelling is determined by the TEM and SEM investigations. The availability of oxygen in the cutting zone is less than the effective oxygen partial pressure of 0.21 (sea-level approximate). Hence, a set of calculations were carried out using these boundary conditions to study the effect of the stated parameters on the coating degradation process. This creates an understanding of which parameters effect the tool wear process and how.

2.5. *Controlled atmosphere machining*

The effect of NMI on the degradation of the alumina coating has shown to not only be dependent on the interaction between the tool and workpiece. It can also be dependent on the cutting environment [26,27]. Therefore, supplementary longitudinal cutting tests were conducted in controlled atmospheres. The removal of oxygen was ensured by the supply of argon at a rate of approximately 400 l/m from the tool holder PCLNL3225P12JETL and three additional nozzles (Fig. 3b). Compressed air was supplied using the same configuration and flow rate. The test was carried out using the same tool, steel and cutting conditions at cutting speed 300 m/min. The thermal camera could not be used to measure the temperature for this set-up. Therefore, each tool was equipped with a thermocouple placed 800 μm from the tool surface (Fig. 3c) instead. Installation of the thermocouples was enabled by blind hole sinking electrical discharge machining (EDM) into the tool from its back side. This was implemented to monitor the effect the extra supply of gas had on the tool temperature.

3. Result and discussion

The result section is categorized by the performed experiments *Onset of the coating wear - Wear mechanism of coating – Temperature measurements - Thermodynamic calculations - Controlled atmosphere machining.* The discussion is combined with the result section, to tie the experiments together and point out the implication of one experiment on the next. The results are then tied together by the section *Proposed degradation mechanisms of the coating.*

3.1. *Onset of the coating wear*

Two distinct wear zones developed on the rake side: a sticking and a sliding zone. These zones are present on all the tools in the tested cutting speed range $v_c = 100$–600 m/min. A sticking zone developed on the rake bordering the flank and a sliding zone developed at the end of the tool-chip interface (Fig. 4a). This is in agreement with similar studies [5,6,17]. The Al_2O_3 coating was intact in the sticking zone and was degraded in the sliding zone.

The size of the sticking zone and the overall contact length decreased with increasing speed, while the sliding zone increased with cutting speed (Fig. 4b and c). Hence, the sliding zone becomes larger and approaches the cutting edge with increasing cutting speed. The decreased contact length is believed to be related to a change in chip formation, as previous research has shown that the chips tend to be increasingly segmented when the cutting speed is increased [21]. The tool wear become more localized when the contact length decreases as the temperature and the pressure increase [21].

The BSE-SEM image of the sliding zone in Fig. 4a indicates that the workpiece material has adhered to the coating. Therefore, the sliding zones are further investigated in Fig. 5. The rake was studied using SE−SEM that render the topography, and XEDS line scans revealed the elemental distribution. The analysis shows presence of abrasive tracks, which are in agreement with previous studies [2–10], and adhered material are present above the Al_2O_3 coating [4]. The XEDS line scans show two main types of deposits, one consisting of Ca and S and one

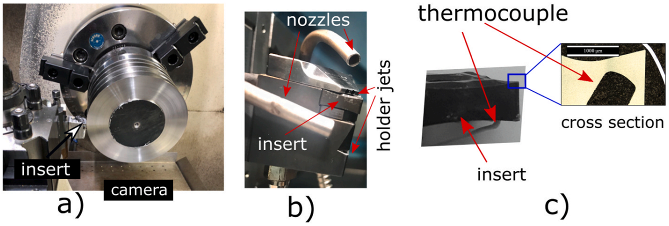

Fig. 3. a) Orthogonal cutting during thermal camera measurements, the bar consists of discs of width equal to the depth of cut. b) The tool holder equipped with nozzles used during machining in argon. c) Insert with an embedded thermocouple and the cross section showing the thermocouple placement.

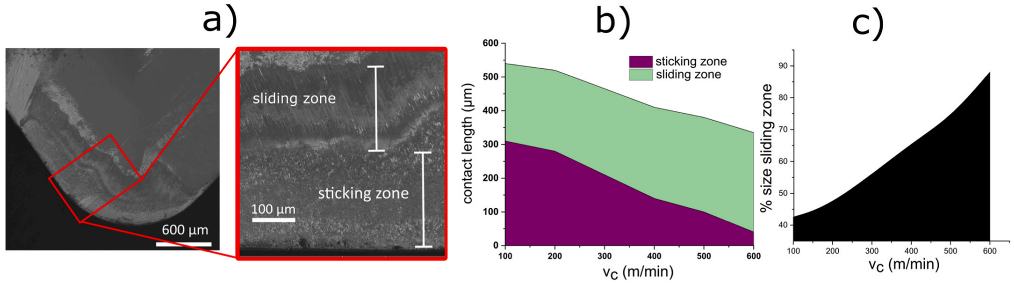

Fig. 4. a) BSE-SEM images of the rake (v_c = 100 m/min). b) Sticking and sliding zone length versus cutting speed after 130 m of engagement. c) Percentage sliding zone in relation to total contact length.

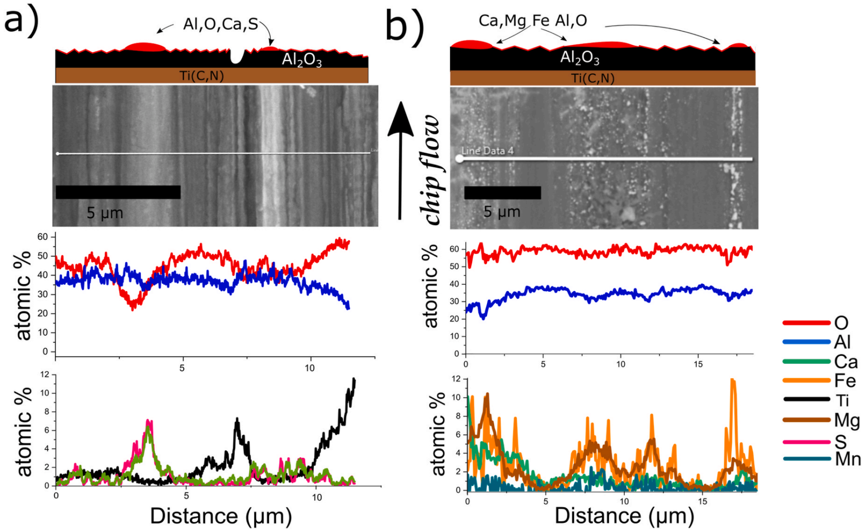

Fig. 5. SE−SEM images and XEDS line scans of the sliding zone of the rake of the tool. Two types of deposits are present: a) CaS and b) Ca, Mg, Fe and potentially Al and O. These deposits are separated by abrasive tracks. The Ti peak in a) is most likely originating from the Ti(C,N) layer.

consisting of Ca, Mg and Fe. The Ca, Mg, and Fe is also present to in the abrasive tracks. Al and O can also be present in the deposits, but the XEDS signal could also originate from the coating due to a large excitation volume. The observed Ti signal is most likely from the intermediate Ti(C,N) coating layer. Further TEM investigation is needed to distinguish the layering, its microstructure and composition. An interpretation of the combined SE−SEM and XEDS is drawn at the top of Fig. 5.

This structure can be related to at least two alternative mechanisms. (*i*) NMI can adhere and not react with the coating to remain as a tribolayer, which mean that NMI elements together with Al and O originate from the steel. Such tribolayer would reduce the wear rate in the sliding zone. (*ii*) Another possibility is that the NMIs react with the alumina coating to form a layer consisting of reaction products as a mechanical and/or chemical mixture of NMI and coating elements. This interaction and deposit would then be less protective or even degrading. Further machining and microscopy are necessary to investigate the actual composition and sequence of this layer formation and mechanisms of its removal.

3.2. *Wear mechanism of coating*

Extended tests using the cutting speed v_c = 300 m/min were carried out to determine the development of the wear mechanism of the coating. The tools were subjected to turning in intervals of approximately 40 s prior to VLM microscopy. Tools used to cut for 40, 70, 100, and 490 s were kept for in-depth SEM and TEM microscopy.

Elements as Ca, Mg, Fe and additionally Mn were present in the sliding zone, in the same manner as the initial test displayed in Fig. 5. Furthermore, Ca and S adhered to the Ti(C,N) coating layer that were exposed once the Al_2O_3 coating was removed; this is colored in green in the XEDS map in Fig. 6a. The Ca and S and the exposed Ti(C,N) creates a clear contrast to the Al_2O_3 coating both using the SE−SEM and the polarizer in VLM. The Al_2O_3 coating appears black in the SE−SEM

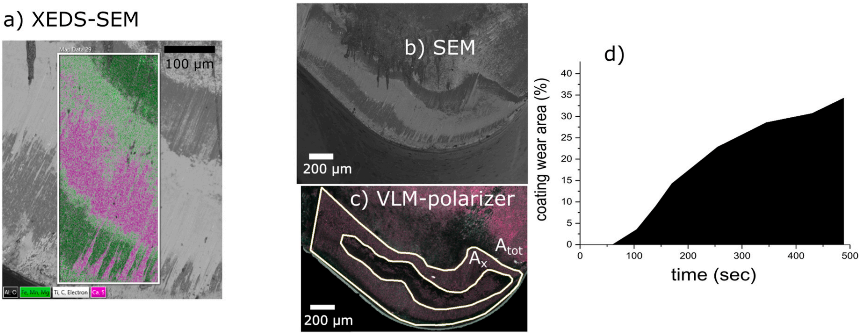

Fig. 6. a) XEDS map of tool rake showing Ca and S adhered to the exposed Ti(C,N) and Fe, Mn and Mg adhered to the alumina coating. b-c) SEM and VLM with polarizer showing the area with Al_2O_3 coating worn through after 490 s of machining. d) Plot of the cutting area with the Al_2O_3 layer worn through time.

(Fig. 6b) and pink in the VLM with the polarizer (Fig. 6c). The SEM analysis has a tendency to overestimate the area of the worn coating if a high accelerating voltage is used due to a deeper excitation volume, which is noted when comparing Fig. 6b and c. The wear development of the alumina coating could be efficiently monitored by measuring the area of exposed Ti(C,N) coating (A_x) to the total cutting area (A_{tot}) using the VLM with a polarizer (Fig. 6c). The measure A_x/A_{tot} is used to monitor the approximate coating wear given in Fig. 6d. The machining was stopped after 490 s. The Al_2O_3 coating was then worn through for approximately 40% of tool-chip interface area, which meant that there was a limited amount of alumina coating left in the crater at this point. There are no signs of flank wear after 490 s of machining, as seen in Fig. 6b.

Additional investigations were conducted on the sliding zone where there was still alumina coating present after 490 s in cut. A lamella perpendicular to the direction of the chip flow was extracted using FIB-SEM. Platinum was used to protect the lamella during the FIB milling, thereby also detected later by STEM-XEDS. Fig. 7 shows two scanning transmission electron microscopy (STEM) images and STEM-XEDS maps of the cross-sections where the boxes indicate the XEDS regions. The XEDS analysis indicates that Ca and Mg has reacted with Al and O. Since a Ca, Mg, Al and O rich area is detected between the remains of the alumina coating and the FIB-platinum. Fig. 7a shows a continuous layer of Ca with trace amounts of sulfur above the alumina coating, followed by a Mg rich layer with trace amounts of Mn. An Fe rich circular area is seen in the middle of the map. The double layer of Ca–Al–O and Mg–Al–O is present on most of the Al_2O_3 coating.

Fig. 7b shows another, often observed layering, where Mg is directly interacting with the Al_2O_3 coating without a Ca layer involvement. These interface areas are probably consisting of $(Mg, Al)_xO_y$ magnesium aluminate and $(Ca, Al)_xO_y$ a calcium aluminate or a mixture $(Mg, Ca, Al)_xO_y$ magnesium calcium aluminate. Such products are present in the steel (Fig. 1) but may have been formed in the interface during the turning process. However, detailed XEDS line scans and point measurements give that these layers are richer in aluminum than the NMI in the steel. This suggests that these layers are reaction products due to chemical interactions of NMI with the Al_2O_3 coating. This is in agreement with published research were Al, Mg, and O pockets formed [24], build up inclusion layers of $(CaO)(Al_2O_3)_6$ [10] and machining with alumina ceramics [19,20]. Very low dislocation densities were observed in the upper region of the Al_2O_3 coating adjacent to the interaction interface, which is in agreement with the result that (001) textured α-Al_2O_3 is more resistant to shear stress [4], and that this was not the initiator of the degradation.

The aluminum and oxygen enrichment of the interaction layer, in comparison to the composition of the NMI is indicative of the degradation of Al_2O_3 coating by a chemical, oxidational, or diffusional interaction with the Ca and Mg rich NMI. This would also contribute to the understanding of why the rake wear is sometimes larger for calcium treated steels compared to non-calcium treated steels [17].

The exposed Ti(C,N) layer experiences the same conditions as the top Al_2O_3 layer, when the Al_2O_3 is worn through. However, CaS does not adhere to the Al_2O_3 coating. Instead, it adheres to the Ti(C,N) sub-layer, when exposed. In addition, the above magnesium calcium aluminates form on the Al_2O_3 layer and not on the Ti(C,N) layer. This clear difference in the chemistry of the layers points towards how the wear is related to the chemical interaction between the coating and NMI.

The removal of the Al_2O_3 coating is more intensive in the sliding zone compared to the sticking zone. The number of NMI interacting with the sliding zone is also larger than in the sticking zone. The availability

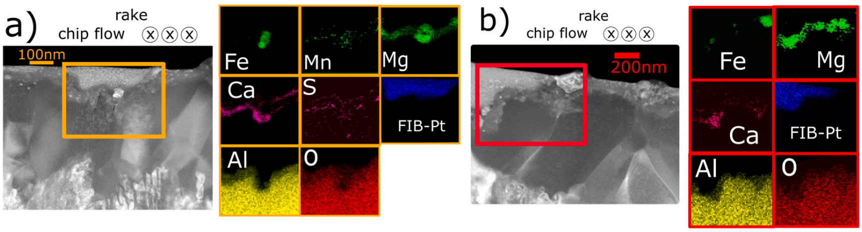

Fig. 7. STEM images and XEDS maps of cross-sectioned lamellas from the sliding zone of the rake after 490 s of machining. Mainly Ca and Mg is interacting with the Al and O shown by the Mg and Ca rich layers and the two shades of Al and O.

of oxygen and the higher temperature in the sliding zone are also contributing factors for an increased chemical interaction. Hence, the abrasive tracks in Fig. 6 could be due to the alumina coating transformation into a magnesium calcium aluminate that eventually forms a tribolayer mixed with iron shown in Fig. 7. Such interaction layers could then be more easily abraded, resulting in the surface structure in Fig. 6. Such assumed process of interaction should be dependent on temperature, chemical activity and oxygen availability. Therefore, further investigation of the temperature, thermodynamics, and oxygen availability is essential.

3.3. *Temperature measurements*

The side-view temperature distribution registered with IR-camera reports that the surface region of the tool was approximately 860 °C at a cutting speed $v_c = 200$ m/min and 910 °C at $v_c = 300$ m/min. The temperature gradient from the cutting edge and inwards into the tool is shown in Fig. 8. Such side-view data are known to underestimate the mid-plane temperature by 10–15% [28], thus, the actual temperature in the cutting zone is within 850–1000 °C depending on the speed. The chip has also reached the same temperature as the coating in the cutting zone.

The temperature and pressure reached in the cutting zone is then high enough for reaction between the coating and the NMI to occur [29]. These temperature data also read that the chip is at comparable temperature to the tool. Therefore, further research of thermodynamic stability and the possibility for chemical, oxidational and diffusional wear within these boundary conditions is of interest.

3.4. *Thermodynamic calculations*

Both Mg and Ca have the ability to deoxidize alumina, and are indeed found in the interaction region with the coating in Figs. 5–7. CaO, CaS, MgO, $(CaO)_x(Al_2O_3)_y$, $MgAl_2O_4$ and $(CaO)_x(Al_2O_3)_y(MgO)_Z$ are common NMI [16], and are also present in this steel (Fig. 1). The amount of NMI participating in the interaction depends on the chip flow and the frequency of NMI in the steel. Hence, the boundary condition for chemical activities is rather broad. The temperature and pressure boundary conditions are previously defined as 850–1000 °C and 10^5–10^9 Pa.

A simplified phase diagram of the MgO–CaO–Al_2O_3 system at 900 °C and at 10^5 Pa is shown in Fig. 9a, calculated using the TCOX10 database. The oxygen activity was arbitrarily set to one relative oxygen gas at ambient pressure and temperature. The alumina phase is modeled as corundum (α-alumina) which is the same as the phase in the coating. The five calcium aluminates $(CaO)_3(Al_2O_3)$, $(CaO)_{12}(Al_2O_3)_7$, $(CaO)_1(Al_2O_3)_1$, $(CaO)_1(Al_2O_3)_2$ and $(CaO)_1(Al_2O_3)_6$ which are solid solutions of calcium oxide and aluminum oxide are grouped into the number “5” $(CaO)_x(Al_2O_3)_y$ for clarity. The three phases $(CaO)_3(Al_2O_3)_2(MgO)_1$, $(CaO)_2(Al_2O_3)_{14}(MgO)_2$ and $(CaO)_1(Al_2O_3)_8(MgO)_2$ which are solid solutions of CaO, MgO and Al_2O_3 are grouped into “6” $(CaO)_x(Al_2O_3)_y(MgO)_z$. The other phases are separate, “1” alumina, “2” calcium oxide, “3” magnesium oxide and “4” magnesium aluminum oxide.

The Al_2O_3 coating is only thermodynamically stable in the left corner (shaded blue region) of the phase diagram (Fig. 9a). Any other composition in the phase diagram can lead to the degradation of the coating into spinel $(MgO)(Al_2O_3)$, calcium aluminate $(CaO)_x(Al_2O_3)_y$ or calcium aluminum magnesium oxide $(CaO)_x(Al_2O_3)_y(MgO)_z$ with varying compositions.

Further, the dimensionless driving force (driving force in J/mol divided by RT) for the first precipitation of the phase is calculated and given in Fig. 9b, for one illustrative point of the phase diagram in Fig. 9a. In this case, the calculation is done for 1 mol of material as a first approximation. This shows that the driving force for the degradation of the coating is favorable for calcium magnesium aluminates in the whole temperature range. The driving force normalized by the gas constant and temperature is decreasing, but the reaction rate might increase since the temperature also effects the rate. Hence, the presence of any magnesium oxide, calcium oxide, calcium aluminate and calcium aluminum magnesium oxide will make the alumina coating thermodynamically unstable, until the reaction layer is saturated with Al and O. Phase diagrams similar to Fig. 9 can be calculated for other possible NMI such as SiO_2 leading to the formation of $(Al_2O_3)_3(SiO_2)_2$. Rendering the same result, which is that they will also degrade the coating if the NMI is not already saturated with aluminum and oxygen. However, the machining tests in Sections 3.1 And 3.2 indicated that Mg and Ca are the most important participants in this case. Ca and Mg are also the strongest oxide formers.

Calculations show that CaS does not react with Al_2O_3 at the given cutting conditions without additional oxygen. However, such excess of oxygen is indeed available in the sliding zone of the tool-chip interface because of the dissolved oxygen in the steel and the presence of oxygen in the atmosphere, at approximately an O_2 effective partial pressure of 0.21. Thermodynamic calculations are therefore carried out within the defined cutting conditions with the addition of oxygen.

Fig. 10 show the calculations at one-to-one ratio of CaS to Al_2O_3, at 900 °C and 10^5 Pa with an increasing partial pressure of oxygen. Fig. 10a demonstrates how calcium aluminates in this case $(CaO)_1(Al_2O_3)_6$ become thermodynamically stable at an O_2 effective partial pressure of 10^{-17} and $(CaO)_1(Al_2O_3)_2$ at 10^{-14}. $CaSO_4$ also becomes stable at an O_2 effective partial pressure of 10^{-12}. Al_2O_3 is thermodynamically stable again at an O_2 effective partial pressure of 10^{-9} and above (Fig. 10a). Fig. 10b gives the dimensionless driving force for the precipitation of the phases. This shows that the driving force is the highest for the formation

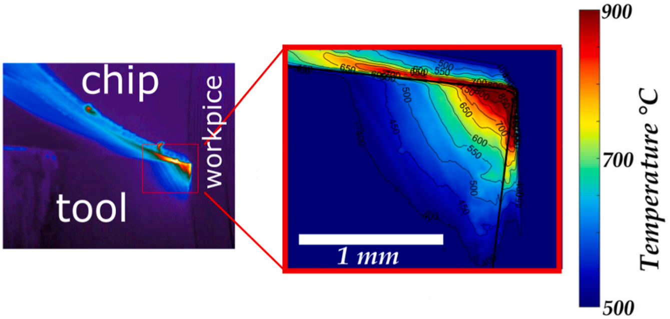

Fig. 8. Single frame example from the continuous temperature measurement of the cutting zone during orthogonal cutting.

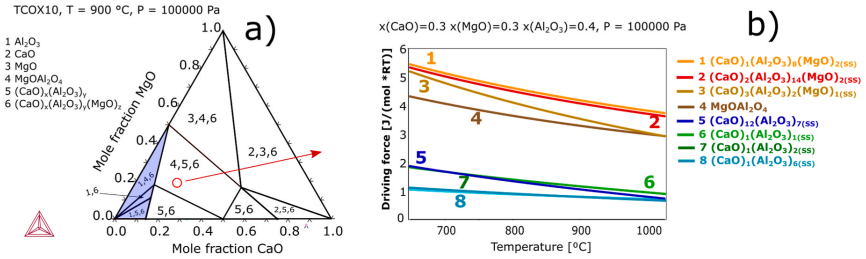

Fig. 9. a) The CaO–Al_2O_3–MgO system at 900 °C and 10^5 Pa, shows that the coating is a stable phase at low fractions of CaO and MgO (blue region). b) The driving force for the formation of the first amount of reaction products for one illustrative composition, showing a positive driving force for the degradation of the alumina coating. (For interpretation of the references to color in this figure legend, the reader is referred to the Web version of this article.)

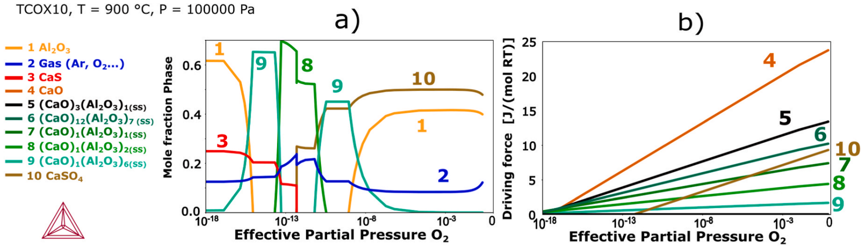

Fig. 10. a) The equilibrium phase composition with increasing oxygen availability, b) the driving force of the formation on different interaction products due to a reaction between CaS, Al_2O_3 and an increasing oxygen availability. CaS can degrade the alumina coating in the presence of oxygen at the machining conditions.

of CaO, and that the driving force for other calcium aluminates are high.

The formation of CaO will also lead to the formation of $(CaO)_3(Al_2O_3)_1$ and other calcium aluminates in accordance with the phase diagram in Fig. 9. Thus, CaS can degrade the Al_2O_3 coating when excess oxygen is available. Increasing the oxygen availability also increases the driving force for degradation. The stable phase and the onset of the degradation depend on the temperature, pressure, and activity. However, the degradation path of the Al_2O_3 is similar in nature within the boundary conditions and ends when reaching the $(CaO)_1(Al_2O_3)_6$ stoichiometry. This might also give an additional explanation to the mechanism behind the findings in Ref. [10] of inclusion deposits of no other calcium aluminates except $(CaO)_1(Al_2O_3)_6$.

Figs. 9 and 10 show that there are two pathways of degradation that would explain the wear of the alumina coating. One path is the degradation due to the formation of a solid solution of MgO, CaO and Al_2O_3 due to the reaction between the oxide NMI and the coating. The other path to degradation is the interaction between CaS with alumina and the ambient oxygen available in the cutting zone.

The products are determined by thermodynamics and the rate is determined by kinetics. Hence, cutting conditions leading to higher temperatures, pressures, and more interactions with NMIs from the chip leads to faster degradation. Such wear would be difficult to limit if it is dependent on the oxygen availability, but it can be limited if it is purely inclusion dependent. Thus, machining tests are needed to differentiate oxygen dependent wear mechanism and only alloy dependent.

Calculations at high pressures were also performed, however only including the molar volume and not bulk modulus. These show an increase in the driving force of the degradation at the high pressures reached in the cutting zone (10^9 Pa). Further investigations of the compressibility of the phases are needed to evaluate the exact result.

3.5. *Controlled atmosphere machining*

The reaction involving CaS that potentially leads to Al_2O_3 degradation is determined by the availability of oxygen. If the available oxygen is suppressed, this path for interaction will be deactivated. If the degradation of the coating is driven by ambient oxygen, then there is a limited possibility to improve the machinability by the addition of sulfates. If the degradation is not driven by the ambient oxygen, then the further control the oxides and oxygen content in the steel to improve the steel machinability.

The controlled atmosphere machining entailed two tests: a temperature assessment and a tool wear assessment. Comparing dry machining in air (dry - unforced air supply) with turning in an argon enriched environment might lead to the wrong conclusions. This is because flooding the cutting zone with 400 l/min of argon will likely introduce an extra cooling effect which influence the temperature in the cutting zone. By turning under the supply of compressed air, in contrast to the argon supply case, might also potentially lead to inaccurate conclusions, because air and argon have different thermal conductivities.

To distinguish between such potential sources of inaccuracy, the temperature was measured in dry, argon enriched, and compressed air environments using an embedded thermocouple inside the insert (Fig. 3c) at vc = 300 m/min. The result of the 50 s of turning is given in Fig. 11. Cutting at dry conditions resulted in a temperature of approximately 540 °C, compressed air in 510 °C, and argon in 507 °C. This is not as accurate as the IR-Camera measurements since the thermocouple is placed 800 μm from the tool-chip interface. However, it indicates the averaged differences. It can be concluded that a supply of compressed air and argon at 400 l/min results in nearly identical process temperatures.

The tool wear test was conducted for 500 s of engagement that is the approximate time at which the 40% of the tool-chip interface was devoid of alumina coating under dry conditions, as determined earlier (Fig. 6d).

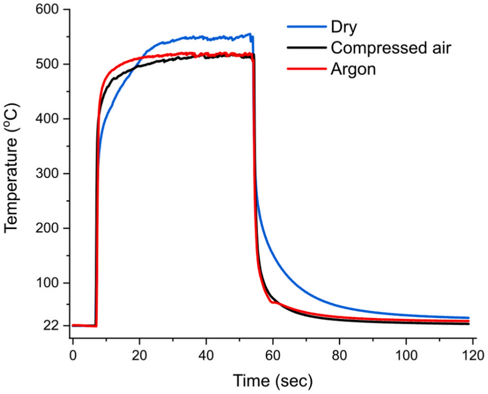

Fig. 11. Temperature measurement by embedded thermocouples 800 μm below the cutting surface. The effect on temperature by flooding the cutting zone with argon and oxygen result in a similar cooling effect.

The tool wear after this engagement time is practically identical between compressed air and argon, as shown in Fig. 12. There is a slight difference between the dry and the other two cases (compressed air and argon). This difference in ambient and compressed air or argon can be assigned to the high flow of gas in the cutting zone that lowers the temperature and improves chip breaking. No signs of flank wear are present.

The SEM-XEDS results of the rake face reveals that the tool surface composition is almost identical for the three cutting conditions. Ca and S is adhered to the exposed Ti(C,N) and Fe, Mg, Mn, and Ca are covering the Al_2O_3 (Fig. 13). This suggests that the degradation of the Al_2O is not driven by the oxygen available in the air, but rather through the reaction between the coating and oxide NMI already present in the workpiece material.

3.6. *Proposed degradation mechanisms of the coating*

The signs of abrasive wear on the alumina coatings have been apparent in the sliding zone in many papers [4–12], studying the wear of alumina coatings during turning machinability improved soft Ca-treated steels. The developments in (001) textured α-Al_2O_3–TiCN coatings and calcium treated steels has led to an increase in the tool life [4,16]. The anomalous wear of the α-Al_2O_3–Ti(C,N) coating when machining Ca-treated steel cannot be attributed to abrasive wear and shear stress alone. Fig. 14 shows a simplified schematic of the results presented in Section 3.1–3.4.

The alumina coating on the flank with no deposits shows limited signs of wear (Fig. 14, step 1). Furthermore, there are no signs of abrasive wear on the flank after 500 s of machining (Fig. 6). This indicates that the alumina coating is rather wear resistant before any thermal and chemical degradation has taken place. This is because the steel is a soft calcium treated steel with suppressed formation of pure oxide inclusions with only sulfides and oxy-sulfides present (Fig. 1). The chip and tool are also at a similar elevated temperature (Fig. 8) which make the inclusions softer than the coating (Fig. 7).

NMI are then deposited and adhered to the alumina coating (Fig. 14, step 2). This occurs mainly in the sliding zone. The composition of theses deposits is a combination of the NMIs, such as (Mn,Ca)S and $(Mg, Ca, Al)_xO_y$ and the workpiece material which is mostly Fe, as is shown in Figs. 5, 6 and 13.

The adhered NMI material reacts with the coating and starts to form a combination of one or several of the solid solution $(CaO)_1(Al_2O_3)_6$, $(MgO)(Al_2O_3)$, $(CaO)_1(Al_2O_3)_8(MgO)_2$ and $(CaO)_2(Al_2O_3)_{14}(MgO)_2$, (Fig. 14, step 3). This is due to the fact that the alumina in the coating is no longer chemically inert, and thus not an equilibrium phase (Fig. 9). There is therefore a positive driving force for it to degrade (Fig. 9b). The temperature and pressure is high enough for a solid-state reaction to take place (Fig. 7). The mixed oxide layer derived from the reaction is drawn in green in Fig. 14, modeled in Section 3.4 and also seen as second shades of Al and O with an overlap with Mg and Ca in Fig. 7.

These reaction products are softer than the original coating and similar in hardness to the NMI. This allows them to be mechanically worn (Fig. 14, step 4). The abrasive tracks appear mostly to be in the adhered layer and reaction products, which has been the focus of earlier works [4–12]. The "ridges" of inclusions and the "valleys" of exposed alumina left between are caused by abrasive particles that remove the reaction layer and the deposited NMI. This is shown by the combination of topography sensitive SE−SEM and XEDS lines cans in Fig. 5. This is a form of abrasive wear, as seen in previous studies [4–12]. However, the origin is the initial chemical degradation of the coating. The results of this current study also explain why Ca-treated steels lead to a decrease in flank wear and increased crater wear for alumina coated and alumina ceramic tools compared to non-calcium treated steel, as shown in earlier works [17,19,20]. The process is repeated as more material is deposited, reacted and abraded (Fig. 14, step 3–5) until the alumina coating is worn through. The Ti(C,N) coating is then exposed which leads to the adhesion of CaS (Figs. 6 and 13).

The interaction system needs to be evaluated at higher pressures, as the driving force would likely increase with an increased pressure, if not offset by a large difference in compressibility. Hence, the high pressure

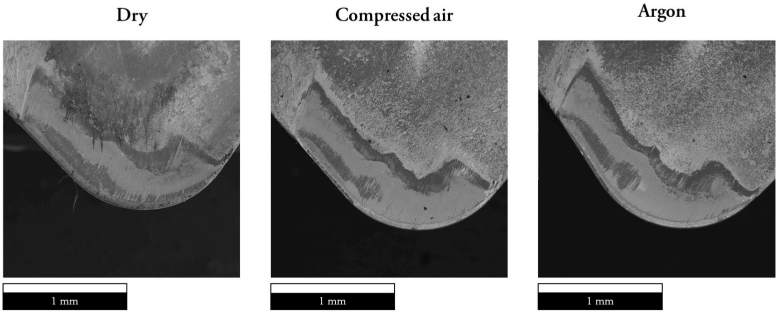

Fig. 12. BSE-SEM images that compare the tools after 500 s of cutting in dry, compressed air, and argon environments.

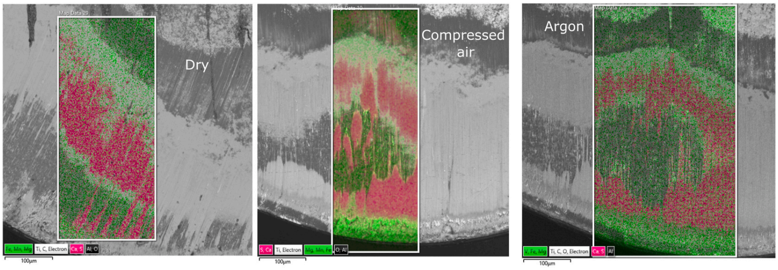

Fig. 13. Comparison of the center of the cutting zone after 500 s of machining in dry, compressed air, and argon conditions. The removal of oxygen by a supply of argon did not affect the wear of the coating measurably.

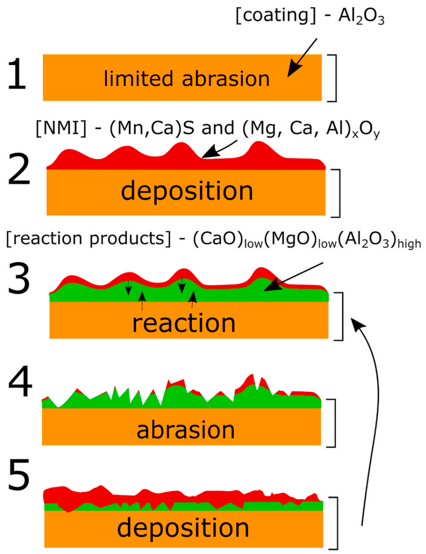

Fig. 14. The process of degradation of the alumina coating, where the green reaction layer is in the order of 100 nm. (For interpretation of the references to color in this figure legend, the reader is referred to the Web version of this article.)

in the cutting zone likely leads to faster degradation than standard experiments carried out in vacuum or at atmospheric pressure [29]. Not taking high pressures, high temperatures and the dynamics of the process under consideration might explain previous overestimates of the inertness of the alumina coating.

4. Conclusions

The anomalous wear of alumina coatings when machining steel that contains NMI can be explained by the initial chemical degradation of the alumina (Al_2O_3). Under there machining conditions, it reacts to form calcium aluminate $(CaO)_x(Al_2O_3)_y$, spinel $MgAl_2O_4$ and calcium magnesium aluminate $(MgO)_x(CaO)_y(Al_2O_3)_z$ by the process outlined in Fig. 14. This shows a sequence of steps leading to a tool surface with signs of abrasive wear. However, the origin is an initial chemical degradation due to the fact that alumina is no longer chemically inert at the prevailing conditions. This is shown by the microstructural investigations and support by the temperature measurements and thermodynamic calculations. Hence, the inertness of alumina coatings in previous studies are overestimated, even more so at higher pressures (1 GPa). The fresh supply of NMI from the steel, as well as the high temperature and pressure in the sliding zone, leads to positive driving forces for the degradation of alumina in the presence of calcium and magnesium mixed oxides and oxi-sulfides.

The degradation of the alumina coating will continue until the deposited NMI are saturated with Al and O, though this layer will be continuously abraded and encounter more NMI. CaS can theoretically lead to the chemical degradation of alumina, but only when an excess of oxygen is available. However, it is shown that oxygen from the ambient air is does not drive such degradation of the coating. This concludes that the degradation is driven by the oxide and NMI available in the steel, and by the ambient oxygen. To understand this interaction even further, detailed investigations of the kinetics of the degradation of alumina in the presence of NMI at high pressures and temperatures are needed. In addition, such an extended study is needed to realize the full benefits of Ca-treatments and NMI without the degradation of the alumina coating.

Declaration of competing interest

The authors declare that they have no known competing financial interests or personal relationships that could have appeared to influence the work reported in this paper.

Acknowledgment

This work was funded by the national strategic innovation program: National action for metallic materials, organized by Vinnova and Jernkontoret (Sweden) under DEMO project (ID 2017–02915). The authors would like to acknowledge the Sustainable Production Initiative (SPI) - a cooperation between Lund University and Chalmers University of Technology. The acknowledgment also extends to Per Alm and Vyacheslav Kryzhanivskyy (Seco Tools AB) for the help with IR thermography.

References

[1] W. König, Einfluss nichtmetallischer Einschlüsse auf die Zerspanbarkeit von Kohlenstoffstählenitle, Maschinenmarkt, 1965.

[2] W. König, Der Einfluss nichtmetallischer Einschlüsse auf die Zerspanbarkeit von unlegierten Baustählen, Ind. Anzeiger 87 (1965).

[3] N. Ånmark, T. Bjork, A. Karasev, P.G. Jonsson, Effect of different inclusions on mechanical properties and machinability of 20NiCrMo carburizing steels, in: Proc. 6th Int. Congr. Sci. Technol. Steelmak. ICS 2015, 2015.

[4] R. M'Saoubi, O. Alm, J.M. Andersson, H. Engström, T. Larsson, M.P. Johansson-Jõesaar, M. Schwind, Microstructure and wear mechanisms of texture-controlled

CVD A-Al2O3 coatings, Wear (2017), https://doi.org/10.1016/j.wear.2017.01.071.

[5] S. Ruppi, Enhanced performance of α-Al2O3 coatings by control of crystal orientation, Surf. Coating. Technol. (2008), https://doi.org/10.1016/j.surfcoat.2008.03.021.

[6] R. Bejjani, M. Collin, T. Thersleff, S. Odelros, Multi-scale study of initial tool wear on textured alumina coating, and the effect of inclusions in low-alloyed steel, Tribol. Int. (2016), https://doi.org/10.1016/j.triboint.2016.01.021.

[7] A. Larsson, M. Halvarsson, S. Ruppi, Microstructural changes in CVD κ-Al2O3 coated cutting tools during turning operations, Surf. Coating. Technol. (1999), https://doi.org/10.1016/S0257-8972(98)00734-8.

[8] M. Gassner, N. Schalk, M. Tkadletz, M. Pohler, C. Czettl, C. Mitterer, Influence of cutting speed and workpiece material on the wear mechanisms of CVD TiCN/A-Al2O3 coated cutting inserts during turning, Wear (2018), https://doi.org/10.1016/j.wear.2017.11.019.

[9] S. Ruppi, M. Halvarsson, TEM investigation of wear mechanisms during metal machining, Thin Solid Films (1999), https://doi.org/10.1016/S0040-6090(99)00413-7.

[10] A. Larsson, S. Ruppi, Structure and composition of built-up layers on coated tools during turning of Ca-treated steel, Mater. Sci. Eng. A (2001), https://doi.org/10.1016/S0921-5093(01)00964-9.

[11] R. M'Saoubi, S. Ruppi, Wear and thermal behaviour of CVD α-Al2O3 and MTCVD Ti(C,N) coatings during machining, CIRP Ann. Manuf. Technol. (2009), https://doi.org/10.1016/j.cirp.2009.03.059.

[12] A. Osada, E. Nakamura, H. Homma, T. Hayahi, T. Oshika, Wear mechanism of thermally transformed CVD Al2O3 layer, Int. J. Refract. Metals Hard Mater. (2006), https://doi.org/10.1016/j.ijrmhm.2005.11.007.

[13] N. Ånmark, T. Björk, Tool wear in soft Part Turning of high performance steel, in: Procedia CIRP, 2016, https://doi.org/10.1016/j.procir.2016.04.043.

[14] N. Ånmark, T. Björk, Effects of the composition of Ca-rich inclusions on tool wear mechanisms during the hard-turning of steels for transmission components, Wear (2016), https://doi.org/10.1016/j.wear.2016.09.016.

[15] N. Ånmark, S. Lövquist, M. Vosough, T. Björk, The effect of cleanliness and micro hardness on the machinability of carburizing steel grades suitable for automotive applications, Steel Res. Int. (2016), https://doi.org/10.1002/srin.201500243.

[16] N. Ånmark, A. Karasev, P.G. Jönsson, The effect of different non-metallic inclusions on the machinability of steels, Materials (Basel) (2015), https://doi.org/10.3390/ma8020751.

[17] R. Bejjani, S. Odelros, S. Öhman, M. Collin, Shift of wear balance acting on CVD textured coatings and relation to workpiece materials, Proc. Inst. Mech. Eng. Part J J. Eng. Tribol. (2020), https://doi.org/10.1177/1350650120926781.

[18] S. Ruppi, B. Högrelius, M. Huhtiranta, Wear characteristics of TiC, Ti(C,N), TiN and Al2O3 coatings in the turning of conventional and Ca-treated steels, Int. J. Refract. Metals Hard Mater. (1998), https://doi.org/10.1016/S0263-4368(98)00039-0.

[19] N. Narutaki, A. Murakoshi, Effect of small quantity inclusions in steels on the wear of ceramic tools, Bull. Jpn. Soc. Precis. Eng. (1977), https://doi.org/10.2493/jjspe1933.42.221.

[20] J. Barry, G. Byrne, Cutting tool wear in the machining of hardened steels. Part I: alumina/TiC cutting tool wear, Wear (2001), https://doi.org/10.1016/S0043-1648(00)00531-7.

[21] J.-E. Ståhl, Metal Cutting : Theories in Practice, SECO TOOLS, Fagersta, Sweden, 2012.

[22] E.M. Trent, P.K. Wright, Metal Cutting, fourth ed., 2000, https://doi.org/10.1016/B978-075067069-2/50015-2.

[23] G. Brandt, Flank and crater wear mechanisms of alumina-based cutting tools when machining steel, Wear (1986), https://doi.org/10.1016/0043-1648(86)90199-7.

[24] S. Shoja, N. Mortazavi, E. Lindahl, S. Norgren, O. Bäcke, M. Halvarsson, Microstructure investigation of textured CVD alumina coatings, Int. J. Refract. Metals Hard Mater. (2020), https://doi.org/10.1016/j.ijrmhm.2019.105125.

[25] J.-O. Andersson, T. Helander, L. Hoglund, P. Shi, B. Sundman, Thermo-Calc & DICTRA, computational tools for materials science, CALPHAD Comput. Coupling Phase Diagrams Thermochem. 26 (2002) 273–312.

[26] P.A. Dearnley, E.M. Trent, Wear mechanisms of coated carbide tools, Met. Technol. (1982), https://doi.org/10.1179/030716982803285909.

[27] V. Bushlya, F. Lenrick, J.E. Ståhl, R. M'Saoubi, Influence of oxygen on the tool wear in machining, CIRP Ann 67 (2018) 79–82, https://doi.org/10.1016/j.cirp.2018.03.011.

[28] M.A. Davies, H. Yoon, T.L. Schmitz, T.J. Burns, M.D. Kennedy, Calibrated thermal microscopy of the tool-chip interface in machining, Mach. Sci. Technol. (2003), https://doi.org/10.1081/MST-120022776.

[29] C. Ghoroi, A.K. Suresh, Solid-solid reaction kinetics: formation of tricalcium aluminate, AIChE J. (2007), https://doi.org/10.1002/aic.11086.

Paper IV

Surface & Coatings Technology 450 (2022) 128997

Contents lists available at ScienceDirect

Surface & Coatings Technology

journal homepage: www.elsevier.com/locate/surfcoat

Understanding wear and interaction between CVD α-Al_2O_3 coated tools, steel, and non-metallic inclusions in machining

Axel Bjerke [a,*], Filip Lenrick [a], Susanne Norgren [a,b], Henrik Larsson [c], Andreas Markström [d], Rachid M'Saoubi [a,e], Igor Petrusha [f], Volodymyr Bushlya [a]

[a] Division of Production and Materials Engineering, Lund University, Ole Römers väg 1, Lund, Sweden
[b] Sandvik Coromant R&D, Lerkrogsv. 13, 126 80 Stockholm, Sweden
[c] Unit of Structures, Department of Materials Science and Engineering, KTH, SE-10044 Stockholm, Sweden
[d] Thermo-Calc Software AB, Råsundavägen 18, SE-169 67 Solna, Sweden
[e] R&D Materials and Technology Development, Seco Tools AB, 737 82 Fagersta, Sweden
[f] Institute for Superhard Materials, NAS of Ukraine, Kiev, Ukraine

ARTICLE INFO

Keywords:
α-Al2O3
Non-metallic inclusions
Diffusion couple
Chemical wear
Machining

ABSTRACT

The aluminum oxide-coating on cemented carbide tools used for metal cutting have been regarded as inert during cutting of steels. Because diffusional dissolution is not possible. Chemical degradation of aluminum oxide coatings is often overlooked, especially in the presence of ambient oxygen and non-metallic inclusions. High-pressure diffusion couples, advanced microscopy, and thermodynamics are used to investigate and predict the chemical degradation of aluminum oxide-coated tools. During interactions with steel and different combinations of inclusions with and without ambient oxygen. The results show that alumina is resistant to chemical degradation by steel in the absence of oxygen. However, this is not the case when oxygen and non-metallic inclusions are present. These experiments and microscopy together with the thermodynamic calculations allow for the creation of a method and guidelines for chemical wear modeling and steel inclusion engineering when machining with aluminum oxide-coated tools.

1. Introduction

The addition of calcium and other compounds during steelmaking to control the composition, morphology and distribution of inclusions in Al-killed steels has been practiced and studied for more than 40 years [1]. Calcium treatment, for example, is used to transform solid alumina (Al_2O_3) into liquid calcium aluminates $(CaO)_x(Al_2O_3)_y$ that improve casting [2]. Adding calcium to the steel melt has also been shown to improve machinability [3]. The inclusions favor chip formation and may be adhered to the cutting tool in the form of a protective layer, which increases the tool life [4,6]. These adhered material can function as a tribofilm, improving tribological contact, reducing mechanical wear, and acting as a barrier to chemical, diffusional, and oxidational wear of the tool material [5,6]. This approach has been successful when machining steels with tool materials such as high-speed steel [4], uncoated cemented carbides [7], polycrystalline cubic boron nitride (PCBN) [8], and cemented carbide with TiC, TiN and Ti(C,N) coatings [9]. However, in comparative studies of calcium- and non-calcium-treated steels [10–12], calcium treatment has been found to increase rake wear, and in some cases decreases the tool life of alumina-coated and alumina-based ceramic tools in machining.

Alumina has limited solubility in the steel phases (austenite, martensite, ferrite and cementite), which limits diffusional wear and should make mechanical wear the main wear mechanism during metal-cutting operations [13]. Studies of the wear of alumina-coated tools with steels containing non-metallic inclusions have revealed the presence of Al-containing mixed oxides atop the Al_2O_3 coatings after machining. These mixed oxides are assumed to be adhered inclusions from the original steel [10,14], but they have also been interpreted as potential reaction products [11,15,16]. In several studies, the worn tools have been etched with HCl [17,18] to remove adhered steel, a process that unfortunately also removes some of the evidence of interactions with calcium oxides. The focus of Al_2O_3 coating studies has therefore been on improving the mechanical properties of alumina coatings by enhanced bonding, phase control and texture, microstructural refinement, multilayering, and texturing of alumina to improve cutting performance

---

[*] Corresponding author.
E-mail address: axel.bjerke@iprod.lth.se (A. Bjerke).

https://doi.org/10.1016/j.surfcoat.2022.128997
Received 18 August 2022; Received in revised form 18 October 2022; Accepted 19 October 2022

[19]. These modifications improve the coating's resistance to mechanical wear such as plastic deformation and abrasion. One recent development is (0001) textured α-Al$_2$O$_3$ which has improved resistance to abrasive wear. This has been shown to be due to the basal slip plane being in the plane of the coating, making uniform plastic deformation and twinning more surface localized [17,19]. In addition, older studies of other Al$_2$O$_3$ coatings such as kappa [21] and not textured α-Al$_2$O$_3$ might not even be relevant today [19].

Still, experiments involving liquid metal and Al$_2$O$_3$-ZrO$_2$ show that the Al$_2$O$_3$ can react with steel in the presence of oxygen [20]. A recent study of the onset of the wear of a (0001) α-Al$_2$O$_3$ coating when machining a calcium-treated steel [16] shows how oxygen, steel, and non-metallic inclusions react with the alumina coating during turning of a calcium-treated 19MnVS6 E470 steel [16]. Similar wear mechanisms were observed in an earlier study on the machining of inclusion engineered steels with a TiC-A$_2$O$_3$-TiN coating [21]. This type of finding is not limited to Al$_2$O$_3$ coatings and is common to machining inclusion engineered steels with Al$_2$O$_3$-based ceramic tool materials [11,12,22–25].

The development of more mechanical-wear resistant alumina coatings and inclusion engineered steels free of hard inclusions has led to an increase in the importance of chemical, oxidational wear as a precursor to mechanical wear [16]. The full potential of turning inclusion engineered steel with alumina-coated tools and ceramics will not be reached without further understanding and limiting of the interaction between alumina, non-metallic inclusions (NMI), steel, and air.

The interaction between alumina and other inclusions has been extensively studied for SiC-Al$_2$O$_3$ ceramics [26–28], with the liquid metal for Al$_2$O$_3$-ZrO$_2$ [20] or under casting conditions [2,29,30]. To our knowledge no studies have investigated the interaction between alumina coatings, rather than ceramics, when the steel and inclusion phases are in the solid state, both in the presence and absence of oxygen. There are few experiments valid for conditions relevant to metal cutting, such as temperatures below 1300 °C and pressures above 2 GPa [16,31,32]. Hence, a set of diffusion couple experiments at 2.5 GPa, 1200 °C and 1300 °C, as well as thermodynamic calculations are performed in this study. The interacting materials include CVD α-Al$_2$O$_3$-coated tools, a range of non-metallic inclusion precursors, and the steel itself. These conditions simulate the interaction environment during the metal-cutting process and aid understanding of the degradation of CVD α-Al$_2$O$_3$ coatings during turning of inclusion engineered steels [16,33]. The generated findings and knowledge can further aid in pairing and developing optimized tools and inclusion engineered steels. In addition, the experimental and modeling solutions developed are not limited to alumina coatings, but also create a basis for understanding the interaction between cutting tools and NMI in general.

2. Methods

2.1. Material & diffusion couple

Previously reported results by Bjerke et.al [16] on the interaction between steel, inclusions and the Al$_2$O$_3$ coating in machining were used when selecting material combinations for the current diffusion couple experiments. The selected steel is a calcium-treated commercial steel 19MnVS6 (E470) shown in Fig. 1a. The tool material used in the diffusion couple experiments is a cemented carbide (WC-Co)-coated insert with a multi-layer CVD coating. The coating consists of a bottom Ti(C,N) layer, a middle Ti(C,N,O) bonding layer, and an outer (001) textured α-Al$_2$O$_3$ layer (Fig. 1b). Additionally, non-metallic inclusion precursors were introduced in the diffusion couple experiments as a set of designed powder mixtures of Al$_2$O$_3$, CaO, Fe$_2$O$_3$, Fe$_3$O$_4$, MgO, MnO and SiO$_2$ prepared by planetary ball milling.

The diffusion couples consisted of three parts: the coated tool material, an inclusion mixture, and a metallic capsule, shown as a schematic cross-section in Fig. 2. The capsule is manufactured from 19MnVS6 steel, and the central cavity is used to encapsulate the round coated cemented carbide insert with the Al$_2$O$_3$ coating facing the inclusions and the steel. The steel capsule was either in as-machined or pre-oxidized state. The inclusion precursor combinations were placed between the steel and the coating. The diffusion couple experiment was performed in a toroid-type high-pressure and high-temperature cell HPAT-30 [34]. The design, assembly, and heating and cooling of the diffusion couples is identical to that described in [34]. The pressure and the holding time were kept constant at 2.5 GPa and 10 min, respectively. Experiments were conducted at temperatures of 1200 °C and 1300 °C. After the heat treatment, the high-pressure cell was instantly oil cooled. The diffusion couple reaches room temperature within a minute, after which the pressure is released. The diffusion couple never came in contact with any air or liquid during the experiment. Table 1 shows the combinations of tool, workpiece, and inclusion mixtures investigated in our study.

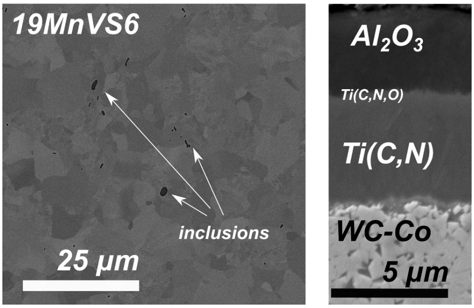

Fig. 1. SEM images of a) the steel 19MnVS6 (non-etched) arrows pointing to non-metallic inclusions introduced during manufacturing; b) the microstructure of coated tool cemented carbide tool material used in diffusion couples. The tool-workpiece combination is identical to the materials [16].

This method has been shown to accurately capture the chemical and diffusional interactions between the tool and metallic materials [33–35]. The chosen conditions aimed to capture the chemical, oxidation, and diffusional degradation of the coating under conditions similar to those during actual machining of the selected tool and workpiece combination. The interaction temperature was intentionally set slightly higher than the actual temperatures in the cutting zone (≈ 1000 °C) [16] in order to compensate for the short interaction time.

2.2. Microscopy

The interaction region of cross-sectioned and polished samples was studied using a Tescan Mira3 scanning electron microscope (SEM), equipped with secondary electron (SE), backscatter electron (BSE), X-ray energy-dispersive spectroscopy (XEDS), and electron backscatter diffraction (EBSD) detectors. Lamellas were extracted and thinned using a FEI Nova NanoLab 600 focused ion beam FIB-SEM. These lamellas were investigated using a transmission electron microscope (TEM) JEOL 3000F additionally equipped with a XEDS detector. Transmission Kikuchi Diffraction (TKD) studies were also conducted on the lamellas using the Tescan Mira3 EBSD detector. This combination of microscopy allowed for investigation of the microstructure, chemistry, and crystal structure of the interaction zone on the millimeter to nanometer scale.

2.3. Thermodynamics

The thermodynamic calculations were conducted using the CALPHAD approach with Thermo-Calc software [36] and the TCFE11 database. The steel was modeled as pure Fe (FCC), since any steel

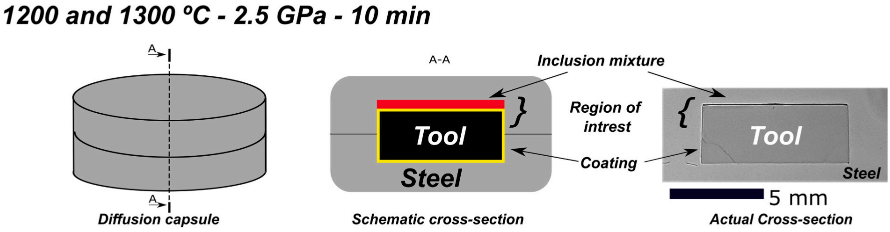

Fig. 2. Schematic and actual cross-sectional view of the diffusion couple assembly.

Table 1
Experimental materials.

#	Coating	Steel capsule	Powder precursors	Pressure [GPa]	Temperature [°C]
1	Al_2O_3	As machined	none	2.5	1200, 1300
2	Al_2O_3	Pre-oxidized	none	2.5	1200, 1300
3	Al_2O_3	As machined	MgO	2.5	1300
4	Al_2O_3	As machined	SiO_2, CaO, MgO, Al_2O_3	2.5	1200, 1300
5	Al_2O_3	As machined	SiO_2, CaO, MgO, Al_2O_3, MnO, Fe_3O_4, Fe_2O_3	2.5	1200, 1300

adhered in the cutting zone will be heated and transformed and this is the case in the diffusion couple. The inclusion mixture as tridymite (SiO_2), halite (CaO, MnO and MgO), corundum (Al_2O_3), spinel (Fe_3O_4) and hematite (Fe_2O_3). The (0001) textured α-Al_2O_3 coating is modeled as corundum. The availability of oxygen in the interaction zone is expressed using the oxygen activity where the reference state is pure oxygen gas. The reference state of oxygen was set as pure oxygen gas at ambient temperature and one bar pressure. The oxygen activity thus corresponds to the partial pressure of O_2 – the latter is, of course, 1 in a pure O_2 environment, approximately 0.21 in the ambient atmosphere, and 0 in an oxygen-free environment. The reactions between the inclusions, steel, oxygen and coating can both be modeled as non-stoichiometric phases and the whole temperature range from 25 °C to 1300 °C is investigated to look for possibly metastable phases.

3. Results

3.1. Al_2O_3 coating vs. steel

The reference sample (Table 1 - #1) is a high-temperature and high-pressure diffusion couple between the coating and the steel in the absence of air. This condition simulates the interface between the coating and the steel that occurs in the sticking zone of the tool–chip interface where the contact is intimate [31,32]. It has been shown that the chemical wear of the coating is also lowest in this zone compared to the mixed and sliding zone when machining these types of steels with Al_2O_3 coatings [10,16].

The reference (#1) diffusion couple between the steel and the alumina coating did not bond together during neither the experiment at 1200 °C nor 1300 °C while being pressed together for 10 min at a pressure of 2.5GPa. The coating also remained its original thickness of approximately 4.5 µm. A gap has formed between the coating and the steel, this gap was partially filled up with mounting material during sample preparation. The gap is indicated in the SEM-BSE image (Fig. 3). This gap formed during the cooling and decompression of the diffusion couple and is related to thermal shrinkage and compressibility during the experiment, of the respective materials. The edges of the Al_2O_3 coating and the edge of the steel has been slightly rounded during sample preparation due to the difference in hardness between the Al_2O_3 coating, the gap partially filled with mounting material and steel. This apparent lack of interaction compared to experiment 2–5 (Table 1) is expected because Fe cannot reduce aluminum oxide [37] and has limited solubility in Al_2O_3 [13]. This agrees with experiments at ambient pressures and higher temperatures [20].

However, air was entrapped in some locations of this sample, which led to a more than 5 µm thick reaction zone forming. Fig. 4 shows a SEM image and XEDS maps of the same diffusion couple (#1) in a location

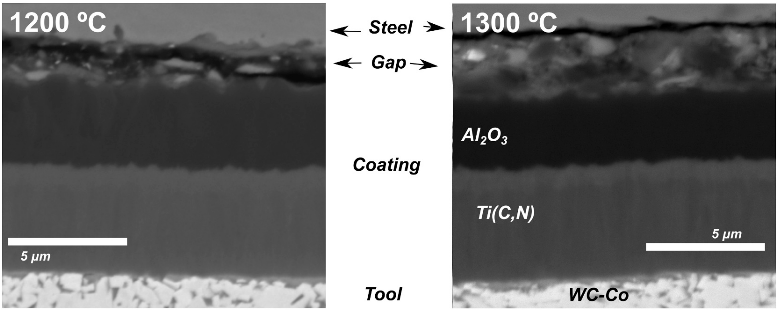

Fig. 3. SEM-BSE image of diffusion couple between steel and coating at 1200 °C and 1300 °C without the presence of inclusions of air, the gap formed during decompression.

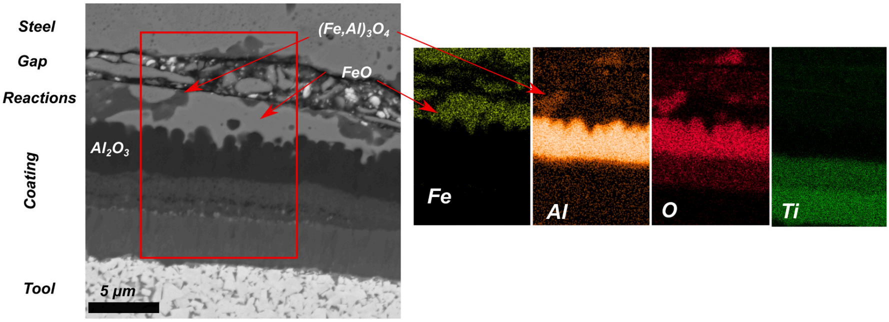

Fig. 4. SEM-BSE image and XEDS maps for the diffusion couple between steel and coating with entrapped oxygen at 1200 °C. $(Fe,Al)_3O_4$ spinel and FeO halite have formed, and the Al_2O_3 coating has been partially consumed.

where air has been trapped. Air can be trapped in the corners of the capsule-insert assembly (Fig. 2), during the manufacturing of the high-pressure and high-temperature experiment. The machined steel capsule has a corner radius of approximately 200 µm, while the coated insert has an edge radius of approximately 25 µm. This difference in radii creates a pocket for air entrapment. The interaction between the tool material and the steel in the presence of air can therefore be studied in these corner regions. This situation represents the interface of the coating and the steel in the presence of oxygen during machining, which occurs in the sliding zone of the tool–chip interface [31,32]. This sliding region is known to exhibit relatively larger wear rates of Al_2O_3 coatings compared to the sticking zone [10,16].

Fig. 4 shows that the Al_2O_3 coating has reacted with oxygen and iron, leading to degradation of the Al_2O_3 coating. An iron aluminum oxide has formed on the interface between the coating and the steel, as shown by the overlapping XEDS maps and the *Z*-contrast contrast difference in the SEM-BSE image (Fig. 4). The gap in this case forms not between the coating and the oxides but between the iron aluminum oxides and the steel. This indicates strong adhesion between the reaction products and the coating. This is different from the areas where excess oxygen cannot access the interface (Fig. 3). Where there is no degradation and oxide formation.

The reaction layer consists of two phases, an aluminum iron oxide with different Al and Fe contents. XEDS and EBSD identified the reaction product as $(Fe, Al)_3O_4$ spinel. A pure iron oxide has also formed that is identified as FeO. The thickness of the Al_2O_3 coating layer has been reduced from the original 4.5 µm to 3.5–4 µm at 1200 °C and to 2.5–3 µm at 1300 °C. This finding is in agreement with a study where mixed ZrO_2-Al_2O_3 ceramic tools were immersed in molten metal containing surface oxides at 1326 °C for 2 min [20]. In the case of the molten metal, the reaction zone was 15 µm, but the same iron alumina spinel was still observed.

3.2. Al_2O_3 coating vs. pre-oxidized steel

The pre-oxidized steel sample was generated by first corroding it in water and then heat-treating it in a furnace at 600 °C for 30 min. The diffusion couple with such pre-oxidized steel (Table 1 - #2) represents machining cases when the coating encounters adhered and oxidized steel, or cases of simultaneous exposure of steel to the air. These situations can occur when machining steels with oxide scales, during intermittent cutting when adhered steel oxidizes, or, most commonly, in the sliding zone of the tool–chip interface where atmospheric oxygen can reach the interface [32].

A SEM-BSE image of the interface between the pre-oxidized scale and the coating after 10 min at 1200 °C and 2.5 GPa is shown in Fig. 5. The result is similar to the case of the reference sample #1 with trapped air (Fig. 4). In the current case, the alumina coating strongly reacts with the iron oxides to form a $(Al,Fe)_3O_4$ spinel phase. A mixture of Fe_xO_y and steel is adhered to the $(Al,Fe)_3O_4$ spinel and Al_2O_3 coating. The absence of a gap between the reaction products and the coating indicates strong adhesion between the reaction products and the coating, which contrasts with the reference sample #1 (Fig. 3). The Al_2O_3 coating layer has reduced in thickness from the original 4.5 µm to 2.5–3 µm at 1200 °C

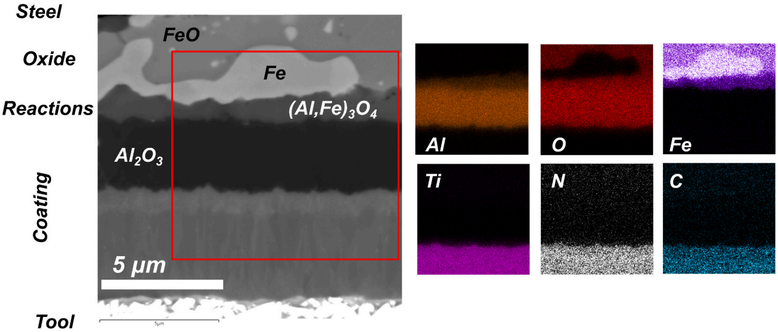

Fig. 5. SEM-BSE image and XEDS maps of the reaction interface between the pre-oxidized steel and the coating at 1200 °C.

and 2.2–2.7 μm at 1300 °C.

A TEM lamella was extracted from the interface and was examined to further identify the reaction products (Fig. 6). The imaging mode used was high-angle annular dark field (HAADF-STEM) which is composition sensitive, and low-angle annular dark field (LAADF-STEM) which is more sensitive to crystallographic differences. This STEM imaging is further combined with TKD and selected area electron diffraction (SAED). The phases identified by XEDS compositional analysis are confirmed by the SAED diffraction and TKD. The ratio of Fe to Al in the $(Al,Fe)_3O_4$ phase varies across the interface but is always spinel of F-d3m space group structure. The FeO is in the Wüstite phase belonging to the space group Fm-3 m. The alumina coating is the corundum R-3c phase. All these reaction products are identical to those in the case of entrapped oxygen (sample #1) and in earlier studies [20]. In this TEM lamella and in multiple instances across the interface, we observed particles of pure iron without the alloying elements of the 19MnVS6 steel.

The Al-Fe-O system is well understood both experimentally and thermodynamically [39]. We can therefore model what happens when steel together with oxygen interacts with the Al_2O_3 coating as seen in Figs. 4, 5 and 6. The thermodynamic calculations were carried out for 5 mol of Fe (steel) and 5 mol of Al_2O_3 (coating) and 1 mol of Ar gas. The presence of oxygen was modeled by continuously increasing the oxygen content of the system (Fig. 7). The calculations reveal the absence of coating interaction and degradation when oxygen is not available in the system, when the effective partial pressure of O_2 (P_{O2}) is below 10^{-17} and the gas phase consists of mostly argon. This computational result is consistent with our experiments (Fig. 3) and [13,20]. Hence, there is no chemical wear in the sticking zone during machining if there are no inclusions and no excess oxygen available [9,17].

However, the Al_2O_3 coating starts to react with the steel when excess oxygen is available and will form $(Al,Fe)_3O_4$, as shown by the increasing amount of $(Al,Fe)_3O_4$ (phase 4, Fig. 7), the decrease in the amount of Fe (phase 3, Fig. 7), and the absence of Al_2O_3 phase between P_{O2} 10^{-17} and 10^{-6} in Fig. 7. FeO is also stable in a part of this region. These results find experimental confirmation in the cases shown in Figs. 4, 5 and 6 where the coating is consumed and replaced by Fe, FeO, and the spinel phase $(Al,Fe)_3O_4$. Alumina and iron are likely to be consumed under excessive amounts of oxygen, which then makes Fe- and Al-rich $(Fe,Al)_2O_3$ the stable phases. This has been experimentally observed in other studies [39], but not in our oxygen-limited cases. Hence, the Al_2O_3 coating is resistive to dissolution and oxidation wear [13,40], but not to chemical wear.

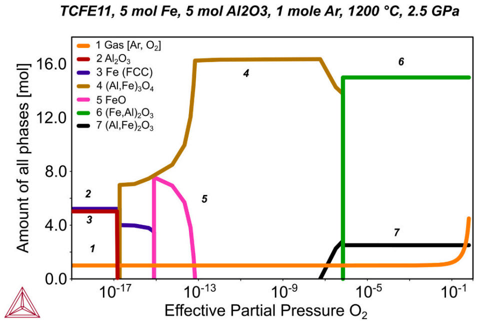

Fig. 7. Diagram of the equilibrium phase composition with varying availability of oxygen at the experimental conditions. The Al_2O_3 coating is not thermodynamically stable in the presence of Fe and O.

3.3. Al_2O_3 coating vs. MgO inclusions

MgO is not commonly used as an NMI for machinability improvement, but it is often found in steels as mixed oxides due to its presence in the steelmaking process. It is often found adhered to tool surfaces during machining [16,41]. A diffusion couple with only MgO precursor was therefore prepared to investigate the effect of the presence of Mg oxides (Table 1 - #3). MgO aggressively reacted with the Al_2O_3 coating, resulting in complete dissolution of the Al_2O_3 layer of the coating in almost all places. Remnants of the coating (well below 1 μm thick) were found in some locations. However in those locations the alumina layer had reacted with MgO to form an Al_2MgO_4 spinel as shown in Fig. 8 Region 1. The more common observation across the coating and MgO interface is the formation of a mixture of different Ti, Mg oxides with only small amounts of Al detectable. Fig. 8 Region 2 is a LAADF-STEM image of an area where a gap formed between the Ti(C,N) coating and the consumed coating and MgO powder. The new $Ti_xMg_yO_z$ phase has the same columnar structure as the Ti(C,N) layer and most likely grew epitaxially when consuming the Ti(C,O,N) bonding layer. The $Ti_xMg_yO_z$

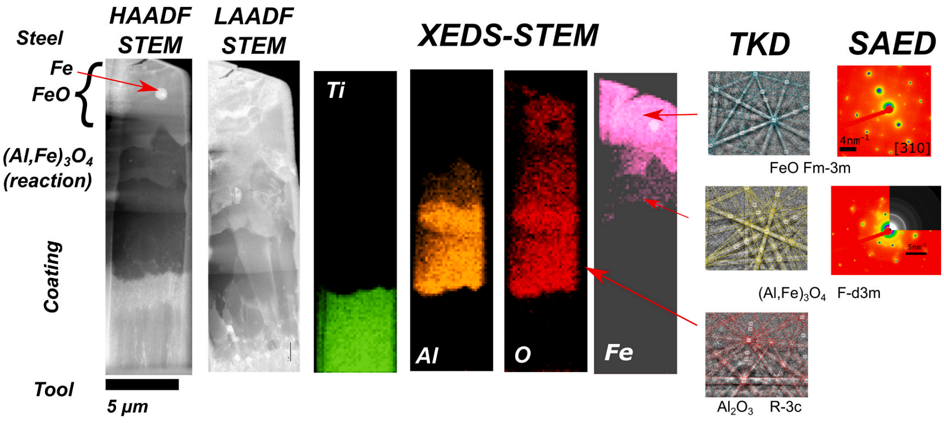

Fig. 6. STEM images, XEDS mapping, TKD, and SAED of the interaction zone and phases found on the interface between the coating and the pre-oxidized steel after 10 min at 1200 °C and 2.5 GPa. The iron oxide has reacted and degraded the Al_2O_3 coating into $(Al,Fe)_3O_4$.

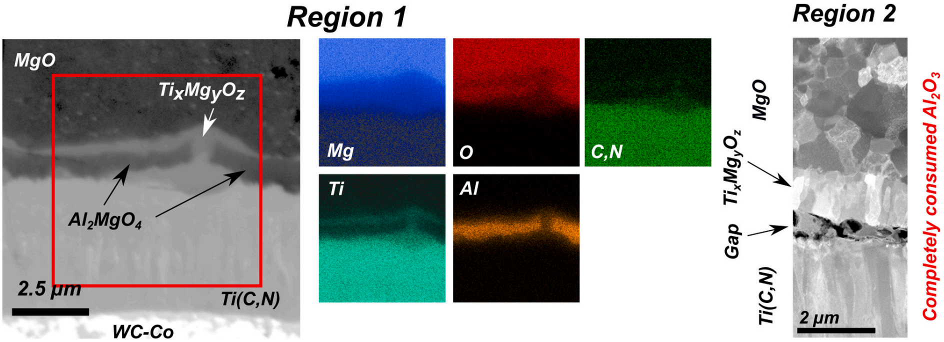

Fig. 8. Region1 shows an SEM-BSE and XEDS-SEM maps of the interface between the coating and MgO powder. Remnants of the Al_2O_3 coating have degraded into Al_2MgO_4 spinel or been completely consumed. Region 2 is a LAADF-STEM image of the interface devoid of Al_2O_3 coating remnants. The $Ti_xMg_yO_z$ formed originates from the interaction of MgO with the Ti(C,O,N) bonding layer and inherits the same columnar structure as the Ti(C,N).

layer is 1.5–2 µm in thickness. Hence MgO inclusions can chemically interact with both the Al_2O_3, as earlier observed in actual machining tests [16,41] and with the Ti(C,O,N) bonding layer as shown in Fig. 8. This finding agrees well with oxidation experiments on ceramics [28]. Furthermore, this behaviour has been observed in machining with ceramics in which the Al_2O_3 binder was chemically attacked [42].

3.4. Al_2O_3 coating vs. (SiO_2, CaO, MgO, Al_2O_3) inclusions

The diffusion couple sample (Table 1 - #4) contained equal moles of precursors of the common NMI SiO_2, CaO, MgO, and Al_2O_3, found both in steels [6] and on the rake of Al_2O_3-coated tools [14,16,41]. Therefore, this is the most representative case of interaction of the coating with inclusions. Fig. 9 contains a SEM-BSE image and XEDS maps of the interface after 10 min at 1300 °C and 2.5 GPa. The Al_2O_3 layer is almost completely consumed by the chemical interaction. Only fragments of Al_2O_3 layer are found in some locations at both 1200 and 1300 °C, with a maximum thickness of 1.7 µm. The Ti(C,N) bottom layer is still intact, but the thin Ti(C,N,O) bonding layer has grown in some locations.

The reaction between the coating and the inclusions resulted in two distinct products. One product is $(Ca,Si,Al)_xO_y$ and the other is a $(Fe,Mg)_1Al_2O_4$ spinel, both in direct agreement with the machining test in [16]. There are also several regions of pure Fe and minor regions of Ca, Si oxides. The reaction oxides are strongly adhered to the original coating, and on decompression of the diffusion couple a gap was formed between the reaction products and the steel.

A TEM lamella was extracted at right angles to the interface between the tool and the reaction products for the sample at 1200 °C in an area where the mixed oxides are found. Fig. 10 shows the combined results from TKD, HAADF-STEM, and XEDS-STEM. The Fe, Mg, Al oxide is clearly identified as $(Fe,Mg)_1Al_2O_4$ spinel by both XEDS and TKD, as further confirmed by SAED. The dominant Ca, Si, Al oxide phase is found to be $Ca_2Al_2Si_1O_7$ melilite. Other solid solutions of SiO_2, CaO, and Al_2O_3 are also present in minor quantities, as identified by XEDS-STEM, but could not be confidently confirmed by SAED and TKD. High-temperature oxidation studies of SiC whisker-reinforced alumina show the presence of crystalline and both glassy and amorphous phases of Si-Mg-Al oxides [28]. However, in our case, all regions give clear diffraction reflexes, and hence the phases in these experiments are neither glassy nor amorphous.

Temperature influences the rate of reactions, as well as the process thermodynamics. If the normalized driving force for the degradation of Al_2O_3 into $(Fe,Mg)_1Al_2O_4$ and $Ca_2Al_2Si_1O_7$ is positive at a given temperature, then the degradation of the coating is thermodynamically

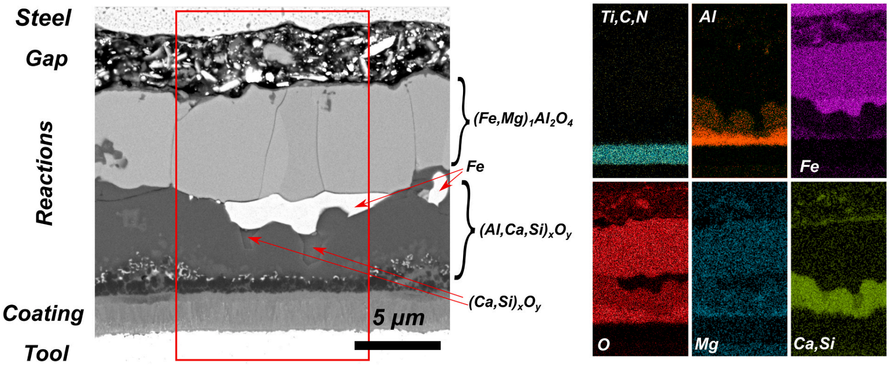

Fig. 9. SEM-BSE image and XEDS maps of the reaction interface between the non-metallic inclusion precursors and the coating at 1300 °C and 2.5 GPa after 10 min. The Al_2O_3 is almost entirely consumed and two new mixed oxides have formed: $(Ca,Si,Al)_xO_y$ and $(Fe,Mg)_1Al_2O_4$.

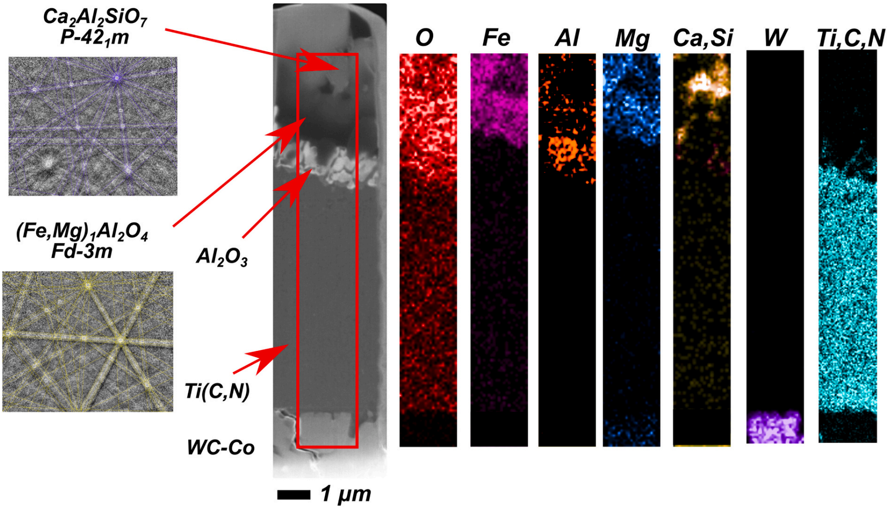

Fig. 10. HAADF-STEM image, XEDS mapping, and TKD patterns of phases in the lamella extracted from the interface between the coating and the inclusion precursor mixture after 10 min at 1200 °C and 2.5 GPa. The Al_2O_3 coating is almost entirely consumed. The two types of oxides formed are (Fe, Mg)$_1$$Al_2O_4$ spinel and solid solutions of SiO_2, CaO and Al_2O_3 such as $Ca_2Al_2Si_1O_7$.

possible and favorable. If it is zero or negative, then the degradation is not possible, as in the case of Fe and Al_2O_3 without additional oxygen (Figs. 3 and 7). Our calculations show that the driving force for the transformation of the coating into the experimentally identified phases is always positive over a wide range of cutting temperatures. This is shown in Fig. 11a, where the normalized driving force for the formation of $Ca_2Al_2Si_1O_7$ and (Fe, Mg)$_1$$Al_2O_4$ from the interaction between the Al_2O_3 coating and the inclusion precursors is plotted from 200 to 1300 °C. This shows that there is thermodynamic potential for coating wear by interacting with inclusions even at lower temperatures than in the diffusion couples, although likely at a slower rate. Hence the degradation of the Al_2O_3 into softer mixed oxides occurs both above the melting and glass transition temperatures [11,21] and as a solid-state reaction as seen in Fig. 8–11, as well as during actual machining [16].

It is interesting that the reaction phases found in diffusion couple experiments (Figs. 9 and 10) are identical to the phases observed in machining low-alloyed steel (19MnVS6) and stainless steel 316L [16,42]. Fig. 11b shows the results of calculations regarding how these two types of products are thermodynamically favorable over other mixed oxides when Si, Ca, Mg oxides interact with the Al_2O_3 coating in the presence of oxygen and increasing amounts of iron. The computational data agree well with the diffusion couple data in Figs. 9 and 10, where a Si and Al-rich oxide and one Fe, Mg and Al-rich oxide were observed. Other mixed oxides, such as a Ca, Si and Al-rich oxide with small amounts of Fe, Mg and Al, may also be present depending on the exact ratio between the NMI, steel, oxygen, and coating. However, the reaction trend of the two types of oxides remains.

3.5. Al_2O_3 coating vs. (SiO_2, CaO, MgO, Al_2O_3, Fe_3O_4, Fe_2O_3, MnO) inclusions

The diffusion couple sample (Table 1 - #5) contained an equal

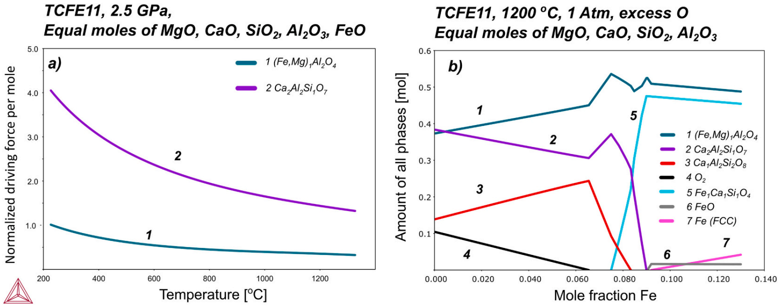

Fig. 11. a) The normalized driving force for the formation of $Ca_2Al_2Si_1O_7$ and (Fe,Mg)$_1$$Al_2O_4$ from equal moles of SiO_2, CaO, MgO, Al_2O_3, and FeO. This shows how the Al_2O_3 coating degradation is thermodynamically favorable. b) The thermodynamic equilibrium phase composition with increasing amount of Fe, showing that a Ca, Si and Al-rich oxide and Fe, Mg and Al-rich oxide are equilibrium phases at conditions of excess O_2 and Fe.

number of moles of the oxides of SiO_2, CaO, MgO, Al_2O_3, Fe_3O_4, Fe_2O_3, and MnO. This is the most representative condition where the Al_2O_3 coating interacts with inclusions, the steel itself, and atmospheric oxygen. All Fe_3O_4, Fe_2O_3, and MnO may originate during oxidation of steel at the tool–chip interface. Additionally, MnO may also be present together with any of the other inclusions [11,14]. The experiment reveals that the results are somewhat similar to the sample without MnO. In the current case, Mn contributes to the spinel with Al, Fe, Mg, and O (Fig. 12). For this combination of inclusions, the Al_2O_3 coating is completely consumed at both 1200 and 1300 °C. The Ti(C,N,O) bonding layer has also started to further oxidize, leading to the formation of TiO_2. Still, in the interaction region, the same two main types of oxides are formed: $(Al,Si,Ca)_xO_y$, and $(Fe,Mg,Mn)_1Al_2O_4$. It is interesting that these reaction products are also found on worn tools from machining with Al_2O_3 coatings and ceramics. Several Mg, Si, Mn, Ca, Fe oxides on Al_2O_3 coatings have been shown in [14,41], and on alumina ceramics tools [11,23]. This indicates that what is generally perceived as an adhered inclusion on the tool (i.e., "belag" or built-up layer) might actually be the selective reaction products of the inclusions with the Al_2O_3 coating.

4. Discussion

Earlier publications [9,14,17,41,43] suggest that surface localized plastic deformation and abrasion have been the prevailing wear mechanisms of Al_2O_3-coated tools during turning of both inclusion and not inclusion engineered steels. A (0001) α-Al_2O_3 textured coating has therefore shown to be a superior coating orientation due to its resistance to these types of wear [17,41,44]. It is suggested that from a mechanistic perspective, oxide inclusions (e.g., $Ca_xAl_yO_z$) are expected to cause lower wear rates on the rake compared to flank wear on uncoated and most coated tools [43]. It has been demonstrated that soft oxides deform and likely lose their abrasiveness as they pass through the primary and secondary shear zones [14]. Additionally, the relative speed of inclusions against the tool is lower on the rake. The flank is exposed to the cutting speed v_c, while the rake is exposed to the chip speed, which is lower by the chip compression ratio λh. Yet it was shown [10] that calcium treated steels cause more rake wear, while clean steels cause more flank wear on Al_2O_3 coated tools during turning. The formation of a melt suggested in early works [21] was not found in these studies.

Inclusion engineering may thus exhibit contrary effects on tool performance when machining with Al_2O_3 coated tools. Calcium treatment facilitates a decrease in abrasive wear by transforming hard alumina inclusions into soft aluminates [6]. This has been shown to protect uncoated cemented carbides from wear by diffusional dissolution [5], and so increasing tool performance. It is shown in this paper and other works [13] that Al_2O_3-coated tools are intrinsically resistant to wear by diffusional dissolution into steel phases. But it is shown here that inclusion engineering transforms the alumina coating into softer mixed oxides by chemical reactions, and in machining studies [16], this decreases tool performance. This competition between abrasive wear and chemical wear depends on the inclusion composition and is a well know effect when machining with Al_2O_3-TiC ceramic tools [11,12], but is often overlooked when using coated Al_2O_3 tools. Hence this paper does not contradict the importance of plastic deformation and abrasion in machining with Al_2O_3-coated tools, especially with a limited presence of non-metallic inclusions [43]. However, this paper show and explain why this picture is drastically changed when non-metallic inclusions are used. Since Fe, Mg, Ca, Si and Mn mixed oxides chemically react and degrade the Al_2O_3 coating, which is both shown here and in machining experiments of the same tool and workpiece material [16].

How does these diffusion in a static cell and thermodynamic calculations at equilibrium give insight in the much more complicated and dynamic process of metal cutting and turning? The temperature during metal cutting of an identical tool and inclusion engineered steel is measured by thermography to 800–900 °C [16]. Thermography cannot measure the temperature inside the cutting zone where the interaction is taking place. The temperature is expected to be higher in this zone since Al_2O_3 is an insulator, Soler et al. [45] even suggest a temperature difference of 30 % or more between measured thermography and the cutting zone. Thermodynamic calculations preformed show that the reactions in this experiment at 700 °C and 1300 °C are the same, but the rate is different, hence it is representative thermodynamically, but enhanced kinetically. Studies using the same methods have also shown how the method is applicable for understanding diffusion and chemical wear during metal cutting of other materials [46–48]. This imitational experiment resulted in the equivalent reaction products forming when cutting and the process is comparable to what is seen in [10,16,43]. The type of inclusion, steel and oxidized steel adhering in the cutting zone depends on the inclusion engineering, cutting conditions and tool geometry. The combination of experimental results from cutting and diffusion couples combined with thermodynamic modeling can add to the understanding tool/coating selection, wear modeling [49] and inclusion engineering in this paper. Section 4.1 and 4.2 are two such examples developed from the results of this study.

4.1. Implications for wear and performance of Al_2O_3-coated tools

Having understood the nature of chemical degradation of Al_2O_3 coatings, allows us to link thermodynamics, diffusion couple experiments, and machining to predict the interactions and degradation when different inclusions and workpiece materials meet the coating.

For example, the equilibrium phase for the reaction between Al_2O_3 and MgO is the spinel phase $Mg_1Al_2O_4$, and the normalized driving force for Al_2O_3 is −0.55 at 700 °C. Since the driving force is strongly negative,

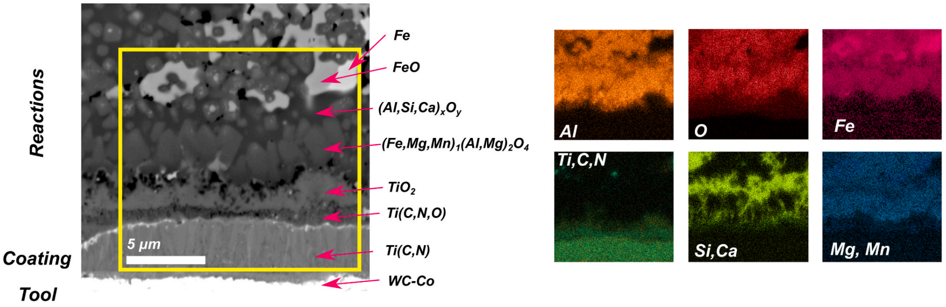

Fig. 12. SEM-BSE image and XEDS mapping of the Al_2O_3 coating and the oxidation of Ti(C,N,O) bonding layer in the presence of inclusion precursors after 10 min at 1300 °C and 2.5 GPa.

Al_2O_3 is not a stable phase. This means that the Al_2O_3 coating is likely to degrade when MgO inclusions are introduced to the tool–chip interface during machining and then form $Mg_1Al_2O_4$ (seen experimentally in Fig. 8). Evidently, the higher the fraction of inclusions in the steel and the more negative the driving force, the more rapid the tool degradation. This calculation can be done for any combination of inclusions or workpiece material. Fig. 13a rates the inclusions in order of potential to degrade the coating. Fig. 13a shows this for several selected examples of Ca, Si, and Mg oxides interfacing with an Al_2O_3 coating. Similar calculations can readily be done for more complicated mixed oxide or sulfide inclusions such as $CaO–SiO_2–MnS-Al_2O_3$.

An interesting simple case is CaO, which can form an entire series of calcium aluminates when interacting with Al_2O_3 as shown in Fig. 13b. The reaction product and the driving force depend on the ratio between Al_2O_3-CaO and temperature (see Fig. 13a). These parameters depend on cutting conditions and inclusion engineering. Interaction with CaO and degradation of the coating can progress until $Ca_1Al_{12}O_{19}$ is formed, which is in equilibrium with Al_2O_3 (Fig. 13 a and b). This will stop further degradation by chemical reactions. It thus can be argued that $Ca_1Al_{12}O_{19}$ is a type of inclusion that would not degrade the Al_2O_3 coating.

4.2. *Implications for steelmaking*

Removing all inclusions and only machining ultra-clean steels would be one route to avoid the observed type of chemical coating degradation. However, this would lead to many other adverse effects, such as worsened chip breaking. Inclusions are an important part of the steelmaking process. Non-metallic inclusions can ease chip formation, decrease abrasive tool wear, improve the tribological contact, and decrease diffusional dissolution of other tool and coating materials [6].

Chemical degradation of Al_2O_3-coated tools can be limited by saturating the steel, and hence the inclusions, with aluminum. The level of aluminum should be such that the NMI in the steel and the adhered material on the tool during machining are Al-saturated endmembers that will not react with and degrade the Al_2O_3 coating. Based on our results. Examples of Al-saturated inclusions are $(Fe, Mg)_1Al_2O_4$ (Fig. 10) in the Fe-Mg-Al-O system and $Ca_1Al_{12}O_{19}$ (Figs. 10 and 13) in the Ca-Al-O system. Combinations and more complicated systems can also form depending on the combinations of the inclusions. The benefits of inclusion engineering can then be maintained without experiencing chemical degradation of the coating.

Fig. 14 is an example of such a hypothetical steel with Ca, Si and Al oxide inclusions. If the Al content is pushed to the end of the green zone, then there are no inclusions that can degrade the alumina coating, as only $Ca_2Al_2Si_1O_7$ and $Ca_1Al_2Si_2O_8$ are present, which cannot degrade the coating. If the Al content extends beyond the green zone, then hard Al_2O_3 inclusions could form in the steel, thus making it very abrasive. As shown before, $Ca_1Al_{12}O_{19}$ is the $CaO-Al_2O_3$ endmember (Fig. 13b) and is a saturated non-metallic inclusion. It is also the calcium aluminate inclusion found on worn tools after machining a steel containing several different calcium aluminates, and has proved to be a beneficial inclusion [43].

5. Conclusions

This study investigated chemical degradation mechanisms of Al_2O_3-coated tools that are relevant in the context of machining all steels that are not completely clean and of course inclusion engineered steels with a variety of non-metallic inclusions. The machining conditions were simulated using a high-temperature (1200 and 1300 °C) and high-pressure (2.5 GPa) diffusion couple method where nine diffusion couples were produced and investigated using advanced microscopy (SEM, XEDS, TEM and TKD) and thermodynamic calculations. The results have been compared to both literature and experimental studies for the same and other comparable tool–workpiece combinations.

As expected, the Al_2O_3 coating is resistant to wear by diffusional dissolution when in contact with steel. However, Al_2O_3 degrades into softer spinel type $(Al,Fe)_3O_4$ mixed oxides when interacting with steel in the presence of O_2. The presence of Ca, Si, Mn, Mg, and Fe oxides in contact with the coating results in the formation of two distinct reaction products, $Ca_2Al_2Si_1O_7$ and $(Fe, Mg, Mn)_1Al_2O_4$. It appears that MgO is among the most aggressive inclusions, as the formation of $Mg_1Al_2O_4$ spinel or complete coating dissolution was observed. All these products formed in a solid-state reaction at temperatures well below melting and glass transformation. These findings show that chemical degradation of Al_2O_3-based tooling has been an underestimated wear mechanism and explain the earlier contradictory results as regards to flank and rake wear when machining inclusion engineered steels. The results also show how this degradation mechanism can be predicted and quantitatively ranked using thermodynamic calculations, which can both aid wear modeling and steel inclusion engineering.

CRediT authorship contribution statement

Axel Bjerke: Conceptualization, Methodology, Software, Validation, Formal analysis, Investigation, Data curation, Writing – original draft, Visualization. **Filip Lenrick:** Conceptualization, Methodology, Validation, Formal analysis, Writing – review & editing, Visualization, Supervision. **Susanne Norgren:** Conceptualization, Methodology, Software, Validation, Formal analysis, Writing – review & editing. **Henrik Larsson:** Conceptualization, Methodology, Software, Validation, Formal analysis, Resources, Writing – review & editing. **Andreas Markström:** Conceptualization, Methodology, Software, Validation,

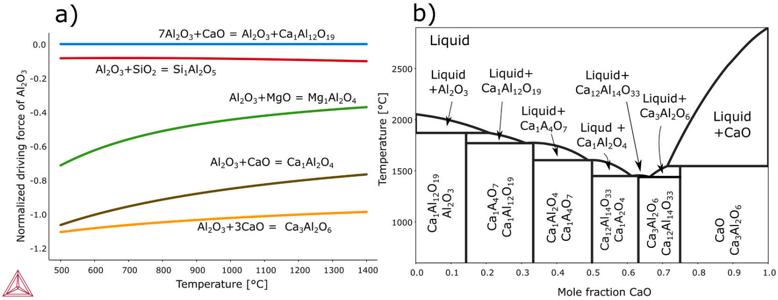

Fig. 13. a) The normalized driving force for Al_2O_3 with reference to several different mixed oxides. b) The $CaO-Al_2O_3$ phase diagram showing how calcium aluminates will degrade the Al_2O_3 coating, except for $Ca_1Al_{12}O_{19}$.

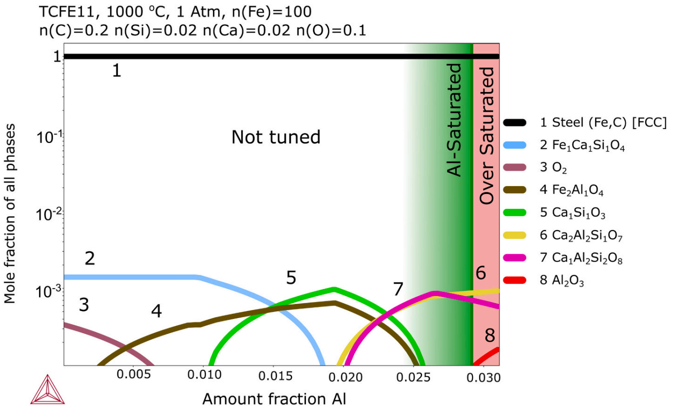

Fig. 14. The thermodynamic equilibrium phase composition of a hypothetical inclusion engineered steel. The case of Al-saturated steel (end of green zone) only contains non-metallic inclusions that will not react with the Al_2O_3 coating. (For interpretation of the references to colour in this figure legend, the reader is referred to the web version of this article.)

Formal analysis, Resources, Writing – review & editing. **Rachid M'Saoubi:** Conceptualization, Methodology, Validation, Resources, Writing – review & editing. **Igor Petrusha:** Conceptualization, Methodology, Validation, Resources. **Volodymyr Bushlya:** Conceptualization, Methodology, Validation, Formal analysis, Resources, Writing – review & editing, Visualization, Supervision, Project administration, Funding acquisition.

Declaration of competing interest

The authors declare that they have no known competing financial interests or personal relationships that could have appeared to influence the work reported in this paper.

Data availability

Data will be made available on request.

Acknowledgments

This work was funded by the national strategic innovation program known as the National Action for Metallic Materials program, organized by Vinnova and Jernkontoret (Sweden) under DEMO project (ID 2017-02915). The authors would like to acknowledge the support of the Sustainable Production Initiative (SPI), a cooperation between Lund University and Chalmers University of Technology. We also thank Dr. Thomas Björk from Ovako AB for support with the workpiece material and fruitful discussions. We would like to thank Ryszard Wierzbicki and Mikael Hörndahl for their help in manufacturing and assembly of the diffusion couple, and Dr. Ofentse Makgae for assistance during TEM imaging, all of Lund University.

References

[1] D.C. Hilty, J.W. Farrell, Modifications of inclusions by calcium 1, Iron and Steelmaker (I and SM) 2 (1975) 17–22.

[2] M. Lind, L. Holappa, Transformation of alumina inclusions by calcium treatment, Metall. Mater. Trans. B Process Metall. Mater. Process. Sci. 41 (2010) 359–366, https://doi.org/10.1007/s11663-009-9337-9.

[3] W. König, Einfluss nichtmetallischer einschlüsse auf die zerspanbarkeit von kohlenstoffstählenitle, Maschinenmarkt 87 (1965).

[4] H. Yamada, S. Yoshida, A. Kimura, K. Kato, T. Ito, On the relationship between machinability and inclusion morphology of Ca bearing free machining steels, 57 Tetsu-to-Hagane (1971) 2111–2127, https://doi.org/10.2355/tetsutohagane1955.57.13_2111.

[5] X.D. Fang, D. Zhang, An investigation of adhering layer formation during tool wear progression in turning of free-cutting stainless steel, 197 Wear (1996) 169–178, https://doi.org/10.1016/0043-1648(96)06924-4.

[6] N. Ånmark, A. Karasev, P.G. Jönsson, The effect of different non-metallic inclusions on the machinability of steels, 8 Materials (2015) 751–783, https://doi.org/10.3390/ma8020751.

[7] N. Matsui, K. Watari, Wear reduction of carbide tools observed in cutting Ca-added steels for machine structural use, 46 ISIJ International (2006), https://doi.org/10.2355/isijinternational.46.1720.

[8] N. Ånmark, T. Björk, Effects of the composition of ca-rich inclusions on tool wear mechanisms during the hard-turning of steels for transmission components, Wear 368–369 (2016) 173–182, https://doi.org/10.1016/j.wear.2016.09.016.

[9] S.Ruppi B. Högrelius, M. Huhtiranta, Wear characteristics of TiC, Ti(C,N), TiN and Al2O3 coatings in the turning of conventional and Ca-treated steels, International Journal of Refractory Metals and Hard Materials 16 (1998) 353–368, https://doi.org/10.1016/S0263-4368(98)00039-0.

[10] R. Bejjani, S. Odelros, S. Öhman, M. Collin, Shift of wear balance acting on CVD textured coatings and relation to workpiece materials, Proceedings of the Institution of Mechanical Engineers, Part J: Journal of Engineering Tribology 235 (2021) 114–128, https://doi.org/10.1177/1350650120926781.

[11] Y. Yamane, H. Usuki, B. Yan, N. Narutaki, The formation of a protective oxide layer in machining resulphurized free-cutting steels and cast irons, 139 Wear (1990) 195–208, https://doi.org/10.1016/0043-1648(90)90045-C.

[12] J. Barry, G. Byrne, Cutting tool wear in the machining of hardened steels, 247 Wear (2001) 139–151, https://doi.org/10.1016/S0043-1648(00)00531-7.

[13] B.M. Kramer, P.K. Judd, Computational design of wear coatings, J. Vac. Sci. Technol. A 3 (1985) 2439–2444, https://doi.org/10.1116/1.572854.

[14] R. Bejjani, M. Collin, T. Thersleff, S. Odelros, Multi-scale study of initial tool wear on textured alumina coating, and the effect of inclusions in low-alloyed steel, Tribol. Int. 100 (2016) 204–212, https://doi.org/10.1016/j.triboint.2016.01.021.

[15] R. M'Saoubi, S. Ruppi, Wear and thermal behaviour of CVD α-Al 2 O 3 and MTCVD Ti(C, N) coatings during machining, CIRP Ann. 58 (2009) 57–60, https://doi.org/10.1016/j.cirp.2009.03.059.

[16] A. Bjerke, A. Hrechuk, F. Lenrick, R. M'Saoubi, H. Larsson, et al., Onset of the degradation of CVD α-Al2O3 coating during turning of Ca-treated steels, 477 Wear (2021) 203785, https://doi.org/10.1016/j.wear.2021.203785.

[17] S. Ruppi, Enhanced performance of α-Al2O3 coatings by control of crystal orientation, Surf. Coat. Technol. 202 (2008) 4257–4269, https://doi.org/10.1016/j.surfcoat.2008.03.021.

[18] S. Ruppi, M. Halvarsson, TEM investigation of wear mechanisms during metal machining, Thin Solid Films 353 (1999) 182–188, https://doi.org/10.1016/S0040-6090(99)00413-7.

[19] K.D. Bouzakis, N. Michailidis, G. Skordaris, E. Bouzakis, D. Biermann, R. M'Saoubi, Cutting with coated tools: coating technologies, characterization methods and performance optimization, CIRP Ann. Manuf. Technol. 61 (2012) 703–723, https://doi.org/10.1016/j.cirp.2012.05.006.

[20] J.A. Yeomans, T.F. Page, Studies of ceramic-liquid metal reaction interfaces, J. Mater. Sci. 25 (1990) 2312–2320, https://doi.org/10.1007/BF00638021.

[21] A. Nordgren, A. Melander, Tool wear and inclusion behaviour during turning of a calcium-treated quenched and tempered steel using coated cemented carbide tools, 139 Wear (1990) 209–223, https://doi.org/10.1016/0043-1648(90)90046-D.

[22] N. Narutaki, A. Murakoshi, Effect of small quantity inclusions in steels on the wear of ceramic tools, journal of the Japan society of, Precis. Eng. 42 (1976) 221–226, https://doi.org/10.2493/jjspe1933.42.221.

[23] G. Brandt, M. Mikus, An electron microprobe and cathodoluminescence study of chemical reactions between tool and workpiece when turning steel with alumina-based ceramics, 115 Wear (1987) 243–263, https://doi.org/10.1016/0043-1648(87)90215-8.

[24] G. Brandt, Flank and crater wear mechanisms of alumina-based cutting tools when machining steel, Wear 112 (1986) 39–56, https://doi.org/10.1016/0043-1648(86)90199-7.

[25] G. Brandt, M. Mikus, Z. Senesan, S. Hogmark, Wear mechanisms when machining grey cast iron with ceramic tools, Surf. Eng. 3 (1987) 211–225, https://doi.org/10.1179/sur.1987.3.3.211.

[26] L.X. Han, S. Suresh, High-temperature failure of an alumina-silicon carbide composite under cyclic loads: mechanisms of fatigue crack-tip damage, J. Am. Ceram. Soc. 72 (1989) 1233–1238, https://doi.org/10.1111/J.1151-2916.1989.TB09713.X.

[27] K.L. Luthra, H.D. Park, Oxidation of silicon carbide-reinforced oxide-matrix composites at 1375° to 1575°C, J. Am. Ceram. Soc. 73 (1990) 1014–1023, https://doi.org/10.1111/J.1151-2916.1990.TB05150.X.

[28] C.C. Lin, A. Zangvil, R. Robert, Phase evolution in silicon carbide–whisker-reinforced mullite/zirconia composite during long-term oxidation at 1000° to 1350°C, J. Am. Ceram. Soc. 83 (2000) 1797–1803, https://doi.org/10.1111/J.1151-2916.2000.TB01466.X.

[29] R.V. Väinölä, L.E.K. Holappa, P.H.J. Karvonen, Modern steelmaking technology for special steels, J. Mater. Process. Technol. 53 (1995) 453–465, https://doi.org/10.1016/0924-0136(95)02002-4.

[30] L.E.K. Holappa, A.S. Helle, Inclusion control in high-performance steels, J. Mater. Process. Tech 53 (1995) 177–186, https://doi.org/10.1016/0924-0136(95)01974-J.

[31] J.-E. Ståhl, Metal Cutting: Theories in Practice, SECO TOOLS, Fagersta, Sweden, 2012.

[32] E.M. Trent, P.K. Wright, Metal cutting, fourth ed., Butterworth-Heinemann, 2000.

[33] V. Bushlya, A. Bjerke, V.Z. Turkevich, F. Lenrick, I.A. Petrusha, K. A. Cherednichenko, J.-E. Ståhl, On chemical and diffusional interactions between PCBN and superalloy inconel 718: imitational experiments, J. Eur. Ceram. Soc. 39 (2019) 2658–2665, https://doi.org/10.1016/j.jeurceramsoc.2019.03.002.

[34] M. Olsson, F. Lenrick, R. M'Saoubi, H. Larsson, A. Markström, , et al.I. Petrusha I, Study of wear mechanisms of cemented carbide tools during machining of single-phase niobium, 450–451, Wear (2020) 203244, https://doi.org/10.1016/j.wear.2020.203244.

[35] V. Bushlya, F. Lenrick, A. Bjerke, H. Aboulfadl, M. Thuvander, J.-E. Ståhl, et al., Tool wear mechanisms of PcBN in machining inconel 718: analysis across multiple length scale, 70 CIRP Annals (2021), https://doi.org/10.1016/j.cirp.2021.04.008.

[36] J.-O. Andersson, T. Helander, L. Höglund, P. Shi, B. Sundman, Thermo-Calc & DICTRA, computational tools for materials science, 26 Calphad (2002) 273–312, https://doi.org/10.1016/S0364-5916(02)00037-8.

[37] H.J.T. Ellingham, Reducibility of oxides and sulphides in metallurgical processes, J. Soc. Chem. Ind. 63 (1944) 125–160, https://doi.org/10.1002/JCTB.5000630501.

[39] L. Dreval, T. Zienert, O, fabrichnaya, calculated phase diagrams and thermodynamic properties of the Al2O3-Fe2O3-FeO system, J. Alloys Compd. 657 (2016) 192–214, https://doi.org/10.1016/J.JALLCOM.2015.10.017.

[40] B.M. Kramer, B.F. von Turkovich, A comprehensive tool wear model, 35 CIRP Annals (1986) 67–70, https://doi.org/10.1016/S0007-8506(07)61840-X.

[41] R. M'Saoubi, O. Alm, J.M. Andersson, H. Engström, T. Larsson, M.P. Johansson-Jõesaar, M. Schwind, Microstructure and wear mechanisms of texture-controlled CVD α-Al2O3 coatings, 376–377 Wear (2017) 1766–1778, https://doi.org/10.1016/j.wear.2017.01.071.

[42] H. Persson, F. Lenrick, J.-E. Ståhl, V. Bushlya, L. Franca L, Wear mechanisms of PcBN tools when machining AISI 316L, 47 Ceramics International (2021) 31894–31906, https://doi.org/10.1016/j.ceramint.2021.08.075.

[43] A. Larsson, S. Ruppi, Structure and composition of built-up layers on coated tools during turning of ca-treated steels, Mater. Sci. Eng. A 313 (2001) 160–169, https://doi.org/10.1016/S0921-5093(01)00964-9.

[44] S. Shoja, S. Norgren, H.-O. Andrén, O. Bäcke, M. Halvarsson, On the influence of varying the crystallographic texture of alumina CVD coatings on cutting performance in steel turning, Int. J. Mach. Tools Manuf. 176 (2022), 103885, https://doi.org/10.1016/j.ijmachtools.2022.103885.

[45] Soler D., Childs T.H.C., Arrazola P.J. A note on interpreting tool temperature measurements from thermography (2015) Machining Science and Technology, 19 (1), pp. 174 – 181, DOI: 10.1080/10910344.2014.991027.

[46] L. von Fieandt, R. M'Saoubi, M. Schwind, B. Kaplan, Chemical interactions between cemented carbide and difficult-to-machine materials by diffusion couple method and simulations, J. Phase Equilib. Diffus. 39 (4) (2018) 369–376, https://doi.org/10.1007/s11669-018-0639-y.

[47] O. Hatt, H. Larsson, F. Giuliani, P. Crawforth, B. Wynne, and M. Jackson, "Predicting Chemical Wear in Machining Titanium Alloys Via a Novel Low Cost Diffusion Couple Method," Procedia CIRP, vol. 45, pp. 219-222, doi:10.1016/j.procir.2016.01.196.

[48] R. Lindvall, A. Bjerke, A. Salmasi, F. Lenrick, R. M'Saoubi, J.-E. Ståhl, V. Bushlya, Predicting wear mechanisms of ultra-hard tooling in machining Ti6Al4V by diffusion couples and simulation, ISSN 0955-2219, Journal of the European Ceramic Society (2022), https://doi.org/10.1016/j.jeurceramsoc.2022.10.005.

[49] A. Bjerke, A. Hrechuk, F. Lenrick, A. Markström, H. Larsson, S. Norgren, R. M'Saoubi, T. Björk, V. Bushlya, Thermodynamic modeling framework for prediction of tool wear and tool protection phenomena in machining, Wear (2021) 484–485, https://doi.org/10.1016/j.wear.2021.203991, art. no. 203991.

Paper V

International Journal of Refractory Metals and Hard Materials 124 (2024) 106806

Contents lists available at ScienceDirect

International Journal of Refractory Metals and Hard Materials

journal homepage: www.elsevier.com/locate/IJRMHM

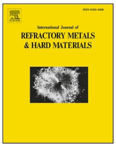

On the wear mechanisms of uncoated and coated carbide tools in milling titanium alloys

Rebecka Lindvall [a,*], Juan Manuel Bello Bermejo [a], Axel Bjerke [a], Jon M. Andersson [b], Elias Vikenadler [b], Rachid M'Saoubi [a,b], Volodymyr Bushlya [a]

[a] Division of Production and Materials Engineering, Lund University, Ole Römers väg 1, 221 00, Lund, Sweden
[b] R&D Materials and Technology Development, Seco Tools AB, Björnbacksvägen 2, 737 82 Fagersta, Sweden

ARTICLE INFO

Keywords:
Milling
Titanium
Cemented carbide
Tool wear

ABSTRACT

Titanium alloys are known for being difficult to machine. Within the groups of Ti alloys, the machinability is reduced when going from the α-alloys, to α + β, and finally to near-β or β-alloys. Uncoated cemented carbide is traditionally used for machining these alloys and finding a suitable coating to improve the performance is a challenge due to the high strength of Ti alloys and the high chemical reactivity of Ti with tool and coating materials at the temperatures achieved during cutting. The PVD applied $Ti_xAl_{1-x}N$ (x = 0.4–0.7) is generally recommended for machining Ti alloys and a top layer of NbN has shown promising performance in milling applications. This study systematically explores the wear mechanisms of either uncoated WC-12%Co or its $Ti_{0.45}Al_{0.55}N$-NbN coated version in the milling of Ti alloys ranging from near-α (Ti-6Al-2Sn-4Zr-2Mo), α + β (Ti-6Al-2Sn-4Zr-6Mo), and near-β (Ti-5Al-5Mo-5 V-3Cr) alloys. The wear evolution is explored by studying as-worn tools and their cross-section using SEM-XEDS and EBSD after having reached 10%, 30%, 50%, and 100% of the full tool life at a flank wear criterion *VB* = 200 μm. The coating is removed within seconds of engagement and fails by cracking within the bulk and PVD droplet defects can initiate such cracks. Diffusional dissolution of the coating may be active on a minor scale, but the rapid mechanical failure shows the need for a more robust coating formulation. Exposed cemented carbide is worn at varying intensities when machining the Ti alloys. The highest wear rate is achieved in milling α + β Ti-6246, followed by a moderate wear rate in near-β Ti-5553, and with a slower wear rate in milling near-α Ti-6242 which is explained varying intensities in oxidation wear, diffusional dissolution, and mechanical cracking. Diffusional loss of C gives rounder WC grains and remaining W at the interface is removed by the chip flow. Diffusional loss of Co gives reduced grain bonding and loss of the dampening effect that leads to fractures in WC grains. Specifically in milling α + β Ti-6246 and in minor scale in near-α Ti-6242, there is formation of $CoWO_4$ ceramic present several μm into the tool and its formation is facilitated by the oxidation of binder with resolved W. Fractures within the $CoWO_4$ explains the high wear rate. Cracks also propagate in binder regions initiated from weakened interface regions due to diffusional loss of C and Co.

1. Introduction

Ti alloys are popular engineering materials due to their high strength to weight ratio, high corrosion resistance, low thermal conductivity, and low thermal expansion [1]. The same properties also makes these alloys difficult to machine, in combination with a high chemical affinity of Ti which causes reactions with tools during machining and results in high wear rates [2]. There are many Ti alloys with different mechanical properties and phase distributions, and these range from commercially pure Ti with only α-phase, to a mix of α- and β-phase, and to metastable β-phased Ti alloys [3]. In general, α-phased or near-α phased Ti are easier to machine than α + β, near-β or β-alloys, as the latter have a higher strength and hardness [3]. A higher bcc β-phase fraction may also contribute to more extensive diffusional or chemical wear as it is more ductile and adhesive than the hcp α-phase and promote a higher mobility of substitutionally diffusing elements [1].

Ti alloys are used in aerospace, automotive, chemical, and medical industries [4]. Previous machining studies in milling Ti alloys have

---

[*] Corresponding author.
E-mail address: rebecka.lindvall@iprod.lth.se (R. Lindvall).

https://doi.org/10.1016/j.ijrmhm.2024.106806
Received 19 March 2024; Received in revised form 19 June 2024; Accepted 28 June 2024

reported a higher performance of uncoated tools than coated ones [5–7]. Finding a suitable coating for machining Ti alloys is a challenge, and the coatings that tool manufacturers recommend using is a physical vapor deposited (PVD) $Ti_xAl_{1-x}N$ with stoichiometry ratio x = 0.4–0.7 [8,9]. These coatings are reported to wear by delamination, abrasion, oxidation, and/or cracking in machining Ti alloys and steel [10–13]. An extra coating layer with NbN has shown promising performance in milling Ti alloys due to its higher hardness than other binary nitrides [14] and its formation of tribo-oxides that can reduce the wear rate [15,16]. Coatings tend to delaminate quickly when milling Ti alloys and expose cemented carbide to wear. Reported wear modes in cemented carbide in milling Ti alloys include brittle fractures like chipping, fractures, and flaking, with sporadic occurrence of plastic deformation and comb cracks, while adhesion and diffusional dissolution are suggested wear mechanisms without experimental validation [7,11,17–21]. Oxidation of cemented carbide can be promoted by the intermittent conditions in milling and controlled oxidation experiments show the formation of WO_3, $CoWO_4$, and Co_3O_4 after treatment at 600 °C [22,23]. In sliding tests, formation of WO_3 and Co_3O_4 were observed [24], while $CoWO_4$ and WO_3 were detected after laser-induced oxidation assisted micro milling [25]. These oxides are brittle and can promote failure of cutting tools suffering from oxidation.

There is a lack of in-depth investigations of the causes of the cracking phenomena and evidence of diffusional dissolution and oxidation wear of cemented carbide tooling when milling Ti alloys. This study explores the diffusional dissolution and oxidation wear mechanisms in addition to mechanical wear in external circular milling in Ti alloys with varying α and β phase fractions, including near-α Ti-6Al-2Sn-4Zr-2Mo (Ti-6242), α + β Ti-6Al-2Sn-4Zr-6Mo (Ti-6246), and near-β Ti-5Al-5 V-5Mo-3Cr (Ti-5553) using uncoated or $Ti_{0.45}Al_{0.55}N$-NbN coated tools.

2. Experimental work

The tools were either uncoated WC-12%Co or PVD applied $Ti_{0.45}Al_{0.55}N$-NbN on the same WC-12%Co substrate, and their microstructures are shown in Fig. 1a. The milling tools were of XOEX120408R-M07 geometry with a 30 μm edge radius that were mounted in an R220.69–0040-12-5AN holder (40 mm diameter) supplied by Seco Tools AB. This combination provided a 14° rake angle, 9° inclination angle, and 90° major cutting edge angle. Three Ti alloys were machined: near-α Ti-6Al-2Sn-4Zr-2Mo (Ti-6242), α + β Ti-6Al-2Sn-4Zr-6Mo (Ti-6246), and near-β Ti-5Al-5 V-5Mo-3Cr (Ti-5553). Their respective microstructure is shown in Fig. 1b–d respectively and their mechanical properties are presented in Table 1. The chemical composition is presented in Table 2. The Ti alloys were sub-transus solution treated and aged.

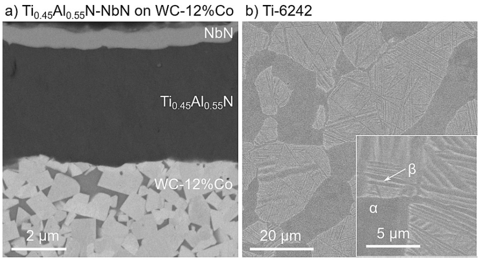

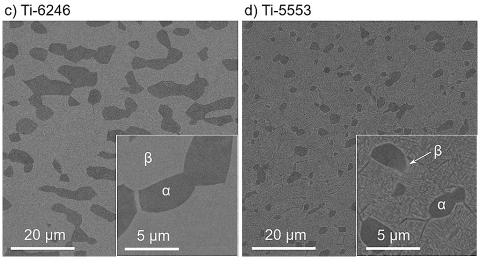

Fig. 1. SEM-BSE images of microstructures. (a) WC-12%Co and $Ti_{0.45}Al_{0.55}N$-NbN. (b) Near-α Ti-6242. (c) α + β Ti-6246. (d) Near-β Ti-5553.

External circular down milling with a single tooth installed was done in a Mori Seiki SV 500 CNC mill which has a spindle speed rated up to 10,000 rpm. The cutting data was a constant depth of cut $a_p = 2$ mm, width of cut $a_e = 2$ mm, feed rate $f_z = 0.10$ mm/tooth, 13° engagement angle Θ, and the cutting speed was $v_c = 80$ m/min for near-α Ti-6242 and α + β Ti-6246, and $v_c = 60$ m/min for near-β alloy Ti-5553 due to its higher strength (Table 1). An 8% oil-water emulsion coolant was delivered externally to avoid chip ignition. Fig. 2 shows the setup with the workpiece fixtured by the chuck on the table of the machining center. The external circular down milling method was used because the three different Ti alloy workpieces were supplied as bars and this method allows workpiece material effective tool wear testing. The descriptive sketch in Fig. 2 partly explains the external circular down milling process and the cutting data. With a cutting width of $a_e = 2$ mm and an engagement angle of $\Theta = 13°$, the maximum chip thickness h_{1max} will be smaller than the feed rate of $f_z = 0.10$ mm. The theoretical maximum chip thickness is calculated using eq. 1 [26]:

$$h_{1max} = r - \sqrt{f_z^2 + r^2 - 2 \bullet f_z \bullet \sqrt{2 \bullet a_e \bullet r - a_e^2}} \quad (1)$$

Where r is the radius of the cutter (20 mm), $f_z = 0.10$ mm, and $a_e = 2$ mm, resulting in a theoretical maximum chip thickness of 44 μm. However, the actual contact width may be larger due to the chip flow over the rake surface. After finishing one full circle of the workpiece and reducing the diameter from D_{outer} to D_{inner}, the tool head was moved 2 mm further down along the axis of the workpiece to attain the correct cutting depth at the next revolution.

Tool life tests were done by incremental measurements of the flank wear until reaching of the flank wear criterion of $VB = 200$ μm and repeated two times to average the stochastic behavior of the milling process. Knowing the average time in cut to reach the tool life criterion, three tool edges were machined at 10%, 30%, and 50% of that time in cut to study the wear evolution. One cutting tool was mounted at each tested condition. Some additional coated tools were machined in the three alloys for only 5 and 30 s to investigate early stage coating degradation. As-worn and cross-sectioned tools were studied in scanning electron microscope (SEM) Tescan Mira3 using secondary electron (SE) and backscatter electron (BSE) detectors that render surface topography and *Z*-contrast respectively. X-ray energy-dispersive spectroscopy (XEDS) and electron backscatter diffraction (EBSD) were used to study reaction products at the tool-chip-workpiece interface using 15 mm working distance and 8–10 kV and 20 kV respectively. Phase diagrams are created using the CALPHAD methods in the Thermo-Calc software

Table 1
Mechanical properties of the Ti alloys.

		Ultimate tensile strength [MPa]	0.2% yield strength [MPa]	Elongation [%]	Reduction in area [%]
Near-α	Ti-6242	1004	895	19	42
α + β	Ti-6246	1214	1118	13	37
Near-β	Ti-5553	1270	1210	7.5	23

Table 2
Elemental composition of the Ti alloys in wt%.

		Al	V	Sn	Zr	Mo	Si	Fe	Cr	Y	O	C	N	H	Res.	Ti
Near-α	Ti-6242	6.00	–	2.00	4.01	2.01	0.095	0.25	–	–	0.15	0.08	0.05	0.01	<0.40	Bal.
α + β	Ti-6246	6.00	–	2.00	4.01	6.01	0.095	0.25	–	–	0.15	0.04	0.04	0.01	<0.40	Bal.
Near-β	Ti-5553	5.28	4.78	–	<0.005	4.58	<0.030	0.32	3.02	<0.001	0.16	0.021	0.007	–	<0.30	Bal.

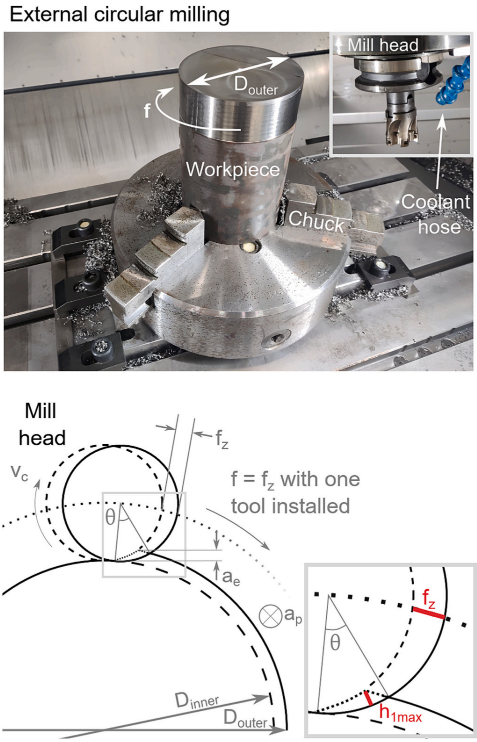

Fig. 2. Setup of workpiece in the mill and description of external circular down milling.

using the SSOL8 and SSUB6 databases [27].

3. Results and discussion

3.1. Performance and wear behavior

Tool performance in the form of flank wear evolution data is presented in Fig. 3 for the three Ti alloys and the uncoated and $Ti_{0.45}Al_{0.55}N$-NbN coated cemented carbide. Tool performance was evaluated twice for both types of tooling. The presented engagement times are the accumulated time in contact with the workpiece material and does not include the time the tool revolves in air. The total machining time includes the time that the tool revolves in air and the time in contact with the workpiece material. The total machining time is much longer than the accumulated time in contact considering the 13° engagement angle and is presented above each wear curve.

The wear evolutions are identical in case of milling with uncoated tools in Ti-6242 (Fig. 3a) and for coated tools in milling Ti-6246 (Fig. 3b). There is a spread of 1–2 min corresponding to an about 50% increase in tool life in cases when using coated tools in milling Ti-6242, uncoated tools in milling Ti-6246, and for both uncoated and coated tools in milling Ti-5553. A longer tool life is attained in milling near-α alloy Ti-6242 (Fig. 3a) at the same cutting speed as to α + β-alloy Ti-6246 (Fig. 3b). This was expected as Ti-6242 has a lower strength (Table 1) than Ti-6246.

The coated tool provides 40–80% longer tool life than the uncoated at the tested conditions when milling near-α Ti-6242 (Fig. 3a). Further in-depth analysis in Section 3.2 reveals the reason for the observed differences in machining performance. In milling α + β Ti-6246 (Fig. 3b), no appreciable improvement is obtained when using a coated tool. This can be explained by the higher hardness and strength and by the higher β-phase fraction that causes such intense and fast wear of the tools. In milling near-β Ti-5553 (Fig. 3c) that has a higher β-phase fraction than α + β Ti-6246 (Fig. 1c–d) and also higher yield and tensile strength (Table 1), the tool life attained are closer to that of near-α Ti-6242 than the expected α + β Ti-6246. This can be explained by the 25% lower cutting speed. It is unclear if the coating provides longer tool life depending on which test is studied when milling this alloy.

Figs. 4–9 shows the as-worn tools in the left column and its cross-section in the right column. The outlined dotted line on the as-worn tool represents the approximate location of the cross-section. The location of the cross-section is similar but not identical for all cases and is thus not marked for all tools. Each row represents the state of wear based on engagement time or tool life, where 100% is at the end of tool life. The partly worn tools and their cross-sections removed after 10%, 30%, and 50% of the full tool life are also presented.

Milling near-α alloy Ti-6242 with an uncoated cemented carbide tool in Fig. 4 shows a low degree of wear and minor removal of tool material up to half of the engagement time (Fig. 4a–c). This is also represented in the flank wear evolution data (Fig. 3a). After 50% engagement time, the wear rate increased and at the end of tool life chipping has occurred on the rake face, there is damage to the edge line and the flank has also loss of material (Fig. 4d–e). The cross-sections reveal a network of cracks in both tools, which are difficult to see at this magnification and they are therefore highlighted with arrows. In-depth exploration of the wear mechanisms is presented in Section 3.2. The new edge line at the end of tool life is uneven. There is a thin (<5 μm) adhered layer of Ti-6242 on the rake until 50% engagement time (Fig. 4a–c) but non at the wear region at the end of tool life (Fig. 4d–e).

The wear evolution when milling the same near-α alloy Ti-6242 but with $Ti_{0.45}Al_{0.55}N$-NbN coated cemented carbide is displayed in Fig. 5. Cross-sections reveal a rapid removal of the coating already after 10% engagement time which exposed the cemented carbide in the wear region. As for the uncoated tool (Fig. 4a–c), the wear to 50% engagement time is minor (Fig. 5a–c) and follows the wear evolution (Fig. 3a). However, the tool wear is not as severe at the end of tool life (Fig. 5d–e) as in the case with uncoated tools (Fig. 4d–e), and about half of the edge in the cutting depth direction is retained while the other half close to the nose radius is worn, and cross-sections reveal an uneven topography. There is one small crack observed here and mechanical cracking has likely caused the uneven topography. There is some adhered Ti alloy on the wear region that can facilitate diffusional wear.

Fig. 6 displays the as-worn uncoated cemented carbide tools and their cross-sections after milling at varying engagement times in α + β alloy Ti-6246. More wear is attained when milling this alloy compared

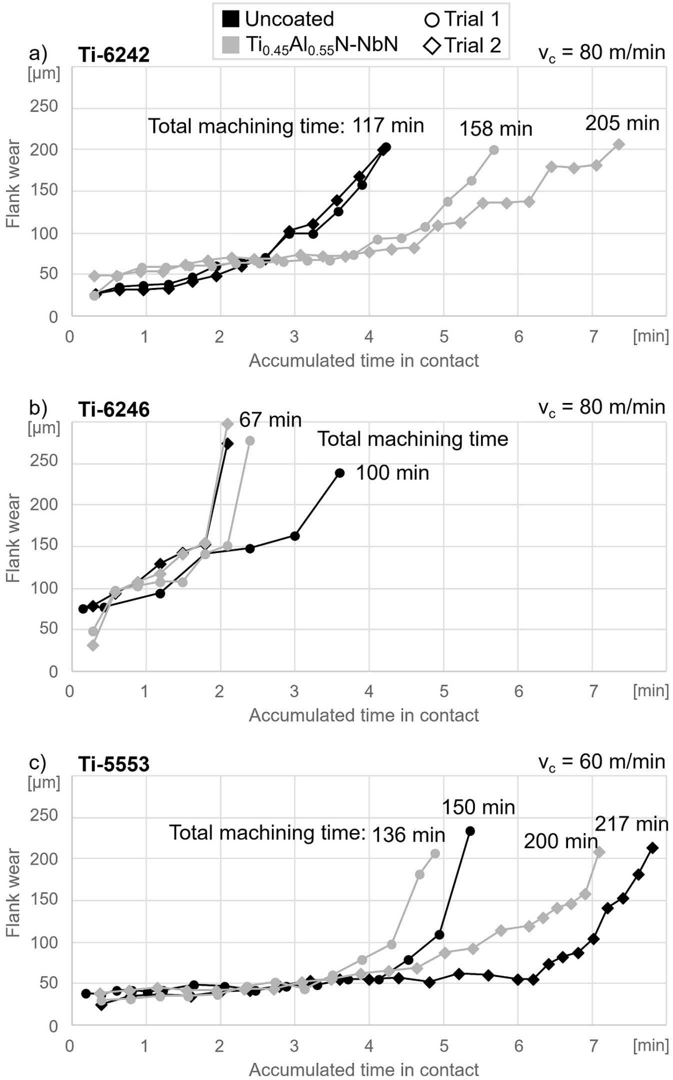

Fig. 3. Flank wear evolutions in milling the Ti alloys with uncoated or $Ti_{0.45}Al_{0.55}N$-NbN coated cemented carbide. (a) Near-α Ti-6242 at $v_c = 80$ m/min. (b) α + β Ti-6246 at $v_c = 80$ m/min. (c) Near-β Ti-5553 at $v_c = 60$ m/min.

to the previous near-α Ti-6242 and is in line with the wear evolution data (Fig. 3b). Cracks are noted in the edge line region already after 10% engagement time which represents about 12 s of contact (Fig. 6a). There is distinct edge line damage already at 30% engagement time and the wear regions increase in size with engagement time. The cross-sections reveal the development of a chamfer-like shape of the cutting edge as tool wear progresses. Some cracks are visible at 10–50% engagement times (Fig. 6a–c) and more cracks are present at the end of tool life (Fig. 6d). These are responsible for the chipping observed on the as-worn tools and can be the cause of removal of smaller parts of cemented carbide. The α + β Ti-6246 alloy adheres to the wear surfaces to a larger extent than the earlier near-α Ti-6242 alloy. The contact of Ti alloy to cemented carbide can accelerate diffusional wear process and the increased adhesion level of Ti-6246 can contribute to the faster wear rate of Ti-6246 compared to Ti-6242.

The wear evolution when milling the same α + β Ti-6246 but with $Ti_{0.45}Al_{0.55}N$-NbN coated cemented carbide is displayed in Fig. 7. The coating is removed already before 10% engagement time (Fig. 7a). The

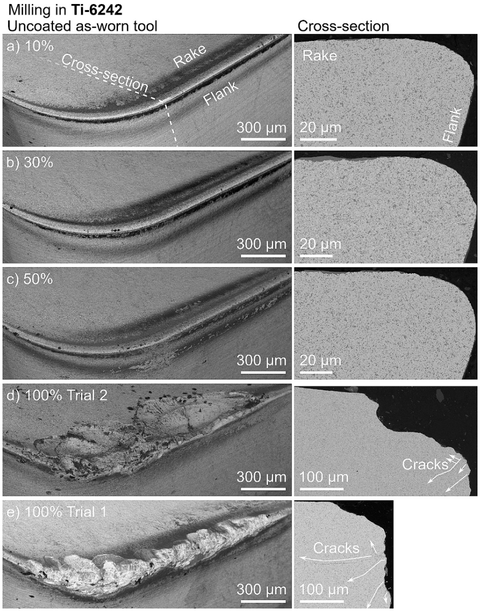

Fig. 4. Wear evolutions of uncoated cemented carbide tools in milling near-α Ti-6242 at $v_c = 80$ m/min. SEM-BSE images of as-worn tools (left column) and their cross-sections (right column) after (a) 10%, (b) 30%, (c) 50%, and (d–e) 100% engagement time.

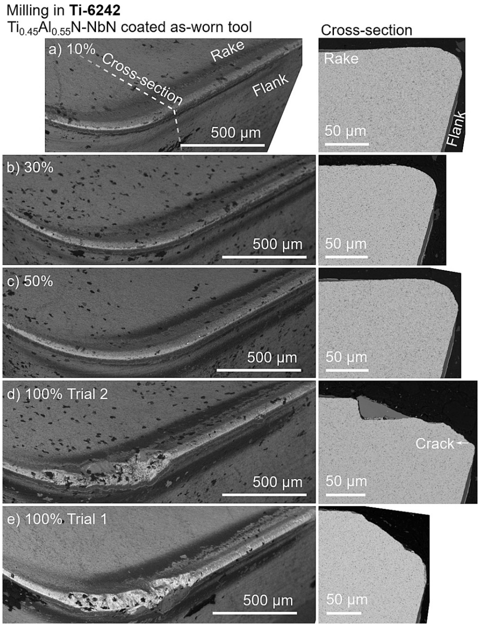

Fig. 5. Wear evolutions of $Ti_{0.45}Al_{0.55}N$-NbN coated cemented carbide tools in milling near-α Ti-6242 at $v_c = 80$ m/min. SEM-BSE images of as-worn tools (left column) and their cross-sections (right column) after (a) 10%, (b) 30%, (c) 50%, and (d–e) 100% engagement time.

wear evolution and wear morphology are similar to the uncoated tools (Fig. 6). The crack network at the end of tool life (Fig. 7d) display how flaking, chipping, and fragments of cemented carbide are removed from the tool.

Fig. 8 displays the as-worn uncoated cemented carbide tools and their cross-sections after milling near-β Ti-5553. This alloy has a higher strength as to the previous alloys and was therefore milled at a 25% lower cutting speed of $v_c = 60$ m/min instead of $v_c = 80$ m/min. The as-worn tools show a low degree of wear at 10–50% engagement time (Fig. 8a–c), but the cross-sections reveal that the edge line has suffered minor loss of material on the rake side. The wear shown in the cross-sections at different engagement times are in line with the wear rate shown in the flank wear evolution (Fig. 3c). Early stage plastic deformation is also present when milling this alloy. At the end of tool life (Fig. 8d–e), the wear regions have grown due to chipping, flaking, and mechanical wear caused by the crack network seen in the cross-section.

The as-worn tools and their cross-sections used when milling near-β Ti-5553 with $Ti_{0.45}Al_{0.55}N$-NbN coated cemented carbide are shown in Fig. 9. Some coating remains on the edge line after 10% engagement time (Fig. 9a) as opposed to when milling the other two alloys. However, the exposed cemented carbide begins to wear in minor scale even at such short engagement time. Once the coating is removed after 10% engagement time, the topography of the worn cemented carbide is similar to the uncoated tools used in milling the same alloy (Fig. 9b–c). At the end of tool life, chipping, flaking, and mechanical fractures are present. The as-worn tool after trial 1 (Fig. 9e) has a similar wear to the uncoated ones (Fig. 8d–e) but the as-worn tool after trial 2 has minor wear. This difference in wear degree is likely due to the stochasticity of the cracking phenomena in the milling process.

The tool life variations when using coated tools in milling of near-α Ti-6242, with uncoated tools in α + β Ti-6246, and with uncoated and coated tools in near-β Ti-5553 at the given flank wear criterion can be explained by studying Fig. 4–Fig. 9. At the end of tool life, chipping and flaking are prominent and there are often more or less developed crack networks within the tools. Rapid coating removal expose cemented carbide and cracking within the cemented carbide is not prevented by the coating on the yet unworn regions. The wear evolution data in Fig. 3 should not be interpreted as that the coating in case of milling Ti-6242 and Ti-5553 prolongs the tool life solely by its protective function. Instead, the wear evolution data merely indicates the stochastic cracking phenomena and likelihood to appear on the flank side where the wear criterion is measured explaining the variations in tool life. At the end of tool life, catastrophic tool failure is prominent as expected considering the total machining time range of 67–217 min.

The wear evolution for both uncoated and coated tools reveal an almost unaffected tool just over 50% engagement time when milling near-α Ti-6242, and similarly minor wear of exposed cemented carbide when milling near-β Ti-5553, while tool material loss starts earlier in case of milling α + β Ti-6246. After 50% to the end of tool life, chipping and crack propagation are present in all cases of milling in Ti-6242, Ti-6246, and Ti-5553. Crack networks within the cemented carbide eventually cause tool material loss and are contributing to an uneven topography seen in the cross-sectioned tools. The wear evolutions in Fig. 5, Fig. 7, and Fig. 9 has shown the absence of coating in the contact region even after 10% engagement time, with an exception of some present on the edge line when milling near-β Ti-5553 (Fig. 9a). Similar flaking and chipping were observed in [28] after milling Ti-64, however comb cracks were also observed which are not present in tools used in this work. The narrow rake contact width can explain such absence

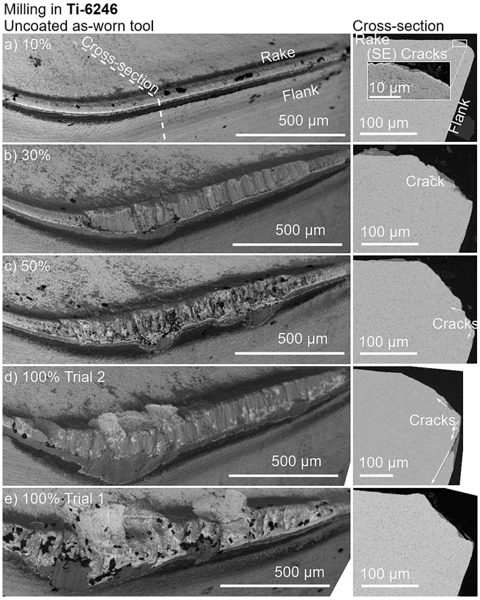

Fig. 6. Wear evolutions of uncoated cemented carbide tools in milling α + β Ti-6246 at v_c = 80 m/min. SEM-BSE images of as-worn tools (left column) and their cross-sections (right column) after (a) 10%, (b) 30%, (c) 50%, and (d–e) 100% engagement time.

which decreases the volume of tool material that is repeatedly heated and cooled and makes comb cracks difficult to form. The narrow contact width is 44 µm according to Eq. 1, however it is expected to be larger considering the chip sliding. When studying the early wear of the tools after 10% engagement time, the contact width is approximately 50–70 µm. Considering the initial edge radius of 30 µm, the rake contact is quite narrow and gives a high load on the tool edge which is compensated for by the high cutting depth of 2 mm, resulting in a long but narrow contact area. This explains the absence of a crater because the contact width is too short and instead the edge wear results in the shape of a chamfer. Such negative geometry creates stresses that favor flaking and chipping.

3.2. *In-depth analysis of wear mechanisms*

As the coating was removed already before 10% engagement time, initial coating degradation was investigated at shorter engagement times of 5 s and 30 s (Fig. 10). However, even after such a short time as 5 s, most of the coating is removed from the edge line in all cases. The NbN is removed in the contact zone in milling Ti-6242 (Fig. 10a) and Ti-5553 (Fig. 10c). The $Ti_{0.45}Al_{0.55}N$ is worn but still present in the contact zones after milling Ti-6242 but is removed in the crater and flank region in Ti-5553 and some remains around the edge line. In milling Ti-6246, both coating layers remains around the edge line but are removed in the crater and flank regions (Fig. 10b). The inset image displays a crack within the bulk of the $Ti_{0.45}Al_{0.55}N$ which goes out through the NbN (Fig. 10b) and thus points to the mechanical degradation of the coating by cracking. After 30 s of engagement time, the coating is completely removed within the contact regions and has exposed the cemented carbide which is already worn after milling in Ti-6246 (Fig. 10e) and minor material loss in milling Ti-5553 (Fig. 10f). Early sign of plastic deformation of the cemented carbide edge line is present after milling Ti-5553 after 5 s of engagement time (Fig. 10c) and previously observed after 10% engagement time in milling the same Ti-5553 (Fig. 8a), and after milling Ti-6242 for 30 s (Fig. 10d). Plastic deformation is not observed in milling Ti-6246.

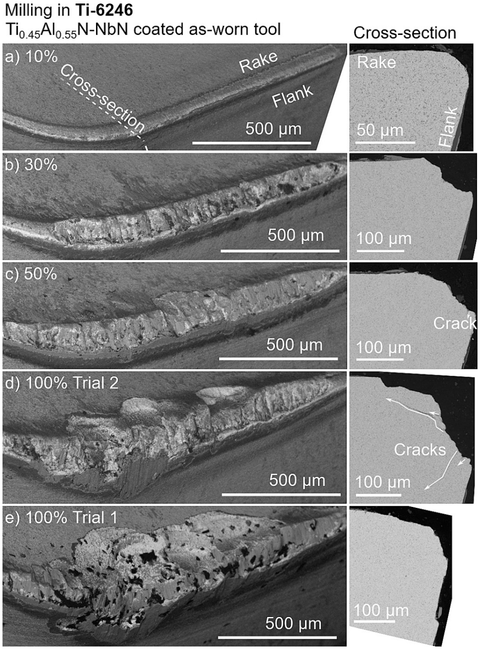

Fig. 7. Wear evolutions of $Ti_{0.45}Al_{0.55}N$-NbN coated cemented carbide tools in milling α + β Ti-6246 at v_c = 80 m/min. SEM-BSE images of as-worn tools (left column) and their cross-sections (right column) after (a) 10%, (b) 30%, (c) 50%, and (d–e) 100% engagement time.

More coating wear phenomena are explored in tools machined for longer times as shown in Fig. 11. Common PVD droplet defects are present sporadically in the coating and can be locations of crack initiation and propagation (Fig. 11a). In milling near-α Ti-6242, adhered Ti alloy at the coating surface (Fig. 11a–c) can contribute to its diffusional dissolution but the uneven topography of the $Ti_{0.45}Al_{0.55}N$ indicate mechanical wear by cracking. A crack within the adhered Ti alloy on the flank side (Fig. 11c) is likely formed due to the thermal cycling during the milling operation. This crack is not damaging the coating but could be if the adhesive force is strong.

In milling α + β Ti-6246, other wear mechanisms of the coating are displayed. Within the adhered Ti alloy on the rake side, parts of µm-sized dislodged NbN and $Ti_{0.45}Al_{0.55}N$ are embedded (Fig. 11d). This clearly displays the mechanical wear by likely local cracking or adhesive wear of both coating layers. On the flank side, a crack is present within the $Ti_{0.45}Al_{0.55}N$ and NbN (Fig. 11e) and shows the mechanical wear by cracking of both coating layers. Such small volume removal could explain the smooth interface of $Ti_{0.45}Al_{0.55}N$ toward Ti alloy in Fig. 11f or it can be explained by the diffusional dissolution of the coating. In milling near-β Ti-5553, the cross-section reveals no significant work material adhesion to the coating. The $Ti_{0.45}Al_{0.55}N$ is unevenly worn on the rake and edge line (Fig. 11g–h) due to cracking. There is a crack within the $Ti_{0.45}Al_{0.55}N$ on the flank side (Fig. 11j), but on another tool,

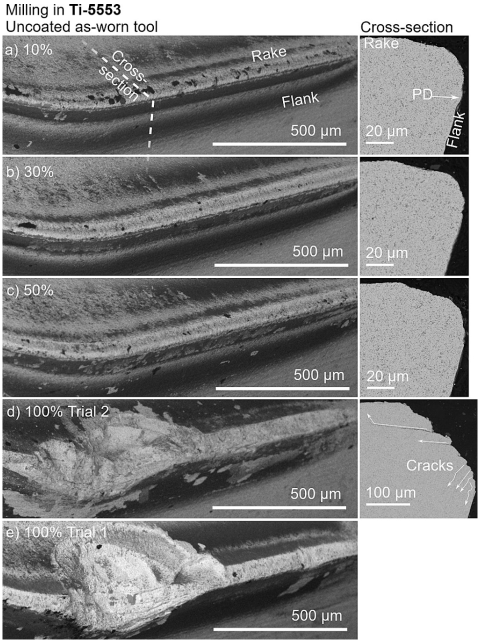

Fig. 8. Wear evolutions of uncoated cemented carbide tools in milling near-β Ti-5553 at $v_c = 60$ m/min. SEM-BSE images of as-worn tools (left column) and their cross-sections (right column) after (a) 10%, (b) 30%, (c) 50%, and (d–e) 100% engagement time.

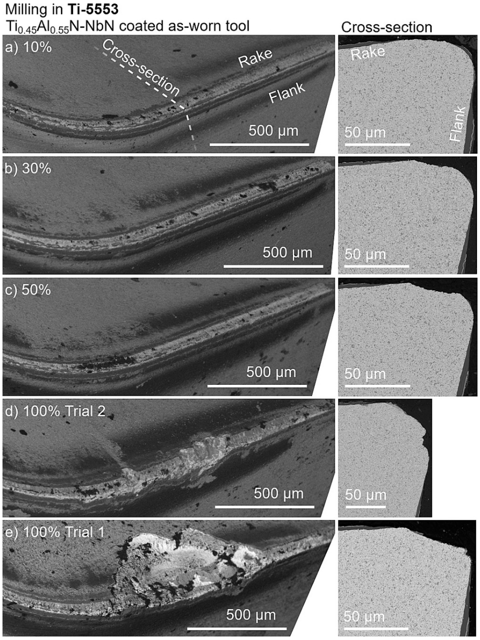

Fig. 9. Wear evolutions of $Ti_{0.45}Al_{0.55}N$-NbN coated cemented carbide tools in milling near-β Ti-5553 at $v_c = 60$ m/min. SEM-BSE images of as-worn tools (left column) and their cross-sections (right column) after (a) 10%, (b) 30%, (c) 50%, and (d–e) 100% engagement time.

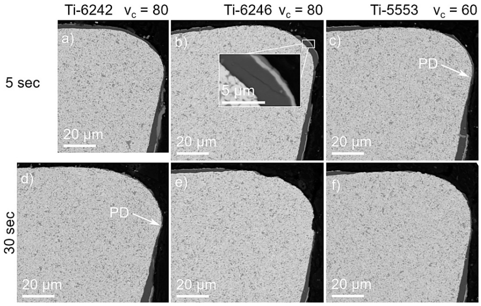

Fig. 10. Initial coating wear. SEM-BSE images of cross-sectioned tools after (a–c) 5 s or (d–f) 30 s of engagement time in milling near-α Ti-6242 (a,d), α + β Ti-6246 (b,e), and near-β Ti-5553 (c,f).

the $Ti_{0.45}Al_{0.55}N$ on the flank is smoothly worn (Fig. 11i) indicating diffusional dissolution.

Based on the cross-sections in Fig. 10 and Fig. 11, the coating is worn by mechanical wear with crack propagation and presence of PVD droplet defects work as local start points for such cracks, while debonding is not an issue. Broken off fragments of both coating layers are removed with the superficial shear of the Ti alloys. Cracking within the coating layers due to thermal cycling is excluded because such cracks would be perpendicular to the cemented carbide surface in a cross-section [29], which are not observed. Instead, cracks are parallel to the cemented carbide surface.

Fig. 11k shows the rake of a cross-sectioned tool in milling α + β Ti-6246. Some coating remains on the left side of the dashed line, but it has been removed to the right side. The figure shows the fast degradation of the cemented carbide once it becomes exposed to the α + β Ti-6246 as also seen in Fig. 7b. The similar was also observed when milling near-β Ti-5553 (Fig. 8 and Fig. 9) but not in milling near-α Ti-6242 (Fig. 4 and Fig. 5). This can be explained both by the higher mechanical properties of α + β Ti-6246 and near-β Ti-5553 compared to near-α Ti-6242, but also that they have a higher β-phase fraction which is more ductile and adhesive that promotes contact between Ti alloy and cemented carbide during the cutting operation. This contact is essential for diffusional dissolution that weakens the surface integrity and makes it more prone to damage by the cyclic impact during milling.

Fig. 12 shows the cemented carbide and Ti alloy contact regions and focus on the wear of cemented carbide. The morphologies shown in the figure have been observed in machining the three alloys. Fig. 12a, d shows smoothly worn WC grains on the rake and flank regions and the microstructure is identical within the bulk and up to the interface. The smooth interface and gradual wear of the WC and absence of mechanical damage is likely due to the outward diffusion of C from WC. The loss of C results in a layer of remaining W, as observed in Fig. 12b, because W has a limited solubility in Ti [30], which is a known phenomenon reported on in previous works [31–37]. Such W layer can be removed by the superficial shear of the Ti alloy as it moves over the contact regions during cutting and can explain why a W-layer is not observed in Fig. 12a, d.

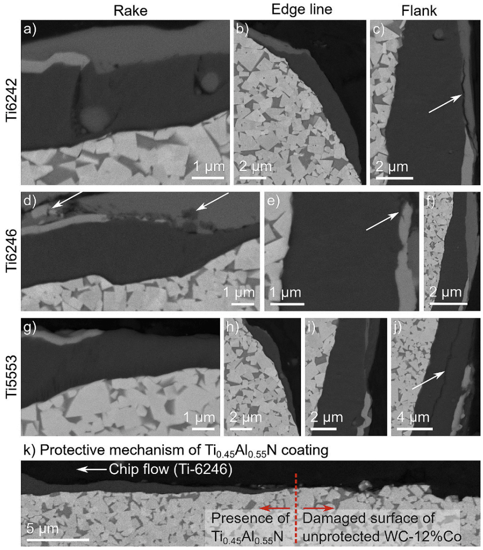

Fig. 11. Coating wear mechanisms. SEM-BSE images of cross-sectioned tools after milling (a–c) near-α Ti-6242, (d–f) α + β Ti-6246, and (g–j) near-β Ti-5553.

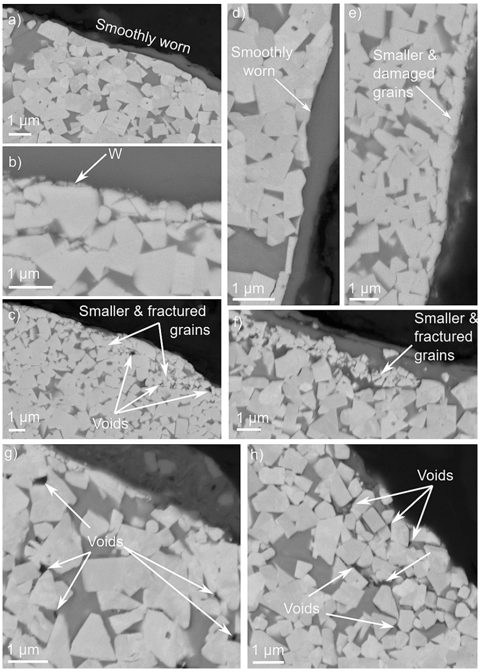

Fig. 12. SEM-BSE images of worn cemented carbide.

Outward diffusion of C into Ti is also known to form TiC which work as a diffusion block for further C loss and is reported in previous work [34–40]. TiC formation is likely occurring which is observed by the dark *Z*-contrast rim in the Ti alloy bordering the cemented carbide, like in Fig. 12a–d. If its presence would be confirmed, the TiC may also block the outward diffusion of Co, which explains the homogeneous microstructure all the way to the interface in Fig. 12a,d. Studying Fig. 12c,e, there are smaller and damaged grains, which are densely packed at the interface. The denser packing is due to lack of Co binder in the near interface region. Without the dampening effect of Co, the cyclic loading of the milling process imposed on the WC grains is the most probable cause of their damage. A combination of Co and C outward diffusion has likely caused the structure in Fig. 12f where even smaller WC fragments are clustered at the interface. Titanium alloy has propagated under them, and they are subsequently removed by the chip flow.

The empty Co regions near the interface in Fig. 12c is observed also in Fig. 12g–h. This phenomenon is observed when milling all Ti alloys but most prominent in Ti-6246, on a minor scale in Ti-6242, and less frequent in Ti-5553. They are present to a depth of about 4 µm from the interface and are not observed within the bulk of the cemented carbide tools and should thus not be formed during sintering. At least two mechanisms could cause these voids, where the first is plastic deformation and the second is Kirkendall porosity. Plastic deformation of the ductile Co in WC-Co is suggested to start by void formation in the Co binder and new voids are formed further into the binder which eventually merge into larger ones that finally form a crack that goes within the Co binder [41,42]. If there is substantial difference in diffusion rate between two bordering elements, vacancies accumulate and eventually form voids, which is called Kirkendall porosity [43]. In another study investigating the mechanisms in as-worn tools and in diffusion couples, such voids were observed, and their location near WC grains is explained by a lower nucleation energy there [44].

The outward diffusion of C from WC grains makes their grains rounder as opposed to the original faceted sides which can weaken their strength and make them more easily damaged by the cyclic loading during milling. Loss of Co due to diffusion also makes the WC grains less attached to the bulk which enables their detachment and removal with the chip flow, and Co loss reduces the impact resistance further contributing to the damage of weaker WC grains. Fig. 13 shows these phenomena. There are detached and rounded WC grains that have been removed by the chip flow as seen by their presence within the adhered Ti alloy (Fig. 13a,c,e). Even clusters of WC grains with Co binder are removed with the chip flow (Fig. 13b,d). Smaller and damaged WC grains that are densely packed at the interface due to Co diffusion is observed in Fig. 13d. Fig. 13e shows empty Co regions near the interface seen by the dark Z-contrast, which can be caused either by plastic deformation of the Co binder or by Kirkendall porosity. These wear specific phenomena related to the diffusional dissolution of cemented

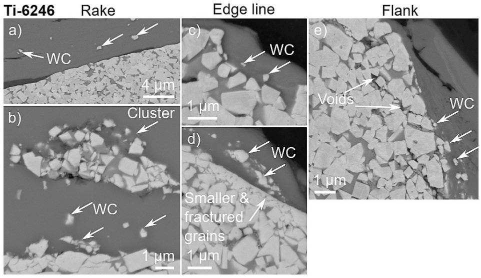

Fig. 13. SEM-BSE images of detached WC grains or clusters that are moved from the interface by the chip flow after milling α + β Ti-6246.

carbide is observed in major scale when milling $\alpha + \beta$ Ti-6246, and in minor scale when milling near-α Ti-6242 and near-β Ti-5553.

Another wear topography that was common for cemented carbide in the milling of the three Ti alloys were the Co interface regions to the Ti alloy along the contact regions on the rake, edge line, and flank as displayed in Fig. 14a–b. In the previous Fig. 12, only WC faced the Ti alloy, but in Fig. 14, regions of Co binder directly face the Ti alloy as well. This morphology is present where volumes of cemented carbide were recently broken off. The cemented carbide has thus had little time in contact with the Ti alloy which can explain the Co presence. Outward diffusion of Co is a known mechanism which can stabilize the β-phase of Ti locally at the interface [34,37,38,45]. The XEDS linescan of the interface region of Co and Ti are shown in Fig. 14c–d and the exact location on the sample is displayed in Fig. 14a. The dashed line at 0.3 μm distance from the start point marks the border between the Co and Ti alloy. The Co concentration increases from the start point to the interface and has a declining concentration within the Ti alloy pointing to its outward diffusion. When such diffusion proceeds, the surface Co becomes removed and results in only WC facing the Ti alloy as seen in Fig. 12.

Additionally, W and C has a declining concentration from the start point to the interface which could be due to the closeness to a WC grain at the start point, or it could indicate the diffusion of C and W from the WC through the Co binder. There is no ingress of Ti to the Co, which could be the case when they are in contact for a longer time forming intermetallic Ti_2Co [34] that act as a diffusion block. The Ti alloy can be oxidized based on the presence of O, and the similar concentration in the Co points to its potential oxidation as well.

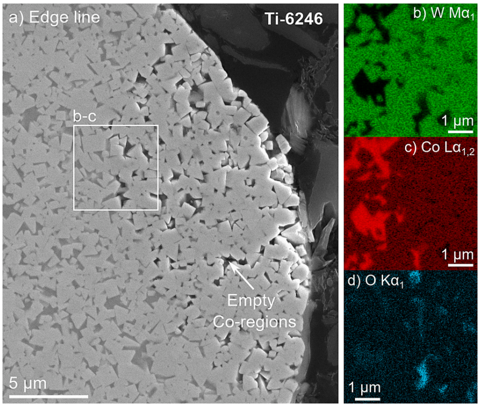

Fig. 15. (a) SEM-SE image of the edge line of a cross-sectioned tool used in milling $\alpha + \beta$ Ti-6246 after 10% engagement time showing empty Co binder regions and (b–d) XEDS maps of such region.

Fig. 15a shows an SEM-SE image of the edge line of a cross-sectioned tool used in the milling of $\alpha + \beta$ Ti-6246 after 10% engagement time, which corresponds to about 12 s. The near interface region has empty Co binder sites seen by darker contrast areas with brighter edges on surrounding WC grains. The Co loss has proceeded about 10 μm into the tool. A region with both empty and original Co binder sites is highlighted with a square in Fig. 15a and the XEDS maps of this region are shown in Fig. 15b–d. This clearly shows the Co presence in the original binder sites and the absence in the empty sites. The Ti alloy has not replaced Co in those sites which remain empty. This Co deficient edge could either be a defect occurring during edge grinding, a sign of rapid diffusional loss during machining, or formed by oxidation. It could be argued that grinding defects would be present along the whole edge line, and when studying other locations outside the cutting zone on the same tool, no Co loss was observed. The other alternative of Co loss by diffusion seems intuitively unlikely due to the short engagement time and a commonly lower cutting temperature in milling than in turning, but the O presence in the voids could point to binder oxidation in combination with diffusional dissolution. Although the mechanism behind the Co loss is unknown, the dampening effect of the Co binder is lost in the edge region. The cyclic loading hits the WC grains repeatedly and the breakaway of individual grains or their clusters are expected if the cutting continues, and this location can be an initial point for crack formation.

Images of cracks within the cemented carbide after milling in the three Ti alloys are shown in Fig. 16. These are propagating between WC grains within the Co binder as marked with the arrows. The

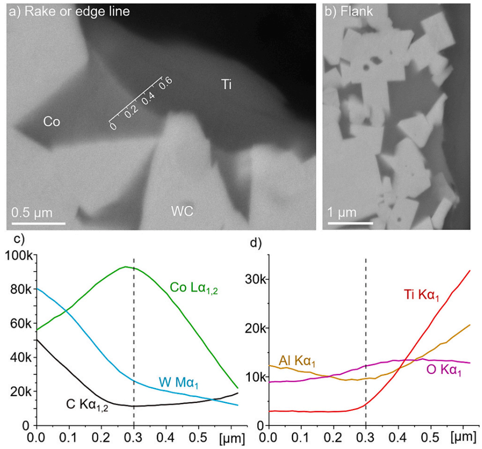

Fig. 14. SEM-BSE images of cemented carbide which has Co regions facing the Ti alloy and XEDS linescan over such interface.

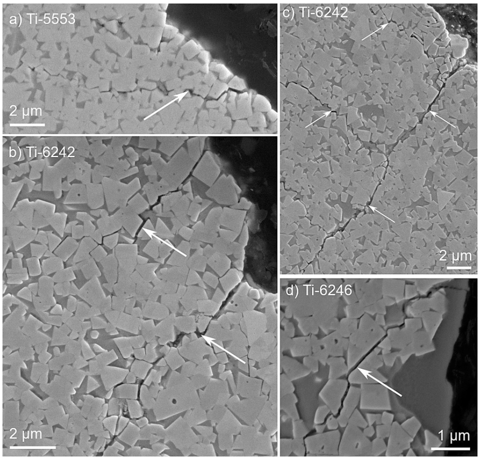

Fig. 16. SEM-SE images of crack networks in cemented carbide after milling near-α Ti-6242 and near-β Ti-5553.

microstructure is the same up to the interface and applies to Fig. 16a,b,d which is in all three Ti alloys and this indicates the plastic deformation of the ductile Co binder phase [41,42] to be the likely mechanism behind the cracks. In Fig. 16c, the microstructure is different near the interface and shows rounder WC grains where C diffusion is promoted because WC are in contact with the Ti alloy. The WC grains become faceted during sintering and attains a prism shape based on a truncated triangle [46] however WC grains with a more round shape can occur at longer sintering times with higher binder content [47]. Rounder WC grains occur sporadically within the cemented carbide but not in the concentration seen at the interface in Fig. 16c pointing to the likelihood of diffusional dissolution.

Another type of crack is occurring in major scale after 50–100% engagement time is displayed in Fig. 17. Cracks of this type are observed frequently in the cases of milling α + β Ti-6246 and in near-α Ti-6242 but less often, but they are not observed in tools used to cut near-β Ti-5553. Fig. 17a shows a crack that propagates through the cemented carbide, and at its base in the interface region, the WC grains have a round shape and there is a lack of Co binder between and become a natural start site for a crack. Such round WC grains with little attachment to the bulk are easily removed with the chip flow, and can allow Ti to propagate in the crack as seen in Fig. 17b. Thermal cycling will open up such crack and result in massive tool material loss and the Ti ingress weaken the tool by diffusional wear further into the tool.

Diffusional loss of C and Co have been observed in the cutting tools, and Fig. 17c shows another example of C loss with smaller WC grains that are also mechanically damaged. Fig. 17c hints on an additional wear mechanism. Along the crack, the binder material has a brighter *Z*-contrast than within the bulk. This phenomenon is observed in several locations especially when milling α + β Ti-6246 but also in near-α Ti-6242 but less often, like in Fig. 17d where the brighter Z-contrast binder region is fragmented. A brighter Z-contrast indicates the presence of larger mass elements, and the fragments indicate the nucleation and growth of a new phase. Such fragments of brighter Z-contrast in binder regions are often accompanied by cracks between the fragments or near the WC grain interfaces, as exemplified in Fig. 17e–f. XEDS spectrums indicate that the brighter Z-contrast regions are oxidized, and that there is presence of Co and W where the presence of W can explain the brighter Z-contrast. Additionally, fragments about 1 μm from the interface also contains Cr which originates from the binder.

Fig. 18 shows an SEM-BSE image with XEDS and EBSD maps of a cross-sectioned as-worn tool after milling α + β Ti-6246. Fig. 18a shows an at least 16 μm long ingress of oxidized binder, with brighter Z-contrast than Co binder in the bulk, along which cracks propagate. This phase is formed during the milling operation and presence of larger grains near the interface compared to smaller fragments further into the tool indicate that the smaller fragments are recently formed showing the growth path of the new phase. XEDS maps captures an area with both Z-contrasts of the binder in Fig. 18b. The bright Z-contrast phase is rich in O and has presence of Co and W, while the darker Z-contrast or original binder sites contains mostly Co. The combination of Co, W, and O could be either CoWO, Co_3W_3O, or $CoWO_4$. The presence of Co_3W_3O and CoWO is considered unlikely because of their difficulties to form [48].

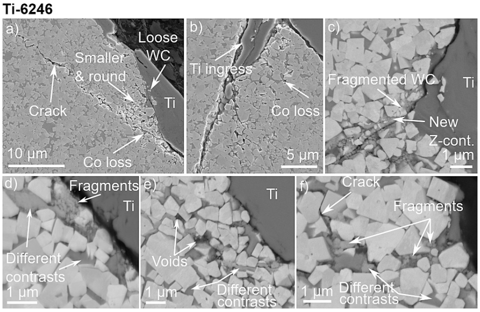

Fig. 17. SEM images attained with (a–b) SE and (c–f) BSE detector of cross-sectioned tools used in milling α + β Ti-6246 at longer engagement times or end of tool life.

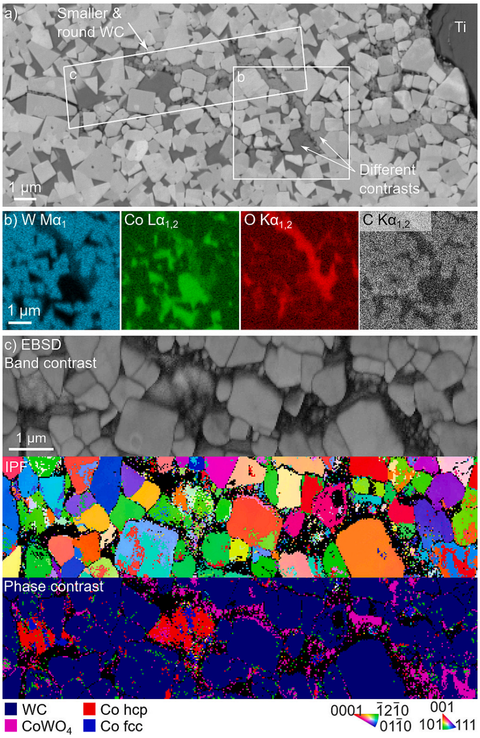

Fig. 18. (a) SEM-BSE image of the near interface region of a cross-sectioned tool used in milling α + β Ti-6246 after 50% engagement time and (b) XEDS maps and (c) EBSD capturing the two contrast regions of the binder.

The oxide was investigated using EBSD and the results are shown in Fig. 18c which contain band contrast, inverse pole figure (IPF), and phase contrast. The band contrast further confirms the small fragments of the oxide that are recognized as the $CoWO_4$. The darker Z-contrast binder that is rich in Co is recognized as mainly hcp Co but there is also presence of fcc Co. Along the 16 μm long $CoWO_4$ ceramic, neighboring WC have a rounder shape (Fig. 18a). There is some W dissolved in the Co binder after sintering [49] but it may not be sufficient in quantity to form $CoWO_4$, and it is speculated that this ceramic phase could form on the cost of neighboring W in WC grains which can explain their round shape.

After sintering, Co has the fcc crystal structure [49], and the EBSD results show mostly hcp (Fig. 18c). This can be explained by the work hardening of the Co phase that results in a transformation from fcc to hcp [50]. In the original binder, there is Cr added as a grain growth inhibitor during sintering [49] and Cr can stabilize the hcp phase of Co. However, XEDS spectrums from these Co sites contain no Cr peaks and this explanation is thus not probable. However, a lack of Cr in these binder regions is rather unexpected. Studying the Ellingham diagram [51], less energy is required to form CrO than WO or CoO and it should thus likely form initially. A hypothesis is that CrO forms first near the interface regions, as indicated in Fig. 17f, and that Cr diffuse to the interface region, or that CrO form small precipitates next to the subsequent formation of $CoWO_4$. The oxides near the interface in Fig. 17d–f and in Fig. 18 are fragmented, and Barbatti et al. [22] observed that such oxides contain defects like porosity, voids, and cracks after performing controlled oxidation experiments on cemented carbide. After treatment at 600 °C, they observed WO_3, $CoWO_4$, and some Co_3O_4. Oxidation of WC grains leading to the formation of WO_3 can also explain the rounder shape of the WC grains near the $CoWO_4$ in Fig. 18. They also observed that the oxides are compact, porous, and brittle with low adhesion to the substrate, where the gases formed during oxidation expand the voids and cracks, and that there are stresses occurring within the oxides upon their formation. With oxide formation within the cemented carbide tool, cracking and fractures are furthermore formed by the cyclic loading conditions.

Diffusion and oxidation modeling of milling is inherently difficult due to the fact that the process is highly dynamic. The tool is in intermittent contact with coolant, air, and fresh workpiece material which leads to a temperature fluctuation in the tool edge. This work shows the diffusional dissolution of WC grains and Co binder, the oxidation of binder, and the mechanical cracking that results in tool material loss.

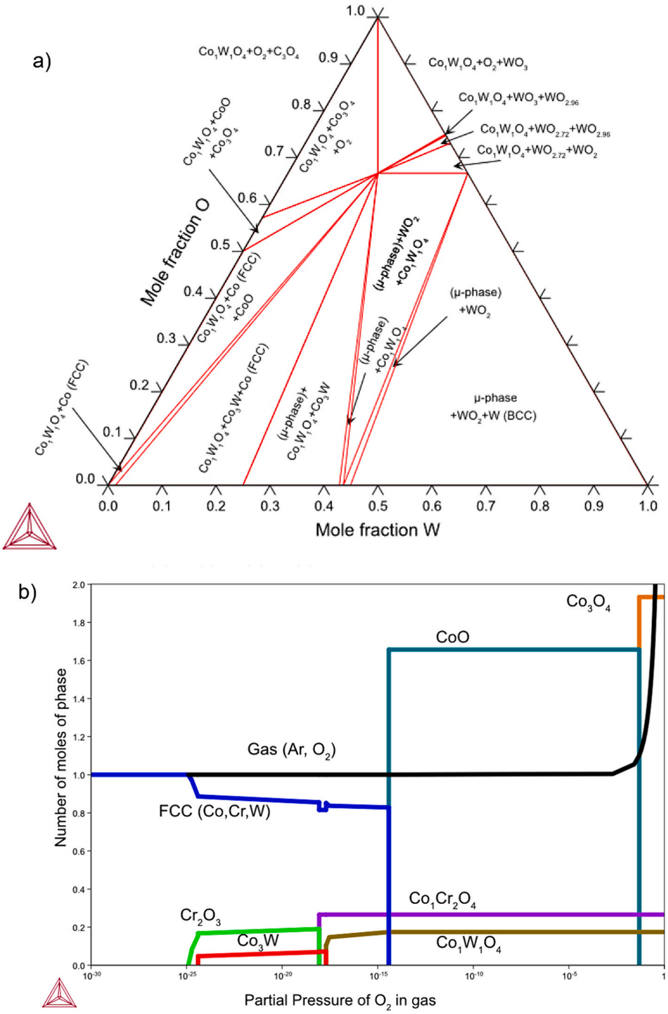

Fig. 19. (a) Ternary phase diagram for Co-W-O and (b) diagram of thermodynamic modeling when the oxygen pressure to the binder is increased and the phases formed.

The comparative effect of the diffusional and oxidative wear mechanisms can be approximated by using thermodynamic modeling and diffusion simulations [37]. Diffusion of Co and C into to bcc β-Ti has also been studied in turning experiments [52]. The permeability, which is the combination of mobility and solubility, and hence the ability of Co and C to diffuse into β-Ti is comparable, while W has limited solubility in Ti [30]. The diffusivity of Co and C is several orders of magnitude smaller in hcp α-Ti compared to bcc β-Ti [53] and the diffusion rate in the α + β Ti-6246 and near-β Ti-5553 is thus likely higher than in near-α Ti-6242 which partly explains their higher wear rate.

The XEDS of Co facing Ti alloy in Fig. 14 and rounding of WC grains shown in Fig. 12, Fig. 13, Fig. 17, and Fig. 18 are the result of diffusional dissolution. However, the approximately 10 μm Co depleted region of the edge in Fig. 15 should not be possible after 12 s of engagement time in the Ti alloy, and about 7 min of total machining time. Such diffusion lengths are achieved in diffusion couple experiments after 10 min of static contact at an expectedly higher temperature of >900 °C [37,52]. While the dynamic nature of a machining process has the continuous supply of fresh Ti alloy for the C and Co to diffuse into gives space for a deeper diffusion loss. Based on the O presence in the voids in Fig. 15, it is possible that an oxide has formed which is brittle and that falls out during polishing. This could explain the 10 μm deep zone containing voids where diffusional dissolution of Co is accompanied by its oxidation.

The binder can oxidize to form CoO and Co_3O_4 [22] which are more brittle than the Co binder. Oxidation of WC grains leads to the formation of CO and CO_2, but more importantly to WO_x which leads to a volume expansion and crack formation [54]. A combination of Co and W oxides can also form, such as the $CoWO_4$ [55] identified in this work. There is always W dissolved in the binder phase and hence the oxidation of the binder results in a mix of Co and W oxides. The ternary phase diagram of Co-W-O in Fig. 19a shows that the $CoWO_4$ phase is stable except in the W-rich corner. The formation of CoO, Co_2O_3, and WO_x are also possible, but these were not included in the EBSD analysis. These phases including the $CoWO_4$ lead to a volume increase and cracking in addition to embrittlement, which adds to the crack growth observed. The cracks may also be growing due to thermal fatigue and the thermal expansion of gas and coolant trapped in the cracks during machining.

By assuming that the binder oxidizes faster than W diffuse into the binder after outward C diffusion, the oxidation process can be modelled by increasing the partial pressure of oxygen to the Co binder. The Co binder contains Cr and dissolved W and C, where C forms CO and CO_2 upon oxidation. Oxidation modeling in Fig. 19b is done at 900 °C and 1 atm which resembles the conditions just after the tool exited the workpiece material. 1 mol of Ar is added to the calculation to be able to calculate the partial pressure of O_2. Fig. 19b shows that the Cr in the binder oxidize initially, followed by the formation of $CoCr_2O_4$, $CoWO_4$, and CoO, where Co_3O_4 might also form if there is complete oxidation. Fig. 19b shows that no oxidation of the WC grains is needed to form $CoWO_4$, because the amount of dissolved W in the binder during sintering is enough for its formation. The rounded WC grains near the $CoWO_4$ in Fig. 18 could therefore be explained by the oxidation of the WC or its earlier diffusional dissolution.

With increasing β-fraction, the strength of the Ti alloy is increased as shown in Table 1, and so the strength increases from relatively lower near-α Ti-6242, to relative medium α + β Ti-6246, and finally to relative high strength near-β Ti-5553 in this group of Ti alloys. When changing from near-α to near-β, the cutting force must increase and if using the same cutting conditions, the cutting temperature is expected to increase [56]. The decrease in cutting speed to $v_c = 60$ m/min for near-β Ti-5553 compared to $v_c = 80$ m/min for α + β Ti-6246 and near-α Ti-6242 probably results in a lower temperature than in α + β Ti-6246. Because α + β Ti-6246 and near-α Ti-6242 are machined at the same cutting speed, the temperature is expected to be higher in case of α + β Ti-6246. The oxidation forming $CoWO_4$ is also prominent when machining in α + β Ti-6246 and is also noted when milling near-α Ti-6242 but to a minor extent. That means that the cutting temperature is over 570 °C above which the WC-Co system oxidizes [22]. The oxidation and diffusional wear mechanisms further facilitate the mechanical wear of the stronger α + β Ti-6246 compared to near-α Ti-6242. Oxide products are not noted when milling near-β Ti-5553 and it can be the case that the onset temperature for oxidation may not have been reached due to the use of a lower cutting speed. However, the temperature has been high enough for diffusional dissolution to take place when milling all alloys, as such indications have been observed when machining the three Ti alloys. The lack of oxidation and the lower cutting speed explain why the higher strength near-β Ti-5553 has a lower wear rate compared to the relatively medium strength α + β Ti-6246.

Rapidly exposed cemented carbide in milling either of the Ti alloys at the selected cutting conditions has resulted in similar wear mechanisms but in different intensities. It is suggested that the high wear rate when milling α + β Ti-6246 is due to the combination of extensive oxidation and diffusional dissolution with, in this group of alloys, medium strength material. The second highest wear rate is attained when milling near-β Ti-5553 because of its high strength and diffusional dissolution, while the lowest wear rate when milling near-α Ti-6242 is due to a combination of diffusional dissolution and minor oxidation wear.

4. Conclusions

This study explores the wear mechanisms of uncoated and $Ti_{0.45}Al_{0.55}N$-NbN coated WC-12%Co tools in external circular milling three different Ti alloys including near-α Ti-6242, α + β Ti-6246, and near-β Ti-5553. The major conclusions are:

- The coating in the contact regions is removed already after 5–30 s. The main wear mechanism is crack formation within the bulk of the coating. PVD droplet defects can initiate such cracks, and superficial shear of the Ti alloys removes broken off fragments. Delamination or thermal cracks are not present, while diffusional dissolution of the coating may be active but on a minor scale. The mechanical wear of the coating is extensive and shows the need for a more robust coating formulation.
- Extensive flaking and chipping and formation of crack networks within the cemented carbide are causing tool material loss. Crack networks propagate within the Co binder and in between WC grains. The variations in tool life are explained by the stochasticity of the cracking phenomena.
- Diffusional dissolution of WC grains is observed by rounder WC grains in near surface regions and residual W layers that are removed with the superficial shear by the chip flow. Diffusional loss of Co leads to the removal of surface WC grains or clusters of surface material with the chip flow. Lack of dampening Co and force fluctuations results in damaged or fractured WC grains in the near interface region and can result in crack propagation. Voids in Co phase in the near surface regions could be explained by its plastic deformation or by Kirkendall porosity.
- Oxidation of Co binder results in the formation of ceramic $CoWO_4$ initially in near surface regions which grows several μm into the tool. The nucleation of the ceramic results in fine and brittle grains which allows crack propagation. WC attains a rounder shape near the $CoWO_4$ pointing to its diffusional dissolution or oxidation. Neighboring Co binder has the hcp structure which can indicate its deformation that causes a transformation from fcc.
- The highest wear rate is achieved when machining α + β Ti-6246 at $v_c = 80$ m/min, followed by medium wear rate in near-β Ti-5553 at lower cutting speed of $v_c = 60$ m/min, and the lowest wear rate is attained when milling near-α Ti-6242 at $v_c = 80$ m/min. The high wear rate when milling α + β Ti-6246 is explained by the combination of oxidation, diffusional dissolution, and mechanical wear. The moderate wear rate in milling near-β Ti-5553 is explained by absence of oxidation wear but high mechanical wear and diffusional

dissolution, while the low wear rate in near-α Ti-6242 is explained by diffusional dissolution and minor oxidation wear.

CRediT authorship contribution statement

Rebecka Lindvall: Writing – review & editing, Writing – original draft, Visualization, Project administration, Methodology, Investigation, Formal analysis, Conceptualization. **Juan Manuel Bello Bermejo:** Writing – review & editing, Project administration, Methodology, Investigation, Formal analysis. **Axel Bjerke:** Writing – review & editing, Visualization, Methodology, Investigation, Formal analysis. **Jon M. Andersson:** Writing – review & editing, Supervision, Resources. **Elias Vikenadler:** Writing – review & editing, Supervision, Resources, Project administration, Methodology. **Rachid M'Saoubi:** Writing – review & editing, Supervision, Resources, Project administration, Methodology, Funding acquisition, Conceptualization. **Volodymyr Bushlya:** Writing – review & editing, Supervision, Resources, Project administration, Methodology, Funding acquisition, Formal analysis, Conceptualization.

Declaration of competing interest

The authors declare that they have no known competing financial interests or personal relationships that could have appeared to influence the work reported in this paper.

Data availability

Data will be made available on request.

Acknowledgements

This research was funded by Seco Tools AB and the strategic research programme of Sustainable Production Initiative (SPI) that involves cooperation between Lund University and Chalmers University of Technology. Adnan Agic and Per Alm (Seco Tools AB) are acknowledged for contributing to the experimental milling setup, and Sören Hägglund (Seco Tools AB) is acknowledged for clarifications on the calculations and definitions related to the theoretical maximum chip thickness in external circular milling. Susanne Norgren (Sandvik AB and Lund University) is acknowledged for valuable discussions on the wear phenomena and thermodynamic modeling. Yvon Millet (formerly at TIMET Savoie) is acknowledged for supplying the titanium workpiece alloys used in this work.

References

[1] R.E. Smallman, A.H.W. Ngan, Physical Metallurgy and Advanced Materials Engineering, 7th edition, Butterworth-Heinemann, Oxford, 2007.

[2] A. Pramanik, Problems and solutions in machining of titanium alloys, Int. J. Adv. Manuf. Technol. 70 (2014) 919–928, https://doi.org/10.1007/s00170-013-5326-x.

[3] T.R. Bieler, R.M. Trevino, L. Zeng, Alloys: titanium, in: F. Bassani, G.L. Liedl, P. Wyder (Eds.), Encyclopedia of Condensed Matter Physics, Elsevier, Oxford, 2005, pp. 65–76.

[4] W.D. Callister Jr., Materials Science and Engineering – An Introduction, 7th edition, John Wiley & Sons, Inc., 2007.

[5] J. Sun, Y.B. Guo, A comprehensive experimental study on surface integrity by end milling Ti-6Al-4V, J. Mater. Process. Technol. 209 (2009) 4036–4042, https://doi.org/10.1016/j.jmatprotec.2008.09.022.

[6] H. Zhang, J. Zhao, F. Wang, J. Zhao, A. Li, Cutting forces and tool failure in high-speed milling of titanium alloy TC21 with coated carbide tools, Proc. Inst. Mech. Eng. B J. Eng. Manuf. 229 (2014) 20–27, https://doi.org/10.1177/0954405414526578.

[7] C.H. Che Haron, A. Ginting, H. Arshad, Performance of alloyed uncoated and CVD-coated carbide tools in dry milling of titanium alloy Ti-6242S, J. Mater. Process. Technol. 185 (2007) 77–82, https://doi.org/10.1016/j.jmatprotec.2006.03.135.

[8] R. M'Saoubi, D. Axinte, S.L. Soo, C. Nobel, H. Attia, G. Kappmeyer, S. Engin, W.-M. Sim, High performance cutting of advanced aerospace alloys and composite materials, CIRP Ann. Manuf. Technol. 64 (2015) 557–580, https://doi.org/10.1016/j.cirp.2015.05.002.

[9] S. Koseki, K. Inoue, K. Sekiya, S. Morito, T. Ohba, H. Usuki, Wear mechanisms of PVD-coated cutting tools during continuous turning of Ti-6Al-4V alloy, Precis. Eng. 47 (2017) 434–444, https://doi.org/10.1016/j.precisioneng.2016.09.018.

[10] B. Wang, A. Li, G. Liu, Cutting performance and Wear mechanisms of TiAlN PVD-coated cemented carbide tool in high speed turning of Ti-5Al-2Sn-2Zr-4Mo-4Cr alloy, J. Mech. Sci. Technol. 34 (2020) 2997–3006, https://doi.org/10.1007/s12206-020-0631-4.

[11] F. Wang, K. Ji, Z. Guo, Microstructural analysis of failure progression for coated carbide tools during high-speed milling of Ti-6Al-4V, Wear 456-457 (2020) 203356, https://doi.org/10.1016/j.wear.2020.203356.

[12] D. Boing, A.J. De Oliveira, R.B. Schroeter, Evaluation of Wear mechanisms of PVD and CVD coatings deposited on cemented carbide substrates applied to hard turning, Int. J. Adv. Manuf. Technol. 106 (2020) 5441–5451, https://doi.org/10.1007/s00170-020-05000-x.

[13] A. Bjerke, F. Lenrick, A. Hrechuk, K. Slipchenko, R. M'Saoubi, J.M. Andersson, V. Bushlya, On chemical interactions between an inclusion engineered stainless steel (316L) and (Ti,Al)N coated tools during turning, Wear 532-533 (2023) 205093, https://doi.org/10.1016/j.wear.2023.205093.

[14] V.N. Zhitomirsky, Structure and properties of cathodic vacuum arc deposited NbN and NbN-based multi-component and multi-layer coatings, Surf. Coat. Technol. 201 (2007) 6122–6130, https://doi.org/10.1016/j.surfcoat.2006.08.125.

[15] L. Ning, S.C. Veldhuis, K. Yamamoto, Investigation of Wear behavior and Chip formation for cutting tools with Nano-multilayered TiAlCrN/NbN PVD coating, Int. J. Mach. Tools Manuf. 48 (2008) 656–665, https://doi.org/10.1016/j.ijmachtools.2007.10.021.

[16] G.S. Fox-Rabinovich, K. Yamamoto, A.I. Kovalev, S.C. Veldhuis, L. Ning, L. S. Shuster, A. Elfizy, Wear behavior of adaptive Nano-multilayered TiAlCrN/NbN coatings under dry high performance machining conditions, Surf. Coat. Technol. 202 (2008) 2015–2022, https://doi.org/10.1016/j.surfcoat.2007.08.067.

[17] J.A. Ghani, C.H.C. Haron, S.H. Hamdan, A.Y.M. Said, S.H. Tomadi, Failure mode analysis of carbide cutting tools used for machining titanium alloy, Ceram. Int. 39 (2013) 4449–4456, https://doi.org/10.1016/j.ceramint.2012.11.038.

[18] A. Jawaid, S. Sharif, S. Koksal, Evaluation of Wear mechanisms of coated carbide tools when face milling titanium alloy, J. Mater. Process. Technol. 99 (2000) 266–274, https://doi.org/10.1016/S0924-0136(99)00438-0.

[19] Y. Jiang, H. Tian, J. Yin, Y. Yang, G. Zhao, L. Li, Investigation on the machinability of metastable β titanium alloy M28, Int. J. Adv. Manuf. Technol. 121 (2022) 2135–2148, https://doi.org/10.1007/s00170-022-09423-6.

[20] M. Nouari, A. Ginting, Wear characteristics and performance of multi-layer CVD-coated alloyed carbide tool in dry end milling of titanium alloy, Surf. Coat. Technol. 200 (2006) 5663–5676, https://doi.org/10.1016/j.surfcoat.2005.07.063.

[21] D. Lv, B. Wang, J. Hou, H. Wang, R. Bian, Characteristics of Chip formation and its effects on cutting force and tool Wear/damage in milling Ti-25 V-15Cr (Ti40) Beta titanium alloy, Int. J. Adv. Manuf. Technol. 124 (2023) 2279–2288, https://doi.org/10.1007/s00170-022-10637-x.

[22] C. Barbatti, J. Garcia, P. Brito, A.R. Pyzalla, Influence of WC replacement by TiC and (Ta,Nb)C on the oxidation resistance of Co-based cemented carbides, Int. J. Refract. Met. Hard Mater. 27 (2009) 768–776, https://doi.org/10.1016/j.ijrmhm.2008.12.009.

[23] C. Qian, Y. Liu, X. Zhang, K. Li, H. Cheng, J. Zhang, S. Zhang, Oxidation behavior of functionally graded cemented carbides with CoNiFeCr multi-principal-element alloy binder, J. Alloys Compd. 968 (2023) 172069, https://doi.org/10.1016/j.jallcom.2023.172069.

[24] X. Liang, Z. Liu, B. Wang, Physic-chemical analysis for high-temperature tribology of WC-6Co against Ti-6Al-4V by pin-on-disc method, Tribol. Int. 146 (2020) 106242, https://doi.org/10.1016/j.triboint.2020.106242.

[25] G. Zhao, H. Xia, Y. Zhang, L. Li, N. He, H.N. Hansen, Laser-induced oxidation assisted Micro milling of high aspect ratio microgroove on WC-Co cemented carbide, Chin. J. Aeronaut. 34 (2021) 465–475, https://doi.org/10.1016/j.cja.2020.08.011.

[26] J.-E. Ståhl, Metal Cutting – Theories and Models, Seco Tools AB, Lund, 2012.

[27] J.O. Andersson, T. Helander, L. Höglund, P. Shi, B. Sundman, Thermo-Calc & DICTRA, computational tools for materials science, Calphad 26 (2002) 273–312, https://doi.org/10.1016/S0364-5916(02)00037-8.

[28] M.I. Sadik, S. Isakson, The role of PVD coating and coolant nature in Wear development and tool performance in cryogenic and wet milling of Ti-6Al-4V, Wear 386-387 (2017) 204–210, https://doi.org/10.1016/j.wear.2017.02.049.

[29] R. Stylianou, D. Velic, W. Daves, W. Ecker, M. Tkadletz, N. Schalk, C. Czettl, C. Mitterer, Thermal crack formation in TiCN/α-Al_2O_3 bilayer coatings grown by thermal CVD on WC-Co substrates with varied Co content, Surf. Coat. Technol. 392 (2020) 125687, https://doi.org/10.1016/j.surfcoat.2020.125687.

[30] M. Ångqvist, J.M. Rahm, L. Gharaee, P. Erhart, Structurally driven asymmetric miscibility in the phase diagram of W-Ti, Phys. Rev. Mater. 3 (2019) 073605, https://doi.org/10.1103/PhysRevMaterials.3.073605.

[31] P. Olander, J. Heinrichs, Initiation and propagation of tool Wear in turning of titanium alloys – evaluated in successive sliding Wear test, Wear 426-427 (2019) 1658–1666, https://doi.org/10.1016/j.wear.2019.01.077.

[32] S. Saketi, S. Odelros, J. Östby, M. Olsson, Experimental study of Wear mechanisms of cemented carbide in the turning of Ti6Al4V, Materials 12 (2019) 2822, https://doi.org/10.3390/ma12172822.

[33] S. Odelros, B. Kaplan, M. Kritikos, M. Johansson, S. Norgren, Experimental and theoretical study of the microscopic crater wear mechanism in titanium machining, Wear 376 (2017) 115–124, https://doi.org/10.1016/j.wear.2017.01.104.

[34] R. Lindvall, F. Lenrick, R. M'Saoubi, J.E. Ståhl, V. Bushlya, Performance and Wear mechanisms of uncoated cemented carbide cutting tools in Ti6Al4V machining, Wear 477 (2021) 203824, https://doi.org/10.1016/j.wear.2021.203824.

[35] M.I. Sadik, M. Lattemann, J. García, Specific carbide substrate design to enhance tool performance in machining of Ti5553, Procedia CIRP 77 (2018) 598–601, https://doi.org/10.1016/j.procir.2018.08.203.

[36] B. Kaplan, S. Odelros, M. Kritikos, R. Bejjani, S. Norgren, Study of tool Wear and chemical interaction during machining of Ti6Al4V, Int. J. Refract. Met. Hard Mater. 72 (2018) 253–256, https://doi.org/10.1016/j.ijrmhm.2017.12.012.

[37] R. Lindvall, A. Bjerke, A. Salmasi, F. Lenrick, R. M'Saoubi, J.-E. Ståhl, V. Bushlya, Predicting wear mechanisms of ultra-hard tooling in machining Ti6Al4V by diffusion couples and simulation, J. Eur. Ceram. Soc. 43 (2023) 291–303, https://doi.org/10.1016/j.jeurceramsoc.2022.10.005.

[38] S. Zhang, J.F. Li, J.X. Deng, Y.S. Li, Investigation on diffusion wear during high-speed machining Ti-6Al-4V alloy with straight tungsten carbide tools, Int. J. Adv. Manuf. Technol. 44 (2009) 17–25, https://doi.org/10.1007/s00170-008-1803-z.

[39] P. Olander, J. Heinrichs, On Wear of WC-Co cutting inserts in turning of Ti6Al4V – a study of wear surfaces, Tribol. - Mater. Surf. Interfaces (2020) 1–12, https://doi.org/10.1080/17515831.2020.1830251.

[40] M. Latteman, E. Coronel, J. Garcia, and I. Sadik, "Interaction between cemented carbide and Ti6Al4V alloy in cryogenic machining", Proceedings of the 19th Plansee Seminar, Reutte, Austria, vol. (2017) pp. 1–12.

[41] L.S. Sigl, P.A. Mataga, B.J. Dalgleish, R.M. McMeeking, A.G. Evans, On the toughness of brittle materials reinforced with a ductile phase, Acta Metall. 36 (1988) 945–953, https://doi.org/10.1016/0001-6160(88)90149-6.

[42] H.F. Fischmeister, S. Schmauder, L.S. Sigl, Finite element modelling of crack propagation in WC-Co hard metals, Mater. Sci. Eng. A 105-106 (1988) 305–311, https://doi.org/10.1016/0025-5416(88)90711-2.

[43] A. Paul, T. Laurila, V. Vuorinen, S. Divinski, Interdiffusion and the Kirkendall Effect in Binary Systems, 2014, pp. 239–298.

[44] C. Botermans, Study of porosity in uncoated cemented carbide tools during titanium alloy machining, in: Production and Materials Engineering, Lund University, 2023.

[45] D. Jianxin, L. Yousheng, S. Wenlong, Diffusion wear in dry cutting of Ti-6Al-4V with WC/Co carbide tools, Wear 265 (2008) 1776–1783, https://doi.org/10.1016/j.wear.2008.04.024.

[46] A. Delanoë, S. Lay, Evolution of the WC grain shape in WC-Co alloys during sintering: effect of C content, Int. J. Refract. Met. Hard Mater. 27 (2009) 140–148, https://doi.org/10.1016/j.ijrmhm.2008.06.001.

[47] M. Pellan, S. Lay, J.-M. Missiaen, S. Norgren, J. Angseryd, E. Coronel, T. Persson, R. Bordia, Effect of binder composition on WC grain growth in cemented carbides, J. Am. Ceram. Soc. 98 (2015) 3596–3601, https://doi.org/10.1111/jace.13748.

[48] N. Schönberg, On the existence of ternary transition metal oxides, Acta Chem. Scand. 8 (1954) 932–936.

[49] J. Garcia, V.C. Cipres, A. Blomqvist, B. Kaplan, Cemented carbide microstructures: a review, Int. J. Refract. Met. Hard Mater. 80 (2019) 40–68, https://doi.org/10.1016/j.ijrmhm.2018.12.004.

[50] K.P. Mingard, B. Roebuck, J. Marshall, G. Sweetman, Some aspects of the structure of cobalt and nickel binder phases in hardmetals, Acta Mater. 59 (2011) 2277–2290, https://doi.org/10.1016/j.actamat.2010.12.004.

[51] J.H.E. Jeffes, Ellingham Diagrams, in: K.H.J. Buschow, R.W. Cahn, M.C. Flemings, B. Ilschner, E.J. Kramer, S. Mahajan, P. Veyssière (Eds.), Encyclopedia of Materials: Science and Technology, Elsevier, Oxford, 2001, pp. 2751–2753.

[52] A. Graves, A. Salmasi, S.J. Graham, W. Wan, C. Xiao, M. Jackson, H. Larsson, S. Norgren, An experimental and theoretical investigation on Ti-5553/WC-Co(6%) chemical interactions during machining and in diffusion couples, Wear 516-517 (2023) 204604, https://doi.org/10.1016/j.wear.2022.204604.

[53] H. Nakajima, M. Koiwa, Diffusion in titanium, ISIJ Int. 31 (1991) 757–766.

[54] F. Lofaj, Y.S. Kaganovskii, Kinetics of WC-Co oxidation accompanied by swelling, J. Mater. Sci. 30 (1995) 1811–1817, https://doi.org/10.1007/BF00351615.

[55] J.A. Bustnes, D. Sichen, S. Seetharaman, Kinetic studies of reduction of CoO and $CoWO_4$ by hydrogen, Metall. Mater. Trans. B Process Metall. Mater. Process. Sci. 26 (1995) 547–552, https://doi.org/10.1007/BF02653872.

[56] V. Bushlya, F. Lenrick, J.-E. Ståhl, R. M'Saoubi, Influence of oxygen on the tool wear in machining, CIRP Ann. Manuf. Technol. 67 (2018) 79–82, https://doi.org/10.1016/j.cirp.2018.03.011.

Paper VI

Journal of the European Ceramic Society 43 (2023) 291–303

Contents lists available at ScienceDirect

Journal of the European Ceramic Society

journal homepage: www.elsevier.com/locate/jeurceramsoc

Predicting wear mechanisms of ultra-hard tooling in machining Ti6Al4V by diffusion couples and simulation

Rebecka Lindvall [a,*], Axel Bjerke [a], Armin Salmasi [b], Filip Lenrick [a], Rachid M'Saoubi [a,c], Jan-Eric Ståhl [a], Volodymyr Bushlya [a]

[a] *Production and Materials Engineering, LTH, Lund University, 221 00, Lund, Sweden*
[b] *Unit of Structures, Department of Materials Science and Engineering, KTH, 100 44 Stockholm, Sweden*
[c] *R&D Materials and Technology Development, Seco Tools AB, 737 82 Fagersta, Sweden*

ARTICLE INFO

Keywords:
Diffusion couple
PCD
pcBN
Cemented carbide
Ti6Al4V

ABSTRACT

Conventional cemented carbide is recommended for machining Ti6Al4V. However, polycrystalline diamond (PCD) and polycrystalline cubic boron nitride (pcBN) also show promise. Demands for higher productivity accelerate diffusional dissolution and chemically driven wear mechanisms in these tool materials. This study investigates active wear mechanisms by studying the interactions between Ti6Al4V and PCD, pcBN, and cemented carbide tools in diffusion couples at temperatures from 900° to 1300°C. All tool materials suffered from diffusion to varying degrees, and different chemical reactions occurred. Titanium carbide with minor vanadium alloying (Ti,V)C reaction products act as diffusion barriers when using PCD and cemented carbide, while the reaction products acting as diffusion barrier in pcBN is $(Ti,V)B_2$. The presence of Mo and W in binder sites of pcBN reduces diffusional dissolution of cBN. Diffusion simulations agreed well with microscopy investigations and were enabled by the known temperature and pressure conditions of the static diffusion couples.

1. Introduction

The recommended tool material for machining the most common titanium alloy Ti6Al4V (Ti-64) at low/medium cutting speeds is uncoated cemented carbide [1]. However, polycrystalline diamond (PCD) and polycrystalline cubic boron nitride (pcBN) have shown promise as they can operate at higher cutting speeds [2–5]. But higher machining rates may shift the balance between wear mechanisms, accelerating diffusional dissolution and chemically driven wear mechanisms [6]. Understanding the wear mechanisms is thus crucial to be able to predict productivity.

When studying wear mechanisms in as–worn tools, only small volumes of reaction products are present, and these may be difficult to detect even with advanced microscopy techniques. In addition, workpiece material chip flow on the tool surface may have resulted in partial or even complete removal of reaction products. Uncertainties regarding the actual contact pressure and the temperature gradient within the cutting zone also make it challenging to use thermodynamic and diffusion models to verify wear mechanisms computationally.

By contrast, diffusion couple experiments are performed at fixed temperature and pressure conditions over a given period, and reaction products remain at the interface due to the static conditions. The volume of these reaction products tends to be larger than in as-worn tools, and are thus easier to detect and characterize. However, the lack of dynamics distinguishes diffusion couples from the cutting tools used in machining.

The chemical reactions taking place in diffusion couple experiments provide invaluable information about chemical wear during cutting. This data can be used to validate thermodynamic and diffusion models. Such an approach was used in previous work by Vleugels et al. in machining steel with ceramic tooling [7–9]. Reliable models can aid in predicting wear mechanisms in similar material systems without costly and time–consuming machining trials, sample preparation, and microscopy [10].

Previous studies of diffusion couples based on titanium alloys have largely combined $\alpha + \beta$ titanium alloys such as Ti-64, Ti-54 M, and Ti-6246 with uncoated cemented carbide [11–17]. At high machining rates, degradation of cemented carbide is governed by outward carbon diffusion of surface WC grains while residual tungsten remains at the interface [18–20]. The same phenomenon is observed in diffusion couples [11–16,21]. Simultaneously, outward diffusion of Co binder

---

* Corresponding author.
E-mail address: rebecka.lindvall@iprod.lth.se (R. Lindvall).

https://doi.org/10.1016/j.jeurceramsoc.2022.10.005
Received 28 June 2022; Received in revised form 26 September 2022; Accepted 2 October 2022

increases the risk of grain pluck-out [11,12,16]. In-operando formation of TiC, intermetallic TiCo$_2$, and intermetallic Co$_3$W creates tool protection layers that retard further WC dissolution [13–18,21–23].

Ultra-hard tool materials including pcBN and PCD have been combined with Fe- or Ni-based alloys in diffusion couples [24–27], but no similar published work was found for titanium alloys. In machining titanium alloys with PCD, wear mechanisms based on graphitization, partial oxidation of diamond, and carbon diffusion are responsible for tool degradation [5,28–31]. At the same time, in-operando formation of TiC, (Ti,V)C, and intermetallic Co$_3$W$_3$C that is facilitated by the liquid Co binder retards dissolution of carbon [6,22,29,31]. For pcBN tools, the reported wear mechanism is outward diffusion of B and N, which is retarded by in-operando formations of TiB$_2$ [32,33], (Ti,V)B$_2$, and (Ti,V,Cr)B$_2$ where the latter is found in metallic binder sites [31]. TiN has also been identified as a potential reaction product [33].

This study aims to employ the diffusion couple method on Ti-64 combined with PCD, pcBN, and cemented carbide tools. Previous studies involving diffusion couples have been performed at ambient pressures, which are different from actual machining conditions. In this study, known process conditions under high pressure–high temperature (HP-HT) conditions at temperatures from 900° to 1300°C facilitate tracking of the change and intensity of active wear mechanisms. In addition, the results are compared to diffusion simulations using DICTRA software for the same controlled conditions as the diffusion couples.

2. Materials and methods

The titanium alloy used in the diffusion couples was mill-annealed α + β Ti-64 alloy with 31 HRC hardness. Its composition is shown in Table 1. Its microstructure is illustrated in Fig. 1a after etching with Kroll's reagent.

Tools were supplied by Seco Tools AB in ISO RNGN060300 geometry. The PCD and pcBN grades are commercially available and were sintered on cemented carbide substrate. The PCD grade had a 12% Co binder and multi-modal diamond grain size distribution of 3–15 µm. The pcBN was a high cBN content grade with 15% metallic binder consisting of several phases that contain mainly Mo, Co, Ni, W, Cr, Ti, and Al. The cemented carbide was medium grain sized WC with 15% Co binder. The microstructures of PCD, pcBN, and cemented carbide are shown in Fig. 1b–d respectively.

2.1. Preparation of diffusion couples

Diffusion couples were prepared by combining a Ti-64 cylindrical capsule with a tool material. The HP-HT rig was based on an HPAT–30 toroid-type high-pressure apparatus that ensured uniform heating across the tool–titanium interface. The process includes rapid heating (250 °C/s), and instant quenching. For a more detailed description, see the study by Olsson et al. [34]. Five PCD and cemented carbide couples were treated at temperatures of 900–1300 °C in 100 °C steps, while four pcBN couples were treated at 1000–1300 °C. The couples with PCD and cemented carbide were subjected to 3 GPa pressure while those with pcBN were subjected to 2.5 GPa, and all diffusion couples were exposed to a holding time of 10 min each. The different pressures were selected to avoid graphitization of diamond [35] and to suppress cBN-to-hBN transformation [36].

After HP-HT treatment at given temperatures, pressure transfer media, graphite heater and hBN gasket were removed from the Ti-64 and tool capsule. The remaining diffusion couple was then cross-sectioned using wire electrical discharge machining (WireEDM). The cross-section was hot-mounted in a conductive resin, ground, polished, and ultrasonically cleaned in ethanol. An example of such cross-section for a PCD with substrate cemented carbide and Ti-64 diffusion couple is illustrated in (Fig. 2).

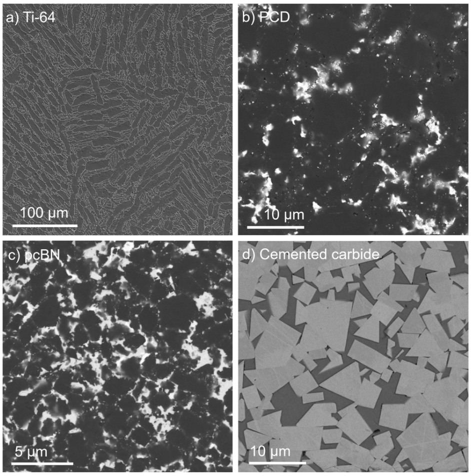

Fig. 1. Microstructure of (a) Ti-64, (b) PCD, (c) pcBN, and (d) cemented carbide.

2.2. Microscopy methods

The cross-sectioned diffusion couples were studied in a scanning electron microscope (SEM) Tescan Mira3 FEG–SEM equipped with an Oxford X-ray energy-dispersive spectroscopy (XEDS) detector and electron backscatter diffraction (EBSD) detector using 15 kV and 20 kV respectively. The tool and titanium alloy interfaces were investigated using an X-ray diffractometer (XRD) STOE Darmstadt with Cu Kα source. The interface was shielded from the bulk material by creating a slit of amorphous silica glass fixed on the diffusion couple.

Selected locations on the interface were subjected to focused ion beam (FIB) lift-out procedure using a combined FIB–SEM FEI Nova NanoLab 600. The lamellae were studied in a transmission electron

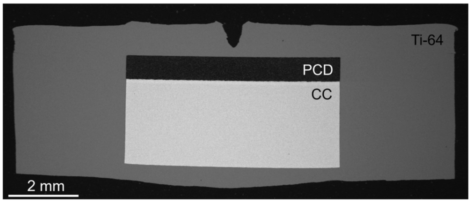

Fig. 2. Cross-section of diffusion couple after HP-HT treatment.

Table 1
Elemental composition of Ti-64 workpiece material.

Element	Fe	C	N	H	O	Y	Al	V	Ti
wt%	0.17	0.021	0.006	0.0013	0.141	< 0.005	6.03	4.05	Balance

microscope (TEM) JEOL 3000 F Field Emission Electron Microscope equipped with an Oxford XEDS detector using 300 kV. Selected area electron diffraction (SAED) was also used to verify reaction products.

2.3. Modeling background and setup

Thermodynamic calculations using Thermo–Calc software [37] provided the basis for setting up the diffusion calculations. They also provided the necessary thermodynamic and kinetic data for the diffusion simulations with the DICTRA software. The DICTRA homogenization model [38,39] was used for 1D simulations of the diffusion-reaction process during HP-HT treatment of the diffusion couples.

All diffusion processes were assumed to occur only in fcc and bcc solid solution phases, though all stable phases that affect the process are considered in the thermodynamics. From a computational point of view, the multiphase problem is transformed into a single-phase problem through a coarse-graining homogenization procedure. The primary expression for the flux of element k in each phase α (α is not to be confused with the hcp α-phase in Ti) is

$$J_k^\alpha = -M_k^\alpha \bullet c_k^\alpha \bullet \nabla \mu_k^\alpha$$

where M_k^α, c_k^α, and μ_k^α respectively represent the mobility, concentration, and chemical potential of element *k* in phase *α*. The permeability of phase *α* in relation to element *k* is specified by $\Gamma_k^\alpha = M_k^\alpha \bullet c_k^\alpha$. The coarse-graining procedure assumes that the system is locally fully equilibrated, so that the chemical potential of each constituent is the same in all locally stable phases. Local phase information such as fractions and compositions were also obtained from the premise of local equilibration set by the overall local composition, temperature, and pressure. The effective permeability of the multiphase mixture is given by

$$\Gamma_k^* = \sum_\Phi f^\Phi \Gamma_k^\Phi$$

where f^Φ is the local volume fraction of the *Φ* phase, and the flux through the multiphase mixture is

$$J_k = -\Gamma_k^* \bullet \nabla \mu_k^{l.eq.}$$

where the *l.eq.* indicates the assumption of a locally equilibrated structure. The implementation details of the homogenization model are discussed in [38,39].

Minor elements were excluded from the model to improve its clarity. The simulations therefore considered only diffusion reaction between the Ti alloy and certain elements of interest in the tool materials. The compositions used in the simulations are listed in Table 2. All simulations were done using the TCFE9 thermodynamic database [40] and the MOBFE5 mobility database [41]. The diffusion taking place during heating and cooling was ignored.

To simulate each diffusion couple, the composition on one side of the domain was set to the simplified composition of the studied cutting tool. On the opposite side, the composition was set to that of Ti-64, with a sharp step in between. In simulations of PCD and pcBN, the left-hand side boundary condition was set to the appropriate activity boundary condition representing the activity of cemented carbide. In all simulations, boundary conditions were applied individually for each element. The simulated time was 10 min, which is the same as the holding time of the diffusion couples.

To stabilize the metastable diamond in simulations of the PCD- based diffusion couples, graphite must be removed from the thermodynamic system. However, graphitization was observed in the experiment, particularly at highest temperature. Unfortunately, thermodynamic calculations of a system containing both metastable diamond and stable graphite are impossible. Therefore, it is assumed that the diamond in PCD is stable at all conditions.

It is also necessary to remove the nitrogen gas from the thermodynamic system to stabilize the metastable cBN in the pcBN- based diffusion couple. It is thus impossible to control the partial pressure of nitrogen gas and degasification. However, given that no evidence of gas formation was observed in the experimental samples, this approach is justified.

3. Results and discussion

3.1. PCD and Ti-64

The interfaces of PCD and Ti-64 at the selected temperatures are shown in Fig. 3. The images were obtained with backscatter electron (BSE) detector and show the effect of the Z-contrast mechanism (average atomic number contrast). The image of the sample exposed to 1300 °C was also obtained with secondary electron (SE) detector to visualize its topography.

At 900–1200 °C (Fig. 3a–d), there are distinct 5–10 μm wide gaps between the PCD and Ti-64. The different thermal expansion coefficients of PCD and Ti-64 affect the size of the gap at ambient pressures. However, this gap is to a greater degree controlled by a difference in compressibility under HP-HT conditions. The compressibility is characterized as the inverse of bulk modulus, which is 432^{-1} GPa^{-1} for diamond [42], 290^{-1}–383^{-1} GPa^{-1} for cBN [43], 390^{-1} GPa^{-1} for WC [44], and only 116^{-1}–148^{-1} GPa^{-1} for Ti-64 [45]. Ti-64 thus expands nearly three times more than the tool materials on decompression after HP-HT treatment and therefore tends to de-bond.

At 900–1000 °C, there are no visual signs of a chemical interaction (Fig. 3a–b). However, a reaction occurs at 1100 °C and is visible as a

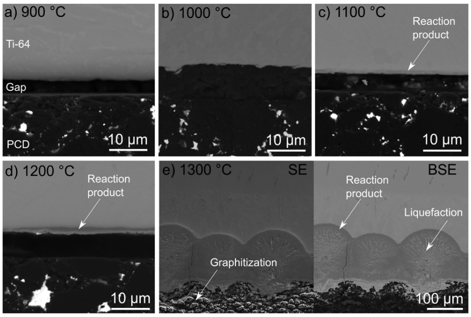

Fig. 3. Overview SEM-BSE images of PCD and Ti-64 interface at 900–1300 °C, with arrows pointing to reaction products, graphitization, and liquefaction of some phase. The 1300 °C sample also has an SE image for topography contrast.

Table 2
Simulated composition of Ti alloy and tool materials in wt%.

	Ti	Al	V	W	C	B	N	Co
Ti-64	Balance	6	4	$4 \cdot 10^{-4}$	$2.6 \cdot 10^{-5}$	–	–	$1 \cdot 10^{-4}$
PCD	$3 \cdot 10^{-4}$	$2 \cdot 10^{-4}$	$3 \cdot 10^{-4}$	$1 \cdot 10^{-3}$	Balance	–	–	35.5
pcBN	$3 \cdot 10^{-4}$	$2 \cdot 10^{-4}$	$3 \cdot 10^{-4}$	$1 \cdot 10^{-3}$	$7 \cdot 10^{-5}$	28.5	Balance	34.5
Cemented carbide	$5 \cdot 10^{-5}$	$3 \cdot 10^{-5}$	$6 \cdot 10^{-5}$	Balance	5.1	–	–	15.0

layer with dark Z-contrast. It becomes thicker (approximately 2 μm) at 1200 °C (Fig. 3c–d, marked by arrows). At 1300 °C the formation of a massive reaction product with a spheroid shape and 100–200 μm thickness creates strong enough bonding that suppresses gap formation (Fig. 3e).

Studying the interface region of the 1300 °C sample (Fig. 3e) shows that several events are taking place. The use of SE mode demonstrates partial graphitization of individual diamond grains, as seen by strong removal of material at the grain boundaries during polishing, indicating that the inverse diamond-to-graphite transformation could be an active wear mechanism even at 3 GPa pressure, which is representative of the cutting process. Further, within the spheroid-shaped reaction product, distinct dendritic morphology indicates probable presence of a liquid during HP-HT treatment. The Ti alloy above the reaction layer has an approximately 150 μm thick brighter Z-contrast region where the reactions at the interface caused substantial alloying of original Ti-64.

The extreme reaction between tool and Ti alloy after treatment at 1300 °C is unlikely to occur during machining to the same extent. Temperatures as high as this are not expected at the PCD–Ti-64 interface due to the high thermal conductivity of the PCD tool. Actual cutting temperatures of 1150 ± 50 °C were reported for PCD machining of Ti-64 [31], though partial graphitization should not be excluded [29]. Therefore, in-depth investigation was focused on the diffusion couple exposed to 1200 °C. Initial SEM-XEDS analysis of that interface is shown in Fig. 4. The darker Z-contrast streak (Fig. 4a) on the upper side of the gap has presence of Ti, V, and C (Fig. 4b, d), which indicates formation of TiC or more likely (Ti,V)C. Aluminum is not present within that reaction layer (Fig. 4c), thus demonstrating its absence as an interactive element.

Other features on the interface are frequent W-containing inclusions (Fig. 4e). This presence of W is related to sintering of PCD, as W-Co-C eutectic is infiltrated into the diamond powder bed and forms the typical by-product Co_3W_3C [30]. Diffusional dissolution of diamond grains would expose the W-containing phase to the Ti-64 interface, where it remains as metallic W has shown poor solubility in Ti [46].

Further TEM-based analysis of the same sample is summarized in Fig. 5, which is focused on the interface of the reaction product and the Ti alloy. The STEM HAADF image (Fig. 5a) displays needle-shaped Ti-grains and reveals a crack in the reaction layer. The XEDS map (Fig. 5c) and line scan (Fig. 5l) show a stronger α-stabilizing Al presence in the Ti region (Fig. 5b,j, region iv), and SAED confirms that the near-interface Ti is of α-phase (Fig. 5f).

The reaction layer contains carbon (Fig. 5d, l, region iii), but the apparent concentration of carbon is disturbed by the contaminated gap. The presence of carbon indicates TiC, as was confirmed by SAED (Fig. 5i). Vanadium is present in the same area as Ti (Fig. 5b, k), and therefore titanium carbide has minor V alloying, eventually creating the reaction product (Ti,V)C. Co is present in between TiC grains (Fig. 5e), which indicates its outward diffusion.

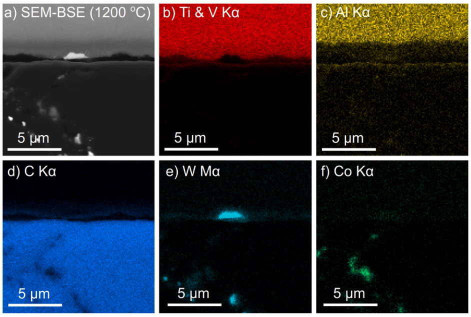

Fig. 4. PCD and Ti-64 interface after treatment at 1200 °C including (a) SEM-BSE image and (b–f) related XEDS maps.

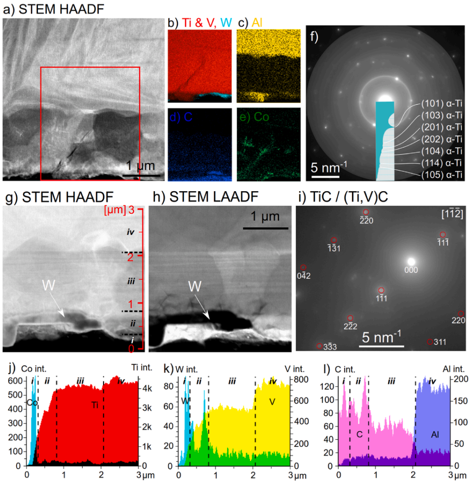

Fig. 5. PCD and Ti-64 interface after treatment at 1200 °C. (a) STEM HAADF image of reaction layer with (b–e) related XEDS maps. SAED showing diffraction pattern of (f) α-Ti and (i) TiC or (Ti,V)C. (g) STEM HAADF and (h) STEM LAADF images of another interface region with (j–l) corresponding XEDS line scan.

Using high and low angle annular dark field (HAADF and LAADF) modes exposed a Z-contrast mechanism and crystal structure contrast, respectively, on another interface region (Fig. 5g–h). Individual TiC grains were exposed, as well as the accumulation of a heavier element than Ti bordering the gap, based on the Z-contrast. XEDS line scan data (Fig. 5j–l) reveal the presence of Co and W at that border (region i–ii). Even under HP-HT treatment, W shows its limited dissolution in Ti [46] and therefore remains on the diamond side of the TiC reaction layer.

Despite the extreme reaction of the diffusion couple exposed to 1300 °C, some information on factors that control the reaction rate can be determined. The investigation of this sample was based on SEM–XEDS and EBSD and is summarized in Fig. 6. The SEM–BSE image (Fig. 6a) shows the partially graphitized diamond grains, the spheroid-shaped reaction layer with innate dendritic structure, and the alloyed Ti-64. Regions analyzed using EBSD and XEDS are highlighted by red boxes.

Overview XEDS maps indicate formation of TiC or (Ti,V)C in the reaction layer (Fig. 6b, d), while the dendritic structure seems to contain at least Co (Fig. 6f). The region between the presumed TiC layer and the partly graphitized diamond grains shows the presence of W and Co (Fig. 6e–f), which may be η-phase Co_3W_3C or Co_6W_6C. Aluminum is still not an interactive element even at this temperature (Fig. 6c).

Additional XEDS analysis captures the presumed TiC layer and the diffusionally alloyed Ti-64. The SEM-BSE image (Fig. 6g) shows the columnar grown grains of presumed TiC and a brighter Z-contrast region marked by an arrow. XEDS maps indeed confirm TiC or (Ti,V)C presence in the reaction layer (Fig. 6h, i, l). Co is present in between these grains (Fig. 6k). Co is also concentrated in the bright Z-contrast region in the Ti alloy, while the presence of Ti, V, and Al is reduced. Instead, the surrounding phase has higher Al concentration (Fig. 6j).

EBSD analysis of the reaction layer bordering the Al and Co alloyed Ti-64 (Fig. 6m–n) yielded new information on reaction products and

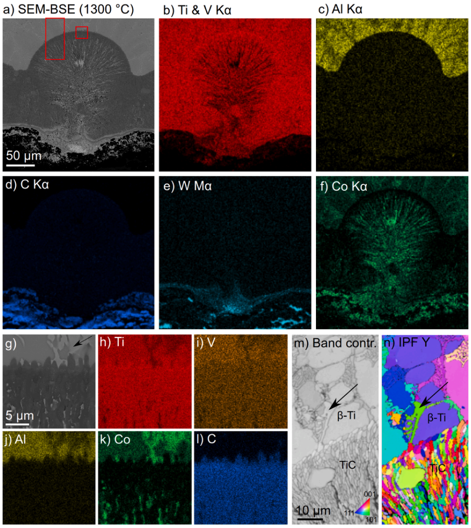

Fig. 6. PCD and Ti-64 interface after treatment at 1300 °C. (a) SEM-BSE image with (b–f) related XEDS maps. (g) SEM-BSE image of TiC grains bordering doped Ti alloy with (h–l) related XEDS maps. EBSD analysis with (m) band contrast and (n) inverse pole figure (IPF).

grain size. As expected, EBSD correlated TiC or (Ti,V)C reaction products with the columnar grains and also demonstrated their polycrystalline structure. XEDS demonstrated Co presence in the dendritic structure between TiC grains (Fig. 6f, k), yet neither hcp nor fcc Co was identified by using EBSD. Hence the Co must consist of some other phase.

The formation of a liquid may explain the dendritic morphology. A liquid phase would greatly increase the transport of carbon from parts of the diamond that are stable or partly graphitized to the TiC–Ti interface. That would explain the massive thickness of the TiC layer. In addition, the liquid phase containing Co reaches through the TiC layer and alloys the Ti-64.

The alloyed Ti-64 seems to consist of two phases with individual Z-contrasts. The brighter Z-contrast region marked by arrows (Fig. 6g) has smaller grains (Fig. 6m) than those in the darker Z-contrast. Quantification of elements in the brighter Z-contrast region revealed 50:40:5 at % distribution of Ti:Co:Al and traces of C and V. These concentrations point to the formation of intermetallic (Ti,Al)Co according to the ternary phase diagram of the Ti-Co-Al system [47]. The surrounding darker Z-contrast has double the Al content with a distribution of 65:15:12 at% of Ti:Co:Al while V is at 4 at%. This distribution of elements alloys Ti to its β-phase [47], which was the phase identified in EBSD.

Fig. 7 shows the two-phase region of diamond and Co in the isopleth for PCD. There is a eutectic transformation at 1250 ℃. Therefore, at 1300 ℃, the Co binder should melt and the diamond in PCD should transform into graphite. Consequently, more C can be dissolved into the Co (fcc) and melt with increasing temperatures. However, the C content needed for formation of TiC is less affected by the increase in temperature. This increase in the ability to transport C may explain the significant increase in TiC formation at the interface (Fig. 6a).

Fig. 8a shows the permeability of C and Co from PCD into Ti-64 at 1000 °C, 1200 °C, and 1300 °C. It shows the temperature dependence and the decrease of permeability with distance. The permeability of Co is expected to be less than that of C due to the lower mobility. However,

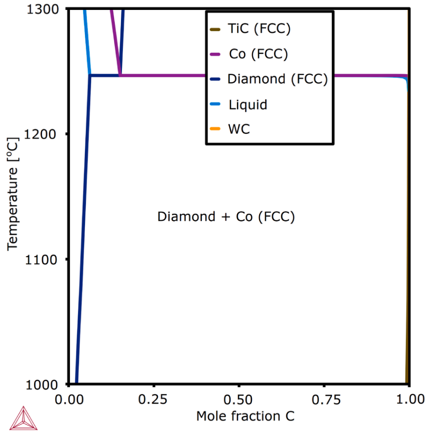

Fig. 7. Isopleth of PCD showing the two-phase region of diamond and Co.

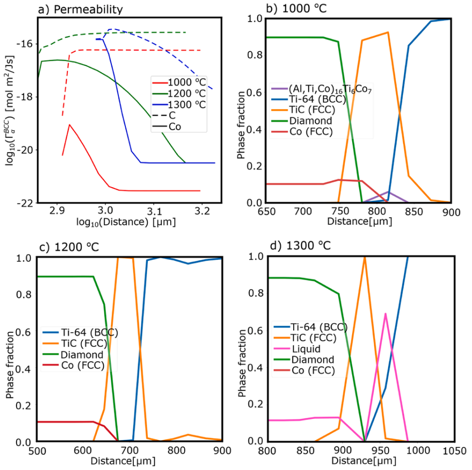

Fig. 8. (a) Permeabilities of C and Co in Ti-64 for PCD at 1000 °C, 1200 °C, and 1300 °C after 10 min; DICTRA simulations of PCD and Ti-64 diffusion couple at (b) 1000 °C, (c) 1200 °C, and (d) 1300 °C.

the higher solubility of Co compared to C in Ti-64 makes the mobility of Co and C surprisingly similar at higher temperatures and short distances.

Fig. 8b–d show simulated results of the diffusion and chemical reactions taking place at the PCD and Ti-64 interface at 1000 °C, 1200 °C, and 1300 °C. At 1000 °C (Fig. 8b), the simulated reaction layer consists mainly of TiC with minor presence of intermetallic $(Al,Ti,Co)_{16}Ti_6Co_7$. This intermetallic phase is absent in simulations at higher temperatures. However, a similar compositional phase (Ti,Al)Co was detected in the diffusion couple exposed to 1300 °C (Fig. 6).

The simulated reaction layer thickness at 1000 °C is around 100 µm (Fig. 8b) and consists of TiC, but no such reaction was detected on the actual diffusion couple. The simulated reaction layer grows to about 150 µm in case of 1200 °C (Fig. 8c), while the actual reaction layer thickness in the diffusion couple exposed to 1200 °C is approximately 2 μm. The simulated reaction layer at 1200 °C consists solely of TiC and smaller TiC precipitates in the Ti-64. This precipitation may be due to the diffusion of C before reaching the solubility limit, but no such TiC precipitates were found in the diffusion couple. However, such precipitates have been found in the adhered Ti alloy in a crater region of a cemented carbide tool after turning Ti-64 [18].

At 1300 ℃ (Fig. 8d), the simulated reaction layer is similar to that at lower temperatures and includes a TiC reaction product, but its size is comparable to that in the actual diffusion couple. The simulation shows that the Co binder is in the liquid state, which is in line with the suggested phenomena occurring in diffusion couples that cause the dendritic morphology (Fig. 6a). In addition, the high C activity in diamond should result in the melting of the Co binder within the cemented carbide substrate.

3.2. pcBN and Ti-64

The interfaces of pcBN and Ti-64 at the selected temperatures are shown in Fig. 9. Reaction products are present at all temperatures (marked by arrows) and the thickness increases with temperature. A thin layer already occurs at 1000 °C (Fig. 9a) instead of 1100 °C as for PCD, showing that pcBN has a higher dissolution rate than PCD. This observation applies to all the selected temperatures up to 1200 °C after which PCD graphitizes and thus exceeds the wear rate of pcBN. The thickness of pcBN reaction products reaches 3 μm after treatment at 1300 °C (Fig. 9d).

Diffusional loss of B and N into the Ti-64 induces formation of reaction products, but also alloys the Ti-64 since nitrogen is an interstitial α-stabilizer. Higher temperatures increase the diffusional loss and increase the α-phase distribution. This phenomenon is visible as the α- and β-phases of Ti-64 have similar grain size and shape at 1000 °C (Fig. 9a), but the α-phase becomes needle-shaped at 1100–1300 °C and dominates the interface region (Fig. 9b–d).

Increased diffusional loss of cBN also leads to accumulation of binder material at the interface. That is due to the limited solubility of some elements of the binder in Ti-64 and the reaction layer. This phenomenon becomes prominent at 1200 °C and at 1300 °C. The accumulation of binder elements may locally reduce B and N diffusion, as demonstrated by the wavy interface (Fig. 9d).

This interface region with binder separating BN grains from the reaction layer was studied using SEM–XEDS maps and line scans (Fig. 10) of the sample exposed to 1300 °C. As in the case with PCD, both Ti and V are present bordering the binder (Fig. 10b–c, n, region i–iii). However, Al is present only up to the reaction layer, although it is also present in the binder (Fig. 10d, n, region i). Other binder elements include Ni, Co, and Cr (Fig. 10e, i–j, region iv). Mo and W are not typical binder elements but are present in the same regions (Fig. 10k–l, region iv). Mo originates from the sintering cell during pcBN production [48] and W originates from the tool substrate. The XEDS line scan shows higher Mo and W concentrations (Fig. 10p) compared to Ni, Co, and Cr (Fig. 10q) at the binder interface (region iv), and they are thus important diffusional barriers.

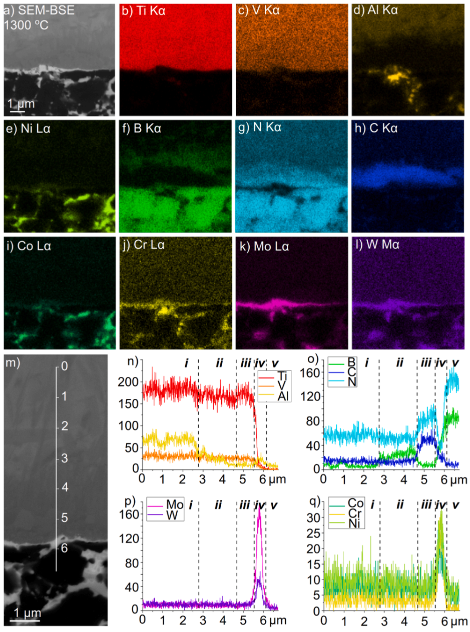

Fig. 10. pcBN and Ti-64 interface after treatment at 1300 °C. (a) SEM–BSE image with (b–l) related XEDS maps, (m) SEM–BSE image with (n–q) corresponding XEDS line scans.

Above the binder layer, reaction products are formed in two sublayers. The first layer, which borders the binder material, is rich in C and N (Fig. 10g–h, o, region iii). The N is sourced from diffusional dissolution of cBN, while the C originates from the cemented carbide substrate and has moved through the binder. Due to the presence of Ti in the same region, it is likely that Ti(C,N) has formed. The other layer bordering the Ti alloy contains Ti, V, and B. Thus, it is likely that formation of Ti and V boride has occurred (Fig. 10 f, o, region ii). The above Ti alloy is presumed to be in its hcp α-phase as the Al and N are α-stabilizers.

The reaction layers were further studied using TEM and EBSD techniques. Fig. 11 summarizes the TEM analysis. The STEM LAADF

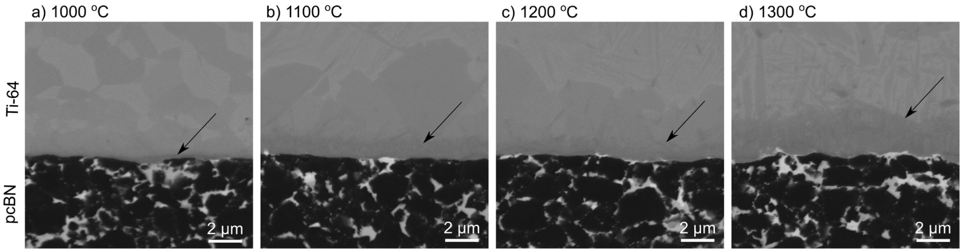

Fig. 9. Overview SEM–BSE images of pcBN and Ti-64 interface at 1000–1300 °C, with arrows pointing to reaction product layers.

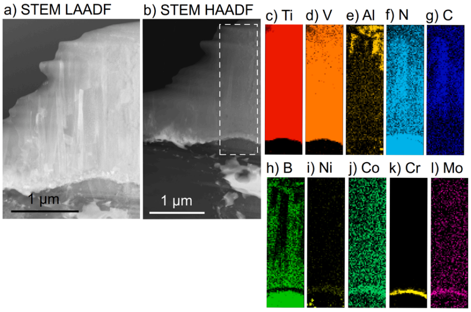

Fig. 11. pcBN and Ti-64 interface after treatment at 1300 °C with (a) STEM LAADF image, (b) STEM HAADF image and related (c–l) XEDS maps.

image of the reaction layer (Fig. 11a) exposes contrast differences that indicate long and thin grains. Thus the reaction products may be epitaxially grown, similar to the findings of Ding et al. [49]. The STEM HAADF image (Fig. 11b) displays the Z-contrast mechanism. Specifically, the binder region to the left appears diffuse and occurs repeatedly across the interface. These phenomena point to a miscibility gap between the binder elements present and Ti alloy. From SEM–XEDS analysis, it is known that Mo and W as well as Cr and Al are present. The other binder elements, Ni and Co, have diffused into the Ti alloy. This loss may increase the risk of adhesive wear as cBN grains become less attached to the bulk.

The dashed rectangle in the STEM HAADF image (Fig. 11b) shows the region analyzed by the XEDS maps and captures binder material atop a cBN grain. As found previously, Ti and V are present in the reaction layer all the way down to the binder layer (Fig. 11c, d), while Al remains a non-interactive element (Fig. 11e). Enrichment of N and C is present in the same regions in the reaction layer (Fig. 11f–g), and they have a columnar shape as indicated by STEM LAADF (Fig. 11a). Surrounding the enrichment, B is present (Fig. 11 h), which in combination with Ti and V may have formed a boride phase. As expected, the cBN grain shows strong B and N concentration, while only N is present in the binder layer at the interface. Ni, Co, Cr, and Mo (Fig. 11i–l) are also present in the binder layer, but Cr has a significant concentration, pointing to formation of a chromium nitride phase.

The final analysis steps of this diffusion couple involve EBSD and SAED, which are presented in Fig. 12. The band contrast image (Fig. 12a) shows the needle-shaped grains of the Ti alloy. The phase contrast (Fig. 12b) demonstrates its composition of α-Ti with a P63/mmc (194) space group. The reaction layer is polycrystalline and consists of Co and Ni in a Fm-3 m (225) space group, as is Ti(C,N) with the same space group. The presence of Mo, W, and Cr with Im-3 m (229) space group were also registered but are present only to a minor degree. This correlates well with border residues on the interface.

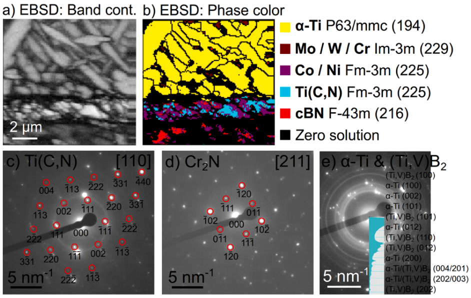

Fig. 12. pcBN and Ti-64 interface after treatment at 1300 °C with EBSD showing (a) band contrast and (b) phase contrast. SAED of (c) Ti(C,N), (d) Cr_2N, and (e) α–Ti and $(Ti,V)B_2$.

More phases were verified using SAED. The presence of N and C in the reaction layer is as expected Ti(C,N) (Fig. 12c). The layer closest to cBN with strong presence of Cr and N in Fig. 11b has a suitable fit to Cr_2N with P-31 m (162) space group. This reaction product originates from excess N and residues of Cr from the binder, and is an artifact that forms under static conditions as this phase has not been identified in as-worn tools [31].

Surprisingly, although XEDS indicated a strong boron presence, EBSD did not return any boride phase (Fig. 11 h). This may be due to a fine grain size. However, when using SAED on the reaction layer neighboring the Ti(C,N) grains, diffraction patterns returned a mix of α-Ti with P63/mmc (194) space group and $(Ti,V)B_2$ with P6/mmm (191) space group. SEM–XEDS data demonstrated a boron-rich particle within the Ti alloy above the reaction layer, which indicates that the $(Ti,V)B_2$ layer may be saturated.

The extremely narrow stability range of the pcBN-Co two-phase region is shown in the calculated isopleth in Fig. 13. Co was selected as it is the main constituent in the pcBN binder. The narrow stability range is due to the limited solubility of B and N in Co, with BN being stochiometric. Hence, AlN and $(V,Co)_2B$ or liquid at high temperatures will form if B or N leaves the tool. This narrow two-phase region bordering non-diffuse phases creates numerical difficulties for the DICTRA simulation, since these phases immediately stabilize at the pcBN and Ti-64 interface. This forces the calculations to stall at infinitely small time steps. DICTRA simulations are thus inconclusive in this case.

However, even simulation results corresponding to the very beginning of the diffusion couple experiment can offer insights into the reaction mechanism. With an entirely non-diffuse reaction layer, it can be expected that the layer will remain roughly unchanged through the rest of the simulation. However, diffusion reactions can still happen on the sides of the layer.

Calculated permeabilities of B, N, and Co in Ti-64 (bcc) are shown in Fig. 14a. The right side of the plot corresponds to the permeabilities of components in an unchanged Ti-64. In contrast, the left side shows the effect of composition change on the permeabilities imposed by diffusion.

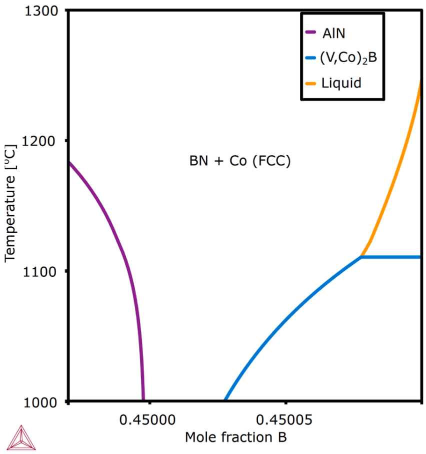

Fig. 13. Isopleth of pcBN showing the two-phase region of BN and Co.

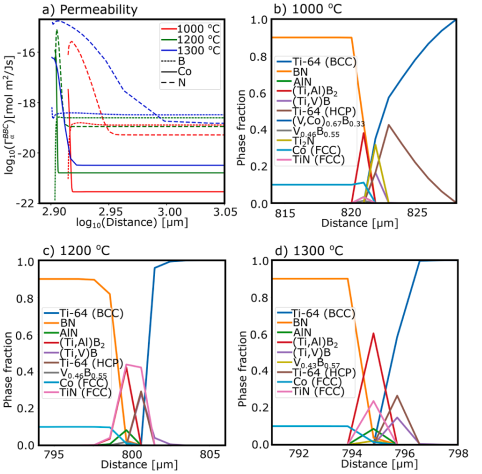

Fig. 14. (a) Permeabilities of B, Co, and N in Ti-64 for pcBN at 1000 °C, 1200 °C, and 1300 °C after 10 min; DICTRA simulations of pcBN and Ti-64 diffusion couple at (b) 1000 °C, (c) 1200 °C, and (d) 1300 °C.

In the unchanged Ti-64, the permeability of B is the largest at all temperatures. The permeability of N comes second, and Co has the lowest permeability. However, the permeabilities of B and N are temperature dependent. It seems that diffusion of B has the fastest rate in unchanged Ti-64, while the high concentration of N results in the highest permeability at the interface.

At 1300 °C, the high permeability of B results in the instantaneous formation of non-diffuse borides. The high fraction of non-diffuse boride phases reduces the fraction of the available diffusion matrix and limits the diffusion of N. Consequently, the impingement of N results in the precipitation of nitrides in the reaction layer. This could explain why (Ti, V)B_2 covers the Ti(C,N) and Cr_2N layers (Fig. 10) in the diffusion couple.

Still, given the low solubility of B in Ti-64, borides should form in the reaction layer instantaneously. The simulated reaction taking place at 1000 °C is shown in Fig. 14b. Unlike with unchanged Ti-64, N has the largest permeability which results in the formation of hcp Ti in Ti-64. When B and N reach their solubility limit, $(Ti,Al)B_2$, (Ti,V)B, $(V,Co)_2B$, and V_xB_{1-x} borides as well as TiN and AlN nitrides are present in the reaction layer. At 1000 °C, Ti_2N is a simulated reaction product that is not present at the higher temperatures. However, the other simulated reaction products are present at 1000 °C, 1200 °C, and 1300 °C. Specifically, the $(Ti,V)B_2$ phase fraction increases with temperature. The simulated reaction layer stays at a constant 3 μm thickness at the chosen temperatures, which agrees with the thickness in the diffusion couple at 1300 °C (Fig. 9d).

The formation of borides, nitrides, and α-Ti (hcp) in the simulation agrees with the observed diffusion couples. Elements in the binder such as Mo, Cr, Ni, and W were not included in the calculations. Diffusion between the formed borides and nitrides cannot be captured by the homogenization model, but the initial diffusion is.

3.3. Cemented carbide and Ti-64

The interfaces of cemented carbide and Ti-64 at all temperatures are shown in Fig. 15. A gap at the interface occurs only at the lowest temperature of 900 °C (Fig. 15a), while reaction products (Fig. 15b–e, marked by arrows) bond cemented carbide and Ti alloy at the higher temperatures. Already at 1000 °C, a reaction occurs at the interface. Based on the darker Z-contrast (Fig. 15b marked by an arrow), the reaction product consists of a lighter compound than Ti-64. The reaction layer thickness increases with temperature and reaches 2.5 μm at 1300 °C (Fig. 15c–e), similar to pcBN (Fig. 9d). Clusters of dissolving WC grains are prominent at higher temperatures of 1200–1300 °C, but occur to a small degree at 900–1100 °C. Additionally, at 1300 °C, WC grains have lost their facets and have instead become rounded.

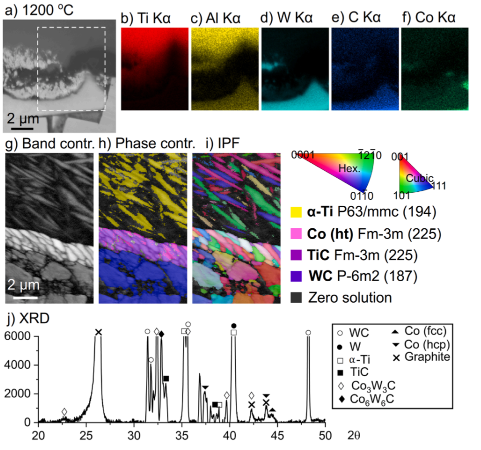

Fig. 15. Overview SEM–BSE images of cemented carbide and Ti-64 interface at 900–1300 °C with arrows pointing to reaction products.

Fig. 16 includes SEM–XEDS maps, EBSD, and XRD analyses of the cemented carbide and Ti-64 interface after treatment at 1200 °C. The SEM–BSE image (Fig. 16a) displays both a darker Z-contrast layer and fragments with bright Z-contrast. XEDS maps indicate the presence of TiC (Fig. 16b, e) in the region of darker Z-contrast. The brighter particles are a mix of WC and W (Fig. 16d–e). As in the case of PCD and pcBN, Al is not an interactive element in the reaction layer (Fig. 16c). Co binder is present between WC grains (Fig. 16f).

EBSD analyses of another interface region in the same sample (Fig. 16g–i) display the needle-shaped grains of titanium alloy, similar to the pcBN diffusion couple (Fig. 12a–b). These correspond to the α-phase of Ti where C and Al act as α-stabilizers. The reaction layer, which has darker Z-contrast in BSE mode, has smaller grains than the WC below. These consist mainly of a TiC reaction product, but Co (in ht-phase) is present as well.

XRD analysis of the interface (Fig. 16j) gives no spatial resolution but adds to the findings from XEDS and EBSD. Indeed, the Ti alloy is in the α-phase, there is TiC presence as well as Co in both the fcc and hcp phase, there are WC grains, and the presence of metallic W is linked to the bright Z-contrast fragments (Fig. 15b–e). The graphite detected is related to epoxy resin. However, η-phase Co_3W_3C and Co_6W_6C were not indicated in previous EBSD analyses but are detected now by using XRD.

Fig. 17 includes SEM– and STEM–XEDS as well as SAED analyses of the cemented carbide and Ti-64 interface in the 1300 °C sample. As in the 1200 °C sample, SEM–XEDS suggests TiC or more likely (Ti,V)C in the darker Z-contrast layer (Fig. 17a–f), as does STEM–XEDS (Fig. 17g–l). STEM HAADF shows at least two individual (Ti,V)C grains that are much larger than the (Ti,V)C grains in the 1200 °C sample (Fig. 16g–i) as the effect of a higher holding temperature. TiC or (Ti,V)C presence is verified by using SAED (Fig. 17m).

Above the TiC layer, Al is present in the Ti alloy (Fig. 17c, i). SAED (Fig. 17n) confirms that the Ti is in the α-phase. Another feature worth noting in STEM–XEDS are the bright Z-contrast streaks between WC

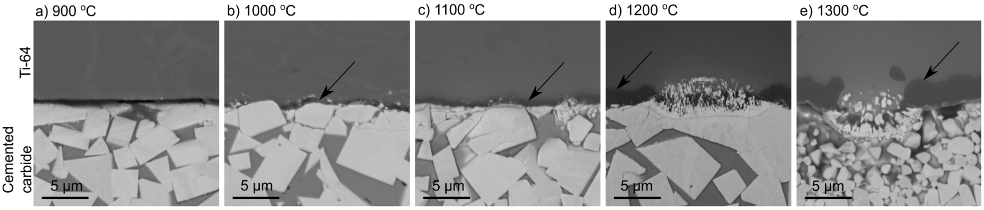

Fig. 16. Cemented carbide and Ti-64 interface after treatment at 1200 °C. (a) SEM–BSE image with (b–f) related XEDS maps. EBSD analysis with (g) band contrast, (h) phase contrast, and (i) inverse pole figure (IPF), (j) XRD spectrum.

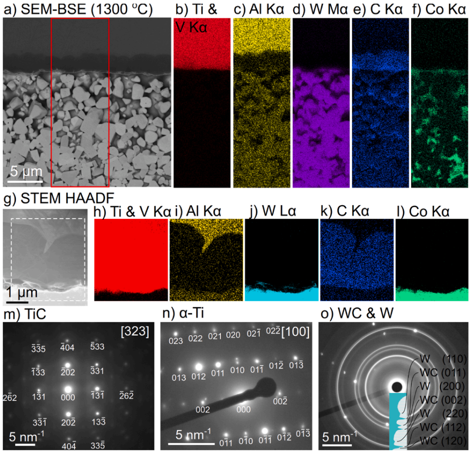

Fig. 17. Cemented carbide and Ti-64 interface after treatment at 1300 °C. (a) SEM–BSE image with (b–f) related XEDS maps. (g) STEM HAADF image of reaction layer with (h–l) related XEDS maps. SAED of selected regions showing diffraction pattern of (m) TiC, (n) α-Ti, and (o) a mix of WC and W.

grain and TiC, where the W signal is prominent. SAED from that region reports a mix of WC and metallic W (Fig. 17o).

A major difference between the 1300 °C sample and the 1200 °C sample is the rounded WC grains. The red box indicating the XEDS map location (Fig. 17a) captures the gradual change of WC grain shape. The grains at the bottom are typically faceted, while toward the interface the grains become rounder. The spacing between grains increases as the rounding increases. The XEDS map of Co (Fig. 17f) shows a gradual decline in Co concentration toward the interface. The mechanism behind the grain rounding is outward diffusion of carbon from WC grains, where C is transported from the grains with Co. As WC is stochiometric, W is released from the WC grain and forms M_6C or $M_{12}C$ with C and Co.

Fig. 18 shows the carbon window in the isopleth of cemented carbide. Graphite and two η-phases (Co_3W_3C and Co_6W_6C) can be stable depending on the carbon activity, but formation of these phases depends on the nucleation rate. The $M_{12}C$ is already present at 1000 °C while M_6C forms at 1150 °C. Both phases were detected in the diffusion couple exposed to 1200 °C. A liquid of Co binder forms at 1300 °C, which accelerates the outward diffusion of carbon. This explains the rounded WC grains in the diffusion couple exposed to 1300 °C compared to the one exposed to 1200 °C (Fig. 15d–e).

Fig. 19a shows the permeabilities of C and Co from cemented carbide

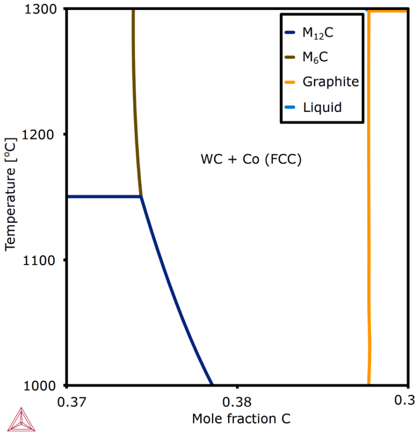

Fig. 18. Isopleth of cemented carbide showing the two-phase region of WC and Co.

in Ti-64 at 1000 °C, 1200 °C, and 1300 °C. At 1000 ℃, the permeability of Co in Ti-64 is comparable to the permeability of C, while they are similar at 1200 °C and 1300 °C at shorter distances (high Co concentration). While the permeability of Co decreases with distance, the C permeability stays comparatively unchanged and surpasses that of Co. This is because the solubility of Co in the Ti alloy is relatively more significant than that of C (0.12 mol fraction at 1000 ℃). In contrast, the mobility of Co is comparable to the mobility of C. The combination of high mobility and more significant solubility of Co results in substantial permeability of Co in Ti-64 compared to C at 1000 ℃, meaning that Co diffuses further inside Ti-64 without triggering any phase transformation. This is not the case for carbon as it triggers carbide formation.

The formation of a reaction layer between cemented carbide and Ti-64 is controlled by outward diffusion of C from WC directly to the Ti-64 and through Co to the Ti-64. Additional thermodynamic calculations on the cemented carbide system at 1000 ℃ showed that reducing the Co content decreases C activity when the C content is fixed, since WC is stochiometric. The formation of TiC or (Ti,V)C at the interface of cemented carbide and Ti-64 is an inevitable consequence of C diffusion. It happens when the C content in Ti-64 exceeds the solubility limit, which is relatively low (roughly $6 \cdot 10^{-4}$ mole fraction [50] at 1000 ℃).

Fig. 19b–d show simulated results of the diffusion and chemical reactions taking place at the cemented carbide and Ti-64 interface at 1000 °C, 1200 °C, and 1300 °C. At 1000 °C (Fig. 19b), the formation of TiC or (Ti,V)C in combination with Co depletion from cemented carbide results in a roughly fixed C composition in the Co binder. The phase

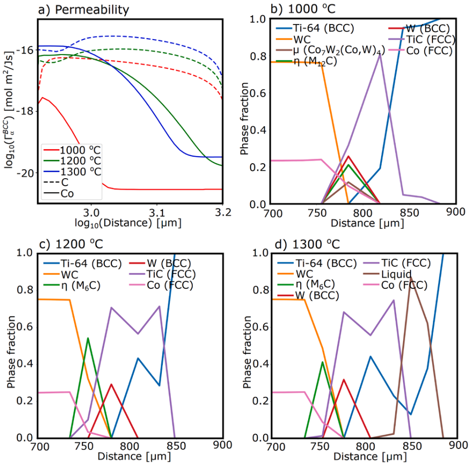

Fig. 19. (a) Permeabilities of C and Co in Ti-64 for cemented carbide at 1000 °C, 1200 °C, and 1300 °C after 10 min; DICTRA simulations of cemented carbide and Ti-64 diffusion couple at (b) 1000 °C, (c) 1200 °C, and (d) 1300 °C.

stability is dictated by the C activity depending on the distance from the cemented carbide interface. It follows the order of $M_{12}C$, bcc W, and finally titanium carbide, which forms at the Ti-64 interface. Simulations also point to the formation of intermetallic $Co_7W_2(Co,W)_4$ at 1200 °C and 1300 °C. Although the thermodynamics predict the stability of this phase, it is unclear if the phase can nucleate.

At higher temperatures, partial melting of the Co binder changes the order and stability of the phases. At 1200 ℃ and 1300 ℃, C permeability is the same as for Co (Fig. 19a), which means a similar diffusion rate of C and Co in Ti-64. A direct effect of this regime change is the higher subsurface decarburization of cemented carbide. Consequently, larger quantities of TiC, bcc W, M_6C and $M_{12}C$ are formed. In addition, higher C content pushes the cemented carbide toward the eutectic point, and partial melting of Co occurs. This may explain the round shape of WC at 1300 °C (Fig. 15e) as partial Co liquid accelerates outward diffusion of carbon.

4. Analysis

The HP-HT diffusion couple method has provided knowledge of when and in which intensity certain reaction products form. This information has been used to develop modeling solutions using DICTRA software to predict the nature of chemical interactions and active wear mechanisms in ultra-hard tooling in contact with Ti-64. The wear mechanisms are discussed in detail in the order PCD, pcBN, and cemented carbide. Finally, the wear mechanisms are connected to the wear rate and its effect on productivity in the context of machining Ti-64.

4.1. Wear of PCD

Titanium is a strong carbide former. Due to outward carbon diffusion of original diamond grains, formation of titanium carbide is expected. Minor alloying of vanadium leads to the formation of (Ti,V)C in the interaction layer, as was found in a previous study by some of the authors [31]. Hartung and Kramer [22] also verified TiC formation while machining Ti-64 with PCD, as did Sadik et al. [29] after turning Ti-5553. Thus, TiC formation occurs both in actual machining, in diffusion couples, and in simulations. Formation of TiC or (Ti,V)C reaction products can serve as a tool protection layer that reduces the wear rate.

The onset temperature of TiC formation in diffusion couples is between 1100 and 1200 °C at 3 GPa pressure, but it already occurs at 1000 °C in the simulation. The disparity between the modeling and the diffusion couples is related to when equilibrium is reached. Variation of pressure is expected across the tool–chip interface in machining, with peak pressure of 3 GPa and lower pressure further from the edge line. Lower pressure decreases the temperature at which TiC formation can occur. However, the extent of the pressure difference that affects the onset reactive temperature is low according to the thermodynamic calculations. Temperature measurement when turning Ti-64 with PCD has reported a tool tip temperature of 1150 °C, with the presence of TiC [31], so the effect of pressure differences in this case is assumed to be marginal.

The pressure of 3 GPa was selected to suppress graphitization, which nevertheless occurred at 1300 °C. It remains unknown whether graphitization occurred to a lesser degree on samples exposed to lower temperatures, but it seems likely based on the study by Qian et al. [51]. They found that a negligibly small amount of diamond was converted into graphite at 1000 °C and 2.5 GPa, while about 30% was converted at 1400 °C. Their results also showed that graphitization increased in the presence of water, a finding that needs to be balanced against the potential productivity gains achieved by using water-based cutting fluid solutions. This result is ignored in the diffusion simulations as graphite has had to be excluded because metastable diamond and graphite cannot both be considered in the same calculation.

However, it remains unknown from which form carbon diffused, as it could be from diamond with sp^3 hybridization or from graphite with sp^2 hybridization. The former seems more likely as graphite has higher cohesive energy than diamond and therefore more energy is needed for carbon with sp^2 hybridization to react with titanium [29]. Graphite is easily removed in machining by the chip flow, and hence graphitization would contribute to tool wear.

At 1300 °C, extreme reactions between PCD and Ti-64 resulted in a reaction layer 100 times thicker than in the 1200 °C sample. Assuming that carbon in the form of graphite requires more energy than in the diamond form to react with titanium, it appears that the liquefaction causing the dendritic structure is responsible for the massive carbon transportation. However, conditions leading to such massive liquefaction of the binder phase are rarely achieved in machining.

4.2. Wear of pcBN

Previous studies conducted on an as-worn tool of the same tool material also identified nanometer-sized grains consisting of reaction products $(Ti,V)B_2$ or $(Ti,V,Cr)B_2$ [31]. Other studies found TiB_2 [32] and potentially TiN reaction products [33]. These products work as tool protection layers and can reduce further outward diffusion of B and N. However, the diffusion couples and simulations show more complexity and additional reaction products because of the static conditions and higher temperatures compared to machining.

SEM–XEDS indicated that the reaction layer atop the binder was two-phased. STEM–XEDS showed its epitaxial growth, and EBSD showed that it was polycrystalline. Outward diffusion of B and N facilitated a sufficiently saturated environment to form diboride and carbonitride of Ti and V, which agrees with simulations. It remains unclear which of these forms first, but the simulations indicate almost instant boride formation followed by nitride formation. If $(Ti,V)B_2$ forms initially, then Ti, N, and C must diffuse through this layer but around grain boundaries and form carbonitrides. A two-phased reaction layer could be beneficial if formed during machining by acting as a tool protection layer.

An additional feature identified in the diffusion couples is the function of Mo and W in binder regions. As shown in Fig. 9d, local binder sites at the reaction layer interface protected underlying cBN grains or at least reduced their outward diffusion. Neighboring cBN grains that were not protected by Mo and W were at a lower level due to outward BN diffusion. The limited solubility of Mo and W in Ti [46,52] may be beneficial in tools to reduce the wear rate when the wear mechanism is based on diffusion. If adding Mo and W to the binder mix and increasing their concentration in the binder could result in the formation of a more stable and substantial layer atop cBN, the wear rate might be drastically reduced. The outward diffusion of binder elements Co, Ni, and Cr might also be reduced. Their rapid outward diffusion may result in tool material loss as grain binding of cBN is reduced, which may increase the risk of adhesive wear.

4.3. *Wear of cemented carbide*

Outward diffusion of carbon and cobalt are previously known wear mechanisms [11–21] in cemented carbide tooling. Carbon diffusion into titanium alloy typically results in TiC or (Ti,V)C reaction products [13–18,21–23], as shown in the simulations, assuming that the temperature and chip flow conditions are such that there is enough saturated carbon to form them, which may differ across the tool–chip contact zone [23]. However, the presence of TiC may reduce or completely block further outward diffusion of carbon and cobalt, and hence work as a tool protection layer. Polycrystalline TiC layers such as those in the 1200 °C sample (Fig. 16g–i) allow for diffusion around grain boundaries.

The TiC layer is not homogeneously spread across the interface; it is thinner or absent at places with W clusters, as can be seen in samples at 1200–1300 °C (Fig. 15d–e). These W clusters are easily detached by the chip flow during machining. However, it seems that the presence of metallic W suppresses TiC formation, possibly because of the decreasing C activity with decreasing Co content. Previous studies [23,46] have shown that W acts as a β-stabilizer of titanium in, for example, W-rich regions at the interface of as-worn tools. The presence of β-Ti was not verified in this study, but it may be present around clusters of W. Alternately, outward diffusion of α-stabilizing carbon may have suppressed its phase change. It can be speculated that the limited TiC presence at W-rich regions is due to the low solubility of carbon in β-Ti [53] and the consequently lower cobalt content.

Fig. 20 illustrates the basic routes of diffusion and wear mechanisms in cemented carbide tooling when machining Ti alloys. Diffusion of C from original WC grains can go either directly from WC into the adhered Ti alloy or may travel through the Co binder into the Ti alloy. Either way, WC grain damage includes increased defects and cracking of the grain (Fig. 15d) or rounding of the faceted grains. Diffusion of C releases W due to stochiometric WC, which may travel the same route as C and precipitate at the interface [54].

TiC layers and clusters of W that outline the interface may suppress further diffusion of C and Co. In parallel, the release of W when C diffuses causes the formation of the η-phase Co_3W_3C or Co_6W_6C that surround rounded WC grains. This occurred in both the diffusion couples and simulations. Formation of such phases appears at 1200–1300 °C in diffusion couples, but already at 1000 °C in diffusion simulations. However, temperatures above 1200 °C are rarely attained during machining with cemented carbide. The brittle η-phase is easily removed by adhesive wear caused by chip flow, and its formation results in tool material loss.

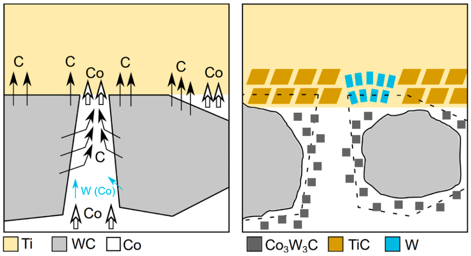

Fig. 20. Illustration of the formation of η-phase Co_3W_3C, TiC, and W by the diffusion of carbon and W precipitation at the interface of cemented carbide and Ti-64.

4.4. *Connection between wear mechanisms and wear rate*

Due to the extreme reaction of PCD at 1300 °C, the tool materials after treatment at 1200 °C are compared in Fig. 21a–c. Reaction products are marked by arrows. A discrete increase in reaction layer thickness is identified from PCD to pcBN and from pcBN to cemented carbide. The resulting reaction layers are formed by outward diffusing elements from tool materials and are C and Co for PCD, B and N for pcBN, and primarily C and Co for cemented carbide.

All those elements, except Co, are interstitial α-stabilizers [45] and have affected the original α + β Ti-64 alloy within the interface region to attain the α-phase (Fig. 5f, Fig. 12e, and Fig. 17n). However, the thickness of the α-phase bordering the reaction layer varies among the tool materials. Therefore, the intensity of the α-Ti stability region is another indicator of diffusional loss of the tool materials. By modifying the brightness and contrast in SEM–BSE mode and using XEDS, the approximate thickness of those layers was identified as 5–7 µm for PCD, 10–12 µm for pcBN, and 15–20 µm for cemented carbide.

The thickness of the reaction products and α-phase region corresponds well to the tool wear rate. To validate this claim, tool wear data from previous research by some of the authors were used [23,31]. In those studies, the same grades of PCD, pcBN, and cemented carbide were used in turning of the same workpiece material as in this study. Finishing conditions with cutting depth 0.3 mm and feed rate 0.1 mm/rev were used. Coolant was delivered at the rake face at 90 bar pressure. Cutting speeds were 350 m/min for PCD, 300 m/min for pcBN, and 250 m/min for cemented carbide.

The flank wear evolutions of those three tools are displayed in Fig. 21d. Although PCD was used to machine at the highest cutting speed, it has the longest engagement distance and the highest performance, followed by pcBN. Cemented carbide demonstrated the fastest wear rate and lowest material removal rate at the lowest cutting speed in the test series. The wear resistance is hence highest for PCD, followed by pcBN, and lowest for cemented carbide. This corresponds to the

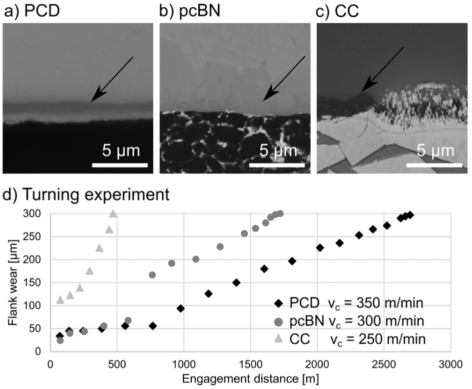

Fig. 21. Comparison of reaction layer thickness marked by arrows at 1200 °C of (a) PCD, (b) pcBN, and (c) cemented carbide. (d) Evolution of flank wear based on engagement distance during turning with the tool materials.

thickness of the reaction layer and α-phased region.

This wear rate can change radically if diffusion barriers or tool protection layers that form on the tool surface slow down chemical and diffusional wear processes. The diffusion simulations predicted diffusion and chemical reaction processes, but the reaction layer thicknesses were not accurately predicted. Diffusion couples are exposed to a static process that would correspond to total workpiece adhesion on the tool surface. An infinite chip flow would correspond to fixed elemental activity of the workpiece material at the interface rather than fixed initial composition. Hence, the initial agreement between the simulation, diffusion, and machining can be used to explore the effect of Ti alloy composition, tool composition, and chip flow on tool wear mechanisms based on chemical reactions and diffusion.

5. Conclusions

This study has demonstrated the application of HP-HT diffusion couple method in combination with diffusion simulations for study and prediction of chemical and diffusional interactions at the tool–workpiece interface and their correlation to wear mechanisms in PCD, pcBN, and cemented carbide tooling when machining Ti-64. The observed interactions under known pressure, temperature and time of the HP-HT treatment have served as the input data for diffusion simulations. The majority of wear mechanisms found in diffusion couples were identical to those observed in actual machining, with some exceptions for the case of pcBN tooling.

For PCD and cemented carbide, TiC or (Ti,V)C formation occurred already at 1000 °C and such reaction products work as a tool protection layer. For PCD, presence of a liquid phase and diamond graphitization at 1300 °C accelerated carbon transport thus increasing the wear rate. For pcBN, formation of $(Ti,V)B_2$ reaction product due to diffusional dissolution of B and N was identical to the actual machining. However, Ti(C, N) and Cr_2N were the artefacts of the diffusion couple method. All these refractory reaction products act as a diffusion barrier. Mo and W in binder has a low solubility in Ti and creates metallic diffusion barriers, and thus increasing their volume in the binder could increase pcBN wear resistance. For cemented carbide, formation of W clusters inhibits TiC formation while brittle η-phase Co_3W_3C reaction product results in a high wear rate. η-phase has not been found in as-worn tools and can be explored by changing the boundary conditions in diffusion simulations.

The use of diffusion couples and diffusion simulation has proven to be valuable means in detecting and predicting the wear mechanisms in machining. This method is mainly applicable when the wear mechanisms are primarily diffusional dissolution and chemical wear. Such conditions are very common when machining titanium alloys or other difficult-to-cut materials at high cutting speeds. The proposed method serves economic benefits as costly machining trials can be kept to a minimum or even avoided, thus allowing investigation of wider materials systems. For instance, it can be used in designing tool materials or metallic alloys which promote the formation of tool protection layers that reduce the wear rate. Alternatively, it can be employed for identification of temperatures and thus cutting conditions which minimize negative interactions and promote formation of diffusion barriers.

Declaration of Competing Interest

The authors declare that they have no known competing financial interests or personal relationships that could have appeared to influence the work reported in this paper.

Acknowledgments

The collaboration and financial support of Seco Tools AB during this research are greatly appreciated. The Sustainable Production Initiative (SPI), a cooperation between Lund University and Chalmers University of Technology, also supported the work. This work was partly funded by the Swedish Foundation for Strategic Research (SSF), contract RMA15-0062.

References

[1] R. M'Saoubi, D. Axinte, S.L. Soo, C. Nobel, H. Attia, G. Kappmeyer, S. Engin, W.-M. Sim, High performance cutting of advanced aerospace alloys and composite materials, 2015/01/01/, CIRP Ann. 64 (2) (2015) 557–580, 2015/01/01/.

[2] G.A. Oosthuizen, G. Akdogan, N. Treurnicht, The performance of PCD tools in high-speed milling of Ti6Al4V, Int. J. Adv. Manuf. Technol. 52 (9–12) (2011) 929–935.

[3] L.R. da Silva, O.S. da Silva, F.V. dos Santos, F.J. Duarte, G.V. Veloso, Wear mechanisms of cutting tools in high-speed turning of Ti6Al4V alloy, Int. J. Adv. Manuf. Technol. 103 (1–4) (2019) 37–48.

[4] F. Nabhani, Wear mechanisms of ultra-hard cutting tools materials, J. Mater. Process. Technol. 115 (3) (2001) 402–412.

[5] N. Corduan, T. Himbart, G. Poulachon, M. Dessoly, M. Lambertin, J. Vigneau, B. Payoux, Wear mechanisms of new tool materials for Ti-6Al-4V high performance machining, 2003/01/01/, CIRP Ann. 52 (1) (2003) 73–76, 2003/01/01/.

[6] E.O. Ezugwu, Z.M. Wang, Titanium alloys and their machinability - a review, J. Mater. Process. Technol. 68 (1997) 262–274.

[7] J. Vleugels, O. Van Der Biest, Chemical interaction between SiAlON ceramics and iron-based alloys, Key Eng. Mater. (1998) 127–176.

[8] J. Vleugels, O. Van Der Biest, Chemical wear mechanisms of innovative ceramic cutting tools in the machining of steel, 1999/04/01/, Wear 225–229 (1999) 285–294, 1999/04/01/.

[9] J. Vleugels, P. Jacobs, J.P. Kruth, P. Vanherck, W. Du Mong, O. Van Der Biest, Machining of steel with sialon ceramics: influence of ceramic and workpiece composition on tool wear, 1995/10/01/, Wear 189 (1) (1995) 32–44, 1995/10/01/.

[10] A. Bjerke, A. Hrechuk, F. Lenrick, A. Markström, H. Larsson, S. Norgren, R. M'Saoubi, T. Björk, V. Bushlya, Thermodynamic modeling framework for prediction of tool wear and tool protection phenomena in machining, 2021/11/15/, Wear 484–485 (2021), 203991, 2021/11/15/.

[11] D. Jianxin, L. Yousheng, S. Wenlong, Diffusion wear in dry cutting of Ti–6Al–4V with WC/Co carbide tools, Wear 265 (2008) 1776–1783.

[12] S. Zhang, J.F. Li, J.X. Deng, Y.S. Li, Investigation on diffusion wear during high-speed machining Ti-6Al-4V alloy with straight tungsten carbide tools, 2008/11/04, Int. J. Adv. Manuf. Technol. 44 (1) (2008) 17, 2008/11/04.

[13] S. Odelros, B. Kaplan, M. Kritikos, M. Johansson, S. Norgren, Experimental and theoretical study of the microscopic crater wear mechanism in titanium machining, 2017/04/15/, Wear 376–377 (2017) 115–124, 2017/04/15/.

[14] D.G. Bhat, V.A. Bedekar, S.A. Batzer, A preliminary study of chemical solubility of ultra-hard ceramic AlMgB14 in titanium: reconciliation of model with experiment, 2004/12/30, Mach. Sci. Technol. 8 (3) (2004) 341–355, 2004/12/30.

[15] O. Hatt, H. Larsson, F. Giuliani, P. Crawforth, B. Wynne, M. Jackson, Predicting chemical wear in machining titanium alloys via a novel low cost diffusion couple method, 2016/01/01/, Procedia CIRP 45 (2016) 219–222, 2016/01/01/.

[16] C. Ramirez, A. Idhil Ismail, C. Gendarme, M. Dehmas, E. Aeby-Gautier, G. Poulachon, F. Rossi, Understanding the diffusion wear mechanisms of WC-10% Co carbide tools during dry machining of titanium alloys, 2017/11/15/, Wear 390–391 (2017) 61–70, 2017/11/15/.

[17] O. Hatt, P. Crawforth, M. Jackson, On the mechanism of tool crater wear during titanium alloy machining, 2017/03/15/, Wear 374–375 (2017) 15–20, 2017/03/15/.

[18] B. Kaplan, S. Odelros, M. Kritikos, R. Bejjani, S. Norgren, Study of tool wear and chemical interaction during machining of Ti6Al4V, Int. J. Refract. Met. Hard Mater. 72 (2018) 253–256.

[19] P. Olander, J. Heinrichs, On wear of WC–Co cutting inserts in turning of Ti6Al4V–a study of wear surfaces, Tribol. Mater. Surf. Interfaces (2020) 1–12.

[20] S. Saketi, S. Odelros, J. Östby, M. Olsson, Experimental study of wear mechanisms of cemented carbide in the turning of Ti6Al4V, Materials 12 (17) (2019) 2822.

[21] L. von Fieandt, R. M'Saoubi, M. Schwind, B. Kaplan, Chemical interactions between cemented carbide and difficult-to-machine materials by diffusion couple method and simulations, J. Ph. Equilib. Diffus. 39 (4) (2018) 369–376.

[22] P.D. Hartung, B.M. Kramer, B.F. von Turkovich, Tool wear in titanium machining, 1982/01/01/, CIRP Ann. 31 (1) (1982) 75–80, 1982/01/01/.

[23] R. Lindvall, F. Lenrick, R. M'Saoubi, J.E. Ståhl, V. Bushlya, Performance and wear mechanisms of uncoated cemented carbide cutting tools in Ti6Al4V machining, Wear 477 (2021).

[24] S. Giménez, O. Van der Biest, J. Vleugels, The role of chemical wear in machining iron based materials by PCD and PCBN super-hard tool materials, 2007/03/01/, Diam. Relat. Mater. 16 (3) (2007) 435–445, 2007/03/01/.

[25] N. Narutaki, Y. Yamane, Tool wear and cutting temperature of CBN tools in machining of hardened steels, Ann. CIRP 28 (1) (1979) 23–28.

[26] K. Katuku, A. Koursaris, I. Sigalas, Structural features of the austempered ductile iron–PcBN cutting tool interaction interface as captured through static diffusion couple experiments, 2012/09/14/, Solid State Ion. 224 (2012) 41–50, 2012/09/14/.

[27] V. Bushlya, A. Bjerke, V.Z. Turkevich, F. Lenrick, I.A. Petrusha, K. A. Cherednichenko, J.E. Ståhl, On chemical and diffusional interactions between PCBN and superalloy Inconel 718: Imitational experiments, J. Eur. Ceram. Soc. 39 (8) (2019) 2658–2665.

[28] W. König, A. Neises, Wear mechanisms of ultrahard, non-metallic cutting materials, Wear 162 (1993) 12–21.

[29] M.I. Sadik, E. Coronel, M. Lattemann, Influence of characteristic properties of PCD grades on the wear development in turning of β-titanium alloy (Ti5Al5V5Mo3Cr), Wear 426 (2019) 1594–1602.

[30] J.E. Westraadt, “Thermal Degradation of Diamond Compacts: A TEM Investigation,” 2011.

[31] R. Lindvall, F. Lenrick, H. Persson, R. M'Saoubi, J.-E. Ståhl, V. Bushlya, Performance and wear mechanisms of PCD and pcBN cutting tools during machining titanium alloy Ti6Al4V, Wear (2020).

[32] Y. Zhang, Y.S. Sato, H. Kokawa, S.H.C. Park, S. Hirano, Stir zone microstructure of commercial purity titanium friction stir welded using pcBN tool, Mater. Sci. Eng. A 488 (1–2) (2008) 25–30.

[33] H. Xiao, W. Ma, S. Wang, S. Liu, Brazing of cBN to 0.45% C steel via Cu-Sn-In-Ti active alloy in a continuous tunnel furnace, 2021/03/15/, Mater. Lett. 287 (2021), 2021/03/15/.

[34] M. Olsson, F. Lenrick, R. M'Saoubi, H. Larsson, A. Markström, I. Petrusha, J.-E. Ståhl, V. Bushlya, Study of wear mechanisms of cemented carbide tools during machining of single-phase niobium, 2020/06/15/, Wear 450–451 (2020), 2020/06/15/.

[35] F.P. Bundy, H.P. Bovenkerk, H.M. Strong, R.H. Wentorf Jr, Diamond-graphite equilibrium line from growth and graphitization of diamond, J. Chem. Phys. 35 (2) (1961) 383–391.

[36] V.L. Solozhenko, V.Z. Turkevich, W.B. Holzapfel, Refined phase diagram of boron nitride, 1999/04/01, J. Phys. Chem. B 103 (15) (1999) 2903–2905, 1999/04/01.

[37] J.O. Andersson, T. Helander, L. Höglund, P. Shi, B. Sundman, Thermo-Calc & DICTRA, computational tools for materials science, 2002/06/01/, Calphad 26 (2) (2002) 273–312, 2002/06/01/.

[38] H. Larsson, A model for 1D multiphase moving phase boundary simulations under local equilibrium conditions, 12/01, Calphad 47 (2014) 1–8, 12/01.

[39] H. Larsson, L. Höglund, Multiphase diffusion simulations in 1D using the DICTRA homogenization model, 2009/09/01/, Calphad 33 (3) (2009) 495–501, 2009/09/01/.

[40] "Thermo-Calc Software TCFE Steels/Fe-alloys database version 9 (accessed 14 March 2022)."

[41] "Thermo-Calc Software MOBFE5 Steels/Fe-alloys mobility database (accessed 14 March 2022)."

[42] E. Mazhnik, A. Oganov, A model of hardness and fracture toughness of solids, J. Appl. Phys. 126 (2019), 125109.

[43] M. P. D′Evelyn, T. Taniguchi, Elastic properties of translucent polycrystalline cubic boron nitride as characterized by the dynamic resonance method, 1999/08/01/, Diam. Relat. Mater. 8 (8) (1999) 1522–1526, 1999/08/01/.

[44] Z. Lin, L. Wang, J. Zhang, Y. Zhao, Nanocrystalline tungsten carbide: as incompressible as diamond, pp. 211906-211906, 11/25, Appl. Phys. Lett. 95 (2009), pp. 211906-211906, 11/25.

[45] T.R. Bieler, R.M. Trevino, L. Zeng, Alloys: titanium, in: F. Bassani, G.L. Liedl, P. Wyder (Eds.), Encyclopedia of Condensed Matter Physics, Elsevier, Oxford, 2005, pp. 65–76.

[46] M. Ångqvist, J.M. Rahm, L. Gharaee, P. Erhart, Structurally driven asymmetric miscibility in the phase diagram of W-Ti, Phys. Rev. Mater. vol. 3 (7) (2019).

[47] E.S. Eberhard, and M. Materials Science International Team, "Liquidus surface: Datasheet from MSI Eureka in SpringerMaterials ⟨(⟩https://materials.springer.com/msi/phase-diagram/docs/sm_msi_r_10_010909_01_full_LnkDia2)," MSI, Materials Science International Services GmbH, Stuttgart.

[48] M.O. Peicheng, C.H.E.N. Jiarong, Z.H.A.N.G. Zhe, C.H.E.N. Chao, P.A.N. Xiaoyi, X.I.A.O. Leyin, L.I.N. Feng, The effect of cBN volume fraction on the performance of PCBN composite, 2021/11/01/, Int. J. Refract. Met. Hard Mater. 100 (2021), 105643, 2021/11/01/.

[49] W.F. Ding, J.-H. Xu, M. Shen, Y.-C. Fu, B. Xiao, Behavior of titanium in the interfacial region between cubic BN and active brazing alloy, 2006/11/01/, Int. J. Refract. Met. Hard Mater. 24 (6) (2006) 432–436, 2006/11/01/.

[50] H. Nakajima, M. Koiwa, Diffusion in titanium, Isij Int. 31 (1991) 757–766.

[51] J. Qian, C. Pantea, G. Voronin, T.W. Zerda, Partial graphitization of diamond crystals under high-pressure and high-temperature conditions, J. Appl. Phys. 90 (3) (2001) 1632–1637.

[52] S. Barzilai, C. Toher, S. Curtarolo, O. Levy, The molybdenum-titanium phase diagram evaluated from ab-initio calculations, Mater. Sci. (2016).

[53] Z.Q. Chen, Y.G. Li, M.H. Loretto, Role of alloying elements in microstructures of beta titanium alloys with carbon additions, 2003/10/01, Mater. Sci. Technol. vol. 19 (10) (2003) 1391–1398, 2003/10/01.

[54] M. Walbrühl, D. Linder, J. Ågren, A. Borgenstam, Diffusion modeling in cemented carbides: solubility assessment for Co, Fe and Ni binder systems, 2017/11/01/, Int. J. Refract. Met. Hard Mater. 68 (2017) 41–48, 2017/11/01/.

Paper VII

Journal of the European Ceramic Society 39 (2019) 2658–2665

Contents lists available at ScienceDirect

Journal of the European Ceramic Society

journal homepage: www.elsevier.com/locate/jeurceramsoc

Original Article

On chemical and diffusional interactions between PCBN and superalloy Inconel 718: Imitational experiments

V. Bushlya[a,*], A. Bjerke[a], V.Z. Turkevich[a,b], F. Lenrick[a], I.A. Petrusha[b], K.A. Cherednichenko[c], J.-E. Ståhl[a]

[a] *Division of Production and Materials Engineering, Lund University, Ole Römers väg 1, Lund, Sweden*
[b] *Institute for Superhard Materials, NAS of Ukraine, Avtozavodska 2, Kiev, Ukraine*
[c] *LSPM–CNRS, Université Paris Nord, 93430, Villetaneuse, France*

ARTICLE INFO

Keywords:
PCBN
Inconel 718
Diffusional wear
Chemical wear
Diffusion couple

ABSTRACT

During a metal cutting process, chemical wear can become the dominant mechanism of tool degradation under the high temperatures and contact pressures that arise between the tool and the metal workpiece. This study focuses on the chemical and diffusional interactions between superalloy Inconel 718 and cubic boron nitride (cBN) tool material with and without TiC binder. It covers thermodynamic modeling and experimental tests in the pressure range of 0.1 Pa to 2.5 GPa at temperatures up to 1600 °C. The methods used include diffusion couples under both vacuum and high pressure, transmission electron microscopy (TEM) analysis and *in-situ* synchrotron observations. It is shown that cBN is prone to diffusional dissolution in the metal and to reactions with niobium, molybdenum, and chromium from Inconel 718. Adding TiC binder changes the overall degradation process because it is less susceptible to these interaction mechanisms.

1. Introduction

Polycrystalline cubic boron nitride (PCBN) tools are widely used in machining hardened steels and superalloys due to their high hardness, wear resistance, and thermal conductivity. These beneficial mechanical and thermal properties are slightly lower than those of polycrystalline diamond. However, PCBN is substantially more chemically inert than polycrystalline diamond. At high cutting speeds, the advantage of the high hardness and abrasion resistance loses its significance because chemical and diffusional mechanisms are activated as the cutting process temperatures increase [1].

While there is evidence of chemical and diffusional mechanisms with cemented carbide tooling [2–4], less is known about PCBN tooling. A diffusion couple study [5] of cubic boron nitride and elemental iron did not register a chemical interaction. Another diffusion couple study of iron and PCBN with TiC binder carried out under vacuum showed that chemical interaction occurs at temperatures above 1300 °C [6]. The authors of that study demonstrate that the interaction is related to the binder and not to cBN. The mechanism was believed to be formation of cementite due to dissolution of carbon from the TiC binder. A diffusion couple study of PCBN with austempered ductile iron also indicated reactions between iron and silicon from the workpiece with the TiC binder phase and not with the cBN phase [7].

Oxidation of PCBN, another type of chemical interaction, has also been investigated. The presence of boron oxide among the wear products on a PCBN tool has been experimentally verified [8]. Similarly, oxidation wear of PCBN has been found in machining hardened tool steel, activated only under accelerated process conditions [9].

More complications are introduced when machining alloyed materials containing Cr, Ni, Mo, Nb, etc., such as hardened tool steels or superalloys as there are indications of the formation of metal borides and their subsequent eutectic melting [10]. The chemical reactivity of cBN and elemental nickel when annealing compacted powders in vacuum at 1300 °C results in the formation of nickel borides [11].

There has, however, been no extensive study of the reactivity between PCBN and highly alloyed workpiece materials. This study thus focuses on chemical and diffusional interaction of PCBN in machining superalloys.

When machining superalloys, temperatures as high as 1250 °C are reached in the cutting zone [12]. High contact pressures also develop there, with estimated average pressures of up to 2.5 GPa [13]. Therefore, in this study, thermodynamic calculations were experimentally compared to three *imitational situations* to investigate the effect of temperature and pressure on chemical and diffusional interactions of

---

[*] Corresponding author.
E-mail address: volodymyr.bushlya@iprod.lth.se (V. Bushlya).

https://doi.org/10.1016/j.jeurceramsoc.2019.03.002
Received 15 January 2019; Accepted 1 March 2019

PCBN with superalloy Inconel 718 (also known as Alloy 718). The three *imitational situations* were:

1 Low vacuum (0.1 Pa) annealing of powdered PCBN and Inconel 718 mixture
2 High pressure (2.5 GPa) annealing of powdered PCBN and Inconel 718 mixture
3 High pressure (2.5 GPa) annealing of bulk PCBN and Inconel 718 (diffusion couple)

These *imitational situations* were designed to reproduce different aspects of metal cutting relevant to chemical and diffusional wear. Specifically, the influence of pressure and diffusion length were set as key variables. Additionally, the influence of PCBN composition on the interaction was investigated. It is known that high-cBN tools have a higher wear rate in continuous machining than low-cBN materials with ceramic binders [14]. Therefore, this study also aims to investigate the mechanisms responsible for the discrepancy in wear between high- and low-cBN tool materials. For each of the *imitational situations* two cases were examined: high-cBN material (case H) and low-cBN material with TiC binder (case L).

The powder samples treated in low vacuum (*imitational situation* 1) were annealed at temperatures ranging from 900 °C to 1250 °C. These samples were later analyzed using laboratory source X-ray diffraction (XRD). The powder samples annealed under high pressure (*imitational situation* 2) were analyzed *in-situ* from 20 °C to 1600 °C using synchrotron source energy dispersive X-ray diffraction (EDXRD). A constant pressure of 2.5 GPa was applied to these samples. The bulk diffusion couple samples annealed at high pressure (*imitational situation* 3) consisted of round tool inserts placed in Inconel 718 capsules and heated to 1300 °C at a constant pressure of 2.5 GPa. These samples were later analyzed using TEM.

2. Materials and methods

As can be seen in Fig. 1a, the microstructure of commercial aged Inconel 718 includes six phases: Ni-γ solid solution with face-centered cubic (FCC) crystal structure; γ' FCC $Ni_3(Ti,Al)$ precipitates; γ'' precipitates of body-centered tetragonal (BCT) structured Ni_3Nb; δ orthorhombic Ni_3Nb; and the carbides NbC and TiC. The δ Ni_3Nb phase forms plate-like precipitates at the grain boundaries (Fig. 1c). Aged Inconel 718 material in a machining operation initially includes all the phases listed above; however in the machining process the precipitates (γ', γ'', δ) are dissolved into the Ni-γ phase [15,16], creating a supersaturated solution in the near surface region. This means that in high speed machining, the tool material interacts with solutionized Inconel 718 instead of multi-phase aged material. To insure that the Inconel 718 was also solutionized in the three *imitational situations* tested, a high pressure high temperature (HPHT) experiment on commercial aged Inconel 718 was conducted. A solid cylindrical block of aged Inconel 718 was subjected to flash HPHT treatment (2.5 GPa and 1300 °C) involving rapid heating (250 °C/s) and immediate quenching. XRD analyses prior to and after the HPHT treatment are shown in Fig. 1a and b. The data show dissolution of the precipitates (γ', γ'', δ) and carbides into the Ni-γ solid solution during the short treatment time. Such rapid dissolution indicates that the material phase composition present at the beginning of the *imitational situations* is the same as in high speed machining.

Situation 1 and 2 use powdered materials to yield large quantities of reaction products and so facilitate their detection. The difference between *situation* 1 and 2 is the pressure used. *Situation* 2 employs high pressure to imitate high speed machining, while *situation* 1 under low vacuum and reflects a conventional high-throughput setup. *Situation* 3 uses bulk materials in a diffusion couple arrangement. This *situation* imitates both diffusional dissolution (mass transport) and chemical reactivity. The downside is that smaller amount of reaction products are formed, which means it is more difficult to detect them.

For the *situations* involving powder material (1 and 2), cBN powder was synthesized at the Institute for Superhard Materials from hexagonal BN (hBN) in a catalyst-solvent system of magnesium and its compounds. Powdered TiC was supplied by H.C. Starck, while LPW Technology LTD supplied gas atomized powder of Inconel 718 in solutionized state with the composition shown in Table 1. For *situation* 3, two grades of PCBN tool material were selected to represent case H and case L. Case H is a binderless cBN grade (BCBN) which has 5–7 µm cBN grains and 3% stress-inducing inclusions of β-Si3N4 (see Fig. 2a and b). Case L is a commercial low-cBN content grade by Seco Tools AB (L-CBN) with a TiC-based binder and other secondary phases (see Fig. 2c and d), constituting approximately 50% by volume. Commercial aged Inconel 718 was supplied by Siemens Industrial Turbomachinery AB (see Table 1).

Before vacuum annealing in *situation* 1, the powders were dry mixed in ratios representing the tools in case H and case L (see Table 2) and cold pressed in a cemented carbide die at 2.5 GPa. The compacted pellets were annealed in a low vacuum furnace (see Table 2), and then sectioned, polished and analyzed using XRD and SEM/XEDS. *Situation* 2 tests were conducted at the PSICHÉ beamline, SOLEIL synchrotron in France, using the Paris–Edinburgh press and 10 mm assembly equipped with graphite resistive heater [17]. The mixed powders for both cases were placed into hBN capsule and, thus were shielded from graphite furnace. Energy dispersive X-ray diffraction (EDXRD) patterns were recorded during heating at intervals of 25 °C. The pressure values at room temperature were estimated using hBN equation of states [18], whereas temperature was controlled with help of the corresponding power (W)-temperature (°C) calibration curve [17]. EDXRD patterns were collected in white beam mode (25–80 keV) using Canberra solid state Ge-detector with angle fixed to 8.021°. The heating rate was set to 20 °C/min, EDXRD acquisition time was 1 min. The overall conditions

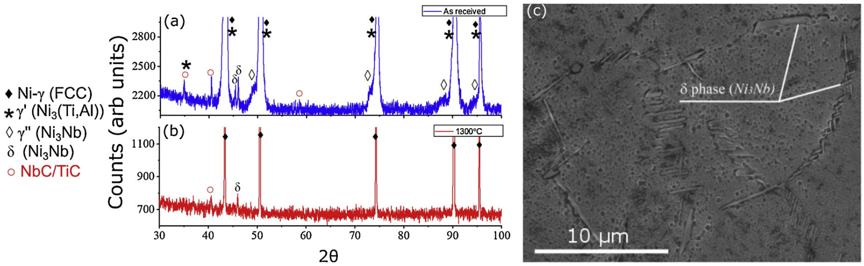

Fig. 1. Microstructure of Inconel 718: (a) XRD analysis of as received aged Inconel 718, (b) XRD analysis of the HPHT treated Inconel 718 and (c) SEM image of as received Inconel 718.

Table 1
Chemical composition of Inconel 718 by wt. %.

	Ni	Cr	Fe	Mo	Nb	Ti	Al	Co	Cu	Mn	Si	C	P	S
Bulk	bal.	18.2	17.8	2.92	5.04	1.01	0.32	0.17	0.04	0.06	0.07	0.03	0.008	0.001
Powder	bal.	19.0	18.0	3.0	5.0	1.0	0.5	–	–	–	–	0.04	–	–

are listed in Table 2.

For *situation* 3, the diffusion couples were subjected to high pressure and heated using an hBN-sleeved graphite heater in the conditions shown in Table 2. A toroid type high pressure apparatus [19] HPAT-30 was used for the treatment. Once the temperature and pressure had been reduced, the samples were cut in the axial direction, polished and analyzed using SEM, TEM, and XEDS.

The computer coupling of phase diagrams and thermochemistry (CALPHAD) method using Thermo-Calc [20] succeeds in evaluating the phase stability of Inconel 718 [21]. Thermo-Calc has also been successful in simulating diffusion and chemical interaction between a workpiece and cemented carbide tooling [2,3]. Thermo-Calc calculations of Inconel 718 at high pressure and high temperature have not been assessed in literature, and neither has the interaction between Inconel 718 and tool materials. Thermodynamic calculations of the interaction between the tool materials (case H and case L) and Inconel 718 were performed at pressures ranging from 0.1 MPa to 2.5 GPa for temperatures between 400 and 1700 °C.

3. Results and discussion

3.1. *Thermodynamic modeling*

Thermodynamic modeling of the chemical interaction between the elements of case H and case L with Inconel 718 at 0.1 MPa was performed using Thermo-Calc. The TCNI8 database, which describes the properties of nickel superalloys and nickel compounds, was used. The results of the calculation are shown in Fig. 3a and c. Among the products at atmospheric pressure are borides and nitrides of molybdenum, chromium, iron, niobium, nickel, aluminum, and titanium. Case L with TiC binder also results in the formation of carbides of titanium, niobium, and chromium.

The influence of pressure on the expressions for the temperature dependence of the Gibbs energy can be added to the Thermo-Calc modeling by adding the change in Gibbs energy due to an increase in pressure to every phase. The values of the molar volumes of phases are taken from Landolt–Börnstein [22] and the Thermo-Calc TCNI8 databases. The bulk moduli and the coefficients of thermal expansion of all competing phases make a negligible difference to the results of the change in Gibbs energy between phases present. Thus, the bulk moduli and the coefficients of thermal expansion for competing phases were assumed to be equal. Fig. 3b and d show the modeling results at 2.5 GPa.

Applying pressure of 2.5 GPa significantly reduces the number of reaction products, as only phases with low specific volume remain stable at high pressures (Fig. 3b and d). Different configurations of (Mo,Cr)B, (Ti,Nb,Cr)N are stable in case H, while (Ti,Nb)C, (Cr,Nb)C and $(Cr,Mo)_5B_3$ are stable in case L due to the presence of the TiC binder. The temperature of initial melting increases by over 100 °C under high pressure.

3.2. *Imitational situation 1 – vacuum annealing of powdered cBN and Inconel 718*

The results from the XRD and SEM analysis in *imitational situation* 1 (Fig. 4) show the formation of reaction products. These new phases are identified by combining data from both XRD and XEDS. Chromium mono- and diboride and nickel boride are identified by XRD phase analysis. In the case of chromium boride, it corresponds to space group Cmcm with lattice parameters a = 0.298 nm, b = 0.787 and c = 0.293 nm. But XEDS indicates that the phase is rich in Cr, Mo, Nb and B; thus (Cr,Mo,Nb)B is identified as the reaction phase. Similarly, $(Cr, Mo)B_2$ and $(Ni, Fe, Nb)_{23}B_6$ are confirmed. It is worth noting that formation of nickel borides has been reported for vacuum annealing [11]. The eutectic of Ni-γ and nickel boride is also seen in Fig. 4b.

Attention should be drawn to the absence of nitrides among the

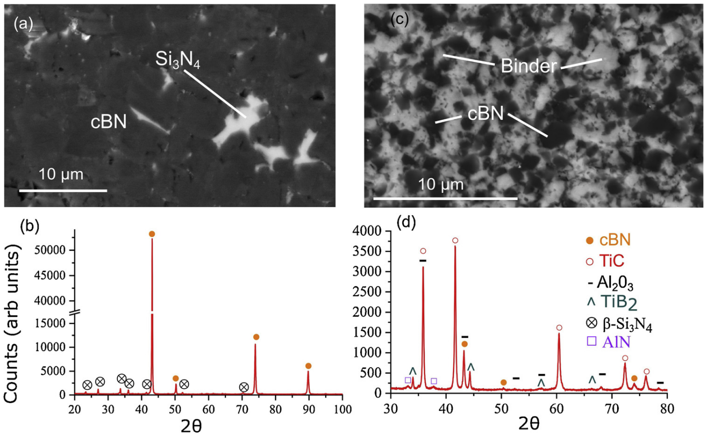

Fig. 2. SEM and XRD showing the microstructure of the tool materials used in imitational situation 3: (a–b) case H, binderless cBN; and (c–d) case L, PCBN with TiC binder.

Table 2
Conditions for the treatments in the three imitational situations.

Imitational situation	Pressure	Temperature range [°C]	Case	Powder mixture ratio [wt.%], or bulk sample	A718 powder particle size [µm]	cBN powder particle size [µm]	TiC powder particle size [µm]	Duration [min]
1	$< 10^{-1}$ Pa	900-1250	H	cBN: 29.8 A 718: 70.2 TiC: 0.0	15–45	14–20	–	120
			L	cBN: 14.1 A 718: 19.9 TiC: 66.0	15–45	14–20	1.5–2	120
2	2.5 GPa	25-1600	H	cBN: 29.8 A 718: 70.2 TiC: 0.0	15–45	14–20	–	100
			L	cBN: 14.1 A 718: 19.9 TiC: 66.0	15–45	14–20	1.5–2	100
3	2.5 GPa	1300	H	6.35 mm ø BCBN insert	Bulk	Bulk	–	5
			L	6.35 mm ø L-CBN insert	Bulk	Bulk	Bulk	5

interaction products. It is assumed that nitrogen does not participate in the reactions because it leaves the interaction system under vacuum as a gaseous phase due to cBN sublimation.

3.3. Imitational situation 2 – high-pressure annealing of powdered cBN and Inconel 718

The EDXRD results of the synchrotron studies from *situation* 2 are shown in Fig. 5. In case H, the first observed reaction products were AlN and (Ti, Nb)N, detected above 350 °C. The AlN lines disappeared completely before the sample had reached 1000 °C, while (Ti, Nb)N was stable until 1400 °C and disappeared before 1500 °C. At around 1200 °C three metal borides, MoB, MoB_2 and CrB_2, were detected. These were joined by Cr_2B_3 at around 1500 °C. All four metal borides remain stable throughout the experiment and after quenching.

In Fig. 6, *post-mortem* XEDS analysis of case H is shown for a sample quenched from 1250 °C and another sample quenched from 1600 °C. Quenching at 1250 °C leaves 10 µm large cBN grains surrounded by borides rich in Cr, Mo and Nb and nitrides rich in Ti and Nb. Quenching at 1600 °C leaves a network of Cr, Mo and Nb rich borides while no nitrides were found.

AlN was also the first observed reaction product in case L. It appears at 350 °C and disappears before the sample reaches 1000 °C. No other nitrides were detected in this case, although it is likely that the diffraction lines from many nitrides and carbonitrides overlap with the lines from TiC so that they are not conclusively identifiable. The metal borides MoB, MoB_2, and CrB_2 were detected at around 1200 °C, and Cr_2B_3 at around 1500 °C. Similarly to the thermodynamic calculations, the application of 2.5 GPa pressure shifts the melting point of Inconel 718 (Fig. 5, case L) compared to ambient conditions.

Residues of cBN phase in a sample quenched from 1250 °C were extracted by ultrasonically-assisted etching in an HF-based solution and compared to as received cBN powder. Fig. 7 shows the formation of pits due to diffusional dissolution of boron and nitrogen into Ni-γ solid solution during HPHT treatment. This confirms that diffusion is one of the active mechanisms in the wear of PCBN.

3.4. Imitational situation 3 – high-pressure annealing of bulk PCBN and Inconel 718

Fig. 8b shows a cross section of a high pressure annealed diffusion couple for case H. Both case H and L diffusion couples show an interaction layer at the interfaces with Inconel 718. Precipitation of new phases is observed primarily along the grain boundaries. Machining the Inconel 718 capsules resulted in sub-surface plastic deformation and reduced grain-size and a developed network of grain boundaries after annealing. Fig. 8a shows new precipitated phases in case H with an increased concentration of Nb, Mo, B, and partly N and Ti. A sharp increase in the concentration of C, Nb, Ti, Mo, B, and N was detected in case L, as seen in Fig. 8c. Reaction products were generally found up to 15 µm deep from the original interface.

Fig. 9 shows that for case L diffusional dissolution of cBN grains takes place at the contact region between the PCBN insert and Inconel 718. Note that the same type of dissolution occurred in *imitational situation* 2 (Fig. 7). The locations occupied by cBN before high pressure annealing are replaced by a solutionized Ni-γ after treatment. The SEM image indicates the relative stability and invariable position of the TiC binder grains. At the same time, XEDS analysis shows an increase of the carbon content in the interaction layer due to diffusion. The source of this carbon, which diffuses into Ni-γ solid solution, is the TiC phase. An increase in the number of vacancies on the carbon sublattice of titanium carbide is possible without a collapse of the lattice at the elevated temperatures. Titanium carbide can reach a composition of $TiC_{0.7}$ at 1300 °C [23], which fully explains how TiC can remain stable while losing carbon to the counterface metal.

The original interface between PCBN and Inconel 718 can be

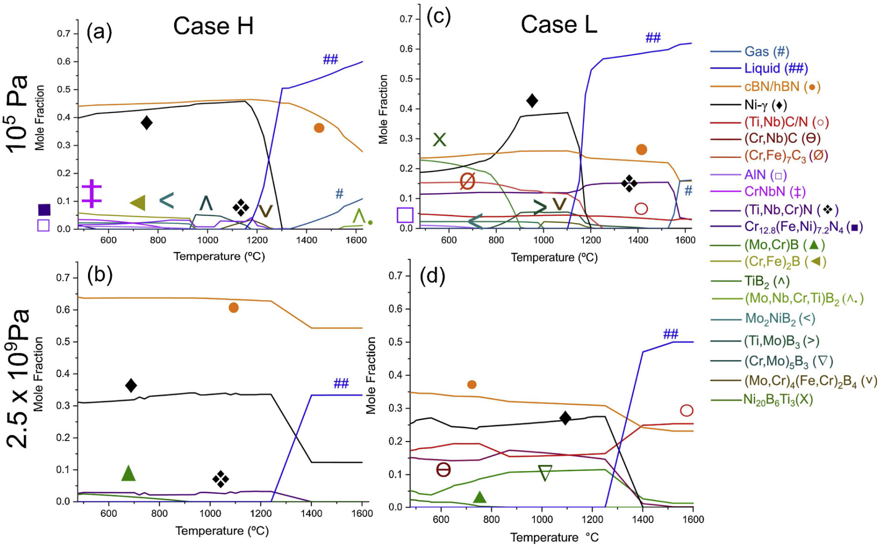

Fig. 3. Results from thermodynamic calculations for case H (a–b) and case L (c–d).

identified by a trail of Al_2O_3 grains shown in the STEM HAADF (high-angle annular dark field) image and XEDS maps (Fig. 10). The oxygen trapped inside the diffusion couple capsule before annealing was limited, and after an initial oxidation of Al from Inconel 718, all oxygen would have remained in Al_2O_3 form during the high pressure annealing. The presence of this Al_2O_3 reference allows quantitative measurement of diffusional loss (mass transport) of the cBN phase. No reaction products are found directly on the metal-cBN interface (Fig. 10), whereas Ni-γ is epitaxial to cBN.

Precipitates of (Nb, Ti)N were found inside the Inconel 718 grains and along the grain boundaries. These precipitates are shown in Fig. 11. The diffraction pattern is well-matched with epitaxial Ni-γ and (Nb, Ti) N, which causes extra, so-called double, diffraction spots. The precipitates are epitaxial with the Ni-γ phase (Fig. 11a) as can be seen in

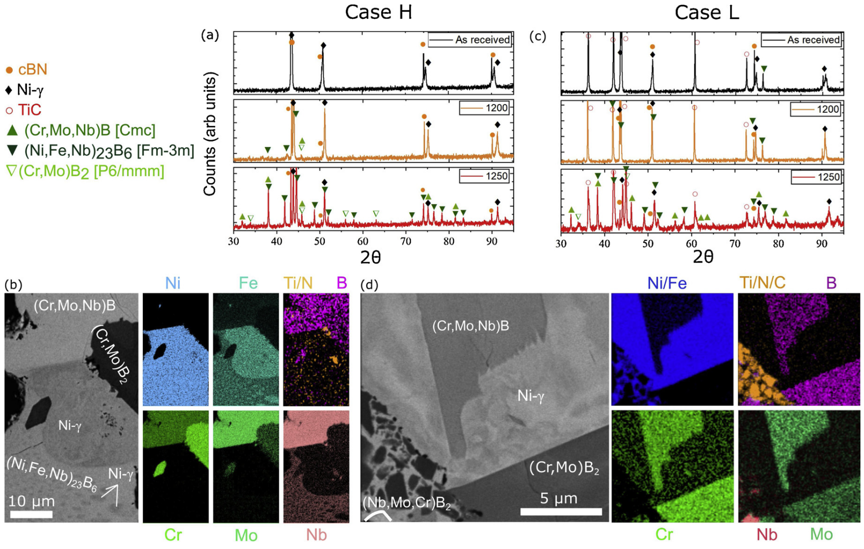

Fig. 4. XRD and SEM/XEDS of the vacuum annealed powder samples in situation 1 at 1250 °C: case H in (a–b) and case L in (c–d).

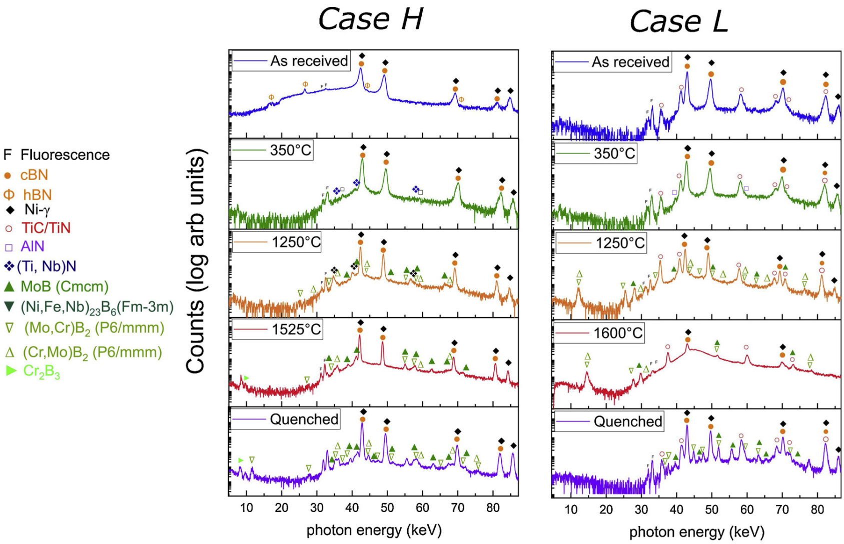

Fig. 5. In-situ EDXRD imitational situation 2.

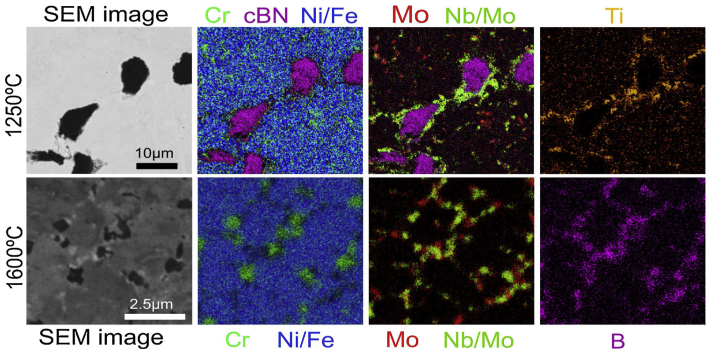

Fig. 6. Post-mortem SEM/XEDS of the quenched high pressure annealed powder samples in imitational situation 2.

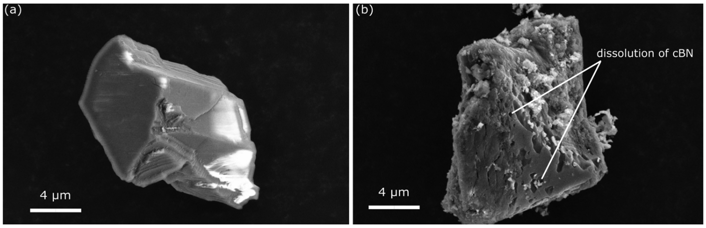

Fig. 7. SEM images of cBN grains a) as received and b) after imitational situation 2 and etching. Dissolution pits can be seen in b) where partly dissolved cBN is visible.

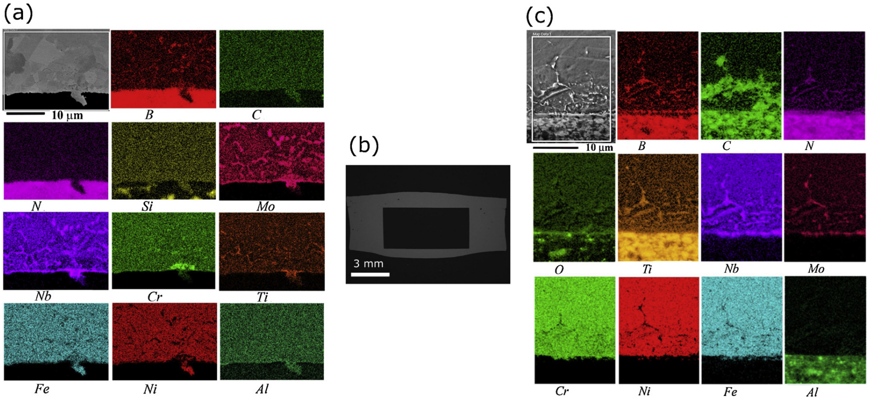

Fig. 8. SEM/XEDS of diffusion couples in situation 3: (a) case H, (b) SEM overview of diffusion couple, and (c) case L.

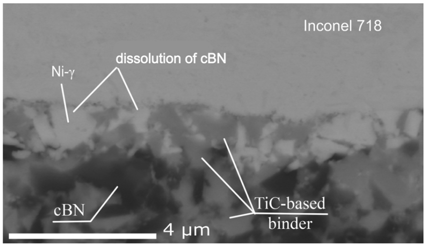

Fig. 9. SEM image of dissolution of cBN in the Ni-γ solid solution in situation 3 case L.

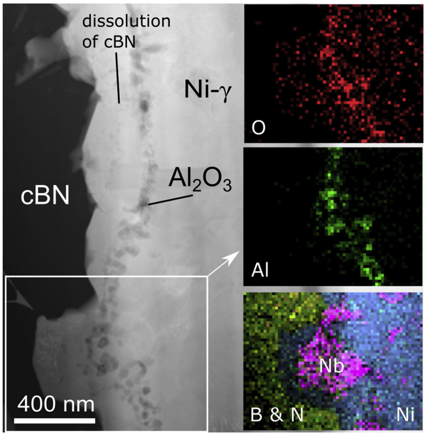

Fig. 10. STEM HAADF and XEDS of original interface and post-treatment interface, Imitational situation 3 case H.

the SAED in Fig. 11c. In case L, formation of carbonitrides was observed.

Fig. 12 shows another reaction product, with approximate stoichiometry (Cr, Nb)$_3$B$_4$. The SAED pattern is shown in Fig. 12c and matches Nb$_3$B$_4$ well. These (Nb, Ti)N and (Cr, Nb)$_3$B$_4$ reaction products were found roughly 3 μm from the interface on the Inconel 718 side of the diffusion couple.

The thermodynamic modeling is in good agreement with both high pressure experimental series (case H and case L) where borides and nitrides of Nb, Cr, Mo, and Ti are formed. However, vacuum annealing, which results in nitrogen loss due to cBN sublimation, changes the interaction system. In this case, formation of nickel boride is observed. This (Ni,Fe,Nb)$_{23}$B$_6$ boride has a low temperature melting eutectic with Ni [24], as shown in Fig. 4a. This result shows that low-vacuum imitational situation is not representative of the machining conditions.

4. Conclusions

The paper addresses the mechanisms of diffusional and chemical interactions encountered under conditions similar to high speed machining of superalloy Inconel 718 with PCBN tools. The approach using *imitational situations* involves the use of thermodynamic modeling, low vacuum powder annealing, HPHT *in-situ* EDXRD of powders, and HPHT diffusion couples of both high-cBN and low-cBN tool materials.

The results of thermodynamic modeling and *imitational situations* 2 and 3 are in reasonable agreement. The annealing under low vacuum in *imitational situation* 1 leads to a loss of nitrogen and formation of nickel boride, which creates a low temperature eutectic with Ni-γ solid solution.

Under high pressure (2.5 GPa) and high temperature (up to 1600 °C), conditions that are often reached in machining, the mechanisms of interaction include the diffusion of boron and nitrogen from cBN into Inconel 718, formation of their solid solutions, saturation and precipitation of new phases. In this way, the diffusional mechanism is responsible for the loss of cBN, while formation of nitrides of Ti and Nb and borides of Cr, Mo, and Nb governs the chemical interaction.

Both experimental and theoretical results show that presence of titanium carbide binder in PCBN (case L) changes quantitative aspects of the interaction. Despite the diffusional loss of carbon, TiC remains more stable than cBN and acts as an inert obstacle to further diffusional loss of the cBN phase. The results obtained make it possible to explain the significantly lower wear rate of PCBN tools with low-cBN content and ceramic binders compared to grades with high-cBN.

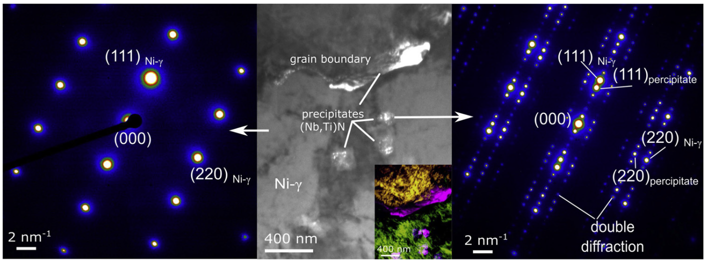

Fig. 11. Imitational situation 3 case H: (a) SAED image of Ni-γ area, (b) Overview TEM and false color DFTEM triplet and (c) SAED image of area with (Nb, Ti)N precipitates epitaxial with the Ni-γ solid solution.

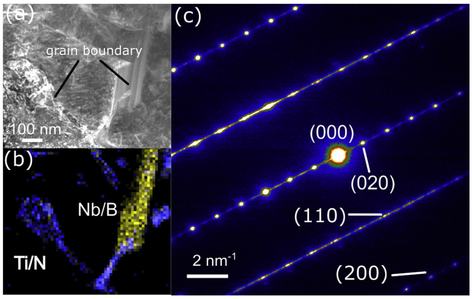

Fig. 12. Imitational situation 3 case H: (a) STEM LAADF, (b) XEDS map of Ti/N and Nb/B, and (c) SAED image of $(Cr, Nb)_3B_4$.

Acknowledgments

This research was supported by the European Union's Horizon 2020 Research and Innovation Programme under the Flintstone2020 Project (grant agreement No. 689279). The acknowledgment also extends to the Sustainable Production Initiative - a cooperation between Lund University and Chalmers University of Technology. The authors are grateful to Dr. Y. Le Godec for assistance at beamline PSICHÉ, SOLEIL, and Prof. V.L. Solozhenko (LSPM-CNRS) for helpful discussions. The *in-situ* high-pressure experiments were carried during beamtime kindly provided by SOLEIL.

References

[1] Y. Huang, Y.K. Chou, S.Y. Liang, CBN tool wear in hard turning: a survey on research progresses, Int. J. Adv. Manuf. Technol. 35 (5–6) (2007) 443–453.
[2] O. Hatt, H. Larsson, F. Giuliani, P. Crawforth, B. Wynne, M. Jackson, Predicting chemical wear in machining titanium alloys via a novel low cost diffusion couple method, Procedia Cirp 45 (2016) 219–222.
[3] S. Odelros, B. Kaplan, M. Kritikos, M. Johansson, S. Norgren, Experimental and theoretical study of the microscopic crater wear mechanism in titanium machining, Wear 376-377 (2017) 115–124.
[4] L. von Fieandt, R. M'Saoubi, M. Schwind, B. Kaplan, C. Århammar, B. Jansson, Chemical interactions between cemented carbide and difficult-to-machine materials by diffusion couple method and simulations, J. Phase Equilibria Diffus. 39 (4) (2018) 369–376.
[5] N. Narutaki, Y. Yamane, Tool wear and temperature of cBN tools in machining of hardened steels, Ann. CIRP 28 (1) (1979) 23–28.
[6] S. Gimenez, O. Van der Biest, J. Vleugels, The role of chemical wear in machining iron based materials by PCD and PCBN super-hard tool materials, Diam. Relat. Mater. 16 (2007) 435–445.
[7] K. Katuku, A. Koursaris, I. Sigalas, Structural features of the austempered ductile iron-PcBN cutting tool interaction interface as captured through static diffusion couple experiments, Solid State Ion. 224 (2012) 41–50.
[8] K. Katuku, A. Koursaris, I. Sigalas, Wear mechanisms of PCBN cutting tools when dry turning ASTM Grade 2 austempered ductile iron under finishing conditions, Wear 268 (2010) 294–301.
[9] V. Bushlya, F. Lenrick, J.-E. Ståhl, R. M'Saoubi, Influence of oxygen on the tool wear in machining, CIRP Ann. 67 (1) (2018) 79–82.
[10] S.A. Klimenko, Y.A. Mukovoz, V.A. Lyashko, A.N. Vashchenko, V.V. Ogorodnik, On the wear mechanisms of cubic boron nitride base cutting tool, Wear 157 (1992) 1–7.
[11] V.P. Bondarenko, A.P. Khalepa, E.S. Cherepanina, E.A. Pugach, Chemical interaction of cubic boron nitride with nickel, Synth. Diam. 6 (1978) 15–18 (in Russian).
[12] K. Shintani, H. Kato, T. Maeda, Y. Fujimura, A. Yamamoto, Cutting performance of CBN tools in machining of nickel based superalloy, J. Jpn. Soc. Precis. Eng. 58 (10) (1992) 1685–1690.
[13] J.-E. Stahl, Metals Cutting: Theories and Models, SECO TOOLS, Fagersta, Sweden, 2012.
[14] V.M. Bushlya, O.A. Gutnichenko, J.M. Zhou, J.-E. Ståhl, S. Gunnarsson, Tool wear and tool life of PCBN, binderless cBN and wBN-cBN tools in continuous finish hard turning of cold work tool steel, J. Superhard Mater. 36 (1) (2014) 49–60.
[15] R. M'Saoubi, T. Larsson, J. Outeiro, Y. Guo, S. Suslov, C. Saldana, S. Chandrasekar, Surface integrity analysis of machined Inconel 718 over multiple length scales, CIRP Ann. Manuf. Technol. 61 (2012) 99–102.
[16] Zhe Chen, Magnus Hörnqvist Colliander, Gustav Sundell, Ru Lin Peng, Jinming Zhou, Sten Johansson, Johan Moverare, Nano-scale characterization of white layer in broached Inconel 718, Mater. Sci. Eng. 684 (2017) 373–384.
[17] Y. Le Godec, G. Hamel, D. Martinez-Garcia, T. Hammouda, V.L. Solozhenko, S. Klotz, Compact multianvil device for in situ studies at high pressures and temperatures, High-Press. Res. 25 (2005) 243–253.
[18] V.L. Solozhenko, G. Will, F. Elf, Isothermal compression of hexagonal graphite-like boron nitride up to 12 GPa, Solid State Commun. 96 (1) (1995) 1–3.
[19] L.G. Khvostantsev, L.F. Vereschagin, A.P. Novikov, Device of toroid type for high pressure generation, High Temp.-High Press 9 (1977) 637–639.
[20] J.O. Andersson, T. Helander, L. Höglund, Thermo-Calc & DICTRA, computational tools for materials science, Calphad 26 (2002).
[21] S.H. Fu, J.X. Dong, M.C. Zhang, X.S. Xie, Alloy design and development of INCONEL718 type alloy, Mater. Sci. Eng. A 499 (1–2) (2009) 215–220.
[22] Springer Materials' database: https://materials.springer.com/ (last accessed 2018-12-10).
[23] K. Frisk, A revised thermodynamic description of the Ti-C system, Comput. Coupl. Phase Diagrams Thermochem. 27 (2003) 367–373.
[24] F. Liu, J. Xu, D. Zhang, Z. Jian, Solidification of highly undercooled hypereutectic Ni-Ni3B alloy melt, Metall. Mater. Trans. A: Phys. Metall. Mater. Sci. 45 (11) (2014) 4810–4819.

Paper VIII

CIRP Annals - Manufacturing Technology 70 (2021) 73–78

Contents lists available at ScienceDirect

CIRP Annals - Manufacturing Technology

journal homepage: https://www.editorialmanager.com/CIRP/default.aspx

Tool wear mechanisms of PcBN in machining Inconel 718: Analysis across multiple length scale

Volodymyr Bushlya[a], Filip Lenrick[a], Axel Bjerke[a], Hisham Aboulfadl[b], Mattias Thuvander[b], Jan-Eric Ståhl[a], Rachid M'Saoubi (1)[a,c,*]

[a] *Division of Production and Materials Engineering, Lund University, Ole Römers väg 1, 22100 Lund, Sweden*
[b] *Division of Microstructure Physics, Chalmers University of Technology, 41296 Gothenburg, Sweden*
[c] *R&D Material and Technology Development, Seco Tools AB, SE-73782 Fagersta, Sweden*

ARTICLE INFO

Article history:
Available online 15 May 2021

Keywords:
Machining
Wear
Diffusion

ABSTRACT

Recently, PcBN tooling have been successfully introduced in machining Ni-based superalloys, yet our knowledge of involved wear mechanisms remains limited. In this study, an in-depth investigation of PcBN tool degradation and related wear mechanisms when machining Inconel 718 was performed. Diffusional dissolution of cBN is an active wear mechanism. At high cutting speed oxidation of cBN becomes equally important. Apart from degradation, tool protection phenomena were also discovered. Oxidation of Inconel 718 resulted in formation of γ-Al_2O_3 and $(Al,Cr,Ti)_3O_4$ spinel that were deposited on the tool rake. Also on the rake, formation of (Ti,Nb,Cr)N takes place due to cBN-workpiece interaction. This creates a sandwich tool protection layer forming continuously as tool wear progresses. Such *in operando* protection enabled counterbalancing tool wear mechanisms and achieved high performance of PcBN in machining.

1. Introduction

Inconel 718, despite its 60 years of history, remains the most used superalloy [1]. Because of its high temperature strength and other properties, it is a difficult-to-cut-material, yet a number of machining strategies and tool materials are readily available. Ceramic tools, notably Al_2O_3-SiC_w and SiAlON are commonly employed for roughing and semi-finishing operations, while coated cemented carbide is a common solution for finishing [2].

In the past decade, polycrystalline cubic boron nitride (PcBN) has been introduced as a viable tooling solution for machining Inconel 718. Under finishing cutting conditions ($f \leq 0.2$ mm/rev, $a_p \leq 0.3$ mm) the recommended cutting speed range is within $v_c = 200–450$ m/min [3,4]. PcBN with low-cBN content ($\leq$ 75 vol.%) and ceramic binder offers higher performance over grades with high-cBN ($\geq$80 vol.%) [4,5]. PcBN tooling, when provided with tailored tool geometry [3], provides higher tool life than ceramics up to $v_c = 300–350$ m/min [6]. Further improvement of PcBN tool life was achieved with high pressure coolant (up to 200 bar) which substantially reduced cratering compared to low pressure coolant supply [7]. Apart from expected higher productivity, PcBN offers improvement of surface quality as compared to coated carbide tooling [8].

Such high efficiency of PcBN in machining Ni-based superalloys is rather unexpected because this tool material is designed for machining martensitic steels and consistently demonstrates poor performance with austenitic alloys [9]. Still, most of the available literature does not focus on wear mechanisms of PcBN tooling in machining Inconel 718. It is a general consensus that involved wear mechanisms are diffusion [4,6], abrasion [3] and adhesive wear [3,5], yet such findings are based on macro- or microscopic analysis of wear scars. Diffusion couple experiments [10,11] demonstrated diffusional dissolution of cBN and chemical interaction resulting in formation of metal nitrides and borides, yet these mechanisms have not been validated in actual machining. In this study, in-depth analysis of PcBN wear mechanisms in machining Inconel 718 is carried out across multiple length scale.

2. Experimental work

Performance and wear of PcBN tools was investigated in longitudinal turning of aged Inconel 718 (HRC 45.1) on CNC lathe SMT 500 (Swedturn). The composition of the superalloy is given in Table 1. The microstructure of the alloy in an aged state (Fig. 1a) consists of Ni–Cr–Fe–Mo solid solution (γ phase) and is primarily strengthened by Ni_3Nb (γ") precipitates (see inset of Fig. 1a). Minor quantities of $Ni_3(Ti,Al)$ γ' and orthorhombic Ni_3Nb (δ) on grain boundaries are also present. Fine carbides of TiC and NbC dispersed in γ matrix are responsible for abrasiveness of Inconel 718 during machining.

Table 1
Chemical composition of Inconel 718 in wt%.

Elem.	Ni	Cr	Mo	Nb	Ti	Al	Fe
min	50.0	17.0	2.8	4.75	0.65	0.2	bal
max	55.0	21.0	3.3	5.50	1.15	0.8	

---

[*] Corresponding author at: Division of Production and Materials Engineering, Lund University, Ole Römers väg 1, 22100 Lund, Sweden.
E-mail address: rachid.msaoubi@secotools.com (R. M'Saoubi).

https://doi.org/10.1016/j.cirp.2021.04.008

Machining experiments were performed at constant feed (f = 0.15 mm/rev) and depth of cut (a_p = 0.25 mm). Cutting speed (v_c) range was between 200 m/min and 450 m/min. Each test was repeated three times. Flood coolant with 8% Cimstar 501-02 concentration was used.

PcBN grade CBN170 (Seco Tools) was used in the experiments, which has 65 vol.% content of cBN and ceramic binder reinforced with SiC whiskers (Fig. 1b). The binder is comprised of titanium carbonitride (TiCN) and smaller fraction of Al_2O_3 originating from reaction of molten Al with powder surface oxygen during PcBN sintering process. Solid ISO DNGN110308 inserts with edge hone of r_β = 25 µm and without chamfer were installed on CDJNL3225P11 toolholder.

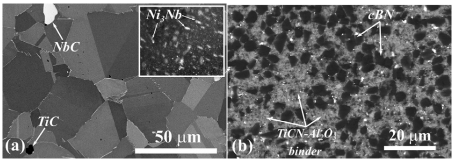

Fig. 1. Backscatter electron images of (a) Inconel 718 and (b) PcBN.

Optical microscopy and 3D profilometry analysis was done on an Alicona Infinite Focus microscope. A field emission Tescan Mira3 scanning electron microscope (SEM) with Oxford XEDS detector was used for chemical analysis at the micrometre scale. A focus ion beam (FIB) lamella was prepared on a FEI Nova NanoLab 600 dual beam FIB/SEM. Standard *in-situ* lift-out procedure was employed where the lamellae were thinned to electron transparency (approx. 100 nm) using 10 kV Ga + ions. Transmission electron microscopy (TEM) was performed on a JEOL 3000F equipped with Oxford XEDS detector. Atom Probe Tomography (APT) analysis was carried out in laser pulsing mode in an IMAGO LEAP 3000X HR instrument using 0.3 nJ at 200 kHz repetition rate and 60 K base temperature. TEM and APT were used to examine the material degradation at the nanometre scale.

3. Results and discussion

3.1. Machining performance

Fig. 2 summarizes the performance of PcBN machining termed as flank (VB), notch (VB_{notch}) and crater (KT) wear. Fig. 2a reports the level of tool wear attained for constant cutting length of 820 m. As expected, an increase of cutting speed intensifies both flank and crater wear, however the rate is not constant. It can be seen that a reduced wear rate is observed within the speed range between v_c = 300 m/min and v_c = 350 m/min and further accelerates, especially at v_c = 450 m/min.

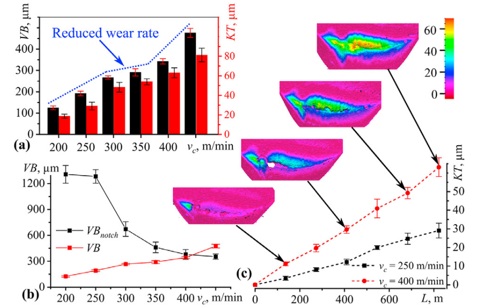

Fig. 2. (a) Flank (VB) and crater (KT) wear for tested cutting speeds. (b) Comparison of flank and notch wear. (c) Development of crater wear over cutting length and respective 3D images of worn tool.

Notch wear, on the contrary, reduces with higher cutting speed and becomes commensurate with flank wear already at v_c = 400 m/min (Fig. 2b). Machining performance data also show that the crater wear increases linearly with the cutting length (Fig. 2c), thus pointing towards stable continuous wear mechanisms. Only at highest speeds, excessive cratering (Fig. 2c) led to cutting edge fracture and chipping. Other morphological features of worn tools include presence of cracks parallel to the cutting edge (Fig. 3c), sporadic adhesion of workpiece material on the rake and strong adhesion on the flank (Fig 3a). Of particular interest is the instability and fragmental delamination of adhered material on the flank under conditions of large VB, denoted with “red” arrows in Fig. 3b.

Backscatter electron (BSE) imaging was used to further distinguish microstructural changes within the wear scar through the Z-contrast mechanism which is sensitive to average atomic mass of present phases. Fig. 3c shows original cBN and binder phases, where adhered Inconel 718 are observed as bright streaks in the chip flow direction. However, BSE imaging of the same region at low acceleration voltage of 5 kV (Fig. 3d), thus constricted to tool surface information, revealed the presence of a film covering the tool-chip interface. High Z-contrast analysis of the film is indicative of new phases with average atomic mass higher than cBN. Inspection of all worn tools over a range of acceleration voltages revealed that the thickness of such film qualitatively appears to be smallest at v_c = 200 m/min and continuously increases at higher cutting speeds.

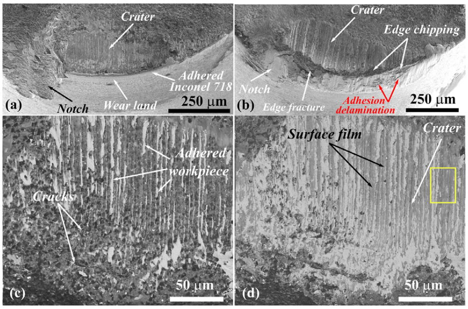

Fig. 3. PcBN wear scar at (a) v_c = 250 m/min and (b) v_c = 400 m/min. Detailed BSE view of the crater (v_c = 400 m/min) taken at (c) 20 kV and (d) 5 kV acceleration voltage.

Local XEDS analysis (Fig. 4) of such film on the crater (yellow area in Fig. 3d) revealed high concentration of binder elements Ti, Al, N and O even in regions of parental cBN. *In-operando* formation of TiAlN in argon machining and TiN with Al_2O_3 in dry cut has been previously reported [12], thus either of the products can be expected in the current case. Additionally, an overlap of Nb and B signals points towards formation of NbB_2 earlier shown to form in reaction of cBN and Inconel 718 powders [11].

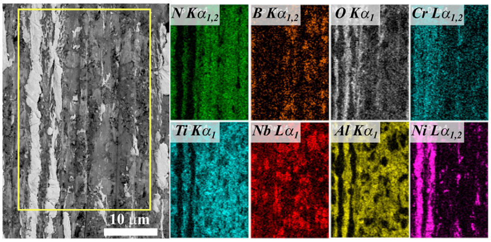

Fig. 4. Detailed BSE image of the crater and respective XEDS maps (v_c = 400 m/min).

3.2. In-depth analysis of wear mechanisms

It should be noted that XEDS in combination with SEM has limited sensitivity for surface characterization due to large excitation volume and therefore the above analysis must be treated as preliminary. Hence, TEM characterisation of lamellae prepared by FIB extracted from the crater and flank wear zones of worn tools has been carried out.

Fig. 5 reports high angle annular dark field scanning TEM (STEM-HAADF) image of tool surface region. This imaging mode shares similar Z-contrast mechanisms to BSE. It is seen that a reaction layer (100–200 nm) forms above cBN grain, consisting of two sub-layers of darker and brighter Z-contrast. XEDS confirms that the top layer has high concentration of Al and O, implying *in-operando* formation of Al_2O_3 due to reaction of Al in Inconel 718 (see Table 1) with atmospheric oxygen. Water vapour from coolant is known to accelerate such oxidative reaction [13] and hence facilitate build-up of such layer. Selected area electron diffraction (SAED) analysis of this zone (Fig. 5d) confirms cubic γ-Al_2O_3 in space group Fd$\bar{3}$m, which is a spinel M_3O_4 type phase with vacancies in Al atomic positions [14]. It is also seen that this γ-Al_2O_3 has high Cr concentration in upper part and high Ti concentration in its lower part, both presumably occupying spinel sites, thus formation of two spinels $(Al,Cr)_3O_4$ and $(Al,Ti)_3O_4$ is highly likely. The bottom of reaction layer has high N concentration and absence of B, and thus the suggested formation of NbB_2 is a misinterpretation of the XEDS map in Fig. 4. This bottom layer is rich in Ti, Nb, Cr, hence *in-operando* formation of (Ti,Nb,Cr)N film as a result of reaction of cBN and Inconel 718 takes place, as confirmed by respective SAED (Fig. 5c).

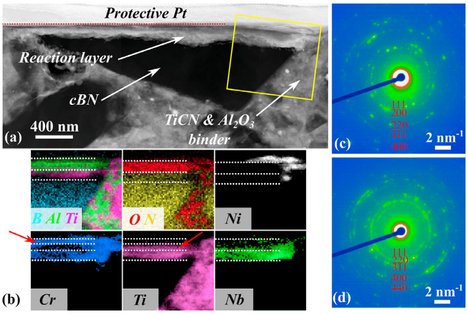

Fig. 5. (a) STEM-HAADF image of crater lamella (v_c = 350 m/min) and (b) XEDS maps. SAED of (c) nitride and (d) oxide reaction phases.

It is also seen that preferential removal of cBN takes place as its level is below the level of PcBN binder material. This is driven by diffusional dissolution of cBN in Inconel 718, where solubility of boron in Ni is negligible even up to 1200 °C [15] but its diffusivity is rather high [16], thus favoring its fast outward diffusion. Because cBN is a binary compound with fixed 1:1 stoichiometry of B and N, simultaneous diffusion of nitrogen occurs, but it is followed by an immediate chemical reaction to form (Ti,Nb,Cr)N. Both nitride and γ-alumina layers act as local diffusion barriers and retard rapid dissolution of cBN. Obviously, formation of protective nitride layer does not occur atop the PcBN binder phases, but γ-Al_2O_3 was also sparsely present.

Surprisingly, in several locations, the reaction layer has exhibited a columnar type grain morphology (Fig. 6) similar to a typical PVD coating, as seen in both bright field TEM and low angle annular dark field (LAADF) STEM, where the LAADF mode (Fig. 6b) displays additional crystallographic information of the layer. It is likely that such columnar grains are the result of epitaxial material growth on cBN. Columnar grains were only rarely observed which suggests that only specific cBN facets seem to promote such growth. This additional information also implies that the protective layer somewhat resembles a tool coating which forms continuously as tool wear progresses.

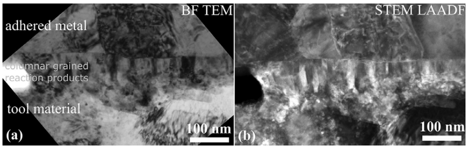

Fig. 6. (a) Bright field TEM and (b) STEM-LAADF images of columnar morphology of the same region of reaction products.

TEM lamella extracted from the worn flank reveals that the protective layers do not form on the flank. STEM-XEDS of Region X (Fig. 7a) demonstrates an unreacted cBN-workpiece interface (see red arrow) and only a minor presence of γ-Al_2O_3. Instead, diffusional dissolution of boron and nitrogen in the adhered Inconel 718 results in formation of nanometric Ti- and Nb-rich precipitates close to the interface (Fig 7 Regions Y and Z). Two distinct types of reaction products are observed: nitrides and borides with high Ti and Nb content (Region Y) as well as carbonitrides with high B concentration (Region Z). A combination of XEDS and SAED data (Fig. 7) confirms formation of TiN, (Ti,Nb)N and (Ti,Nb)B_2, as well as (Nb,Ti)(C,B,N) within the adhered material. Presence of carbon in the carbonitride precipitates is attributed to diffusional dissolution of TiCN binder of the PcBN grade. Similar reaction products were found in diffusion couples [11] in absence of workpiece material flow. Strong adhesion of Inconel 718 on the flank likely promotes local stagnation of workpiece flow and facilitates the saturation of B, C and N needed to form these products.

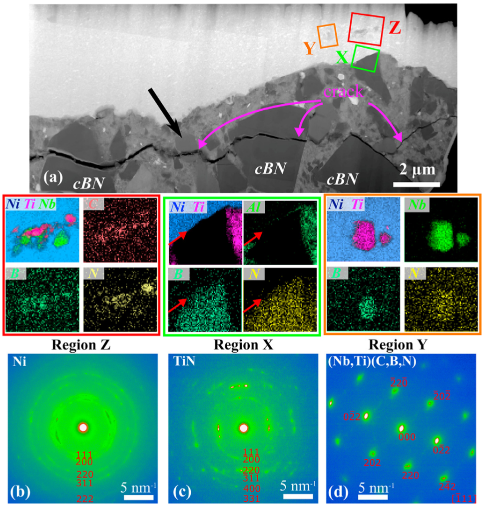

Fig. 7. (a) STEM-HAADF image of lamella from flank wear land (v_c = 350 m/min) with respective XEDS maps of 3 regions. SAED of (b) adhered Inconel 718, (c) TiN and (d) (Nb,Ti)(C,B,N) precipitates.

Under conditions of workpiece seizure, the ingress of oxygen and respective formation of Al_2O_3 film is strongly limited, and hence tool protection layer as on the tool flank is not generated. Therefore, despite higher cutting temperature on the rake, lesser loss of tool material by volume takes place as compared to the flank. Such strong adhesion on the flank plays a further negative role. Formation of a crack parallel to the flank wear land is observed (Fig. 7a) which explains previously observed flank delamination (Fig. 3b). The strength of adhesive bond is so high that the crack propagates through individual cBN grains and even fractures SiC whiskers (black arrow in Fig. 7a). It can be summarized that active wear mechanisms on the flank are dissolution of cBN and TiCN binder, adhesive wear, and limited oxidation, though abrasion by TiC and NbC carbides in the alloy microstructure (Fig. 1a) is also likely.

TEM analysis of the sample extracted from the crater of a tool worn at v_c = 450 m/min (Fig. 8) revealed that the thickness of reaction layer is nearly three times as high compared to v_c = 350 m/min and ranges 200–500 nm. Similar to the other case, a sub-layer of Al-rich concentration and a Nb- and Cr-rich sub-layer are observed at this speed. However, oxygen is uniformly present in both sub-layers. This implies that oxidation of the nitride layer is actively ongoing, with an ingress of atmospheric oxygen directly towards cBN. SAED (Fig. 10c) of the reaction zone confirmed presence of only M_3O_4 spinel lattice type, but XEDS data (Fig. 8) revealed co-existence of several compositions: pure γ-Al_2O_3, and two spinels of $(Al,Ti)_3O_4$ and $(Al,Cr,Ti)_3O_4$. This means that diffusional dissolution of cBN is accompanied by an intensive oxidation process in absence of the protective (Ti,Nb,Cr)N layer present at lower cutting speeds.

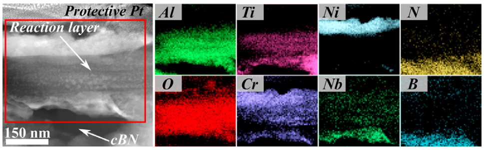

Fig. 8. (a) STEM-HAADF image of crater lamella (v_c = 450 m/min) with respective XEDS maps.

It thus can be argued that the insufficient thickness of protective layers at lower cutting speeds is responsible for the high wear rate (Fig. 2a). The presence of thick sandwich of γ-Al_2O_3 and (Ti,Nb,Cr)N at v_c = 300–350 m/min results in a reduces the wear rate as it acts as a tool protection layer (TPL). At higher cutting speeds, despite even thicker reaction products, the loss of nitride sub-layer due to its through-oxidation and ingress of oxygen to parental PcBN tool material gives rise to accelerated wear rate.

Additional effort was invested into modelling the observed type of chemical interactions in the cutting zone. Thermodynamic calculations were performed using the CALPHAD phenomenological approach in Thermo-Calc [17] software, using TCNi10 database which describes the properties of nickel superalloys and nickel compounds. The calculation of the interaction between tool, workpiece materials and ambient atmosphere rests on minimizing the Gibbs energy among all competing phases at given composition, temperature and pressure. Previously [11], it was shown that neglecting the influence of pressure may corrupt the modelling outcomes. Therefore, as the first step, Finite element modelling (FEM) simulation of 3D oblique cutting process was performed with an aim to extract temperature and contact pressure within the tool-chip interface. Coupled Eulerian–Lagrangian technique in Abaqus/Explicit was employed, with the PcBN tool in a Lagrangian formulation and the workpiece by a Eulerian formulation. The Johnson–Cook damage model combined with material softening by stiffness degradation constituted the damage initiation for adequate chip formation and segmentation according to previous [18] orthogonal case and further adapted to current oblique machining case. Thermal steady state analysis of the cutting tool was performed prior to FEM machining simulation. This was done to create initial tool preheating. 900 °C was applied on the tool-chip interface and the underside of the PcBN insert was set to 230 °C as this temperature was registered when machining with thermocouple embedded in the toolholder anvil. Fig. 9a reports that the interface temperature rapidly increases up to 1000 °C even at v_c = 250 m/min and fluctuates between 950–1050 °C during a chip segmentation cycle. High temperature is thus expected for increased cutting speed. Peak contact pressure (Fig. 9b) in excess of 2.5 GPa are yielded by the FE simulation, while an average of 2.3 GPa is registered. It is seen that such peak pressure is located near the cutting edge and subsides towards the crater end side.

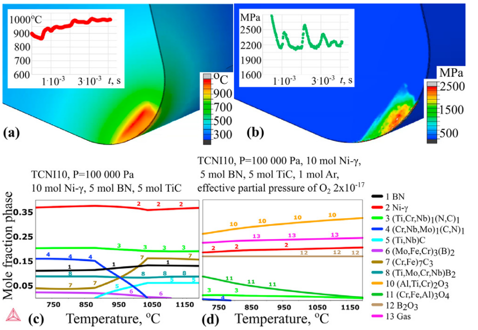

Fig. 9. Results of FE simulation of (a) temperature and (b) contact pressure within tool-chip interface (v_c = 250 m/min). Results of thermodynamic modelling of interaction (c) without oxygen and (d) with oxygen partial pressure.

Fig 9c shows the thermodynamically stable phases and the phase fractions for the thermodynamic equilibrium between the cBN, TiCN binder and Inconel 718. The calculations confirm the stability of (Ti, Cr,Nb)N reaction product between cBN and Inconel 718 (Fig. 5 and Fig. 7). Also stable are a range of Ti, Cr, Mo and Al borides, similar to those observed experimentally (Fig. 7). It further shows that the formation of (Cr,Nb,Mo)(C,N) is not favored at higher temperatures, thus explaining stability of TiCN binder as it lacks a driving force for dissolution. Fig. 9d shows similar calculation, but with the addition of oxygen at an effective partial pressure of 2×10^{-17}, with the liquid phase suspended. The data reveal that the $(Al,Ti,Cr)_2O_3$ spinel (Fig. 5 and Fig. 8) is more favorable at higher temperatures compared to the spinel $(Cr,Fe,Al)_3O_4$ more commonly observed in machining steels.

A further TEM analysis of a sample from the crater at v_c = 450 m/min revealed an anomalous wear aspect which does not follow the established thermodynamic framework. A local reduction in boron and nitrogen concentration in cBN grains is observed within 100–200 nm in the proximity of the wear surface, as seen in the inset of Fig. 10a. Typically, such concentration gradient is associated with the adjacent metal being diffusionally saturated [19], yet in our case the counter material is M_3O_4 spinel (Fig. 10b). A detailed view of the near-surface region and respective XEDS (Fig. 10c) reveals that a rapid drop in B concentration is observed within cBN grain itself. Yet, cBN is a stoichiometric compound with fixed ratio of B to N [20] and solution phase of type $B_{1-x}N$ is not supported. Another interesting observation is related to a 'droplet' shape formation in the cBN surface region (Fig. 10c) as noticed by higher Z-contrast inclusions inside the cBN grain. XEDS data attests ingress of Ni-Fe-Cr solid solution. Such encapsulated metal inclusions were observed throughout the sample in all 6 investigated locations.

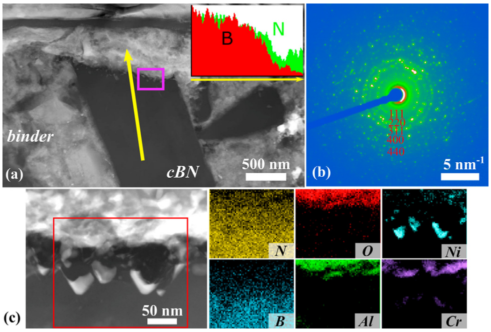

Fig. 10. (a) STEM-HAADF image of crater lamella (v_c = 450 m/min). (b) SAED of oxide reaction product. (c) STEM-HAADF image of cBN surface region with respective XEDS maps.

Additionally, STEM-HAADF imaging of these ‘droplets’ (Fig. 11a) displays much darker Z-contrast or lower average atomic mass above the metal ‘droplets’ than the original cBN grain. In practice, such image may originate if: (i) local sample perforation happened during FIB milling and the observed region is simply vacuum, (ii) cBN-to-hBN reverse phase transformation has taken place locally, or (iii) this region of cBN grain has high concentration of vacancies. STEM-LAADF imaging (Fig. 11b) excludes presence of vacuum (perforation) as the sample is crystalline, also confirmed by SAED. Selected area electron diffraction (Fig. 11c) shows that diffused Ni-Fe-Cr metal is epitaxial to cBN and that the upper darker region has the same Zincblende type structure as the original cBN, and this excludes reverse transformation. On the contrary, XEDS data (Fig. 11d) confirms a dramatic decrease in B concentration atop metal ‘droplets’ – more than half of the original. Similarly, loss of N within the same region also takes place, but to a lesser degree. This means these formations are cBN phase with high vacancy density and can be described as $(B_x,Va_{1-x})(N_y,Va_{1-y})$. Presence of vacancies in cBN has been predicted [21], yet at far lower concentration. XEDS data also show that this cBN region exhibits traces of oxygen (2.6–5.6 at.%) and by aluminium (< 1 at.%). It is likely that such doping by larger atoms prevents the lattice collapse under high vacancy density. Presence of vacancies also explains diffusional ingress of Ni-Fe-Cr metal into cBN, which would otherwise be impossible for close-packed Zincblende structure. Metal-filled thin pathways connecting the metal droplets with worn surface are visible (Fig. 11a).

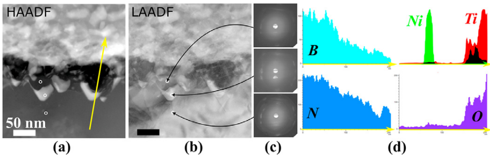

Fig. 11. (a) STEM-HAADF and (b) STEM-LAADF images of cBN region with droplets. (c) nano-beam diffraction of cBN and a metal inclusion, and (d) XEDS linescans across droplets and adjacent regions.

APT analysis was performed to further examine the compositional details in this sample at the nanoscale. The specimens were prepared from the same crater area as previous TEM sample ($v_c = 450$ m/min). Fig. 12 displays an APT reconstruction showing the binder region as well as nanometric clusters of cBN surrounded by Al_2O_3 and C segregations. No agglomerations of Ni or Cr were observed in the proximity of the detected fine cBN clusters.

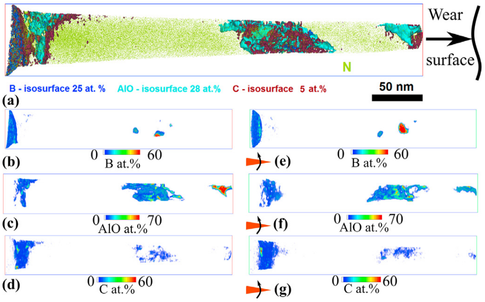

Fig. 12. APT analysis of the TiCN binder region with fine clusters of cBN. (a) N atoms with isoconcentration surfaces of B, AlO and C. (b–d) 3D concentration maps of B, AlO and C. (e–g) 90-degree rotated view.

It is seen that diffusional transport of carbon has taken place in the subsurface region. The bulk of TiCN grains is practically devoid of C signal, whereas carbon has migrated towards grain boundaries or interfaces (Fig. 12) and further outwards into the Inconel 718 chips. XRD data of the PcBN material (Fig. 13) report that the original TiCN binder has varying C:N ratio within this phase with strong skewness towards TiC (Fig. 13a). The original binder composition can be averaged as $Ti(C_{0.38},N_{0.72})$, but carbon diffusion during the wear process resulted in its near-complete loss. Yet, nitrogen in TiCN is more stable and thus, as a result of carbon loss and respective vacancy generation, the remaining phase can be described as Ti(N,Va). TiN is a solution phase of wide range of N solubility where composition of $TiN_{0.83}$ can be maintained at 20 °C and as low as $TiN_{0.7}$ at 1050 °C without phase transformations [22]. Previously reported data from diffusion couples [11] also demonstrated active diffusional loss of carbon from the binder. This direct validation of carbon dissolution supports the mechanisms of formation of C-rich precipitates on the tool flank (Fig. 7a and 7d).

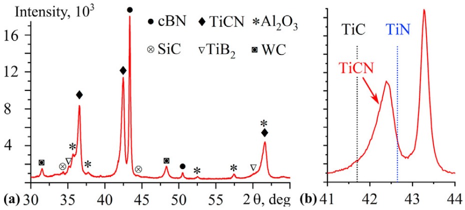

Fig. 13. (a) XRD phase analysis of PcBN grade, (b) Detail of XRD pattern of TiCN (200) reflection.

This finding of preferential C loss implies that TiN-based binders have a potential to better withstand tool degradation. Special series of PcBN tools and machining experiments have been implemented to check this assumption.

3.3. Implications for PcBN material design

Three PcBN grades were specially sintered in toroid type high pressure apparatus (T = 2000 °C, $p = 7.7$ GPa) with final insert geometry ISO RNGN090300. Binders based on TiC, TiCN and TiN precursor powders were used for sintering PcBN with 60 vol.% cBN concentration. Fig. 14a shows XRD of sintered materials. It is seen that TiC binder has partially increased N concentration as a results of cBN-TiC interaction during the sintering process and hence can be averaged as $Ti(C_{0.95},N_{0.05})$. TiCN binder attains a bi-modal C:N ratio during the sintering and can be averaged as $Ti(C_{0.46},N_{0.54})$, while TiN binder remains unaffected.

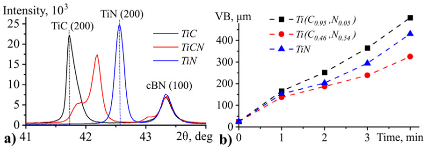

Fig. 14. (a) Fragment of XRD patterns of TiC, TiCN and TiN (200) reflections attesting to binder C:N ratio. (b) Evolution of flank wear land for experimental PcBN grades.

Machining experiments were conducted under following cutting conditions: $v_c = 300$ m/min, $f = 0.1$ mm/rev, $a_p = 0.3$ mm, flood coolant. Flank and crater wear were assessed up to a given time-in-cut (t = 4 min), with three repetitions for each test. Fig. 14b summarizes PcBN performance and indeed TiN binder outperforms TiC-based binder by almost 20%. Yet, surprisingly the grade of TiCN binder demonstrated the best performance with over 50% lesser tool wear over PcBN with TiC binder. It is worth noting that not only diffusion, but the oxidation resistance of the binder phases is different. Detectable oxidation of TiN begins at 700 °C while for TiC this starts at 800 °C [23]. Yet not only the onset of oxidation, the kinetics of the oxidation process are also higher for TiN [23]. The kinetics of TiCN oxidation fall between TiN and TiC [24] and therefore a balance between diffusion and oxidation wear mechanisms is attained for TiCN binder. It can be argued that, at different cutting conditions, varying C:N ratio in Ti(C_x, N_{1-x}) will provide the optimal resistance to diffusion and oxidation, and so the binder can be tailored to a specific machining operation.

4. Conclusions

In-depth investigation of PcBN tool degradation and related wear mechanisms when high-speed machining Inconel 718 was performed in this study. Diffusional dissolution of cBN with outwards diffusion of boron and nitrogen was found to be an active wear mechanism. At high cutting speed oxidation of cBN became equally important mechanism. Diffusional loss of carbon from TiCN binder was documented, yet the binder as a whole was less prone to diffusion than cBN phase. However, macroscopic tool wear means that loss of binder and cBN eventually occurs at a similar rate, thus other mechanisms are involved in degradation of binder phases and would require additional investigation. Adhesive wear was found to be active on flank wear land, resulting in microscopic removal of both cBN and binder.

Apart from degradation, tool protection phenomena were also discovered. Oxidation of Inconel 718 resulted in formation of γ-Al_2O_3 and $(Al,Cr,Ti)_3O_4$ spinel that were deposited on the tool rake. Also on the rake, outwards diffusional flux of nitrogen ended in a solid state chemical reaction with formation of (Ti,Nb,Cr)N above cBN grains. This creates a sandwich *tool protection layer* consisting of bottom (Ti,Nb,Cr)N and top γ-Al_2O_3 coating on cBN forming continuously as tool wear progresses. Such in operando protection enabled counterbalancing tool wear mechanisms and achieved high performance of PcBN in machining.

Declaration of Competing Interest

The authors declare that they have no known competing financial interests or personal relationships that could have appeared to influence the work reported in this paper.

Acknowledgments

This research was partly funded by European Union's Horizon 2020 Research and Innovation Programme under Flintstone2020 project (grant agreement No. 689279). It was also co-funded by strategic research programme of Sustainable Production Initiative (SPI), involving cooperation between Lund University and Chalmers University of Technology. The authors also would like to express their gratitude to Dr. Mathias Agmell for the help with FEM simulations. Authors are grateful to E. Brug (University of Cambridge) for fruitful and inspiring discussions.

References

[1] Paulonis DF, Schirra JJ (2001) Alloy 718 at Pratt & Whitney - Historical perspective and future challenges. *Proceedings of the International Symposium on Superalloys and Various Derivatives* 1:13–23.
[2] M'Saoubi R, et al. (2015) High performance cutting of advanced aerospace alloys and composite materials. *CIRP Annals - Manufacturing Technology* 64/2:557–580.
[3] Khan SA, et al. (2012) Tool wear/life evaluation when finish turning Inconel 718 using PCBN tooling. *Procedia CIRP* 1:283–288.
[4] Costes JP, Guillet Y, Poulachon G, Dessoly M (2007) Tool-life and wear mechanisms of CBN tools in machining of Inconel 718. *International Journal of Machine Tools and Manufacture* 47:1081–1087.
[5] Bushlya V, Gutnichenko O, Zhou J, Avdovic P, Ståhl J-E (2013) Effects of cutting speed when turning age hardened Inconel 718 with PCBN tools of binderless and low-CBN grades. *Machining Science and Technology* 17/4:497–523.
[6] Bushlya V, Zhou J, Avdovic P, Ståhl J-E (2013) Performance and wear mechanisms of whisker-reinforced alumina, coated and uncoated PCBN tools when high-speed turning aged Inconel 718. *International Journal of Advanced Manufacturing Technology* 66:2013–2021.
[7] Hsin LC, Sugihara T, Enomoto T (2020) High speed machining of Inconel 718 with high pressure coolant focusing on material structures of CBN tools. *International Journal of Automation Technology* 14:1045–1050.
[8] M'Saoubi R, et al. (2012) Surface integrity analysis of machined Inconel 718 over multiple length scales. *CIRP Annals - Manufacturing Technology* 61:99–102.
[9] Liew WYH, Ngoi BKA, Lu YG (2003) Wear characteristics of PCBN tools in the ultra-precision machining of stainless steel at low speeds. *Wear* 254:265–277.
[10] Shintani K, Kato H, Maeda T, Fujimura Y, Yamamoto A (1992) Cutting performance of CBN tools in machining of nickel based superalloy. *Journal of Japan Society for Precision Engineering* 58/10:1685–1690.
[11] Bushlya V, et al. (2019) On chemical and diffusional interactions between PCBN and superalloy Inconel 718: Imitational experiments. *Journal of the European Ceramic Society* 39:2658–2665.
[12] Bushlya V, Lenrick F, Ståhl J-E, M'Saoubi R (2018) Influence of oxygen on the tool wear in machining. *CIRP Annals* 67/1:79–82.
[13] Kim H-E, Moorhead A J (1991) Corrosion and strength of SiC whisker-reinforced alumina exposed at high temperatures to H2-H2O atmospheres. *Journal of the American Ceramic Society* 74/6:1354–1359.
[14] Samain L, et al. (2014) Structural analysis of highly porousγ-Al2O3. *Journal of Solid State Chemistry* 217:1–8.
[15] Hansen M, Anderko K (1958) *Constitution of Binary Alloys*, 2 ed McGraw-Hill Companies. New York. 256.
[16] Karlsson L, Norden H (1986) Grain boundary segregation of boron. an experimental and theoretical study. *Journal de Physique* 47/7:257–262.
[17] Andersson J-O, et al. (2002) Thermo-Calc & DICTRA, computational tools for materials science. *CALPHAD Comput. Coupling Phase Diagrams Thermochem.* 26:273–312.
[18] Agmell M, et al. (2020) Investigation of mechanical and thermal loads in pcBN tooling during machining of Inconel 718. *The International Journal of Advanced Manufacturing Technology* 107:1451–1462.
[19] Matsui N, et al. (2011) Microscopic observation of the interface between a tool wear surface and deposits from a low carbon free cutting steel machined. *Journal of the Japan Institute of Metals* 75/9:516–523.
[20] Solozhenko V, Turkevich V (2018) Phase Diagram of the B–BN System at Pressures up to 24 GPa: Experimental Study and Thermodynamic Analysis. *The Journal of Physical Chemistry* 122/15:8505–8509.
[21] Orellana W, Chacham H (1999) Atomic geometry and energetics of vacancies and antisites in cubic boron nitride. *Applied Physics Letters* 74/20:2984–2986.
[22] Wriedt HA, Murray JL (1987) The N-Ti (Nitrogen-Titanium) system. *Bulletin of Alloy Phase Diagrams.* 8:378–388.
[23] Tampieri A, Belossi A (1991) Oxidation Resistance of Alumina-Titanium Nitride and Alumina-Titanium Carbide Composites. *Journal of the American Ceramic Society* 75/6:1688–1690.
[24] Komratov GN (1997) The oxidation kinetics of titanium carbide, nitride, and carbonitride powders in air. *Powder Metallurgy and Metal Ceramics* 36:9–10.

Paper IX

Wear 484-485 (2021) 203991

Contents lists available at ScienceDirect

Wear

journal homepage: www.elsevier.com/locate/wear

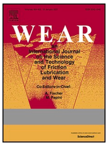

Thermodynamic modeling framework for prediction of tool wear and tool protection phenomena in machining

Axel Bjerke [a,*], Andrii Hrechuk [a], Filip Lenrick [a], Andreas Markström [b], Henrik Larsson [c], Susanne Norgren [d], Rachid M'Saoubi [e], Thomas Björk [f], Volodymyr Bushlya [a]

[a] *Division of Production and Materials Engineering, Lund University, Ole Römers väg 1, Lund, Sweden*
[b] *Thermo-Calc Software AB, Råsundavägen 18, SE-169 67, Solna, Sweden*
[c] *Unit of Structures, Dept Materials Science and Engineering, KTH, SE-10044, Stockholm, Sweden*
[d] *Sandvik R&D, Lerkrogsv. 13, 126 80, Stockholm, Sweden*
[e] *R&D Materials and Technology Development, Seco Tools AB, 737 82, Fagersta, Sweden*
[f] *Ovako Group, Olof Hjorts väg 2, 813 35, Hofors, Sweden*

ARTICLE INFO

Keywords:
Wear modelling
Thermodynamic modeling
Steel
Ultra-hard materials
Cutting tools
Electron microscopy

ABSTRACT

Chemical, oxidational and diffusional interactions between the tool, chip and cutting environment are known tool wear mechanisms in machining. However, the interaction between tool, coating, workpiece, coolant and atmospheric oxygen can, under favorable conditions, lead to formation of reaction products that retard tool wear. A method with the ability to predict theses interactions, would therefore enable a better control over tool life in machining. An attempt to create such a modelling framework is developed in this study. This method can predict the phase composition and the driving force for degradation and the formation of protective interaction products in the cutting zone. This modeling approach is applicable across cutting processes in which chemical, diffusional and oxidational wear are dominant or present. This framework has been applied to investigate the interactions occurring in the cutting zone during turning of a medium alloyed low-carbon steel (Hybrid Steel® 55). A range of degradation events are predicted, as well as the formation of a protective corundum $(Al,Fe,Cr)_2O_3$ or spinel $(Al,Fe,Cr)_3O_4$ film due to an interaction between the Al-alloyed steel and the environment. Validation of the modeling was performed by studying tool wear and reaction products formed when machining with ceramics, PcBN and coated carbide tooling. Inserts are studied by the use of scanning and transmission electron microscopy, after cutting tests were performed. Additional tests were performed in different environments (dry, argon and coolant). The results confirmed the model predictions of oxidation and diffusion wear as well as the formation of an $(Al,Fe,Cr)_3O_4$ tool protection layer. Thus, the proposed thermodynamic framework seem promising to serve as a predictive instrument for the correct pairing of existing tool and workpiece combinations and cutting parameters, or for tailoring respective material compositions for intentional formation of a tool protection layer. As well as guidance on how to apply present and future kinetic models when concurrent interaction mechanisms are present. Which lead to a reduction and minimization of costly experimental machining tests.

1. Introduction

Predictive models of metal cutting are an essential tool to reach optimum productivity [1]. Tool life modelling originated with the development of Taylor's equation [2] which relates the cutting speed to the tool life, and was later extended by Colding to include an equivalent chip thickness [3]. These equations and their derivatives are empirical models describing tool life expectancy for a narrow window of process conditions and materials. These models are routinely used in industry [4], despite their heavy reliance on large arrays of repetitive experimental data and absence of relations to occurring physical phenomena.

The limitations of empirical models were recognized early and this lead to the interest in physics-based analytical tool wear models, designed to have a predictive power independently of process conditions. One of the earliest models is the abrasive wear model by Archard [5] operating with the single wear mechanism of abrasion. Similar single-mechanism models predicting the kinetics of tool wear by diffusion [6,7] and thermodynamic models of the chemical interactions [8]

---

[*] Corresponding author.
E-mail address: axel.bjerke@iprod.lth.se (A. Bjerke).

https://doi.org/10.1016/j.wear.2021.203991
Received 12 February 2021; Received in revised form 25 May 2021; Accepted 21 June 2021

are among the original attempts to model tool wear. However, it should be recognized that many such models are physics-based but not entirely analytical, because they rely on experimental cutting data to calibrate the underlying equations.

Modern high-speed machining generates high temperatures in the cutting zone, which activate multiple interdependent wear mechanisms, such as chemical, oxidational and diffusional wear [9]. These multiple and interdependent wear mechanism cannot be modeled by the early single wear mechanism models. This problem motivated the development of hybrid models build-up of multiple single wear mechanisms models with assumed weight coefficients. Kramer and von Turkovich [10] combined abrasive and dissolution wear models into a composite model and proposed a series machining procedures to estimate the weightings. Huang and Dawson [11] further extended this approach to combine three mechanisms of abrasion, adhesion and diffusion for the case of PcBN wear in hard turning. Malakizadi et al. [12] developed a thermodynamics approach to assess the potential solubility of W and C in the steel for uncoated tools. This model was further combined with finite element (FEM) simulations to map process temperature for a range of cutting data and tool wear. Empirical coefficients was then used to transform the calculated potential solubility at the modeled temperature into tool material loss.

Unfortunately, the tool life determining wear mechanisms are not known before conducting a machining test. Thus, an accurate assignment of weight coefficients for each of the mechanisms or even predicting what mechanism will occur, is not possible before a machining test and its rigorous analysis has been conducted. The predictive power of such hybrid models are consequently limited, because each unique combination of cutting data and conditions, will affect such weightings in their unique way. At the same time, current kinetic and analytical models are unable to handle concurrent wear mechanisms for multi-component interaction systems. Hence, a model that can predict the tool life determining wear mechanisms is needed for degradation driven by thermodynamics and chemistry in addition to mechanical wear. Either to reduce the complexity the modeling problem to be able to develop completely analytical kinetic models or to analytically predict the weighing coefficients, before cutting tests are carried out.

Further complications, even for single-mechanism modeling, can arise when the interaction between tool and workpiece or environment does not lead to tool degradation. Interactions have shown to result in the build-up of tool protective layers and reaction products retarding tool wear. Gutnichenko et al. [13] demonstrated the formation of an Al_2O_3 film on PcBN tools while machining white cast iron, which resulted in suppressed crater wear, thereby acting as a tool protection layer (TPL). A tool protection layer differs from well-known mechanisms such as built-up layers (BUL), transfer layers (TL), tribofilms [14] or deformed binder material [15]. A TPL represents a new phase that is formed on the surface of the tool *in-operando*, due to the reaction between the tool, cutting environment and workpiece [16]. The formation of such a TPL has been reported for tool and workpiece interaction in which NbC [17], (Ti,V)C or (Ti,V,Cr)B_2 [18], (Ti,Nb)N [19] and (bcc) W [20] films formed during the cutting process. Experimental observations have also reported on the formation of Al_2O_3 [21], Al–O and AlN [22] as a result of interaction between the tool and workpiece as well as atmospheric air. The understanding and predictive modeling of the TPL formation and its stability is absent in literature, despite the benefits of retarding tool wear that are offered by a tool protection layer. Not being able to predict the formation and stability of TPLs hinders the correct pairing of existing tool and workpiece material, or the tailoring of material compositions and machining parameters for the intentional formation of build-up of such a protection layer.

This study develops a modeling framework based on thermodynamic calculations, which act as a predictive instrument for chemical, thermal, oxidational and diffusional interactions in machining. This is in contrast to works using thermodynamic modeling to describe and rank degradation mechanism based on experiments results [23,24], rather than predicting it. This modeling framework has also been developed to predict the potential formation of a tool protection layers in addition to degradation and the conditions for its existence and stability.

Hence, this method predicts which phenomena will occur, their driving forces and provides an assessment of their relative importance. However, it is not capable of predicting the rate at which the mechanisms will result in degradation or protection. Rates are predicted by kinetic models, which currently cannot model the concurrent multi-component interaction system of metal cutting without empiric fitting. However this model's predictive power can reduce the complexity of the wear process, to potentially allow current analytical and kinetic models to be used without empirical fitting. The proposed thermodynamic predictive framework has been exemplified and validated for machining a medium alloy low-carbon steel (Hybrid Steel® 55) using six tool materials. The validation has also been supported by scanning and transmission electron microscopy, infrared thermography and cutting tests in different environments (dry, argon and coolant). The results demonstrate how the thermodynamic model can currently be used to select tool materials, alloying compositions and cutting parameters that lead to the formation of tool protection layers. While also potentially reducing the reliance on empirical fitting parameters, when applying kinetic models.

2. Methods

The thermodynamic and chemical interactions during the cutting process involves close contact between a cutting tool and a workpiece in a specific environment. Such interactions can be divided into three individual categories (i–iii) or their combination (iv). (Fig. 1):

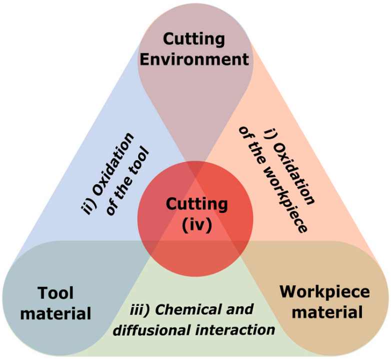

Fig. 1. Schematic illustration showing three individual interactions (corners), their interplay during the cutting process (sides) and their combined effect (center).

ii) Oxidation of the tool material. The tool material itself can react with atmospheric oxygen or oxygen in the workpiece during the cutting process, which may lead to the formation of softer, deformable or even vaporable oxides, all of which can result in rapid tool degradation [27]. The rate of oxidation depends on the process temperature, contact pressure, material system and the availability of oxygen during the cutting process [28].

iii) Chemical and diffusional interaction. The tool and the workpiece can also react or dissolve by diffusion into to each other, leading to chemical [29] and diffusional wear mechanisms [30]. The pressure, temperature and composition of the tool and workpiece materials will determine the possibility and rate of such reactions [12].

iv) The cutting process. The above three interactions: oxidation of the workpiece (i), oxidation of the tool (ii) and chemical and diffusional interaction (iii) frequently occur concurrently in the cutting process. However, the cutting process may also involve an extra layer of interactions, such as the interaction between the tool and workpiece oxides formed *in-operando.*

i) Oxidation of the workpiece material. The workpiece itself, the generated chips and workpiece material adhered to the tool, can react with oxygen from the environment. This phenomenon leads to formation of oxides which, in turn, can protect the tool from oxidation [22,25], or react with the tool and accelerate the degradation of the tool material [26].

There are currently several categories of models, and their development is briefly outlined in the Introduction (Section 1). They may be divided into empirical models that rely on technological variables such as cutting speed, feed, depth of cut and tool geometry [4]. There are early physics-based models that describe a single mechanism [7,31]. Then there are hybrid models that combine analytical models with empirical coefficients [10,12,29]. Finally there are analytical models based on only thermodynamics and kinetics which are used to describe the observed phenomenon [17,23,24,32].

The framework developed in this paper (Fig. 1) is an analytical model based on thermodynamics. This relies on the physical quantities such as temperature, pressure and chemical potential, as outlined in Section 2.1 and Appendix A, this makes it possible to create predictive results before any machining tests are performed, regarding the thermal and chemical wear. This allows for predicting protective interaction phenomena, which models found in literature have not attempted to do.

2.1. *Computational framework*

CALPHAD is a phenomenological approach for calculating thermodynamic, kinetic, and other properties of multicomponent materials systems. It is based on describing the properties of the fundamental building blocks of materials, namely the phases, starting from pure elements and binary and ternary systems. CALPHAD predicts the properties of higher order alloys, with extrapolation from the binary and ternary systems, Over the last decades, the CALPHAD method has successfully been used for development of numerous engineering materials. It has also been used to study and describe different types of tool – workpiece interactions, see e.g. Refs. [17,32], however it has not to the authors' knowledge been used to create generic tool wear models.

In CALPHAD the Gibbs energy (G^{α}) of each phase *(α, β …)* is described as a function of pressure (*P*), temperature (*T*) and composition (x_i^{α}). The thermodynamic modeling of Gibbs energy is based on physical models and is described in Appendix 1. Gibbs energy is chosen since in an isothermal isobaric system, equilibrium is reached when the Gibbs energy reaches its minimal value. The current study uses Thermo-Calc [33], a CALPHAD-based software. This method can calculate all the thermodynamic properties of the system at a given composition (X_i), temperature (*T*) and pressure (*P*).

Thus, the task is to translate the cutting parameters into thermodynamic quantities. The physical state (P, T, X_i,) in the cutting zone depend on cutting parameters such as cutting speed (v_c), feed (*f*), depth of cut (a_p), materials, tool geometry, etc. It should also be noted that conditions vary across the tool/chip and tool/workpiece contact zones. The contact pressures can reach above 10^9 Pa and temperatures often range from 500 °C to 1300 °C [34,35]. The availability of oxygen in the cutting zone, is in this paper expressed using the oxygen activity where the reference state is pure oxygen gas; the oxygen activity thus correspond to the partial pressure of O_2 *(dimenionless)*, it is 1 in a pure O_2 environment, approximately 0.21 in the ambient atmosphere and 0 in an oxygen-free environment. Hence, a partial pressure in the range of 0–0.21 is expected across the seizure zone, sliding zone and transition zone [36]. The state will also in general change during the cutting process. The tool will initially encounter a continuous supply of workpiece material, but adhered metal or a reaction product might also separate the tool from the chip and workpiece as the cutting progresses. The effect of any change in the composition and cutting parameter space can therefore be explored before any cutting tests are executed. Thus predict the formation of different reaction products at the tool/chip interface assuming that all phases have equal nucleation energy e.g. disregarding the kinetics of the reactions.

The above translation allows us to calculate the equilibrium phase composition (x_i^{α}, x_i^{β} …) in the cutting zone (Eq. (1)). The calculation results show if the tool material is thermodynamically stable at elevated process temperatures and pressures. The result also give the equilibrium phase composition in the cutting zone. These results then indicate what phases will form in the cutting zone.

$$G(P, T,\ X_i\ , ..) = G^{\alpha}(P, T, x_i{}^{\alpha}, ..) + G^{\beta}(P, T, x_i{}^{\beta},\ ..) + \dots \tag{1}$$

This also allows the normalized driving force per mole *(dimensionless)* for the precipitation of these reaction products to be calculated. To do this, the phase composition of the tool, workpiece and the environment are first defined, then followed by the equilibrium state calculations. It is then possible to obtain the driving force for the formation of the first infinitesimal amount of reaction products, for the given equilibrium state. This allows the driving forces to be evaluated independently of any conceivable reaction products. The driving force for phases likely to form defined by the initial equilibrium calculations (Equation (1)) are shown in the results, however the driving force of any other phase can also be calculated using this method.

Consequently, careful translation of the cutting conditions into thermodynamic boundary conditions is crucial because correct translation makes it possible to calculate whether the tool and workpiece materials are stable or will react with each other or the environment (interactions *i–iv*). The equilibrium phase composition and the driving force for the reaction products to be formed can then be calculated and identified, if a reaction occurs. These procedural steps are performed for the given boundary conditions of temperatures, pressures, cutting environments, tools and workpiece combinations.

2.2. *Experimental framework*

The above-described methodology of investigating the interactions between tool, workpiece and the environment during metal cutting is independent of the materials, tool and cutting parameters in question. The selected material for this particular machining test is Hybrid Steel® 55 (X20NiCrAlMoV6-5-2-1), a medium alloy low-carbon steel. Hybrid Steel® 55 alloyed with Mn, Cr, Ni, Mo, V and Al according to Table 1. This kind of alloying should allow for a wide range of potential interactions.

Machining was performed for the steel supplied in a quenched and aged condition, which resulted in a microstructure of tempered martensite, fine carbides and precipitates of a Ni_3Al intermetallic phase. Fig. 2a is the X-ray diffraction (XRD) spectrum indicate the presence of tempered martensite and the Ni_3Al phase. Fig. 2b shows the backscatter electron (BSE) image of the material displaying a martensitic lath structure. The Vickers hardness of aged steel is measured to HV10 = 4.8 GPa.

The machining was longitudinal finish turning on a CNC SMT500 lathe (70 kW) at a constant cutting speed of $v_c = 300$ m/min, feed $f = 0.1$ mm/rev and depth of cut of $a_p = 0.3$ mm under dry cutting conditions. Through an iterative increase in cutting speed, these test conditions were found to provide sufficient tool life for investigation of wear processes and reflect an actual production viewpoint.

Six different tool materials (Table 2) were tested to investigate the machinability of the steel and to explore the widest range of interactions. The tools were a titanium aluminum nitride ((Ti,Al)N) physical vapor deposition (PVD) coated cemented carbide (WC–Co), four ceramic tools and a polycrystalline cubic boron nitride (PcBN) with low cBN concentration (50 vol %) and TiC binder. The four ceramic tools among which three contained silicon-based phases were silicon nitride (Si_3N_4), SiAlON, and whisker-reinforced alumina (Al_2O_3-SiC_w). The fourth ceramic tool is a mixed alumina (Al_2O_3–TiC). This choice of workpiece and tool material is selected to allow for the studying of

Table 1
Hybrid Steel® 55 composition by wt. % [48].

	C	Si	Mn	P	Cr	Ni	Mo	V	Al	Fe
Min (mass %)	0.16	0	0.20	0	4.80	5.80	0.60	0.45	2.00	balance
Max (mass %)	0.20	0.20	0.40	0.015	5.20	6.20	0.80	0.55	2.40	

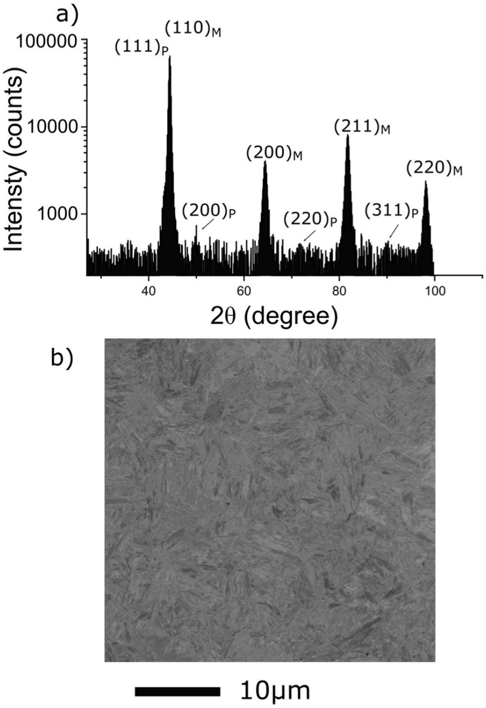

Fig. 2. a) XRD spectrum showing tempered martensite (M) and Ni_3Al precipitates (P) and b) backscatter image (BSE) of the martensitic lath structure of aged Hybrid Steel® 55 precipitates.

Table 2
List of tools materials and geometry.

Tool material	Geometry
WC–Co (substrate), (Ti,Al)N (coating)	CNMG120408-MF1
Si_3N_4 (solid ceramic)	CNGA120408T02020
Al_2O_3 - SiC_w (whisker reinforced ceramic)	CNGA120408T01020
SiAlON (solid ceramic)	CNGA120408E
Al_2O_3 - TiC (mixed ceramic)	CNGA120408T00520
50% cBN (grains) and TiC (binder)	CNGA120408S-01020-L1-U

several types of chemical and thermodynamic interactions, rather than abrasive wear.

The machining test was initially conducted at intervals of 15 s. However, longer intervals were used for higher preforming tools (Al_2O_3–TiC and cBN-TiC). The cutting test was used to measure wear development, tool life and investigate interaction mechanisms. All cutting tests were also repeated for every tool at an engagement time exceeding the tools obtained tool life. Flank wear, rake wear and cutting forces were continuously measured. Flank wear measurements were performed using an Olympus SZX7 stereo light optical microscope, while an Alicona Infinite Focus 3D microscope was used for crater wear analysis. The wear criteria were set to flank wear VB = 200 μm due to the tolerances needed for finish machining of bearing steel and the crater wear criteria was set to KT = 30 μm due to the risk of tool breakage. A PCLNL2525M12 tool holder was used and the cutting forces was monitored using a Kistler 9129AA dynamometer.

Worn tools were investigated using a Tescan Mira3 Scanning Electron Microscope (SEM), with both secondary (SE) and backscatter electron (BSE) detectors. It is also equipped with an X-ray Energy Dispersive Spectrometer (XEDS), used in this study to investigate the elemental composition. Focused ion beam (FIB) samples for transmission electron microscopy (TEM) were extracted from the tools using a FEI Nova NanoLab 600 FIB-SEM. A JEM-3000F TEM, also equipped with an XEDS, this was used to investigate the chemical and phase composition of worn tools and interaction products.

3. Results and discussion from the theoretical prediction

The results from the thermodynamic predictions are given in this section. The results are grouped into the oxidation of the workpiece material (*interaction i*) in 3.1, the oxidation of the tool materials (*interaction ii*) in 3.2, the chemical and diffusional interaction (*interaction iii*) and the overall cutting process (*iv)* in 3.3. Section 3.1, 3.2 and 3.3 are further divided in the following tool material categories: 1. Silicon containing tools (Si_3N_4, Al_2O_3-SiC_w, SiAlON), 2. The coated cemented carbide tool ((Ti,Al)N coated WC–Co) and 3. Titanium carbide containing tools (Al_2O_3–TiC, cBN-TiC).

3.1. Oxidation of workpiece material (i)

The equilibrium phase composition was modeled at different pressures, temperatures and effective O_2 partial pressures (see Fig. 3a). This creates the possibility of mapping the physical quantities of machining parameters to specific areas of the cutting zone. This modeling section aims to illustrate and predict potential oxides that might form in the cutting zone as a result of a reaction between the workpiece material and the environment. The results in this section show all phases that are thermodynamically stable under the prevailing conditions, for reactions in category *i) oxidation of the workpiece*. The calculations were performed for temperatures from 25 °C and up to 1200 °C, for pressures from 10^5 Pa up to 10^9 Pa and from an effective O_2 partial pressure of 0–0.21. For ease of comparison, all figures were plotted at 1000 °C and 10^5 Pa as these conditions were found to be most illustrative. Additional figures and comments are introduced when a change in temperature and pressure results in a significant change in the behavior of the interaction. The databases contain information about molar volume, but not its volume dependence on pressure, which is a good approximation of these phases when the pressure is below 10^9 Pa [37]. Gases such as Ar, O_2 and CO_2 is modeled as one phase (gas) with different constituents (Ar, O_2, CO_2 etc.).

Fig. 3a reports the equilibrium phase fraction as a function of the effective O_2 partial pressure at 1000 °C and 10^5 Pa for Hybrid Steel® 55. FCC (austenite) is the equilibrium phase of the steel at this temperature and pressure. Fig. 3b gives the driving force for the formation of these oxides from a gas (Ar and O_2) and Hybrid Steel® 55, versus increasing effective partial pressure of O_2 at 1000 °C and 10^5 Pa. Fig. 3 reports the modeling results which predict that $(Al,Fe,Cr)_2O_3$ mixed corundum

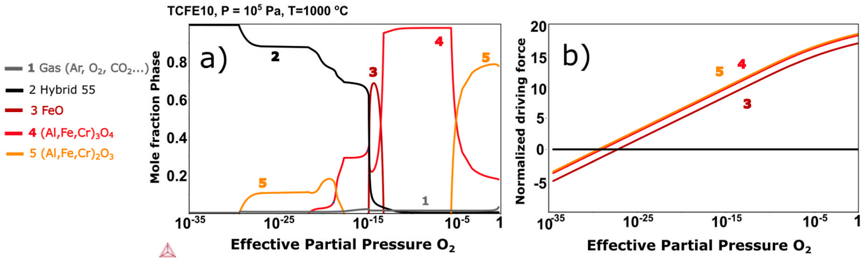

Fig. 3. a) show which oxides may form in the cutting zone due to oxidation of the workpiece, it is the equilibrium phase fractions when Hybrid 55 reacts with oxygen as a function of the effective partial pressure of O_2 b) The driving force for these phases to form dependent on the effective partial pressure of O_2. This show which phases are more likely to form. The corundum phase $(Al,Fe,Cr)_2O_3$ and spinel phase $(Al,Fe,Cr)_3O_4$ have a higher driving force than FeO.

oxide is stable at low effective partial pressures (below 10^{-17}) and high partial pressures (above 10^{-6}). $(Al,Fe,Cr)_2O_3$ has the highest driving force for formation, while FeO is only stable in the range of 10^{-15}-10^{-13} and has the lowest driving force of formation. $(Al,Fe,Cr)_3O_4$ spinel phase is stable above a partial pressure of 10^{-20} and has a driving force close to $(Al,Fe,Cr)_2O_3$ (Fig. 3). The steel can also dissolve a small amount of oxygen before an oxide forms (Fig. 3a). These general trends are robust for temperatures from 25 °C and up to 1200 °C and for pressures from 10^5 Pa up to 10^9 Pa.

$(Al,Fe,Cr)_2O_3$ and $(Al,Fe,Cr)_3O_4$ are both stable at high and low O_2 partial pressures (Fig. 3a) and have a high driving force for formation (Fig. 3b). Thus, they are the most likely to form and remain stable. FeO on the other hand is stable in a narrow range of effective oxygen partial pressures and has a lower driving force for formation than the other two reaction products (Fig. 3). Modeling was also performed for a hypothetical steel that do not contain aluminum and chromium, these show a reverse trend dominated by the formation of FeO.

Oxides such as aluminum oxide, can act as a barrier to oxidational tool wear of multilayer CVD coated cemented carbide tool [22]. However, FeO can react with a cBN tool and cause tool degradation [27]. Hence, both positive and negative effects are expected from the formation of workpiece oxides on tool surfaces. It can protect against oxidation or catalyze the oxidation. The effect depends on the interaction between the formed product and the tool material, determined by cutting process interactions (*interaction iv*).

3.2. Oxidation of the tool material (ii)

The reaction between the tool and the environment can be modeled in the same way as the interaction between workpiece and environment. Hence, the section below relates to category *ii) Oxidation of the tool.* This section aims to shed light on whether the tool degraded by oxidational wear mechanisms and under which conditions such wear processes take place.

3.2.1. Silicon-containing tools (Si_3N_4, Al_2O_3-SiC_w, SiAlON)

The silicon nitride (Si_3N_4) tool material is not thermodynamically stable (metastable) at ambient total gas pressures. Hence, the amount of

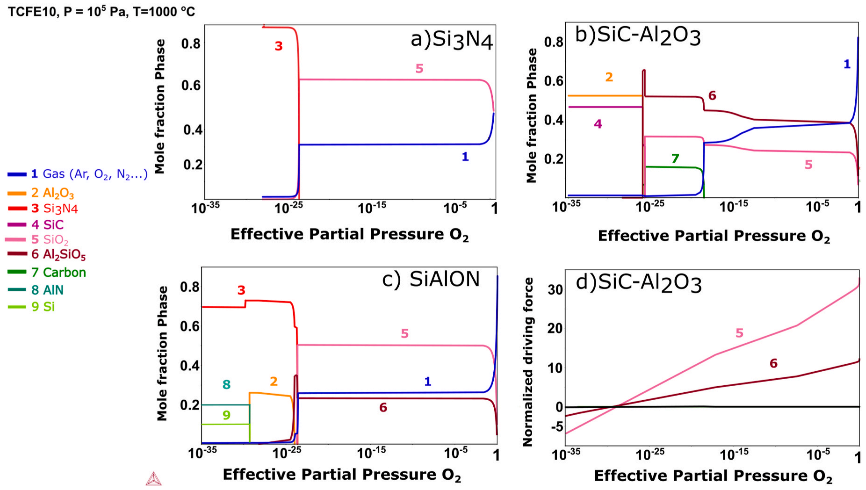

Fig. 4. a) Modeling results showing the oxidation of Si_3N_4, leading to formation of SiO_2 with increasing effective partial pressure of O_2 b) and c) showing similar calculation results for Al_2O_3-SiC_w and SiAlON tools, both reactions leading to the formation of Al_2SiO_5 in addition to SiO_2. d) The driving force for formation of SiO_2 and Al_2SiO_5 versus increasing oxygen availability in the representative case of the Al_2O_3–SiC_w tool.

Si_3N_4 decreases to zero at an effective O_2 partial pressure of 10^{-23}, as it decomposes to SiO_2 and gas as the effective partial pressure of O_2 increases, given a high enough temperature and time. This is seen in Fig. 4a where the molar phase fractions is plotted as function of increasing effective oxygen partial pressure. The trend remains unchanged within the range of cutting temperatures and pressures investigated in this study. However, calculations show that increasing the temperature increases the effective partial pressure at which SiO_2 becomes stable. Decreasing the pressure increases the effective O_2 partial pressure at which SiO_2 becomes stable. The behavior of Al_2O_3-SiC_w is similar insofar as the trends are stable across cutting temperatures and pressures. However, Al_2O_3-SiC_w degrades into SiO_2, Al_2SiO_5 and graphite, as shown in Fig. 4b. This is followed by the oxidation of graphite and the formation of CO_2 gas at elevated temperatures.

Finally, SiAlON is a more complicated phase to model, since it basically inherits the lattice structure of Si_3N_4 but with partial replacement of Si–N bonds by Al–O and Al–N bonds [38]. Fig. 4c show that Al_2SiO_5, SiO_2 and gas phases are the most stable as the effective partial pressure of O_2 increases. Thus, SiAlON resembles both Si_3N_4 and Al_2O_3-SiC_w decomposition. Fig. 4d show the driving force for the formation of SiO_2 and Al_2SiO_5 versus an increasing effective partial pressure of O_2 in the case of Al_2O_3-SiC_w. The trend is the same for all three silicon-containing tools since the carbon present in SiC transform into graphite and CO_2 and excess nitrogen transform into a gas when thermodynamic equilibrium is reached.

Silicon-containing tools have different mechanical properties [39] but are predicted to degrade in an oxygen environment in a similar manner (Fig. 4a–c). The silicon will react with the oxygen to form SiO_2 (Fig. 4). The presence of aluminum, as in the case of SiAlON and Al_2O_3-SiC_w, additionally results in the formation of Al_2SiO_5 (Fig. 4b–d). Neither of the elements C or N are likely to participate in the formation of protective reaction products (Fig. 4b and c). Both the predicted formation of SiO_2 and Al_2SiO_5 would lead to a rapid degradation of these tool materials [28].

3.2.2. *Coated cemented carbide tools (WC–Co, (Ti,Al)N)*

For the purpose of modeling, the cemented carbide tool with a PVD (Ti,Al)N coating can be divided into the following four phases: two for the substrate WC and cobalt metal and two for the coating TiN and AlN. Such a representation of the (Ti,Al)N coating is related to the fact that (Ti,Al)N is a metastable phase at the modeled conditions. Although modeled, WC and cobalt phases are not shown in Fig. 5 for reasons of clarity. The substrate is known to oxidize and the focus of the study is the coating. The wear rate of cemented carbide is also more rapid and more studied than (Ti,Al)N [34,35]. Fig. 5a shows the equilibrium phase fractions for TiN and AlN, versus an increased effective partial pressure of O_2. (Ti,Al)N will degrade into TiO_2 and $(Al,Ti)_2O_3$ while nitrogen will form N_2. Fig. 5b shows that the driving force for the formation of TiO_2 and $(Al,Ti)_2O_3$ is steadily increasing with an increasing availability of oxygen.

The coating will tend to oxidize but the rate of the oxidation will depend on the temperature in the cutting zone and the availability of oxygen (Fig. 5). Hence, the degradation of the coating by the formation of TiO_2 and $(Al,Ti)_2O_3$ is predicted to be the main oxidational wear mechanism for the (Ti,Al)N coating (Fig. 5).

3.2.3. *Titanium carbide-containing tools (Al_2O_3–TiC, cBN-TiC)*

Fig. 6a gives the equilibrium phase fractions for the TiC phase present in the tool dependent on the effective partial pressure of O_2. This calculation is valid for the oxidation of only the TiC binder in both Al_2O_3–TiC and cBN-TiC tools. First, Ti_2O_3 forms at lower partial pressures and TiO_2 at higher partial pressures of O_2 and the carbon will form CO_2 gas (Fig. 6a). The driving force for the formation of TiO_2 and Ti_2O_3, in turn, depends on the partial pressure of O_2. The driving force for the formation of Ti_2O_3 is initially higher. Then driving force for formation of TiO_2 surpasses than of Ti_2O_3 at higher effective partial pressures (Fig. 6b). However the difference between TiO_2 and Ti_2O_3 is small (Fig. 6a). Al_2O_3 does not react with oxygen at any machining temperatures and pressures. Hence, the Al_2O_3–TiC tool should only experience an oxidational attack on the TiC and not Al_2O_3.

The TiC-cBN tool will not only experience oxidational attack on TiC but also on the BN phase. Hexagonal boron nitride is the equilibrium BN phase at these temperatures and pressures, since cubic-BN is metastable at these conditions. Oxygen reacts with BN to form B_2O_3 (Fig. 7), which has a melting temperature of approximately 450 °C. Fig. 7 also shows that the driving force for the formation of B_2O_3 increases at higher effective O_2 partial pressure. The formation of B_2O_3 might potentially form a protective film on the tool surfaces, but such a product might melt or be abraded away during the cutting process. Calculations also show that increased pressures will increase the melting point of B_2O_3 without affecting other aspects of interaction.

3.3. *Chemical and diffusional wear (iii) and the cutting process (iv)*

Chemical and diffusional wear should be studied in addition to wear by oxidation, this is done by investigating whether the tool material is likely to react or dissolve into the workpiece material. In this section we also combine all three components of tool degradation: *oxidation of workpiece material (i)*, *oxidation of tool material (ii)* and *chemical and diffusional wear (iii)*. The calculations were also performed for temperatures from 25 °C and up to 1200 °C, for pressures from 10^5 Pa up to 10^9 Pa. This combination of mechanisms can predict whether the workpiece oxides or tool/workpiece reaction products could protect the tool from oxidation, diffusion and chemical wear or whether, on the contrary, if it will accelerate the degradation of the tool material. Technically, this can be performed in one single calculation because the workpiece material always has minor concentrations of dissolved oxygen, and an effective partial pressure of O_2 equaling zero is the same as a direct tool/

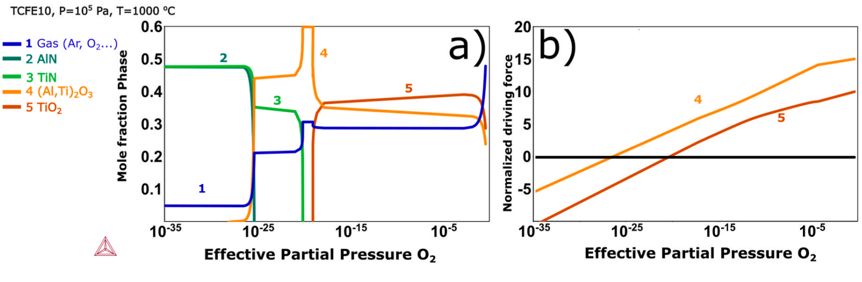

Fig. 5. a) Results from the equilibrium calculations between the modeled (Ti,Al)N coating and oxygen. (Ti,Al)N degrades into TiO_2 and $(Al, Ti)_2O_3$ together at increasing effective partial pressures of O_2. b) Showing the driving force for the formation of TiO_2 and $(Al, Ti)_2O_3$.

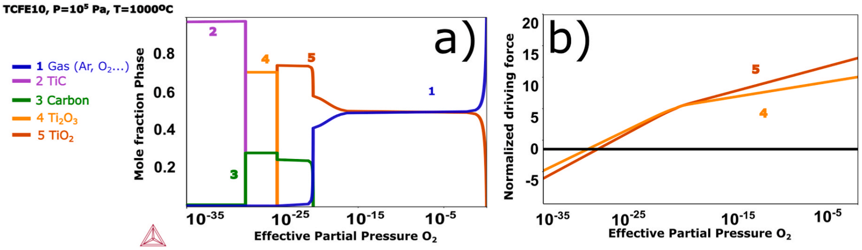

Fig. 6. a) The TiC present in both the Al_2O_2 and cBN tools can react with oxygen and form TiO_2 or Ti_2O_3. b) The driving force for formation of TiO_2 and Ti_2O_3. Ti_2O_3 has a higher driving force at a low effective O_2 partial pressure and TiO_2 at high effective O_2 partial pressures.

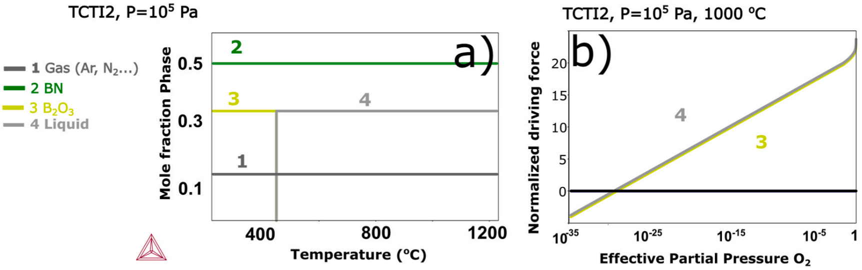

Fig. 7. Showing the molar phase fractions a) and driving force for formation b) for the interaction between BN and O_2. The formation of B_2O_3 is a result of BN oxidation. Under static conditions, B_2O_3 acts as an oxidation barrier, yet it melts and lacks the mechanical properties to function under the thermo-mechanical loads of cutting.

workpiece interaction *(iii)*. Hence this section models the combination of all the multi component interactions in cutting process *(iv)*.

3.3.1. *Silicon-containing tools (Si_3N_4, Al_2O_3-SiC_w, SiAlON)*

Silicon-containing tools are highly prone to oxidational wear according to earlier calculations given in Fig. 4. Fig. 8 gives the equilibrium phase composition of Hybrid Steel® 55 in contact with Si_3N_4 simultaneously under an increasing partial pressure of O_2. The phases in the red zone of Fig. 8 show the interaction at low O_2 partial pressures, where no new oxides are stable. This red zone represents the interaction *(iii)-chemical and diffusional wear* between the steel (workpiece/chip) and Si_3N_4. The region outside the red area represents the combined effect of (i), (ii) and (iii), the *cutting process (iv)*.

Si_3N_4 is in a stable phase at low effective oxygen partial pressures (red zone). Nevertheless, some N has formed AlN and (V,Cr)N (Fig. 8), a chemical interaction has to occur for these nitrides to form. Si_3N_4 is a stoichiometric phase and no new Si phase is formed at these low effective oxygen partial pressures. This result indicates that the Si has dissolved in the steel. This dissolution of Si indicates the possibility for diffusional interactions. This might not be obvious form Fig. 8, however the calculation contains all the thermodynamic properties of the system (Section 2.1 and Appendix A). Fig. 9 give the mole fraction of phases as a function of small additions of Si_3N_4 to the system. Showing that the steel can dissolve all the Si in Si_3N_4, up to an addition corresponding to the dotted line. It also shows the stability of the AlN and (V,Cr)N reaction products.

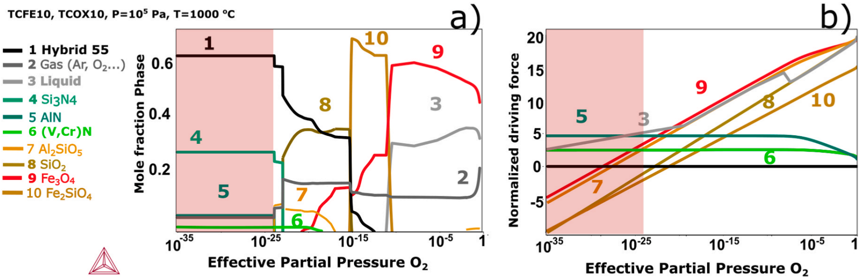

Figure 8. Showing the interactions (iii) and (iv) for the Si_3N_4 tool material. The products $(Al,Fe,Cr)_2O_3$, $(Al,Fe,Cr)_3O_4$ and SiO_2 in Figs. 3 and 4 are the results of the interaction (i) and (ii), which are now replaced by the reaction products Al_2SiO_5 and Fe_2SiO_4. Because combining interaction (i), (ii) and (iii) results in combination effects, hence (iv)-the cutting process shown by the schematic in Fig. 1.

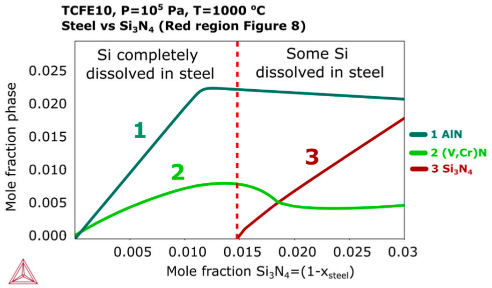

Fig. 9. Showing how Si can be completely dissolved in steel while N forms AlN and (V,Cr)N, indicating possible Si diffusion during machining.

SiO_2, Al_2SiO_4 and Fe_2SiO_4 become stable at even higher effective O_2 partial pressures (Fig. 8). However, Fe_2O_3 and a liquid phase containing silicon, metals and oxygen are both more thermodynamically favorable when the effective O_2 partial pressure is approximately 10^{-10} or above. The calculations predict that the mole fraction of products will differ for the Al_2O_3-SiC_w and SiAlON tools. However, the reaction products and their behavioral trend are similar since both carbon and aluminum are already present in the steel (Fig. 8).

Silicon-containing tools, as exemplified in the case of Si_3N_4, are likely to degrade by oxidational wear by the formation of SiO_2 and N_2 (Fig. 8). Additionally, Si tends to dissolve in the workpiece material (Fig. 9). Furthermore, Si will also react with any of the metal oxides from the workpiece oxidation (Fig. 3), thereby forming glassy phases such as Al_2SiO_5 and Fe_2SiO_4 (Fig. 8). Another possible and positive scenario might occur if the nitrogen reacts with the steel alloys Al, V and Cr, thereby forming nitrides instead of becoming gaseous N_2. The formation of such nitrides on the interface might retard tool degradation, however it might lead to abrasion if formed as particles. The iron-rich spinel Fe_3O_4 has a slightly higher driving force than the other phases in the predictions (Fig. 8) and this stable phase might protect the tool by acting as a barrier for further oxidation or diffusional dissolution. However, Si from the tool can react with this spinel and form Fe_2SiO_4 (Fig. 8), which would decrease its ability to protect the tool as it melts slightly above 1100 °C [40]. Fe, Ni and Cr can diffuse into the whiskers while Si diffuses out or oxidizes [41]. However, this would not lead to the formation of any tool protective layer. Changing the pressure and temperature does not significantly change the above interactions, but rather shifts the point at which the phases forming under high effective O_2 partial pressure become thermodynamically favorable.

3.3.2. Coated cemented carbide tool (WC–Co, (Ti,Al)N)

Oxidation can be significant in the case of the (Ti,Al)N coating as reported earlier in Fig. 5. The calculation results for the interaction with the addition of Hybrid Steel® 55 steel are shown in Fig. 10. Previously, the excess nitrogen released due to oxidation of (Ti,Al)N can now promote the formation of refractory nitride (V,Cr)N (Fig. 10), similar to the results in (Fig. 8). However, the oxidation of the coating remains the most significant interaction. The driving force for the formation of $(Al,Ti,Fe)_2O_3$ and $(Al,Fe)_3O_4$ still remains the largest and both phases are stable under high partial pressures of O_2.

Corundum $(Al,Ti,Fe)_2O_3$ and spinel $(Fe,Al)_3O_4$ (Fig. 10) are more capable of protecting the coating from oxidation than the oxides containing silicon (Fig. 8), as these interaction products are not glassy phases. The calculations also predict that the solubility of Ti, Al and N in steel is less than of Si. The metal oxides that form between the tool and the workpiece (Fig. 10) might also limit further oxidation and dissolution of the tool (Figs. 5 and 10).

3.3.3. Titanium carbide-containing tools (Al_2O_3–TiC, cBN-TiC)

Titanium carbide can degrade due to oxidation by transforming into Ti_2O_3 and TiO_2, as shown in Fig. 5. Alumina does not oxidize, while cBN will oxidize with a release of N_2 gas and the formation of B_2O_3, which becomes liquid above 450 °C at 10^5 Pa (Fig. 5). The calculation results in Fig. 11 show that the alumina phase with different compositions of $(Al,Fe,Cr)_2O_3$ is stable (Fig. 11a) and has a high driving force for formation. $(Al,Fe,Cr)_3O_4$ spinel is also thermodynamically stable and has virtually the same high driving force. Fig. 11 illustrate that Al_2O_3–TiC tool material will degrade through oxidation of TiC followed by the formation of Ti_2O_3 and the simultaneous dissolution of carbon in the steel. However, the dissolution of TiC is less favorable than its oxidation. Boron and nitrogen can also dissolve in the workpiece and chips similar to Si (Figs. 8 and 9), thus fulfills the criteria for diffusional wear and they can react and form borides and nitrides leading to chemical wear (Fig. 11).

The predictions also reveal that the cBN-TiC material is less resistant to chemical, oxidational and diffusional wear compared to the Al_2O_3–TiC material (Fig. 11). Both materials share the same TiC component but Al_2O_3 is essentially inert while cBN has many possible degradation paths. The calculation predict that the ratio of metallic elements in the spinel phases $(Al,Fe,Cr)_3O_4$ and corundum phases $(Al,Fe,Cr)_2O_3$ will be determined by the effective oxygen partial pressure. Starting from Al and Ti based oxides and shifting towards Fe and Cr. The formation of all such phases would have the possibility to form a TPL and slow down the tool degradation (Figs. 6, 7 and 11).

4. Experimental validation

The results from the cutting tests and microscopy are given in this section, it is divided in 3 parts as the previous Section 3 thus 1. Silicon-containing tools (Si_3N_4, Al_2O_3-SiC_w, SiAlON), 2. Coated cemented carbide tools (WC–Co, (Ti,Al)N) and 3. Titanium carbide-containing tools (Al2O3–TiC, cBN-TiC). The tool life criteria is set to VB = 200 μm and

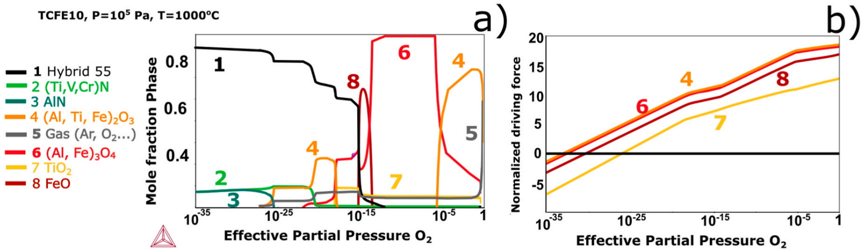

Fig. 10. The equilibrium calculation and driving force calculation for the interaction products forming due to interactions between the (Ti,Al)N-coated carbide tool, the steel and oxygen. The reactions between Fe–Al–Ti–O are the most prominent reaction products that might hamper further oxidation of the tool material.

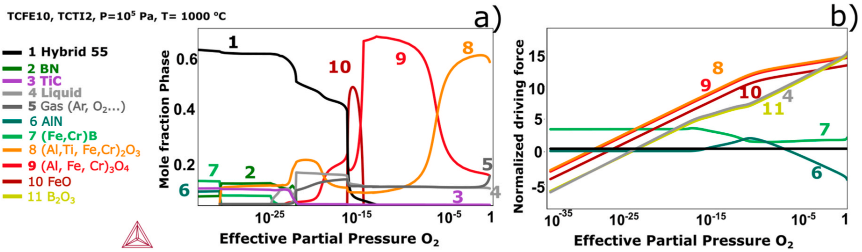

Fig. 11. a) The phase fractions for cBN with TiC binder and Hybrid steel 55 as a function of increasing effective partial pressure of oxygen, and, b) corresponding driving force for the formation of the reaction products.

KT = 30 (Section 2.2).

4.1. *Silicon-containing tools (Si_3N_4, Al_2O_3-SiC_w, SiAlON)*

Fig. 12 shows the development of flank wear and crater wear for silicon-containing tools versus engagement time. The Si_3N_4 tool displayed the shortest tool life of around 30 s and the process was stopped due to excessive cratering. The Al_2O_3-SiC_w had a tool life of 75 s and failed due to crater wear. The SiAlON tool had the longest tool life, lasting for 200 s then reached the crater wear criteria. Such excessive cratering behavior is indicative of chemical and diffusional degradation [34,35]. The SiAlON tool developed the largest degree of flank wear, which points to a concurrent abrasive wear mechanism, whereas the short tool life of Al_2O_3-SiC_w and Si_3N_4 tools did only allow for small amounts of flank wear to develop (Fig. 12).

Fig. 13 show BSE-SEM images and XEDS spectra of the worn SiC–Al_2O_3 tool taken of the ejection, sliding and sticking zones of the cutting edge after 90 s of machining. This is representative of the main wear mechanism of the Si-based tools. In addition BSE-SEM images and a spectra of the unworn tool material, was also collected and compared to the different regions of the cutting zones. The spectra are acquired from an area scan and also a point analysis of a whisker from the respective wear zones. This kind of comparative analysis is performed for *a)* the new tool and the different zones of a worn tool (after 75 s of machining) - *b)* the debris ejection zone, c*)* sliding zone and d*)* sticking zone.

The ejection zone b*)* is located outside the tool/chip interface and has high concentrations of Mg, O, Fe, Ca, Cr and Mn indicating that this is oxidized workpiece material deposited outside the cutting zone (Fig. 13, surface spectra *b*). The SiC whiskers are not detectable through this thick layer of metal and oxides.

For the sliding zone *c*), high concentration of Fe, Cr, Ni, Ca and O on the tool surface and a significant decrease of Si and loss of C is detected (Fig. 13, surface spectra *c*). The BSE image reveals the presence of a thin film across the entire surface of the sliding zone. A spectrum from the remnants of the whiskers in this area (Fig. 13, whisker spectra *c*) shows a critical loss of Si, which is replaced by Fe, Ni, V, Cr and Mn, indicating a counter-diffusion of elements. This indicates a preferential degradation of the whiskers in this contact region.

Within the sticking zone d) a smaller loss of Si and a greater loss of C is observed, if compared to the sliding zone *c*). Additionally, XEDS also indicate the presence of Fe, Ni, V, Cr and Mn, similarly to the sliding zone. Yet the former whisker region is practically devoid of Si in the sliding zone *c)*, while some Si is present in the whiskers in the sticking zone d) (Fig. 13: whisker spectra c and d).

Compering and combining the results from machining and modeling show that the Si from the whisker can react with oxygen and steel to form SiO_2, Al_2SiO_5, Fe_2SiO_4 due to the high driving forces of this phases, predicted by the calculations shown in Fig. 8 and Section 3.3.1. Which is due to oxygen generally being available in the sliding zone c). Thus, this kind of reaction lead to the depletion of Si from the whiskers, shown by the smaller Si peak in whisker spectrum c in Fig. 13. This is in agreement with loss of the SiC phase in Fig. 4b. The BSE-SEM image of the sliding zone shown by a glassy appearance which is in agreement with the calculation of the formation of a of Al_2SiO_5, Fe_2SiO_4 (Fig. 8), shown by the Fe, Al, Si and O peaks in surface spectra c in Fig. 13. This is also in agreement with other studies of Si-tools [41]. Additionally, the Si and C peaks are replaced by with workpiece elements peaks in the whisker spectra d) Fig. 13 which reflects a counter-diffusional process of Si and workpiece metals in agreement with [42] and predictions in Figs. 8 and 9. Thus, diffusional and oxidational wear is present in the sliding zone, in agreement with predictions Section 3.3.1. Oxidation is suppressed and only the diffusional loss of silicon (Section 3.3.1) is active [28], due to the limited oxygen availability in the sticking zone d). This leads to the replacement of silicon by Fe, Ni, Cr and V in the whisker (Fig. 13) and an absence of a glassy phase in this contact zone d).

4.2. *Coated cemented carbide tool (WC–Co, (Ti,Al)N)*

The coated cemented carbide tool initially displayed limited crater

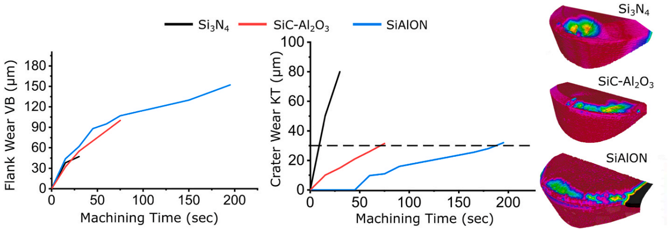

Fig. 12. Tool wear evolution of silicon-based tools and 3D scans of the worn tools.

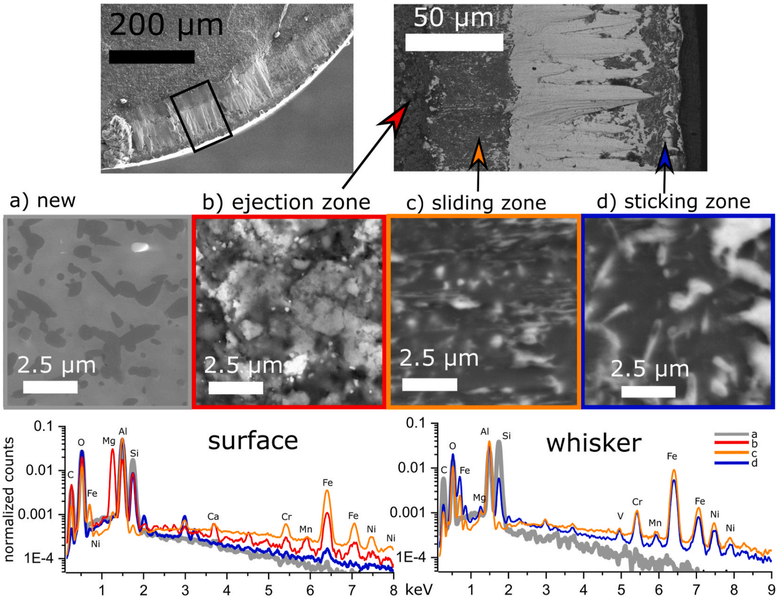

Fig. 13. BSE-SEM images and the tool and cutting zone after 90 s of machining with the SiC–Al_2O_3 tool. Additional BSE-SEM image of the unworn tool material compared to the different regions of the cutting zone. The XEDS spectra are collected and compared, one type of spectra are collected from the whole surface and one from point measurements of the whiskers.

wear and flank wear (Fig. 14). The crater wear was absent until 150 s of machining which was followed by flank wear. This rapid growth of wear resulted in plastic deformation of the cutting edge.

Fig. 15 shows a topography-sensitive SE image, a composition-sensitive BSE image and XEDS spectra of the rake of the tool after 90 s in cut. Three coating perforations or pits are filled with workpiece material, as indicated by the yellow arrows Fig. 15. The growth and coalescence of such pits led to the sudden large increase in rake wear (Fig. 14). Two distinct surface morphologies can be seen in the contact zone, as compared to the original coating spectrum a) Fig. 15. The first area of interest spectrum b) reflects the adhered workpiece material and area/spectrum c) has a visible thin film. In the BSE image, the thin film *c)* is brighter than the original coating a), but not the ahead metal b), due to the Z-contrast mechanism. As expected, the adhered metal b) mainly comprises of Fe, C, Cr and Ni. However, since the thickness of the adhered metal film is less than the XEDS interaction volume Ti and N from underlying coating, are also detected. The area within the detected film c) shows a strong signal of Al, Fe and O but is depleted of Ti, compared to the original coating.

Linking the results from calculations and machining can explain how the (Ti,Al)N coated tool had a tool life comparable to the SiAlON tool and longer than the Si_3N_4 and Al_2O_3-SiC_w. Such a favorable performance is likely related to the more limited solubility of Ti and Al in the steel compared to Si (Section 3) rather than the addition of the chip breaker. A chip breaker changes the cutting conditions, but no the general thermodynamic trends. Additionally, the coating is more resistant to oxidation due to a smaller driving force for formation of reaction products than then the Si tools (Figs. 8 and 10). However, the formation of the film (Fig. 15) on top of the coating in the contact length play a larger role. The glassy film in Fig. 13 allowed Si to leave the whiskers while the film in Fig. 15 protect the coting. The expected reaction products (Fig. 10) point to the formation of $(Al,Fe)_2O_3$ and $(Al,Fe)_3O_4$,

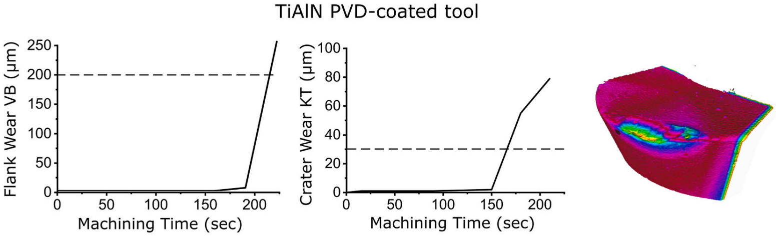

Fig. 14. Evolution of flank and crater wear of PVD (Ti,Al)N-coated cemented carbide, showing limited wear progression then a sudden increase after 150 s. The rapid increase in crater wear after 150 s led to the collapse of the cutting edge.

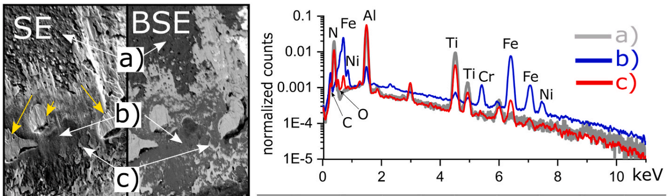

at. %	N	Al	Ti	O	Fe	C	Cr	Ni
a) Coating	45.61	25.43	22.55	2.35	0	4.05	0	0
b) Adhered metal	0	3.50	0.71	2.66	61.81	21.20	3.17	6.95
c) Film	46.04	30.19	6.30	5.06	3.90	8.51	0	0

Fig. 15. SE and BSE images of the rake face of the (Ti,Al)N coated tool after 90 s of machining. Comparison of XEDS spectra and corresponding calculated compositions between the original coating a), adhered metal b) and film c). Yellow arrows indicating pits. (For interpretation of the references to colour in this figure legend, the reader is referred to the Web version of this article.)

which form *in operando* during the machining process. The regenerative and continuous formation of such a protective film on the tool surfaces that comprises of stable oxide phases would then explain the longer tool life [21], whereas for Si-containing tools, similar *in-operando* interaction leads to the formation of non-protective glassy phases [28].

4.3. Titanium carbide-containing tools (Al_2O_3–TiC, cBN-TiC)

The cBN-TiC tool outperforms the Al_2O_3–TiC tool with regard to resistance to flank wear (Fig. 16), which is explained by the differences in mechanical properties between the two materials [34,35]. However, cBN is expected to degrade from intensive chemical, diffusional and oxidational wear, while Al_2O_3 is affected by none of these, as shown in Section 3.2.3 and 3.3.3. Despite such expectations, crater wear for the cBN-TiC tool was less than for the mixed alumina tool (Fig. 16). Additionally, the progression of crater wear for the cBN-TiC tool significantly slowed down after 300 s (Fig. 16).

This kind of crater wear behavior is contrary to the classical relationship between solubility and driving forces and tool wear [12]. However, the formation of an (Al, Ti, Fe, Cr)$_2$O$_3$ or Al, Fe, Cr)$_3$O$_4$ (Fig. 11 and Section 3.3.3) tool protection layer might potentially explain this anomalous behavior [16]. Electron microscopy and spectroscopy (Fig. 17) show that a metal oxide film has formed on the contact surface of the cBN tool, similar to the film on the (Ti,Al)N-coated tool (Fig. 15). The thickness of such film can be approximated to several hundred nanometers based on the excitation volume of the SEM [43]. It is transparent at an accelerating voltage of 15 kV and visible at 5 kV (Fig. 17). XEDS confirms the presence of Fe, Cr, Al and O within this region. However, conclusive detection of Al and O is not possible as the tool material also contains Al_2O_3, since it is used as a sintering aid for PcBN manufacturing [44], thereby affecting the baseline of the Al and O signal.

5. Oxidation and temperature investigation

Further investigation of the Al, Fe, Cr thin film (Figs. 15 and 17) and its dependence on cutting speed and oxygen availability is of considerable interest because predictive modeling show that this effect is driven by oxygen availability (Figs. 10 and 11) and its rate depends on the process temperature. The presence of high amounts of Al in the (Ti,Al)N-coated tool and the Al_2O_3–TiC mixed ceramic makes the analysis of Al-based TPLs difficult. Hence, the investigation reported in this section will focus on cBN-TiC due to the observed stable TPL and low amount of Al present in the tool material. Thus enabling a clearer distinction to be made between parental tool material and a tool protection layer.

5.1. Method

The formation of reaction products and TPLs is a thermodynamic and kinetic process (Fig. 1). Thus, the temperature and chemical potential of the elements in the system will be determine the rate of TPL formation. Temperature measurements were conducted using a high-speed Flir x6580sc IR camera with an imaging frequency of 350 FPS (Hz) and a temperature range of 300–1150 °C. Orthogonal cutting was carried out rather than longitudinal cutting to enable correct imaging. Repeated orthogonal cutting experiments were performed with cutting speeds in the range of $v_c = 50$–300 m/min and a feed rate $f = 0.1$ mm/rev using the same CBN010 insert material, but in a grooving geometry (LCGN160304-0300S0125LF) the width of cut equaling the tool geometry (3 mm). The implemented orthogonal cutting of the preliminarily prepared groove side and the camera-moving system enabled the measurement of the temperature field on the insert side view. The selected emissivity level was 0.55 for PcBN [45]. The temperature values were extracted from the image zone corresponding to the cBN-TiC part of the tool/chip contact zone (Fig. 18).

The investigation of the influence of oxygen was carried out by comparing an oxygen-reduced environment, ambient conditions and the

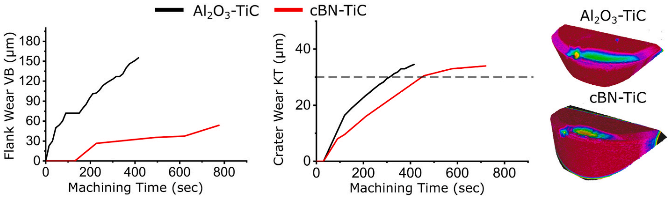

Fig. 16. Evolution of flank and crater wear for Al_2O_2–TiC and cBN-TiC tools. The PcBN tool shows better resistance to flank wear, as expected from its mechanical properties. High resistance to crater wear was observed, while the tool material is expected to be less resistant to chemical wear.

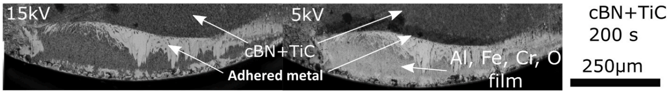

Fig. 17. Side-by-side BSE-SEM images of the rake of a cBN-TiC tool. A thin film of Al, Fe, Cr and O was detected when reducing the accelerating voltage (HV) to 5 kV.

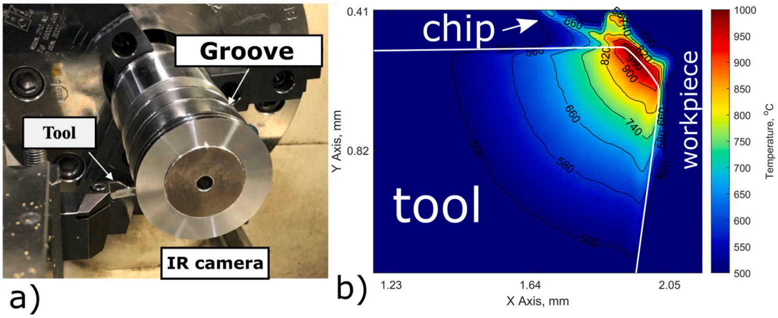

Fig. 18. a) The setup of the temperature measurements using an IR camera. The IR camera is out of view and filming orthogonal to the grroving. (b) A processed frame of a temperature field acquired for the orthogonal turning using CBN010 at $v_c = 300$ m/min and $f = 0.1$ mm/rev.

use of coolant. To perform such a comparison a special chamber was developed and used to control the availability of oxygen (Fig. 19). The chamber comprises a sheet metal frame covering the tool holder and partly the workpiece, it also contains internal tubing for gas supply. The chamber was subsequently purged with argon or compressed air to control the availability of oxygen. The gas was supplied through the chamber itself and through the tool holder having two rake and one flank jet nozzle. Argon gas supply at the flow rate of 400 l/m, which creates an essentially oxygen-free environment [21].

5.2. Results and discussion of oxidation and temperature investigation

As expected, the temperature in the cutting zone increases with increased cutting speed (Fig. 20) [46]. However, the temperature stabilizes at a cutting speed of $v_c = 200$ m/min (Fig. 20). Scanning electron microscopy at a low acceleration voltage of 5 kV was performed on tools after they have been used in the orthogonal temperature measurement tests. The BSE-SEM images in Fig. 20 give that there was no formation of a tool protection layer at low temperatures and speeds $v_c = 50$–100 m/min. However a thin film identical to the TPL in Fig. 17, forms on the chamfer at speeds above 150 m/min. Thus, the TPL increases in thickness and coverage with increased speed and temperature. However, the rate at which the TPL is removed also increases, leading to its continuous build-up and removal. Thus, the layer does not grow much beyond several hundred nanometers (Fig. 20). The formation and stabilization of the TPL with increased temperature limits the otherwise expected rapid tool wear because it acts as a barrier to further degradation [13].

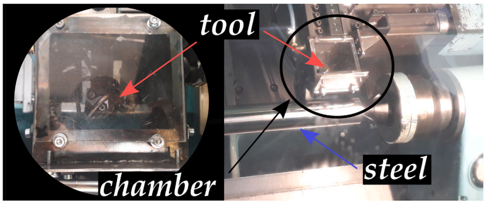

Fig. 19. Machining setup for cutting tests with limited oxygen in the cutting zone. Ar is supplied at a flow rate of 400 l/min from the jet nozzles in the tool holder and through the piping system in the chamber.

Fig. 21 shows how the oxygen availability and the environment influence the performance and degradation of the respective tools. The machining in an oxygen-reduced environment was interrupted after 30 s due to severe vibrations, surface damage and chipping of the tool. Further SEM show that such anomalous process behavior was due to the strong adhesion of the chip to the tool, resulting in fractures on both the tool rake and flank. Also anomalous compared to machining in air, the use of a coolant had a negligible effect on both the flank and crater wear compared to the ambient conditions, despite the generally expected lowering of cutting temperature.

Comparing these results to previous calculations, show that such severe adhesion in an oxygen-reduced environment at a cutting speed of 300 m/min is likely due to the chemical and diffusional interaction between the steel and the cBN-TiC tool material, as seen in the calculation in Section 3.3.3 and Fig. 11. The potential formation of interfacial nitrides and borides could increase the strength of the adhesive bond, as known from the active brazing process [47]. The same calculation and Fig. 11 also show that $(Al, Fe, Cr)_3O_4$ and $(Al, Fe, Cr)_2O_3$ should form when there is more oxygen available, also seen in the SEM Fig. 17. This explains the longer tool life during machining in ambient and coolant conditions (Fig. 21). The benefit of using coolant instead of machining dry/ambient conditions is not significant for this combination of tool and workpiece at these cutting conditions, since the TPL is stable during dry conditions.

TEM lamellas were produced to further study the rake zone of the tools used in ambient and coolant conditions, this enabled an in-depth investigation of the film formed. The central image of Fig. 22 shows a Scanning Transmission Electron Microscopy (STEM) image of a lamella region with adhered metal on top and an interaction layer marked by red dashed lines on top of the cBN-TiC tool material. Selected Area Electron Diffraction (SAED) patterns were taken from the different areas indicated by the arrows, and XEDS-STEM line scans were made across the interaction layer shown at the bottom of Fig. 22.

The XEDS line scans indicate a decrease in Fe and Cr and an increase

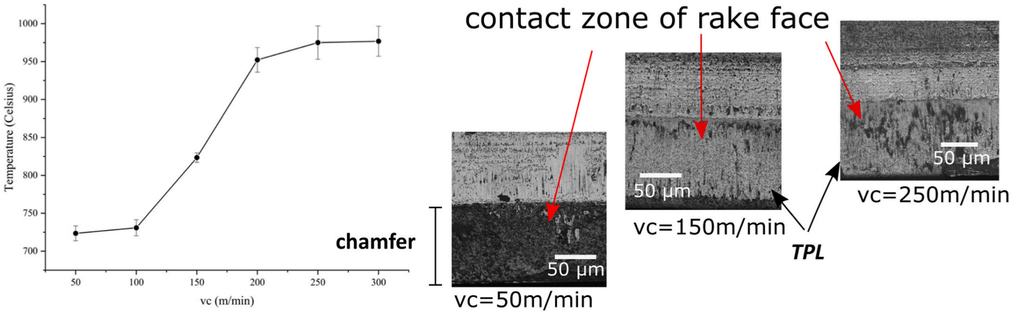

Fig. 20. Influence of cutting speed on process temperature for the cBN-TiC tool, with accompanying SEM-BSE images at surface-sensitive low acceleration voltages (HV = 5 kV), indicating the formation of TPL like the TPLs in Figs. 14 and 16.

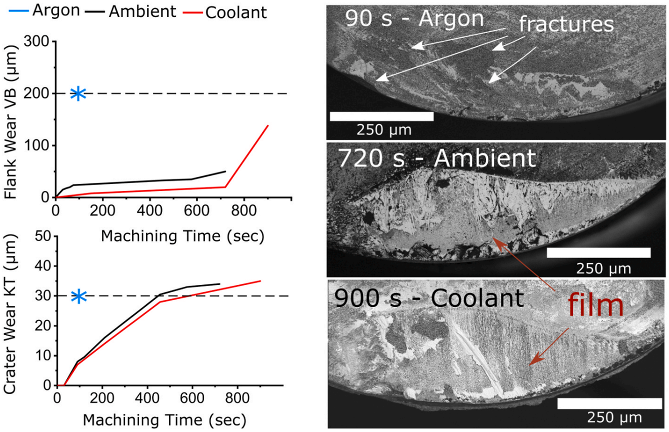

Fig. 21. Evolution of flank and crater wear for the cBN-TiC tools used in argon, ambient and coolant machining conditions. Accompanying low acceleration voltage (HV = 7 kV) BSE images showing the TPL in the case of ambient and coolant condition. Machining in an oxygen-reduced environment led to vibrations, adhesion, tool chipping and fractures.

in Al and O in the interaction zone. The B and N signals then increase at the edge of a cBN grain. The diffraction pattern from the adhered metal is consistent with iron in the bcc structure. Combining this information with XEDS-STEM indicates that it is adhered Hybrid Steel® 55 steel. The diffraction pattern from the interaction zone is not in agreement with any of the phases in the tool, binder, steel or FeO. The diffraction pattern is consistent with Al_2FeO_4. However, conclusively ruling out Al_2O_3 was not possible. The observed Al_2FeO_4 is the same phase as the $(Al, Fe)_3O_4$ predicted by the thermodynamic calculations. Thus, the thermodynamic predictions and the XEDS-STEM and XEDS-SEM analyses are all in agreement. Two lamella from different areas and tools were investigated using this combination of XEDS, SEM, TEM and SAED, and the investigation showed the same result. The observed Cr signal in the XEDS-STEM is in agreement with predicted solubility of Cr in the metal oxide phase. Thus, the formation of $(Al, Fe, Cr)_3O_4$ takes place on the tool surface and between the tool and the adhered metal. The third diffraction pattern is from the tool just below the interaction layer showing the cubic structure of the cBN grain in the [1-1-2] direction.

6. Conclusions

Both the predictive modeling and the experiments showed that silicon-based ceramics tools suffered from degradation by reactions with the metal, atmospheric oxygen and metal oxides formed on the tool surface. The Si dissolved in the workpiece material by diffusion, it reacted with oxygen and workpiece metal oxides and formed glassy phases such as Al_2SiO_5 and Fe_2SiO_4. Hence, reaction products formed on the tool surface *in-operando* are unable to retard the degradation of Si-based tools.

The predictive modeling indicated that machining Hybrid Steel® 55 with Al_2O_3–TiC, (Ti,Al)N-coated carbide and PcBN should lead to the formation of stable metal oxides of either Al_2O_3 or Al_2FeO_4. Such oxides are expected to form a tool protection layer (TPL) that retards further tool degradation. Cutting tests, microscopy, spectroscopy and diffraction investigations confirmed the formation of $(Al, Fe, Cr)_2O_4$ spinel predicted by the thermodynamic calculations, which slowed down the wear process. Additionally, machining in an oxygen-reduced environment and the temperature measurements showed that there is a minimum temperature and oxygen availability necessary for a stable TPL to

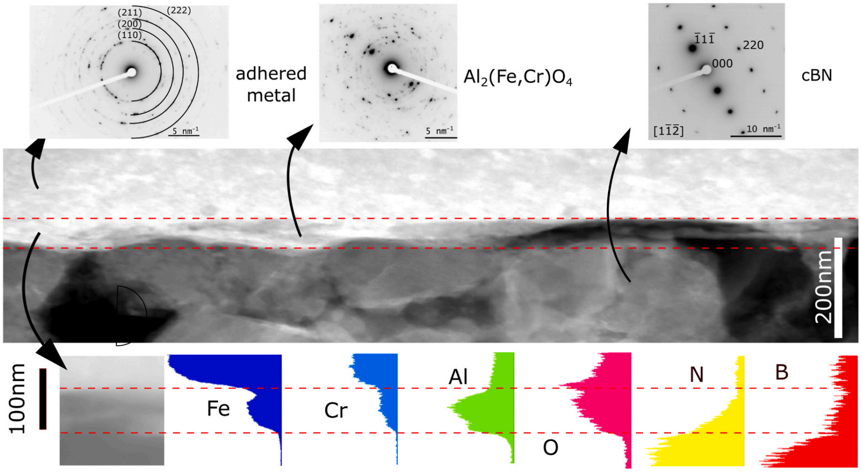

Fig. 22. SAED, combined with a STEM image and XEDS-STEM line scans showing the formation of an Al_2FeO_4 layer between the parental tool and the adhered workpiece metal. This film likely slows down further chemical, diffusional and oxidational wear.

form, in accordance with the modeling. Thus, a distinct improvement in tool wear resistance was demonstrated when the TPL formed, since it retarded otherwise expected chemical, diffusional and oxidational wear mechanisms.

Tool degradation during metal cutting due to chemical reactions, dissolution, diffusion and oxidation is well known. However, few models can make predictions about the result of these mechanisms when they occur concurrently and involve multi-component interaction systems, and no models found in literature have been able to predict the formation of tool protection layers. This study developed a thermodynamics-based modeling framework for prediction of such concurrent degradation mechanisms. Apart from tool degradation, the modeling was also constructed to enable prediction of *in-operando* formation of new phases which act as berries to tool wear. This framework was applied to the machining of Al-alloyed Hybrid Steel® 55 and 6 tool materials. Machining tests, microscopy, characterization of wear mechanisms and interaction products, control of machining environment and IR thermography constituted the experimental validation.

The developed modeling framework allows for the correct pairing of tool materials and workpiece alloying, leading to the formation of tool protection layers, before any machining is performed. Further modeling work, especially kinetic modeling enabling wear rate predictions, will benefit from using this method to predict what phenomena will influence the tool life. Since current kinetic models are not able to model all phenomena simultaneously. This framework also allows for combining and building on mechanical wear based models. Furthermore, the proposed modeling approach can predict what modification to the workpiece and tool composition will promote the formation of oxide, nitride, carbide or boride tool protection layer. Since it can predict the *in-operando* reactions occurring between the tool, workpiece and cutting environment.

CRediT authorship contribution statement

Axel Bjerke: Conceptualization, Methodology, Software, Validation, Formal analysis, Investigation, Data curation, Writing – original draft, Writing – review & editing, Visualization. **Andrii Hrechuk:** Conceptualization, Methodology, Validation, Formal analysis, Investigation, Data curation, Writing – original draft, Writing – review & editing, Visualization. **Filip Lenrick:** Conceptualization, Methodology, Validation, Formal analysis, Investigation, Data curation, Writing – review & editing, Visualization, Supervision, Funding acquisition. **Andreas Markström:** Conceptualization, Methodology, Software, Validation, Formal analysis, Investigation, Resources, Writing – review & editing, Supervision, Funding acquisition. **Henrik Larsson:** Conceptualization, Methodology, Software, Validation, Formal analysis, Investigation, Resources, Writing – review & editing, Supervision, Funding acquisition. **Susanne Norgren:** Conceptualization, Methodology, Software, Validation, Formal analysis, Investigation, Resources, Writing – review & editing, Supervision, Funding acquisition. **Rachid M'Saoubi:** Conceptualization, Methodology, Validation, Resources, Writing – review & editing, Supervision, Funding acquisition. **Thomas Björk:** Conceptualization, Methodology, Validation, Resources, Writing – review & editing, Supervision, Funding acquisition. **Volodymyr Bushlya:** Conceptualization, Methodology, Validation, Formal analysis, Investigation, Resources, Data curation, Writing – review & editing, Visualization, Supervision, Project administration, Funding acquisition.

Declaration of competing interest

The authors declare that they have no known competing financial interests or personal relationships that could have appeared to influence the work reported in this paper.

Acknowledgements

This work was funded by the national strategic innovation program – national action for Metallic Materials, organized by Vinnova and Jernkontoret (Sweden) under the DEMO project (ID 2017-02915). The authors would like to acknowledge the Sustainable Production Initiative (SPI) – a cooperation between Lund University and Chalmers University of Technology. This acknowledgment also extends to Per Alm and Vyacheslav Kryzhanivskyy (Seco Tools AB) for their help with IR thermography.

Appendix A. Supplementary data

Supplementary data to this article can be found online at https://doi.

org/10.1016/j.wear.2021.203991.

References

[1] C.A. van Luttervelt, T.H.C. Childs, I.S. Jawahir, F. Klocke, P.K. Venuvinod, Y. Altintas, E. Armarego, D. Dornfeld, I. Grabec, J. Leopold, B. Lindstrom, D. Lucca, T. Obikawa, Shirakashi, H. Sato, Present situation and future trends in modelling of machining operations progress report of the CIRP working group 'modelling of machining operations', CIRP Ann. 47 (1998) 587–626, https://doi.org/10.1016/S0007-8506(07)63244-2.

[2] F.W. Taylor, On the art of cutting metals, Trans. ASME 28 (1907) 31.

[3] B.N. Colding, A three-dimensional, tool-life equation—machining economics, J. Eng. Ind. 81 (1959) 239–249, https://doi.org/10.1115/1.4008313.

[4] D. Johansson, S. Hägglund, V. Bushlya, J.-E. Ståhl, Assessment of commonly used tool life models in metal cutting, Procedia Manuf 11 (2017) 602–609, https://doi.org/10.1016/j.promfg.2017.07.154.

[5] J.F. Archard, Contact and rubbing of flat surfaces, J. Appl. Phys. 24 (1953) 981–988, https://doi.org/10.1063/1.1721448.

[6] T.N. Loladze, Of the theory of diffusion wear, CIRP Ann. 30 (1981) 71–76, https://doi.org/10.1016/S0007-8506(07)60898-1.

[7] E. Usui, T. Shirakashi, T. Kitagawa, Analytical prediction of cutting tool wear, Wear 100 (1984) 129–151, https://doi.org/10.1016/0043-1648(84)90010-3.

[8] P.D. Hartung, B.M. Kramer, B.F. von Turkovich, Tool wear in titanium machining, CIRP Ann. 31 (1982) 75–80, https://doi.org/10.1016/S0007-8506(07)63272-7.

[9] X. Hong, Wear behaviour and wear mechanism of ceramic tools in machining hardened alloy steel, Wear 139 (1990) 439–451, https://doi.org/10.1016/0043-1648(90)90061-E.

[10] B.M. Kramer, B.F. von Turkovich, A comprehensive tool wear model, CIRP Ann. 35 (1986) 67–70, https://doi.org/10.1016/S0007-8506(07)61840-X.

[11] Y. Huang, T.G. Dawson, Tool crater wear depth modeling in CBN hard turning, Wear 258 (2005) 1455–1461, https://doi.org/10.1016/j.wear.2004.08.010.

[12] A. Malakizadi, B. Shi, P. Hoier, H. Attia, P. Krajnik, Physics-based approach for predicting dissolution−diffusion tool wear in machining, CIRP Ann. 69 (2020) 81–84, https://doi.org/10.1016/j.cirp.2020.04.040.

[13] O. Gutnichenko, V. Bushlya, J. Zhou, J.-E. Ståhl, Tool wear and machining dynamics when turning high chromium white cast iron with pcBN tools, Wear 390–391 (2017) 253–269, https://doi.org/10.1016/j.wear.2017.08.005.

[14] N. Ånmark, A. Karasev, P.G. Jönsson, The effect of different non-metallic inclusions on the machinability of steels, Materials 8 (2015) 751–783, https://doi.org/10.3390/ma8020751.

[15] D. Nguyen, S. Tooptong, K.-H.H. Park, P. Kwon, Formation mechanism of alumina layer in protecting cubic boron nitride inserts in turning cast irons, Int. J. Mach. Tool Manufact. 153 (2020) 103539, https://doi.org/10.1016/j.ijmachtools.2020.103539.

[16] J.-E. Ståhl, Requirements and potential for high performance cutting tools based on superhard phases in new applications Title, in: De Beers Diamond Conference Hosted by Warwick University, UK, 2016.

[17] M. Olsson, F. Lenrick, R. M'Saoubi, H. Larsson, A. Markström, I. Petrusha, J.-E. Ståhl, V. Bushlya, Study of wear mechanisms of cemented carbide tools during machining of single-phase niobium, Wear 450–451 (2020) 203244, https://doi.org/10.1016/j.wear.2020.203244.

[18] R. Lindvall, F. Lenrick, H. Persson, R. M'Saoubi, J.-E. Ståhl, V. Bushlya, Performance and wear mechanisms of PCD and pcBN cutting tools during machining titanium alloy Ti6Al4V, Wear (2020) 454–455, https://doi.org/10.1016/j.wear.2020.203329.

[19] V. Bushlya, A. Bjerke, V.Z.Z. Turkevich, F. Lenrick, I.A.A. Petrusha, K.A. A. Cherednichenko, J.-E.E. Ståhl, On chemical and diffusional interactions between PCBN and superalloy Inconel 718: imitational experiments, J. Eur. Ceram. Soc. 39 (2019) 2658–2665, https://doi.org/10.1016/j.jeurceramsoc.2019.03.002.

[20] S. Odelros, B. Kaplan, M. Kritikos, M. Johansson, S. Norgren, Experimental and theoretical study of the microscopic crater wear mechanism in titanium machining, Wear 376–377 (2017) 115–124, https://doi.org/10.1016/j.wear.2017.01.104.

[21] V. Bushlya, F. Lenrick, J.-E. Ståhl, R. M'Saoubi, Influence of oxygen on the tool wear in machining, CIRP Ann. 67 (2018) 79–82, https://doi.org/10.1016/j.cirp.2018.03.011.

[22] T. Aiso, U. Wiklund, M. Kubota, S. Jacobson, Effect of Si and Al additions to carbon steel on material transfer and coating damage mechanism in turning with CVD coated tools, Wear 368–369 (2016) 379–389, https://doi.org/10.1016/j.wear.2016.10.011.

[23] J. Vleugels, O. Van Der Biest, Chemical wear mechanisms of innovative ceramic cutting tools in the machining of steel, Wear 225–229 (1999) 285–294, https://doi.org/10.1016/S0043-1648(98)00362-7.

[24] S. Giménez, O. Van der Biest, J. Vleugels, The role of chemical wear in machining iron based materials by PCD and PCBN super-hard tool materials, Diam. Relat. Mater. 16 (2007) 435–445, https://doi.org/10.1016/j.diamond.2006.08.017.

[25] V. Bushlya, F. Lenrick, A. Bjerke, H. Aboulfadl, M. Thuvander, J.-E. Ståhl, R. M'Saoubi, Tool wear mechanisms of PcBN in machining Inconel 718: analysis across multiple length scale, CIRP Ann. (2021), https://doi.org/10.1016/j.cirp.2021.04.008.

[26] G.J. Tennenhouse, F.D. Runkle, The effects of oxygen on the wear of tungsten-carbide-based materials, Wear 118 (1987) 365–375, https://doi.org/10.1016/0043-1648(87)90078-0.

[27] J. Angseryd, H.-O.O. Andrén, An in-depth investigation of the cutting speed impact on the degraded microstructure of worn PCBN cutting tools, Wear 271 (2011) 2610–2618, https://doi.org/10.1016/j.wear.2010.11.059.

[28] G.J. Tennenhouse, F.D. Runkle, The effects of oxygen on the wear of Si3N4 against cast iron and steel, Wear 110 (1986) 75–81, https://doi.org/10.1016/0043-1648(86)90153-5.

[29] R.F. Silva, F.J. Oliveira, F.P. Castro, J.M. Vieira, Modeling of chemical wear in ferrous alloys/silicon nitride contacts during high speed cutting, Acta Mater. 46 (1998) 2501–2507, https://doi.org/10.1016/S1359-6454(98)80034-7.

[30] P.A. Dearnley, E.M. Trent, Wear mechanisms of coated carbide tools, Met. Technol. 9 (1982) 60–75, https://doi.org/10.1179/030716982803285909.

[31] J.F.F. Archard, W. Hirst, The wear of metals under unlubricated conditions, Proc. R. Soc. London Ser. A. Math. Phys. Sci. 236 (1956) 397–410, https://doi.org/10.1098/rspa.1956.0144.

[32] O. Hatt, H. Larsson, F. Giuliani, P. Crawforth, B. Wynne, M. Jackson, Predicting chemical wear in machining titanium alloys via a novel low cost diffusion couple method, Procedia CIRP 45 (2016) 219–222, https://doi.org/10.1016/j.procir.2016.01.196.

[33] J.-O.J.-O. Andersson, T. Helander, L. Höglund, P. Shi, B. Sundman, L. Hoglund, P. Shi, B. Sundman, Thermo-Calc & DICTRA, computational tools for materials science, Calphad 26 (2002) 273–312, https://doi.org/10.1016/S0364-5916(02)00037-8.

[34] J.-E. Ståhl, Metal Cutting: Theories in Practice, SECO TOOLS, Fagersta, Sweden, 2012.

[35] N.M. Major, S.T. Crawford, Elbow effusions in trauma in adults and children: is there an occult fracture? AJR Am. J. Roentgenol. 178 (2002) 413–418. http://www.ncbi.nlm.nih.gov/pubmed/11804906.

[36] E.D. Doyle, J.G. Horne, D. Tabor, Frictional interactions between chip and rake face in continuous chip formation, Proc. R. Soc. Lond. A. Math. Phys. Sci. 366 (1979) 173–183, https://doi.org/10.1098/rspa.1979.0046.

[37] X.-G. Lu, M. Selleby, B. Sundman, Implementation of a new model for pressure dependence of condensed phases in Thermo-Calc, Calphad 29 (2005) 49–55, https://doi.org/10.1016/j.calphad.2005.04.001.

[38] S. Hampshire, H.K. Park, D.P. Thompson, K.H. Jack, α′-Sialon ceramics, Nature 274 (1978) 880–882, https://doi.org/10.1038/274880a0.

[39] R. Riedel, I.-W. Chen, Ceramics science and technology, in: Materials and Properties, 2, Wiley, 2011.

[40] W.-G. Seo, F. Tsukihashi, Thermodynamic and structural properties for the FeO–SiO2 system by using molecular dynamics calculation, Mater. Trans. 46 (2005) 1240–1247, https://doi.org/10.2320/matertrans.46.1240.

[41] V. Bushlya, J. Zhou, P. Avdovic, J.-E. Ståhl, Wear mechanisms of silicon carbide-whisker-reinforced alumina (Al2O3–SiCw) cutting tools when high-speed machining aged Alloy 718, Int. J. Adv. Manuf. Technol. 68 (2013) 1083–1093, https://doi.org/10.1007/s00170-013-4899-8.

[42] G. Brandt, A. Gerendas, M. Mikus, Wear mechanisms of ceramic cutting tools when machining ferrous and non-ferrous alloys, J. Eur. Ceram. Soc. 6 (1990) 273–290, https://doi.org/10.1016/0955-2219(90)90019-C.

[43] R. Reichelt, Scanning electron microscopy, in: P.W. Hawkes, J.C.H. Spence (Eds.), Sci. Microsc., Springer, New York, NY, 2007, pp. 133–272, https://doi.org/10.1007/978-0-387-49762-4_3.

[44] K.E. Lindgren, A. Kauppi, L.K.L. Falk, Development of matrix microstructure in polycrystalline cubic boron nitride ceramics, J. Eur. Ceram. Soc. 37 (2017) 3017–3026, https://doi.org/10.1016/j.jeurceramsoc.2017.03.010.

[45] I. Gonzalez De Arrieta, T. Echaniz, R.B. Perez-Saez, M.J. Tello, I.G. de Arrieta, T. Echániz, R.B. Pérez-Sáez, M.J. Tello, Thermo-radiative and optical properties of a cutting tool based on polycrystalline cubic boron nitride (PCBN), Mater. Res. Express 3 (2016), 045904, https://doi.org/10.1088/2053-1591/3/4/045904.

[46] M. Bacci da Silva, J. Wallbank, Cutting temperature: prediction and measurement methods—a review, J. Mater. Process. Technol. 88 (1999) 195–202, https://doi.org/10.1016/S0924-0136(98)00395-1.

[47] W.F. Ding, J.H. Xu, Y.C. Fu, B. Xiao, H.H. Su, H.J. Xu, Interfacial reaction between cubic boron nitride and Ti during active brazing, J. Mater. Eng. Perform. 15 (2006) 365–369, https://doi.org/10.1361/105994906X108747.

[48] A.B. Ovako, Hybrid steel 55. https://steelnavigator.ovako.com/steel-grades/20nicrmov24-20-7/, 2020 accessed July 1, 2020.

Appendix A: Thermodynamic modeling

By adopting the CALPHAD [i, ii, iii] technique, all available thermochemical information is used to fit the model parameters used to describ the Gibbs energy of individual phases. The purpose is to obtain a consistent set of model parameters that can describe the thermodynamic properties of the system in a realistic way. The thermodynamic parameters are evaluated using the PARROT module [iv] in the Thermo-Calc software [v]. The module works by minimizing an error sum where each piece of information is given a certain weight according to its estimated accuracy and allows the simultaneous concideration of various types of thermochemical and phase diagram data.

The Gibbs energy of each phase is described using the compound energy formalism [vi]. The structure of a phase is represented by a sublattice model $(A, B)_k(D, E, F)_l(\ldots)\ldots$, where A and B mix on the first sublattice, and D, E and F mix on the second sublattice, and similarly if more sublattices are added. The sublattices (s) are indexed with the stoichiometric coefficients $k, l, \ldots (n^s)$ and one mole of formula units thus contains $k+l+\ldots+n^s$ moles of atoms. The expression for the Gibbs energy of each phase is given by,

$$G_m = \sum {}^{\circ}G_{end} \prod y_J^s + RT \sum \sum n^s y_J^s \ln(y_J^s) + {}^E G_m + G_m^{magn}. \tag{A.1}$$

The first term represents the surface of reference and is constructed by a summation over all end-members and the product $\prod y_J^s$ contains one site fraction from each sublattice and they are identified by the constituents, J, in the end-member. The Gibbs energy of one formula unit of the compound represented by the end-member is ${}^{\circ}G_{end}$. The second term is the ideal entropy of mixing, ${}^E G_m$ represents the excess energy and G_m^{magn} the magnetic contribution. The excess energy is described by a generalized regular solution expression,

$${}^E G_m = \prod y_J^s \sum y_B^t L_{A,B:D:G\ldots} + \prod y_J^s \sum \sum y_B^t y_D^u L_{A,B:D,E:G\ldots} + \ldots \tag{A.2}$$

The commas in the subscript separates constituent on the same sublattice and the colons separates constituents in different sublattices. For the L parameters Redlish-Kister terms [vii] in site fractions are used. $L_{A,B:D:G}$ is then described as

$$L_{A,B:D:G} = \sum_{v=0}^{k} (y_A^s - y_B^s)^v \cdot {}^v L_{A,B:D:G} \tag{A.3}$$

where ${}^v L_{A,B:D:G}$ can be temperature dependent.

Inden [viii] was the first to describe the magnetic contribution in terms of heat capacity. This was later integrated to a Gibbs energy expression by Hillert and Jarl [ix]

$$G_m^{magn} = nRT\ln(\beta+1)f(\tau) \qquad \text{(A.4)}$$

where *n* is the number of atoms per formula unit that have the average magnetic moment β and the function $f(\tau)$ is

for τ < 1

$$f(\tau)=1-\left[\frac{79\tau^{-1}}{140p}+\frac{474}{497}(p^{-1}-1)\left(\frac{\tau^{3}}{6}+\frac{\tau^{9}}{135}+\frac{\tau^{15}}{600}\right)\right]/A.$$

For τ > 1 (A.5)

$$f(\tau)=\left[\frac{\tau^{-5}}{10}+\frac{\tau^{-15}}{315}+\frac{\tau^{-25}}{1500}\right]/A$$

Where $A=\left(\frac{518}{1125}\right)+\left(\frac{11692}{15975}\right)\left(p^{-1}-1\right)$ and p depends on the structure. $\tau=T/T_C$, where T_C is the Curie temperature.

The temperature dependence of the Gibbs energy of an end member, $°G_{end}$, is often described by a power series [iv] as

$$°G_{end}-\sum_i b_i H_i^{SER} = a_0 + a_1T + a_2T\ln(T) + a_3T^2 + a_4T^{-1} + a_5T^3 + \ldots \qquad \text{(A.6)}$$

where $\sum_i b_i H_i^{SER}$ represents the sum of enthalpies of the elements in their reference state. By describing the Gibbs energy as above one may derive entropy S, enthalpy H, heat capacity c_p among with many other quantities by using the following thermodynamic relations:

$$S_m^{\theta}=-\left(\frac{\partial G_m^{\theta}}{\partial T}\right)_{p,N_i} = -a_1 - a_2(1+\ln(T)) - 2a_3T + a_4T^{-2} - 3a_5T^2 \ldots$$

$$H_m^{\theta}-\sum_i b_i H_i^{SER} = G_m^{\theta} - T\left(\frac{\partial G_m^{\theta}}{\partial T}\right)_{p,N_i} = a_0 - a_2T - a_3T^2 + 2a_4T^{-1} - 2a_5T^3 + \ldots \qquad \text{(A.7)}$$

$$c_p^{\theta}=-T\left(\frac{\partial^2 G_m^{\theta}}{\partial T^2}\right)_{p,N_i} = -a_2 - 2a_3T - 2a_4T^{-2} - 6a_5T^2 + \ldots$$

The number of coefficients that are used in the modeling are determined by the available experimental information. But, as seen from the above expressions, at least a_0, a_1 and a_2 should be determined in order to also get a description of the entropy, enthalpy and heat capacity for the compound.

---

[i] L. Kauffman and H. Bernstein, Computer Calculations of Phase Diagrams with Special Reference to Refractory Metals, Academic Press, New York, NY, 1970.

[ii] N. Saunders and A. P. Miodownik, Calphad Calculations of Phase Diagrams: A Comprehensive guide, Pergamon Materials Series, Vol. 1, (ed. R. W. Cahn, 1998)

[iii] H. L. Lukas, S. G. Fries and B. Sundman, Computational thermodynamics, Cambridge university press, 2007.

[iv] B. Jansson, Ph. D. Thesis, Royal Inst. Of Technology, Stockholm, Sweden, 1984.

[v] B. Sundman, B. Jansson and J.-O- Andersson, CALPHAD, 9, 1985, pp. 153-190

[vi] M. Hillert, Journal of Alloys and Compounds, 320, 2001, pp. 161-176

[vii] O. Redlish, A. Kister, Ind. Eng. Chem., 40 (1948) pp 345

[viii] G. Inden, Physica, 103B, 1981, pp. 82-100.

[ix] M. Hillert and M. Jarl, Calphad, 2 , 1978, pp. 227-238

Paper X

Journal of Materials Processing Tech. 330 (2024) 118496

Contents lists available at ScienceDirect

Journal of Materials Processing Tech.

journal homepage: www.elsevier.com/locate/jmatprotec

Research article

Machinability improvement by in-operando Tool Protection Layers through designed steel alloying: The case of manganese steel

Axel Bjerke[a,*], Susanne Norgren[a,b], Henrik Larsson[c,d], Andreas Markström[c], Filip Lenrick[a], Rachid M'Saoubi[a,e], Jörgen Petersson[f], Latifa Melk[f], Volodymyr Bushlya[a]

[a] *Division of Production and Materials Engineering, Lund University, Ole Römers väg 1, Lund, Sweden*
[b] *Sandvik Coromant R&D, Lerkrogsvägen 13, Stockholm 12680, Sweden*
[c] *Thermo-Calc Software AB, Råsundavägen 18, Solna SE-16967, Sweden*
[d] *Unit of Structures, Dept Materials Science and Engineering, KTH, Stockholm SE-10044, Sweden*
[e] *R&D Materials and Technology Development, Seco Tools AB, Fagersta 73782, Sweden*
[f] *Sandvik SRP, Svedala 233 31, Sweden*

ARTICLE INFO

Keywords:
Machinability
Thermodynamic modeling
Tool wear
Electron microscopy

ABSTRACT

Improvements in machinability by alloying of the workpiece often adversely impact the end user properties of a material. For example, the common use of non-metallic inclusions can lead to improved tool life during turning or milling, but often adversely affects weldability, corrosion, and wear resistance. A cutting tool material meets kilometers of workpiece material during a machining operation. Hence elements in small quantities in the workpiece may insignificantly affect the end user properties but may have large effects on tool wear. One such effect is the formation of refractory and wear resistant reaction products between the workpiece and tool. Such reaction products forming on tool surfaces may lead to improved machinability. This paper proposes the use of small amounts of alloying to induce such a Tool Protection Layer. Additionally, the paper develops a computational framework for designed alloying which balances formation of Tool Protection Layers, its in-process retention, and the functional properties of the alloy. The method has been validated for a case of manganese steel. The calculations were validated first by a wide range of diffusion experiments. Then by industrial turning of cast alloys, by comparing one reference and two newly designed alloys based on the alloying concept. The alloy with 0.003 mol fractions of Al resulted in more than 3 times increase in tool life, due to in-operando formation of Al_2O_3 Tool Protection Layer. The designed manganese steel maintained its functional properties with respect to abrasive wear resistance and retained its ability to work harden.

1. Introduction

For the past 50 years the standard approach to improve the machinability of steel has been to change the amount, morphology, and composition of non-metallic inclusions (NMI) [1,2]. This machinability improvement often comes at the expense of inferior tensile strength, fatigue performance, weldability, and corrosion resistance [3]. Consequently, using NMI as a means of machinability improvement results in a trade-off between machinability and any negative effects on the functional properties. Bearing steel and Hadfield steel are examples where a clean steel is preferred over NMI engineered steel at the cost of inferior machinability. This is due to the requirements of the final functional properties, such as resistance to crack formation [4,5]. Recent research efforts have discovered that a thin protective layer can sometimes form between the tool and the workpiece, which leads to improved machinability without the use of NMI [6,7]. These layers form due to reactions between the elements in the workpiece, the surrounding air or coolant, and the tool, without the presence of inclusions.

Such a layer is sometimes referred to as a Tool Protection Layer (TPL) [8]. A TPL is distinctly different from inclusions from the steel getting deposited on the tool, and protecting the tool from mechanical, chemical, diffusional, and oxidational wear [3]. TPLs are also distinctly different from a tribofilm [3], a built-up edge (BUE) [9], deformed binder material [10], a built-up layer (BUL), or transfer layers [11]. TPLs are by definition layers formed as a result of reactions between the workpiece elements, the cutting tool, and the environment (air or

---

* Corresponding author.
E-mail address: axel.bjerke@iprod.lth.se (A. Bjerke).

https://doi.org/10.1016/j.jmatprotec.2024.118496
Received 16 May 2024; Received in revised form 30 June 2024; Accepted 1 July 2024

coolant), and consists of phases such as oxides, nitrides, carbides, and borides formed during machining [7]. Hence, this effect can occur in clean steels and alloys and limit tool wear by acting as a chemical, diffusional, or oxidational barrier. The tool encounters kilometers of tool material during metal cutting, hence elements in small quantities in the workpiece might not affect the end user properties but may have large effects on tool wear.

Examples of the protective functions of TPLs can be found in recent literature. Machining Si alloyed Pb-free brass using (Ti,V,Zr,Hf,Nb,Ta)N-coated tools results in a reaction between the coating, oxygen, and Si and Al in the alloy that leads to the formation of β-SiAlON and SiO_2 layers, which blocked diffusional wear [12]. An NbC diffusion barrier has been observed to form between cemented carbide tools and pure Nb workpieces during machining, blocking further diffusional wear [13]. TiN, (Ti,Al)N, and Al_2O_3 can form at a range of different machining conditions during machining of Alloy 718 with a cubic boron nitride (cBN) tool, which prevents oxidation and diffusion [14,15]. (Ti,V)C or $(Ti,V,Cr)B_2$ layers that act as a diffusional barrier have formed when Ti6Al4V is machined with polycrystalline diamond (PCD) or cBN respectively; both have been observed during machining studies [16] and studies of diffusion couples imitating machining [17].

A similar but different effect can occur when machining Ti-alloys with cemented carbide [18,19]. The diffusional wear of Co and C can be limited by a protective tungsten (W) layer that forms because W does not diffuse into the alloy, and not because of a reaction between the workpiece and the tool. The W layer then limits the diffusion of other tool elements. Machining AD730 with polycrystalline cBN (PcBN) resulted in the formation of layers of γ-Al_2O_3, (Ti, Nb, Zr)N, and (Ti, Cr, N, Zr)N, which resulted in a reduction in tool wear caused by diffusion and oxidation [20].

Adding either 1 mass % of Si or Al in a solid solution to low carbon steel also showed a reduction in tool wear. The study demonstrated that alloying with either Al or Si led to the formation of mixed oxides and nitrides on the tool surface during turning with a TiN-Al_2O_3-Ti(C,N) CVD-coated cemented carbide tool [21] and on high speed steel tools PVD-coated with (Ti,Al)N during gear cutting [22]. These oxides and nitrides protected and lubricated the tool, thereby reducing wear.

A comparison of the machining of a medium-alloy low-carbon steel with five different ceramic tools and one (Ti,Al)N-coated cemented carbide tool showed how pairing different tool materials with the same steel led to the formation of different layers on the tool surface [7]. This work used thermodynamics to predict which tool–workpiece combination and cutting conditions were likely to form protective layers and which combinations led to tool degradation [7].

Fig. 1 schematically presents the difference between clean alloys, inclusion engineered alloys, and alloys that can form a TPL. The tool material is in contact with the workpiece, chip, and air or coolant when machining clean steel. This can lead to wear caused by elements in the tool diffusing into the chip [23], oxidational attack of the tool [6], and elements of the workpiece diffusing into the binder and/or reacting with the tool material [14] (Fig. 1a). The addition of non-metallic inclusions in the steel can lead to protective deposits that limit these effects [24] (Fig. 1b), but this often leads to degraded functional properties. Small amount of alloying paired with the correct tool material at certain cutting conditions can lead to phases forming on the tool surface such as borides [16], nitrides [21], oxides [7], and carbides [13] during machining, which limit wear by diffusion, reactions, and oxidation (Fig. 1c) without changing the functional properties.

To the best of our knowledge, there are no previously published works that intentionally alloy a workpiece material with the aim of forming a TPL. Previous work has either focused on showing that a TPL exists [13,20], selecting a tool material that leads to TPL formation [7], changing the cutting conditions to from a TPL [6,14], or the workpiece was alloyed in some manner but they alloying was not intentionally matched with the tool or coating material to form a TPL [21,22]. Hence, no methods have shown how to intentionally match alloying, tool material, and cutting conditions to form a TPL. This paper aims to initiate the development of such a method of designed alloying for TPL formation.

The aim of the method presented in this paper is to alloy a material such that a TPL will form between the workpiece and tool, which hinders further diffusion, reactions, and oxidation that otherwise would lead to rapid tool wear. This TPL is to be achieved without degrading the functional properties of the workpiece. Finding this balance requires a good understanding of the materials of both the workpiece and the tool. However, changing the alloying is not always necessary, the appropriate selection of cutting conditions, coatings, and tool materials can in certain cases lead to the formation of a protective film without the need for additional alloying. A proposed method for tool material selection has been previously been shown [7]. Inclusion engineering generally leads to thicker protective deposits than TPLs. However, inclusions are not acceptable in some materials and selecting different tool materials or cutting conditions might not be sufficient for the formation of a TPL. Alloying by "small amounts" or "microalloying", meaning alloying with

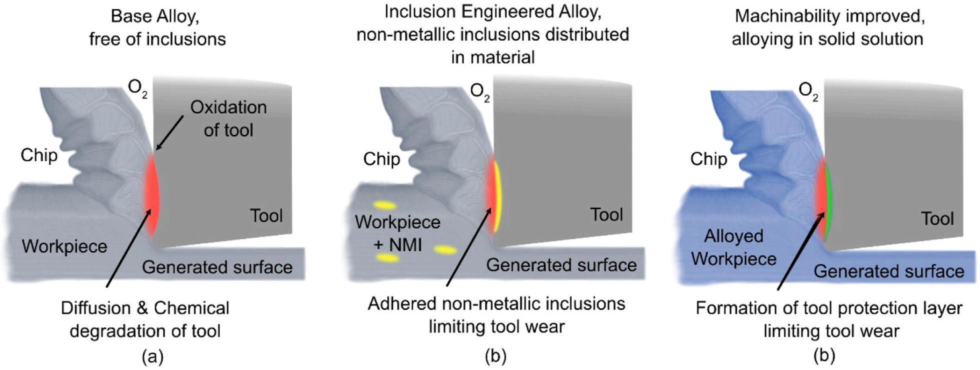

Fig. 1. Schematic difference between inclusion engineering and this papers method. (a) a clean/base alloy where the tool suffers from oxidation, diffusion and chemical degradation during machining, (b) an inclusion engineered version of (a) were the inclusions decrease tool wear but change the functional properties of the workpiece, and (c) designed TPL alloy version of (a), leading to an interaction between the alloy, tool, and oxygen resulting in a protective layer, with retained functional properties of the workpiece material.

amounts minor enough that the functional properties does not change can therefore offer another approach to achieve machinability improvement. This paper develops a method and shows by a case study how to achieve this microalloying balance.

2. Experimental design

The method presented here is a combination of thermodynamic calculations that are used to evaluate alloying and tool combinations to minimize time consuming and expensive casting, machining, microscopy, and tool material experiments. The paper also uses a range of diffusion couple studies to verify the thermodynamic calculations. The alloying selected from the thermodynamic screening calculations are then cast into bars to validate the method and the improvements in machinability and to test the functional properties workpiece.

2.1. Workpiece material for validation of the method

An austenitic Hadfield or high manganese steel for rock crushing and heavy industrial applications (12–15 wt% Mn) is selected as a case study material for validating the method. Hadfield steels should contain minimal amount of inclusions (carbides, oxides, and sulfides) because inclusions become sites that initiate crack formation [5]. Hadfield steel is able to harden under load due to transformation induced plasticity (TRIP) into martensite and due to twinning induced plasticity (TWIP) [25,26]. It is therefore also difficult to machine [27], hence machinability improvement is of interest. Changing the alloying composition is more acceptable compared to nickel and titanium aerospace alloys, while the demands for the functional properties of manganese steels remain high. This compositional flexibility makes Hadfield steel suitable for this study. The composition of the reference material is shown in Table 1.

2.2. Tool material and alloying for validation of the method

A TPL typically consists of carbides, borides, nitrides, or oxides because these phases can protect the tool during machining. The recommended tool material for machining Hadfield steels at higher cutting speeds is PcBN [27]. Mixed Al_2O_3/TiC ceramics are also a possible choice [28], but they together with uncoated and coated cemented carbides have poor performance at higher speeds [27], and PCD is a poor choice for machining ferrous alloys when high temperatures are reached in the cutting zone [29]. Hence PcBN is the recommended tool material to machine Hadfield steel at high speeds due to its hardness and chemical stability. The choice of tool grades and binders are limited when machining Hadfield steel at high speeds, but a commercial high cBN (90 %) grade with a mean grain size of 20 μm sintered with Al binder has shown success in industry and is thus selected. The Al binder reacts with the cBN during sintering forming AlN, AlB_2 and AlB_{12}, leading to a tougher and harder tool with low porosity compared to other commercial binder systems [30]. There are also metallic binders available for interrupted machining, however this study focuses on continuous machining.

Forming a carbide TPL such as NbC and (Ti,V)C as in the case of machining pure Nb with WC-Co [13] and Ti-alloys with PCD [16,17], is not a possible route because adding enough carbide forming elements to form a carbide based TPL would lead to carbides in the workpiece material which already contains the source of carbon. Hence the best possibility for alloying would be adding boride-, nitride-, and oxide-forming elements. The elements that are commercially available to alloy steel and form refractory materials with B, N, and O are the group 4–6 elements Ti, V, Zr, Nb, Mo, Ta, and W, in addition to Al. Cr and Si oxides and nitrides are also good candidates. However, Cr and Si are already present and defined in the reference alloy.

To reach the goal of finding the correct alloying with these elements, which leads to improved machinability (by TPL formation) without degrading the functional properties would be an extremely time-consuming and expensive experimental screening process. Hence the method of theoretical screening to limit experimental testing is therefore essential and is outlined in the next section.

Table 1
Composition of reference alloy in mass %. *represents the composition used for calculations.

	Fe	Mn	C	Si	Cr
Min	balance	12	1.0	0.40	1.0
Max	balance	15	1.4	0.90	1.6
*	balance	14.0	1.14	0.50	1.50

2.3. Thermodynamic screening

The specific calculations depend on the tool material and the functional properties of the workpiece materials, but the underlying method is the same. The limit of how the material can be alloyed needs to be defined. Some grades, such as nickel [14] and titanium alloys [16], might only be alloyed within a specified composition range. While other grades, such as cast iron, steels, and aluminum alloys most often contain recycled material and hence trace elements [31] or may contain certain elements up to a limit [20,32]. But there is always a window of opportunity for alloying and selecting tool materials.

Modelling the effect on machinability due to alloying within this range is then the next step. This modeling depends on what tool wear mechanism should be limited by TPL formation. Tool materials can suffer from oxidation, diffusion, chemical degradation or a combination. This method of thermodynamic screening and TPL formation is not aimed at preventing tool wear that is purely abrasive and mechanical. Such wear can often be avoided by selection of a different tool grade. Many coatings, ceramics, and superhard tool materials do not mainly suffer from abrasive wear, but by a combination wear by chemical degradation, oxidational attack, or diffusional loss of tool elements leading to degradation of mechanical properties resulting in abrasive wear. Hence a TPL can limit such wear by creating an in-operando barrier as outlined in the introduction.

Two alloying criteria are defined for the case study of manganese steel. Alloying must be limited so that it retains its functional properties (defined by ***criteria 1*** and ***2***).

(1) ***The steel must be austenitic, with only a limited fraction of carbides after quenching.***
(2) ***The abrasive wear resistance must be in parity with the current reference material.***

Calculating the maximum amount of alloying possible while still meeting ***criteria 1***, a fully austenitic steel with a low fraction of carbides after quenching, can be readily performed using thermodynamic modeling. The fastest method for doing this for a wide alloy range is to calculate at what alloying fraction the steel is not fully austenitic at the quenching temperature. This is not as accurate as performing precipitation simulations [33], but performing equilibrium calculations at the quenching temperature is a time-efficient method to explore the alloying range.

Modeling ***criteria 2*** requires that the material should retain its functional properties and hence remain resistant to wear by work hardening. Work hardening by forming twins or a phase transformation from austinite, a face-centered cubic (FCC) structure, to ε-martensite, a hexagonal close packed (HCP) structure, is mainly determined by the material's stacking fault energy (SFE) [34]. Calculating the SFE of an alloy is currently an open and active research area, especially for medium Mn-steels. Three main methods are used for predicting the SFE of an alloy: ab initio-based methods such as density functional theory (DFT) [35], thermodynamics based methods [36,37], and empirical fitting of experimental data [34]. The thermodynamics based approach has shown to give reasonable agreement with measurements with limited effort, given the availability of good thermodynamic models and data [38,39]. Hence this method will be used to model ***criteria* 2**.

The next step is to calculate the effect of the acceptable alloys (in this case alloys meeting ***criteria 1*** and ***2***) on tool wear by diffusion, oxidation, and chemical degradation. ***Criteria 1*** and ***2*** and the calculations might be performed for several different tool materials and coatings. Hence alloys that meet ***criteria 1*** and ***2*** are used for evaluation with ***criteria 3***, the formation of a TPL, and ***criteria 4***, the stability of the TPL and an increase in tool life. The tool life is modeled with thermodynamics based on the method used in earlier papers [7,15].

(3) The tool and workpiece combination must support the formation of a tool protection layer (TPL).

(4) The tool protection layer (TPL) must be stable and result in an increase in tool performance.

The positive or negative effect of the possible interactions in the cutting zone between the steel, tool and air is then studied by modeling the interaction products formed and their stability at machining conditions, which further narrows the final experimental matrix.

Criteria 1 and ***2*** and how to calculate and model them are alloy specific, while ***Criteria 3*** and ***4*** and the method of calculation are general. However, the boundary conditions of the calculations have to be selected appropriately depending on the cutting conditions and if it is turning, milling, or another machining operation.

2.4. Experimental validation

The first step to validate the results from the thermodynamic modeling is by high-temperature and high-pressure diffusion couple experiments between the tool, steel, and air. The diffusion couple experiments can function as a controlled study that provides a connection between the thermodynamic calculations and machining [17,40]. This will be used to evaluate whether ***criteria 1*** and ***3*** are met. This step is focused on validation of the modeling and might not be needed when modeling a well understood tool and workpiece combination.

Evaluation of an increase in tool performance in ***criteria 4*** is best done with machining experiments. Validation of ***criteria 2*** is done with a controlled rock grinding abrasion test between the alloy and rock.

3. Methods

Thermodynamic calculations are performed using the CALPHAD approach, which is a phenomenological approach for calculating thermodynamic, kinetic, and other properties of multicomponent materials systems. CALPHAD is preformed using Thermo-Calc software [41] and the databases TCFE12 and MOBFE7 as well as additional borides and nitrides appended from TCNI12. Thermo-Calc was also coupled with Python using TC-Python, enabling the calculation for efficient screening of alloy combinations.

Thermo-Calc uses the compound energy formalism [42] to describe the Gibbs energy (G^{α}) of each phase *(α, β …)* as a function of pressure (*P*), temperature (*T*), and composition (${x_i}^{\alpha}$). The expression for the molar Gibbs free energy of a phase with two or more sublattices can be given by Eq. 1.

$$G_m = \sum \overset{\circ}{G}_{end} \prod y_J^s + RT \sum \sum n^s y_J^s \ln(y_J^s) + {}^{E}G_m + G_m^{magn} \tag{1}$$

The first term represents the surface of reference and is a weighted average of all the endmembers. ${}^{\circ}G_{end}$ is the Gibbs energy of one formula unit of the compound represented by the endmember. y_J^s represents the site fractions, s identifies the sublattice, J the constituent, and the product $\prod y_J^s$ then contains one site fraction from each sublattice identified by the constituent. The second term is the ideal entropy of mixing, where n^s is the stoichiometric coefficient indexed by *s, R* is the gas constant, and *T* is the temperature in K. The ${}^{E}G_m$ term is the excess Gibbs energy representing the deviation from an ideal mixture and the G_m^{magn} term is the magnetic contribution. A full description of this can be found in the literature [42].

Thermodynamic equilibrium is reached when the Gibbs energy of the entire system is minimized in an isothermal isobaric system. This is done by minimizing $G(P, T,\ x_i\ , ..)$ (Eq. 2), where the Gibbs energy $G^{\alpha}(P, T, {x_i}^{\alpha},$ $..)$ of each phase *(α, β …)* is described by Eq. 1.

$$G(P, T, \quad X_i \quad , ..) = G^{\alpha}(P, T, {x_i}^{\alpha}, ..) + G^{\beta}(P, T, {x_i}^{\beta}, \quad ..) + \dots \tag{2}$$

This method enables us to calculate what phases are stable, what phases can form, their driving forces, the solubility of elements in each phase, their diffusivities, and all other thermodynamic properties of the system during casting, quenching, and machining. Further details and examples of the application of the CALPHAD method to study tool wear can be found elsewhere [23,43]. This modeling is then the base for the evaluation of the prospect of a potential alloy using ***criteria 1–4***.

The effect of alloying on the SFE must be evaluated to meet ***criteria 3.*** The SFE should not drastically change from the reference alloy. Work hardening by a phase change from FCC to HCP is thought to occur when the SFE is ~10–18 mJ/m^2 [26,44], hardening by twinning is thought to occur when the SFE is 12–35 mJ/m^2, and both can occur in the region of the overlap [26,38].

Eq. 3 is used to calculate the SFE per unit area (γ_{SFE}) [36,37]

$$\gamma_{SFE} = 2\rho^{HCP}\left(G_m^{FCC\rightarrow HCP} + R_m^{str}\right) + 2\sigma \tag{3}$$

where ρ^{hcp} is the molar surface density in the HCP plane, $G_m^{FCC\rightarrow HCP}$ is the Gibbs energy difference per mol between FCC and HCP, R_m^{str} is the strain energy per mol, and σ is the interfacial energy between FCC and HCP per unit area.

A small change in the alloy composition mainly affects the $\Delta G_m^{FCC\rightarrow HCP}$ since the density of atoms ρ^{HCP} is dependent on the lattice parameter, which does not change considerably with low amounts of alloying [45,46] compared to the changes in $\Delta G_m^{FCC\rightarrow HCP}$. The value of σ can to some extent be assumed to be independent of composition [47]. The effect of composition on R_m^{str} is negligible compared to its effect on $\Delta G_m^{FCC\rightarrow HCP}$ [48]. We can then simplify Eq. 3 if we only consider the change in SFE ($\Delta\gamma_{SFE}$) from the reference alloy. Then the relevant factor is the change in the Gibbs energy between FCC and HCP ($\Delta G_m^{FCC\rightarrow HCP}$), which can be calculated using thermodynamics. The density of atoms (ρ^{HCP}) of this material can be calculated from the lattice a_{FCC} parameter of the FCC phase [48], which is 0.361 nm for this alloy, giving a $2\rho^{HCP}$ of 5.9×10^{-5} moles/m^2. Hence, we want to maintain a sufficiently low alloying concentration so that the change in SFE (Eq. 4) is limited.

$$\Delta\gamma_{SFE} \approx 2\rho^{HCP}\left(\Delta G_m^{FCC\rightarrow HCP}\right) \tag{4}$$

Microscopy analysis is preformed using a scanning electron microscope (SEM, TESCAN Mira3) equipped with a topography sensitive secondary electron (SE) detector, a composition sensitive backscatter electron (BSE) detector, an X-ray energy dispersive spectroscopy (XEDS) detector, and crystallographic sensitive electron backscatter diffraction (EBSD) detector. Lamellae for analysis with a transmission electron microscope (TEM) are prepared by a lift-off procedure using a focused ion beam (FIB, FEI Nova NanoLab 600). A TEM (JEOL 3000 F) equipped with XEDS is used to investigate the lamellae. Scanning transmission electron microscopy (STEM) and selected area electron diffraction (SAED) is also performed. The compositions of the materials are measured with a spark optical emission spectrometer (OES, Thermo Fisher). Flank wear is measured using an Olympus SZX7 stereo visible light microscope (VLM), while an Alicona Infinite Focus 3D VLM based on focus variation is used for crater wear analysis.

Experimental tests include casting, diffusion couple tests, and machining. Casting for the diffusion couples is performed in a resistance tube furnace carried out by first pumping down to vacuum (10^{-6} mbar) then flooding with Ar. The samples are held at 1500 °C for 1 hour, then cooled. The samples are then heat-treated at 1100 °C and quenched.

The cast samples for each alloying composition are machined to produce two cylindrical cups creating a capsule into which the PcBN tool material in the form of a RNGN 060300–01520 insert is placed. The diffusion couple experiments were performed in a toroid-type high pressure and high temperature cell (HPAT-30) as described in detail in the literature [13,40]. The diffusion experiment was conducted for 10 min at a pressure of 2.5 GPa and temperatures of 1200 and 1300 °C. The high-pressure cell was then water cooled to room temperature in less than 1 minute.

The final versions of the alloyed Hadfield steels and the reference material were produced as round bars. These bars for machining and abrasion tests were cast in a pilot foundry using an induction furnace and cast into molds. These materials were oil quenched at 1100 °C following an industrially standard heat treatment routine.

Abrasion resistance is evaluated by longitudinal rock turning [49, 50] using pins manufactured from the cast Mn-steel bars. The counter surface is red granite, the Mn-steel pins are 10 mm in diameter with a hemispherical surface. The pins are pressed against the rock at a pressure of 100 N, the travel length is 100 m at a speed of 53 m/min and the test is preformed dry. The test is repeated three times for every material and the mass loss is measured.

The ***machining test*** is performed on a SMT 500 Swedturn CNC-lathe, which has a motor power of 70 kW and a spindle speed rated up to 4000 rpm. The toolholder used is an ISO CRSNL3225P12 and the insert geometry is round, chamfered, and solid ISO RNMN120400S. The cutting conditions are based on industrially relevant cutting conditions that are aimed to have a high enough cutting depth (a_p) and feed (f) to avoid machining the hardened surface from the previous pass while still providing an acceptable surface finish. The speed is selected based on reaching the condition leading to the desired temperature enabling the formation of a TPL. The machining test and abrasion tests are performed on material from the same bar.

4. Results

4.1. Thermodynamic and theoretical screening

The aim of the thermodynamic screening is to determine which elements and their respective concentrations in the alloy satisfy ***criteria 1–4***. More alloying results in a higher possibility for formation of a TPL (***criteria 3 and 4***) but may change the functional properties of the material (***criteria 1 and 2***),. Thus, the aim of the calculations is to find the boundary conditions for alloying. Fig. 2 is a schematic summarizing the method to find the elements and amount of alloying to meet ***criteria 1–4.***

4.1.1. Calculating the maximum permissible alloying (criteria 1 & 2)

Calculating and measuring the SFE is not yet an exact science [51], and there is also not an exact link between the SFE and abrasive wear resistance. In addition, the steel should be "carbide free", but a small amount is almost always present [52]. Carbides can and might form during quenching. The aim in the screening stage is to find the range of successful alloying with Ti, V, Zr, Nb, Mo, Ta, W, and Al.

The first boundary condition is to find how much boride-, nitride-, and oxide-forming elements can be added into the FCC phase in the Mn-steel without forming carbides that are stable above 1100 °C (the quenching temperature). The reference alloy is fully FCC at the quenching temperature. Fig. 3a shows the maximum solubility of the

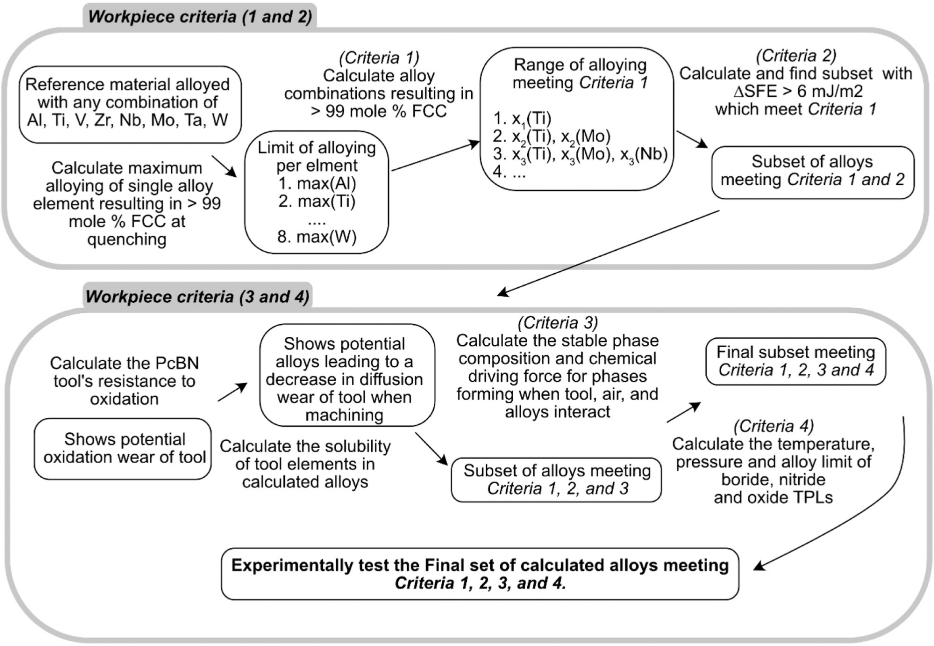

Fig. 2. A schematic of the thermodynamics based computational method. Starting with a large set of all potential alloying combinations. Then modeling and successive exclusion of alloys not meeting the criteria, to find the most promising alloy subset, leading to improved machinability with retained functional properties.

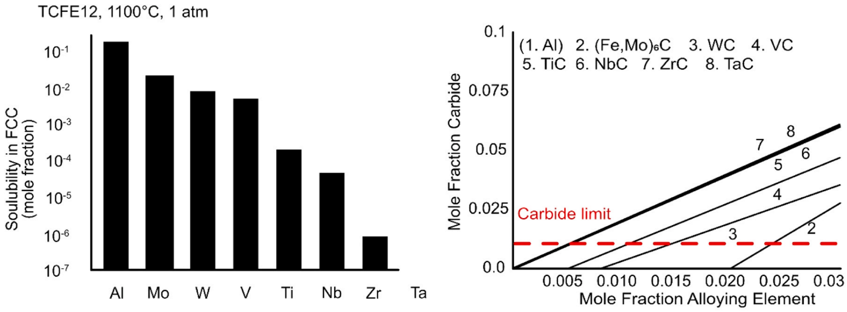

(a)

(b)

Fig. 3. Calculating maximum alloying with regards to carbide formation. (a) The mole fraction of an element that can be added to the reference steel before a carbide is stable at the quenching temperature. (b) The mole fraction of carbide that forms as the alloying increases. The red line indicates the acceptable alloying limit, Al is not a carbide former and hence not limited by carbide formation.

different elements in the FCC phase in the Mn-steel. This indicates how much the steel can be alloyed before carbides form. For example, adding a mole fraction of 0.02 of Mo is the maximum amount of Mo that can be dissolved in FCC at 1100 °C (Fig. 3a). Al is however not a carbide former but an FCC stabilizer (at 1100 °C), and therefore carbide formation is not a limiting factor for Al. Fig. 3b shows the resulting carbide that forms when alloying above the solubility limit. For example, alloying with a mole fraction of 0.025 Mo results in 0.014 mol fractions of $(Fe,Mo)_6C$ being stable at the quenching temperature of 1100 °C. This calculation is also performed for all possible combinations of all the alloying elements. For example, alloying with a combination of W and Mo leads at low quantities to the formation of $(Fe,Mo,W)_6C$ rather than both WC and $(Fe,Mo)_6C$. However, the maximum "carbide free" alloying for a single alloy element is always maximized when not combined with other carbide formers.

Over-alloying can also lead to a decrease in abrasive wear resistance (***criteria 2***). This second boundary condition is finding the maximum amount of alloying which can be added without changing the wear properties. This is modeled by calculating the change in SFE using Eq. 4. These calculations are performed for all elements, but results are only shown for Al, Mo, W, and V because carbide formation is by far the limiting factor for V, Ti, Nb, Zr and Ta. The value of $\Delta G_m^{FCC \rightarrow HCP}$ is calculated at 300 K (27 °C) and 10^5 Pa (1 atm) using the Thermo-Calc TCFE12 database. Fig. 4 is the calculated change in the SFE with the addition of Al, Mo, W, or V to the reference material. This method for calculating the change in SFE is in this narrow range of alloying in good agreement with published calculations [35] and experimental measurements [39,53].

The limit of the change in SFE is set to 6 mJ/m^2. A smaller change in SFE can be offset by tuning of the reference alloy and heat treatment. The limit of carbide formation is set to a mole fraction of 0.01 at the quenching temperature, (~1 vol%, depending on the carbide). Table 2 shows the maximum limit of alloying per element based on ***criteria 1*** and ***2***.

Combining elements leads to a smaller amount of alloying than the maximum shown in Table 2. The one exception is for the combination of Al with elements lowering the SFE, (mainly Mo or W). There are other effects of alloying not calculated here. Some examples are Al capturing O and P in the melt [54]. Ti and Al are also known to reduce the grain size of the material and change the fracture toughness at low temperatures [54]. However these changes can be neglected or offset at these low alloying amounts for a steel used for heavy industrial applications [54].

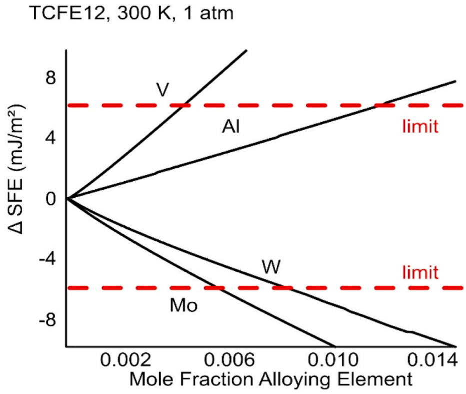

Fig. 4. Calculating the maximum alloying with regards to Δ SFE. The red line indicates the maximum allowable change in SFE.

Table 2
The maximum amount of alloying of each element. The subscripts SFE and C indicate that the element is limited by the change in SFE and carbide formation, respectively.

	Al_{SFE}	W_{SFE}	Mo_{SFE}	V_{SFE}	Ti_C	Nb_C	Zr_C	Ta_C
at%	1.50	1.10	0.80	0.55	0.52	0.5	0.5	0.5

4.1.2. Calculating the potential for and stability of a TPL (criteria 3 & 4)

The next step is to screen for alloying combinations of the elements in Table 2 that meet ***criteria 3*** and ***4***. There is a crucial difference when modeling the steel and tool interaction in a static diffusion couple and when it is being machined. The PcBN tool continuously meets fresh Mn-steel as it is engaged in the cutting. Hence the chemical activity of the elements in the steel are nearly constant while the chemical activity of some of the elements in the tool will decrease as the tool is worn by diffusion, reactions, and/or oxidation [17]. Thus, an intentional small amount of alloying (0.4–1 at% [14]) or unintentional amounts of alloying from recycled materials (<1 at% [32]) can have a large effect on machinability if they react or oxidize and accumulate on the tool surface. The aim of this section is to evaluate what alloying element and amount might be able to form a protective layer that decreases tool wear caused by diffusion, oxidation, and chemical reaction wear mechanisms.

The tool material can degrade by oxidation, the binder (AlN, AlB_2 and AlB_{12}) can oxidize into Al_2O_3, and the cBN grains can oxidize into B_2O_3 and N_2 gas. This has been shown in oxidation experiments [55] and machining experiments [56], and can be shown by the thermodynamics presented in Fig. 5. Complete oxidation of the cBN phase into B_2O_3 and the formation of the B_2O_3 melt is thermodynamically possible. However, this does not happen kinetically in oxidation experiments because B_2O_3 forms a passivation layer on cBN, which makes cBN resistant to oxidational attack and the consequent melting of B_2O_3 [57], unless at very high temperature where B_2O_3 may evaporate.

The tool material elements (B, N, and Al) can diffuse into the workpiece material. This has been shown in diffusion couple experiments [15] and machining experiments [58]. Wear by diffusion can be calculated using diffusion simulations, which would be more accurate, but would also be rather a time-prohibitive endeavor for screening all alloy combinations. An efficient approximation of tool wear by diffusion is permeability [19,59]. The permeability is the product of concentration (how much of an element from the tool is transported into the steel) and the diffusivity (how fast an element from the tool can diffuse into the steel). The maximum permeability is when the concentration has reached the solubility limit in the steel phase. This maximum can be reached for B when Fe_2B forms and for N when N_2 gas forms at normal pressure (1 atm) or when CrN forms at high pressure (2.5 GPa) (Fig. 6 and Table 3). Al is an austenite stabilizer (Fig. 3), hence the solubility is not limited by the formation of a new phase but rather by an equilibrium between the tool and the steel.

Comparing the permeability (mobility times concentration) of B, N, and Al can approximate the potential for diffusional wear of the tool. Fig. 6 is a ternary diagram between the Hadfield steel, B, and N that shows how much of the elements can be dissolved. Table 3 shows the maximum solubility and what phase is formed, the mobility of the element, and the theoretical maximum permeability. This shows that all elements from the tool can diffuse into the steel. B diffuses the fastest, but it might lead to the formation of borides. N diffuses more slowly, but a larger amount can dissolve in the steel or even form N_2 if the contact between the tool and the workpiece does not lead to elevated pressures. Al diffuses more than four orders of magnitude slower than B and N, but a large amount of Al can dissolve in the steel. This will only happen in diffusion couples or in a BUL during machining and not at the tool chip interface because the diffusion rate is insufficient for such substantial mass transfer.

The tool can also chemically degrade by reacting with both air (mainly O_2) and the steel. Fig. 7 shows the equilibrium phase

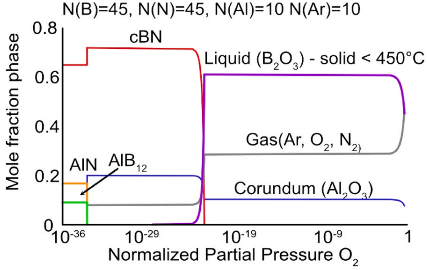

Fig. 5. Modeling the oxidation of the tool. The Al-based binder oxidizes into alumina (Al_2O_3) and the cBN grains become B_2O_3 and N_2. B_2O_3 is solid at low temperatures and high pressures, and liquid at higher temperatures and lower pressures.

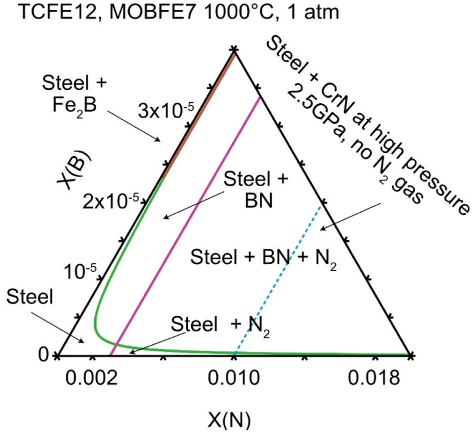

Fig. 6. Ternary phase diagram of B-N-Steel. B and N (tool material) can dissolve (and potentially diffuse) into the steel. N will likely to form CrN or N_2 gas, B will likely form Fe_2B above the solubility limit in the steel.

Table 3
The solubility limit, what phases will form when the limit is reached, the mobility, and the permeability. This indicate the ability of the tool element to diffuse into the steel potentially lead to tool wear.

	Solubility limit in steel	Phase formed	Mobility in steel phase $[m^2/J\ s]$	Theoretical maximum permeability $[mol\ m^2/J\ s]$
B	2.3×10^{-5}	Fe_2B	4.4×10^{-15}	1.0×10^{-19}
N	0.003 (at 1 atm) 0.01 (at 2.5 GPa)	N_2 (gas) CrN	8.2×10^{-16}	8.2×10^{-18}
Al	0.1*	-	6.5×10^{-20}	6.5×10^{-21}

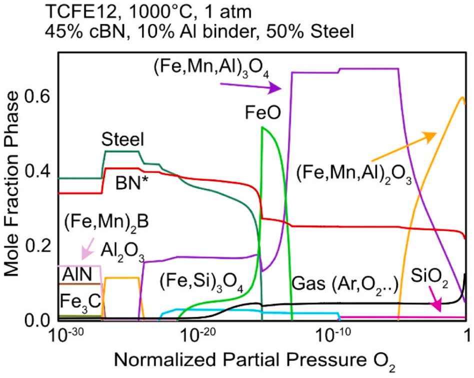

Fig. 7. Modeling the interaction between the tool, steel as more oxygen is available at the tool chip interface. * The BN becomes B_2O_3 at an oxygen partial pressure of 10^{-21} but this is suspended in the calculation because it is kinetically unlikely in turning [57] and does not affect the rest of the calculation.

composition at an increasing availability of O_2. A normalized partial pressure of O_2 equal to 10^{-30} represents no air/coolant in the cutting zone, which is representative of the sticking zone at the tool-chip interface, where the contact is intimate. A normalized partial pressure of O_2 equal to 0.21 represents the end of the cutting zone where air is fully present. The steel can react with the AlB_{12} to form $(Fe,Mn)_2B$ when no air is present, but AlN is resistant to chemical attack by the steel. The Al-based binder can then oxidize into Al_2O_3 as air is available at a normalized O_2 partial pressure of approximately 10^{-26}. But a spinel phase $(Fe,Mn,Al)_3O_4$ consisting of both the binder and steel elements can form at higher oxygen availability. Hence different oxides that might not be as wear resistant can form on the tool when it is in the presence of steel (Fig. 7) compared to when the tool oxidizes by itself (Fig. 5). The formation of B_2O_3 from cBN and the subsequent melting is suspended in this calculation (Fig. 7). Including B_2O_3 leads to the BN line being separated into three phases, as shown in Fig. 5.

These same calculations (Table 3 and Figs. 5, 6, and 7) are performed with the addition of the alloying from Table 2 and their combinations. The results of the calculations can be used to understand what alloying can limit diffusion, oxidation, or chemical degradation of the tool by the formation of stable borides, nitrides, oxides or by lowering the solubility and mobility. The formation of $(Fe,Mn)_2B$ without any alloying could be a boride candidate (Fig. 7), but it melts above 1070 °C at 1 atm in this system and it would be soft at temperatures reached during machining. Therefore, it does not meet ***criteria 4***.

The alloying elements Ta, Nb, Zr, and W can form carbide TPLs if the activity of C in the steel increases. The carbon activity in the steel, chip, or workpiece material adhered to the tool can increase during machining if for example Fe and Mn reacts with B from the binder or if Cr, Mn, or Si react with oxygen. However, this is not a promising TPL, as it forms in the steel rather than on the tool surface to limit wear. Hence such potential carbides that would meet ***criteria 1*** but do not meet ***criteria 4***.

Alloying with Mo could lead to the formation or stabilization of the metal boride by forming $(Fe,Mn,Mo)_2B$. This boride has a low melting point (similar to $(Fe,Mn)_2B$) at ambient pressures (1 atm) but the boride is more stable at higher pressures (>1 GPa).

Adding Zr and V can lead to the formation of nitrides in the cutting zone, limiting N diffusion and the outgassing of N_2. Fig. 8a shows how the addition of V leads to the formation of VN, which is stable even up to 2000 °C. This can only happen at the interface between the steel and cBN. Because V cannot degrade the AlN binder into VN, the binder phase is not included in Fig. 8a. Fig. 8a also shows how $(Fe,Mn)_2B$ is stable at higher temperatures (1200 °C) at pressures > 1 GPa.

Ti and Al are the most promising as they are both nitride formers (TiN and AlN), and oxide formers combined either independently as part of steel in contact with the cBN or air, or together with the binder (Al_2O_3 and $(Al,Ti)_2O_3$). Al also decreases the chemical potential for the binder to diffuse into the steel because the binder is Al-based. Fig. 8b shows how the addition of Ti leads to both $(Al,Ti)_2O_3$ (corundum) and TiN (FCC), which are both stable at temperatures beyond those reached in the cutting zone in the presence of cBN, binder, steel, and oxygen.

Additionally, the alloying elements should not chemically attack the cBN grains and binder phases, but rather form TPL phases with elements leaving the tool phases. This is similar to the problem of how Mg- and Ca-oxides in non-metallic inclusions can attack Al_2O_3 coatings and degrade them into spinel and calcium aluminates rather than forming protective deposits [40,60]. None of the alloying elements can degrade AlN. However, all alloying elements can degrade the AlB_{12} binder phase into other metal borides such as B_2W_9, $(Mo,Fe)_xB_y$, and $(Fe,Ta)B_2$. Similar to Fe degrading AlB_{12} into $(Fe,Mn)_2B$ shown in Fig. 7 and 8.

4.1.3. Summary of results from thermodynamic and theoretical screening

Micro-alloying with less than 1.50 at% of Al is the most promising. There is also no lower boundary for when Al has a positive effect. Al is an austenite stabilizer and not a carbide former ***(criteria 1)***. Alloying with close to or more than 1.50 at% Al can change the SFE and the abrasive wear properties ***(criteria 2*** and Fig. 4). The binder of the tool is Al-based (AlB_2/AlB_{12} and AlN). Any addition of Al to the steel does not attack the binder or grains and limits the solubility of the tool elements in the steel. Additionally, Al promotes the formation of a TPL of either AlN, AlB_x, or Al_xO_y (***criteria 3***). AlN, AlB_x, and Al_xOy are stable at high temperatures (Fig. 8b) (***criteria 4***).

Small amounts (<0.52 at%) of Ti are also promising because Ti is both an oxide former together with Al and a nitride former. V and Zr are nitride formers that could limit N diffusion and outgassing. Mo forms borides together with Fe and Mn but these are not as stable as the nitrides. However, all these elements lead to carbide formation (Fig. 3), which might not affect the functional properties of the workpiece but might lead to increased abrasive wear. However small amount of Ti, V, Mo, and Zr might still result in carbides that are detrimental to machining performance.

The carbide formers Nb, W, and Ta are not as promising because they form carbides in the steel and not on the tool-chip interface. These might be interesting when machining with carbon-based tools such as cemented carbide or polycrystalline diamond but show little promise for the PcBN tool material system. The Si and Cr originally precent in the steel is also not enough to form a TPL.

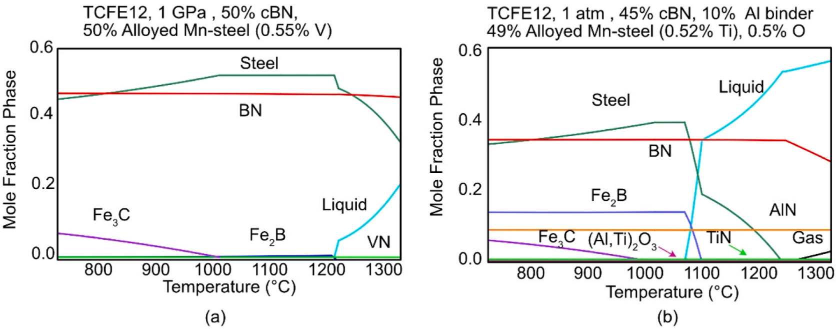

Fig. 8. Modeling the effect of alloying on the steel-tool-O_2 interaction. (a) Alloying with V can lead to the formation of VN, which is a potential TPL. (b) Alloying with Ti can lead to the formation of a TiN and also a $(Al,Ti)_2O_3$ TPL. VN, TiN, and $(Al,Ti)_2O_3$ are stable over a wide range of machining conditions compared to Fe_3C and Fe_2B, which soften, dissolve, or melt at higher temperatures.

4.2. *Experimental evaluation*

4.2.1. *Diffusion couples*

Diffusion couples were made to do wide-range and small-scale tests of the validity of the thermodynamic predictions, since calculations of this material at these conditions have not been published before. A total of 10 different alloys were tested at 2 different temperatures (1200 and 1300 °C) resulting in 20 separate experiments. The materials tested were the reference material (Table 1), each maximum single element alloy (Table 2), and a multiple element alloy of Mo, Ti, and Nb. The diffusion experiments were carried out at high pressure (2.5 GPa) for 10 min. No evidence of liquid or gas formation in the diffusion couple was found due to the high pressure, but glassy or amorphous phases were found. Hence all reactions took place in solid (or glassy) states. This method provided an easier way to analyze experimentally the potential chemical wear products in the cutting zone [40,60].

The diffusion couple between the tool and the reference alloy shows how the tool phases (cBN, AlB_{12}, and AlN) diffuse and dissolve into the steel. The calculations in Figs. 6 and 7 and the experimental results in Fig. 9 all show this. Increasing the temperature to 1300 °C (Fig. 10) shows results similar to those at 1200 °C. However, there is a larger interaction layer (6–13 μm), more metal borides, and even reprecipitation of BN inside the steel.

Air is sometimes trapped in corners of the diffusion couple, because the PcBN inserts are chamfered. As shown in Fig. 11, the trapped air can lead to the formation of a variety of mixed oxides containing Fe, Mn, Cr, and Si from the steel and limited amounts Al from the binder. Si-rich oxides appear as a glassy, amorphous slag and Si deficient oxides are crystalline. This is because Si can lower the glass transition temperature, and these experiments were carried out at temperatures and pressures close to the melting point of Si-rich oxides [61]. The calculation in Fig. 7 assumes thermodynamic equilibrium and no formation of liquid B_2O_3. No B_2O_3 was found using SEM. There might be B_2O_3 formed on the surface of the cBN grains, but they would thinner than 50 nm and create a passivation layer [57]. The three main phases $Metal_3O_4$ (spinel), $Metal_2O_3$ (corundum), and SiO_2 are identified both in the calculation and the diffusion couple experiments.

The carbon activity in the steel would increase if the Fe in the steel leaves and form borides. This might result in carbide-forming elements such as Ta, Nb, Zr, and W forming more carbides then initially predicted (Table 4), which would result in agglomerates of carbides forming inside the steel and on the interface between the tool and the alloy. This can explain what is seen in the diffusion couple experiment between the tool material and Ta-alloyed workpiece material (Fig. 12), the same occurs in the Nb, Zr, and W alloyed workpieces. This would not be a successful TPL and would not protect the tool because these carbides would form in the chip or adhered material rather than protecting the tool surface. It might however lead to a TPL when machining with carbon-containing tools such as cemented carbide or polycrystalline diamond [17,19].

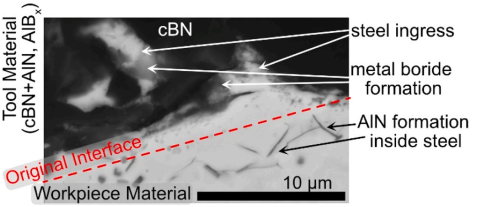

Fig. 9. Diffusion couple between reference alloy and tool after 1200 °C, 10 min and 2.5 GPa. BSE-SEM image with phase identification by XEDS. The original interface is difficult to identify due a lot of interactions between the tool and steel. The grains and binder dissolve and diffuse into the steel, and the steel elements consume the binder. Metal borides form on the interface, and AlN has reprecipitated inside the steel.

Adding Ti and Al resulted in the cBN grains being covered by an AlN or TiN layer that limited diffusion. The effect was the greatest with Al because it was both present in the binder and steel. The effect of this was seen when comparing the Al alloyed sample in Fig. 13 with a small (1–5 μm) interaction layer compared to the large (6–13 μm) layer in the reference alloy in Fig. 10, (a small layer is due to less diffusion). Reprecipitated BN is also not found in the Ti and Al alloyed materials, indicating less diffusion compared to the reference alloy (Fig. 10). Hence the addition of Al and Ti leads to less diffusion on the binder phases and limits cBN dissolution and diffusion.

Alloying with Ti and Al also leads to the formation of more Al-, Ti-, Cr-, and Fe-rich corundum $(Al, Ti, Cr,Fe)_2O_3$ (Fig. 14) rather than a majority of Fe-rich spinel oxides (Fig. 11). Corundum layers should result in harder, more wear resistant oxide layers compared to spinel on the tool surface during machining [7].

Adding Mo is expected to lead to boride formation (Table 4). These borides are iron-rich and similar to the borides in Figs. 9 and 10. Mo does also lead to slightly B- and Mo-enriched areas away from the interface. This shows how fast B diffuses in the austenite phase, especially when there are cracks and grain boundaries (Fig. 15). The combined alloying of Nb, Mo, and Ti results in the same effect as alloying them individually except for the formation of mixed carbides (Mo,Nb)C.

4.2.2. *Casting*

The calculations and the verification by diffusion couple experiments are in good agreement, and therefore Al remains the most promising alloying element. Al is a main constituent of the binder (AlN, AlB_6, and AlB_{12}), hence alloying lowers the difference between the activity of Al in the steel and binder, lowering the driving force for Al from the binder to diffuse into the steel (Table 3, Fig. 13). Al can also form a TPL with O (Table 4, Fig. 14), N, and B (Table 4, Fig. 13). It is also not a carbide former (Fig. 3). Adding Al will change the SFE (Fig. 4) and the abrasive resistance, but the effect can be limited if the alloying is less than 1.5 at % (Table 2). Casting with Al can also capture oxygen leading to formation of oxides, change the shape and distribution of phosphides, and impact grain growth [54]. Proper deoxidation, a low phosphor content, and not changing the grain size between the new alloy and the reference should be considered.

A combination of Al, Ti, V, and Nb is also experimentally interesting based on the calculations (Table 4) and diffusion couple experiments (Fig. 14). Alloying with Ti, V, and Nb leads to some carbide formation (Fig. 3), but it can be limited by low amounts of alloying Table 2. The addition of Ti is interesting because it is both an oxide and nitride former, but not a strong boride former (Table 4, Figs. 8b, and 13). V is only a nitride former (Table 4), hence will likely not form an oxide TPL like Al and Ti do. Nb is a carbide former in this system (Fig. 3 and Table 4) but can combine to form nitride if there is an accumulation of Nb at the interface.

Three bars were made for experimental validation: a reference bar, an Al alloyed bar, and an Al, Ti, V, and Nb alloyed bar. The bars were from the same melt. The reference was cast first then the melt was alloyed, the second bar was then cast, and then the melt was alloyed again, and the third bar was cast.

4.2.3. *Metallographic investigation for criteria 1*

The hardness and composition of the three test bars are shown in Table 5. The hardness and composition are measured after heat treatment using a Vickers hardness indenter and OES, respectively, in six separate locations on the bar. The composition and hardness are homogenous throughout the bars.

There was one reference Hadfield high manganese steel for heavy industrial application. Alloy I contained an addition of Al (0.3 at%), which was below the calculated maximum limit of 1.5 at%. Alloy II had approximately the same amount of Al (0.28 at%) and additions of Ti (0.24 at%), Nb (0.13 %), and V (0.042 at%). Alloy I was well within the

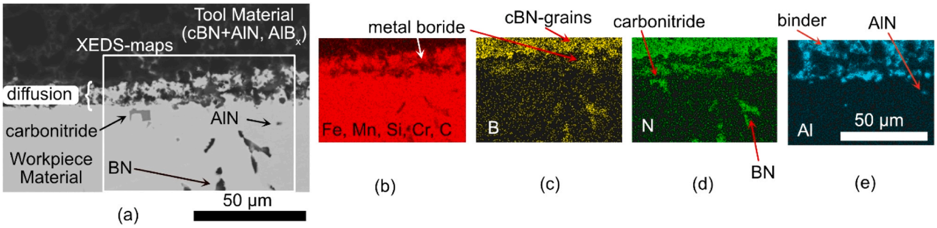

Fig. 10. Diffusion couple between reference alloy and tool at 1300 °C, 10 min and 2.5 GPa. (a) BSE-SEM and (b-e) XEDS maps. The binder and grains are dissolved into the steel. Borides, and carbonitrides have formed in the steel and BN and AlN have reprecipitated. Again, showing the intense diffusion and reaction between the tool material and steel.

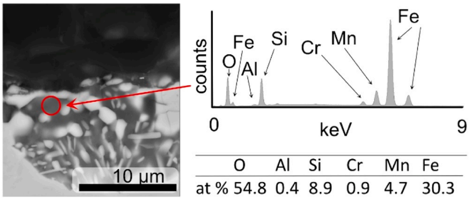

Fig. 11. Diffusion couple between reference alloy and tool at 1200 °C, 10 min and 2.5 GPa with trapped air. BSE-SEM and XEDS spectrum. The steel, binder are oxidized resulting in mixed metal oxides.

Table 4
The potential TPLs formed by alloying with specific elements, and the corresponding potential negative effects of the alloying.

Alloying element	Potential tool protection layer	Potential attack on tool	Comment
Al	Al_2O_3, AlN AlB_{12}	-	Limits oxidation, diffusion and chemical attack, and possible TPL formation.
Ti	TiN, (Al,Ti)2 O_3	cBN, AlB_{12} -> $(Fe,Ti)_2B$	Limits oxidation and TiN formation, attack on AlB_{12} and carbide formation
V	VN	cBN, AlB_{12} -> $(Fe,V)_2B$	Attack on AlB_{12} and carbide formation.
Zr	ZrN	cBN, AlB_{12} -> $(Fe,Zr)_2B$	Risk of ZrC formation, attack on AlB_{12} and carbide formation.
Mo	$(Fe,Mo)_2B$, Mo_3B_2	cBN, AlB_{12} -> $(Fe,Mo)_2B$	$(Fe,Mo)_2B$ not high temperature stable, attack on AlB_{12} and carbide formation.
Nb	NbC	cBN, AlB_{12} -> $(Fe,Nb)_2B$	Risk of NbC formation, attack on AlB_{12}.
W	WC	cBN, AlB_{12} -> B_2W_9, $(Fe, W)_2B$	Risk of WC formation. Attack on AlB_{12}.
Ta	TaC	cBN, AlB_{12} -> $(Fe,Ta)_2B$	TaC formation, attack on AlB_{12}.

calculated limits of carbide formation and changes in SFE. However, Alloy II resulted in a calculated change in stacking fault outside the desired limits (of $\Delta G_m^{FCC \rightarrow HCP} = 16$ mJ/m^2) and a calculated carbide mole fraction of 0.0073 (volume fraction of 0.0065). This was due to the Si from the lining mixing into the melt, as seen by the higher Si content.

The bars were fully austenitic after quenching. The grain size of the bars was the same in all samples. Pores were present but similar between alloys. All the alloys had low S, P, and Ca content, but trace amounts of MnS were present in all three alloys (Fig. 16). The bars were cast from

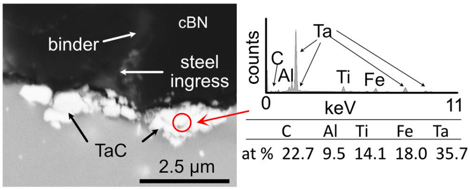

Fig. 12. Diffusion couple between Ta-alloyed material and tool at 1300 °C, 10 min and 25 GPa. BSE-SEM and XEDS spectrum. Fe diffuses into binder pockets leading to increased C-activity in the steel, this then leads to TaC formation.

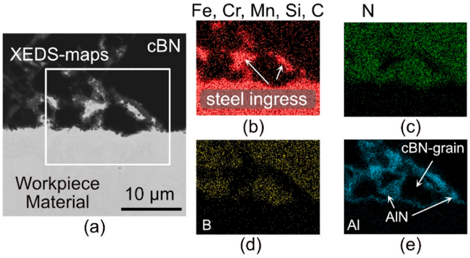

Fig. 13. Diffusion couple with the Al alloyed material at 1300 °C, 10 min and 2.5 GPa. The grains are covered with AlN limiting the wear by diffusion. (a) BSE-SEM and (b-e) XEDS maps.

recycled material and hence both the Reference and Alloy I had some carbo-nitrides. Alloy I was alloyed with Nb, which resulted in an expected but acceptable volume fraction of (Nb,Ti)C. Al_2O_3 and AlN was found in Alloy II but only to a very limited extent. Such precipitates and inclusion are hard and abrasive and will lead to inferior machinability and should hence be avoided.

4.2.4. Abrasion resistance testing for criteria 2

Abrasion resistance tests were performed on 3 pins from each material (Reference, Alloy I, and Alloy II). The mass of each pin was measured before and after 100 m of continuous wear testing. Fig. 17 shows the results of the abrasion tests. Alloy II performed slightly better (6 %) than the Reference and Alloy II performed slightly worse (2 %). As a result, this test showed that ***criteria 2*** was met as Alloy I and Alloy II only had an insignificant change in wear performance.

EBSD from the worn pins shows that all three materials have

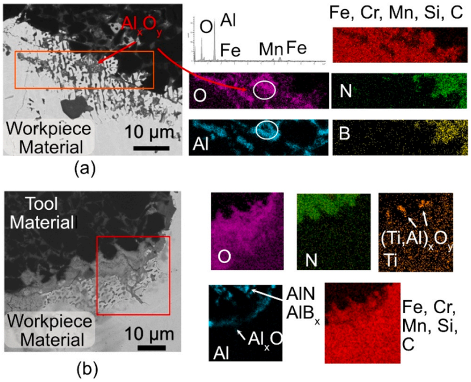

Fig. 14. Diffusion couple at 1300 °C, 10 min and 2.5 GPa for (a) Al and (b) Ti alloyed materials in areas with trapped oxygen. BSE-SEM and XEDS maps and spectrum. There is formation of aluminum and titanium oxides limiting grain and binder degradation, which may function as oxide TPLs during machining.

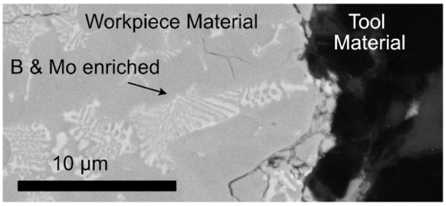

Fig. 15. Diffusion couple of Mo alloyed material at 1300 °C, 10 min and 2.5 GPa. BSE-SEM and identification by XEDS measurements. The Mo-boride that could form would likely not function as a TPL, as it would form in the steel and not on the interface. There is instead Mo and B rich regions inside the steel.

substantially work hardened during contact with the rock both by TWIP and TRIP (Fig. 18). The bulk material is austenitic, the grains become highly strained closer to the surface. ε-martensite grains are detected between the austenite grains, some grains are also identified as α'-martensite. The EBSD-signal is lost 1–5 µm from the edge due to the resolution limit of the microscope detector.

4.2.5. Machining performance testing of criteria 3 and 4

The machining test was performed at a cutting depth of $a_p = 0.5$ mm and a feed of $f = 0.3$ mm/rev to avoid machining the hardened surface from the previous pass. The oxide scale was removed, and the workpieces were cleaned before the machining test to reduce uncertainty. The recommended cutting speed (v_c) for the reference material was 200 m/min. These cutting conditions represented high speed industrially relevant medium finishing conditions of wear parts for this material.

The initial wear mechanism is crater wear, which leads to the chamfer being consumed, this weakens the cutting edge leading to progressive flank wear. This crater wear is often a sign of chemical, diffusional and oxidational wear [1,62], this was confirmed by thermodynamics Figs. 5–7 and diffusion couple experiments Figs. 9–11. The wear criteria were therefore based on flank wear, even if the flank wear was initiated by crater wear. The criteria were set to a flank wear (VB_{max}) of 800 µm because of surface quality requirements and the tool was likely to critically fail beyond this point due to the crater being large and the chamfer consumed. Hence no tool breakage occurred during the final testing.

Cutting the reference material at higher speeds led to aggressive cratering combined with flank wear, which can lead to a collapse of the cutting edge. This could be attributed to the higher speed leading to higher temperatures and therefore higher reaction rates, diffusion, and oxidation. But increasing the speed would also increase the formation of a possible TPL [14]. Hence the machining tests were conducted at $v_c =$ 200, 250, 300, and 350 m/min.

Fig. 19 shows the result of the machining tests, which were stopped around VB_{max}= 800 µm and hence no edge collapse occurred during the machining tests. The progression of the flank wear (VB_{max}) is plotted against cutting length. The crater depth (KT) is monitored using a VLM throughout the test, but only accurately measured using the 3D microscope at the end of test. The location and depth of the crater varies with speed but is located on the chamfer as seen in Fig. 20. The final KT is shown in Fig. 19. The tests were repeated without incremental measurements to confirm the results.

The reference material performed as expected. Machining at $v_c =$ 200 m/min led to a progressive increase in flank wear, until 630 m into the cut when the edge started to collapse, leading to a jump in the flank wear. This was more pronounced at higher speeds. Cutting at v_c =250 m/min led to such a jump at 518 m, and at around 350 m for v_c =300 and 400 m/min. The higher speeds contributed to an unpredictable performance because the edge breakage is not as predictable as the progressive flank wear.

The Al-alloyed material (Alloy I) had more than three times better tool life than the reference material. In contrast, Alloy II, containing Al, Ti, V, and Nb, had worse tool life at speeds 200–250 m/min but equal or slightly better at speeds 300–350 m/min with respect to the reference material. KT was also always less compared to the reference at comparable amounts of flank wear and cutting length (Fig. 19).

The wear progressed differently between the reference material and the two alloys (Fig. 20). The reference material had a large and deep crater, which led to a collapse of the cutting edge and the aforementioned unpredictable increase in flank wear. Alloy I had a small and shallow crater that did not lead to edge collapse and instead exhibited a slow progression of flank wear. Alloy II had a smaller crater that did not lead to an edge collapse, but the carbides in its microstructure led to aggressive flank wear. Hence the carbides present in Alloy II were few enough that they did not affect the functional properties of the material, but they did lead to aggressive abrasive wear even with suppressed crater wear. Again, showing how alloying affects the machinability and end-user properties very differently. These different modes of wear can be seen in Fig. 20, the flank of the Reference material is marked by a continuous collapse of the edge with a large crater. Alloy I have a small crater and limited flank wear. Alloy II has less crater wear than the Reference but clear abrasive marks on the flank.

VLM showed how the wear pattern of the flank and rake differed. SEM images at high accelerating voltage (HV), which led to a large

Table 5
Measured mean composition at% using OES and hardness using a Vickers hardness indenter.

	HV2	Fe	Mn	C	Si	Cr	Al	Ti	Nb	V	P	S
Reference	195	bal	14.00	5.05	0.89	1.22	0.02	0.06	0.009	0.026	0.088	<0.0017
Alloy I	206	bal	13.91	4.91	0.89	1.22	0.30	0.06	0.009	0.027	0.089	<0.0017
Alloy II	209	bal	13.99	4.81	1.66	1.39	0.28	0.24	0.131	0.042	0.092	<0.0017

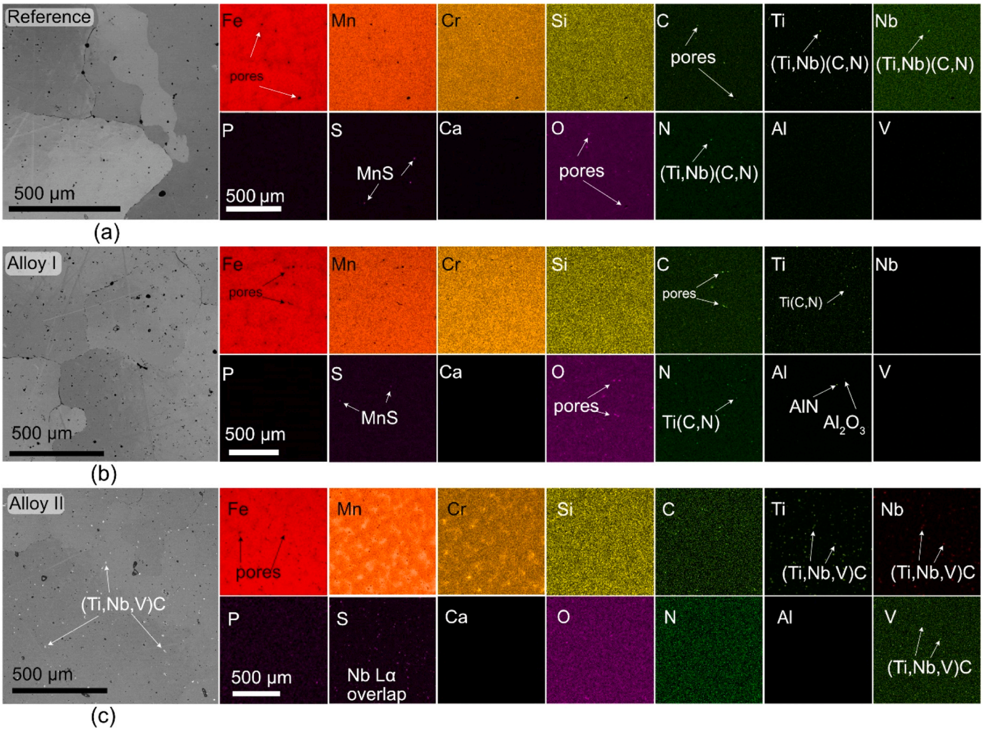

Fig. 16. Casted samples, (a) Reference, (b) Alloy I / Al-alloyed, (c) Alloy II / Al, Ti, Nb, and V alloyed. BSE-SEM and XEDS-maps. The materials contain some pores and very few carbides and sulfates, except Alloy II which resulted in the expected amount of (Ti,Nb,V)C seen as dots in SEM and XEDS images of Alloy II.

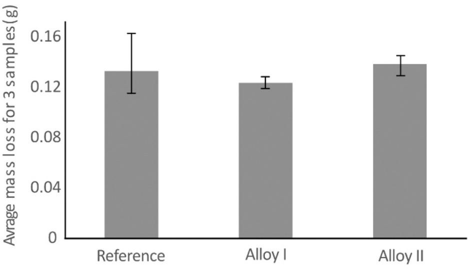

Fig. 17. . Results from the abrasion tests. Alloy I performed slightly better than the Reference and Alloy II slightly worse. Experiments repeated three times, bars indicate average result, whiskers indicate maximum and minimum values.

interaction volume, did not reveal much difference between the chemistries on the tool surfaces used to cut the different alloys.

Lowering the accelerating voltage HV to <8 keV in the SEM and studying the rake revealed that the tools were covered by a thin film approximately hundreds of nanometers (SE-SEM images Fig. 22). The BSE-SEM and XEDS spectrums further revealed a crucial difference between the reference material and the alloys. Dark cBN grains were visible in the BSE image for the tool used to machine the Reference material, but the cBN grains were covered with an oxide film for Alloys I and II (Fig. 22). The only Al oxides present on the tools that cut the reference material were oxidized AlN and AlB_x binder. Seen in XEDS spectrum i) for the Reference material in Fig. 22. The cBN-grains of the tool that was used to machine the material with additional Al (Alloy I) were fully or partially covered by an Al oxide film. Seen in XEDS spectrum i) for Alloy II Fig. 22. Alloy II was also covered by this Al oxide film, but there were carbides scattered across the rake, and oxidized Fe (adhered and oxidized steel) was also present. The thin alumina film was similar to the films studied for TPL formation when machining nickel alloys and stainless steel [7,14].

The film is a couple of hundreds of nanometers thick which makes it difficult to study using SEM. A TEM lamella was extracted from the rake of the tool used to machine Alloy I at v_c =300 m/min for 900 m. Which was a representative case of the thin film on top of a cBN gain in Fig. 23. The Pt was to protect the surface during FIB lift off. The combination of XEDS, SAED, and STEM revealed that 100–200 nm thin film (TPL) was most likely corundum/α-Al_2O_3. The other polymorphs of Al_xO_y were missing major reflections and did not have any reflection at the location of the 116 reflections. Other possible phases that could possibly have similar SAED patterns did not agree with the XEDS spectrum from the layer. Hence the film covering the tool is the Al_2O_3 TPL predicted to lead to increased tool wear by the thermodynamic calculations summarized in Table 4.

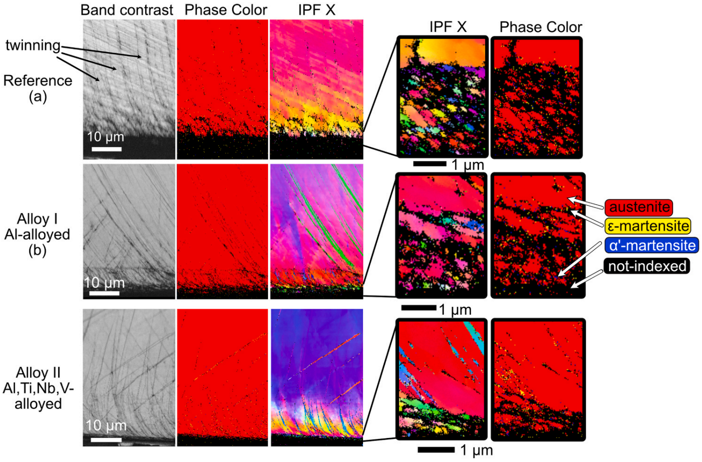

Fig. 18. All three alloys work harden by TWIP and TRIP after abrasion tests. EBSD images and maps. All alloys show twinning and formation of ε-martensite, and some α'-martensite. The grains are also very small and highly strained and indexing of grains becomes increasingly difficult 5 μm from the edge of the worn pin, resulting in the black area.

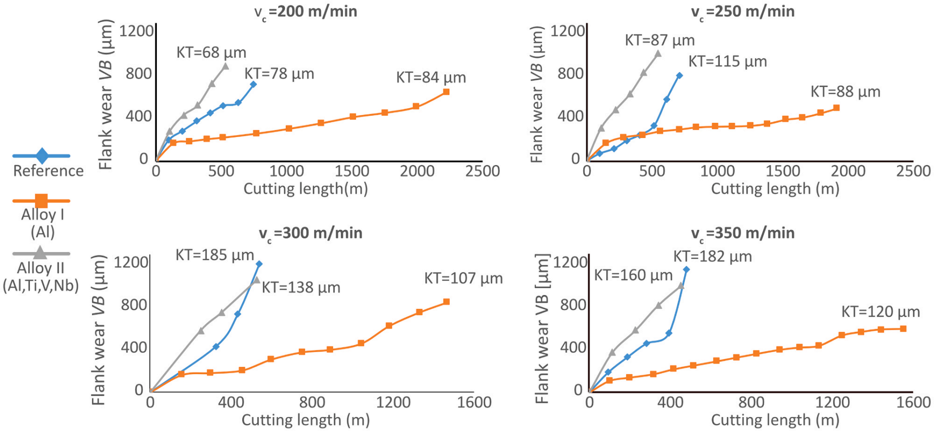

Fig. 19. Flank and crater wear results from machining tests. The performance of Alloy I is threefold with respect to the Reference. Alloy II performed worse than the reference at speeds of 200 and 250 m/min but equal or better at 300 and 350 m/min. However, Alloy II had less crater wear than the Reference at all speeds.

5. Conclusion

Alloying a workpiece material to improve its machinability often comes at the expense of other material properties. However, small amounts of alloying may not affect the end user properties of the workpiece, but can have large effects on machinability due to the cutting tool meeting kilometers of workpiece material during machining. This new method is validated for manganese steel. It avoids the negative effects of machinability improvement due designed alloying and correct pairing of the tool material and cutting conditions, with workpiece alloying to form a tool protection layer composed of refractory and wear resistant reaction products.

The thermodynamic calculations showed that alloying the reference material (Hadfield steel) with at most 0.015 mol fractions of aluminum was the most promising, alloying with 0.0055 mol fractions or less of V, Ti, and Nb also showed promise. The calculations were also evaluated by comparison with diffusion couple experiments. One reference and two new alloys based on the calculations were then cast for validation by abrasion and machining test as well as metallographic investigation. The alloy with 0.003 mol fractions of Al resulted in more than 3 times increase in machining performance which is related to the in-operando formation of Al_2O_3 tool protection layer on the contact surfaces of PcBN tool. The alloy with Al, Nb, V, and Ti resulted in more predictable tool wear but not an overall performance improvement. The two alloys

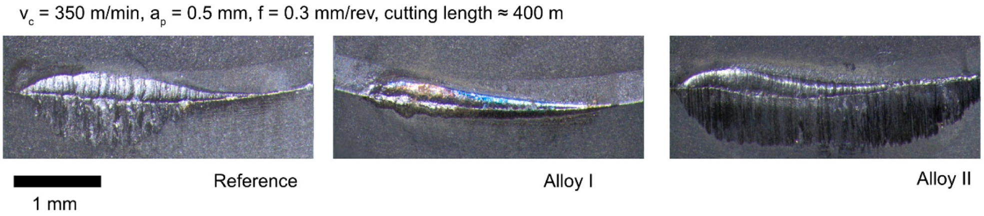

Fig. 20. Comparison between the tool wear during cutting of the different alloys. A Representative overview using VLM images of the tools showing the larger and deeper craters of the Reference (chemical, oxidational and diffusional wear), the more aggressive flank wear of Alloy II (increase in abrasive wear due to carbides), and the limited wear of Alloy I after equal machining (potentially in-operando TPL formation).

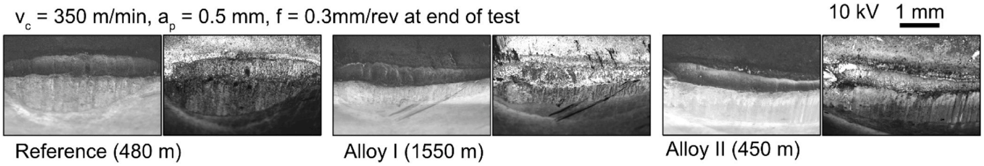

Fig. 21. Comparison between the tool wear during cutting of the different alloys using SEM. SE-SEM and BSE-SEM of tool rakes and flanks at the end of tool life for the tools used to cut the three materials.

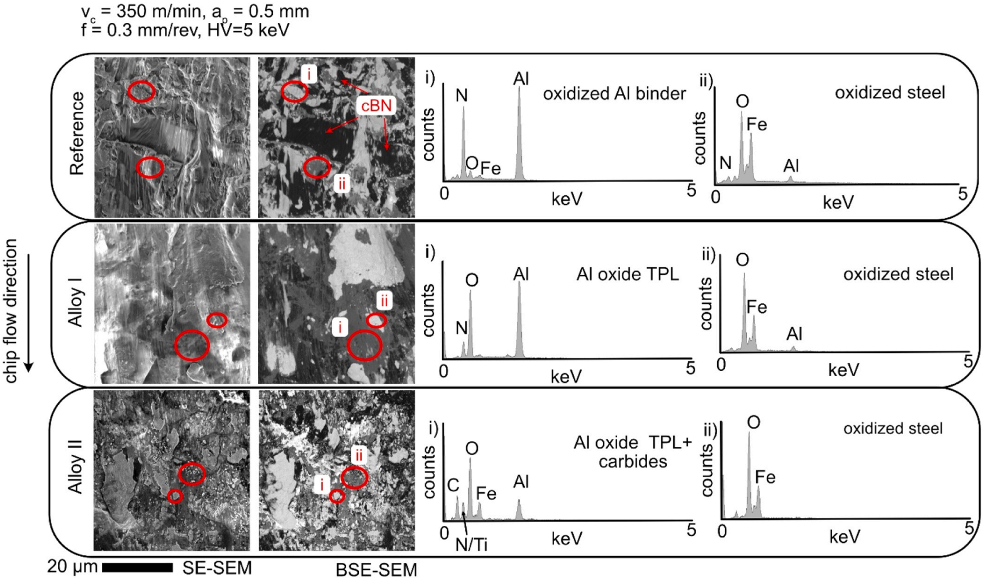

Fig. 22. Center of the crater at the end of machining at 350 m/min from Fig. 21. SEM and XEDS at low accelerating voltages (HV). The crater of the reference material is only covered with iron oxide some oxidized Al binder is also measured, but no Al-oxide film can be found. Alloy I is covered by a thin film of Al-oxide and areas of Fe-oxide. Alloy II is covered with Al-oxides, but some carbides can be found in the layer.

retained their functional properties with respect to abrasive wear resistance and retained their ability to work harden by TWIP and TRIP mechanisms.

This study shows that it is possible to intentionally alloy a workpiece paired with a tool material to form a tool protection layer, thereby increasing the tool life without degrading the workpiece properties. This study also shows that the experimental testing required to do so can be reduced or avoided by employing the proposed thermodynamic

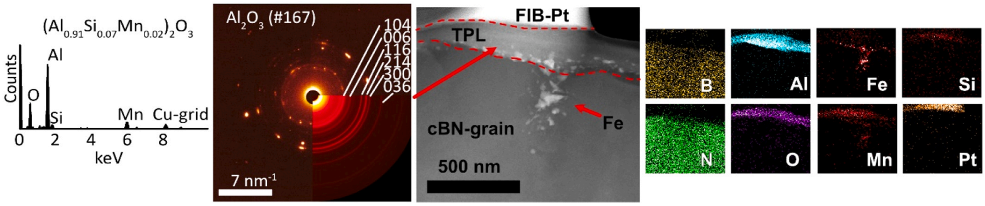

Fig. 23. The thin Al-oxide in Fig. 22 is α-Al_2O_3 TPL formed in-operando on tools when machining Alloy I. STEM-XEDS and SAED from same region, with STEM image and STEM-XEDS maps. The Si and Mn could be noise or part of the Al_2O_3. The Cu signal is from the holder and grid. The layer is 100–200 nm thick on top of a cBN grain, explaining the difficulty of measuring with SEM.

modeling method and modelling framework. The method presented is limited to decrease the effect wear mechanisms initiated or driven by diffusion, oxidation, and chemical degradation, but not conceptually limited to certain tools, materials and cutting conditions. It is validated for turning of manganese steel with PcBN tools in this work. Hence, assessing the method and applying it to other machining conditions, workpieces, and tools is of future interest. The efficiency, accuracy and ease of use of this method will likely improve as material and metal cutting models improve with time. This establishes a new route for machinability improvement, which does not have to lead to a degradation of the functional properties of a workpiece.

CRediT authorship contribution statement

Susanne Norgren: Writing – review & editing, Validation, Supervision, Software, Resources, Methodology, Investigation, Funding acquisition, Formal analysis, Conceptualization. **Axel Bjerke:** Writing – review & editing, Writing – original draft, Visualization, Validation, Software, Resources, Project administration, Methodology, Investigation, Formal analysis, Data curation, Conceptualization. **Andreas Markström:** Writing – review & editing, Validation, Supervision, Software, Resources, Methodology, Investigation, Formal analysis, Data curation, Conceptualization. **Henrik Larsson:** Writing – review & editing, Validation, Supervision, Software, Methodology, Investigation, Formal analysis, Conceptualization. **Rachid M'Saoubi:** Writing – review & editing, Supervision, Resources, Methodology, Investigation, Funding acquisition, Formal analysis, Conceptualization. **Filip Lenrick:** Writing – review & editing, Visualization, Validation, Supervision, Resources, Methodology, Investigation, Funding acquisition, Formal analysis, Data curation, Conceptualization. **Latifa Melk:** Supervision, Resources, Investigation, Conceptualization. **Jörgen Petersson:** Validation, Supervision, Resources, Methodology, Investigation, Formal analysis, Conceptualization. **Volodymyr Bushlya:** Writing – review & editing, Visualization, Validation, Supervision, Resources, Project administration, Methodology, Investigation, Funding acquisition, Formal analysis, Data curation, Conceptualization.

Declaration of Competing Interest

The authors declare that they have no known competing financial interests or personal relationships that could have appeared to influence the work reported in this paper.

Acknowledgements

This work was funded by the national strategic innovation program: National action for metallic materials, organized by Vinnova and Jernkontoret (Sweden) under DEMO project (ID 2017–02915). The acknowledgment also extends to Igor Petrusha at the V. Bakul Institute for Superhard Materials of the National Academy of Sciences of Ukraine, Kyiv, Ukraine for conducting the diffusion couple experiments and to Mikael Hörndahl and Ryszard Wierzbicki both at the Division of Production and Materials Engineering, Lund University for great ideas and help through the project.

References

[1] E.M. Trent, P.K. Wright, Metal Cutting Fourth Edition, 2000.

[2] J.-E. Ståhl, Seco Tools AB, Metal Cutting: Theories and Models, Seco Tools AB, 2012.

[3] Ånmark, N., Karasev, A., Jönsson, P., 2015. The effect of different non-metallic inclusions on the machinability of steels. Materials 8, 751–783. https://doi.org/10.3390/ma8020751.

[4] Bhadeshia, H.K.D.H., 2012. Steels for bearings. Prog. Mater. Sci. 57, 268–435. https://doi.org/10.1016/j.pmatsci.2011.06.002.

[5] Zellagui, R., Hemmouche, L., Bouchafaa, H., Belrechid, R., Aitsadi, H., Chelli, A., Touil, M., Djalleb, N., 2022. Effect of heat treatments on the microstructure, mechanical, wear and corrosion resistance of casted hadfield steel. Int. J. Met. 16, 2050–2064. https://doi.org/10.1007/s40962-021-00751-z.

[6] Bushlya, V., Lenrick, F., Ståhl, J.-E., M'Saoubi, R., 2018. Influence of oxygen on the tool wear in machining. CIRP Ann. 67, 79–82. https://doi.org/10.1016/j.cirp.2018.03.011.

[7] Bjerke, A., Hrechuk, A., Lenrick, F., Markström, A., Larsson, H., Norgren, S., M'Saoubi, R., Björk, T., Bushlya, V., 2021. Thermodynamic modeling framework for prediction of tool wear and tool protection phenomena in machining. Wear 484–485, 203991. https://doi.org/10.1016/j.wear.2021.203991.

[8] J.-E. Ståhl, Requirements and potential for high performance cutting tools based on superhard phases in new applications, in: De Beers Diamond Conference hosted by Warwick University, UK, 2016.

[9] Kümmel, J., Gibmeier, J., Müller, E., Schneider, R., Schulze, V., Wanner, A., 2014. Detailed analysis of microstructure of intentionally formed built-up edges for improving wear behaviour in dry metal cutting process of steel. Wear 311, 21–30. https://doi.org/10.1016/j.wear.2013.12.012.

[10] Nguyen, D., Tooptong, S., Park, K.-H., Kwon, P., 2020. Formation mechanism of alumina layer in protecting cubic boron nitride inserts in turning cast irons. Int. J. Mach. Tools Manuf. 153, 103539 https://doi.org/10.1016/j.ijmachtools.2020.103539.

[11] Tanaka, R., Yamane, Y., Sekiya, K., Narutaki, N., Shiraga, T., 2007. Machinability of BN free-machining steel in turning. Int. J. Mach. Tools Manuf. 47, 1971–1977. https://doi.org/10.1016/j.ijmachtools.2007.02.003.

[12] Bushlya, V., Johansson, D., Lenrick, F., Ståhl, J.-E., Schultheiss, F., 2017. Wear mechanisms of uncoated and coated cemented carbide tools in machining lead-free silicon brass. Wear 376–377, 143–151. https://doi.org/10.1016/j.wear.2017.01.039.

[13] Olsson, M., Lenrick, F., M'Saoubi, R., Larsson, H., Markström, A., Petrusha, I., Ståhl, J.-E., Bushlya, V., 2020. Study of wear mechanisms of cemented carbide tools during machining of single-phase niobium. Wear 450–451, 203244. https://doi.org/10.1016/j.wear.2020.203244.

[14] Bushlya, V., Lenrick, F., Bjerke, A., Aboulfadl, H., Thuvander, M., Ståhl, J.-E., M'Saoubi, R., 2021. Tool wear mechanisms of PcBN in machining Inconel 718: analysis across multiple length scale. CIRP Ann. 70, 73–78. https://doi.org/10.1016/j.cirp.2021.04.008.

[15] Bushlya, V., Bjerke, A., Turkevich, V.Z.Z., Lenrick, F., Petrusha, I.A.A., Cherednichenko, K.A.A., Ståhl, J.-E.E., 2019. On chemical and diffusional interactions between PCBN and superalloy Inconel 718: imitational experiments. J. Eur. Ceram. Soc. 39, 2658–2665. https://doi.org/10.1016/j.jeurceramsoc.2019.03.002.

[16] Lindvall, R., Lenrick, F., Persson, H., M'Saoubi, R., Ståhl, J.-E., Bushlya, V., 2020. Performance and wear mechanisms of PCD and pcBN cutting tools during machining titanium alloy Ti6Al4V. Wear 454–455, 203329. https://doi.org/10.1016/j.wear.2020.203329.

[17] Lindvall, R., Bjerke, A., Salmasi, A., Lenrick, F., M'Saoubi, R., Ståhl, J.-E.E., Bushlya, V., M'Saoubi, R., Ståhl, J.-E.E., Bushlya, V., 2023. Predicting wear mechanisms of ultra-hard tooling in machining Ti6Al4V by diffusion couples and simulation. J. Eur. Ceram. Soc. 43, 291–303. https://doi.org/10.1016/j.jeurceramsoc.2022.10.005.

[18] Odelros, S., Kaplan, B., Kritikos, M., Johansson, M., Norgren, S., 2017. Experimental and theoretical study of the microscopic crater wear mechanism in titanium machining. Wear 376–377, 115–124. https://doi.org/10.1016/j.wear.2017.01.104.

[19] Graves, A., Salmasi, A., Graham, S.J., Wan, W., Xiao, C., Jackson, M., Larsson, H., Norgren, S., 2023. An experimental and theoretical investigation on Ti-5553/WC–Co(6%) chemical interactions during machining and in diffusion couples. Wear 516–517, 204604. https://doi.org/10.1016/j.wear.2022.204604.

[20] Persson, H., Bushlya, V., Franca, L., Zhou, J., Ståhl, J.-E., Lenrick, F., 2022. Performance and wear mechanisms of different PcBN tools when machining superalloy AD730. Ceram. Int. 48, 22733–22742. https://doi.org/10.1016/j.ceramint.2022.04.042.

[21] Aiso, T., Wiklund, U., Kubota, M., Jacobson, S., 2016. Effect of Si and Al additions to carbon steel on material transfer and coating damage mechanism in turning with CVD coated tools. Wear 368–369, 379–389. https://doi.org/10.1016/j.wear.2016.10.011.

[22] Aiso, T., Matsumura, T., 2022. Effect of Si and Al additions to steel on machinability in gear cutting. ISIJ Int. 62, 1957–1966. https://doi.org/10.2355/isijinternational.ISIJINT-2022-145.

[23] Malakizadi, A., Shi, B., Hoier, P., Attia, H., Krajnik, P., 2020. Physics-based approach for predicting dissolution-diffusion tool wear in machining. CIRP Ann. 69, 81–84. https://doi.org/10.1016/j.cirp.2020.04.040.

[24] Ånmark, N., Björk, T., Ganea, A., Ölund, P., Hogmark, S., Karasev, A., Jönsson, P. G., 2015. The effect of inclusion composition on tool wear in hard part turning using PCBN cutting tools. Wear 334–335, 13–22. https://doi.org/10.1016/j.wear.2015.04.008.

[25] Ge, S., Wang, Q., Wang, J., 2017. The impact wear-resistance enhancement mechanism of medium manganese steel and its applications in mining machines. Wear 376–377, 1097–1104 https://doi.org/https://doi.org/10.1016/j.wear.2017.01.015.

[26] Galindo-Nava, E.I., Rivera-Díaz-del-Castillo, P.E.J., 2017. Understanding martensite and twin formation in austenitic steels: a model describing TRIP and TWIP effects. Acta Mater. 128, 120–134. https://doi.org/10.1016/j.actamat.2017.02.004.

[27] Kopac, J., 2001. Hardening phenomena of Mn-austenite steels in the cutting process. J. Mater. Process. Technol. 109, 96–104. https://doi.org/10.1016/S0924-0136(00)00781-0.

[28] Horng, J.-T., Liu, N.-M., Chiang, K.-T., 2008. Investigating the machinability evaluation of Hadfield steel in the hard turning with Al2O3/TiC mixed ceramic tool based on the response surface methodology. J. Mater. Process. Technol. 208, 532–541. https://doi.org/10.1016/j.jmatprotec.2008.01.018.

[29] Giménez, S., Van der Biest, O., Vleugels, J., 2007. The role of chemical wear in machining iron based materials by PCD and PCBN super-hard tool materials. Diam. Relat. Mater. 16, 435–445. https://doi.org/10.1016/j.diamond.2006.08.017.

[30] McKie, A., Winzer, J., Sigalas, I., Herrmann, M., Weiler, L., Rödel, J., Can, N., 2011. Mechanical properties of cBN–Al composite materials. Ceram. Int. 37, 1–8. https://doi.org/10.1016/j.ceramint.2010.07.034.

[31] Windmark, C., Lattanzi, L., Månberger, A., Jarfors, A.E.W., 2022. Investigation on resource-efficient aluminium recycling – a state of the art review. : Adv. Transdiscipl. Eng. 15–27. https://doi.org/10.3233/ATDE220122.

[32] Gutnichenko, O., Bushlya, V., Zhou, J., Ståhl, J.E., 2017. Tool wear and machining dynamics when turning high chromium white cast iron with pcBN tools. Wear. https://doi.org/10.1016/j.wear.2017.08.005.

[33] Chen, Q., Wu, K., Sterner, G., Mason, P., 2014. Modeling precipitation kinetics during heat treatment with calphad-based tools. J. Mater. Eng. Perform. 23, 4193–4196. https://doi.org/10.1007/s11665-014-1255-6.

[34] Schramm, R.E., Reed, R.P., 1975. Stacking fault energies of seven commercial austenitic stainless steels. Metall. Trans. A. 6, 1345–1351. https://doi.org/10.1007/BF02641927.

[35] Choi, Y.W., Dong, Z., Li, W., Schönecker, S., Kim, H., Kwon, S.K., Vitos, L., 2020. Predicting the stacking fault energy of austenitic Fe-Mn-Al (Si) alloys. Mater. Des. 187, 108392 https://doi.org/10.1016/j.matdes.2019.108392.

[36] Olson, G.B., Cohen, M., 1976. A general mechanism of martensitic nucleation: Part I. General concepts and the FCC → HCP transformation. Metall. Trans. A. 7, 1897–1904. https://doi.org/10.1007/BF02659822.

[37] Hirth, J.P., 1970. Thermodynamics of stacking faults, Metall. Mater. Trans. B. 1, 2367. https://doi.org/10.1007/BF03038365.

[38] Allain, S., Chateau, J.-P., Bouaziz, O., Migot, S., Guelton, N., 2004. Correlations between the calculated stacking fault energy and the plasticity mechanisms in Fe–Mn–C alloys. Mater. Sci. Eng. A. 387–389, 158–162. https://doi.org/10.1016/j.msea.2004.01.059.

[39] Park, K.T., Jin, K.G., Han, S.H., Hwang, S.W., Choi, K., Lee, C.S., 2010. Stacking fault energy and plastic deformation of fully austenitic high manganese steels: Effect of Al addition. Mater. Sci. Eng. A. 527, 3651–3661. https://doi.org/10.1016/j.msea.2010.02.058.

[40] Bjerke, A., Lenrick, F., Norgren, S., Larsson, H., Markström, A., M`Saoubi, R., Petrusha, I., Bushlya, V., 2022. Understanding wear and interaction between CVD α-Al2O3 coated tools, steel, and non-metallic inclusions in machining. Surf. Coat. Technol. 450, 128997 https://doi.org/10.1016/j.surfcoat.2022.128997.

[41] Andersson, J.-O., Helander, T., Höglund, L., Shi, P., Sundman, B., 2002. Thermo-Calc & DICTRA, computational tools for materials science. Calphad 26, 273–312. https://doi.org/10.1016/S0364-5916(02)00037-8.

[42] Hillert, M., 2001. The compound energy formalism. J. Alloy. Compd. 320, 161–176. https://doi.org/10.1016/S0925-8388(00)01481-X.

[43] Bejjani, R., Collin, M., Thersleff, T., Odelros, S., 2016. Multi-scale study of initial tool wear on textured alumina coating, and the effect of inclusions in low-alloyed steel. Tribol. Int. 100, 204–212. https://doi.org/10.1016/j.triboint.2016.01.021.

[44] Rémy, L., Pineau, A., 1976. Twinning and strain-induced f.c.c. → h.c.p. transformation on the mechanical properties of Co-Ni-Cr-Mo alloys. Mater. Sci. Eng. 26, 123–132. https://doi.org/10.1016/0025-5416(76)90234-2.

[45] Chu, C.M., Huang, H., Kao, P.W., Gan, D., 1994. Effect of alloying chemistry on the lattice constant of austenitic Fe-Mn-Al-C alloys. Scr. Metall. Mater. 30, 505–508. https://doi.org/10.1016/0956-716X(94)90611-4.

[46] Babu, S.S., Specht, E.D., David, S.A., Karapetrova, E., Zschack, P., Peet, M., Bhadeshia, H.K.D.H., 2005. In-situ observations of lattice parameter fluctuations in austenite and transformation to bainite. Metall. Mater. Trans. A. 36, 3281–3289. https://doi.org/10.1007/s11661-005-0002-x.

[47] Ferreira, P.J., Müllner, P., 1998. A thermodynamic model for the stacking-fault energy. Acta Mater. 46, 4479–4484. https://doi.org/10.1016/S1359-6454(98)00155-4.

[48] Cotes, S.M., Guillermet, A.Fernández, Sade, M., 2004. Fcc/Hcp Martensitic Transformation in the Fe-Mn System: Part II. Driving Force and Thermodynamics of the Nucleation Process. Metall. Mater. Trans. A Phys. Metall. Mater. Sci. 35 A, 83–91. https://doi.org/10.1007/s11661-004-0111-y.

[49] Angseryd, J., From, A., Wallin, J., Jacobson, S., Norgren, S., 2013. On a wear test for rock drill inserts. Wear 301, 109–115. https://doi.org/10.1016/j.wear.2012.10.023.

[50] Johansson, D., Hrechuk, A., Bushlya, V., Mårtensson, M., Can, A., Ståhl, J.-E., 2019. Small scale testing of PCD and WC-Co tooling in rock cutting using longitudinal turning. Wear 426–427, 1515–1522. https://doi.org/10.1016/j.wear.2018.11.036.

[51] Vitos, L., Nilsson, J.-O., Johansson, B., 2006. Alloying effects on the stacking fault energy in austenitic stainless steels from first-principles theory. Acta Mater. 54, 3821–3826. https://doi.org/10.1016/j.actamat.2006.04.013.

[52] Banerjee, M.K., 2017. In: Hashmi, M.S.J.B.T.-C.M.F. (Ed.), 2.8 Heat Treatment of Commercial Steels for Engineering Applications. Elsevier, Oxford, pp. 180–213. https://doi.org/10.1016/B978-0-12-803581-8.09190-6.

[53] Kim, J., Lee, S.-J., De Cooman, B.C., 2011. Effect of Al on the stacking fault energy of Fe–18Mn–0.6C twinning-induced plasticity. Scr. Mater. 65, 363–366. https://doi.org/10.1016/j.scriptamat.2011.05.014.

[54] S.V. Zhytnov, N.G. Davydov, S.G. Bratchikov, High manganese steels, in: Metalurgia publishing, Moscow, 1995: pp. 161–223.

[55] Özkan, İ., Dokumacı, E., Önay, A.B., 2018. Cyclic oxidation behavior of c-BN and h-BN at elevated temperatures. Acta Phys. Pol. A. 134, 61–63 https://doi.org/10.12693/APhysPolA.134.61.

[56] Angseryd, J., Andrén, H.-O., 2011. An in-depth investigation of the cutting speed impact on the degraded microstructure of worn PCBN cutting tools. Wear 271, 2610–2618. https://doi.org/10.1016/j.wear.2010.11.059.

[57] G.E. Spriggs, 13.5 Properties of diamond and cubic boron nitride, in: P. Beiss, R. Ruthardt, H. Warlimont (Eds.), Powder Metall. Data. Refract. Hard Intermet. Mater., Springer-Verlag, Berlin/Heidelberg, n.d.: pp. 118–139. https://doi.org/10.1007/10858641_7.

[58] Johansson, D., Hägglund, S., Bushlya, V., Ståhl, J.-E., 2017. Assessment of commonly used tool life models in metal cutting. Procedia Manuf. 11, 602–609. https://doi.org/10.1016/j.promfg.2017.07.154.

[59] Larsson, H., Höglund, L., 2009. Multiphase diffusion simulations in 1D using the DICTRA homogenization model. Calphad 33, 495–501. https://doi.org/10.1016/j.calphad.2009.06.004.

[60] Bjerke, A., Hrechuk, A., Lenrick, F., M`Saoubi, R., Larsson, H., Markström, A., Björk, T., Norgren, S., Ståhl, J.-E., Bushlya, V., 2021. Onset of the degradation of CVD α-Al2O3 coating during turning of Ca-treated steels. Wear, 203785. https://doi.org/10.1016/j.wear.2021.203785.

[61] Prostakova, V., Shishin, D., Shevchenko, M., Jak, E., 2019. Thermodynamic optimization of the Al2O3–FeO–Fe2O3–SiO2 oxide system. Calphad 67, 101680. https://doi.org/10.1016/j.calphad.2019.101680.

[62] M.C. Shaw, J.O. Cookson, Metal cutting principles (Vol. 2), 2005.